Optimization of Aperture Coupled Microstrip Patch Antennas

M. Dogan[1, 2], **G. K. Sendur**[2], **and F. Ustuner**[1]

[1]TUBITAK-UEKAE, Kocaeli, Turkey
[2]Sabanci University, Istanbul, Turkey

Abstract— Aperture coupled microstrip patch antennas (ACMPA) are special class of microstrip antennas with high gain and wide impedance bandwidth. These antennas differ from other microstrip antennas with their feeding structure of the radiating patch element. Input signal couples to the radiating patch through the aperture that exists on the ground plane of the microstrip feedline. These special antennas are multilayer stacked type of antennas with so many design variables that will affect the antenna performance. This paper presents the design and optimization procedure of ACMPA while taking care of all possible design variables and parameters to get the highest possible antenna gain and minimum VSWR.

1. INTRODUCTION

Microstrip antennas (MSA) are one of the most popular antenna types which were first produced by Deschamps [1]. Because of their low profile and conformal structure, they have been widely used in wireless, aerospace, vehicular and other areas where large antennas are not practical to use. Among several advantages in application, MSAs suffers from major drawbacks such as low gain and narrow impedance bandwidth. In 80s, Pozar [2, 3] invented the multilayer configuration which was named Aperture Coupled Microstrip Patch Antenna. This new microstrip antenna demonstrates improvement on the impedance bandwidth from 5% to 50% and 4–5 dBi gain enhancement. Due to their structural complexity, it is challenging job to get the expected gain and bandwidth improvements. Therefore a well planned optimization process needs to be performed to get the highest possible antenna gain while having minimum VSWR at the antenna input terminal.

A powerful optimizer is implemented with MATLAB optimization toolbox which runs HFSS and collects data via HFSS Script. In this paper, the optimization process is presented step by step from the initial settings of design parameters; variables, bounds on variables, constraint and objectives, to the final optimized results.

2. ANTENNA OPTIMIZATION SETUP

The optimization is performed for designing the ACMPA with highest possible gain and minimum VSWR, while keeping the gain above some lower limit (8 dBi), VSWR below the upper limit (1.5) without exceeding the maximum allowed antenna dimensions (10 cm × 10 cm × 2.5 cm).

Next step in optimization is separating the design parameters which are always constant during the optimization from the design variables that are going to be changed. There are several design parameters and variables of double layer ACMPA as shown in Figure 1. There are several factors that affect the performance of ACMPA such as length of tuning stub, patch dimensions, aperture length and width, relative location of the aperture w.r.t to the patch, shape of coupling aperture, antenna substrate properties, height of each stacked layers from the ground plane, reflector height, thickness of the metal layers on the dielectric materials. The more the number of variables, the slower the optimization process. Thus, we need to decrease the number of variables and set some variables constant and accept them as parameters.

In our ACMPA example, ROGERS 4003C is used as a dielectric material, so the relative dielectric permittivity ε_r (3.38), substrate height (0.81 mm), metal layer thickness (17 μm), tangential loss (0.0027) are all constant. Preliminary simulation demonstrates that reflector height should be around 8 mm, and the radiating patch needs to be placed 13.2 mm above the aperture plane. Impedance of the microstrip feedline should be 50-Ω, so the feedline width (1.78 mm) is constant. Effect of aperture width is negligible and it is fixed at 2 mm.

There are four geometric variables which are highly effective on antenna performance after setting up the optimization parameters. The stub length (L_s) is used to tune the excess reactance of the aperture coupled antenna. Antenna performance is very sensitive to the variations of stub length. The radiating patch length (L_p) determines the resonant frequency of the antenna and the width (W_p) affects the resonant resistance of the antenna. The wider patch results the lower resonant resistance. The aperture length (L_a) mainly determines the coupling level of the input

signal to the radiating patch, so it has direct effect on the resonant resistance. As L_a increases, coupling of the input signal increases and as a result the resonant frequency increases. Upper bounds for all those variables come from the size of the surrounding metal cavity.

Constraints of the optimization and the main objective should be clearly defined before starting the optimization. According to the formal definition of the optimization problem, we need to maximize gain and minimize VSWR while the gain is above 8 dBi (1) and VSWR is below 1.5 (2). Multi-objective design is little bit tricky. The antenna gain is simply related with the patch area however VSWR depends on all four parameters, therefore we keep minimum VSWR as the only objective of the optimization (3). In (1), (2) and (3); $\vec{x}$ is the vector includes variables, $\vec{p}$ is parameter vector, f_i simulation frequencies and λ_i is the weighting coefficient.

$$-\text{Gain}\,(\vec{x},\,\vec{p},\,f_i) + 8.0 \le 0 \ \forall f_i \ \text{ such that } 2.2\,\text{GHz} \le f_i \le 2.4\,\text{GHz} \tag{1}$$

$$\text{VSWR}\,(\vec{x},\,\vec{p},\,f_i) - 1.5 \le 0 \ \forall f_i \ \text{ such that } 2.2\,\text{GHz} \le f_i \le 2.4\,\text{GHz} \tag{2}$$

$$\min\{J\,(\vec{x},\,\vec{p})\} = \min\left\{\sum\nolimits_{i=1}^{i=9} \lambda_i \,(\text{VSWR}\,(\vec{x},\,\vec{p},\,f_i) - 1)^2\right\} \ \text{ where } \sum\nolimits_i \lambda_i = 1 \tag{3}$$

Here, antenna optimization is done with MATLAB optimization toolbox instead of using other commercial EM Design tools. MATLAB runs the HFSS via scripts, takes the output data (VSWR, Gain) from the HFSS, processes them according to the formulas which are based on gradient based optimization, checks whether any constraint violation and finishes the optimization after couple of iterations and function evaluations. The advantage of this method is that during optimization,
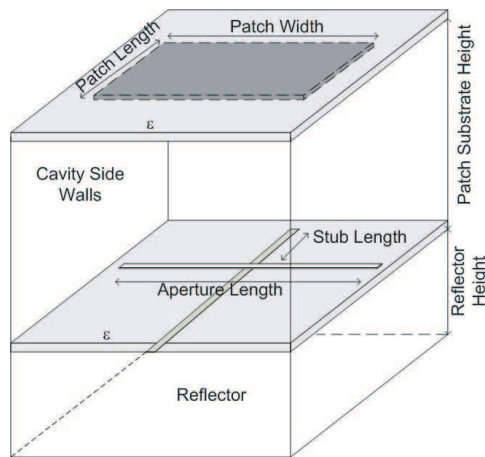

Figure 1: Double layer aperture coupled microstrip patch antenna embedded in a metal cavity.
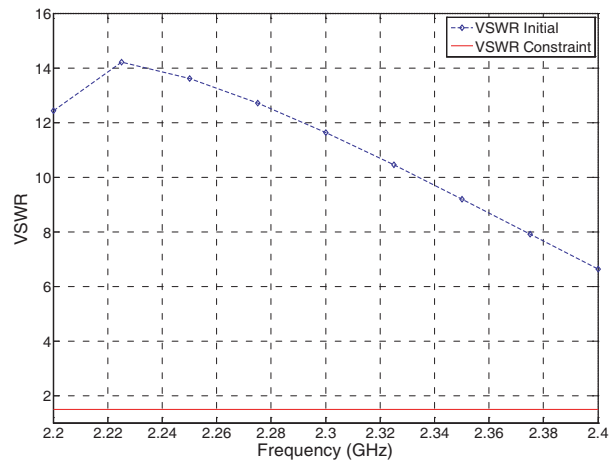

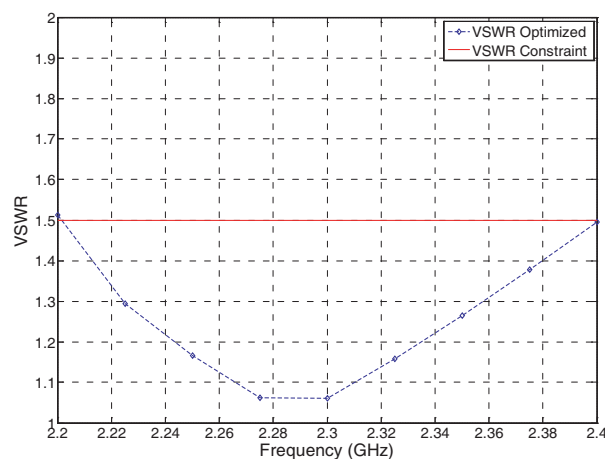Figure 2: VSWR before optimization (1st trial).
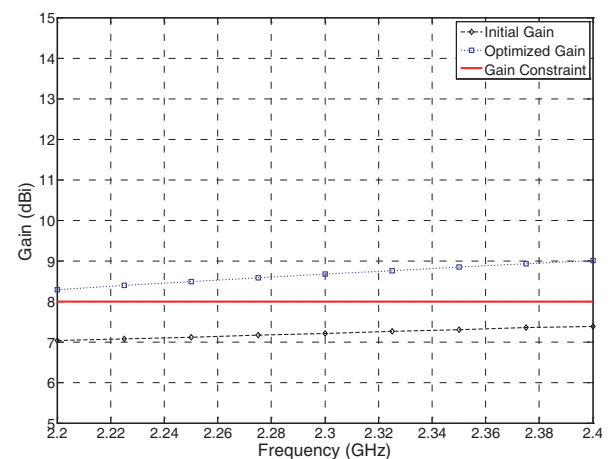

Figure 3: VSWR after optimization (1st trial).

Figure 4: Antenna gain before and after the optimization (1st trial).

designer will able to see and control the optimization process. Additionally, MATLAB did not stop until user defined criteria are met which is not the case in other EM Design Tools.

3. OPTIMIZATION RESULT

Performance of the optimization is directly affected by the weighting coefficients. Initially, weighting coefficient at 2.3 GHz was maximum and gradually decreases as going to 2.2 and 2.4 GHz. This configuration worked pretty well in the neighborhood of the center frequency but VSWR exceeds 1.5 around the corner frequencies. Then all coefficients are equally weighted and the results get better.

In the first optimization trial, the lower and upper bounds of the design variables are relatively close. For instance, the lower bound of design variables is $\vec{x}_{lb} : [L_s \ L_a \ L_p \ W_p] = [1 \ 2 \ 2 \ 2]$ and upper bound is $\vec{x}_{ub} = [45 \ 90 \ 90 \ 90]$. The initial design vector is $\vec{x}_0 = [30 \ 80 \ 70 \ 70]$. The initial value of the objective function $J(x, p)$ is 105.67 and the maximum constraint violation is 12.70. After 27 iteration and 218 function evaluations $J(x_{opt}, p) = 0.096$ and the maximum constraint violation is 0.0132 only at one frequency where the optimum design vector is $\vec{x}_{opt} = [19.6322 \ 73.4904 \ 40.4162 \ 78.4580]$.

4. SENSITIVITY ANALYSIS

The next step in optimization is finding dependency of the design problem on the design variables at the optimum point. Ideally, the optimum design should not be so sensitive to the small variation on the optimal values. For this purpose, the sensitivity of the VSWR and the antenna gain to the all design variables at 2.3 GHz in the $\pm 10\%$ range of the optimal values are performed and depicted from Figure 5 to Figure 12. The rate of change of VSWR and the gain is close to zero in the close
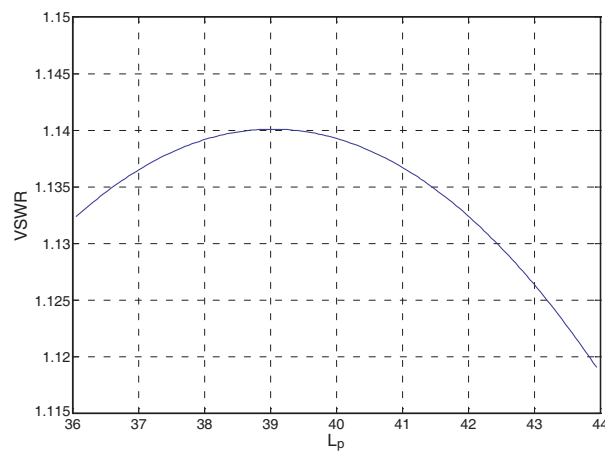

Figure 5: Sensitivity of VSWR to the patch length at 2.3 GHz.
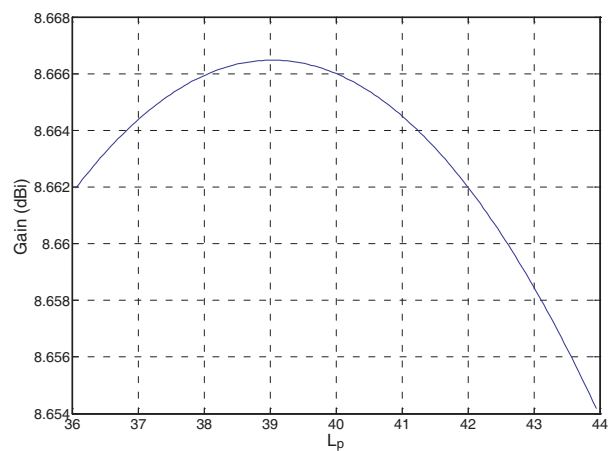
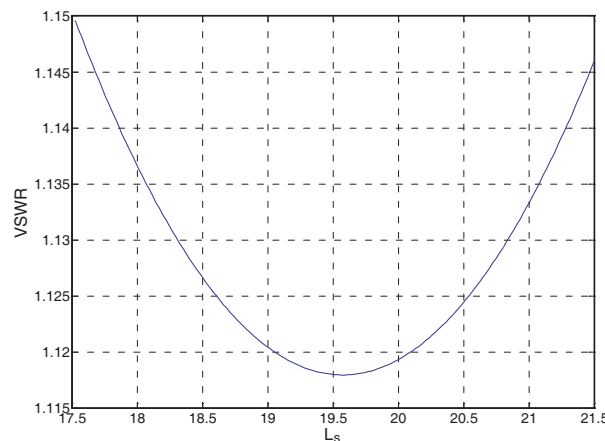Figure 6: Sensitivity of gain to the patch length at 2.3 GHz.

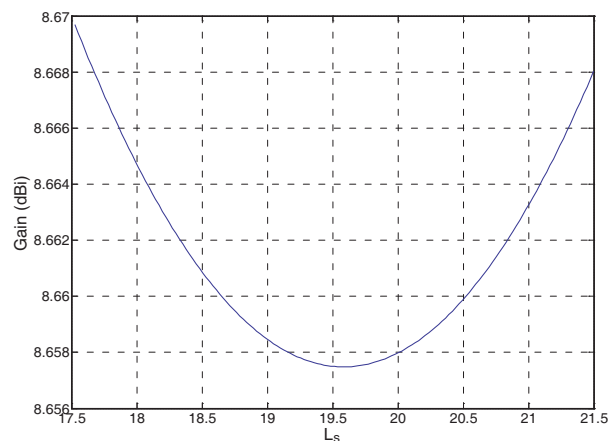Figure 7: Sensitivity of VSWR to the stub length at 2.3 GHz.

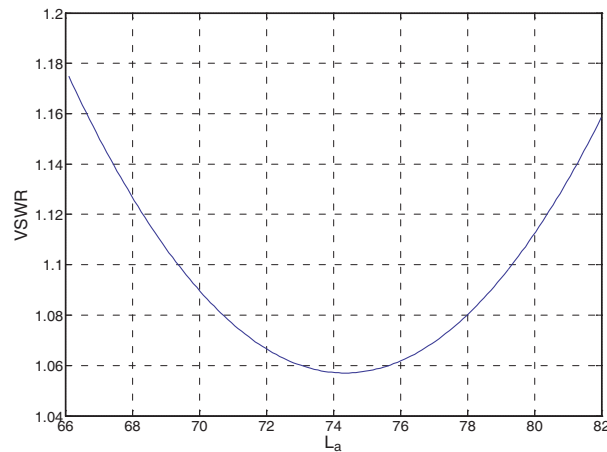Figure 8: Sensitivity of gain to the stub length at 2.3 GHz.

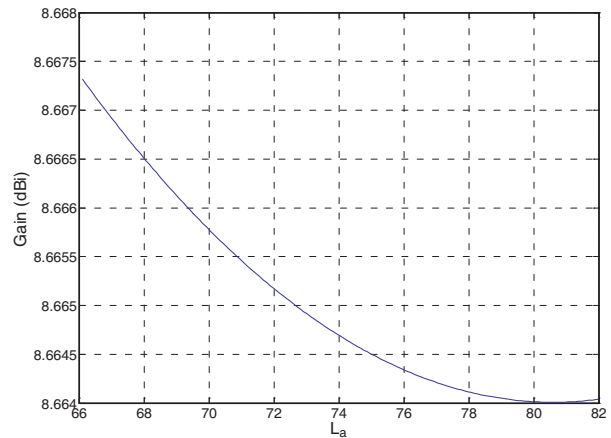Figure 9: Sensitivity of VSWR to the aperture length at 2.3 GHz.

Figure 10: Sensitivity of gain to the aperture length at 2.3 GHz.
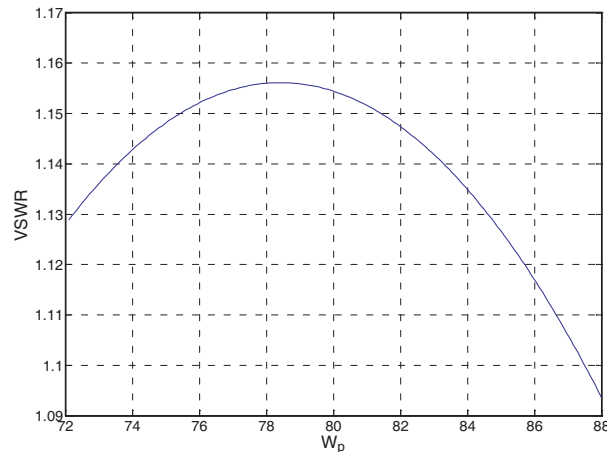

Figure 11: Sensitivity of VSWR to the patch width at 2.3 GHz.
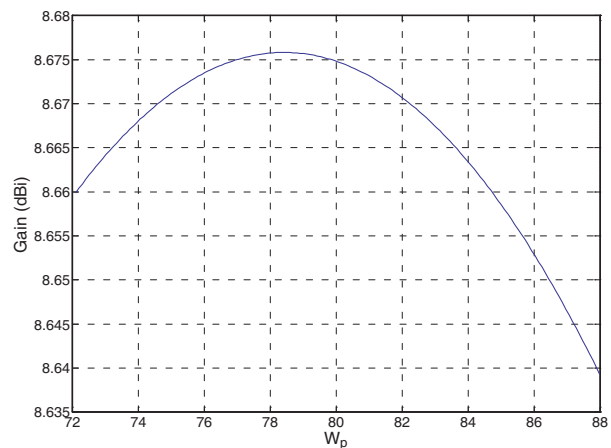
Figure 12: Sensitivity of gain to the patch width at 2.3 GHz.

proximity of the optimum values, so the optimal design is not sensitive to the variation on the final design vector which should be the case.

5. CONCLUSION

The optimization of the ACMPA is explained step by step with the details and then sensitivity analysis performed on the optimal design vector. The optimization process is developed and finalized after several trial and errors. During these trial and errors, the importance of the weighting coefficients, upper and lower bounds on the design variables are observed. The constraints and the objective should be well defined and powerful. Sensitivity analyses are performed to see the dependency of the optimal antenna performance around the neighborhood of the optimal design variables. Results depict that final design is stable at the optimal values.

REFERENCES

1. Deschamps, G. A., "Microstrip microwave antennas," *Proc. 3rd USAF Symposium on Antennas*, 1953.
2. Pozar, D. M., "A review of aperture coupled microstrip antennas: history, operation, development and applications," May 1996.
3. Pozar, D. M., "A microstrip antenna aperture coupled to a microstrip line," *Electronics Letters*, Vol. 21, 49–50, January 17, 1985.

Use of Attachment Functions in the Moment Method for Analysis of Planar Microstrip Structures

O. Nejla and T. Aguili

SysCom Laboratory, Electrical Engineering Department, Engineer School of Tunis, Tunisia

Abstract— In this work, we propose a solution to deal with the problem of the errors introduced by the presence of discontinuities in planar microstrip circuits in computing some physical quantities, like the distribution of the current, by the moment method (MoM).

This approach combines the Moment Method with the generalized equivalent circuit method to analyze a planar circuit. The interest of the method is the use of the attachment functions in the base of trial functions in the moment method, generally one or two functions by interface.

In order to assess its efficiency, the proposed method is developed for analyzing discontinuities in a rectangular microstrip antenna. To achieve this purpose, the current traveling on the feed line toward the patch edge is calculated and the coupling coefficient of a rectangular microstrip antenna array in H-plane configuration is investigated. The convergence study of the matrix in TE and TM mode is highlighted.

1. INTRODUCTION

Among the available numerical techniques, the Method of Moments is a very efficient for the modeling of planar circuits like micro-strip antenna [1, 2].

When adopting this technique, a common issue is related to the proper choice of test functions and the number of basis functions in order to guarantee the convergence of algorithm with a reliable result [3]. The developed method consists in determining the system matrix from the equivalent diagram then make projections of modes on the basis of trial functions in which we use attachment functions.

2. STUDIED STRUCTURE

The studied circuit of the first part, as described in Figure 1 and which parameters are summarized in Table 1, is composed of a rectangular microstrip radiating element (A) and a microstrip line (L) excited by a voltage source E_0 placed on the circuit plane. This structure is embedded in a metallic box which its electric walls are considered too far from the circuit to avoid all interactions. In the second part, we place a second patch antenna identical to the first in H plane configuration to study the mutual coupling phenomena. The used frequency in both cases is $f = 4.9\,\text{GHz}$.
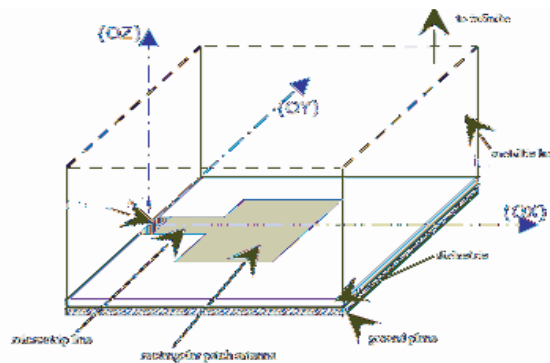
Figure 1: A rectangular microstrip antenna.

3. THEORETICOL DEVELOPMENT: CASE OF A RECTANGULAR MICROSTRIP ANTENNA

The method of generalized equivalent circuits used to implement an electromagnetic problems described by Maxwell's equations in an electrical problem [4]. On the plane of the circuit, the electric tangential field is related to the total current density by the impedance operator.

$$\vec{E}_T = \hat{Z}\vec{J} \tag{1}$$

Table 1: Dimensions of the rectangular microstrip antenna.

	Patch	Feed line	Voltage Source	Box
Length (mm)	$L = 22.76$	$l = 5.69$	$c = 0.7863$	$a = 200$
Width (mm)	$W = 5.99$	$d = 2.812$	$d = 2.812$	$b = 100$

$\hat{Z}$ is a projection operator on the f_{mn}^{TE} and f_{mn}^{TM} of the empty waveguide. The solution of the problem consists in satisfying the following boundary conditions:

$$\vec{E}_T = \vec{0} \text{ on the metal and } \vec{J} = \vec{0} \text{ on the insulator.}$$

We use an arbitrary excitation $\vec{E}_0$ on the micro-strip line subregion. On the plane of the strip, let $\vec{J}_M$ be the current density on the metal region. The planar microstrip antenna can be modeled with equivalent diagram as shown in Figure 2:
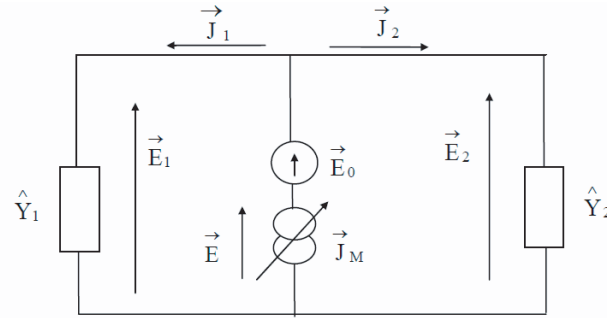

Figure 2: Equivalent diagram of a rectangular microstrip antenna.

$\hat{Y}_1$ and $\hat{Y}_2$ are the admittance operator: $\hat{Z} = (\hat{Y}_1 + \hat{Y}_2)^{-1}$, $\vec{E}_0$ defined on (M), $\vec{E}_0 = V_0\vec{e}_0$, $\vec{e}_0$ is the source function of amplitude V_0. Let g_k be the trial basis functions on the metallic part of the structure. The current density is then described with test functions and expanded on a set of basis functions. This yields the set of linear Equation (2). Thus, we obtain a matrix equation: $AX = B$ (3).

$$\sum_i \langle \vec{g}_i, \hat{Z}\vec{g}_j \rangle X_j = \langle \vec{g}_i, \vec{g}_0 \rangle \forall i \tag{2}$$

$$A = \begin{bmatrix} [A_{LL}] & [A_{LA}] & \langle \vec{g}_1, \hat{Z}\vec{g}_{ATT} \rangle \\ [A_{AL}] & [A_{AA}] & \cdots \\ \langle \vec{g}_{ATT}, \hat{Z}\vec{g}_1 \rangle & \cdots & \langle \vec{g}_{ATT}, \hat{Z}\vec{g}_{ATT} \rangle \end{bmatrix} \begin{bmatrix} X_1 \\ \cdots \\ X_N \end{bmatrix} = \begin{bmatrix} \langle \vec{g}_1, \vec{E}_0 \rangle \\ \cdots \\ \langle \vec{g}_N, \vec{E}_0 \rangle \end{bmatrix} \tag{3}$$

For the study of rectangular planar microstrip antenna, it seems natural to choose the relative solutions of the transverse electric field of a metallic rectangular waveguide as basic functions [5, 6].

The trial functions, as shown in Figure 3, are chosen for our case, so to better describe the current as it passes from one area to another for complex structures composed by several fields metal (assumed rectangular) and this by introducing functions called attachments [3].
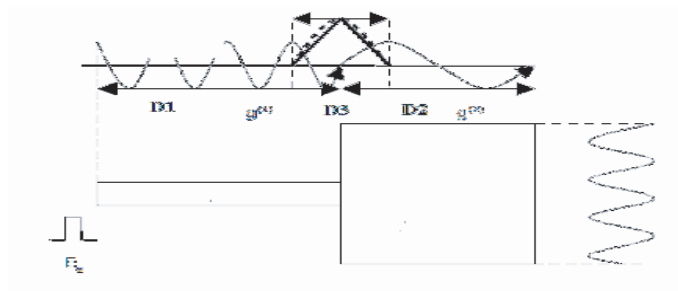
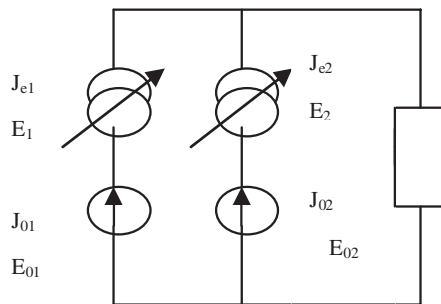Figure 3: Attachment function in a rectangular micro-strip antenna.

Figure 4: Equivalent diagram of a rectangular microsstrip antenna.

4. THEORETICOL DEVELOPMENT: CASE OF A RECTANGULAR MICROSTRIP ANTENNA ARRAY

We extend the approach detailed above. The microstrip antenna array can be modeled by an equivalent diagram as described in Figure 4. The obtained matrix system is:

$$\begin{pmatrix} I_{01} \\ I_{02} \end{pmatrix} = \begin{pmatrix} A_1^t & 0 \\ 0 & A_2^t \end{pmatrix} M^{-1} \begin{pmatrix} A_1 & 0 \\ 0 & A_2 \end{pmatrix} \begin{pmatrix} V_{01} \\ V_{02} \end{pmatrix} \tag{4}$$

$$A_1^t = \left[< \overrightarrow{f_{01}}, \overrightarrow{g_1^1} >, \ldots, < \overrightarrow{f_{01}}, \overrightarrow{g_n^1} > \right]$$

$$A_2^t = \left[< \overrightarrow{f_{02}}, \overrightarrow{g_1^2} >, \ldots, < \overrightarrow{f_{02}}, \overrightarrow{g_n^2} > \right]$$

where

$$M = \begin{pmatrix} y_{11} & y_{12} \\ y_{21} & y_{22} \end{pmatrix} \tag{5}$$

$$y_{11}(i,j) = < \overrightarrow{g_i^1}, \hat{Y}^{-1} \overrightarrow{g_j^1} > = < \overrightarrow{g_i^1}, \hat{Z} \overrightarrow{g_j^1} >$$

$$y_{12}(i,j) = < \overrightarrow{g_i^1}, \hat{Y}^{-1} \overrightarrow{g_j^2} > = < \overrightarrow{g_i^1}, \hat{Z} \overrightarrow{g_j^2} >$$

$$y_{21}(i,j) = < \overrightarrow{g_i^2}, \hat{Y}^{-1} \overrightarrow{g_j^1} > = < \overrightarrow{g_i^2}, \hat{Z} \overrightarrow{g_j^1} >$$

$$y_{22}(i,j) = < \overrightarrow{g_i^2}, \hat{Y}^{-1} \overrightarrow{g_j^2} > = < \overrightarrow{g_i^2}, \hat{Z} \overrightarrow{g_j^2} >$$

Y is the admittance matrix. $\vec{f}_{01}$ (respectively $\vec{f}_{02}$) is the unit vector of the first (respectively second) source. g_i^k is a test function on a patch antenna ($k \in [1, 2]$).

5. NUMERICAL RESULTS

A computer program has been coded in MATLAB language for the first part and in JAVA language for the second part due to the density of the matrix. As shown in Figure 5, according OX, component of J, noted that Jx, vanishes on edges in the x-direction and reached the peak on the transverse edges before reaching quick minimum amplitude (zero) on the dielectric. We Note all the same small oscillations preceding the cancellation of current (Gibbs effect).
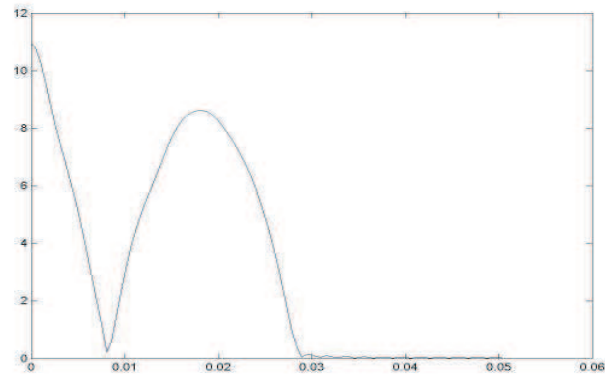
Figure 5: $|Jx|$ on base functions (A-A cut).
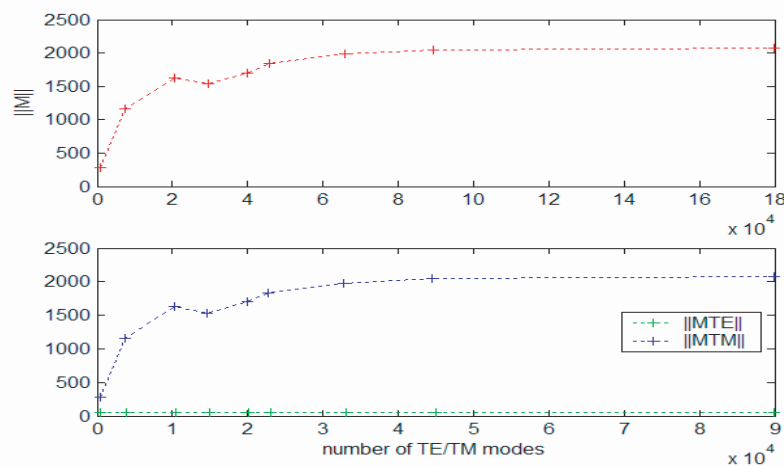
Figure 6: Convergence of the matrix M in modes for 38 test functions
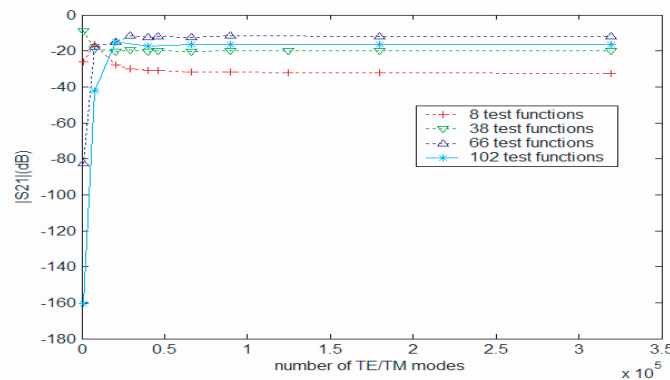
Figure 7: Convergence of $|S_{21}|$ dB in modes and test functions.

Furthermore, by awarding the fact that the current has amplitude nonzero on the interface between the line and the antenna, we can notice the important role of the function of attachment.

The study of convergence in single mode TE and TM alone in case of a microstrip antenna array, as shown in Figure 6, has led the conclusion as designating TM mode role in the structure. Indeed, the number of modes TM needed to describe all of the modes propagating in the structure is too larger than the TE mode. This characteristic reflects the capacitive aspect of the structures studied.

Note that the higher the number of test functions is used, the greater should be the number of modes to obtain a matrix that is well conditioned.

At convergence (in modes and trial functions), we obtain a reasonable approximation of the coupling coefficient at $f = 4.9$ GHz. It should be noted, according to Figure 7, that convergence is achieved for 66 sinusoidal test functions and 89888 modes. We can then conclude that $S_{12} = -11.42$ dB. The structure is simulated by SONNET and the found value is $S_{12} = -11.39$ dB.

6. CONCLUSION

Two structures have been studied. It was shown that the boundaries conditions were respected in the microstrip antenna. At the discontinuity between the feed line and the patch, the current is not zero which highlight the important role of attachment function. It should be noted that measured results, in the second structure, were compared with measured ones and they improve the effectiveness of the method.

REFERENCES

1. Jackson, R. W. and D. M. Pozar, "Full wave analysis of microstrip open-end and gap discontinuity," *IEEE Trans. on MTT*, Vol. 36, No. 10, 1036–1042, 1985.
2. Hill, A., "Quasi-TEM and full wave numerical methods for the characterization of microstrip discontinuities," Ph.D. Thesis, Oregon State University, 1989.
3. Montagna, M., M. Bozzi, and L. Perregrini, "Convergence properties of the method of moments with entire-domain and sub-domain basis functions in the modeling of frequency selective surfaces," *International Journal of RF and Microwave Computer-aided Engineering*, Vol. 20, No. 2, 220–229, 2008.
4. Taha, B. S., "Analysis of planar antenna: Use of attachment function," Master's Diploma Engineer School of Tunis, Tunisia, 2003.
5. Pozar, D. M., "Input impedance and mutual coupling of rectangular microstrip antennas and scatterers," *IEEE-T-AP*, Vol. 30, No. 6, 1191–1196, Nov. 1982.
6. Liu, Z. F., P. S. Kooi, L. W. Li, M. S. Leong, and T. S. Yeo, "A spectral domain analysis of mocrostrip antenna array using method of moment: Theory and experiment," *Journal of Electromagnetic Waves and Applications*, Vol. 12, 1471–1490, 1998.

GA Optimization for Compact Broadband PIFA Application

Wen Pan and Quanyuan Feng

Institute of Microelectronics, Southwest Jiaotong University, Chengdu 610031, China

Abstract— In this paper, a Planar Inverted-F antenna (PIFA) applicable to the digital broadcasting service such as DMB and DVB-H is presented. Between the top plate and ground one part of the substrate is ferrite and the remaining is air-filled. This combined substrate structure as well as the utilization of T-shaped ground plane remarkably broadens the bandwidth and minimizes the antenna size. The optimizer by Genetic Algorithms (GA) cooperated with High Frequency Structure Simulator (HFSS) is adopted to obtain the optimal volume and shape of the PIFA. The mixed optimization program gives the scheme to cut out irregularly shaped slot windows on the patch which makes the Return Loss of the antenna proposed achieve $-51.25\,\text{dB}$ at the operation frequency. Finally, the antenna is fixed on $23\,\text{mm}$ length, $5\,\text{mm}$ width, $1\,\text{mm}$ thick, over 72% reduction in the size compared with the conventional PIFA, relative bandwidth is 70% at $0.7\,\text{GHz}$, and VSWR is 1.05.

1. INTRODUCTION

Recently, the demand for miniaturization, multi-band and broadband antennas have been increased along with the development of multi-system and downsizing handset. For the volume of the antenna is inversely proportional to the desired frequency, miniaturization is a crucial problem to the digital broadcasting services such as DMB and DVB-H which is assigned from $170 \sim 800\,\text{MHz}$. This frequency range is not only relatively lower, but also has a wideband. The attempt to achieve both miniaturization and broadband antenna is manifest.

The hexagonal ferrite substrate is effective for the miniaturization of the antenna and slots on both radiating patch and ground plane can be adopted to realize the miniaturization and broadband performance. But the hexagonal ferrite will put a strangle hold on the electromagnetic field and reduce the bandwidth, which means using the hexagonal ferrite substrate would present contradiction between miniaturization and broadband. This paper proposes miniaturization and broadband PIFA which overcomes this problem. Meanwhile, the optimizer by GA cooperated with HFSS is adopted to get the antenna excellent performance by cut off erose slot windows on the top patch.

2. REALIZATION OF THE OPTIMIZER COMBINED GA AND HFSS

Adding slots can change current distribution on radiating patch and introduce equivalent inductance and capacitance. These create different resonance modes close to each other [1] which can broaden the bandwidth and reduce the operational frequency of a PIFA without additional element. However, it is hard to analyze where and what shape the slots should be to make the antenna best, this also has become an important application in GA optimization for antenna.

This paper adopts the basic GA [2] and creates GA main program by MATLAB. The subprogram which creates VB script with MATLAB to call HFSS [3] calculates the cost function by the simulation result to get the fitness for GA. According to the way in which HFSS builds antenna 3D model, this paper proposes a novel program without dividing the radiating patch into meshes which is the method used to optimize antenna performance with erose slots by GA. The program flow chart is shown in Figure 1. The subprogram builds a intact antenna patch in HFSS and a 'mold' of a rectangle shown in Figure 2 serving as a basic cell. With a given 'mold' size (dx, dy), the chromosome of each individual gives a location (start point), according to which the 'mold' will be cutoff from the patch one at a time. After several cuts, antenna will get an optimal slot. There should be a maximal cut number n that the 'mold' can be cut. When exceed the limit n and not achieve the optimal result, a new intact patch should be built for anther round. Note that the chromosome which denotes the coordinates of start point is expressed by binary string, so the start points are discrete. Make sure that the size of 'mold' is larger than the interval between nearest start points and not the integer times in both x and y axis, which can guarantee the avoidance of connection at a vertex. The mixed optimization program could show the scheme to cut off proper slot on the patch.

The GA optimizes the patch by removing several square metal subsections from the patch region. Design the cost function (1) using the method below [4]. S_{11} of three frequencies are selected in

GA main program
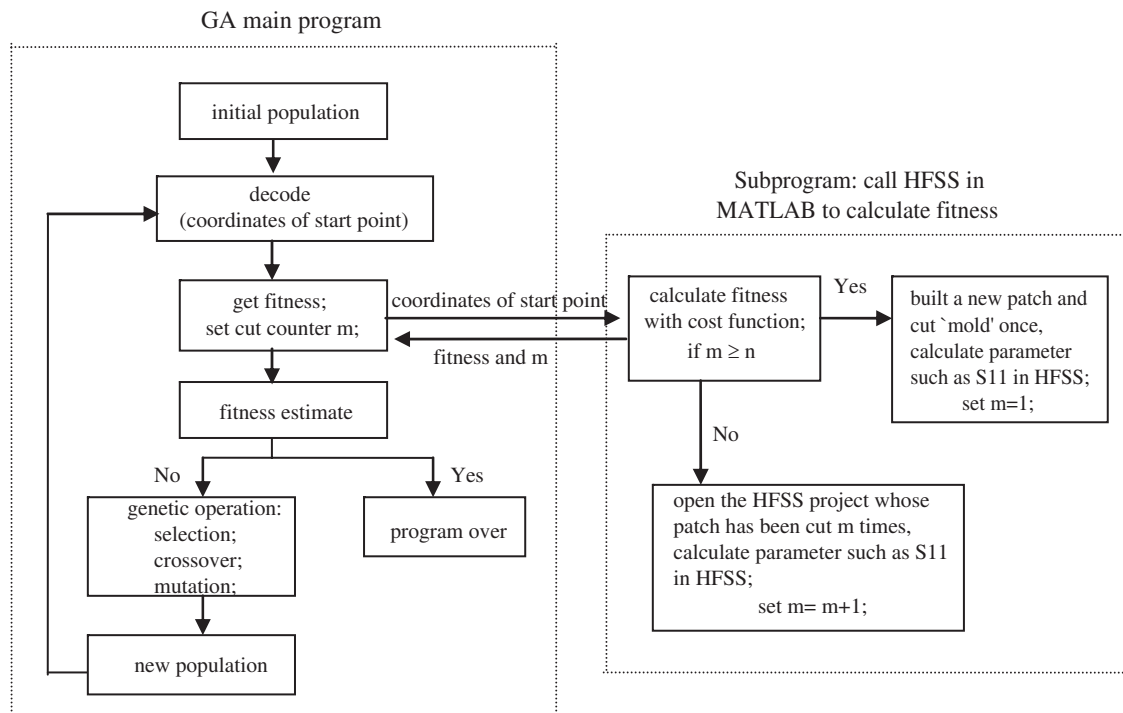
Figure 1: Program flow chart for GA/HFSS.

Start point (x, y)
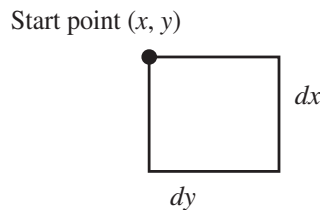
Figure 2: A rectangle 'mold' serves as a basic cell.

the frequency range which needs to be optimized. Table 1 illustrates the parameter set for GA optimizer.

$$F = \sum_{i-1}^{3} S_i/3 \tag{1}$$

$$S_i = \begin{cases} |S_{11}(f_i)|, & 5 \leq |S_{11}| \leq 20 \\ 20, & |S_{11}| > 20 \\ 0, & |S_{11}| < 5 \end{cases} \tag{2}$$

Table 1: Parameter set for GA optimizer.

Population	32 Individuals
Crossover	80%
Mutation	20%
Generation	64
Max-cut-number (n)	15

3. PIFA CONFIGURATION AND RESULT OF OPTIMIZATION

This paper proposes a miniaturization and broadband PIFA based on the investigation of T-shaped ground plane PIFA [1]. As shown in Figure 3, The antenna configuration before optimization has a regular square patch 5×23 mm above a finite ground plane 92×125 mm by 1 mm. Two rectangles 45.4×15 are cutoff from ground plane. It is known that the dielectric material with permittivity ε and permeability μ can be applied to miniaturize antenna. For the size of antenna is directly proportional to $\frac{1}{\sqrt{\varepsilon\mu}}$, hexagonal ferrite with $\varepsilon = 16.5$, $\mu = 2.8$ make the wavelength shorter, which is effective for the miniaturization of the antenna. Then, to solve the contradiction between miniaturization and broadband described in the previous section, the substrate between the top plate and ground is partly filled with hexagonal ferrite and the remaining is air-filled. The air substrate reduces the bandage of hexagonal ferrite to electromagnetic field. Meanwhile, the combined substrate acting as tapered line impedance-matching network in the transmission line theory broadens the bandwidth remarkably. Figure 4 shows the sequence by which the 'mold' is cutoff and the top patch configuration of the PIFA after optimization. The coordinates of start points of the 'mold' (0.5×2 mm) given by 9 individuals of the 13th generation are listed in Table 2.

Table 2: The coordinate list of start points of the 'mold' cut from the patch.

Mold-1	X: −0.8	Y: 66.1	Mold-6	X: −1.8	Y: 72.4
Mold-2	X: 0.1	Y: 70.7	Mold-7	X: −1.7	Y: 64.3
Mold-3	X: 1.2	Y: 74.1	Mold-8	X: 0.1	Y: 68.3
Mold-4	X: 0.9	Y: 76.5	Mold-9	X: 0.4	Y: 66.6
Mold-5	X: −2.3	Y: 63.7			

The results of parameter S_{11} and VSWR of the antenna before and after optimized by the proposed method are presented in Figure 5 and Figure 6. Compared with the conventional PIFA, the optimized antenna is over 72% reduction in size, the relative bandwidth is 70% at 0.7 GHz, the VSWR is 1.05, and the S_{11} can achieve −51.25 dB.
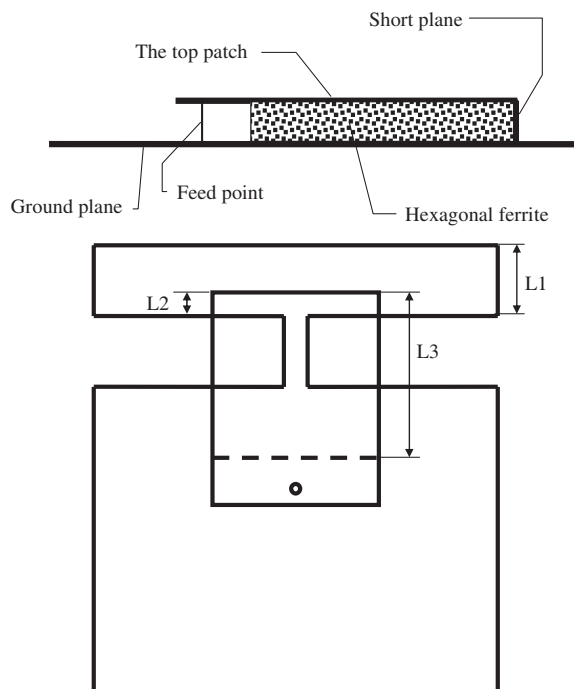
Figure 3: The antenna configuration before optimization.
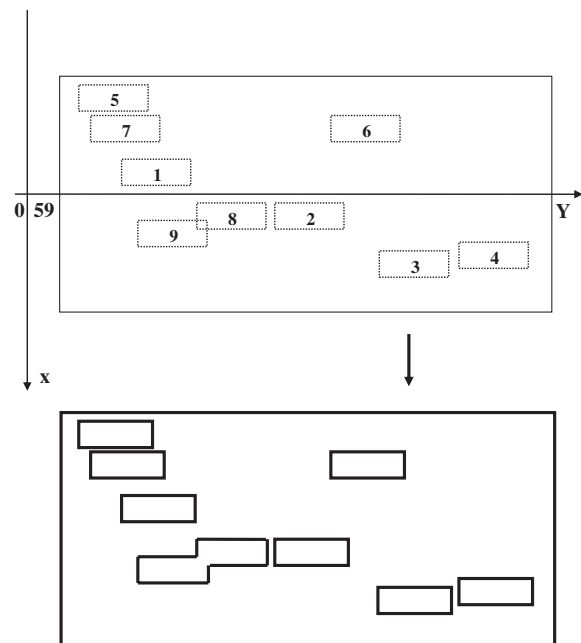
Figure 4: The sequence mold cutting sequence and the top patch configuration of the PIFA after optimization.
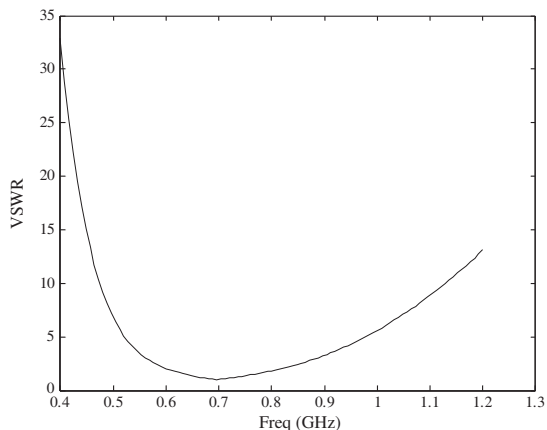
Figure 5: The VSWR of the PIFA.
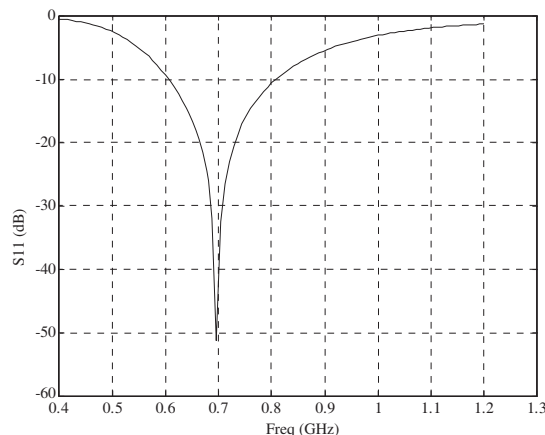
Figure 6: The S_{11} of the PIFA.

4. CONCLUSION

This paper proposed a method combined GA and HFSS to optimize PIFA with erose slots. This method is proved to be effective and finally the optimized PIFA reduces over 72% in size compared with the conventional PIFA, relative bandwidth is 70% at 0.7 GHz.

ACKNOWLEDGMENT

REFERENCES

1. Wang, F., Z. Du, Q. Wang, and K. Gong, "Enhanced-bandwidth PIFA with T-shaped ground plane," *Electronics Letters*, Vol. 40, 1504–1505, 2004.
2. Haupt, R. L., "An introduction to genetic algorithms for electromagnetics," *IEEE Antennas and Propagation Magazine*, Vol. 37, No. 2, 7–15, Apr. 1995.
3. Maruyama, T., F. Kira, and K. Cho, "Novel chromosome generation method for genetic algorithm applied to planar and meander-line antenna design," *IEEE Antennas and Propagation Society International Symposium*, Vol. 1, 527–530, 2004.
4. Yang, F. and X. Zhang, "The application of genetic algorithms in microstrip antenna optimization," *Acta Electronica Sinica*, Vol. 28, No. 9, 91–95, Sep. 2000.

Numerical Computation of Capacitance of Oblate Spheroidal Conducting Shells

Omonowo D. Momoh, Matthew N. O. Sadiku, and Cajetan M. Akujuobi

Department of Electrical and Computer Engineering, Prairie View A&M University
Prairie View, TX 77446, USA

Abstract— In this paper, numerical method for determining the capacitance of a conducting oblate spheroidal shell has been established. An explicit finite difference technique for solving Laplace's equation in oblate spheroidal coordinates systems for an axially symmetric geometry has been developed. An ingenious strategy was created to overcome the singularity problems encountered in the oblate spheroids. Consequently, the finite difference results were used to compute the capacitance of the spheroidal shell in an easy to understand manner. This was achieved using the Dirichlet boundary conditions on the oblate spheroidal surfaces. The shell capacitance results obtained did fall in the same range with those obtained using analytical method.

1. INTRODUCTION

The choice of a particular coordinate system is motivated by the geometrical form of the body under study and can result in a considerably simplified analysis of the problem [1].

In other words, to express boundary conditions in a reasonably simple way, one must have coordinate surfaces that fit the physical boundaries of the problem [2, 3]. In considering heat flow in a bar of elliptic cross section, for instance, one uses elliptic-cylindrical coordinates while in calculating the effect of introducing a dielectric sphere into an electric field, one uses spherical coordinates. Thus the range of field problems that can be handled effectively by an engineer or physicist will depend upon the number of coordinate systems with which the person is familiar [3].

A spheroid is obtained by rotating an ellipse about one of its principal axes. If the ellipse is rotated about its major axis, a prolate spheroid is formed, while an oblate spheroid is formed if the ellipse is rotated about its minor axis. However, if the generating ellipse is a circle, a sphere is formed. Spheroidal coordinates eliminate the cumbersome mathematical expressions obtained with rectangular coordinates and allow the simple determination of areas and volume. They offer an obvious generalization of physical processes described in spherical coordinate systems and in addition yield the extremely interesting limiting cases of the infinitely thin, finite "wire" and the infinitely thin circular disk [4]. For instance, spheroidal antennas can be used to model a variety of different antenna shapes, from wire antennas, through cylindrical antennas, to disk antennas. Subsequently, for antennas that are long and thin, prolate spheroidal coordinates fit the geometry more closely while oblate spheroids should represent antennas in the shape of a disk [5, 6].

The computation of the shell capacitance would help in future research efforts at finding the characteristic impedance and phase velocity in spheroidal shell conductors just like it has already been done for microstrip lines [7]. The authors have been able to compute the capacitance in conducting prolate spheroidal shells both analytically and numerically in their previous work [8]. This research work therefore aims at the computation of the capacitance in a conducting oblate spheroidal shell.

2. OBLATE SPHEROIDAL COORDINATE SYSTEMS

The oblate spheroidal coordinate system is generated by taking an orthogonal family of confocal ellipses and hyperbolas and rotating it about the minor axis of the ellipses. The resulting coordinate surfaces are oblate spheroids, half planes and hyperboloids of one sheet [9]. Oblate spheroidal coordinates have a circular disc as the degenerate element of the system; the two foci of the 2D ellipse form a ring when rotated about the minor axis of the ellipse [10].

The oblate spheroidal coordinates are related to the rectangular coordinates shown in Equations (1)–(3).

$$x = a \cosh \xi \sin \eta \cos \phi \tag{1}$$

$$y = a \cosh \xi \sin \eta \sin \phi \tag{2}$$

$$z = a \sinh \xi \cos \eta \tag{3}$$

where a is the focal length of the oblate spheroid.

The respective scale factor for each of the three coordinates (ξ, η, ϕ) is

$$h_\xi = a\sqrt{\sinh^2 \xi + \sin^2 \eta} \tag{4}$$

$$h_\eta = a\sqrt{\sinh^2 \xi + \sin^2 \eta} \tag{5}$$

$$h_\phi = a \cosh \xi \cos \eta \tag{6}$$

3. NUMERICAL COMPUTATION OF SHELL CAPACITANCE

3.1. Finite Difference Solution of Oblate Spheroid Laplace's Equation

The numerical solution of differential problems defined on general-shape, three-dimensional domains nowadays still presents difficulties, in particular if the boundary conditions involve the normal derivative of the solution. Several recent articles and transactions papers have examined the application of a variety of field solution techniques to electromagnetic problems [11–18]. In this research work, we use the simplest and oldest of all digital schemes — fully explicit finite-difference approximation of partial derivatives to compute the oblate spheroidal shell capacitance. The choice was based on its simplicity over other complicated schemes which make it easier to program from scratch. It has lesser probability to contain elusive errors. That the computation time may be lengthy is not seen as a draw back because nowadays "computer time" is inordinately cheaper than "people time" [19].

The Laplacian equation in oblate spheroidal coordinate systems is

$$0 = \nabla^2 V = \left(\frac{1}{\sinh^2 \xi + \sin^2 \eta} \right) \cdot \left[\begin{array}{l} \left(\sec h^2 \xi \tan^2 \eta + \sec^2 \eta \tanh^2 \xi \right) \dfrac{\partial^2 V}{\partial \phi^2} \\[2mm] + \dfrac{\partial^2 V}{\partial \xi^2} + \tanh \xi \dfrac{\partial V}{\partial \xi} + \dfrac{\partial^2 V}{\partial \eta^2} - \tan \eta \dfrac{\partial V}{\partial \eta} \end{array} \right] \tag{7}$$

The term outside the bracket may be ignored. Also the first term inside bracket may be ignored due to the rotational symmetry about the vertical (z) axis [19]. Therefore, (7) reduces to

$$\frac{\partial^2 V}{\partial \xi^2} + \tanh \xi \frac{\partial V}{\partial \xi} + \frac{\partial^2 V}{\partial \eta^2} - \tan \eta \frac{\partial V}{\partial \eta} = 0 \tag{8}$$

This equation is found to govern the distribution of potential. Equation (8) was discretized by finite difference method and the respective mesh sizes in each of the two coordinates are $\Delta\xi$ and $\Delta\eta$. Consequently, the sampling points are defined by the following coordinate values [20];

$$\begin{array}{ll} \xi = i\Delta\xi, & i = 0, 1, 2, 3, \ldots \\ \eta = j\Delta\eta, & j = 0, 1, 2, 3, \ldots \end{array} \tag{9}$$

The difference equation is developed by expanding the potential at the points i, j in Taylor's series and deriving expressions for the second partial derivative in any direction, which are substituted into the transformed equation in (8) [21]. The finite difference equation in oblate spheroidal coordinates is shown in (10).

Figure 1 shows one-quarter of constant oblate spheroidal surfaces. The figure exhibits symmetry with respect to η coordinate. Therefore, the range of $0 \le \eta \le \frac{\pi}{2}$ is used for simulation. Subsequently, the results computed for capacitance is multiplied by four.

$$\begin{aligned} V(i,j) \;=\; & 0.5 \left[\frac{1}{\left[\dfrac{1}{(\Delta\xi)^2} + \dfrac{1}{(\Delta\eta)^2} \right]} \right] \\[3mm] & \cdot \left[\begin{array}{l} V(i+1,j)\left[\dfrac{1}{(\Delta\xi)^2} + \dfrac{\tanh(i\Delta\xi)}{2\Delta\xi} \right] + V(i-1,j)\left[\dfrac{1}{(\Delta\xi)^2} - \dfrac{\tanh(i\Delta\xi)}{2\Delta\xi} \right] \\[3mm] + V(i,j+1)\left[\dfrac{1}{(\Delta\eta)^2} - \dfrac{\tan(\eta_j)}{2\Delta\eta} \right] + V(i,j-1)\left[\dfrac{1}{(\Delta\eta)^2} + \dfrac{\tan(\eta_j)}{2\Delta\eta} \right] \end{array} \right] \end{aligned} \tag{10}$$
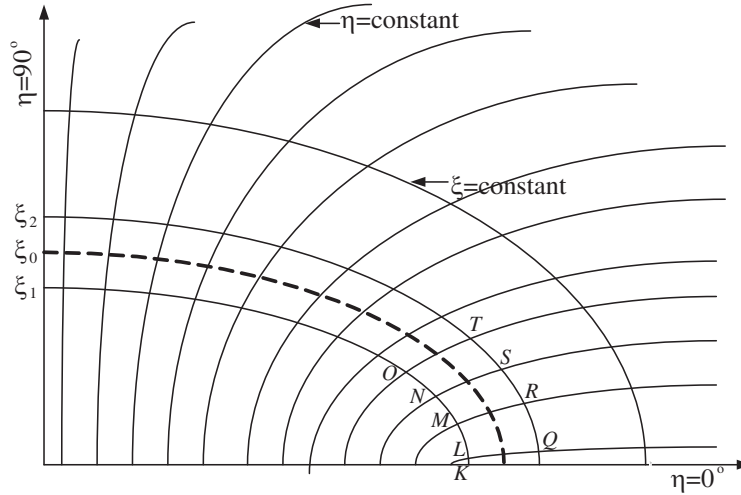
Figure 1: Oblate Spheroidal surface path used in computing the charge enclosed.

The factor 4 is necessary because we are working on only one-quarter of the cross section [7, 8]. Two lines of symmetries are encountered in this range of η. They are $\eta = 0°$ and $\eta = 90°$. On these lines of symmetries, the Neumann boundary condition $\frac{\partial V}{\partial \eta} = 0$ is imposed [7].

Therefore, the finite difference equations in the two lines of symmetries become:
Along $\eta = 90°$, $j = j_{\max}$,

$$V(i, j_{\max}) = 0.5 \left[\frac{1}{\left[\frac{1}{(\Delta\xi)^2} + \frac{1}{(\Delta\eta)^2} \right]} \right]$$

$$\cdot \left[V(i+1, j_{\max}) \left[\frac{1}{(\Delta\xi)^2} + \frac{\tanh(i\Delta\xi)}{2\Delta\xi} \right] + V(i-1, j_{\max}) \left[\frac{1}{(\Delta\xi)^2} - \frac{\tanh(i\Delta\xi)}{2\Delta\xi} \right] + 2V(i, j_{\max} - 1) \left[\frac{1}{(\Delta\eta)^2} \right] \right] \quad (11)$$

Also along $\eta = 0°$, $j = 0$,

$$V(i, 0) = 0.5 \left[\frac{1}{\left[\frac{1}{(\Delta\xi)^2} + \frac{1}{(\Delta\eta)^2} \right]} \right] \cdot \left[\begin{array}{l} V(i+1, 0) \left[\frac{1}{(\Delta\xi)^2} + \frac{\tanh(i\Delta\xi)}{2\Delta\xi} \right] \\ + V(i-1, 0) \left[\frac{1}{(\Delta\xi)^2} - \frac{\tanh(i\Delta\xi)}{2\Delta\xi} \right] + 2V(i, 1) \left[\frac{1}{(\Delta\eta)^2} \right] \end{array} \right] \quad (12)$$

$\eta_{j\,\max}$ and η_0 are obtained by substituting $j = 90°$ and $j = 0°$ into Equation (11) respectively. Equations (10)–(12) are used for the finite difference simulation.

3.2. Effects of Polar Singularities on Potential Distribution

The imposition of the derivative condition ($\frac{\partial V}{\partial \eta} = 0$) along the lines of symmetries helped to eliminate the $\tan(\eta)$ factor in (10) which otherwise could have generated 'infinity' especially along line $\eta = 90°$. This strategy helps to obtain uniform potential distribution on equipotential surfaces which ultimately enhances the accuracy of the spheroidal shell capacitance results. The mesh sizes used were $\Delta\xi = 0.05$ and $\Delta\eta = \frac{\pi}{20}$ respectively, and the shell radial coordinate and potential values ranged from $(\xi_1 = 1.0, V_1 = 0)$ to $(\xi_2 = 2.0, V_2 = 100)$.

Prior to implementing the singularity resolution strategies that gave the uniform potential distributions, the potential values obtained were infinitely large, randomly non-uniform, and sometimes absolutely infinite.

3.3. Shell Capacitance Computation

Based on the results obtained from the simulation, the total charge (Q) enclosed by the oblate spheroidal shell can be calculated. To find Q, we apply Gauss's law to a closed surface S enclosing

the total electric fluxes as follows

$$Q = \oint \bar{D} \cdot d\bar{s} = \oint \varepsilon \frac{\partial V}{\partial n} \bar{a}_n \cdot ds \bar{a}_n = \varepsilon \oint \frac{\partial V}{\partial n} ds \tag{13}$$

The differential normal surface area is calculated with the aid of the scale factors as shown in

$$d\bar{s} = h_\phi h_\eta d\phi d\eta \bar{a}_\xi = a^2 \sqrt{\sinh^2 \xi + \sin^2 \eta} \cosh \xi \cos \eta d\phi d\eta \bar{a}_\xi \tag{14}$$

Therefore, the charge Q can be obtained from (13) as shown in (14)–(18).

$$Q = a^2 \varepsilon \iint \frac{\partial V}{\partial \xi} \left(\sinh^2 \xi_0 + \sin^2 \eta \right)^{0.5} \cdot \cosh \xi_0 \cos \eta d\phi d\eta \tag{15}$$

where $\xi = \xi_0$ is the dotted path shown in Fig. 1.

Solving (18) we have,

$$Q = 2\pi a^2 \varepsilon \int \frac{\partial V}{\partial \xi} \left(\sinh^2 \xi_0 + \sin^2 \eta \right)^{0.5} \cdot (\cosh \xi_0 \cos \eta d\eta) \tag{16}$$

On further simplification, (16) becomes

$$Q = 2\pi a^2 \varepsilon \left[\begin{array}{l} \dfrac{V_p - V_k}{\Delta \xi} \left(\sinh^2 \xi_0 + \sin^2 \eta_p \right)^{0.5} \cdot (\cosh \xi_0 \cos \eta_p \Delta \eta) \\ + \dfrac{V_Q - V_L}{\Delta \xi} \left(\sinh^2 \xi_0 + \sin^2 \eta_Q \right)^{0.5} \cdot (\cosh \xi_0 \cos \eta_Q \Delta \eta) + \ldots \end{array} \right] \tag{17}$$

Equation (17) is put in a more compact form as

$$Q = 2\pi a^2 \varepsilon \frac{\Delta \eta}{\Delta \xi} \sum_{\substack{p=0 \\ k=0}}^{N} \left[(V_p - V_k) \left(\sinh^2 \xi_0 + \sin^2 \eta_p \right)^{0.5} \right] \cdot (\cosh \xi_0 \cos \eta_p) \tag{18}$$

It should be noted again that Fig. 1 represents a quarter of the spheroids. The charge is computed by adding all the net potentials on the nodes of the constant surface spheroid. This implies subtracting the respective potential on the corresponding adjacent nodes P, Q, R, S, T, etc. of constant surface ξ_2, and the nodes K, L, M, N, O, etc. of constant surface ξ_1 in Fig. 1. The net potential so obtained is consequently employed in (18) to compute the charge. The charge is subsequently used to compute the capacitance as shown in (19).

$$C = \frac{4Q}{V_d} \tag{19}$$

V_d represents the potential difference between the spheroidal shell's inner and outer surfaces ($V_d = 100\,\text{V}$ in Fig. 1).

The equation for the analytical solution for oblate spheroidal conducting shell capacitance computation is

$$C = \frac{4\pi a \varepsilon}{[gd(\xi_2) - gd(\xi_1)]} \tag{20}$$

where $gd(\ )$ denoting the Gudermannian function [22] is represented as

$$gd(\xi) = \sin^{-1}(\tanh(\xi)) \tag{21}$$

4. RESULTS

The computation results obtained from both numerical and analytical approaches are shown in Table 1. Six different sample results each typifying oblate spheroidal conducting shell formed between two different spheroidal surfaces ξ_1 and ξ_2 were tabulated. The oblate spheroidal shells used have focal length of 0.85. The values of the radial coordinate used for this study as reflected

Table 1: Oblate spheroidal shell capacitance.

Surface $\xi = \xi_1$	surface $\xi = \xi_2$	Shell Capacitance (nF) Exact	Shell Capacitance (nF) FD
0.2	0.4	0.49499	0.40989
0.2	0.5	0.33572	0.27916
0.4	0.8	0.28108	0.21549
0.4	1.0	0.19867	0.14907
0.7	1.3	0.24269	0.21349
1.0	2.0	0.21691	0.17829

Table 2: Effects of mesh size $\Delta\xi$ and $\Delta\eta$ on numerical results accuracy.

$\Delta\xi$	$\Delta\eta$	Shell Capacitance (nF) Exact	Shell Capacitance (nF) FD
0.5	$\frac{\pi}{180}$	0.21691	0.94589
0.25	$\frac{\pi}{180}$	0.21691	0.30154
0.1	$\frac{\pi}{180}$	0.21691	0.17829
0.05	$\frac{\pi}{180}$	0.21691	0.18331
0.05	$\frac{3\pi}{180}$	0.21691	0.22509
0.05	$\frac{6\pi}{180}$	0.21691	0.22447
0.05	$\frac{9\pi}{180}$	0.21691	0.22225

in Table 2 were chosen randomly. Table 2 shows the effects of the changes of the respective mesh size $\Delta\xi$ and $\Delta\eta$ (representing the two coordinates) on the accuracy of the numerical computation results. This was implemented by varying one mesh size at a time while the other mesh size was kept constant and vice versa. Consequently, $\Delta\eta$ was held constant in rows 1–4, while $\Delta\xi$ was held constant in rows 4–8. The oblate spheroidal shell's inner and outer surfaces were kept constant at $\xi_1 = 1$ and $\xi_2 = 2$ respectively for the study in Table 2.

It can be seen from Table 2 that decreasing the mesh size of either coordinates lead to better accuracy. However, on a closer look, changes in the mesh size of radial coordinate ξ have more impact on the accuracy of the numerical computation results than changes in the mesh size of angular coordinate η.

5. CONCLUSION

Numerical method of computing oblate spheroidal shell capacitance has been implemented. The problems posed by the presence of singularities on the pole regions of the oblate spheroids were successfully tackled. The numerical results approximate that of the analytical approach as expected. Also, the effects of the mesh sizes on the accuracy of the numerical computation results investigated showed that changes in the mesh size of the equivalent radial coordinate ξ affect the accuracy of the numerical computation results more than changes in the mesh size of the angular coordinate η.

REFERENCES

1. De Lima, A. G. B. and S. A. Nebra, "Theoretical analysis of the diffusion process inside prolate spheroidal solids," *Journal of Drying Technology*, Vol. 18, No. 1 & 2, 21–48, 2000.

2. Ricciardi, G. F. and W. L. Stutzman, "A near-field to far-field transformation for spheroidal geometry utilizing an eigenfunctions expansion," *IEEE Trans. Antennas and Propagation*, Vol. 52, No. 12, 3337–3349, Dec. 2004.

3. Moon, P. and D. E. Spencer, *Field Theory Handbook including Coordinate Systems, Differential Equations and their Solutions*, 2nd Edition, 1–31, Springer-Verlag, New York, 1971.

4. Hodge, D. B., "Eigenvalues and eigenfunctions of the spheroidal wave equation," *Journal of Mathematical Physics*, Vol. 11, No. 8, 2308–2312, Aug. 1970.

5. Li, L.-W., M.-S. Leong, T.-S. Yeo, and Y.-B. Gan, "Electromagnetic radiation from a prolate spheroidal antenna enclosed in a confocal spheroidal radome," *IEEE Trans. Antennas and Propagation*, Vol. 50, No. 11, 1525–2402, Nov. 2002.

6. Adams, R. C. and P. M. Hansen, "Evaluation of the quality factor of an electrically small antenna in spheroidal coordinates," *IEEE Int. Symposium on Antennas and Propagation*, 6001–6002, 2007.

7. Sadiku, M. N. O., *Elements of Electromagnetics*, 4th Edition, 740–748, Oxford University Press, New York, 2007.

8. Momoh, O. D., M. N. O. Sadiku, and C. M. Akujuobi, "Analytical and numerical computations of prolate spheroidal shell capacitance," *Microwave and Optical Technology Letters*, Vol. 51, No. 10, 2361–2365, Oct. 2009.

9. Grabner, P., "Electrostatic attitudes of a frequent ophthalmologic bioimplants," *Proc. Int. ISEM Symp. Nonlinear Electromagnetic Systems*, A. J. Moses and A. Basak (Eds.), 358–361, IOS Press, Cardiff, Wales, UK, Sep. 1996.

10. Kuhlman, K. L., "Laplace transform analytic element method for transient groundwater flow simulation," 85–94, Ph.D. Dissertation, Dept. Hydrology & Water resources, Univ., Arizona, 2008, unpublished.

11. Davey, K. R. and M. B. Nair, "A Monte Carlo technique for eddy current problems," *IEEE Trans. Magnetics*, Vol. 29, No. 2, 1376–1379, March 1993.

12. Sadiku, M. N. O., C. M. Akujuobi, S. M. Musa, and S. R. Nelatury, "Monte Carlo analysis of time-dependent cylindrical problems," *Proc. IEEE Southeastcon*, 778–782, Mar. 2007.

13. Sadiku, M. N. O., S. O. Ajose, and Z. Fu, "Applying the exodus method to solve Poisson's equation," *IEEE Trans. Microwave Theory and Tech.*, Vol. 42, No. 4, 661–666, 1994.

14. Sadiku, M. N. O. and C. N. Obiozor, "A comparison of finite difference time-domain (FDTD) and transmission-line modeling (TLM) methods," *Proc. IEEE Southeastcon*, 19–22, Apr. 2000.

15. Sadiku, M. N. O. and F. A. Peterson, "A comparison of numerical methods for computing electromagnetic fields," *Proc. IEEE Southeastcon*, Vol. 1, 42–47, Apr. 1990.

16. Hoole, S. R., "Finite element electromagnetic field computation on sequent symmetry 81 parallel computer," *IEEE Trans. Magnetics*, Vol. 26, No. 2, 837–840, Mar. 1990.

17. Li, L.-W., M.-S. Yeo, and M.-S. Leong, "Method of moment analysis of EM fields in a multilayered spheroids radiated by a thin circular loop antenna," *IEEE Trans. Antennas and Propagation*, Vol. 52, No. 9, 2391–2401, Sep. 2004.

18. Sadiku, M. N. O., C. M. Akujuobi, and R. C. Garcia, "An introduction to wavelets in electromagnetics," *IEEE Microwave Magazine*, Vol. 6, No. 2, 63–72, Jun. 2005.

19. Myland, J. C. and K. B. Oldham, "Modeling diffusion to a disk electrode by fully explicit simulation," *Journal of Electroanalytical Chemistry*, Vol. 576, 353–362, 2005.

20. Eide, H. A., et al., "New method for computing expansion coefficients for spheroidal functions," *Journal of Quantitative Spectroscopy & Radiative Transfer*, Vol. 63, 191–203, 1999.

21. Grabner, P., "Electrostatic attitudes of a frequent ophthalmologic bioimplants," *Proc. Int. ISEM Symp. Nonlinear Electromagnetic Systems*, A. J. Moses and A. Basak (Eds.), 358–361, IOS Press, Cardiff, Wales, UK, Sep. 1996.

22. Spanier, J. and K. B. Oldham, *An Atlas of Functions*, Section 33, No. 14, 317–318, Hemisphere and Springer-Verlag, New York and Berlin, 1987.

Guided and Leaky Modes of Planar Waveguides: Computation via High Order Finite Elements and Iterative Methods

D. Stowell and J. Tausch

Southern Methodist University, USA

Abstract— Guided and leaky modes of planar dielectric waveguides are eigensolutions of a singular Sturm-Liouville problem. This paper describes how this problem can be transformed into a quartic eigenvalue problem, which in turn can be converted into a generalized eigenvalue problem. Thus standard iterative methods, such as Arnoldi methods, can be used to compute the spectrum. We show how the shifts in the Arnoldi methods must be selected to obtain convergence to the dominant modes. In addition, by using high-order finite elements, the resulting solutions can be made extremely accurate. Numerical examples demonstrate the speed and accuracy as well as the stability of the method.

1. INTRODUCTION

It is easy to characterize the modes of planar dielectric waveguides by an algebraic equation. There are numerous papers that discuss numerical methods that are based on finding the roots of the characteristic function, either by using the argument principle of complex analysis [1–3, 11], or by a continuation method [7]. However, the numerical solution of the equation suffers from numerical instabilities which are caused by the exponential scaling of the characteristic function. It is well known that for this reason the standard methods are often unreliable especially if there are many or thick layers present, if the frequency is large or if there are lossy layers, see, e.g., [5, 9, 12].

In [12], we presented a new variational formulation of the Sturm-Liouville problem that characterizes the guided and leaky modes. After discretization, the variational form reduces to either a quadratic or a quartic matrix eigenvalue problem. Solving the eigenvalue problem is numerically stable, even for waveguides with thick layers or arbitrary index profiles. In [12], we used a low-order discretization scheme and solved the eigenvalue problem by a direct method. This demonstrated the general feasibility of the approach, but the convergence of the higher-order modes is slow and the high cost of the numerical linear algebra limits the applicability to relatively simple structures.

In the present paper we address the slow convergence problem by using piecewise high-order polynomial finite elements. Furthermore, we employ an iterative eigensolver that is capable to exploit the sparseness of the finite-element matrices. To ensure that an iterative method converges to a specific eigenvalue one has to shift the problem such that the selected eigenvalue is dominant. We will present a strategy for selecting the shift such that all dominant guided and leaky modes are found. We will conclude with some numerical results that demonstrate the usefulness of our improved method.

2. VARIATIONAL FORMULATION

In this section, we briefly review the derivation of the variational formulation that characterizes the modes of a dielectric waveguide. For more details we refer to [12].

We consider an infinite medium where the refractive index $n(x) = \sqrt{\epsilon(x)\mu}$ is a function of x and we let z be the direction of propagation. In this case the modes are of the form $\mathbf{E}(x, z, t) = \exp(-i\omega t + i\beta z)\phi(x)\hat{\mathbf{y}}$ (TE wave) or $\mathbf{H}(x, z, t) = \exp(-i\omega t + i\beta z)\phi(x)\hat{\mathbf{y}}$ (TM wave). To simplify notations we only discuss the TE waves, as the treatment of TM waves is completely analogous and can be found in [12]. The lateral dependence of the mode is given by the function ϕ which satisfies

$$\phi''(x) + \left(k^2 n^2(x) - \beta^2\right)\phi(x) = 0, \quad x \in \mathbb{R}, \tag{1}$$

see, e.g., [8]. Equation (1) is a singular Sturm-Liouville problem, where the propagation constant β is the unknown eigenvalue. The spectrum consists of a discrete part, corresponding to guided modes, and a continuous part, corresponding to radiation modes. There is a third type of eigensolution, known as leaky modes. These are unbounded solutions of (1) that radiate energy away from the stack. For more information on leaky modes in planar waveguides we refer to the recently published survey articles [6] and [13].

The refractive index $n(x)$ is a piecewise constant function with discontinuities at $x_0, \ldots, x_J$ and function value $n(x) = n_j$ in the j-th layer. It follows that a mode has the general form

$$\phi(x) = \begin{cases} \exp(i\alpha_0 x)\phi(x_0), & x \leq x_0 \\ \cos(\alpha_j(x - x_j))\phi(x_j) + \sin(\alpha_j(x - x_j))/\alpha_j\phi'(x_j), & x_j \leq x \leq x_{j+1}, \\ \exp(-i\alpha_J(x - w))\phi(x_J), & x \leq x_J, \end{cases} \quad (2)$$

where α_j is the lateral propagation constant given by $\alpha_j = \sqrt{k^2 n_j^2 - \beta^2}$.

By considering the exponential form of ϕ in the semi-infinite layers, it follows that the modes are solutions of the non-standard Sturm-Liouville problem

$$\phi''(x) + \left(k^2 n^2(x) - \beta^2\right)\phi(x) = 0, \quad x \in (0, w), \quad (3)$$

$$\phi'(x_0) - i\alpha_0\phi(x_0) = 0, \quad (4)$$

$$\phi'(x_J) + i\alpha_J\phi(x_J) = 0. \quad (5)$$

To derive the variational formulation, we first multiply (3) by a test function, use integration by parts and apply the boundary conditions (4), (5) to obtain

$$-\int_0^{x_J} \bar{\psi}'\phi' + \int_0^{x_J} \left(k^2 n^2 - \beta^2\right)\bar{\psi}\phi - i\alpha_J\bar{\psi}(x_J)\phi(w) - i\alpha_0\bar{\psi}(x_0)\phi(x_0) = 0 \quad (6)$$

Conceivably, one could discretize (6). However, the result would be a nonlinear eigenvalue problem. We circumvent this problem by making use of the change of variable suggested by [10].

$$\zeta = \frac{1}{2i}\left(\sqrt{k^2 n_0^2 - \beta^2} + \sqrt{k^2 n_J^2 - \beta^2}\right). \quad (7)$$

A bit of algebra reveals that

$$\alpha_0 = i\left(\frac{\delta^2}{4\zeta} + \zeta\right) \quad \text{and} \quad \alpha_J = i\left(\frac{\delta^2}{4\zeta} - \zeta\right) \quad (8)$$

where $\delta^2 = k^2 n_J^2 - k^2 n_0^2$. From the definitions of α_0, α_J we have

$$\beta^2 = \frac{k^2(n_0^2 + n_J^2)}{2} - \frac{\alpha_0^2 + \alpha_J^2}{2}. \quad (9)$$

If we let $q(x) = k^2\left[n^2(x) - \frac{1}{2}(n_0^2 + n_J^2)\right]$, we can introduce the bilinear forms

$$a(\psi, \phi) = \int_0^{x_J} \bar{\psi}'\phi' - q\bar{\psi}\phi, \quad (10)$$

$$a^\pm(\psi, \phi) = \bar{\psi}(x_J)\phi(x_J) \pm \bar{\psi}(x_0)\phi(x_0). \quad (11)$$

with these notations the variational formulation of (3) is: Find ζ and ϕ such that for all test functions ψ

$$\frac{\delta^4}{16}(\psi, \phi) + \zeta\frac{\delta^2}{4}a^-(\psi, \phi) + \zeta^2 a(\psi, \phi) + \zeta^3 a^+(\psi, \phi) + \zeta^4(\psi, \phi) = 0 \quad (12)$$

holds. This is a quartic eigenvalue problem in the variable ζ. Once the eigenvalues ζ have been found, β and be recovered using (8) and (9). If the refractive indices in the semi-infinite layers are equal, then $\delta^2 = 0$ and (12) reduces to the quadratic eigenvalue problem.

$$a(\psi, \phi) + \zeta a^+(\psi, \phi) + \zeta^2(\psi, \phi) = 0. \quad (13)$$

3. DISCRETIZATION AND IMPLEMENTATION

A discretization of (12) or (13) can be obtained by letting the trial and test function be restricted to a finite dimensional subspace span $[\varphi_1, \ldots \varphi_n]$. This yields the quartic matrix eigenvalue problem: find ζ such that

$$A_0 + \zeta A_1 + \zeta^2 A_2 + \zeta^3 A_3 + \zeta^4 A_4 \quad (14)$$

is singular. We note these matrices are sparse, since from (11)

$$A_1 = \frac{\delta^2}{4}\text{diag}(-1, 0, \ldots, 0, 1), \quad A_3 = \text{diag}(1, 0, \ldots, 0, 1), \tag{15}$$

and from (10)

$$A_0(i, j) = \frac{\delta^4}{16}(\varphi_i, \varphi_j), \quad A_2(i, j) = (\varphi_i', \varphi_j') - (q\varphi_i, \varphi_j), \quad A_4(i, j) = (\varphi_i, \varphi_j). \tag{16}$$

By using the companion matrix, the quartic eigenvalue problem is converted into an equivalent generalized eigenvalue problem $Ax = \zeta Bx$, where

$$A = \begin{bmatrix} & I & & \\ & & I & \\ & & & I \\ -A_0 & -A_1 & -A_2 & -A_3 \end{bmatrix} \quad \text{and} \quad B = \begin{bmatrix} I & & & \\ & I & & \\ & & I & \\ & & & A_4 \end{bmatrix}. \tag{17}$$

Since the matrices involved are sparse and large, the problem is ideally suited for solution by an iterative method. Iterative methods converge to eigenvalues near the extremes of the spectrum. However, by introducing the shift σ, (17) can be transformed to the equivalent shifted problem

$$Bx = \frac{1}{\lambda - \sigma}(A - \sigma B)x. \tag{18}$$

An iterative method applied to (18) will produce approximations that converge to the eigenvalues near σ. By determining where the eigenvalues of interest are found in the complex ζ-plane we can find a good choice of σ.

It is known that the eigenvalues of (12) accumulate at $\zeta = 0$ and $\zeta = \pm i\infty$, see [13]. The ζ's near the accumulation points are not of interest because they lead to a large value of β. The condition for a guided mode is that α_0 and α_J are purely imaginary and negative for exponential decay of the mode in the semi-infinite layers. From (8) it follows that the corresponding ζ-values are real and satisfy $\zeta > \delta/2$.

The leaky modes have complex β and hence complex ζ. However, not every complex solution of (12) will be a leaky modes. Whether a complex mode is leaky or non-physical depends on the following conditions. For substrate leaky modes $kn_J < \text{Re}(\beta) < kn_0$. For full leaky modes β satisfies $\text{Re}(\beta) < kn_J$. See, [4, 8]. These conditions restrict the eigenvalue search to certain portions of the complex ζ plane. Such regions are depicted in Figure 1. The region labeled R_1 is the search region for the guided modes. R_2 is the region for the substrate leaky modes, and R_3 is where eigenvalues associated with full leaky modes are to be found. The circle is of radius $\frac{\delta}{2}$,
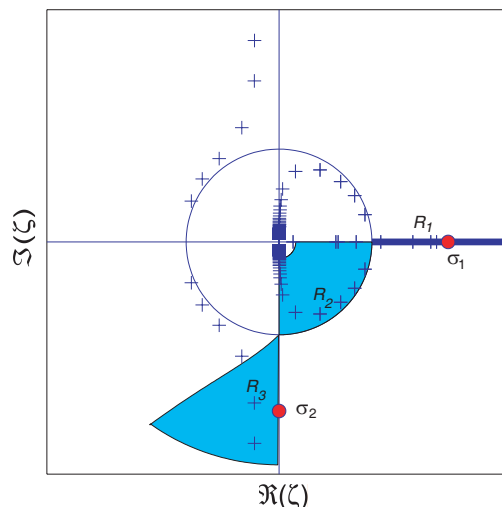

Figure 1: Eigenvalue distribution for a typical quartic eigenvalue problem. Also shown are the search regions in the complex plane as well as a choice of shifts for the eigenvalue problem.

where δ is defined in the previous section. The outer boundary of R_3 is given as a parameter, and allows the search to find all modes up to a given order. The inner boundary of R_2 is also given as a parameter. The appropriate shifts can be chosen using an understanding of these regions.

There are two important considerations in the choice of σ. First, we want to ensure that we find all dominant modes. Second, we want to avoid the accumulation point(s). One way to accomplish these objectives is to use two shifts, σ_1 and σ_2, and execute two searches. The first search will begin in R_1 and will include a portion of R_2. The second will begin in R_3 and will also include a portion of R_2. The search is complete when the union of the searches covers all three regions. To choose σ_1, use that fact that guided modes satisfy $kn_0 < \beta < kn_{\max}$. We have found a good choice of σ_1 to be the value of ζ that corresponds with $\beta = kn_{\max}$. By (8) and (9), this gives

$\sigma_1 = \sqrt{-B + \sqrt{B^2 - \frac{\delta^4}{4}}}$ where $B = \frac{k^2(n_0^2+n_J^2)}{2} - k^2 n_{\max}^2$. Then, let $\sigma_2 = -i\sigma_1$. See Figure 1.

We conclude with two comments. Generally speaking, the eigenvalues of interest in R_2 are found near the outer radius. The inner radius can then be enlarged, if needed. If there is a question as to whether some propagation constants were missed in the search, the inner radius can be adjusted accordingly and the search run again. Finally, for the quadratic eigenvalue problem, since $\delta = 0$, the outer radius of R_2 shrinks to zero, there are no accumulation points, and therefore, the search is simplified.

4. NUMERICAL RESULTS

We demonstrate our method on the waveguide structure with the following parameters (w_j denotes the width of the jth layer):

$$n_0 = 1.5, \ n_1 = 1.66, \ n_2 = 1.6, \ n_3 = 1.53, \ n_4 = 1.6, \ n_5 = 1.0$$
$$w_1 = w_2 = w_3 = w_4 = .5, \quad k = 9.92918$$

This structure has been studied in the literature [7]. In this case, since the characteristic function is stable, the propagation constants can be found using Newton's method. These values will be used for testing the method.

We have implemented our method using polynomial bases of degrees 1, 2 and 4. For the interpolation nodes on each element, the Lobatto nodes are chosen. The computed eigenvalues are then compared with the known values.
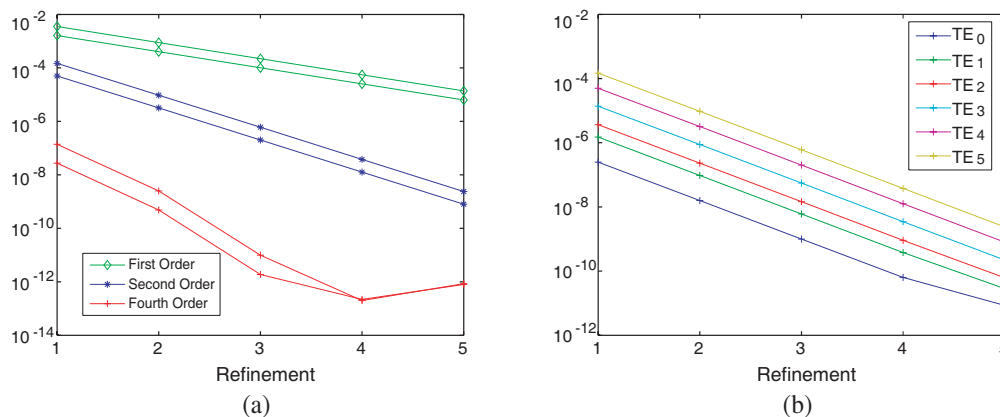

Figure 2: Convergence results. The FE computed eigenvalues are compared with known, exact values. (a) Convergence results using piecewise polynomial basis functions of degrees one, two and four. (b) Convergence results for the first six modes. In this experiment, piecewise-quadratic polynomials were used for the basis functions.

In the first experiment, we compare the convergence for different values of p. Figure 2(a) shows the convergence of TE_4 and TE_5 for $p = 1, 2, 4$. The experiment is designed so that at each step the matrices are of the same size for each order. For example, to begin, we have $p = 1$, $n_e = 40$, $p = 2$, $n_e = 20$, and $p = 4$, $n_e = 10$. The number of elements is doubled at each refinement.

Figure 2(b) shows results from he second experiment. Here we demonstrate the convergence of the first six eigenvalues of the same structure for $p = 2$.

5. CONCLUSION

We have derived a method which is numerically stable and is able to compute all modes up to a given order. Since the discretized version is a polynomial eigenvalue problem, there is no need for a priori knowledge of the location of the modes in the complex plane. However, the physical properties of the modes can be used, in conjunction with an iterative method, to find the eigenvalues quickly and accurately.

ACKNOWLEDGMENT

REFERENCES

1. Anemogiannis, E. and E. N. Glytsis, "Mutlilayer waveguides: Efficient numerical analysis of general structures," *J. of Lightwave Tech.*, Vol. 10, 1344–1351, 1992.
2. Anemogiannis, E., E. N. Glytsis, and T. K. Gaylord, "Determination of guided and leaky modes in lossless and lossy planar multilayer optical waveguides: Reflection pole method and wavevector density method," *J. of Lightwave Tech.*, Vol. 17, 929–941, 1999.
3. Chen, C., P. Berini, D. Feng, S. Tanev, and V. Tzolov, "Efficient and accurate numerical analysis of multilayer planar optical waveguides in lossy anisotropic media," *Optics Express*, Vol. 7, No. 8, 260–272, 2000.
4. Chilwell, J. and I. Hodgkinson, "Thin-film field-transfer matrix theory of planar multilayer waveguides and reflection from prism-loaded waveguides," *J. Opt. Soc. Amer. A*, Vol. 1, No. 7, 742–753, 1984.
5. Hsueh, W. and J. Lin, "Stable and accurate method for modal analysis of multilayer waveguieds using a graph approach," *J. Opt. Soc. Amer. A*, Vol. 24, 825–830, 2007.
6. Hu, J. and C. R. Menyuk, "Understanding leaky modes: Slab waveguide revisited," *Advances in Optics*, Vol. 1, No. 1, 58–106, 2009.
7. Petracek, J. and K. Singh, "Determination of leaky modes in planar multilayer waveguides," *IEEE Photonics Tech. Letters*, Vol. 14, No. 6, 810–812, 2002.
8. Marcuse, D., *Theory of Dielectric Optical Waveguides*, Academic Press, New York and London, 1974.
9. Mehrany, K. and R. Rashidian, "Polynomial expansion for extraction of electromagnetic eigenmodes in layered structures," *J. Opt. Soc. Amer. B*, Vol. 20, 2434–2441, 2003.
10. Smith, R. E., G. W. Forbes, and S. N. Houde-Walter, "Unfolding the multivalued planar waveguide dispersion relation," *IEEE J. Quantum Elect.*, Vol. 29, No. 4, 1031–1034, 1993.
11. Smith, R. E., S. N. Houde-Walter, and G. W. Forbes, "Mode determination for planar waveguides using the four-sheeted dispersion relation, *IEEE J. Quantum Elect.*, Vol. 28, No. 6, 1520–1526, 1992.
12. Stowell, D. and J. Tausch, "Variational formulation for guided and leaky modes in multilayer dielectric waveguides," Technical Report, Southern Methodist University, 2009.
13. Tausch, J., "Mathematical and numerical techniques for open periodic waveguides," *Wave Propagation in Periodic Media — Analysis, Numerical Techniques and Practical Applications*, In M. Ehrhardt, Editor, 51–74, Bentham, 2009.

A Closed Form Solution for Longitudinally Inhomogeneous Waveguides

Mohammad Khalaj-Amirhosseini

College of Electrical Engineering, Iran University of Science and Technology, Tehran, Iran

Abstract— A closed form analytic solution is introduced for arbitrary Longitudinally Inhomogeneous Waveguides (LIWs). First, the differential equations of LIWs are written as a suitable matrix differential equation. Then, the matrix differential equation is solved to obtain the chain parameter matrix of LIWs. Afterward, the electric and magnetic fields at any point and also the scattering parameters are obtained using the chain parameter matrix. The validation of the introduced solution is studied, finally.

1. INTRODUCTION

Longitudinally Inhomogeneous Waveguides (LIWs) can be used in microwaves as phase changers, matching transformers and filters [1–3], especially for high power applications. The differential equations describing LIWs have non-constant coefficients and so except for a few special cases no analytical solution exists for them. There are some methods to analyze the LIWs such as cascading many thin layers [4], finite difference [5], Taylor's series expansion [6], Fourier series expansion [7], the method of Moments [8], the equivalent sources [9] and equivalent circuit method [10]. All of these methods are numerical and do not yield a closed form analytic solutions. However, in this paper, a closed-form analytic solution is introduced for arbitrary LIWs. First, the differential equations of LIWs are written as a suitable matrix differential equation. Then, the matrix differential equation is solved to obtain the chain parameter matrix of LIWs. The obtained solution is applicable to arbitrary lossy and lossless LIWs. The validation of the introduced solution is studied using two comprehensive examples.

2. THE EQUATIONS OF LIWS

Figure 1 shows a typical LIW with dimensions a and b, filled by an inhomogeneous lossy dielectric with complex electric permittivity distribution $\varepsilon_r(z)$ and length d. It is assumed that a TE$_{10}$ mode with electric filed strength E^i propagates towards the positive z direction. The differential equations describing LIWs are given by

$$\frac{dE_y(z)}{dz} = j\omega\mu_0 H_x(z) \tag{1}$$

$$\frac{dH_x(z)}{dz} = j\omega\varepsilon_0 \left(\varepsilon_r(z) - (f_c/f)^2\right) E_y(z) \tag{2}$$

where f_c is the cutoff frequency of the hollow waveguide. Furthermore, the terminal conditions for LIWs are as follows

$$E_y(0) - Z_S H_x(0) = 2E^i \tag{3}$$
$$E_y(d) + Z_L H_x(d) = 0 \tag{4}$$

where

$$Z_S = Z_L = Z_{TE} = \begin{cases} \frac{\eta_0}{\sqrt{1-(f_c/f)^2}}, & f > f_c \\ j\frac{\eta_0}{\sqrt{(f_c/f)^2-1}}, & f < f_c \end{cases} \tag{5}$$

is the waveguide impedance, in which $\eta_0 = \sqrt{\mu_0/\varepsilon_0}$ is the wave impedance of the free space. It is known that the electric and magnetic fields of any arbitrary point z can be related to those of the point $z = 0$ by a chain parameter matrix as follows

$$\begin{bmatrix} E_y(z) \\ -H_x(z) \end{bmatrix} = \boldsymbol{\Phi}(z) \begin{bmatrix} E_y(0) \\ -H_x(0) \end{bmatrix} \tag{6}$$
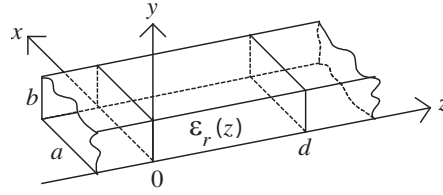
Figure 1: A typical LIW.

The chain parameter matrix of the point $z = d$ can be used to find the S parameters using (3)–(6), as follows

$$S_{11} = \frac{-\mathbf{\Phi}(1,1)Z_{TE} - \mathbf{\Phi}(1,2) + \mathbf{\Phi}(2,1)Z_{TE}^2 + \mathbf{\Phi}(2,2)Z_{TE}}{\mathbf{\Phi}(1,1)Z_{TE} - \mathbf{\Phi}(1,2) - \mathbf{\Phi}(2,1)Z_{TE}^2 + \mathbf{\Phi}(2,2)Z_{TE}} \tag{7}$$

$$S_{21} = S_{12} = \frac{2Z_{TE}}{\mathbf{\Phi}(1,1)Z_{TE} - \mathbf{\Phi}(1,2) - \mathbf{\Phi}(2,1)Z_{TE}^2 + \mathbf{\Phi}(2,2)Z_{TE}} \tag{8}$$

$$S_{22} = \frac{\mathbf{\Phi}(1,1)Z_{TE} - \mathbf{\Phi}(1,2) + \mathbf{\Phi}(2,1)Z_{TE}^2 - \mathbf{\Phi}(2,2)Z_{TE}}{\mathbf{\Phi}(1,1)Z_{TE} - \mathbf{\Phi}(1,2) - \mathbf{\Phi}(2,1)Z_{TE}^2 + \mathbf{\Phi}(2,2)Z_{TE}} \tag{9}$$

3. ANALYTIC SOLUTION OF LIWS

In this section, an approach is proposed to solve the differential equations of LIWs, analytically. First, we define the distributed secondary parameters of LIWs (the waveguide impedance and the propagation coefficient) as follows

$$Z_g(z) = \frac{\eta_0}{\sqrt{\varepsilon_r(z) - (f_c/f)^2}} \tag{10}$$

$$\gamma(z) = j\frac{\omega}{c}\sqrt{\varepsilon_r(z) - (f_c/f)^2} \tag{11}$$

Then, we transform the set of differential Equations (1), (2) to the following ones

$$\frac{d\bar{E}_y(z)}{dz} = -\frac{1}{Z_g(z)}\frac{dZ_g(z)}{dz}\bar{E}_y(z) + \gamma(z)H_x(z) \tag{12}$$

$$\frac{dH_x(z)}{dz} = \gamma(z)\bar{E}_y(z) \tag{13}$$

where

$$\bar{E}_y(z) = \frac{1}{Z_g(z)}E_y(z) \tag{14}$$

is defined as the normalized electric field. Now, the set of differential Equations (12), (13), can be written as the following matrix differential equation

$$\frac{d}{dz}\mathbf{X}(z) = -\mathbf{A}(z)\mathbf{X}(z) \tag{15}$$

where

$$\mathbf{X}(z) = \begin{bmatrix} \bar{E}_y(z) & \bar{E}_y(z) \\ -H_x(z) & -H_x(z) \end{bmatrix} \tag{16}$$

and

$$\mathbf{A}(z) = \begin{bmatrix} \frac{1}{Z_g(z)}\frac{dZ_g(z)}{dz} & \gamma(z) \\ \gamma(z) & 0 \end{bmatrix} \tag{17}$$

From the matrix algebra and using (15), we can write the following

$$d\mathbf{X}(z)\mathbf{X}^{-1}(z) \cong d\left(\ln(\mathbf{X}(z))\right) = -\mathbf{A}(z)dz \tag{18}$$

Integrating (18) gives us the following

$$\ln(\mathbf{X}(z)) - \ln(\mathbf{X}(0)) \cong \ln\left(\mathbf{X}(z)\mathbf{X}^{-1}(0)\right) = -\int_0^z \mathbf{A}(z')dz' \tag{19}$$

Therefore, one can determine the following solution for the unknown matrix in (15).

$$\mathbf{X}(z) = \exp\left(-\int_0^z \mathbf{A}(z')dz'\right)\mathbf{X}(0) = \mathbf{\Phi}(z)\mathbf{X}(0) \tag{20}$$

The approximations used in (18) and (19) are dependent to the matrix $\mathbf{A}(z)$ and its integral. From (14), (16) and (20), the following closed form analytic solution is obtained as the chain parameter matrix of LIWs.

$$\mathbf{\Phi}(z) = \begin{bmatrix} Z_g(z) & 0 \\ 0 & 1 \end{bmatrix} \exp\left(-\int_0^z \mathbf{A}(z')dz'\right) \begin{bmatrix} 1/Z_g(0) & 0 \\ 0 & 1 \end{bmatrix}$$

$$= \begin{bmatrix} Z_g(z) & 0 \\ 0 & 1 \end{bmatrix} \exp\left(-\begin{bmatrix} \ln\left(Z_g(z)/Z_g(0)\right) & \int_0^z \gamma(z')dz' \\ \int_0^z \gamma(z')dz' & 0 \end{bmatrix}\right) \times \begin{bmatrix} 1/Z_g(0) & 0 \\ 0 & 1 \end{bmatrix} \tag{21}$$

The electric and magnetic fields at any point z can be obtained after finding those at the surfaces using the chain parameter matrix of the point $z = d$ and the boundary conditions. The proposed approach to solve the matrix differential Equation (15) is inspired of the approach that is usually used to solve ordinary scalar differential equations, indeed.

4. EXAMPLE AND RESULTS

In this section, the introduced explicit analytic solution is validated using two comprehensive examples. Consider a WRG-90 waveguide ($a = 0.9$ inch and $b = 0.4$ inch) filled by an exponential dielectric with the following electric permittivity function

$$\varepsilon_r(z) = \varepsilon_{r0}\exp(kz/d) \tag{22}$$

This exponential LIW has the following distributed secondary parameters.

$$Z_g(z) = \frac{\eta_0}{\sqrt{\varepsilon_{r0}\exp(kz/d) - (f_c/f)^2}} \tag{23}$$

$$\gamma(z) = j\beta(z) = j\frac{\omega}{c}\sqrt{\varepsilon_{r0}\exp(kz/d) - (f_c/f)^2} \tag{24}$$

Also, the matrix $\mathbf{A}(z)$ of this LIW will be as follows

$$\mathbf{A}(z) = \begin{bmatrix} -\frac{k}{2d}\frac{\varepsilon_{r0}\exp(kz/d)}{\varepsilon_{r0}\exp(kz/d)-(f_c/f)^2} & j\frac{\omega}{c}\sqrt{\varepsilon_{r0}\exp(kz/d)-(f_c/f)^2} \\ j\frac{\omega}{c}\sqrt{\varepsilon_{r0}\exp(kz/d)-(f_c/f)^2} & 0 \end{bmatrix} \tag{25}$$

Therefore, the chain parameter matrix of this LIW will be given by

$$\mathbf{\Phi}(z) = \begin{bmatrix} \frac{\eta_0}{\sqrt{\varepsilon_{r0}\exp(kz/d)-(f_c/f)^2}} & 0 \\ 0 & 1 \end{bmatrix}$$

$$\times \exp\left(-\begin{bmatrix} \ln\left(\frac{\sqrt{\varepsilon_{r0}-(f_c/f)^2}}{\sqrt{\varepsilon_{r0}\exp(kz/d)-(f_c/f)^2}}\right) & G(z) - G(0) \\ G(z) - G(0) & 0 \end{bmatrix}\right) \times \begin{bmatrix} \frac{\sqrt{\varepsilon_{r0}-(f_c/f)^2}}{\eta_0} & 0 \\ 0 & 1 \end{bmatrix} \tag{26}$$

where

$$G(z) = j2\frac{\omega}{c}\frac{d}{k}\left(\sqrt{\varepsilon_{r0}\exp(kz/d)-(f_c/f)^2} - \frac{f_c}{f}\tan^{-1}\left(\frac{f}{f_c}\sqrt{\varepsilon_{r0}\exp(kz/d)-(f_c/f)^2}\right)\right) \tag{27}$$

Now, assume that $\varepsilon_{r0} = 1 - j0$ and $d = 2\,\mathrm{cm}$. A TE_{10} mode wave with the electric field strength $E^i = 1.0\,\mathrm{V/m}$ propagates in the considered lossless LIW. Figures 2, 3, compare the amplitude and phase of the electric field distribution at frequency 10 GHz, obtained from the introduced solution with the exact ones [8-Appendix], considering $k = 1$ and 2. Also, Figures 4, 5, compare the amplitude of the scattering parameters S_{11} and S_{21}, obtained from the introduced solution with the exact ones against to the frequency. One sees that the introduced solution has a good agreement with the exact ones. It is seen that as k decreases, the accuracy of the solution is increased. Also, the error decreases and increases alternately with respect to frequency. According to the above examples, one may be conclude that the accuracy of the introduced solution is increased as the variation of the electric permittivity distribution (k/d in the examples) is decreased. Mathematically, as the diagonal elements of the integral of the matrix $\mathbf{A}(z)$ tend to zero with respect to its anti-diagonal elements, the error is decreased. It is worth to mention that the determinant of the chain parameter matrices obtained in the above examples were exactly equal to one at all frequencies.
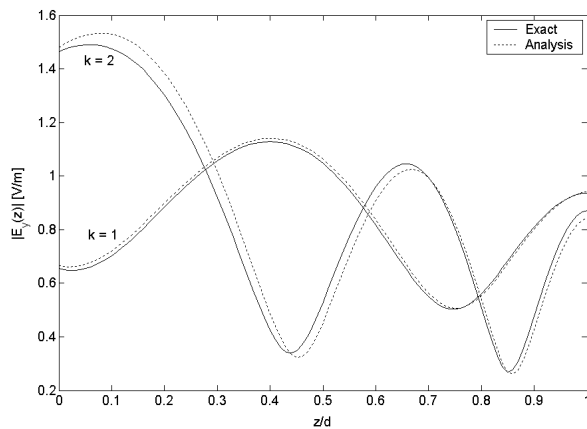

Figure 2: The amplitude of the electric field for exponential LIW at $f = 10$ GHz.
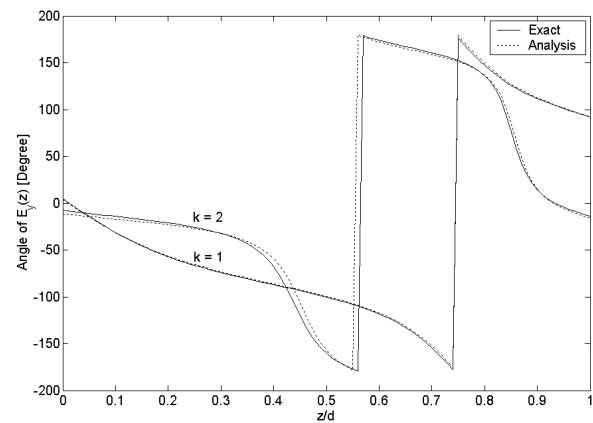

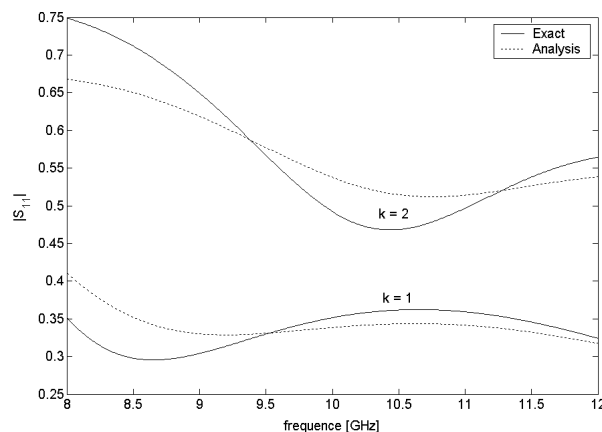Figure 3: The phase of the electric field for exponential LIW at $f = 10$ GHz.

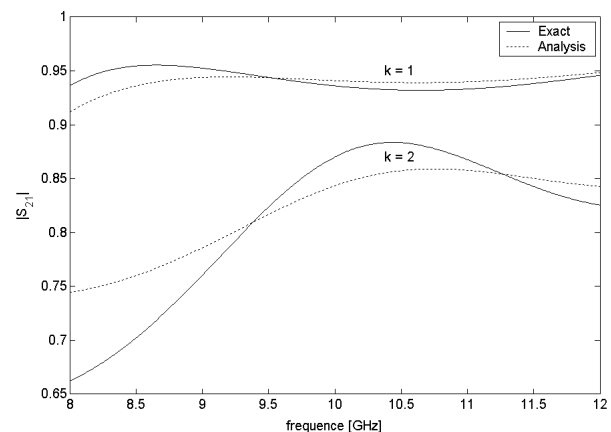Figure 4: The amplitude of the scattering parameter S_{11} for exponential LIW.

Figure 5: The amplitude of the scattering parameter S_{21} for exponential LIW.

5. CONCLUSIONS

A closed form analytic solution was introduced for arbitrary Longitudinally Inhomogeneous Waveguides (LIWs). First, the differential equations of LIWs are written as a suitable matrix differential equation. Then the matrix differential equation is solved to obtain the chain parameter matrix of LIWs. The validation of the introduced solution was studied using a comprehensive example. It was seen that the accuracy of the introduced solution is acceptable for arbitrary LIWs at all frequencies. Moreover, the accuracy of the introduced solution is increased as the variation of the

electric permittivity distribution is decreased. The introduced method can be extended for LIWs, whose magnetic permeability is inhomogeneous solely or along with their electric permittivity.

REFERENCES

1. Collin, R. E., *Field Theory of Guided Waves*, IEEE Press, New York, 1991.
2. Collin, R. E., *Foundations for Microwave Engineering*, McGraw-Hill, New York, 1996.
3. Khalaj-Amirhosseini, M., "Microwave filters using waveguides filled by multi-layer dielectric," *Progress In Electromagnetics Research*, PIER 66, 105–110, 2006.
4. Paul, C. R., *Analysis of Multiconductor Transmission Lines*, John Wiley and Sons Inc., 1994.
5. Khalaj-Amirhosseini, M., "Analysis of longitudinally inhomogeneous waveguides using finite difference method," *Int. Conf. on Inform. and Comm. Tech.: From Theory to Appl. (ICTTA 2006)*, 799–800, Damascus, Syria, Apr. 24–28, 2006.
6. Khalaj-Amirhosseini, M., "Analysis of longitudinally inhomogeneous waveguides using Taylor's series expansion," *Journal of Electromagnetic Waves and Applications*, Vol. 20, No. 8, 1093–1100, Aug. 2006.
7. Khalaj-Amirhosseini, M., "Analysis of longitudinally inhomogeneous waveguides using the Fourier series expansion," *Journal of Electromagnetic Waves and Applications*, Vol. 20, No. 10, 1299–1310, Oct. 2006.
8. Khalaj-Amirhosseini, M., "Analysis of longitudinally inhomogeneous waveguides using the method of moments," *Progress In Electromagnetics Research*, PIER 74, 57–67, 2007.
9. Khalaj-Amirhosseini, M., "Analysis of longitudinally inhomogeneous waveguides using equivalent sources method," *Asia-Pacific Microwave Conf. (APMC 2007)*, Bangkok, Thailand, Dec. 12–14, 2007.
10. Mei, Z. and F. Xu, "Analysis of longitudinally inhomogeneous rectangular waveguide using equivalent circuit method," *Int. Conf. Microwave and Millimeter Wave Technology (ICMMT 2007)*, Guilin, China, April 19–21, 2007.

Simulating Dispersive Left-handed Media with the TLM Method

Cédric Blanchard[1], Didier Felbacq[1], Brahim Guizal[1], Jorge Andrés Porti[2], and Rachid Talhi[3]

[1]Groupe d'Etude des Semi-Conducteurs, Université de Montpellier II, Montpellier, France
[2]Departamento de Física Aplicada, Universidad de Granada, Granada, Spain
[3]CNRS-UMR 6115, Université de Tours, Orléans, France

Abstract— In its conventional form, the Transmission Line Modeling method is not capable of accounting for media whose constitutive parameters are exotic. Permittivity and permeability less than unity can be reached by using a mesh that is the numerical counterpart of a dispersive left-handed transmission line network. In this communication, the dispersion thus introduced in a two-dimensional node is shown to follow a Drude profile. This property is verified on an example involving an infinite cylinder made up of metamaterial.

1. INTRODUCTION

The Transmission Line Modeling (TLM) method is a numerical time domain technique that was introduced by Johns in 1971 [1]. Since then, it has been successfully employed to solve many problems involving the propagation of waves for acoustic, diffusion and, especially, electromagnetic problems.

TLM exploits the analogy between Maxwell's equations and the equations of the transmission line theory. The electromagnetic medium to be simulated is discretized by an analogous mesh of interconnected transmission lines, while the electromagnetic wave is modeled by voltage and current pulses that propagate into such a network. A unitary cell of the mesh, called node, is defined as the intersection of constitutive transmission lines. At low frequency, a node can be understood in terms of lumped capacitors and inductors, i.e., a usual distributed L-C circuit.

Traditionally, in the TLM modeling of conventional materials, the optic constants are supposed to be non-dispersive as long as the wavelength λ is large enough compared to the size of the nodes. On the other hand, considering metamaterials, with exotic parameters, modifies this statement given that the nodes become dispersive in that case as shown by So and his colleagues in [2]. These authors adapted the fact that networks of left-handed transmission lines (with the position of L and C interchanged, i.e., series capacitances and shunt inductances) can support backward electromagnetic waves [3] to construct a TLM node capable of modeling metamaterials. Because of the special characteristics of TLM, it should be noted that modeling such metamaterials with this method is more than a simple extension to account for the negative values of the permittivity, ε, and permeability, μ, it is also a conceptual procedure that can be viewed as the numerical counterpart of what happens in a real left-handed transmission line network. This makes TLM an elegant approach to model metamaterials. This approach includes the assumption of a working frequency at which the required permittivity and permeability are adjusted; both are altered at any other value. As a result, the TLM node for metamaterials is a dispersive system, which means that there is no need to add artificial dispersion, as it is the case for other comparable methods (FDTD for instance). Controling the behavior of the simulated metamaterial in a given frequency range is fundamental; in this sense, it has been recently shown that the inherent dispersion is of Drude type [4] for the Symmetrical Condensed Node (SCN) [5] which is, hitherto, the most accurate and versatile node to study three-dimensional (3D) problems.

However, there is no need to use SCN for the study of two-dimensional (2D) problems as it increases the computational requirements. The less demanding 2D nodes should be preferred. The principal aim of this communication is to derive the dispersion associated with 2D nodes to show that it is also of Drude type. This result will be verified on an example involving the scattering of a dispersive left-handed cylinder that is illuminated by a plane wave.

Furthermore, in the usual TLM procedure, there is a certain degree of freedom in the election of the TLM numerical parameters, such as the impedance of the constitutive transmission lines of the nodes or the time-step. However, causality conditions may alter this statement if metamaterials are involved. In this communication, a particular emphasis will be placed on the restrictions imposed by these conditions.

2. TLM SIMULATION OF METAMATERIALS

Let us consider the 2D node for Transverse Electric (TE) mode [6]. If losses are disregarded, it is made up of 7 lines: 4 principal lines allow the propagation of the pulses into the mesh, 1 capacitive stub line accounts for ε_z, while 2 inductive stub lines account for μ_x and μ_y. The admittance of the capacitive stubs and the impedance of the inductive stubs take the form:

$$Y_z = \frac{2\varepsilon_z\varepsilon_0}{Y_0\Delta t}\frac{\Delta x\Delta y}{\Delta z} - 4, \quad Z_x = \frac{2\mu_x\mu_0}{Z_0\Delta t}\frac{\Delta y\Delta z}{\Delta x} - 2, \quad Z_y = \frac{2\mu_y\mu_0}{Z_0\Delta t}\frac{\Delta x\Delta z}{\Delta y} - 2. \tag{1}$$

In these expressions, Δt is the time-step; Y_0 and Z_0 are the characteristic admittance and impedance, respectively, of the principal lines; while Δx, Δy, and Δz are the dimensions of the node along the three Cartesian directions. An important condition to ensure stability is that the parameters of Eq. (1) must be positive.

Obviously, negative values for ε and μ render Y and Z negative, which means that the TE-node is unable to model left-handed media in its original form. However, by taking into account that a positive inductance L is equivalent to a negative capacitance $C = -1/\omega^2 L$, where $\omega = 2\pi f$ is a temporal frequency, it can be understood that these negative parameters can be easily modeled with TLM by interchanging the position of the inductive and capacitive stubs. As a consequence, the usual expression of the stubs must be modified. Concretely, the regions of space where $\varepsilon < 1$ and $\mu < 1$ must be discretized by using nodes for which Y and Z are given by [7]:

$$Y_z = -\frac{\Delta t^2\omega^2}{4}\left[\frac{2\varepsilon_z\varepsilon_0}{Y_0\Delta t}\frac{\Delta x\Delta y}{\Delta z} - 4\right], \; Z_x = -\frac{\Delta t^2\omega^2}{4}\left[\frac{2\mu_x\mu_0}{Z_0\Delta t}\frac{\Delta y\Delta z}{\Delta x} - 2\right], \; Z_y = -\frac{\Delta t^2\omega^2}{4}\left[\frac{2\mu_y\mu_0}{Z_0\Delta t}\frac{\Delta x\Delta z}{\Delta y} - 2\right]. \tag{2}$$

The unique difference between Eq. (1) and Eq. (2) is the presence of the negative factor $-\Delta t^2\omega^2/4$. Accordingly, if the parameters in Eq. (1) result to be negative, substituting them by the parameters of Eq. (2) make them positive, which again ensures stability. Furthermore, the fact that these values depend on the frequency means that this approach is valid only at one single frequency. As a result, the simulation of metamaterials with TLM requires the assumption of a functional frequency ω_0 at which the optic constants take the desired values.

3. SCATTERING BY A LOSSLESS LEFT-HANDED CYLINDER: EXACT SOLUTION

Let us now consider a plane wave incident upon a lossless cylinder — with radius $r = a$ — embedded into free space. The incoming wave is linearly polarized with the electric field $\bar{E}^i$ parallel to the axis $\hat{z}$ of the cylinder. The wavevector in free space $\bar{k}_0 = k_0\hat{x}$ is perpendicular to the axis of the cylinder. In cylindrical coordinates, $\{r, \varphi, z\}$, we have $\bar{E}^i = \hat{z}E_0\exp(-ik_0x)$. According to the usual procedure, the plane wave is transformed into a superposition of cylindrical waves that satisfy the Helmholtz wave equation in cylindrical coordinates, which leads to [8, 9]:

$$\bar{E}^i = \hat{z}E_0\sum_{n=-\infty}^{\infty} i^{-n}J_n(k_0r)\exp(in\varphi), \tag{3}$$

where J_n represents the Bessel function of the first kind.

In the presence of the lossless cylinder, the total field is the sum of the incident wave, given in Eq. (3), and the scattered wave. Expecting outward waves, the latter quantity can be written in terms of Hankel functions of the second kind

$$\bar{E}^s = \hat{z}E_0\sum_{n=-\infty}^{\infty} a_n H_n^{(2)}(k_0r)\exp(in\varphi), \tag{4}$$

where a_n represents the yet unknown amplitude coefficients. Note that the use of Hankel functions of the second kind means that the choice $e^{i\omega t}$, as time convention to denote the time-harmonic dependence, is assumed. The other representation, $e^{-i\omega t}$, would lead to the use of Hankel functions of the first kind.

Inside the cylinder, the stationary wave can be written as:

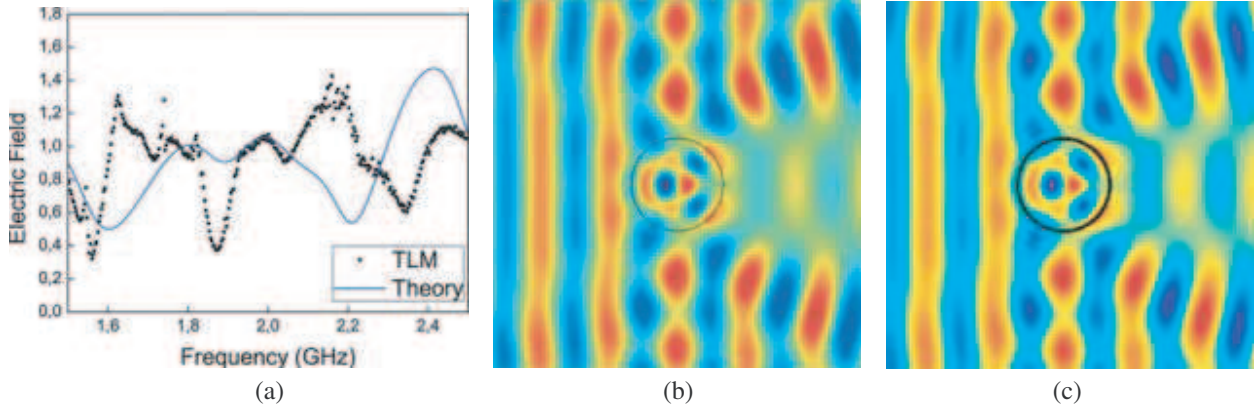$$\bar{E}^c = \hat{z}E_0\sum_{n=-\infty}^{\infty} [b_n J_n(kr) + c_n Y_n(kr)]\exp(in\varphi), \tag{5}$$

Figure 1: (a) Norm of the electric field in terms of the frequency. (b) TLM vs (c) COMSOL at $f = 2\,\text{GHz}$.

where Y_n, b_n, and c_n are the Bessel function of the second kind and the amplitude coefficients, respectively. The wave vector is given by $k = \omega\sqrt{\varepsilon\varepsilon_0\mu\mu_0}$.

The magnetic field $\bar{H}$ is obtained by using the Maxwell-Faraday equation $\nabla \times \bar{E} = -\frac{\partial}{\partial t}\bar{B}$, where $\bar{B} = \mu\mu_0\bar{H}$ is the magnetic flux density, which gives $H_r = -\frac{1}{i\omega\mu\mu_0}\frac{1}{r}\frac{\partial E_z}{\partial \varphi}$ and $H_\varphi = \frac{1}{i\omega\mu\mu_0}\frac{\partial E_z}{\partial r}$.

The unknown amplitude coefficients a_n, b_n, c_n can be found by applying the usual boundary conditions at the interface $r = a$, i.e., conservation of the (i) tangential component of $\bar{E}$, (ii) normal component of $\bar{B}$, and (iii) tangential component of $\bar{H}$ given that there is no surface current density. The result is

$$a_n = i^{-n}\frac{J_n(ka)J_n'(k_0a) - \sqrt{\frac{\varepsilon}{\mu}}J_n(k_0a)J_n'(ka)}{\sqrt{\frac{\varepsilon}{\mu}}H_n^{(2)}(k_0a)J_n'(ka) - H_n^{(2)'}(k_0a)J_n(ka)},$$

$$b_n = i^{-n}\frac{J_n(k_0a)H_n^{(2)'}(k_0a) - H_n^{(2)}(k_0a)J_n'(k_0a)}{H_n^{(2)'}(k_0a)J_n(ka) - \sqrt{\frac{\varepsilon}{\mu}}H_n^{(2)}(k_0a)J_n'(ka)}, \quad c_n = 0.$$

(6)

It is worth noting that the aforementioned series are slowly convergent when λ is not large compared to a.

Let us consider a left-handed cylinder whose constitutive parameters are $\varepsilon = -4$ and $\mu = -1$; accordingly, the refractive index is negative and can be expressed as $n = -\sqrt{\varepsilon\mu}$. By using Eq. (4), $\bar{E}_z(f)$ is calculated at $r = 4a$ and $\varphi = 0$. The result in the range 1.5–2.5 GHz is depicted in Fig. 1(a) (blue line).

The TLM simulation of $\bar{E}$ in terms of the frequency is plotted in Fig. 1(a) (black symbol). The functional frequency $f_0 = \omega_0/2\pi$ has been choosen to be $f_0 = 2\,\text{GHz}$ so that $\varepsilon(f_0) = -4$, and $\mu(f_0) = -1$. It is plain from Fig. 1(a) that the results match only at $f = f_0$. This was expected given the presence of the term ω in Eq. (2), which deviates ε and μ from their initial values by rendering them dispersive. For completion's sake, Figs. 1(b) and 1(c) offer a comparison between the $\bar{E}$-mapping obtained with TLM and with the software Comsol at $f = f_0$, which clearly evinces good agreement. The important remaining concern is to determine the kind of dispersion that is involved in the TE-node when metamaterials are under consideration.

4. DISPERSION OF THE TLM MESH

Let us consider the frequency dependent expressions given in Eq. (2). In practice, and as it has been pointed out in Section 2, a working frequency that defines $\varepsilon(\omega_0)$ and $\mu(\omega_0)$ must be previously chosen. In the numerical procedure, this definitively fixes the values of Y and Z to be

$$Y_z(\omega_0) = -\frac{\Delta t^2\omega_0^2}{4}\left[\frac{2\varepsilon_z(\omega_0)\varepsilon_0}{Y_0\Delta t}\frac{\Delta x\Delta y}{\Delta z} - 4\right], \quad Z_x(\omega_0) = -\frac{\Delta t^2\omega_0^2}{4}\left[\frac{2\mu_x(\omega_0)\mu_0}{Z_0\Delta t}\frac{\Delta y\Delta z}{\Delta x} - 2\right],$$

$$Z_y(\omega_0) = -\frac{\Delta t^2\omega_0^2}{4}\left[\frac{2\mu_y(\omega_0)\mu_0}{Z_0\Delta t}\frac{\Delta x\Delta z}{\Delta y} - 2\right].$$

(7)

On the other hand, from Eq. (2), we could also obtained the expressions of $\varepsilon(\omega)$ and $\mu(\omega)$ in terms of Y and Z or, more precisely, in terms of $Y(\omega_0)$ and $Z(\omega_0)$ given that the values of the stubs have been fixed.

$$\varepsilon_z(\omega) = \frac{Y_0\left[2\Delta t^2\omega^2 - 2Y_z(\omega_0)\right]}{\varepsilon_0\omega^2\Delta t\frac{\Delta x\Delta y}{\Delta z}}, \; \mu_x(\omega) = \frac{Z_0\left[\Delta t^2\omega^2 - 2Z_x(\omega_0)\right]}{\mu_0\omega^2\Delta t\frac{\Delta y\Delta z}{\Delta x}}, \; \mu_y(\omega) = \frac{Z_0\left[\Delta t^2\omega^2 - 2Z_y(\omega_0)\right]}{\mu_0\omega^2\Delta t\frac{\Delta x\Delta z}{\Delta y}}. \quad (8)$$

Therefore, by using Eq. (7), we can get the dispersion relations of the optic constants

$$\varepsilon_z(\omega) = A_{\varepsilon_z} - \frac{\omega_0^2}{\omega^2}\left[A_{\varepsilon_z} - \varepsilon_z(\omega_0)\right], \; \mu_x(\omega) = A_{\mu_x} - \frac{\omega_0^2}{\omega^2}\left[A_{\mu_x} - \mu_x(\omega_0)\right], \; \mu_y(\omega) = A_{\mu_y} - \frac{\omega_0^2}{\omega^2}\left[A_{\mu_y} - \mu_y(\omega_0)\right], \quad (9)$$

where $A_{\varepsilon_z} = \frac{2\Delta t Y_0\Delta z}{\varepsilon_0\Delta x\Delta y}$, $A_{\mu_x} = \frac{\Delta t Z_0\Delta x}{\mu_0\Delta y\Delta z}$, and $A_{\mu_y} = \frac{\Delta t Z_0\Delta y}{\mu_0\Delta x\Delta z}$.

Let $\chi(\omega) = 1 - \omega_p^2/\omega^2$ be either a permittivity or a permeability that follows a Drude dispersion. The quantity ω_p is the plasma frequency that can be easily determined if $\chi(\omega)$ is known at a certain frequency ω_0. Indeed, $\chi(\omega_0) = 1 - \omega_p^2/\omega_0^2$, which means that $\omega_p^2 = \omega_0^2[1 - \chi(\omega_0)]$. Finally,

$$\chi(\omega) = 1 - \frac{\omega_0^2}{\omega^2}\left[1 - \chi(\omega_0)\right], \quad (10)$$

which evinces that Eq. (9) are clearly reminiscent of a Drude dispersion model. Actually, the last statement depends on the value of A_{ε_z}, A_{μ_x}, or A_{μ_y}. Usually, the TLM parameters as Δt, $Z_0 = 1/Y_0$, Δx, Δy, or Δz constitute degrees of freedom as long as the quantities in Eq. (1) remain positive. The procedure described in this communication allows to elude this rule given that we can substitute Eq. (1) by Eq. (2) if the former results to be negative. However, this prescription makes the optic constants strongly dispersive and is thus of limited interest. Since conventional media can be approximated as non-dispersive, at least in a certain frequency range, we do not want them to be described by the strongly dispersive Eq. (1); Eq. (2) are best suited. On the other hand, metamaterials are inherently dispersive [10] and, as a result, should be associated with Eq. (2) rather than with Eq. (1). Consequently, we should ensure that the parameters of Eq. (1) are as follow: $\varepsilon \geq 1 \Rightarrow Y \geq 0$, $\varepsilon \leq 1 \Rightarrow Y \leq 0$, $\mu \geq 1 \Rightarrow Z \geq 0$, and $\mu \leq 1 \Rightarrow Z \leq 0$.

These conditions may restrict the election of Δt and Z_0. For the sake of simplicity, let us consider square nodes, i.e., $\Delta x = \Delta y = \Delta z = \Delta l$. Assuming that ε and μ can take any values, in particular $1 \pm \delta$ with $\delta \to 0$, we reach the conclusion that $\frac{2\varepsilon_0}{Y_0\Delta t}\Delta l - 4 = 0$ and $\frac{2\mu_0}{Z_0\Delta t}\Delta l - 2 = 0$, which leads to

$$Z_0 = \sqrt{2}\eta_0, \qquad \Delta t = \frac{\Delta l}{c\sqrt{2}}, \quad (11)$$

where η_0 and c are the impedance of free space and velocity of light in free space, respectively. If $\delta \nrightarrow 0$, the allowed Z_0 and Δt are not single values anymore and there exists a range of permitted values that becomes larger as δ increases.

Furthermore, the choice of Eq. (11) has another virtue: $A_{\varepsilon_z} = A_{\mu_x} = A_{\mu_y} = 1$, which yields Eq. (9) $\equiv$ Eq. (10), i.e., rigorous Drude's dispersion.

5. DISCUSSION

Since we have clarified the problem of the dispersion of ε and μ for the TE-node if metamaterials are involved, we are now capable of looking into the mismatch that has been observed in Fig. 1(a). While $\varepsilon = -4$ and $\mu = -1$, without regard to the frequency, in the analytical calculation, the cylinder's constitutive parameters in the TLM modeling are as expected only at ω_0 as it can be checked in Eq. (9). At other frequencies, the constitutive parameters disperse. In the numerical calculation that has been performed in Section 3, we chose for Z_0 and Δt the values given in Eq. (11). As a result, the relation of dispersion in the TLM node was described by Eq. (10). The analytical calculation is performed again, but instead of using constant values for ε and μ, Eq. (10) is employed with $\varepsilon(\omega_0) = -4$ and $\mu(\omega_0) = -1$. The comparison between the analytical and numerical results are then displayed in the range 0–6 GHz in Fig. 2(a): They show good agreement between each other. This validates the development that has been provided in Section 4.

Note that the spectral distribution of $\varepsilon(\omega)$ and $\mu(\omega)$ exhibits either positive or negative values. Therefore, the sign of n has to be accordingly picked up in the analytical calculation. In Fig. 2(a),
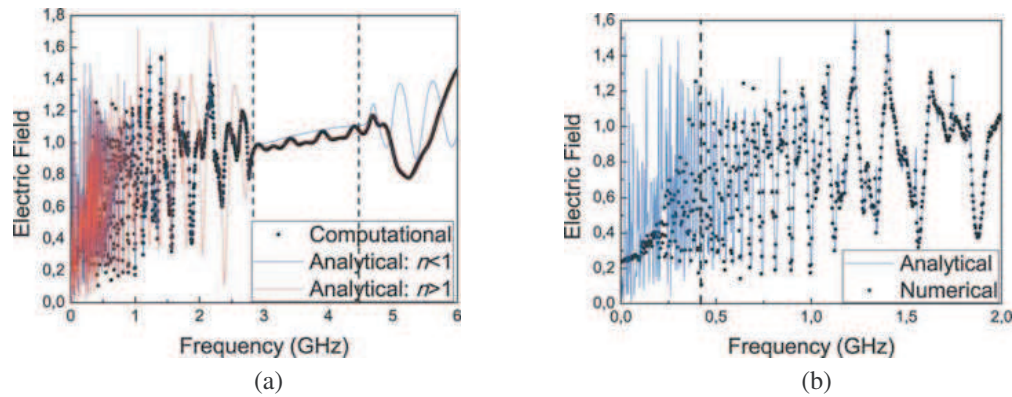
Figure 2: Analytical and numerical norm of the electric field for a dispersive left-handed cylinder. (a) The frequency ranges from 0 to 6 GHz. (b) Enlargement of the previous plot from 0 to 2 GHz.

we have plotted both cases, i.e., $n = \pm\sqrt{\varepsilon(\omega)\mu(\omega)}$. As expected, at low frequency, the negative root matches the computational curve while the positive root matches it at high frequency. The sign of $\varepsilon(\omega)$ and $\mu(\omega)$ turns out to switch at $f = 4.47$ and $f = 2.83$ GHz, respectively. These two frequencies have been plotted, with dashed lines, in Fig. 2(a). We have a clear confirmation that bellow the lower bound we have $n < 0$ and, beyond the upper bound, we have $n > 0$. Nonetheless, the medium is of single-negative (SNG) kind between those bounds, which gives rise to a little mismatching that seems to be ascribable to the numerical method. It is worth mentioning that the same mismatching is also observed for the reflection and transmission coefficients for a SNG infinite slab illuminated by a plane wave. This surprising behavior is currently under study.

In Fig. 2(b), we look more closely at the 0–2 GHz range, it reveals that there is a clear mismatch at low frequency. This was expected given that ε and μ are large as f tends to zero, which results in λ to be small inside the cylinder. Therefore, the series in Eq. (4) converge slowly and we cannot rely on the analytical low frequency values. The problem is similar for the TLM modeling. TLM is a low frequency technique and it can be considered as reliable as long as λ is much larger than Δl. Usually, the lower bound for λ is set to be $\lambda_{\min} = 10\Delta l$, which means that $f_{\max} = \frac{c}{10\Delta l\sqrt{\varepsilon\mu}}$. In our modeling we have chosen $\Delta l = 1$ mm, which means that $f \leq f_{\max} \Rightarrow f \geq 0.42$ GHz. This bound is represented in Fig. 2(b), which suggests that we should be more restrictive than $\lambda_{\min} = 10\Delta l$.

6. CONCLUSION

Metamaterials are inherently dispersive and, as a result, numerical modeling of metamaterials must take this property into account. In this communication, we have proven that the 2D TLM nodes used to simulate metamaterials, which have been shown to be dispersive, exhibit a Drude type dispersion. This special behavior has been illustrated on an example that involves the scattering of a left-handed structure.

ACKNOWLEDGMENT

REFERENCES

1. Johns, P. B. and R. L. Beurle, "Numerical solution of 2-dimensional scattering problems using a transmission-line matrix," *Proc. Inst. Elec. Eng.*, Vol. 118, No. 9, 1203–1208, 1971.
2. So, P. P. M., H. Du, and W. J. R. Hoefer, "Modeling of metamaterials with negative refractive index using 2-D shunt and 3-D SCN TLM networks," *IEEE Trans. Microwave Theory Tech.*, Vol. 53, No. 4, 1496–1505, 2005.
3. Ramo, S., J. R. Whinnery, and T. Van Duzer, *Fields and Waves in Communication Electronics*, John Wiley and Sons, 3rd Edition, 1994.
4. Blanchard, C., J. A. Portí, J. A. Morente, and A. Salinas, "Dispersion inherent to TLM nodes for modelling of metamaterials," *Electron. Lett.*, Vol. 46, No. 2, 110–112, 2010.

5. Johns, P. B., "A symmetrical condensed node for the TLM method," *IEEE Trans. Microwave Theory Tech.*, Vol. 35, No. 4, 370–377, 1987.

6. Portí, J. A., J. A. Morente, A. Salinas, M. Rodriguez-Sola, and C. Blanchard, "On the circuit description of TLM nodes," *Int. J. Electron.*, Vol. 93, No. 7, 479–491, 2006.

7. Blanchard, C., J. A. Portí, B.-I. Wu, J. A. Morente, A. Salinas, and J. A. Kong, "Time domain simulation of electromagnetic cloaking structures with TLM method," *Opt. Express*, Vol. 16, No. 9, 6461–6470, 2008.

8. Kong, J. A., *Electromagnetic Wave Theory*, EMW Publishing, 2008.

9. Balanis, C. A., *Advanced Engineering Electromagnetics*, John Wiley and Sons, 1989.

10. Elefhteriades, G. V. and K. G. Balmain, *Negative-Refraction Metamaterials*, John Wiley and Sons, 2005.

Sensitivity Analysis of Pulse Broadening in Optical Fibres; A Stochastic Approach

F. Emami

Optoelectronic Research Centre
Electronic Department, Shiraz University of Technology, Shiraz, Iran

Abstract— Propagation of the Gaussian-shape pulses, which are generated by sources with Gaussian spectral distribution, is theoretically studied in single mode fibers. Using Fourier transform pair, it is possible to express the pulse transmission behavior considering the effects of the chirp on the pulse width; a parameter which is depends stochastically on the various factors such as dispersion, dispersion slope and the source spectrum. These dependencies and sensitivities are studied and their variational behaviors are derived. It is found that, the pulse width sensitivity is higher for negative chirp factors and smaller wavelengths sources. This width sensitivity is increased for longer length fibers whereas it is low for shorter wavelengths. The pulse width sensitivity is an increasing function with respect to the small dispersion slope and has a maximum at a determined point. This situation for sensitivity is repeated for different wavelengths. If we use wide spectrum sources, the pulse width sensitivity is generally increased. But, with an appropriate spectral source width and wavelength, it is possible to decrease the sensitivity even to zero.

1. INTRODUCTION

Multi-path dispersion in optical fibers is important phenomenon, which can broad a pulse during the propagation through an optical fiber [1, 2]. As a result, the information-carrying capacity of the fiber related to the bit-rate is decreased [3]. A precise relation between the bit rate and the time difference of different components of the propagated pulse was done using stochastic procedure [4]. Usually at the operating wavelengths, the amount of the pulse broadening and bit rate limitations can be expressed by dispersion amount and its slope [5]. Note also that, the width of the input pulse depends on the spectral width of the source which can be minimized by using a monochromatic light source. In practice, the spectral width of the sources is much larger than the signal bandwidth of the pulse and this point must be considered in the applied stochastic theory for pulse propagation in single mode fibers (SMFs) [5]. Chirping of the laser sources, described by chirp parameters, is another important factor which we should consider in pulse width calculations. On the other hand, the propagated pulse width is a sensitive parameter related to some variables such as wavelength, input pulse width and etc. This sensitivity can be controlled by choosing some appropriate values of mentioned parameters.

2. THEORY OF PULSE DISTORTION

The general theory of the propagation of chirped pulses in dispersive media is presented by Marcuse, [4, 5]. Here, dispersive effects up to the third order are considered too. The used expression for our discussion is useful for arbitrary shaped pulses. The pulse propagation equation is solved in spectral (Fourier) domain and if we introduce the slowly varying amplitude of the pulse envelop as $A(z, t)$, and considering the quasi-monochromatic approximation, after expanding the Taylor expansion of the propagation constant up to third order, the solution is in the form of [1]:

$$A(z, t) = \frac{1}{2\pi} \int_{-\infty}^{+\infty} \Im\left[A(0, t)\right] e^{\left[\frac{i}{2}\beta_2 z\omega^2 + \frac{i}{6}\beta_3 z\omega^3 - j\omega t\right]} d\omega \tag{1}$$

where the symbol $\Im$ denotes the Fourier transform, β_2 and β_3 are the group velocity dispersion (GVD), related to the dispersion parameter, and the factor of the dispersion slope respectively. The above relation for $A(z, t)$ can be extended for any higher order dispersion. In general, the propagated pulse does not remain Gaussian during the propagation and would be broaden. This broadening is not uniform and there is a tail with an oscillatory structure in the pulse shape. Hence, a describing factor such as full widths at half maximum (FWHM) is no longer useful. In this case an appropriate estimation for the pulse width is its RMS value, defined as the root of:

$$\sigma^2 = \langle t^2 \rangle - \langle t \rangle^2 \tag{2}$$

where $\langle\rangle$ denotes the different moments as follows:

$$\langle t^n \rangle = \frac{\int_{-\infty}^{+\infty} t^n \, |A(z,t)|^2 \, dt}{\int_{-\infty}^{+\infty} |A(z,t)|^2 \, dt} \tag{3}$$

Now assume the nonlinear effects are negligible, so the different components are propagated by a simple relation in the form of:

$$\Im\left[A(z,t)\right] = \{\Im\left[A(0,t)\right]\} \, e^{(j\beta z)} = \left[P(\omega) \, e^{(j\eta)}\right] e^{(j\beta z)} \tag{4}$$

where the spectrum of the input pulse is shown by $P(\omega)$ and $\eta(\omega)$ describes the input chirp effects. Note that the field propagation constant depends on the frequency (and may be the fiber length). The broadening factor can be normalized to σ_0, the RMS width of the input Gaussian pulse, and it is shown that after some manipulations we can rewrite (3) in the form of [1]:

$$\left(\frac{\sigma}{\sigma_0}\right)^2 = \left(1 + \frac{C\beta_2 L}{2\sigma_0^2}\right)^2 + \left(1 + V_\omega^2\right)\left(\frac{\beta_2 L}{2\sigma_0^2}\right)^2 + \left(1 + C^2 + V_\omega^2\right)^2 \left(\frac{\beta_3 L}{4\sqrt{2}\sigma_0^3}\right)^2 \tag{5}$$

where we assumed that the initial field of the input pulse is chirped Gaussian and it is represented by:

$$A(z,t)_{|z=0} = A(0,t) = A_0 \exp\left[\frac{1+jC}{2}\left(\frac{t}{T_0}\right)^2\right] \tag{6}$$

In (6), C is the chirp factor, A_0 is the peak amplitude and T_0 depends to FWHM of the pulse. Other parameters are L, the fiber length and $V_\omega \equiv 2\sigma_\omega\sigma_0$, where σ_ω is RMS spectral width of the input source spectrum.

3. SENSITIVITY OF THE PULSE WIDTH

Consider a function from n variables $x_1, x_2, \ldots, x_n$; for example $y = f(x_1, x_2, \ldots, x_n)$. Every (relative) change in each of the variables can causes a change in the function y. If the variable variations are stochastic then the function variations will be the random processes too. We can define the function changes due to the x_i variations in the form of:

$$\Delta y \approx \frac{\partial y}{\partial x_i} \Delta x_i \tag{7}$$

To have a dimensionless interpretation of the function changes we can define its sensitivity in the form of:

$$\text{Sensitivity of } y \text{ respect to } x_i = S_{x_i}^y = \left(\left.\frac{x_i}{y}\right|_{\text{Quiescent Point}}\right) \times \frac{\partial y}{\partial x_i} \tag{8}$$

Now, we can study the sensitivity of the pulse width, with the aforementioned conditions, with respect to some variables which are random processes such as chirp, dispersion and input spectral behavior.

4. NUMERICAL RESULTS

Using (8), we can derive the normalized pulse width sensitivity with respect to the chirp factor, C. The results are shown in Fig. 1 for different fiber lengths and different exciting wavelengths. Consider the effects of the fiber lengths at first [Fig. 1(a)]. As seen, the sensitivity goes to zero for some non-zero values of chirp factor and this is occurred for positive and negative chirp factors but in a non-symmetric manner. For example at fiber length of about 6 km, there is zero sensitivity for $C \approx -2.2$ and $C \approx 2.0$. In other words, we can use a source with nonzero chirp factor whereas there is no any sensitivity like the chirp-less case. The selected values for chirp factor are decreased with increasing the fiber lengths. Higher sensitivity is seen for short fibers and it means for shorter fibers we should choose the chirp factor precisely.

Zero sensitivity can be achieved by different source wavelengths too. This is shown in Fig. 1(b). Again it is possible to have zero sensitivity for pulse widths with non-zero chirp factors. Short-wavelengths sources should not be used because of higher sensitivity. Hence long-wavelength sources
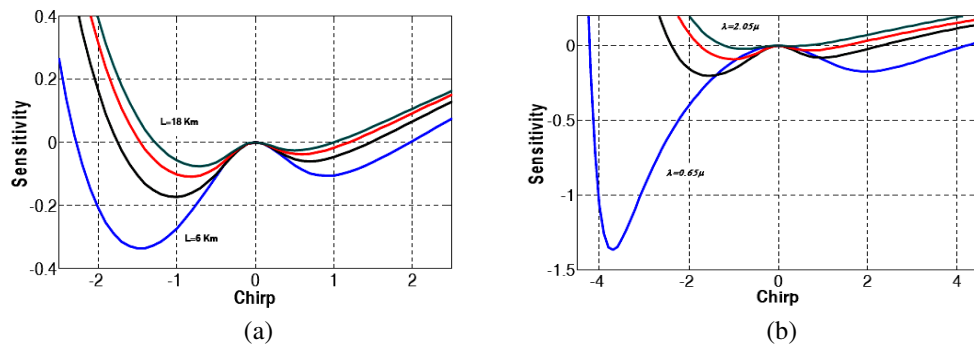
Figure 1: (a) Pulse width sensitivity respect to the chirp factor for different fiber lengths. (b) Sensitivity for different wavelengths.
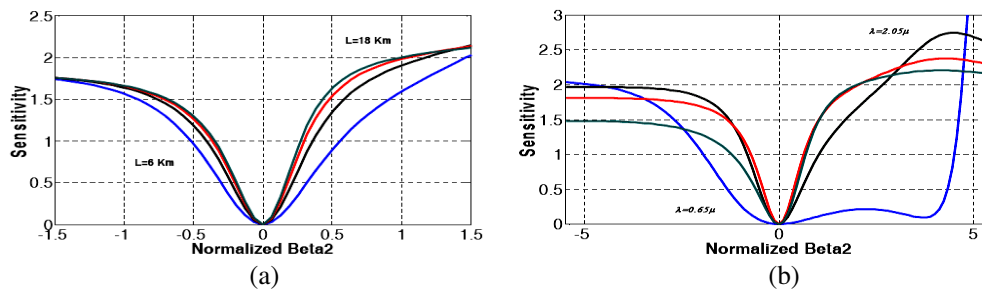

Figure 2: (a) Pulse width sensitivity respect to the dispersion factor for different fiber lengths. (b) Sensitivity for different wavelengths.

are preferred. But, in the case of shorter wavelengths we can have chirp factors in the range of ± 4 or more.

If we use the wavelengths far from the zero-dispersion wavelength for the fiber, the dispersion factor of the medium is dominated and we can ignore the dispersion slope effects.

In this case, β_3 is negligible and the sensitivity calculations are based on the dispersion (or equivalently β_2) factor only. The results are reported in Fig. 2. Generally, the sensitivity is increased for nonzero dispersion factors. But, for the fibers with higher effects of dispersion this increment tends to be saturated. This is independent from positive (negative) or negative (positive) values of β_2 (D, dispersion factor) but in a non-symmetric variations.

The longer fibers are more sensitive respect to the shorter fibers. For a defined dispersion amount, the shorter wavelengths generate less sensitivity and as shown this factor increased for higher dispersions.

Consider the case of excitation with wavelengths near to the zero-dispersion wavelengths. In this case, the effects of β_2 (dispersion) is negligible and we should study the appearance of β_3 which is related to the dispersion slope. The results are plotted in Fig. 3.

Pulse width sensitivity is increased for higher slopes but it has a maximum for determined values of fiber lengths [Fig. 3(a)]. For very large dispersion slopes, the sensitivity is independent from the fiber lengths but for intermediate slopes the fiber length is very important and short fibers are better. Behaviors of the input wavelengths are unexpected. As shown in Fig. 3(b), the sensitivity is increased with increasing the wavelength. But there is an especial wavelength so that the sensitivity has the maximum and after that it will be decreased.

Finally, we can study the source effects. There are two types of the sources; LDs and LEDs which are the optical sources with small and large spectral width, respectively. For LDs we have small FWHM [mathematically we can define $V_\omega \ll 1$ in (5)]. But, for LEDs there is large value of $V_\omega (V_\omega \gg 1)$. To survey these effects, the pulse width sensitivity is calculated for different values of V_ω. The results are drawn in Fig. 4. For LDs the sensitivity is very small and it will be increased for LED sources. For shorter fibers [Fig. 4(a)] there is a value for V_ω where the sensitivity is very small again, like the LD sources. The sources with very wide spectrum have a constant sensitivity independent of the LED types.

By using short-wavelength sources, it is possible to have LD behaviors for LED sources, where
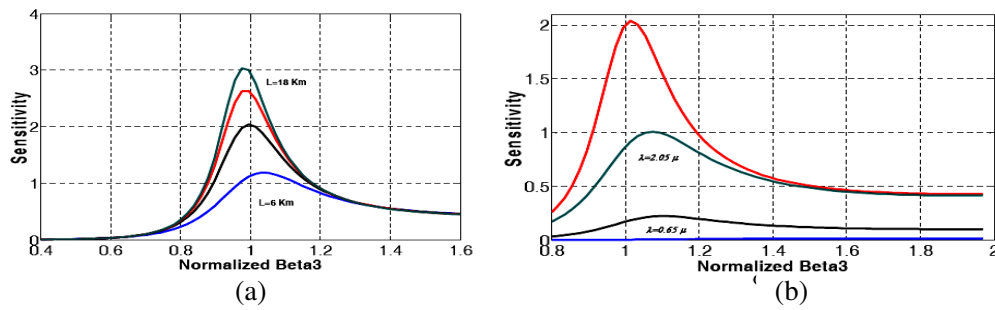
Figure 3: (a) Pulse width sensitivity respect to a factor of dispersion-slope, for different fiber lengths. (b) Sensitivity for different wavelengths.
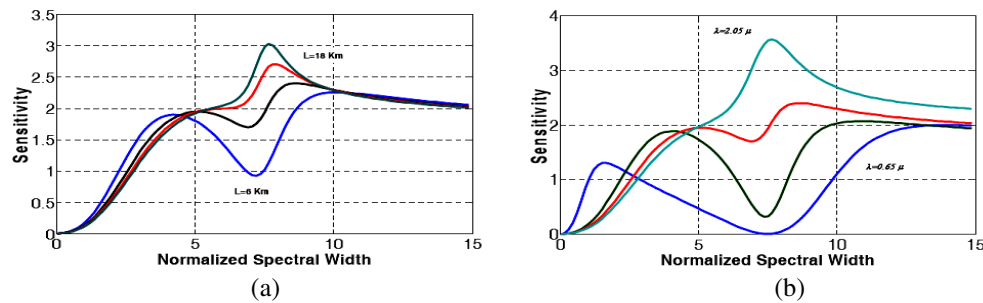

Figure 4: (a) Pulse width sensitivity respect to the normalized source spectral width, for different fiber lengths. (b) Sensitivity for different wavelengths.

sensitivity is zero. For long fibers and long wavelength sources, the sensitivity does not have a sharp decrement and it may has a maximum.

5. CONCLUSION

In conclusion, the sensitivity of the Gaussian pulse with respect to some parameters is studied based on the stochastic formulation for pulse broadening in an optical fiber. It is found that, this sensitivity can be reduced to zero using a proper value of the chirp factor for different fiber lengths and source wavelengths. In the case of dispersive fibers, short fibers excited with the sources of short wavelengths are preferred. When we utilize the dispersion-shifted fibers, short length and wavelength should be used. If LEDs are the exciting sources, it is possible to minimize the sensitivity by the proper selection of fiber length or wavelength.

REFERENCES

1. Agrawal, G. P., *Fiber Optic Communication Systems*, 3rd Edition, Wiley & Sons Inc., New York, 2002.
2. Born, M. and E. Wolf, *Principles of Optics*, 7th Edition, Cambridge University Press, New York, 1999.
3. Agrawal, G. P., *Nonlinear Fiber Optics*, 4th Edition, Academic Press, San Diego, CA, 2007.
4. Marcuse, D., "Pulse distortion in single mode fibers," *Applied Optics*, Vol. 19, No. 10, 1653–1660, 1980.
5. Marcuse, D., "Pulse distortion in single mode fibers — 3: Chirped pulses," *Applied Optics*, Vol. 20, No. 20, 3573–3579, 1981.

Stress and Strain Sensing with Multimode POF Bragg Gratings

Yanhua Luo[1,2]**, Binbin Yan**[1]**, Mo Li**[1]**, Xiaolei Zhang**[1]**, Qijin Zhang**[2]**, and Gang-Ding Peng**[1]

[1]School of Electrical Engineering and Telecommunications, University of New South Wales
Sydney 2052, NSW, Australia
[2]CAS Key Laboratory of Soft Matter Chemistry, Key Laboratory of Optoelectronic Science and Technology
Department of Polymer Science and Engineering, University of Science and Technology of China
Hefei, Anhui 230026, China

Abstract— A longitudinal stress and strain sensor based on the multimode POF Bragg gratings was analyzed. Several fiber modes were propagating in this multimode fiber, but two fiber modes were chosen for the stress and strain sensing. Variations of the peak wavelengths for both modes were approximately linear, but eventual discrepancies may be attributed to a certain viscoelasticity of the fiber and measurement errors. The stress and strain coefficient was estimated to be about 5.3 nm/N and 11.8 nm/%, respectively. Furthermore, the effective strain-optic constant and the Young's modulus of POF were calculated to be about 0.248 and 3.367 GPa. All the results based on such multimode POF gratings sensor for the measurement of refractive index, strain, temperature, etc.

1. INTRODUCTION

Fiber gratings written in POF have attracted much attentions since 1999, for their high sensitivity to strain and temperature, wide tuning wavelength range, good biocompatibility, etc. [1–7]. And different kinds of POF gratings have been fabricated in POF including both single mode fiber Bragg gratings (SM FBGs) and multimode fiber Bragg gratings [1–3, 7–15].

SM FBG in POF has been used in strain and temperature sensing, fiber laser with wide tuning wavelength range, humidity detection, etc. [2–7, 16, 17]. However, for some applications SM-FBGs is not appropriate due to not easy coupling with optical devices except SMF's or laser diodes resulted from a small core diameter [18, 19]. On the other hand, MM FBGs have several merits compared with SM FBGs [20–22]. And they have been used in multiwavelength fiber laser [23, 24] strain and temperature sensors [18, 20, 25–27], refractive index sensor [28], chemical sensor [29] etc. Therefore, the fabrication of fiber sensor gratings in multimode fibers and applications of MM FBGs would be of great interest [26], especially MM FBGs in POF. MM FBGs in POF would have the merits both of easy coupling with low cost light source belong to MM FBGs and high sensitivity to strain and temperature, wide tuning wavelength range, good biocompatibility, etc. However, the studies of MM FBGs in POF are rare. So in this work, stress and strain sensing of MM FBGs in POF was investigated systematically.

2. STRESS SENSING

Using the FBGs made in MM POF [30], the stress sensing using multimode polymer FBGs was performed using the setup shown in Figure 1(a). The change in the Bragg grating spectra is recorded as the stress is applied. The spectrum has more than 10 peaks, with one maximum peak and second maximum peak at 1571.383 and 1572.373 nm, and their spectral widths of 0.2 nm and 0.15 nm, respectively. As the stress increases, the spectrum moves to the right linearly (Figure 1(b)) without change of shape.

When the stress reduced the spectrum returns. However, it could not return to its original position as the stress is released to 0.089 N, in which there is a difference of 0.1 nm. This difference is attributed to the viscoelastic properties of POF [17]. Seen from Figure 1(b), although the intercepts of linear fit for the maximum peak and second maximum peak are different, the stress coefficient is almost the same. The stress coefficient was estimated to be about 5.3 nm/N. The error is very small showing good linear relationship. But the loading and unloading process has some differences which should be resulted from the viscoelastic properties of the materials [17] and measurement error.

3. STRAIN SENSING

The strain tuning of POF Bragg gratings was investigated by the mechanical stretching as shown in Figure 2(a). Figure 2(b) shows the resonant shift of the grating corresponding to the variation

in axial strain. The strain coefficient was estimated to be about 11.8 nm/%, which is comparable with that for conventional silica fiber gratings [31]. But a little lower than the previous result [5], attributed to the different materials. Similarly, the strain response for the loading and unloading also has some difference but the difference is much smaller than that seen from the stress sensing, which may be attributed to the Young's modulus changes with strain rate for the viscoelastic material [32].
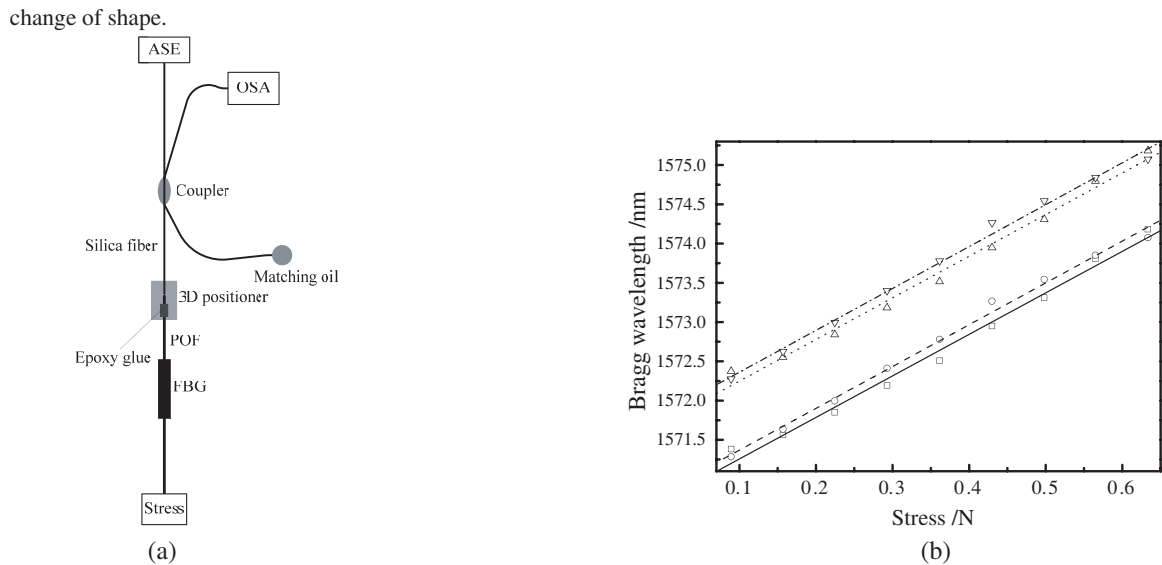

Figure 1: (a) Experiment setup for the stress sensing using multimode polymer FBGs. (b) The maximum Bragg resonant wavelength and their corresponding linear fit with the axial loading ($\square$, ——) and unloading ($\bigcirc$, — —), stress process for FBGs in the MM POF, and the second maximum Bragg resonant wavelength and their corresponding linear fit with the axial loading ($\triangle$, ·········) and unloading ($\triangledown$, — · — · —) stress process for FBGs in the MM POF.
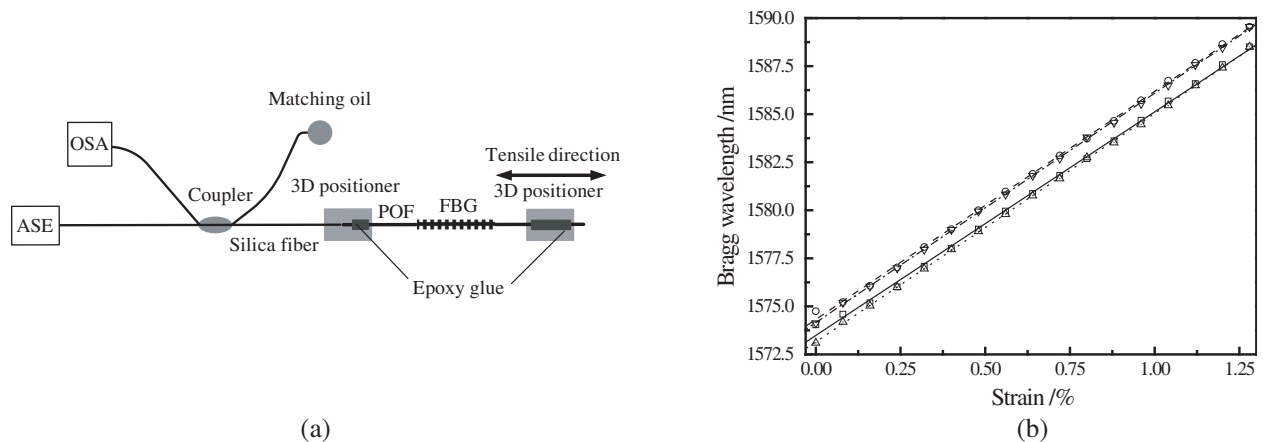

Figure 2: (a) Experiment setup for the strain sensing using multi mode polymer FBGs. (b) The maximum Bragg resonant wavelength and their corresponding linear fit with the axial unloading ($\square$, ——) and loading ($\triangle$, ·········) strain process for FBGs in the MM POF, and the second maximum Bragg resonant wavelength and their corresponding linear fit with the axial unloading ($\bigcirc$, — —), and loading ($\triangledown$, — · — · —) strain process for FBGs in the MM POF.

4. YOUNG MODULUS OF POF

When an axial strain is applied to the Bragg grating in a multimode fiber, the wavelength peak of the ith reflection mode (λ_{pi}) will be shifted by an amount $\Delta\lambda_{pi}$ due to strain induced changes of

the periodicity and the effective index given by [26, 27]

$$\Delta\lambda_{pi} = 2\left(\Lambda\frac{\partial n_{eff}}{\partial L} + n_{eff}\frac{\partial\Lambda}{\partial L}\right)\Delta L, \tag{1}$$

The strain effect may be expressed further as [26, 27]

$$\Delta\lambda_{pi} = \lambda_{pi}(1 - p_{eff})\varepsilon_z, \tag{2}$$

where ε_z is the longitudinal strain suffered by the grating when subjected to a stress. The effective strain-optic constant (p_{eff}) is given by [27]

$$p_{eff} = \frac{\overline{\beta}_i^2}{2}[p_{12} - \nu(p_{11} + p_{12})] \tag{3}$$

where $\overline{\beta}_i = (\beta_i\lambda/2\pi) \approx n_1$, β_1 is the propagation constant of the ith mode, p_{11} and p_{12} are components of the strain optic tensor, and ν is the Poisson ratio. The value of p_{eff} could be about 0.248 obtained from Figure 2(b) by linear fitting. This value is a little larger than the silica fiber (0.22), meaning a little smaller strain sensitivity than the silica fiber [33], which may be attributed to the smaller Poisson ratio of the materials.

For elastomers, the stress (σ) and strain (ε_z) satisfy the following relationship:

$$\sigma = E \cdot \varepsilon_z \tag{4}$$

where E is the Young modulus. If we just consider the elasticity of POF while neglecting the viscoelasticity of POF, the relationship between stress (σ) and axial strain (ε_z) of POF can also be described using the above equation. But in fact, polymer is a viscoelastic material so that the measured Young's modulus changes a little when the stress is applied [32]. That's why the loading and unloading process has some difference as shown in Figure 1(b) and Figure 2(b).

The relationship between the stress (σ) and the force (F) applied upon the fiber is as follow:

$$\sigma = \frac{F}{A} = \frac{4F}{\pi D^2} \tag{5}$$

where A is the area of the cross section of the fiber and D is the diameter of the fiber.

Combining Equations (2), (4) and (5), there would be:

$$\Delta\lambda_{pi} = \lambda_{pi}\frac{4(1 - p_{eff})}{\pi D^2 E}F \tag{6}$$

where $\lambda_{pi}\frac{4(1-p_{eff})}{\pi D^2 E}$ could be obtained by linear fitting in Figure 1(b). Based on this, the value of E could be estimated to be about 3.367 GPa, close to the value of PMMA [32].

5. CONCLUSION

Two fiber modes in this multimode fiber were chosen for the longitudinal stress and strain sensing. Variations of the peak wavelengths for both modes were approximately linear, but eventual discrepancies may be attributed to a certain viscoelasticity of the fiber and measurement errors. The stress and strain coefficient was estimated to be about 5.3 nm/N and 11.8 nm/%, respectively. Through the longitudinal stress and strain measurement, the effective strain-optic constant and the Young's modulus of POF were calculated to be about 0.248 and 3.367 GPa. The result demonstrated that this multimode sensor could be employed for the measurement of stress and strain.

REFERENCES

1. Peng, G. D., Z. Xiong, and P. L. Chu, *Opt. Fiber Technol.*, Vol. 5, 242–251, 1999.
2. Xiong, Z., G. D. Peng, B. Wu, et al., *IEEE Photon. Technol. Lett.*, Vol. 11, 352–354, 1999.
3. Yu, J., X. Tao, and H. Tam, *Opt. Lett.*, Vol. 29, 156–158, 2004.
4. Liu, H. Y., H. B. Liu, G. D. Peng, et al., *Opt. Commun.*, Vol. 266, 132–135, 2006.
5. Liu, H. Y., H. B. Liu, G. D. Peng, et al., *Opt. Commun.*, Vol. 219, 139–142, 2003.
6. Webb, D. J., K. Kalli, C. Zhang, et al., *Proc. SPIE*, Vol. 6990, 69900L-1-10, 2008.
7. Dobb, H., K. Carroll, D. J. Webb, et al., *Proc. SPIE*, Vol. 6189, 618901-1-12, 2006.
8. Zhang, C., X. Chen, D. J. Webb, et al., *Proc. SPIE*, Vol. 7503, 750380-1-4, 2009.
9. Large, M. C. J., J. Moran, and L. Ye, *Meas. Sci. Technol.*, Vol. 20, 034014-1, 2009.
10. Luo, Y., J. Zhou, Q. Yan, et al., *Appl. Phys. Lett.*, Vol. 91, 071110, 2007.
11. Li, Z., H. Y. Tam, L. Xu, et al., *Opt. Lett.*, Vol. 30, 1117–1119, 2005.
12. Dobb, H., D. J. Webb, K. Kalli, et al., *Opt. Lett.*, Vol. 30, 3296–3298, 2005.
13. Hiscocks, M. P., M. A. V. Eijkelenborg, A. Argyros, et al., *Opt. Express*, 14, 4644–4649, 2006.
14. Terblanche, J., D. Schmieder, and J. Meyer, *Proc. SPIE*, Vol. 7503, 75037F-1-4, 2009.
15. Chen, X., C. Zhang, D. J. Webb, et al., *Proc. SPIE*, Vol. 7503, 750327-1, 2009.
16. Zhang, C., D. J. Webb, K. Kalli, et al., "Bragg grating inscription in TOPAS microstructured polymer optical fibre," *Proc. 16th Int. Conf. Polymer Opt. Fiber*, UK, 2007.
17. Peng, G. D. and P. L. Chu, *Proc. SPIE*, Vol. 4110, 123–138, 2000.
18. Lim, J., Q. P. Yang, B. E. Jones, et al., "Strain and temperature sensors using multimode optical fiber bragg gratings and correlation singal processing," *IEEE Instrumentation and Measurement Technology Conference*, 1463–1466, Budapest, Hungary, 2001.
19. Wanser, K. H., K. F. Voss, and A. D. Kersey, *Proc. SPIE*, Vol. 2360, 265–268, 1994.
20. Mizunami, T., T. V. Djambova, T. Niiho, et al., *J. Lightwave Technol.*, Vol. 18, 230–235, 2000.
21. Lu, C. and Y. Cui, *J. Lightwave Technol.*, Vol. 24, 598–604, 2006.
22. Ecke, W., "Applications of fibre bragg grating sensors," Institute of Photonic Technology, Perth, 2008.
23. Feng, X., H.-Y. Tam, W.-H. Chung, et al., *Opt. Commun.*, Vol. 263, 295–299, 2006.
24. Feng, X., H.-Y. Tam, and P. K. A. Wai, *OECC*, 2006.
25. Djambova, T. V. and T. Mizunami, *Jpn. J. Appl. Phys.*, Vol. 39, 1566–1570, 2000.
26. Zhao, W. and R. O. Claus, *Smart Mater. Struct.*, Vol. 9, 212–214, 2000.
27. Cazo, R. M., O. Lisbôa, H. T. Hattori, et al., *Microw. Opt. Technol. Lett.*, Vol. 28, 4–8, 2001.
28. Zhao, C.-L., X. Yang, M. S. Demokan, et al., *J. Lightwave Technol.*, Vol. 24, 879–883, 2006.
29. Sang, X., C. Yu, B. Yan, et al., *Microw. Opt. Technol. Lett.*, Vol. 48, 1739–1741, 2006.
30. Luo, Y., H. Liu, Q. Zhang, and G.-D. Peng, "Grating writing with 355 nm wavelength in polymer optical fibre doped with benzildimethylketal," *The Australasian Conference on Optics, Lasers and Spectroscopy and Australian Conference on Optical Fibre Technology*, Adelaide, 48, 2009.
31. Jin, W., W. C. Michie, G. Thursby, et al., *Opt. Eng.*, Vol. 36, 598–609, 1997.
32. Ishiyama, C. and Y. Higo, *J. Polym. Sci. Pt. B-Polym. Phys.*, Vol. 40, 460–465, 2002.
33. Liu, H., "Polymer optical fiber bragg gratings," University of New South Wales, Sydney, 2003.

Novel Composite Non Reciprocal Right/Left-handed Line Made from Ferrite Material

F. Boukchiche[1], T. Zhou[2], M. L. Berre[2], D. Vincent[1], B. Payet-Gervy[1], and F. Calmon[2]

[1]Laboratoire DIOM, Saint-Etienne University, France
[2]INL-UMR5270, CNRS, INSA de Lyon, France

Abstract— Non reciprocal segments of line are using to connect series capacitors and shunt inductors in order to perform a right/left-handed planar medium. The artificial medium behavior is fixed by the value of L-C components and the transmission line characteristics. The effect of non reciprocal segments of line are studied. From the derivation of the dispersion relation, new behaviors may be expected and are observed for several applied magnetic D.C. values. The concept can be extended to active non reciprocal network.

1. INTRODUCTION

Veselago [1] has given the concept of negative refractive index material (NRI) in 1968. Many bulk 3-D NRI materials including metallic particles in host matrices were studied [2–4]. However, the losses remain too high for microwave applications. On the other hand, devices and circuits on planar structures are suitable for electronic integration. L-C loaded transmission lines are easily used to make planar negative index media [5, 6]. Lumped elements (L, C) are connected through a transmission line network. The effective properties of the left handed media can be changed by varying the effective permittivity or/and effective permeability. For active solutions, varactors could be used in place of capacitors.

When magnetic substrate or magnetic thin-films deposited on a dielectric substrate are used to fabricate a transmission line network, non reciprocal effect can exist and the media properties are different for the two propagation directions. We propose tunable structures using non reciprocal transmission lines made from YIG magnetic materials or magnetic thin-films. Results obtained from simulations and experiments are presented.

2. STRUCTURE UNDER TEST

The composite right/left handed transmission line unit cell is made up of periodic series interdigital capacitors and shunt inductors embedded in the coplanar waveguide. The unit cell is shown on Figure 1. The relevant dimensions of the interdigital capacitor are a finger length of 75 μm and width of 72 μm for a finger spacing of 10 μm. The shunt inductance length is 575 μm. The length of non reciprocal transmission line between the interdigital capacitor and the shunt inductor is 1.05 mm, whereas the length of non reciprocal transmission line connecting the probes is 2.1 mm. The shunt inductance extracted by 3D simulation is around 105 pH and the series capacitance is about 0.25 pf. The magnetic properties of the YIG thin film are: magnetization $M_s = 140$ kA/m, damping factor from Polder model [7] around 0.05. The non-reciprocal effect is due to the gyromagnetic resonance phenomenon occurring when a D.C. magnetic field is applied to the ferrite substrate (or film) along the transverse in-plane direction.
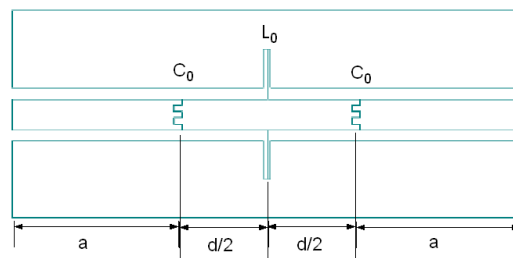

Figure 1: Unit cell of structure network.

3. RESULTS

The properties of such a coplanar waveguide are evaluated experimentally from 1 to 20 GHz. On the other hand, simulations have been made to evaluate the transmission coefficients (Figure 2). These simulation results are in good agreement with experimental results given on Figure 3.

The value of the applied magnetic field being not exactly the same, the gyromagnetic resonance frequency is slightly shifted and the simulated transmission coefficient values are lower than the experimental ones. The experimental and simulated results show that the gyromagnetic resonance frequency of this CPW is centered at 8.2 GHz, and a band gap is obtained for frequencies starting at 11.2 GHz. As expected, we obtain a gyromagnetic resonance from about 7–11 GHz, and a non reciprocal phenomenon is present.

From experimental data the dispersion diagram can be plotted for several D.C. applied fields. Results for zero applied field (small remanent field) are given on Figure 4. The left-handed and band gap regions are clearly observed.
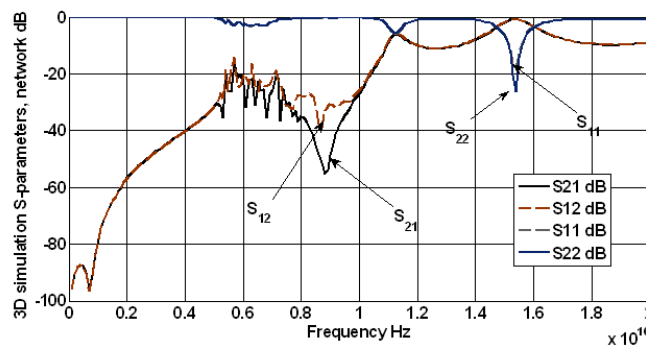

Figure 2: 3D simulated S-parameters in dB when the D.C. applied field is close to 140 kA/m.
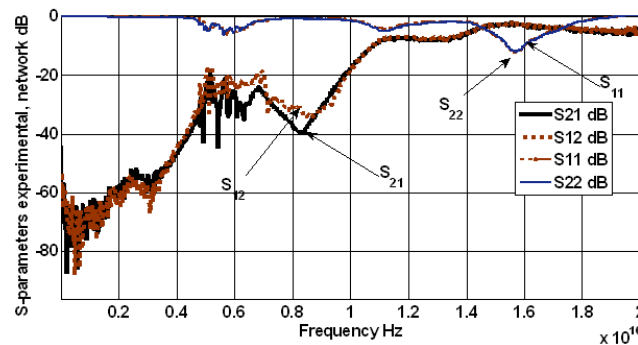

Figure 3: Experimental S-parameters in dB when the D.C. applied field is close to 140 kA/m.
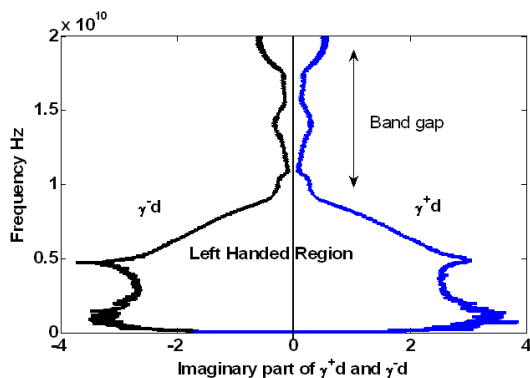

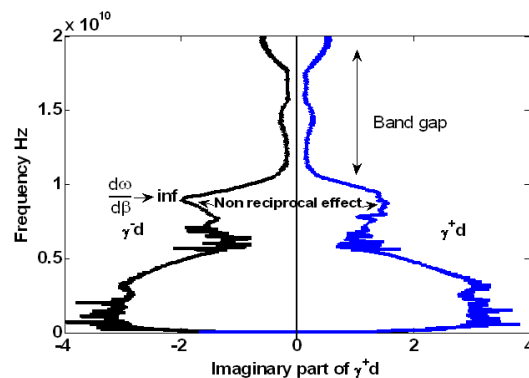Figure 4: Dispersion diagram for zero field.

Figure 5: Dispersion diagram for 210 kA/m D.C. field.

When the D.C. field increases the dispersion diagram varies showing unusual behavior in the gyromagnetic resonance frequency band. On Figure 5 the group velocity could become infinite in a dispersive and lossy material [8]. In this case, it does not keep the energy propagation velocity meaning.

4. CONCLUSION

Planar non reciprocal negative refraction index medium could be carried out on magnetic substrate or thin film. This medium was made from *L-C* loaded non reciprocal coplanar transmission line. Inside this strong dispersive region, unusual propagation behavior may occur and could be an interesting material support to design new components like non reciprocal filters or couplers ... In addition, variation of the D.C. applied field makes possible tunable devices. However, we have to use a low loss material for usual applications. A coplanar isolator with low insertion losses ([9]) is under study. It can work in the LH-passband region and a non reciprocal filter will be performed. Further works are still under consideration to complete this study and to design new microwave devices.

REFERENCES

1. Veselago, V. G., "The electrodynamics of substances with simultaneously negative values of ϵ and μ," *Sov. Phys. Usp.*, Vol. 10, 509–514, 1968.
2. Shelby, R. A. and D. S. Schultz, "Experimental verification of a negative index of refraction," *Science*, Vol. 292, 77–79, May 2001.
3. Lu, K., J. McLean, R. Gregor, C. Parazzoli, and M. H. Tanelian, "Free space focused beam characterization," *Appl. Phys. Letter*, Vol. 82, 2535–2537, 2003.
4. Simovski, C. and S. He, "Frequency range and explicit expressions for negative permittivity and permeability for an isotropic medium formed by a lattice of perfectly conducting Omega-particles," *Phys. Lett. A*, Vol. 311, 254–263, 2003.
5. Eleftheriades, G. and A. I. Kremer, "Planar negative refractive index media using periodically *L-C* loaded transmission lines," *IEEE Trans. Microwave Theory Tech.*, Vol. 50, 2702–2712, 2002.
6. Caloz, C. and T. Itoh, "Transmission line approach of left-handed (LH) materials and microstrip implementation of an artificial LH transmission line," *IEEE Transaction on Antennas and Propagation*, Vol. 52, 1159–1166, 2004.
7. Lax, B. and K. Button, *Microwave Ferrites and Ferrimagnetics*, McGraw-Hill, 1962.
8. Ziolkowski, R. W., "Superluminal tranmission of information through an electromagnetic meta-material," *Phys. Rev. E*, Vol. 63, 1–13, 2001.
9. Kirouane, S., E. Verney, D. Vincent, and A. Chaabi, "Isolateur coplanaire dplacement de champ base de YIG," *Proceedings of Journes Nationales Microondes*, Grenoble, France, May 2009.

A New Profile for Metal Post Circular Waveguide Polarizer

S. H. Mohseni Armaki, F. H. Kashani, and M. Fallah

Department of Electrical Engineering, Iran University of Science and Technology (IUST), Iran

Abstract— This paper presents a new profile for depth of metal posts in circular wave guide polarizer. Simple designs of metal posts depth arrangement are predefined by tangential profile. Finally, exact depths of metal posts are tuned by HFSS. Measurement and simulation result have a good agreement in 18% bandwidth.

1. INTRODUCTION

In circularly polarized antenna feed systems, polarizer are used to convert linearly polarized signals provided at the first interface port (circular waveguide) into circularly polarized signals supplied to the second interface port (antenna). Typical examples of polarizer are a circular waveguide polarizer with metallic posts, a corrugated waveguide polarizer and a dielectric slab waveguide polarizer [1–3].

A circularly polarized wave is represented by the superposition of two orthogonal linearly polarized weaves that posses identical magnitude and a phase difference of $\pm\pi/2$. In conventional polarizer such as metal post (pin) polarizes apart from good matching properties at each port, there are two basic demands on the design of these polarizer type. Firstly, the signals of the linearly polarized modes must be exactly divided (combined) into orthogonal components with identical magnitude. Secondly a differential phase shift of $\pm\pi/2$ between these semi signals has to be accomplished.

Thus, the complete polarizer can be regarded a combination of a power divider and two independent phase shifter. Both tasks must be realized simultaneously by differential phase shifting region that exhibit a physical alignment of 45 deg with regard to the incident linearly polarized mode supplied to import (TE11).

For designing this type of polarizer, we can use equivalent circuit, and then it is reached to desired result by empirical tuning depth of posts [4]. The depth of posts gradually increased from the beginning to the middle of circular waveguide. So far there isn't presented equation for optimum profile of posts depth. In this paper, while presenting optimum profile, performance of polarizer is simulated and tested.

2. CONFIGURATION

Figure 1 depicts the structure of proposed polarizer with metal posts. The polarizer is composed of a circular waveguide and 13 symmetrical metal posts arrange in single line and aligned diagonally with regard to E vector. An equivalent circuit suggests that the inductance of these posts, together with their capacitive coupling, is providing the $E_\parallel$ component with high pass equivalent circuit thus advancing the phase relative to its orthogonal component [4].

Broadband polarizer with metal posts is designed on the basis of the fact that normalized capacitive susceptance of short posts decreases at high frequencies. To obtain the design data, the measurement is made for the optimum post diameter and its length which give negative normalized capacitive susceptance, and the magnitude of the post susceptance for the orthogonal two polarized waves. To obtain good VSWR characteristics, the post depth in the matching sections follows the tangential profile that predefine by following equation:.

$$d(z) = (a/2)\left[(1-A)\frac{z}{l} + A\tan^2\left(\frac{\pi z}{4l}\right)\right] \quad \text{where} \quad A = 0.7 \tag{1}$$

The size of space between metal post and the diameter of post are: $\lambda_g/4$, $0.04\lambda_g$ respectively and length of polarizer is about $2\lambda_g$. Then desired response is obtained by very small depth tuning in HFSS.

3. EXPERIMENTAL RESULT

As a typical design example, a 7–8.4 GHz metal post wc109 circular wave guide polarizer has been fabricated. Fig. 2 shows a photograph of the fabricated polarizer. According to Fig. 3 a very little

(a)   (b)
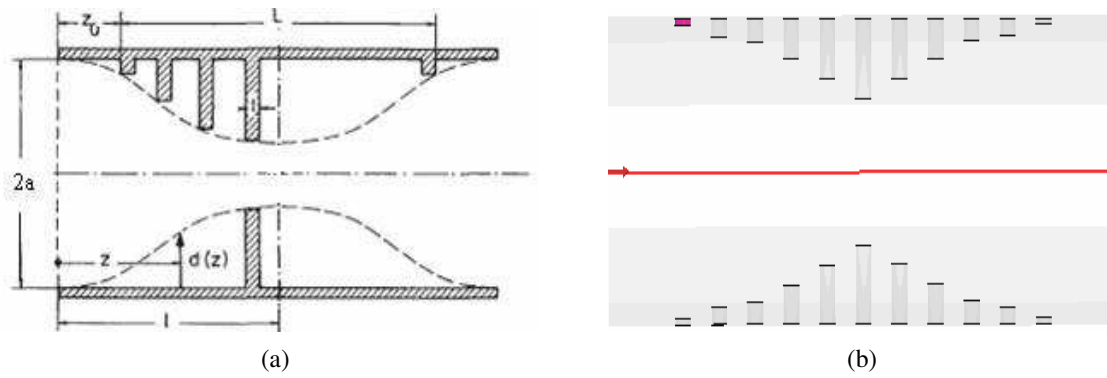
Figure 1: (a) Profile of metal post polarizer [5]. (b) Metal post polarizer in HFSS.
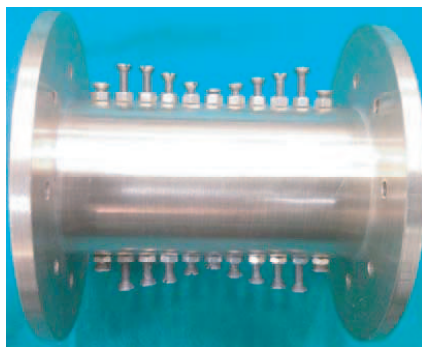

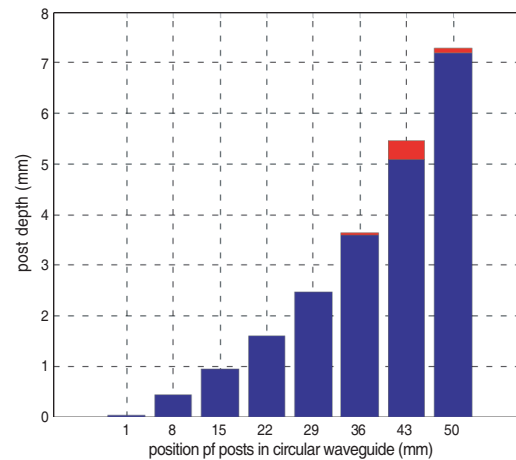Figure 2: Fabricated circular polarizer.

Figure 3: Predefined and tuned post depth.

change in predefined and tuned depth of posts is shown. The polarizer is designed to provide a good match ($s_{11} < -17$ dB) and a good axial ratio (AR < 2 dB) over the frequency range between 7–8.4 GHz. The total length of the designed polarizer is 100 mm and the diameter of circular waveguide is 28.5 mm. A good agreement is obtained between the experimental and simulated data both in Fig. 4 and Fig. 5.
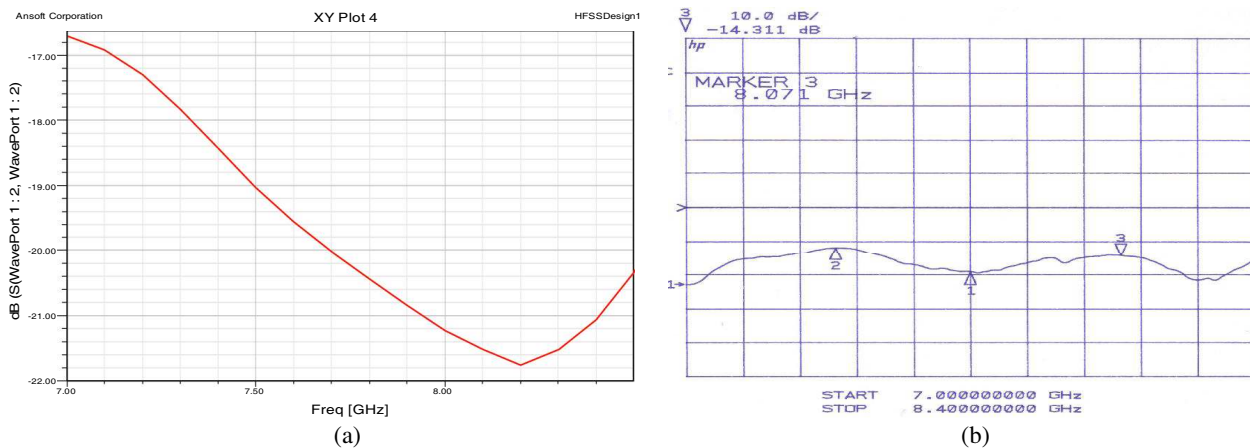

(a)   (b)

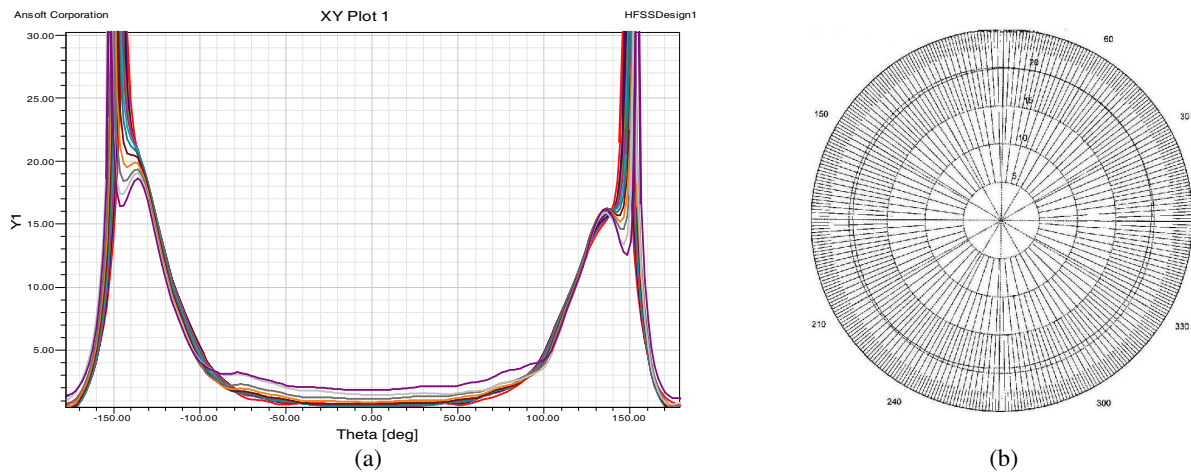Figure 4: (a) Simulated s_{11}. (b) Measured s_{11}.

Figure 5: (a) Simulated AR in different freq. (b) Measured AR in 8.2 GHz.

4. CONCLUSION

A Configuration, design and simulation of metal post circular polarizer with tangential profile for post depths has been introduced in this paper. The presented polarizer doesn't need experimental tuning post depths. Such a polarizer could find application I in earth stations.

REFERENCES

1. Kitsuregawa, T., *Advanced Technology in Satellite Communication Antenna: Electrical and Mechanical Design*, Artech House, 1990.
2. Uher, J., J. Bornemann, and U. Rosenberg, *Waveguide Components for Antenna Feed Systems: Theory and CAD*, Artech House, 1993.
3. Unger, H. J., "Polarization wandler in hohlleitern," Frequentz, Band 16, 117–120, April 1962.
4. Marcuvitz, N., *Waveguide Handbook*, McGraw Hill, New York, 1951.
5. Arndt, F., W. Tucholke, and T. Wriedt, "Design of a wideband compact square waveguide polarizer," *Elecronics Letters*, Vol. 21, No. 12, 74–75, June 1985.

A Parallel Adaptively Modified Characteristic Basis Function Method for Analyzing Electromagnetic Scattering Problems

Fei Dai, **Zichang Liang**, **and Hui Yue**

The State Key-Lab for Electromagnetic Characters of Environment
The 802 Research Institute of Shanghai Academy of Spaceflight Technology, Shanghai 200438, China

Abstract— ElectroMagnetic (EM) scattering analysis, particularly the Radar Cross Section (RCS) evaluations, is a tremendous computational task. For engineering applications, there are a lot of problems with very large number of unknowns to be solved. However, the present computer technology can not provide sufficient memory size to store all of the data in the process of the computation. What is worse, the computational speed is not acceptable. It is not rare to spend several days to gain a solution of a complex target. In order to increase the computational efficiency and overcome the limitation of the computer capacity at the same precision, parallel algorithm has been introduced by many researchers. Characteristic Basis Function Method (CBFM) is a novel approach for analyzing the ElectroMagnetic (EM) scattering from electrically large objects. Based on dividing the studied object into small blocks, the CBFM is suitable for parallel computing. In the past paper, a static load balance parallel method has been presented by combining Message Passing Interface (MPI) with Adaptively Modified CBFM (AMCBFM). The object geometry is partitioned into distinct blocks, and the serial number of blocks is sent to related nodes according to a certain rule. Every node only needs to calculate the data on local blocks. In this paper, we present a hybrid scheduling parallel method that can be used in heterogenous parallel computing environment. A series of numerical results and computing performance are discussed, which show that the hybrid scheduling parallel method is a promising solution for analyzing large-scale problems in electromagnetic field, and confirm the accuracy and efficiency of the proposed method in speeding up solving large electrical scale problems.

1. INTRODUCTION

ElectroMagnetic (EM) scattering analysis, particularly the Radar Cross Section (RCS) evaluations, is a tremendous computational task. The most widespread and generally accepted technique is Moment Method (MM) [1], Fast Multiple Method (FMM) [2] and the Multilevel Fast Multiple Method (MLFMM) [3]. However, the present computer technology can not provide sufficient memory size to store all of the data in the process of the computation. What is worse, the computational speed is not acceptable. In order to increase the computational efficiency and overcome the limitation of the computer capacity at the same precision, parallel algorithm has been introduced by many researchers [4–6].

In 2003, the Characteristic Basis Function Method (CBFM) [7] proposed by Raj Mittra has been successfully incorporated in MM to solve radiation and scattering problems, and its advantage is that it can reduce the size of impedance matrix. Compared with MM, this method reduces considerably the burden on the CPU time as well as memory requirements. It is based on dividing the object structure into small blocks, and evaluating the characteristic functions that are localized in each of these blocks.

In the past paper, a static load balance parallel method has been presented by combining Message Passing Interface (MPI) with Adaptively Modified CBFM (AMCBFM) [8]. The object geometry is partitioned into distinct blocks, and the serial number of blocks is sent to related nodes according to a certain rule. Every node only needs to calculate the data on local blocks. It is very suitable to be used in homogeneous parallel computing environment. In this paper, we present a hybrid scheduling parallel method that can be used in heterogenous parallel computing environment. Compared with the past method, the obtained results confirm the accuracy and efficiency of the proposed methods in speeding up the RCS calculation of large electrical scale objects in the heterogenous parallel computing environment.

2. PARALLEL AMCBFM BASED ON STATIC LOAD BALANCE (SP-CBFM)

In homogeneous parallel computing environment, we can distribute $1/P$ (P is the number of nodes) of the whole problem to every node for executing in parallel. As we have described in Ref. [9], a brief summary of static load balance method are presented as follows:

Step 1. The object geometry is meshed and is divided into M blocks. Subsequently, the task is distributed to every node. The principle of distribution is to make sure that the sum of unknowns located in every node is nearly equal to each other.

Step 2. Primary CBF (PCBF) is generated. As we have distributed task equally to every node, each one generates its own matrix Z_{ii} and PCBF. These tasks are independent and can be processed in parallel. The computed CBFs are broadcasted to the other nodes for generating the Secondary CBF (SCBF). The memory and CPU time used in this step are close to $1/P$ of those in AMCBFM.

Step 3. Solve the coefficients of PCBF. Every node generates the corresponding line of PCBF matrix. In this step, the memory and CPU time are still almost $1/P$ of that needed in conventional AMCBFM.

Step 4. The calculation for higher levels of CBFs is similar with those of Step 2 and Step 3.

Figure 1 shows the flow of the parallel AMCBFM code.

3. PARALLEL AMCBFM BASED ON HYBRID SCHEDULING (HP-AMCBFM)

In heterogenous parallel computing environment, things look different. If we distribute $1/P$ of the whole task to every node, it will be inefficient, and now, we present a hybrid scheduling parallel method which is very efficient in heterogenous parallel computing environment. The difference between BP-AMCBFM and HP-AMCBFM is described as follows:

Step 1. The object geometry is meshed and is divided into M blocks. Then we can sort the blocks according to the unknowns of every block, bring a M members descending queue. The difference is only distributed the serial number of first $\lambda \times M$ ($0 \leq \lambda \leq 1$) block to every node. The value of λ depends on the unknowns of every block and the difference of computation performance of every node.

Step 2. Because the first $\lambda \times M$ block is distributed to every node with static load balance method, the node with higher performance will finish the task earlier. The finished node send a message to main node, and then main node will send the serial number of the next block of the queue until all of the left $(1-\lambda) \times M$ blocks were distributed. The computed CBFs are broadcasted to the other nodes for generating the Secondary CBF

Step 3. Solve the coefficients of PCBF. as we have done in Step 1, the first $\lambda \times M$ line will be distribute with static load balance method, and the next $(1 - \lambda) \times M$ line will be distribute dynamicly.

Step 4. Solve the higher level coefficients of CBFs is different. The matrix equation of SCBF is show in Fig. 2, the elements in Part (1) have been calculated in PCBF. As the line of Part (1) have been calculated in different node, when we calculate Part (2), every node should calculate the same line as Part (1). When we calculate Part (3), the distribute scheme should be executed like Step 3, and the distributed line number may be different from Parts (1) and (2).
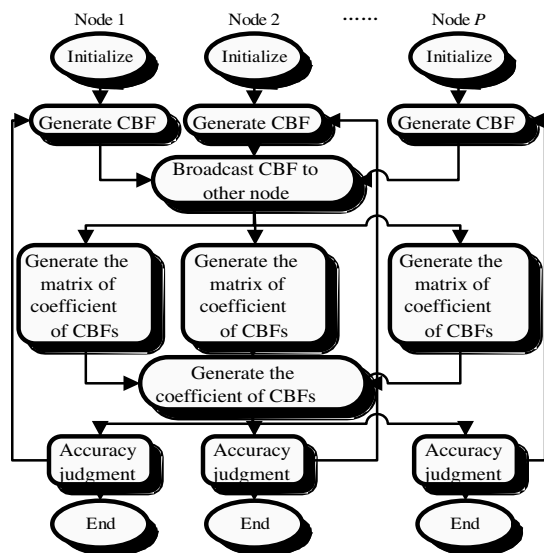

Figure 1: Outline of parallel CBFM.

Figure 2: Matrix equation of SCBF.

4. NUMERICAL RESULTS

As we have discussed in the past, the speed-up ratio of SP-AMCBFM in homogeneous parallel computing environment is very high, even close to the ideal case. But in heterogenous parallel computing environment, the computing ability of every node is different, and the efficiency will be affected.

In this section, two test cases are given as follows, and all of the objects are irradiated normally by plane wave. All numerical results in this paper are implemented on PC clusters based on Message Passing Interface (MPI), and in the homogeneous parallel computing environment, we have 6 Intel Pentium 3.0 GHz CPU/512 MB memory computers and 4 Intel Pentium 3.2 GHz CPU/512 MB memory computers. The difference between the computers is very, that is why λ is chosen closed to 1 in the next two cases. Compared SP-AMCBFM with HP-AMCBFM, we can find that the new is more efficient in heterogenous parallel computing environment.

Case 1: Perfect Electric Conductor (PEC) cube whose length of side is 1.5 m, the total unknowns are 45000. The frequency is 1 GHz. The object geometry has been divided into 98 distinct blocks. In order to prove the correctness, we have compared with the computing result of FEKO. The result of SP-AMCBFM and HP-AMCBFM are the same.

Table 1: Computing time and memory used in Case 1.

Parallel Method	Computing time (s)	Memory (MB)
SP-AMCBFM	20773	166.5 ∼ 170.9
HP-AMCBFM	18549	157.8 ∼ 175.3

Table 2: Computing time and memory used in Case 2.

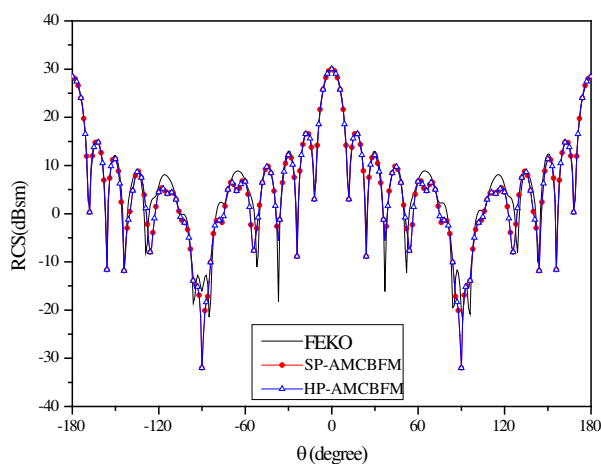| Parallel Method	Computing time	Memory (MB)
SP-AMCBFM	8 h 56 m	228 ∼ 232.6
HP-AMCBFM ($\lambda = 0.9$)	8 h 17 m	205.3 ∼ 241.8
HP-AMCBFM ($\lambda = 0.8$)	8 h 3 m	182.5 ∼ 246.3

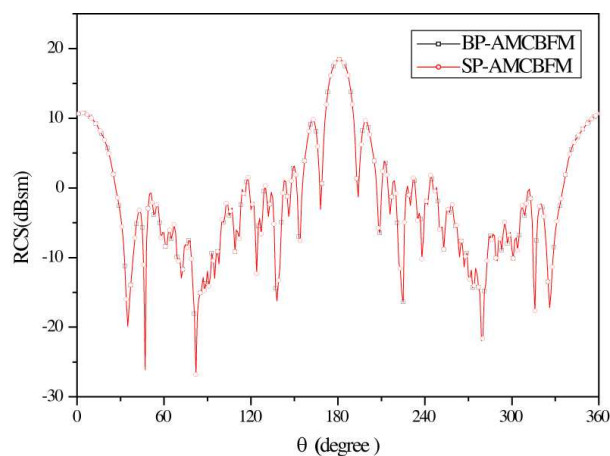
Figure 3: Bi-static RCS of Case 1.
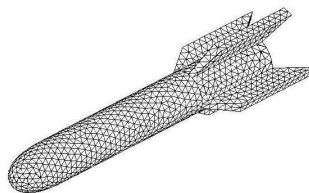

Figure 4: Bi-static RCS of Case 2.

Figure 5: Meshed model of PEC Predigested Missile.

Case 2: PEC predigested missile with the length about 4 m, and the diameter is about 0.5 m. The frequency of the incident wave is 1.5 GHz, and the total unknowns are 57907. The object is divided into 504 blocks. Because the complex structure of missile model, the unknowns of divided blocks is different, and we can see in Table 2, that when $\lambda = 0.8$ the computing time is less.

5. CONCLUSIONS

In this paper, we present a hybrid scheduling parallel method which can be used in heterogenous parallel computing environment. A series of numerical results and computing performance are discussed, which show that the hybrid scheduling parallel method is a promising solution for analyzing large-scale problems in electromagnetic field, and confirm the accuracy and efficiency of the proposed method in speeding up solving large electrical scale problems.

REFERENCES

1. Rao, S. M., D. R. Wilton, and A. W. Glisson. "Electromagnetic scattering by surfaces of arbitrary shape," *IEEE Transactions on Antennas and Propagation*, Vol. 30, No. 5, 409–418, 1982.

2. Song, J. M. and W. C. Chew, "Fast multipole method solution of three dimensional integral equation," *IEEE Antennas and Propagation on Society International Symposium*, 1528–1531, California, USA, June 18–23, 1995.

3. Song, J., C. Lu, and W. C. Chew, "Multilevel fast multiple algorithm for electromagnetic scattering by large complex objects," *IEEE Transactions on Antennas and Propagation*, Vol. 3, No. 4, 1488–1493, 1997.

4. Abd-El-Raouf, H., R. Mittra, and J.-F. Ma, "Solving very large EM problems using the MPI-CBFDTD method," *IEEE Antennas and Propagation on Society International Symposium*, 18–21, Washington, USA, July 3–8, 2005.

5. Velamparambil, S., W. C. Chew, and J. M. Song, "10 million unknowns: Is it that big?" *IEEE Transactions on Antennas and Propagation*, Vol. 45, No. 2, 43–58, 2003.

6. Lin, H., W. F. Cai, H. P. Guo, and X. G. Liu, "Analysis of large-scale EM scattering using the parallel characteristic basis function method," *IEEE 7th International Symposium on Antennas, Propagation & EM Theory*, 1–4, Guilin, China, October 26–29, 2006.

7. Prakash, V. V. S. and R. Mittra, "Characteristic basis function method: A new technique for efficient solution of method of moments matrix equations," *Microwave and Optical Technology Letters*, Vol. 36, No. 2, 95–100, 2003.

8. Han, G. D. and C. Q. Gu, "A hybrid QR factorization with dual-MGS and adaptively modified characteristic basis function method for electromagnetic scattering analysis," *Microwave and Optical Technology Letters*, Vol. 49, No. 11, 2879–2883, 2007.

9. Dai, F., G. D. Han, and C. Q. Gu, "Parallel adaptively modified characteristic basis function method based on static load balance," *Journal of Electronics (China)*, Vol. 26, No. 4, 532–536, July 2009.

Wireless Mass Sensor System with Four Mixers Structure Based on FBAR

Wei-Wei Cheng[1], Shi-Sheng Jin[2], Shu-Rong Dong[1], and Yan Han[1]

[1]Institute of Microelectronics and Optoelectronics, Zhejiang University, Hangzhou, Zhejiang 310027, China
[2]Guizhou Meteorological Information Center, Guiyang, Guizhou 550002, China

Abstract— A new-type wireless mass sensor system with four mixers structure based on FBAR is designed, fabricated and tested, which includes dual-path and a receiver to test the sensor circuit. The mixing-mode makes the result of measurement more accurate than the one which is based on dividing-mode. The result of measurement of mixing-mode depends on the accuracy and stability of the oscillators in mixers. In fact, this measured frequency is the real oscillating frequency which represents the practical change of mass on the FBAR sensor. And this wireless mass sensor system with four mixers structure is programmable of two working modes which are automatic frequency tracking and customizing frequency tracking for application.

1. INTRODUCTION

FBAR (Film Bulk Acoustic Resonator) consists of a piezoelectric resonator based on bulk acoustic film, and there is an operating frequency which is above 1000 MHz of it, while its Q factor may be more than 2000, what's more, its high operating frequency makes it be good candidate of integrated mass sensor chip. In fact, its compatibility to the CMOS and BiCMOS integrated process gives it a good prospect of consuming market, and its small size brings the very possibility of its application for sensor, detector, and filter, duplexer, multi-duplexer, and oscillator in wireless communication [1].

FBAR oscillator is very important to the FBAR mass sensor, and the accuracy of the sensor depends on the stability of oscillator, so the more accurate measurement requires more stable frequency and regular change of frequency which is according to the increasing of mass on the film of FBAR. These parameters are determined by the phase noise of FBAR oscillator. Otherwise, if the bandwidth of frequency is larger, the requirement to the phase noise is more critical. Therefore, this paper represent a wireless mass sensor system with four mixers structure to make the oscillator which is connected to the other port of mixer work in different band range to get the linear working performance.

And considering other practical aspects in application of the sensor, accuracy and stabilization of the measurement of FBAR sensor are disturbed by the temperature, humidity, pressure and other affecting factors of environment, so dual-path architecture and application of programmable logic circuit may compensate the error and process the data of the measurement results precisely and sending them in high speed [2, 3].

2. THEORY

FBAR is modeled by MBVD (Modified Butterworth Van Dyke) model [4], in Fig. 1. FBAR has a series resonant frequency f_s which is set by Equation (1) and a parallel resonant frequency f_p which is determined by Equation (2) [5],

$$f_s = \frac{1}{2\pi\sqrt{L_m C_m}} \tag{1}$$

$$f_p = \frac{1}{2\pi\sqrt{L_m \dfrac{C_m C_0}{C_m + C_0}}} \tag{2}$$

where L_m is the motional inductance, C_m is the motional capacitance, C_0 is the clamped capacitance, and R_m is the motional resistance of FBAR.

3. CIRCUITS DESIGN

The sensor system with dividing-mode is shown in Fig. 2, which includes a pair of differential inputs to sense the tiny mass, and the difference of the two channels is corresponding to the real
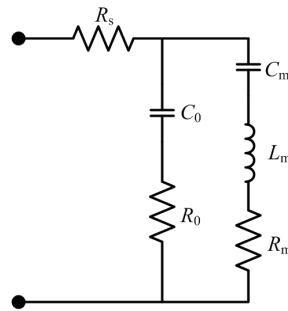
Figure 1: MBVD model.

change of the mass. This is the traditional structure, and the structure with differential inputs is to compensate the error brought from temperature and other factors of environment [17].

Figure 3 shows the differential structure of sensing by the way of mixing, which includes several circuit block: under-tested FBAR sensor oscillator, RF tracking circuit of coarse channel, IF tracking circuit of fine channel, programmable logic processor circuit, reference IF tracking circuit of fine channel, reference RF tracking circuit of coarse channel, reference FBAR sensor oscillator, RF transceiver and antenna.

Figure 4 shows the schematic of differential structure of sensing by the way of mixing. RF tracking circuit of coarse channel includes RF mixer, RF oscillator, amplifier, IF filter; IF tracking circuit of fine channel includes IF mixer, IF oscillator, filter and wave-shaping circuit; reference IF tracking circuit of fine channel includes IF mixer, IF oscillator, filter and wave-shaping circuit; reference RF tracking circuit of coarse channel includes RF mixer, RF oscillator, amplifier, IF filter; programmable logic processor circuit includes programmable logic device circuit and digital signal processing circuit.

In the processing of measurement, the mass loading on FBAR sensor increases, f_s and f_p of FBAR decrease, and this change is the base of mass measurement. The FBAR studied in this work resonates at around 2000 MHz in its fundamental thickness shear mode.

In the testing channel, the radio frequency signal (under-tested FBAR RF signal) which created by the under-tested FBAR sensor oscillator is sent to the RF tracking circuit of coarse channel. RF oscillator creates a reference radio frequency signal to the RF mixer to mix the under-tested FBAR
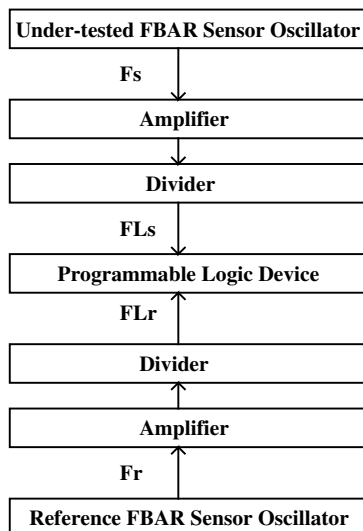

Figure 2: Differential structure of sensing by the way of dividing.
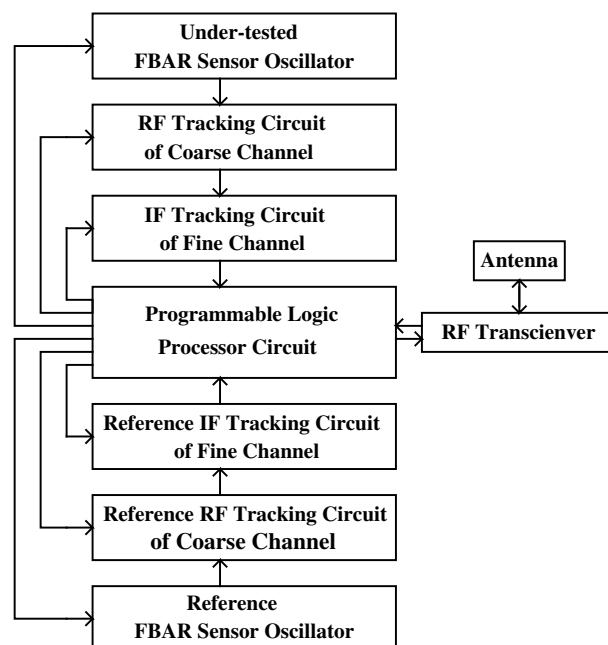
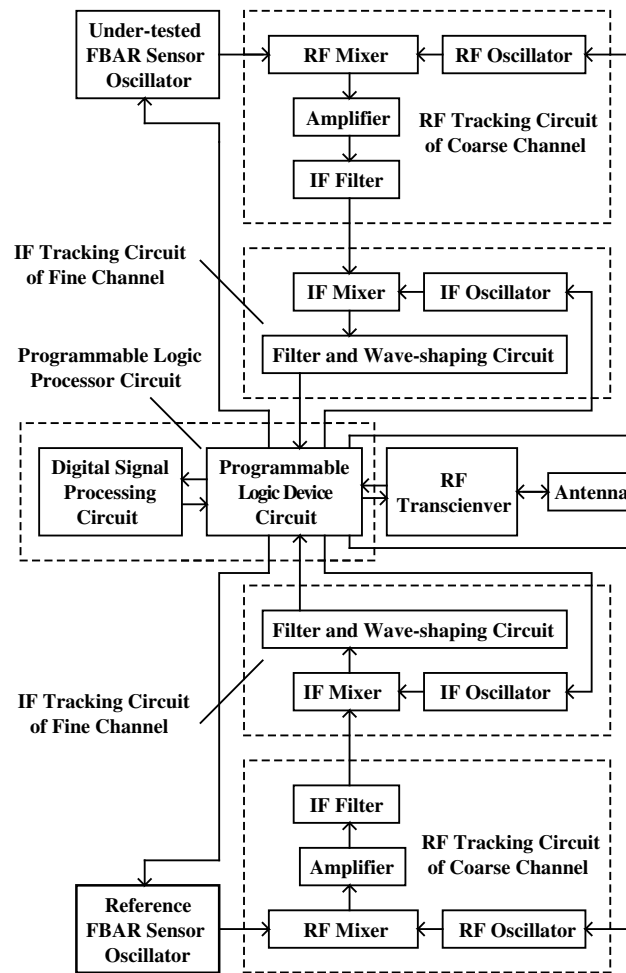Figure 3: Differential structure of sensing by the way of mixing.

Figure 4: Schematic of mass sensor system.

RF signal, then the output of RF mixer is an intermediate frequency signal (under-tested FBAR IF signal), which is sent to the IF filter after being amplified by the amplifier, then it comes in the IF tracking circuit of fine channel. The IF oscillator creates a reference intermediate frequency signal to the IF mixer to mix the under-tested FBAR IF signal, then the output of IF mixer is an low frequency signal (under-tested FBAR LF signal), which is sent to the wave-shaping circuit to make the sine wave to a digital signal to be fit to the programmable logic device circuit after being filtered by the LF filter to remove the noise signal and harmonic waves. Then it outputs the under-tested FBAR digital signal.

The circuit of reference channel is as well as the one of testing channel, and the signal processing of reference channel is same as the one of testing channel. The difference is that the radio frequency signal (reference FBAR RF signal) which created by the reference FBAR sensor oscillator is according to the factors of environment but not the change of mass.

This circuit with four mixers is a dual-channel circuit which is like a super heterodyne receiver. The key point is that the programmable logic processor circuit may control the frequency of the two RF oscillators and the two IF oscillators through a memory storing the frequency table by the look-up-table mode. Then it increases the speed of the signal processing and makes the frequency regulation accurate, and avoids the affect of temperature.

On the other hand, according to the frequency table, the programmable logic processor circuit keeps the linearity of the accordance between the mess change and the frequency change. To a great extent, it compensates the measurement errors brought from the frequency shifting and low stability of oscillators, and the temperature and other environment factors to get a better performance of tiny mess measurement.
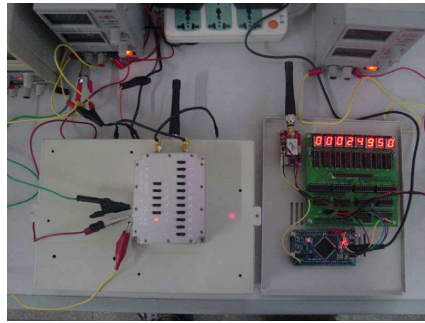
Figure 5: Photo of mass sensor system (under testing).

Table 1: Specifications of the wireless tiny mass sensor system.

Parameter	Typical	Absolute Maximum	Absolute Minimum	Unit
Input Frequency		2400/868/915		MHz
Input Amplitude	0	5.5	−4	dBm
Supply Voltage	5	7	3	V
Distance between Transmitter and Receiver		100 (indoor) 1200 (outdoor)		m
Resolution of Display			0.05	kHz
Range of Error of Display		0.025		kHz
Range of Display	0 ∼ 2.4			GHz
Time of Response		0.8	0.4	s

4. TESTING RESULTS

See the wireless mass sensor system with four mixers structure based on FBAR in Fig. 5, and the testing results are shown in Table 1. In fact, the minimum shifting frequency can decrease to the level below 0.05 kHz, and it owes to the high Q factor of FBAR and the dual-path structure which avoids the error of the mass measurement effectively.

5. CONCLUSION

A new wireless mass sensor system with four mixers structure based on FBAR has been designed, and the dual-path architecture with mixers compensates the interference of environment. In fact, comparing with previous dual-path architecture with dividers, this one with mixers and programmable logic circuits has realized that the mixing-mode makes the result of measurement more accurate than the one which is based on dividing-mode. The measured frequency is the real oscillating frequency which represents the practical change of mass on the FBAR sensor. Moreover, this wireless mass sensor system with four mixers structure is programmable of two working modes which are automatic frequency tracking and customizing frequency tracking for application.

REFERENCES

1. Zhang, H. and E. S. Kim, "Micromachined acoustic resonant mass sensor," *Journal of Microelectromechanical Systems*, Vol. 14, 699–706, Aug. 2005.
2. Cheng, W. W., et al., "A low power, low phase noise fbar oscillator," *Integrated Ferroelectrics*, Vol. 105, 75–86, Jan. 2009.
3. Cheng, W. W., et al., "Wireless tiny mass sensor system based on FBAR," *PIERS Proceedings*, 410–413, Moscow, Russia, Aug. 18–21, 2009.
4. Zhang, H. and E. S. Kim, "Micromachined acoustic resonant mass sensor," *Journal of Microelectro Mechanical Systems*, Vol. 14, 699–706, Aug. 2005.
5. Larson, J. D., et al., "Modified Butterworth-Van Dyke circuit for FBAR resonators and automated measurement system," *IEEE Ultrasonics Symposium*, 863–868, San Juan, Pr, 2000.

Design and Simulation of Low Noise Amplifier for Radio Frequency Front End of Wireless Communication

Shi-Sheng Jin[1], **Wei-Wei Cheng**[2], **Shu Rong Dong**[2], **Yan Han**[2],
Shun Yuan[1], **Jun-Yong Wang**[1], **and Jue Li**[1]

[1]Guizhou Meteorological Information Center, Guiyang, Guizhou 550002, China
[2]Institute of Microelectronics and Optoelectronics, Zhejiang University, Hangzhou, Zhejiang 310027, China

Abstract— This paper presents the design of 2 GHz front end low noise amplifier application. The progress of the 3G wireless communication has the demand for the development of low cost, low power and small size transceiver by using microstrip technology. Design and simulation of low noise amplifier circuits are presented. It is focusing on development of low noise amplifier operating at 2000 MHz for the third generation wireless communication application. The amplifier design comprised AT-41411 and lumped elements to implement the matching networks. Hewlett-Packard's AT-41411 is a general purpose NPN bipolar transistor that offers excellent high frequency performance. The target simulation are gain (S-21) > 10 dB, noise figure as low as possible (given the bias conditions) with < 10 dB, and input and output return loss < -10 dB at 2000 MHz.

1. INTRODUCTION

The frequency band of the third generation wireless communication is 1900 MHz–2200 MHz [1, 2]. Low noise amplifier is a basic building block of modern communication systems, which is the key part of radio frequency front-end module and a receiver section. And the low noise amplifier is the first stage amplifier of the radio frequency module and is very important to the noise figure of the whole wireless communication system [2–5]. The received signal from antenna is very weak in practical systems and must be amplified before it's demodulation. Otherwise, the components of the module add kinds of noise to the received signal, when amplifying a very low-level signal. In fact, at the same time, the amplifier noise may amplify itself. Low noise amplifier has some characters: Maximum gain with minimum noise figure which can deal with the above problems. The fabrication of modern low noise amplifier adopts different technologies: SiGe, Bipolar, BiCMOS, MCM, GaAs, MMIC, SOI CMOS, MEMS and microstrip technology [2–7]. In this paper, we simulated a low noise amplifier with the microstrip technology which comprises the printed circuit board, bipolar transistor AT-41411 and lumped components to implement the matching networks.

2. CIRCUIT DESIGN

The requests of the low noise amplifier are that gain (S-21) > 10 dB, noise figure as low as possible (given the bias conditions) with < 10 dB, and input and output return loss < -10 dB at 2 GHz.

The formulas give source and load reflection coefficients to make the maximum power gain of LNA.

$$\Gamma_{in} = S_{11} + \frac{S_{12}S_{21}\Gamma_L}{1 - S_{22}\Gamma_L}$$
$$\Gamma_{out} = S_{11} + \frac{S_{12}S_{21}\Gamma_L}{1 - S_{22}\Gamma_L}$$

The stability of the low noise amplifier which is given bias point is determined by the following.

$$K = \frac{1 - |S_{11}|^2 - |S_{22}|^2 + |\Delta|^2}{2|S_{12} \cdot S_{21}|}$$
$$\Delta = S_{11} \cdot S_{22} - S_{12} \cdot S_{21}$$

If $K > 1$ and $|\Delta| < 1$, the low noise amplifier is unconditionally stable, while if $K > 1$ and $|\Delta| > 1$, or $K < 1$ and $|\Delta| < 1$, it is potentially stale.

3. CIRCUIT SIMULATIONS

On account of the advantages above, a novel power controller of wireless sensor network node circuit for energy saving is designed, which is shown in Figure 1. There is only transmitting channel of communication, and the wakeup circuit only receiving the low frequency signal to accumulate the energy and without the function to demodulating the information of the low frequency signal.

It consists of LF antenna (low frequency antenna), RF antenna (radio frequency antenna), wakeup circuit, logic control switch, battery which is composed of three power supply modules, power switch array which is composed of three power array modules, duplexer, monitor circuit which is composed of detector, filter and comparator, radio frequency transmitting circuit which is composed of PA (power amplifier), gain amplifier and modulator, DSP (digital signal processing), and data sampling circuit which is composed of A/D (analogue to digital converter) and sensor.

3.1. *S*-parameters and Noise Parameters

It is a simulation of the *S*-parameters and noise parameters of the amplifier before the addition of input and output matching networks.

Figure 1 shows the main circuit structure of the low noise amplifier, while Figure 2 shows the available gain, noise, and power gain circles, as well as the minimum noise figure, optimal source impedances, etc., and shows the source and load stability circles as well as the source and load impedances for simultaneous conjugate matching.

3.2. Matching Design

A shunt-L, series-C network is used to generate a source impedance that is in between the optimal source impedances for noise figure and available gain. it may be necessary to use a series-C, shunt-L, series-C network if it is undesirable to have a DC short to ground at the input of the finished amplifier.
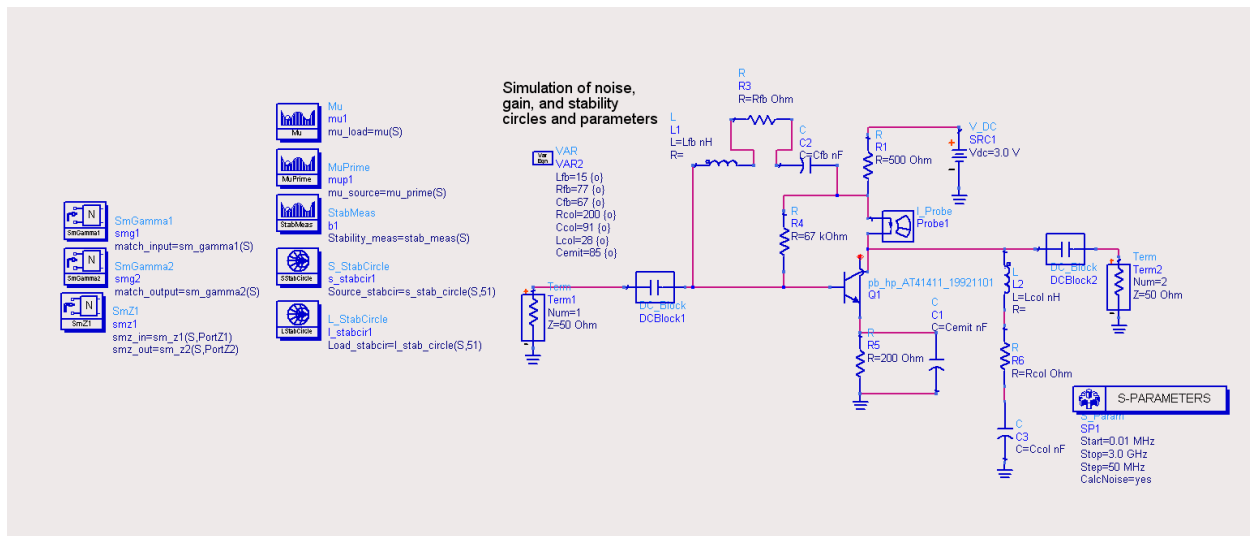
Figure 1: Main circuit structure of the low noise amplifier.
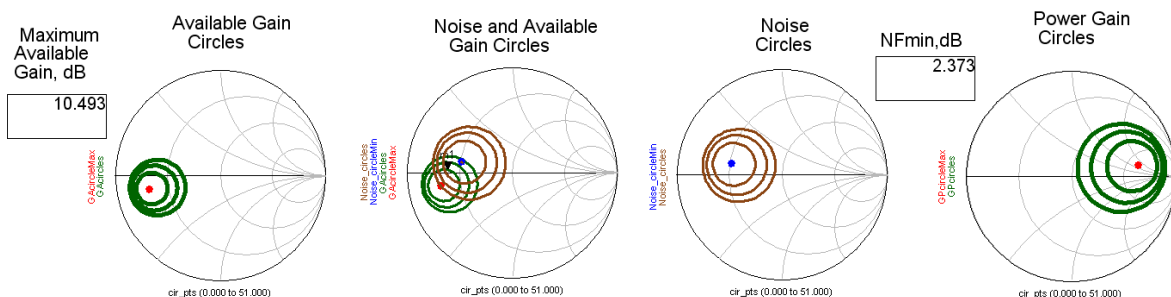
Figure 2: Circles simulation.

Figure 3 shows a simple, LC matching network design to generate a source impedance that is a compromise between the optima for gain and noise figure.

The marker in Figure 4 is midway between optimal source impedances for noise figure and available gain. With this source impedance, a noise figure of about 2.5 dB and a gain of about 10 dB should be achievable.
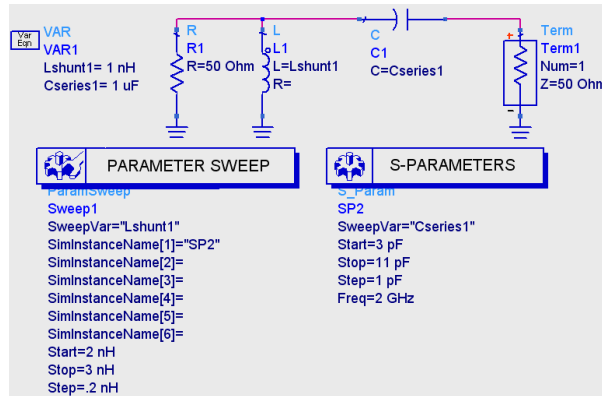
Figure 3: Input impedance matching.
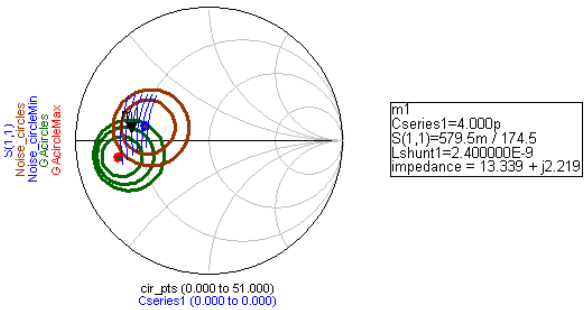
Figure 4: Simulation of input impedance matching.
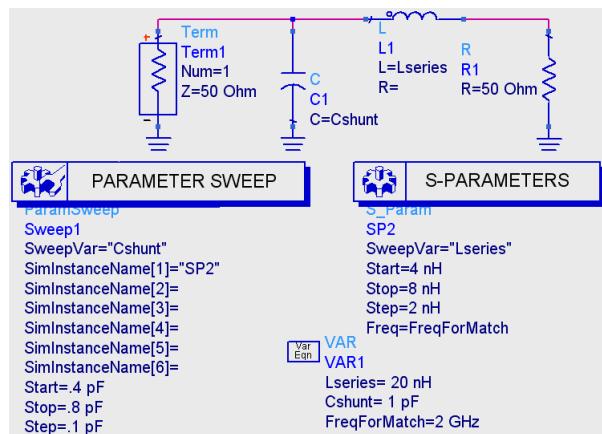
Figure 5: Output impedance matching.
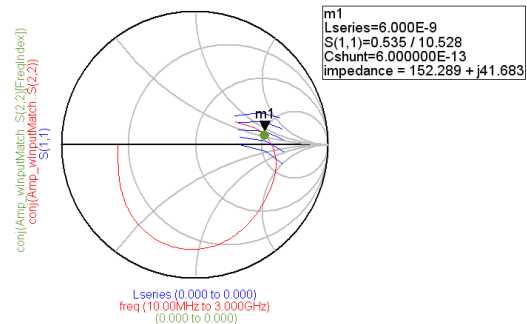
Figure 6: Simulation of output impedance matching.
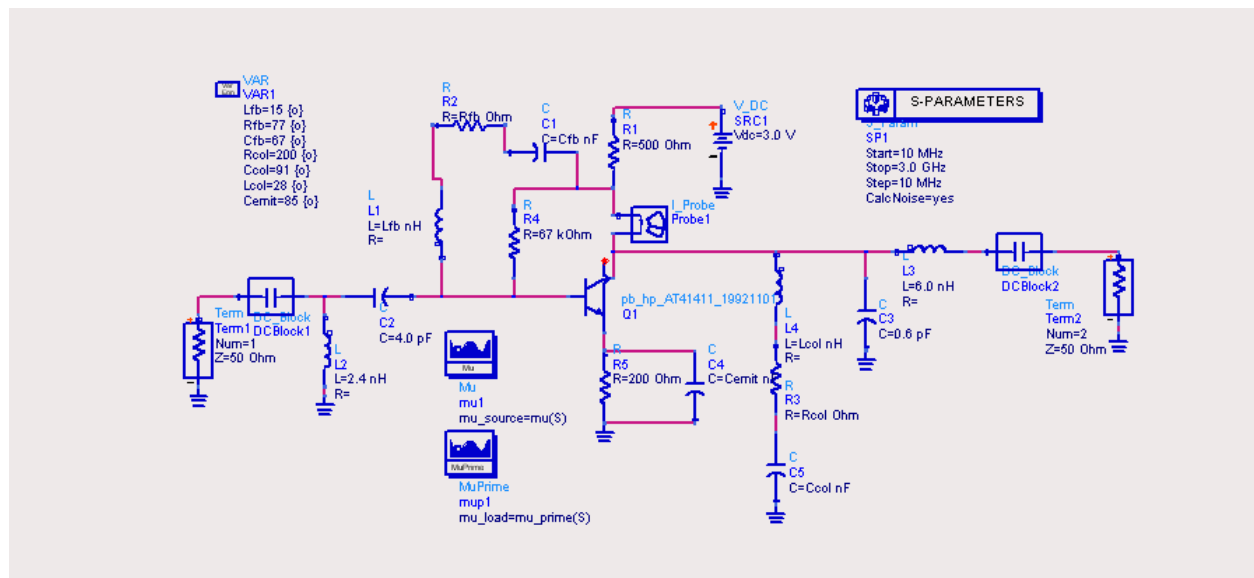
Figure 7: The amplifier with stability networks.

Figure 5 shows a simple, LC matching network design to generate a load impedance close to that required for simultaneous conjugate match..

A series-L, shunt-C network is used to generate a load impedance that is close to that required for simultaneous conjugate matching. With this matching network, it will be necessary to add a DC blocking capacitor to the output of the finished amplifier.

A matching network has been added to the input, and the external source impedance has been set to 50 Ohms. So, given that the input matching network is fixed, the conjugate of S_{22} will be the optimal load reflection coefficient. The marker is close to this impedance, and the L-series and C-shunt values below will generate it.

3.3. Stability and Noise Figure

It shows a simulation of the amplifier with stability networks, and both impedance matching networks added. The resulting gain and noise figure are close to what is predicted by the available gain and noise figure circles, as shown in Figure 7 and Figure 8.
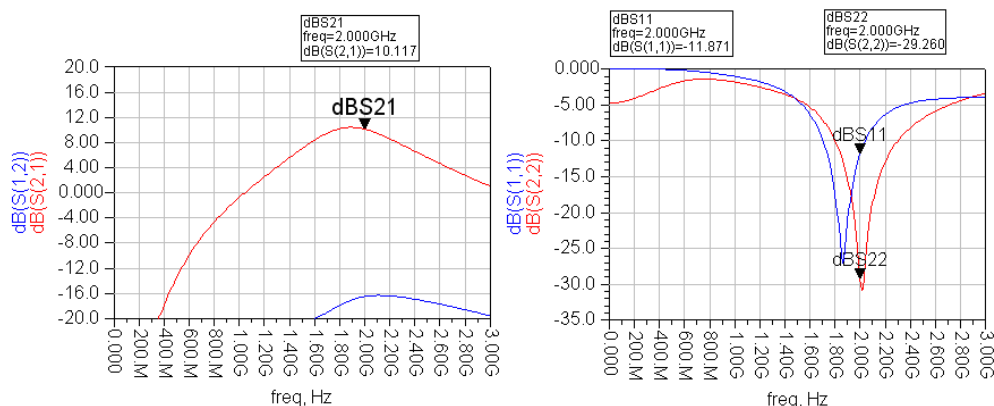
Figure 8: Simulation of the amplifier with stability networks.
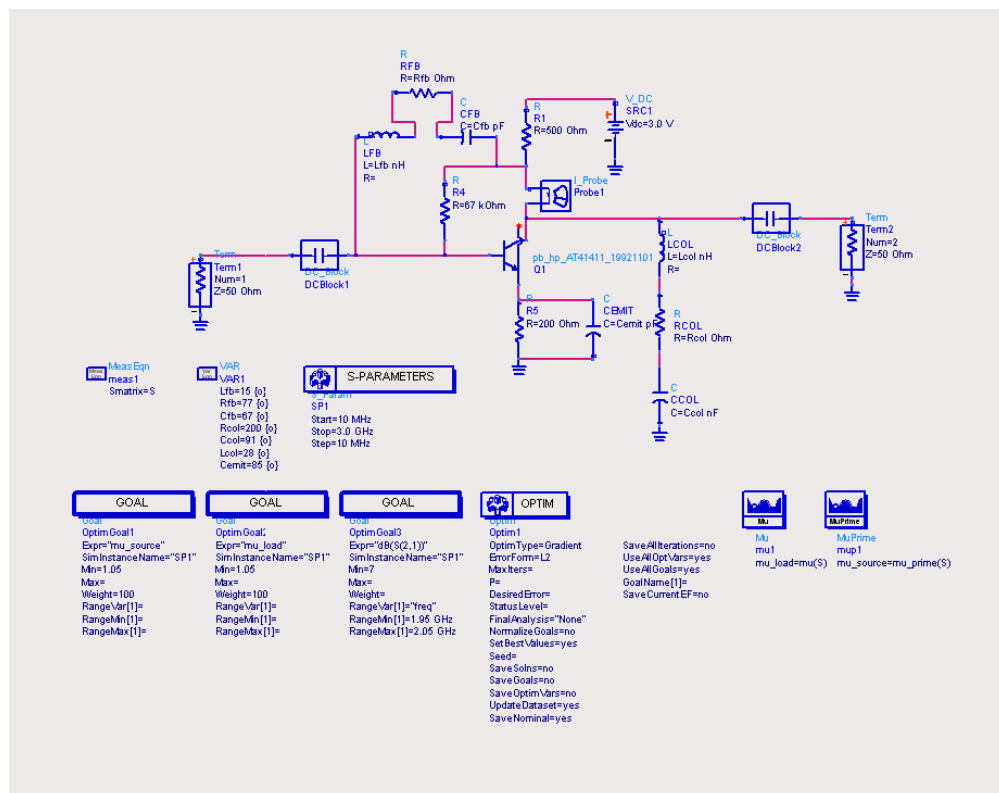
Figure 9: Optimization.
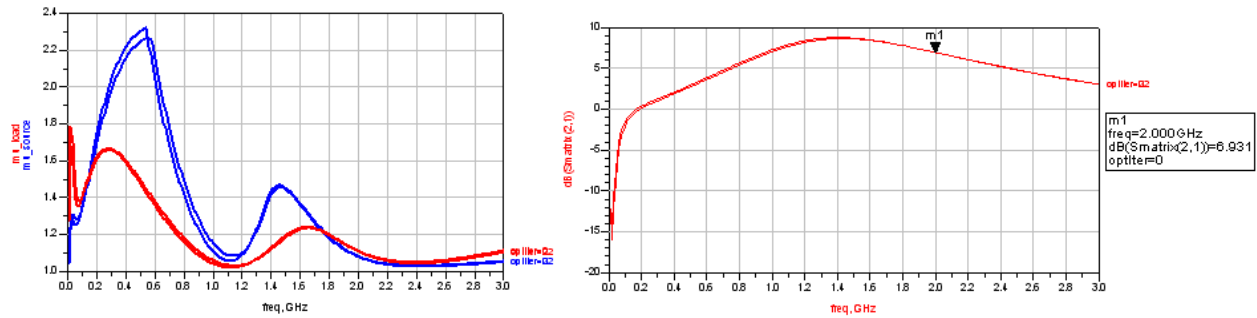
Figure 10: Simulation of optimization.

4. OPTIMIZATION

Gain optimization and Stability optimization show the addition of stabilizing networks added between the base and collector, and from the collector to ground. The component values are optimized to achieve unconditional stability, as simulated from 0 to 3 GHz.

5. CONCLUSION

We designed a 2 GHz front end low noise amplifier application by using microstrip technology. The amplifier design comprised AT-41411 and lumped elements to implement the matching networks. The lumped element configuration provides better performances than the circuit structures based on distributed elements. The results of the low noise amplifier are gain (S-21) > 10 dB, noise figure as low as possible (given the bias conditions) with < 10 dB, and input and output return loss < -10 dB at 2 GHz. The results are according to the desired requirements based on this designing method in the frequency band of wireless communication.

REFERENCES

1. Jin, H. and C. A. T. Salama, "A 1-V, 1.9-GHz CDMA, CMOS on SOI, low noise amplifier," *IEEE International SOI Conference*, 2000.
2. Harada, M., T. Tsukahara, J. Kodate, A. Yamagishi, and J. Yamada, "2-GHz RF front end circuits in CMOS/SMOX operating at an extremly low voltage of 0.5 V," *IEEE J. of Solid-state Circuits*, Vol. 35, No. 12, 2000–2004, Dec. 2000.
3. Kim, C. S., M. Park, C. H. Kim, H. K. Yu, K. Lee, and K. S. Nam, "A fully integrated 1.9 GHz CMOS low noise amplifier," *IEEE Microwave and Guided Wave Letters*, Vol. 8, No. 8, Aug. 1998.
4. Zhang, L. and Y. X. Xia, "Design and simulation of microwave band-pass filter based on SERENADE," Amphibious Technique and Product for Military and Civilian, 36–37, Dec. 2005.
5. "Tuning, optimization and statistical design," *Agilent Technologies*, May 2003.
6. Rohde, U. L. and D. P. Newkirik, *RF/Microwave Circuit Design for Wireless Application*, John Wiley & Sons, Inc., 2000.
7. Le Ny, J., B. Thudi, and J. McKenna, "A 1.9 GHz low noise amplifier," *EECS 522 Analog Integrated Circuits Project*, 1–6, Winter 2002.

A Chaos Based Waveform Approach to Radar Target Identification

F. J. Rachford and T. L. Carroll

Naval Research Laboratory, Washington, D.C. 6362, USA

Abstract— We present a low resolution method for radar target identification. The method employs optimized waveforms in cross correlation with the return from a low frequency chirp to distinguish between similar candidate targets. Target signature waveforms were generated every degree in azimuth for generic wing-body-tail targets using FDTD simulation. The targets were four to five meters in length with approximately two meter wing spans. The transmitted linear chirp had a 20% band width and 250 MHz center frequency. We generated candidate waveforms using a simple chaotic map to cross correlate with the target returns. The waveforms were generated by passing chaotic time series through a bandpass filter. Alternately the waveforms were constructed by concatenating constant amplitude sinusoids whose periods were specified by the amplitudes of the chaotic time series. In both cases waveforms were constructed with the same bandwidth and center frequency as the transmitted chirp. A large number of test waveforms were generated by random variation of the generating chaotic map parameters. These test waveforms were cross correlated with the return waveforms from two similar targets. Waveforms that maximized (minimized) the cross correlation amplitude ratio difference between targets were retained and fine tuned with simplex optimization. Optimization was conducted over target azimuthal windows up to 10° in width. Best maximizing and minimizing test waveforms were retained for each data window. Using this method pairwise discrimination between candidate targets could be achieved over most aspects where the signature of the respective targets are not varying too rapidly with angle.

1. INTRODUCTION

The problem of identifying targets seen in radar returns has important civilian and military applications. The current methods seek to identify a particular complex target by resolution of individual scatterers [1] or by recognizing characteristic resonances [2, 3]. Here we set out to devise a method that will distinguish between two candidate known targets, A and B by generating and optimizing waveforms to cross correlate with their known simulated or measured radar returns [4, 5]. With the advent of modern fast gigahertz electronics complex real time radar signals can be readily constructed, digitized and processed. In principal these waveforms can be fabricated to enhance or null the signature of a single known target from detailed knowledge of its geometry and surface properties. Constructing waveforms that will simultaneously maximize (minimize) the radar return from one target while simultaneously minimizing (maximizing) the return from a second target is considerably more difficult. We use chaos based waveform optimization to perform this task. Employing an appropriate chaotic map allows us to generate a very wide variety of deterministic reproducible waveforms from random variation of a few parameters. We select and optimize these test waveforms by cross correlation with the simulated or measured return of fast radar chirps reflected from two known targets at multiple angles of incidence. With our optimized waveforms we can form ratios of cross correlations of the two targets with both maximizing and minimizing chaos based test waveforms. We then use the difference between cross correlation ratios to discriminate between the targets.

2. METHOD

In this work, we assume that the radar transmitted pulse is a simple linear chirp, Ψ_{chirp}, transmitted with a (20%) bandwidth. The transmitted pulse could be any waveform with sufficient bandwidth but we simplify the problem by limiting it to a fast linear chirp. In this paper, we also assume, for convenience, that the target of interest is in level flight at a substantial distance and is monitored by a mono-static radar. We assume that in practice standard radar tracking will provide Doppler correction and angle of approach information.

We also assume that the radiation patterns returned from the two known complex scatterers, Ψ^A, Ψ^B are normalized to the average amplitude of the return and are faithfully digitized. Radar range data (or simulations) for each target are collected at multiple azimuthal angles Θ as individual targets are rotated in the far field. We also assume that the returned waveforms vary slowly with azimuth. Since in practice the angle of approach information is approximate, a number of waveforms within an azimuthal window are analyzed together.

We wish then to find a waveform for each azimuthal data window, $\Phi_{\max}^{A|B}$, that will maximize the averaged cross correlation amplitude, $\langle|R(\Phi_{\max}^{A|B}\Psi^A)\rangle$ with return from target A while minimizing the the cross correlation amplitude with target B, $\langle|R(\Phi_{\max}^{A|B}\Psi^B)|\rangle$. Also we wish to find another waveform, $\Phi_{\min}^{A|B}$, that will minimize $\langle|R(\Phi_{\min}^{A|B}\Psi^A)\rangle$ while maximizing $\langle|R(\Phi_{\min}^{A|B}\Psi^B)|\rangle$. Taking the ratios of the maximizing to minimizing cross correlations for each target defines their respective characteristic contrast ratio in the angular window of interest. The difference in these contrast ratios is used to distinguish between targets.

We have constructed the trial waveforms, Φ, by two methods; 1) the concatenation of single unit amplitude sinusoids whose periods are specified by a chaotic time series and 2) band pass filtering of a chaotic time series. In both cases the time series was constructed by evaluating the modulus of an iterated six parameter analog shift register sum [4, 5]. The resulting chaotic time series is a sequence of floating point values bounded in value between 0 and 1. In the first instance, the time series is mapped onto sinusoids with periods within the desired band width and center frequency. In the second case the center frequency and bandwidth of the band pas filter are similarly specified. In both cases we require that the center frequency and band width match that of the transmitted chirp, Ψ_{chirp}. In the first case we further required that the test waveform conform to the same number as sinusoidal elements present Ψ_{chirp}. In the second case we required that the test waveform conform to the length of the identically windowed return waveforms from the two targets, Ψ^A and Ψ^B.

For simplicity we first consider the process of finding Φ at a single azimuth. In practice we iterate to a solution first composing a random chaos based test waveform. Then compute the cross correlation amplitude with the waveforms Ψ^a and Ψ^B returned from both targets A and B at the angle of interest, We then compare amplitudes to previous iterations our best $\Phi_{\max}^{A|B}$ and $\Phi_{\min}^{A|B}$. If the new waveform maximizes the correlation ratios when subsitiuted for the previous best $\Phi_{\max}^{A|B}$ or $\Phi_{\min}^{A|B}$ it is retained. The three ratios to be maximized are summed in Eq. (1).

$$G = \frac{\langle|R(\Phi_{\max}^{A|B}\Psi^A)|\rangle}{\langle|R(\Phi_{\min}^{A|B}\Psi^A)|\rangle} + \frac{\langle|R(\Phi_{\max}^{A|B}\Psi^A)|\rangle}{\langle|R(\Phi_{\max}^{A|B}\Psi^B)|\rangle} + \frac{\langle|R(\Phi_{\min}^{A|B}\Psi^B)|\rangle}{\langle|R(\Phi_{\min}^{A|B}\Psi^A)|\rangle} \tag{1}$$

We in fact calculate our ratio comparisons over a number of azimuthal angles contained in a window. This is necessary since the angle of approach is only approximately known. While computationally more complex this is a straightforward extension of the single angle process.

The process is repeated many times. After this iteration process is complete the two best test waveforms, $\Phi_{\max}^{A|B}$ and $\Phi_{\min}^{A|B}$, generated in each angular window are then optimized using the down hill simplex amoeba optimization routine [6]. In the same process waveforms $\Phi_{\max}^{B|A}$ and $\Phi_{\min}^{B|A}$, are also generated selecting target B over A. Due to the nature of the selection process $\Phi_{\max}^{A|B} \neq \Phi_{\min}^{B|A}$ and $\Phi_{\min}^{A|B} \neq \Phi_{\max}^{B|A}$. We then distinguish target A from target B by computing the contrast $C_i^{A|B}$ and contrast difference $D_i^{A|B}$ in each azimuthal window centered at Θ_i,

$$C_i^{A|B}(A, \Theta) = 20 \log_{10}\left(\frac{\langle|R(\Phi_{\max}^{A|B}(i)\Psi^A(\Theta))\rangle}{\langle|R(\Phi_{\min}^{A|B}(i)\Psi^A(\Theta))\rangle}\right) \tag{2}$$

$$C_i^{A|B}(B, \Theta) = 20 \log_{10}\left(\frac{\langle|R(\Phi_{\max}^{A|B}(i)\Psi^B(\Theta))\rangle}{\langle|R(\Phi_{\min}^{A|B}(i)\Psi^B(\Theta))\rangle}\right) \tag{3}$$

$$D_i^{A|B}(\Theta) = 20 \log_{10}\left(\frac{\langle|R(\Phi_{\max}^{A|B}(i)\Psi^A(\Theta))\rangle/\langle|R(\Phi_{\min}^{A|B}(i)\Psi^A(\Theta))\rangle}{\langle|R(\Phi_{\max}^{A|B}(i)\Psi^B(\Theta))\rangle/\langle|R(\Phi_{\min}^{A|B}(i)\Psi^B(\Theta))\rangle}\right) \tag{4}$$

As part of the same process we can save chaos based waveforms $\Phi_{\max}^A$ and $\Phi_{\min}^B$ which maximize the contrasts C_i^A and C_i^B in window i,

$$C_i^A(\Theta) = 20 \log_{10}\left(\frac{\langle|R(\Phi_{\max}^A(i)\Psi^A(\Theta))\rangle}{\langle|R(\Phi_{\min}^A(i)\Psi^A(\Theta))\rangle}\right) \tag{5}$$

$$C_i^B(\Theta) = 20 \log_{10}\left(\frac{\langle|R(\Phi_{\max}^B(i)\Psi^B(\Theta))\rangle}{\langle|R(\Phi_{\min}^B(i)\Psi^B(\Theta))\rangle}\right) \tag{6}$$

A large contrast C_i^A does not necessarily select target A itself but when used in combination with the $C_i^{A|B}$ and $D_i^{A|B}$ will serve to confirm that the identification of target A. Thus in order

to distinguish A from B, we save the parameters used to generate $\Phi_{\max}^{A|B}$ and $\Phi_{\max}^{A|B}$ and, if desired, $\Phi_{\max}^{A}$ and $\Phi_{\min}^{A}$ for each angular window using the same chaotic map and generation procedure. With fast parallel computation the contrasts and contrast differences can be rapidly generated for a large number of target combinations.

3. EXAMPLE

In order to test this scheme we created computer models of several similar generic wing/body/tail objects approximately five meters in length with features like engine ducts and radomes. The two of the target models considered here are shown in Fig. 1. Target 14 is 4.9 m long and target 16 is 4.8 m long. Both are two meters wide at the wings. None of the models simulate real military or civilian targets. The models are all right-left symmetric and have enough complexity to scramble the transmitted pulse upon reflection. We used a finite difference time domain (FDTD) code to launch linear chirps at the models at various angles (one degree steps between 0° and 180°). The short chirp had 50 MHz (20%) band width centered at 250 MHz. The low frequency and bandwidth were chosen to slow the angular variation of the returned waveforms while still imparting enough complexity to the waveforms to enable us to distinguish between targets. The same chirp was employed for each model simulation. A mono-static far field return waveform was calculated at each angle. Care was taken to terminate the simulations before the build-up of rounding errors invalidated the return signal. FDTD error constraints limited our available target size and chirp waveform length. We split the data into overlapping ten degree wide azimuthal windows taken five degrees apart.

The transmitted chirp was constructed by concatenating thirty three individual unit amplitude sinusoids spanning 225 to 275 MHz. The optimization code calculated and compared chaos based test waveforms, Φ, in cross correlation with all $\Psi^A(\Theta)$ and $\Psi^B(\Theta)$, at all angles Θ to find the best, $\Phi_{\max}^{A|B}(i)$ and $\Phi_{\min}^{A|B}(i)$ for all windows i.

In Fig. 2, we plot the calculated cross correlation amplitudes for the two best chaos based waveforms $\Phi_{\max}^{A|B}$ and $\Phi_{\min}^{A|B}$ optimized to distinguish target 16 from target 14 in the angular window
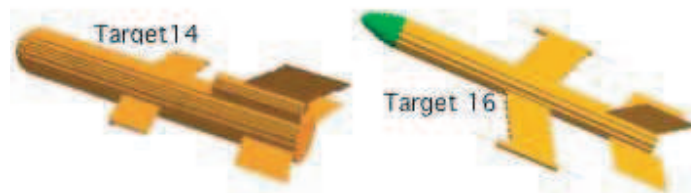
Figure 1: Shown are the two targets studied in this paper, targets 14 and 16. The gridding was selected to be less than one twentieth of a wavelength at 275 MHz. Gold or orange indicates metal and green indicates radome. Both are approximately 5 m in length.
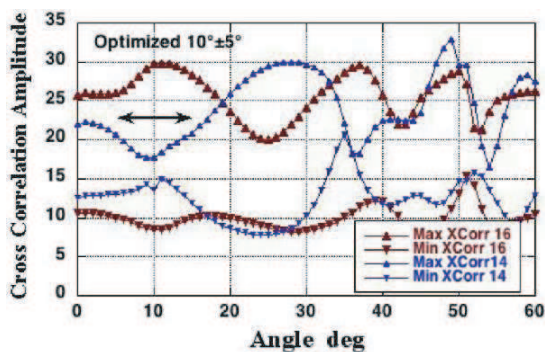
Figure 2: Cross correlation amplitudes for targets 16 and 14. Waveforms $\Phi^{16|14\max}$ and $\Phi^{16|14\max}$ optimized for a 10° window centered at 10° azimuth, 0° elevation. (See arrow). The cross correlations with returned waveforms Ψ^{16} and Ψ^{14} are shown extended over the 0° to 60° forward sector.
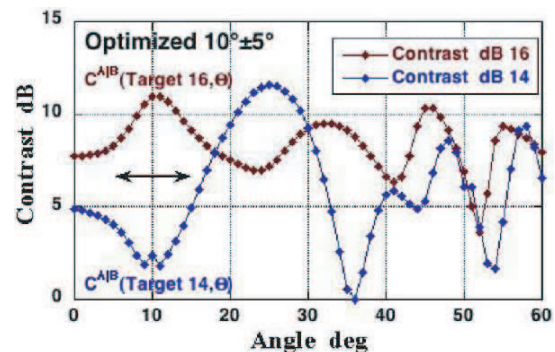
Figure 3: The cross correlation ratios $C^{16|14}(16,\Theta)$ and $C^{16|14}(14,\Theta)$ optimized for the 10° window centered at 10° azimuth, 0° elevation. (See arrow).
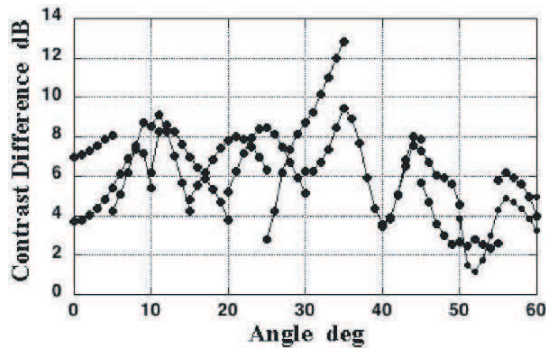
Figure 4: Contrast differences between targets 16 and 14, $D^{16|14}(\Theta)$, calculated for 10° azimuthal windows spaced 5° apart and 0° elevation.
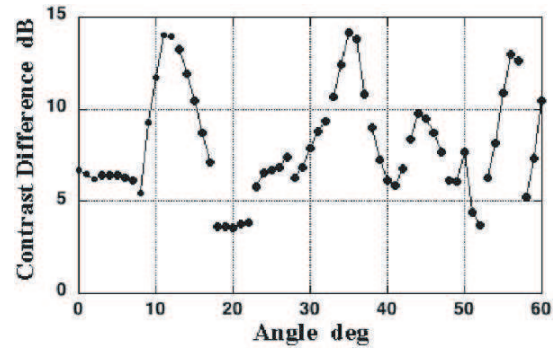
Figure 5: Contrast differences, $D^{16|14}(\Theta)$, between targets 14 and 16 for 4° windows spaced 5° apart for the same received data sets as in Fig. 4.

10°±5° (arrow). In that region $\langle|R(\Phi_{max}^{16|14}\Psi^{16}(\Theta))\rangle > \langle|R(\Phi_{max}^{16|14}\Psi^{14}(\Theta))\rangle$ and $\langle|R(\Phi_{min}^{16|14}\Psi^{16}(\Theta))\rangle < \langle|R(\Phi_{min}^{16|14}\Psi^{14}(\Theta))\rangle$.

Taking the ratios of the cross correlations in Fig. 2 we find the contrasts shown in Fig. 3.

In Fig. 4, we plot the ten degree window contrast differences, $D_i^{16|14}(\Theta)$, for 5° angular increments between 0° and 60° in the forward sector. Since the models are symmetric these results apply over the range −60 to +60. In each case the optimization is driven by the least compatible returned waveform in the window. If the returned waveforms vary rapidly within a window the optimization becomes more difficult. The contrast difference can be increased by narrowing the window and thus reducing the received waveform variation. This can be seen in Fig. 5. In general, narrowing the optimization window increases the contrast difference between targets but may limit the applicability of the method in real situations with angle of approach uncertainty.

4. CONCLUSIONS

We demonstrate that one can distinguish between two similar radar targets using a method based on the optimization of chaos based test waveforms. Two methods were used to construct the test waveforms, concatenation of sinusoids and band pass filtering of the chaotic time series. Both methods resulted in similar optimizations. The optimization process included a Monte Carlo selection of test waveforms with later simplex optimization. The simplex amoeba optimization routine employed was prone to divergences since tweaking the chaotic map parameters can lead to sudden departures from the starting test waveform. Work is proceeding in incorporating more stable optimization routines in the code. We also will be studying the effect of additive noise on the calculated contrasts and the overall discrimination between targets. Angular window size and choice of bandwidth and center frequency and target dimension trade off with contrast difference target discrimination through the rapidity of variation of the waveform pattern with angle of approach.

REFERENCES

1. Rihaczek, A. W. and S. J. Hershkowitz, *Theory and Practice of Radar Target Identification*, Artech House, Boston, 2000.
2. Rothwell, E., D. P. Nyquist, K. M. Chen, and B. Drchman, "Radar target discrimination using the extinction-pulse technique," *IEEE Trans. Antennas Propag.*, Vol. 33, No. 9, 929–936, 1985.
3. Rothwell, E., K. M. Chen, D. P. Nyquist, and W. Sun, "Frequency domain E-pulse synthesis and target discrimination," *IEEE Trans. Antennas Propag.*, Vol. 35, No. 4, 426–434, 1987.
4. Carroll, T. L., "Using a phase space statistic to identify resonant objects," *Chaos*, Vol. 16, No. 2, 23113–2311, 2006.
5. Carroll, T. L., "Optimizing chaos-based signals for complex radar targets," *Chaos*, Vol. 17, No. 3, 033103, 2007.
6. Press, W. H., B. P. Flannery, S. A. Teukolsky, and W. T. Vetterling, *Numerical Recipes*, 289–293, Cambridge University Press, Cambridge, UK, 1989.

Using Chaos to Detect IIR and FIR Filters

T. L. Carroll

US Naval Research Lab, Code 6362, Washington, DC 20375, USA

Abstract— In many signal processing applications, IIR and FIR filters may be used inter-changeably, as in the long delay limit, an FIR filter looks like an IIR filter. It is known in nonlinear dynamics that a properly tuned IIR filter can change the dimension of a chaotic signal. This occurs because the feedback in an IIR filter makes it a dynamical system, so it may be characterized in terms of dynamical quantities such as Lyapunov exponents. An FIR filter, on the other hand, is not a dynamical system, and should not change the dimension of a chaotic signal. In practice, however, an FIR filter with a long tail mixes parts of the chaotic signal that are uncorrelated in time, so that a finite length chaotic signal filtered with an FIR filter will appear to have a larger dimension.

I will show in this paper that it is possible to use a recently developed dimension estimation method to distinguish an IIR filtered chaotic signal from an unfiltered signal, or a signal filtered by an FIR filter. I can also distinguish different IIR filters from each other. I can even detect the presence of an IIR filter when I use a chaotic signal whose bandwidth is much smaller than the filter bandwidth. Possible applications of this filter ID method could be in identifying radar or sonar targets based on resonant structures, or remotely identifying chemical compounds based on their resonance properties.

1. INTRODUCTION

If one is remotely detecting an object using a signal that reflects off the object (such as radar, sonar, or an optical signal), it may be useful to determine if the object has resonant properties. One example is an object where reflections off different parts of the object produce constructive or destructive interference in the signal; this sort of resonance acts as an FIR filter. Detection of FIR resonances is used in radar for target identification. On the other hand, a resonance line used to detect a particular chemical is an IIR filter, as is a magnetic resonance line [1].

It has been shown that filtering a chaotic signal with an infinite impulse response (IIR) filter, a type of filter that uses recursion, can increase the dimension of a chaotic signal [2, 3]. A finite impulse response (FIR) filter does not use recursion, and so should not increase the dimension of a chaotic signal [4], but if the FIR filter includes a long delay time, the filtered chaotic signal may appear to numerical algorithms to have a higher dimension [5]. While analysis of the reflected power spectrum can reveal the presence of a resonance, this analysis may not be enough to distinguish if the resonance is caused by an IIR filter or an FIR filter.

2. FIR FILTER

A simple example of an FIR filter that is found naturally is the reflection of a sound wave from an infinite plate [6]. If a sound wave propagates in a medium such as water, with an acoustic impedance of R_1, and strikes a plate at normal incidence, then the reflection coefficient and transmission coefficients at the front of the plate are

$$R_{12} = \frac{R_2 - R_1}{R_2 + R_1} \qquad T_{12} = \frac{2R_2}{R_2 + R_1} \tag{1}$$

where R_2 is the acoustic impedance of the plate.

After traveling through the plate thickness of d, the sound wave is encounters the rear surface, which has a reflection coefficient

$$R_{21} = \frac{R_1 - R_2}{R_2 + R_1} \tag{2}$$

After a time delay of $t = 2d/c$, where c is the sound velocity in the plate, the sound wave emerges from the front surface of the plate with a transmission coefficient of

$$T_{21} = \frac{2R_1}{R_2 + R_1} \tag{3}$$

The result is a sum of delayed versions of the original sound wave. In principle, the sum of reflections is infinite, so the term "finite impulse response" is not completely accurate, but we will keep the standard language, where infinite impulse response (IIR) refers to a system with feedback, while finite impulse response (FIR) refers to a system without feedback.

3. IIR FILTER

The IIR filter used in this work is a model of a simple dynamical system. A linear ODE model is used:

$$
\begin{aligned}
\frac{dy_1}{dt} &= \alpha_f \left(-\beta y_1 + y_2\right) + x_d \\
\frac{dy_2}{dt} &= \alpha_f \left(-y_1 - \beta y_2\right)
\end{aligned}
\tag{4}
$$

where x_d is the driving signal. The 2 Lyapunov exponents for this filter are $-\beta \alpha_f$, corresponding to a complex conjugate pair of eigenvalues.

4. DIMENSION

For a dynamical system with Lyapunov exponents $\lambda_1 \geq \lambda_2 \ldots \geq \lambda_d$, the Lyapunov dimension of the attractor is

$$
D_L = j + \sum_{k=1}^{j} \frac{\lambda_k}{|\lambda_{j+1}|}
\tag{5}
$$

where j is the largest index for which the sum over k is non negative. If the signal is filtered, then the Lyapunov exponents η_i of the filter will also be included in the sum of Eq. (5). The additional exponents may alter the Lyapunov dimension of the signal [2], as demonstrated below.

5. MEASURING DIMENSIONS

After embedding a chaotic signal in a phase space by the method of delays [7], the dimension of the chaotic signal could be measured using the method of [8]. Applying this method produces an average phase space radius $\langle \epsilon^*(\tau) \rangle$, further described in [9]. The change in this radius as the embedding dimension changes is related to the actual dimension of the chaotic signal.

In order to calculate the attractor dimension, it is necessary to pick a series of multidimensional index points on the attractor and find other points on the attractor that are nearby in phase space. This set of phase space neighbors forms a reference, and the indices of the set are stored in a reference file. References are created for both filtered and unfiltered signals, and are used below when comparing $\langle \epsilon^*(\tau) \rangle$ values for different signals.

6. CHAOTIC SYSTEM

To generate the chaotic signal, we use a map of the form

$$
x(n+1) = a_c x(n) \bmod 1
\tag{6}
$$

where a_c is to be determined. The initial condition was $x(0) = 0.2$, and the first 500 iterates from the map were discarded. The resulting signal was frequency modulated onto a sinusoidal carrier. The frequency of the modulated signal $s(i)$ was determined by $\zeta(n) = 1.0 + 0.1[x(n) - 0.5]$, so that the n'th cycle of the signal $s(i)$ was given by

$$
s(i) = \sin\left(2\pi t / [20\zeta(n)]\right) \quad [i = 0, 1, 2 \ldots, i < 20\zeta(n)]
\tag{7}
$$

If $\zeta(n) = 1$, then $s(i)$ will have a period of 20 points. The signal $s(i)$ has a constant envelope. For the map of Eqs. (6) and (7), the Lyapunov exponent is $\log(|a_c|)/\text{cycle}$, where log is the natural logarithm.

The chaotic signal $s(i)$ is filtered through the IIR filter of Eq. (4), with a time step of 0.1 s. The filter time constant α_f is set to 3.256 so that the signal $s(i)$ is at the center of the filter passband. The damping constant β is chosen so that $\alpha_f \beta$ is less than the Lyapunov exponent of the chaotic signal.

When $a_c = 1.1$, the Lyapunov exponent of the chaotic signal is $\log(1.1)/(20 \, \text{pts} \times 0.1 \, \text{s/pt}) = 0.048 \, \text{s}^{-1}$. The damping constant β is set to 0.01, so $\alpha_f \beta = 0.03256$ (or the Lyapunov exponents are both -0.03256).

Figure 1 shows $\langle \epsilon^*(\tau) \rangle$ vs. dimension for the map signal with $a_c = 1.1$ modulated onto a sine wave. The reference signal is derived from the IIR filtered signal. The lowest values of $\langle \epsilon^*(\tau) \rangle$ occur for the IIR filtered signal, the highest values for the unfiltered signal, and the sum of signals gives an intermediate value of $\langle \epsilon^*(\tau) \rangle$.

7. NOISE MODULATION

As the value of $\alpha_f \beta$ in the IIR filter increases, the Lyapunov exponent of the chaotic signal must also increase if the IIR filter is to increase the signal dimension. As the Lyapunov exponent of the map of Eq. (6) becomes larger, the map signal looks more and more like noise. Taking the limit of this trend, β for the IIR filter of Eq. (4) was increased to 0.04, and the signal $x(n)$ in Eqs. (6) and (7) was replaced by computer generated uniformly distributed random noise. Figure 2 shows that the noise signal, when modulated onto a sinusoidal carrier, is also useful for distinguishing an IIR filtered signal from an unfiltered signal.

While the noise signal itself is infinite dimensional, the sine wave onto which the noise is modulated is 2 dimensional, so the resulting signal appears to have a dimension between 2 and 3. Figure 3 shows the normalized power spectrum of the chaotic signal used for Figure 2, along with the response of the IIR filter for $\alpha_f = 3.256$ and $\beta = 0.04$.

The dimension increase of the chaotic signal depends on the relative Lyapunov exponents of the filter and the chaotic signal, not on the relative bandwidths. Modulating the chaotic signal onto a carrier allowed the Lyapunov exponent and bandwidth of the chaotic signal to be varied independently, so Figure 3 shows that the chaotic signal used to detect the presence of the IIR filter occupies only a narrow portion of the filter response function. The full width at half maximum (FWHM) for the chaotic signal is 7.5×10^{-4} Hz, while the FWHM for the IIR filter response is 4.3×10^{-2} Hz. If the chaotic signal bandwidth was as large or larger than the filter response, then detecting the IIR filter could be done with spectral methods. Since the chaotic signal bandwidth is much smaller than the filter response, detection using spectral methods would be difficult.
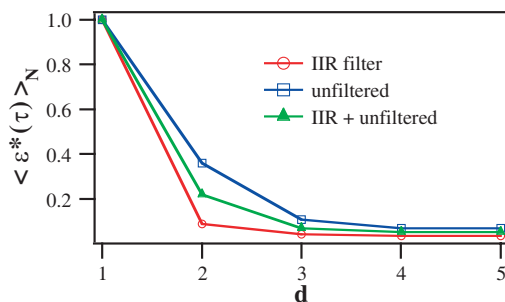
Figure 1: $\langle \epsilon^* \rangle$ for an unfiltered signal generated by frequency modulating a chaotic signal onto a sine wave (Eqs. (6) and (7)), $\langle \epsilon^* \rangle$ for the same signal filtered by an IIR filter, and $\langle \epsilon^* \rangle$ for a sum of the 2 signals.
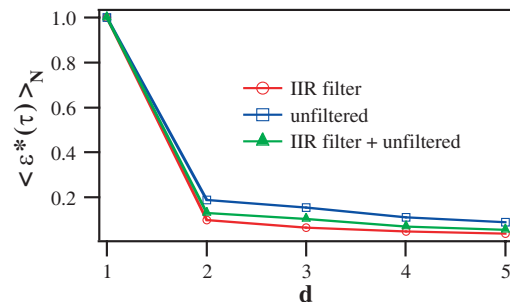
Figure 2: $\langle \epsilon^* \rangle$ for a filtered and unfiltered signal when a noise signal is substituted for the chaotic signal $x(n)$ in Eq. (7).
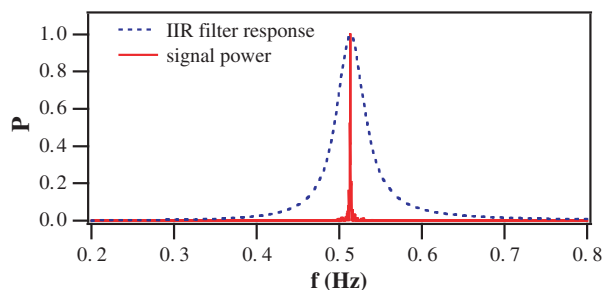
Figure 3: Frequency response of the IIR filter of Eq. (4) with $\alpha_f = 3.256$ and $\beta = 0.04$, and power spectrum of the signal created by using uniformly distributed noise to modulate a sine wave in Eq. (7).
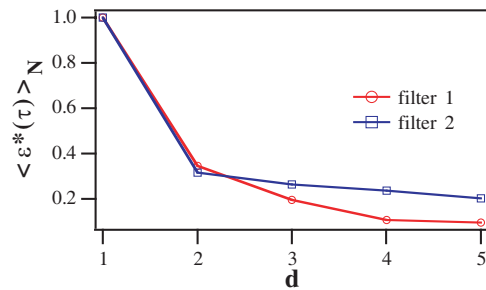
Figure 4: $\langle \epsilon^*(\tau) \rangle$ for 2 filters with a 10% difference in frequency, showing the ability to distinguish between 2 different IIR filters. Both filters were driven by a noise modulated sine wave, and the reference file for filter 1 was used.
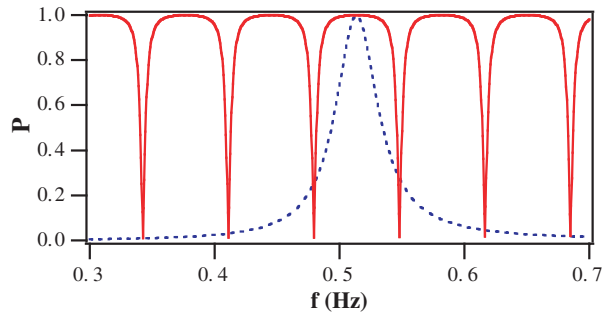
Figure 5: Frequency response of the IIR filter of Eq. (4) (dashed line) with $\alpha_f = 3.256$ and $\beta = 0.04$, and the FIR filter from the infinite plate model with a thickness of 3.56 wavelengths of the noise modulated sine wave.
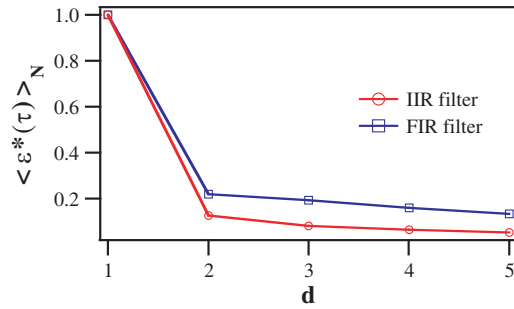
Figure 6: Comparison of $\langle \epsilon^*(\tau) \rangle$ for a noise modulated sine wave signal filtered by an IIR filter and an FIR filter based on the infinite plate model. The reference file comes from the IIR filter, so the values of $\langle \epsilon^*(\tau) \rangle$ resemble the values that would be seen for an unfiltered signal.

8. SENSITIVITY

A different measure of the usefulness of the dimension change of the chaotic signal as a detector of IIR filtering is the sensitivity of the method to a change in the IIR filter; can we distinguish 2 different IIR filters? The time constant of the IIR filter of Eq. (4) was increased by 10%, from $\alpha_f = 3.2256$ to 3.582, while the damping constant β was decreased by 10%, from 0.04 to 0.036, leaving the product $\alpha_f\beta$ constant. The unmodified filter will be refered to as filter 1, while the modified filter is filter 2. The noise modulated sine wave signal was used to drive both filters. A reference signal was produced for the IIR filtered signal from filter 1 and both filtered signals were compared to this reference.

Figure 4 shows $\langle \epsilon^*(\tau) \rangle$ vs dimension for filter 1 and filter 2 when compared to a reference from filter 1. The values for filter 2 are larger for dimensions of 3 and above, but the difference is not large. It is possible to distinguish between 2 different IIR filters using the dimension increase method, but the method is not very sensitive to filter differences when using a noise modulated sine wave. The bandwidth of the noise modulated sine wave is much narrower than the filter response, so one would not expect great sensitivity.

9. FIR FILTER

The FIR filter was derived from the infinite plate model described above, with a thickness of 3.56 average wavelengths of the modulated signal. The response functions for the IIR and FIR filters are shown in Figure 5. The FIR filter response is periodic in frequency, but the noise modulated signal is narrow enough in bandwidth that it will not see the periodicity. The same noise modulated signal was used to drive both filters.

Figure 6 shows $\langle \epsilon^*(\tau) \rangle$ vs. dimension for the noise modulated signal filtered by both IIR and FIR filters when compared to a reference generated by the IIR signal. In this case, the values of $\langle \epsilon^*(\tau) \rangle$ for the FIR filter are very close to the values of $\langle \epsilon^*(\tau) \rangle$ for an unfiltered signal.

10. CONCLUSION

While it is not always possible to distinguish between IIR and FIR filters using conventional methods, this paper shows that these filter types can be distinguished by taking advantage of the dimension increase in filtered chaotic signals. Furthermore, because the bandwidth and Lyapunov exponent of a chaotic signal may be varied independently when modulating it onto a carrier, is is possible to identify an IIR filter with a signal that is much narrower than the filter bandwidth.

REFERENCES

1. Slichter, C. P., *Principles of Magnetic Resonance*, Springer, New York, 1980.
2. Badii, R., G. Broggi, B. Derighetti, M. Ravini, S. Ciliberto, and A. Politi, "Dimension increase in filtered chaotic signals," *Physical Review Letters*, Vol. 60, No. 11, 979, 1988.
3. Davies, M. E. and K. M. Campbell, "Linear recursive filters and nonlinear dynamics," *Nonlinearity*, Vol. 9, 487–499, 1996.

4. Sauer, T. D. and J. A. Yorke, "Are the dimensions of a set and its image equal under typical smooth functions?" *Ergodic Theory and Dynamical Systems*, Vol. 17, 941–956, 1997.

5. Broomhead, D. S., J. P. Huke, and M. R. Muldoon, "Linear filters and non-linear systems," *Journal of the Royal Stastical Society B*, Vol. 54, No. 2, 373–382, 1992.

6. Crawford, F. S., *Waves*, McGraw-Hill, New York, 1968.

7. Abarbanel, H. D. I., R. Brown., J. J. Sidorowich, and L. S. Tsmring, "The analysis of observed chaotic data in physical systems," *Reviews of Modern Physics*, Vol. 65, No. 4, 1331–1392, 1993.

8. Pecora, L. M., L. Moniz, J. Nichols, and T. L. Carroll, "A unified approach to attractor reconstruction," *Chaos*, Vol. 17, No. 1, 013110-9, 2007.

9. Carroll, T. L., submitted to *Chaos*, 2010.

Development of Polarimetric Ground Based-SAR System with Compact VNA and Vivaldi Antenna Array

M. Matsumoto and M. Sato

Tohoku University, Japan

Abstract— A polarimetric Ground Based-SAR system that can achieve continuous scanning is evaluated in this paper. Our laboratory has developed compact and continuous scanning system with a compact VNA and a box type Vivaldi antenna array composed by four Vivaldi antennas. Weight of the VNA is reduced from 22 kg to 3 kg, and we also reduced weight of the antenna from 8 kg to 1 kg in order to develop more compact system. After we developed the continuous scanning system with the VNA and the array antenna, we evaluated effects of continuous scanning in this system. First, we measured a metallic sphere with both of Stop & Go scanning and continuous scanning. After that, we evaluated the difference of both scanning methods by comparing radar images. As a result, we confirmed that there was no significant difference between two scanning methods.

1. INTRODUCTION

A polarimetric Ground Based-SAR (GB-SAR) system can be used not only to examine a scattering property of any target, but also to monitor vegetation or a landslide. Our laboratory has developed the system for several years. The system is a SF-CW (Stepped-Frequency Continuous-Wave) radar system with a VNA (Vector Network Analyzer) and a dual ridged horn antenna. Our system could detect seasonal changes of trees by using polarimetric analysis [1]. While we carry out a measurement, we need to move the VNA with the antenna scanning due to a limit of coaxial cables which connect the VNA and the antenna. Therefore, antenna scanning was Stop & Go scanning, which is slow scanning and caused oscillation of the coaxial cables and the dual ridged horn antenna when the antenna stops. Besides, the VNA and the dual ridged horn antenna in this system is excellent quality, but the equipments are relatively large.

In order to solve such problems, we developed a compact VNA and a box type Vivaldi antenna array. The compact VNA which was developed by Anritsu and our laboratory achieves high speed measurement, because it is specialized for S_{21} measurement. Therefore, it can be attached to antenna positionner, and we can adopt continuous scanning. By using the compact VNA and the antenna array, we could develop a more compact GB-SAR system.

In this paper, effects of continuous measurement in our system will be evaluated. First, we measured a metallic sphere with both of Stop & Go scanning and continuous scanning. After that, we evaluated the difference of both scanning methods.

2. POLARIMETRIC GROUND BASED-SAR SYSTEM

Figure 1(a) shows a block diagram of the compact polarimetric GB-SAR system. Main part of the system consists of three components. First is a compact VNA whose measurement frequency range is from 2 MHz to 6 GHz. Weight of the compact VNA, which is 3 kg, was reduced to 13.6% of a conventional VNA.

Second is a linear antenna positioner which carries the array antenna and the VNA. The VNA measures when it catches a trigger signal from a controller of the antenna positioner in order to achieve continuous scanning.

Third is an antenna system. In order to achieve full polarimetric measurement, we developed a box type antenna array which consists of four Vivaldi antennas. The array antenna is shown in Fig. 1(b). Weight of the array antenna is 1 kg and we could reduce the weight to 12.5% of the dual ridged horn antenna. Fig. 2 shows antenna direct coupling of the array antenna measured in anechoic chamber. If the antenna array has symmetrical structure, we can expect that HH and VV component have almost same characteristics. And we can also expect that HV and VH component have same characteristics. Figs. 2(a) and (b) shows power spectrum and time domain signal, respectively. We can see that HH and VV component, HV and VH component have almost same characteristics. So we can conclude that the antenna has almost symmetrical structure. The characteristic of our system is a SF-CW, bistatic and continuous scanning radar system.

(a)   (b)
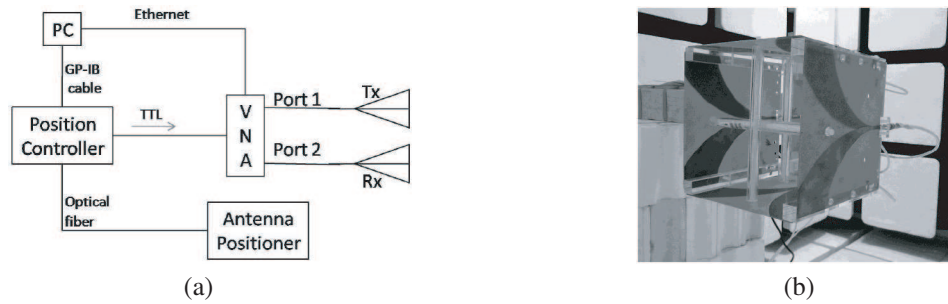
Figure 1: (a) Configuration of polarimetric GB-SAR system. (b) A box type Vivaldi antenna array composed by four Vivaldi antennas. This array antenna is used in our system.

(a)   (b)
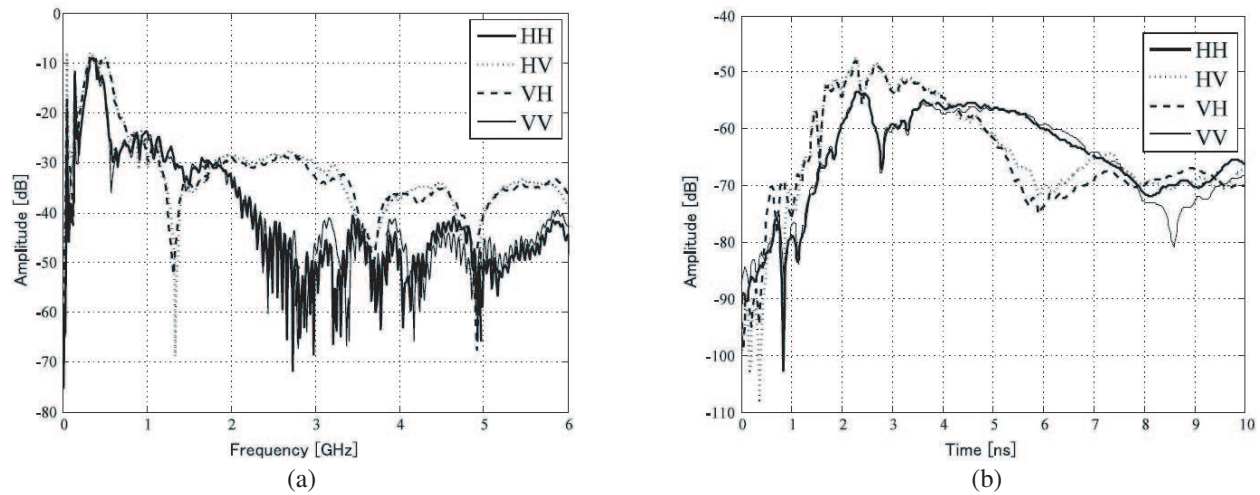
Figure 2: Antenna direct coupling of the array antenna which is used in polarimetric GB-SAR. (a) Spectrum in frequency domain. (b) Signal amplitude in time domain.
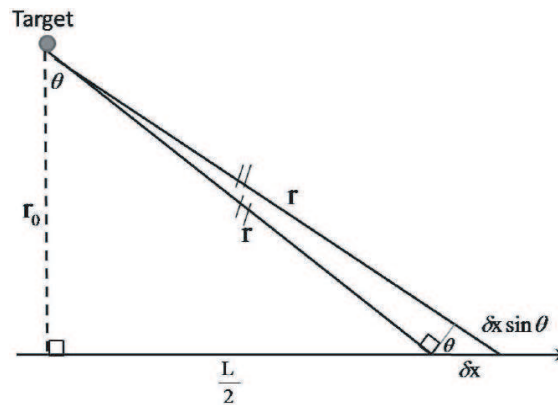
Figure 3: Diagram to explain the effect of continuous scanning. r_0 is 1.7 m, L is 3 m in this measurement.

3. EVALUATION OF CONTINUOUS SCANNING IN OUR SYSTEM

We measured two times with different scanning method in order to evaluate the effect of continuous scanning. At first, we scanned continuously with the speed of 1.9 cm/sec. After that, we scanned with Stop & Go scanning. As a target, we used metallic sphere whose diameter is 15 cm. Measurement frequency is from 1 GHz to 4 GHz. Scan aperture is 3 m and scan interval is 2 cm. The distance between target and scan line is 1.7 m. In this measurement, we measured VV polarization. We also measured background in order to subtract undesirable reflection from surroundings. We can consider two effects of continuous scanning. One is the effect of Doppler frequency shift caused by antenna scanning. We can ignore it because the scan speed is enough slow compared to the

speed of light. Another is difference of antenna position when the system measures lowest frequency and highest frequency. Fig. 3 shows a diagram to explain the effect of continuous scanning, where L is scan aperture, δx is a movement of antenna during sweep time. The difference along the line of sight can be expressed as $\delta x \cdot \sin \theta$. This value can be maximum when antenna is at the end of scan. In this measurement, sweep time of the VNA is 0.4 sec. The antenna moves 0.76 cm during sweep time. Therefore, maximum value of $\delta x \cdot \sin \theta$ is 0.5 cm. This value is only one fifteenth of shortest wave length of this measurement. Therefore, we can expect that there is no significant difference between two scanning methods in this system.

4. RESULT

Figure 4 shows B-scan images after background subtraction. (a) and (b) show continuous scanning and Stop & Go scanning, respectively. We can see clearly the curvature of the hyperbolic trajectory which represents the reflection from the metallic sphere in both figures. In Fig. 4(b), there are some discontinuities. The reason is that we failed to subtract the background data from original data completely. The shape and amplitude of the curvature are almost same. It is difficult to detect the differences between two scanning methods.

Figure 5 shows reconstructed images calculated by diffraction stacking algorithm. (a) and (b) show continuous scanning and Stop & Go scanning, respectively. Due to migration, the effect of discontinuity is vanished in Fig. 5(b). We could get almost same image.
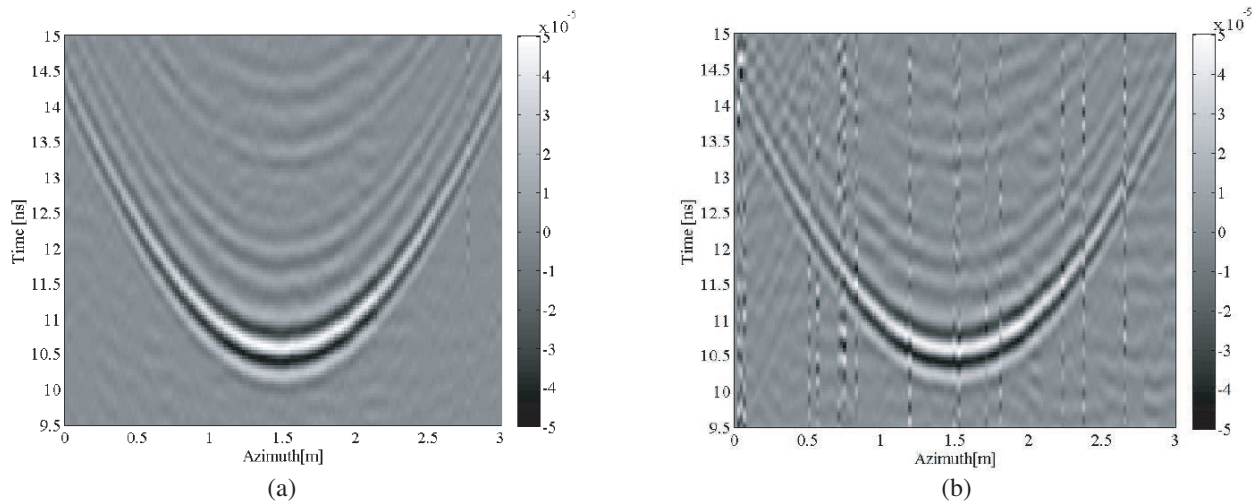
Figure 4: B-scan image. (a) Continuous scanning. (b) Stop & Go scanning.
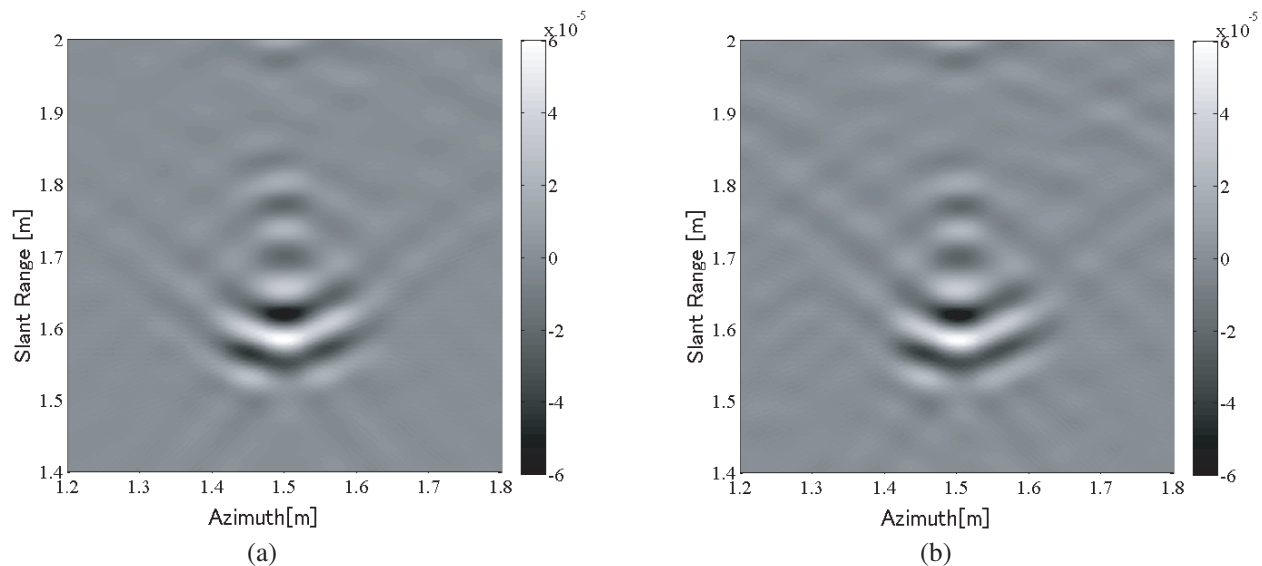
Figure 5: Reconstructed image. (a) Continuous scanning. (b) Stop & Go scanning.
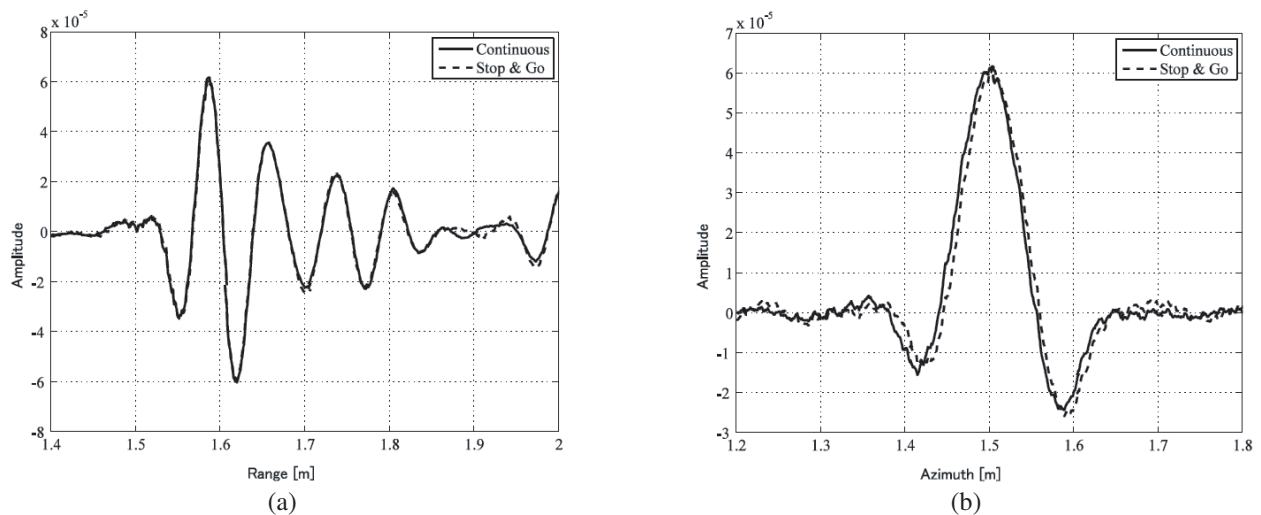
Figure 6: Cross-section of reconstructed images. (a) Cross-section along range direction where azimuth is 1.5 m. (b) Cross-section along azimuth direction where range is 1.58 m.

Figure 6(a) is a cross-section of reconstructed images along range direction where azimuth is 1.5 m. Solid line and dashed space line represent continuous scanning and Stop & Go scanning, respectively. We can see that both signals are exactly same in this figure. Therefore, we can conclude that there is no effect of continuous scanning along azimuth direction. Fig. 6(b) is a cross-section of reconstructed images along azimuth direction where range is 1.58 m. Solid line and dashed space line represent continuous scanning and Stop & Go scanning, respectively. We can see that both signals are almost same in this figure but there are very small differences.

5. CONCLUSION

In this paper, we discussed the effect of continuous scanning in polarimetric GB-SAR. In this system, we used the compact VNA and the box type Vivaldi antenna array. As a result of using these two equipments, we could reduce weight of the system and achieve continuous scanning. In order to evaluate the effect of continuous scanning, we measured the metallic sphere with different scanning method. After that we reconstructed the radar images by diffraction stacking algorithm. From the cross-sections of reconstructed images, we confirmed the two different scanning methods give same results.

ACKNOWLEDGMENT

REFERENCES

1. Zhou, Z.-S., W.-M. Boerner, and M. Sato, "Development of a ground-based polarimetric broad-band SAR system for non-invasive ground-truth validation in vegetation monitoring," *IEEE Transactions on Geoscience and Remote Sensing*, Vol. 42, No. 9, 1803–1810, 2004.

Full Polarimetric Calibration of Ground Based-SAR System with Thin Wire

M. Matsumoto and M. Sato

Tohoku University, Japan

Abstract— Full polarimetric calibration procedure of a polarimetric Ground Based-SAR system is proposed. As a calibration target, we used a thin wire because the wire can be put more easily than other deterministic target like a dihedral corner reflector. At first, we measured 0 degree, 45 degree and 90 degree inclined thin wire. By using the measured data sets, we derived antenna calibration parameters. After that, we calibrated the system by using the estimated parameters. In order to evaluate this calibration method, we tested the parameters by using 60 degree and 30 degree inclined wire. As a result, we could calibrate 60 degree wire from 1 to 2 GHz but not calibrate 30 degree wire as for amplitude. As for phase term, cross-polarization component could be calibrated for both wires case. But co-polarization component could not be calibrated. The differences between theoretical and calibrated value are within 60 degree up to 3 GHz.

1. INTRODUCTION

A polarimetric Ground Based-SAR system can be used not only to examine a scattering property of any target, but also to monitor vegetation or a landslide. In a full polarimetric measurement, systematic errors can arise in a transmitter and a receiver antenna due to misalignment of antenna and so on. This errors result in distortion of a scattering matrix. Therefore we need a full polarimetric calibration in order to acquire the correct scattering matrix. The full polarimetric calibration requires three different targets. For example, we can use a metallic sphere, 0 degree and 45 degree oriented dihedral corner reflector as the calibration targets [1]. Although the dihedral corner reflector has relatively large RCS (Radar Cross Section), it has a strong dependency as for incident angle of electromagnetic wave. Therefore it is difficult to deploy the dihedral corner reflector correctly. On the other hand, a thin wire can be put more easily than the dihedral corner reflector because one of rotation axes can be neglected.

In this paper, we measured reflection from 0 degree, 45 degree and 90 degree inclined wire. By using these data sets, we derived calibration parameters. Derivation of calibration parameters of thin wire case is discussed in [2]. After we obtained calibration parameters, we tested the parameters for 60 degree and 30 degree inclined wire case.

2. POLARIMETRIC GROUND BASED-SAR SYSTEM

Main part of our Ground Based-SAR system consists of compact VNA (Vector Network Analyzer) and a box type Vivaldi antenna array. Measurement frequency range of the VNA is from 2 MHz to 6 GHz. As for antenna system, we made a box type antenna array which consists of four Vivaldi antennas. The Vivaldi antenna and the array antenna are shown in Fig. 1. Our radar system is a SF-CW (Stepped-Frequency Continuous-Wave) and bistatic radar system.
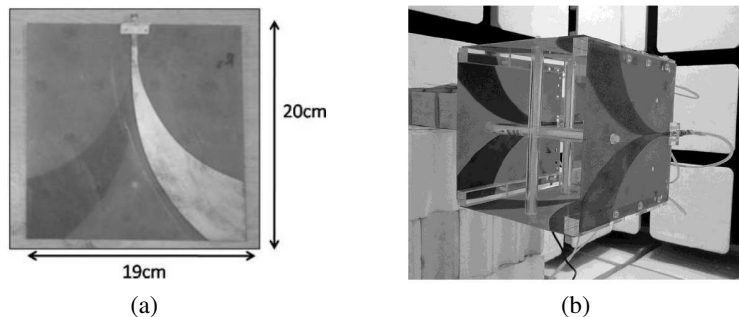

Figure 1: Antenna system used in polarimetric Ground Based-SAR. (a) Vivaldi antenna. (b) A box type antenna array which consists of four Vivaldi antennas.

3. CALIBRATION ALGORITHM

In general, a scattering matrix $\mathbf{M}$ can be expressed by (1) and (2) in a polarimetric GB-SAR system.

$$\mathbf{M} = \mathbf{RST} + \mathbf{N} \tag{1}$$

$$\begin{bmatrix} M_{xx} & M_{xy} \\ M_{yx} & M_{yy} \end{bmatrix} = \begin{bmatrix} R_{11} & R_{12} \\ R_{21} & R_{22} \end{bmatrix} \begin{bmatrix} S_{xx} & S_{xy} \\ S_{yx} & S_{yy} \end{bmatrix} \begin{bmatrix} T_{11} & T_{12} \\ T_{21} & T_{22} \end{bmatrix} + \mathbf{N} \tag{2}$$

$\mathbf{R}$ is a distortion matrix of a receiver antenna, $\mathbf{S}$ is a scattering matrix of a target, $\mathbf{T}$ is a distortion matrix of a transmitter antenna, $\mathbf{N}$ is a noise matrix caused by undesirable reflection from surroundings and thermal noise of the VNA. We measured thermal noise and it was relatively small compared to reflection from wire. Therefore, we concluded that the noise matrix can be ignored. Then, (2) can be rewritten as (3).

$$\begin{bmatrix} M_{xx} & M_{xy} \\ M_{yx} & M_{yy} \end{bmatrix} = \begin{bmatrix} 1 & r_{12} \\ r_{21} & r_{22} \end{bmatrix} \begin{bmatrix} S_{xx} & S_{xy} \\ S_{yx} & S_{yy} \end{bmatrix} \begin{bmatrix} 1 & t_{12} \\ t_{21} & t_{22} \end{bmatrix} \tag{3}$$

In this equation, we normalized distortion matricides $\mathbf{R}$ and $\mathbf{T}$ by R_{11} and T_{11} respectively. In order to acquire correct scattering matrix, we need to determine each element of distortion matrices like r_{12}, r_{21}, r_{22}, t_{12}, t_{21} and t_{22}. In an ideal radar system, r_{12}, r_{21}, t_{12} and t_{21} are equal to zero. And r_{22} and t_{22} are equal to one. In this particular case, R and T become identity matrix and does not distort scattering matrix at all. Let theoretical scattering matrix of 0 degree, 90 degree and inclined wire be $\mathbf{S}_1$, $\mathbf{S}_2$ and $\mathbf{S}_3$ respectively.

$$\mathbf{S}_1 = \begin{bmatrix} 1 & 0 \\ 0 & 0 \end{bmatrix}, \quad \mathbf{S}_2 = \begin{bmatrix} 0 & 0 \\ 0 & 1 \end{bmatrix}, \quad \mathbf{S}_3 = \begin{bmatrix} c & d \\ d & e \end{bmatrix}, \quad d^2 = ce \tag{4}$$

And let measured scattering matrices of 0 degree, 90 degree and inclined wire be $\boldsymbol{\alpha}$, $\boldsymbol{\beta}$ and $\boldsymbol{\gamma}$ respectively.

$$\boldsymbol{\alpha} = \begin{bmatrix} \alpha_{11} & \alpha_{12} \\ \alpha_{21} & \alpha_{22} \end{bmatrix}, \quad \boldsymbol{\beta} = \begin{bmatrix} \beta_{11} & \beta_{12} \\ \beta_{21} & \beta_{22} \end{bmatrix}, \quad \boldsymbol{\gamma} = \begin{bmatrix} \gamma_{11} & \gamma_{12} \\ \gamma_{21} & \gamma_{22} \end{bmatrix} \tag{5}$$

By substituting (4) and (5) for (3), we can obtain t_{12} and r_{21} as following equations.

$$t_{12} = \frac{\alpha_{12}}{\alpha_{11}}, \quad r_{21} = \frac{\alpha_{21}}{\alpha_{11}} \tag{6}$$

And we obtain two sets of solutions as following equations.

$$r_{22} = \frac{c}{d} \frac{\beta_{22}}{\alpha_{11}} \frac{\alpha_{11}\gamma_{21} - \alpha_{21}\gamma_{11}}{\beta_{22}\gamma_{11} - \beta_{12}\gamma_{21}}, \quad r_{12} = \frac{\beta_{12}}{\beta_{22}} r_{22}, \quad t_{22} = \frac{c}{d} \frac{\beta_{22}}{\alpha_{11}} \frac{\alpha_{11}\gamma_{12} - \alpha_{12}\gamma_{11}}{\beta_{22}\gamma_{11} - \beta_{21}\gamma_{12}}, \quad t_{21} = \frac{\beta_{21}}{\beta_{22}} t_{22} \tag{7a}$$

$$r_{22} = \frac{d}{e} \frac{\beta_{22}}{\alpha_{11}} \frac{\alpha_{11}\gamma_{22} - \alpha_{21}\gamma_{12}}{\beta_{22}\gamma_{12} - \beta_{12}\gamma_{22}}, \quad r_{12} = \frac{\beta_{12}}{\beta_{22}} r_{22}, \quad t_{22} = \frac{d}{e} \frac{\beta_{22}}{\alpha_{11}} \frac{\alpha_{11}\gamma_{22} - \alpha_{12}\gamma_{21}}{\beta_{22}\gamma_{21} - \beta_{21}\gamma_{22}}, \quad t_{21} = \frac{\beta_{21}}{\beta_{22}} t_{22} \tag{7b}$$

Detail of derivation of above equations is discussed in [2]. We have two sets of solutions, because the number of equations acquired by substituting six matrices for (3) exceeds number of unknown parameters. In the following chapters, we name a calibration procedure using (7a) and (7b) as Cal.1 and Cal.2, respectively. We carried out experiment in the anechoic chamber. We measured 0 degree, 30 degree, 45 degree, 60 degree, and 90 degree inclined wire in frequency domain. The 30 degree and 60 degree oriented wire can be used to evaluate this calibration method. After we converted to time domain by Inverse Fourier Transform, we extracted reflection from wires by using time window. Then, we applied Fourier Transform to convert frequency domain, and calculated the calibration parameters.

4. RESULT

Figure 2 shows normalized amplitude of scattering matrix in case of 60 degree oriented wire. Figs. 2(a) and (b) are calculated by Cal.1 and Cal.2, respectively. Here S, M and T represent calibrated, measured and theoretical values of each element of scattering matrix, respectively. In this case, each value is normalized by yy component. From this figure, we can see the calibrated values S_{xy}, S_{yx} and S_{xx}, are approaching theoretical values T_{xy} and T_{xx} up to around 2 GHz in both

calibration cases. Fig. 3 shows normalized phase of scattering matrix. Figs. 3(a) and (b) are calculated by Cal.1 and Cal.2, respectively. Theoretically, normalized phase of xy and yx component must be 180 degree. And normalized phase of xx component must be 0 degree. Fig. 3 represents that how much degree is different from theoretical value. As for cross-polarization, we can see that the calibrated values S_{xy} and S_{yx} get worse by Cal.1. On the other hand, Cal.2 makes S_{xy} and S_{yx} approach 0 degree. As for co-polarization, S_{xx} gets worse than M_{xx} in both calibration cases.

Figure 4 shows normalized amplitude of scattering matrix in case of 30 degree oriented wire. Figs. 4(a) and (b) are calculated by Cal.1 and Cal.2, respectively. In this case, each value is normalized by xx component. In both cases, S_{yx} component between 2.2–3.8 GHz gets better due to the calibration. But other components like S_{xy} and S_{yy} get worse than M_{xy} and M_{yy}. Fig. 5 shows normalized phase of the scattering matrix. Figs. 5(a) and (b) are calculated by Cal.1 and Cal.2, respectively. At this figure, we applied same manner used in Fig. 3 in order to represent normalized phase. As for cross-polarization, although we could not calibrate xy and yx component by Cal.2, we could calibrate cross-polarization successfully within few degree in Cal.1 up to 3 GHz. As for co-polarization, we failed to calibrate.
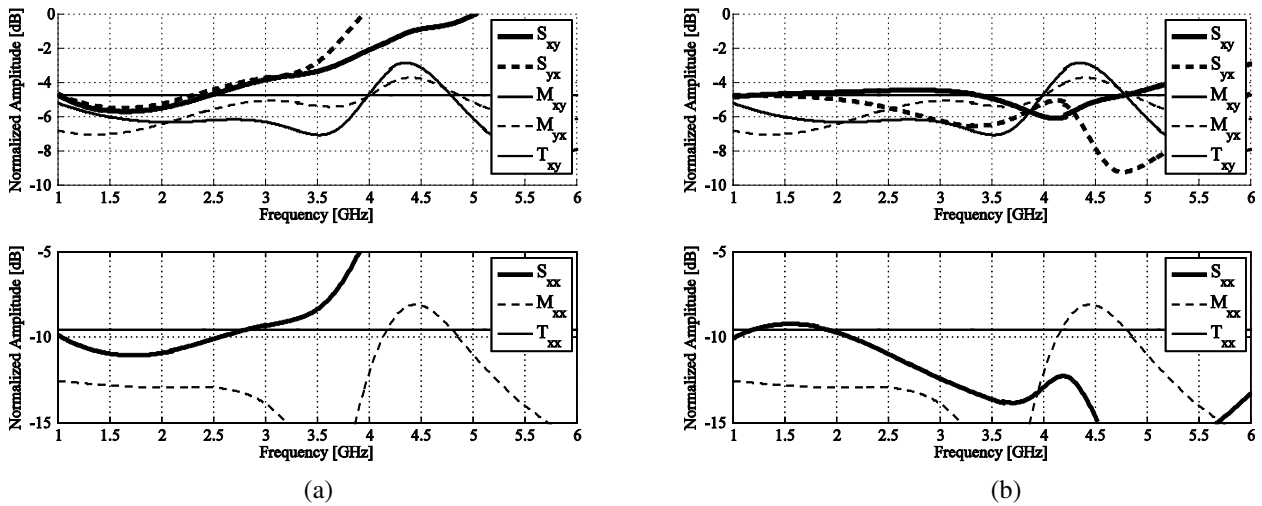
Figure 2: Normalized amplitude of scattering matrix at 60 degree inclined wire. (a) Cal.1. (b) Cal.2. Top figures show cross-polarization component. Bottom figures show co-polarization component.
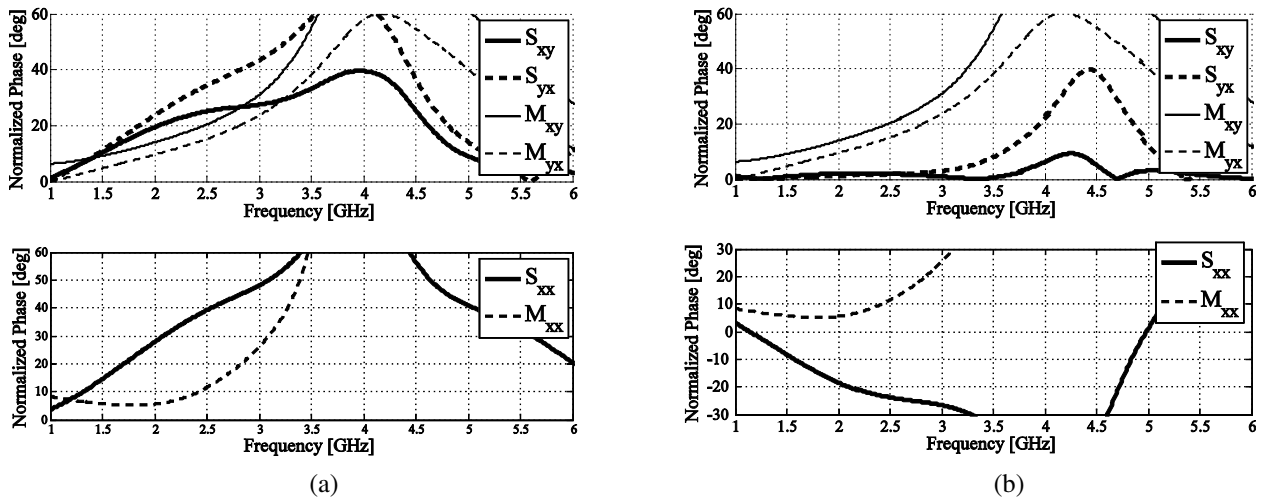
Figure 3: Normalized phase of scattering matrix at 60 degree inclined wire. (a) Cal.1. (b) Cal.2. Top figures show cross-polarization component. Bottom figures show co-polarization component.
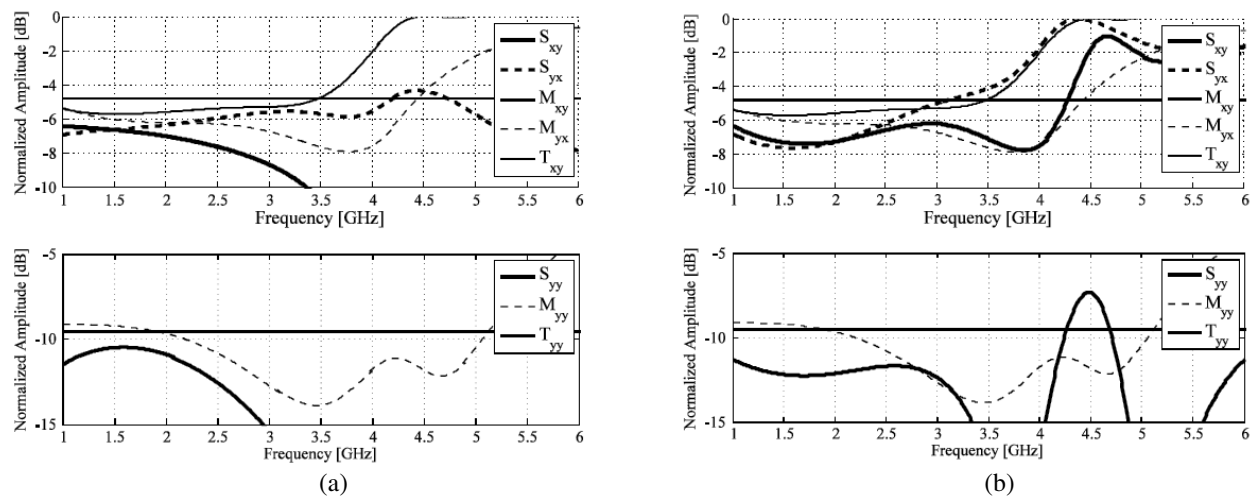
Figure 4: Normalized amplitude of scattering matrix at 30 degree inclined wire (a) Cal.1. (b) Cal.2. Top figures show cross-polarization component. Bottom figures show co-polarization component.
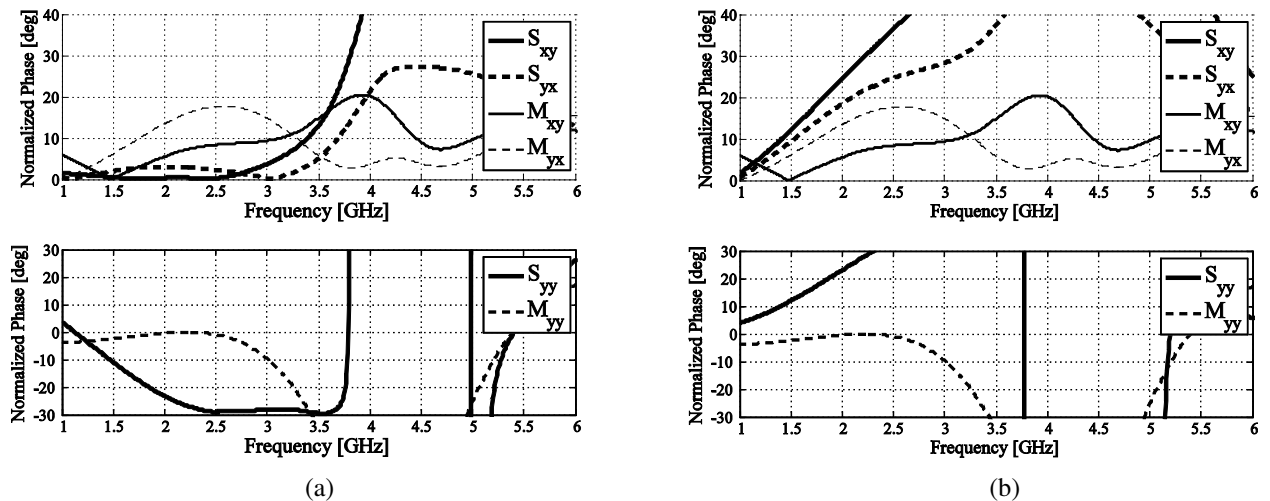
Figure 5: Normalized phase of scattering matrix at 30 degree inclined wire. (a) Cal.1. (b) Cal.2. Top figures show cross-polarization component. Bottom figures show co-polarization component.

5. CONCLUSION

In this paper, we discussed full polarimetric calibration of polrarimetric Ground based-SAR system. As a calibration target, we used a thin wire in order to avoid a difficulty of deploying calibration targets. According to [2], we obtained two sets of solutions namead as Cal.1 and Cal.2 by using theoretical and measured scattering matrices of 0 degree 45 degree and 90 degree inclined wires. After that we calibrated the system and evaluated by using 30 degree and 60 degree oriented wire.

As for amplitude, we could calibrate the system successfully from 1 to around 2 GHz in case of 60 degree wire. On the other hand, we could not calibrate in case of 30 degree wire for amplitude. As for phase term, Cal.2 worked well to calibrate cross-polarization component in case of 60 degree wire, but Cal.1 did not work well. On the other hand, Cal.1 worked well to calibrate cross-polarization component in case of 30 degree wire, but Cal.2 did not work. As for phase term of co-polarization component, we could not calibrate in both wires and both calibration cases. The calibration does not work in some cases. We need to investigate why such a phenomenon happens.

REFERENCES

1. Wiesbeck, W. and S. Riegger, "A complete error model for free space polarimetric measurements," *IEEE Transactions on Antennas and Propagation*, Vol. 39, No. 8, 1105–1111, August 1991.
2. Yueh, S. H., J. A. Kong, R. M. Barnes, and R. T. Shin, "Calibration of polarimetric radars using in-scene reflectors," *Journal of Electromagneitc Waves and Applications*, Vol. 4, No. 1, 27–48, 1990.

Input Characteristics of Coated Thin Wire Helix Antenna

S. A. Adekola[1], **A. I. Mowete**[1], **A. Ogunsola**[1, 2], **and A. Ayorinde**[1]

[1]Department of Electrical and Electronics Engineering, Faculty of Engineering
University of Lagos, Lagos, Nigeria
[2]Parsons Group International, Rail Transit Division, London, United Kingdom

Abstract— In this paper, we investigate the effects of the dielectric insulation on the input impedance and admittance characteristics of coated thin-wire helical antennas, using the quasi-static moment-method approach described elsewhere by Adekola et al. [1]. For the dielectric insulation modeled by a Schelkunoff's volume polarization current, the unknown quantity is the electric field in the dielectric region due to the distribution of current along the axis of the un-insulated wire, which is also an unknown quantity. The quasi-static approach assumes that both unknowns are related in the manner specified by Richmond and Newman [2], and Lee and Balmain [3], so that the problem then becomes completely solved, when using the method of moments, the unknown current distribution is obtained. One interesting feature of the paper is the demonstration that the circuit-geometric character of the moment-methods enables the formulation for the coated elliptical cylindrical helical antenna to serve as a general case for certain regular thin-wire geometries. Numerical results obtained for the representative examples of a coated monofilar helix (backed by a large ground plane) describe effects of coating these antenna types as consistent with those reported by Desplanches et al. [4].

1. INTRODUCTION

In addition to protecting against the undesirable effects of direct contact with the ambient medium, dielectric coatings on thin-wire antennas also serve the practically important ends of increasing the antenna's electrical length and enabling the definition of equivalent radii for thin-wire cylindrical structures, [4, 5]. These and other considerations informed the various analytical investigations, to which the characteristic properties of coated thin-wire antenna structures have been subjected, over the years. Notable among these are the contributions of Richmond and Newman, [2], Lee and Balmain, [3], Huddlestson et al., [6], Chatterjee et al. [7], and Popovic and Nesic, [8], whose efforts have not only provided significant insight into the nature of the physics of the problem, but have also yielded numerical results that describe the performance characteristics of coated-thin-wire antennas. Adekola et al. [1], advanced arguments to support certain modifications to the analytical models described in [2, 3, 7], leading to the quasi-static model of interest to this paper.

Majority of the analyses referred to in the foregoing, like most others on the subject in the open literature, focused on the problem of coated linear thin-wire antennas; and only a few, to the best of our knowledge, have investigated the characteristics of coated thin-wire helical antennas. Examples of the latter include the contributions of Yamauchi and Nakano, [5], who derived a Hallen-type equation for use in the analysis of dielectric-coated thin-wire antennas. Numerical results were presented in [5], for the current distribution along the axis of a 2-turn coated-helical antenna, but no analytical details were provided. Desplanches et al., [4], utilized a moment-method formulation for the analysis of a monofilar helical antenna backed by a cylindrical cavity as well as a dielectric-coated quadrifilar helical antenna backed by a small ground plane. Their development followed the approach earlier described by Moore and West, [9], and numerical results were obtained for the radiation field and input impedance characteristics.

An analysis is presented in this paper of a dielectric-coated thin-wire monofilar helical antenna backed by a very large plane. Using the image theory, the ground plane is replaced by a mirror image of the helix, and for the dielectric insulation, the quasi-static theory described elsewhere is utilized, in a moment solution. Numerical results obtained for input impedance and admittance characteristics, for various coating sizes and dielectric permittivities are presented and discussed in the paper.

2. ANALYSIS

For the un-insulated thin-wire monofilar helical antenna defined by the problem geometry of Figs. 1(a) and 1(b), current distribution is specified by the moment-method solution specified [10],

$$\begin{bmatrix} I_n^p \\ I_n^i \end{bmatrix} = \begin{bmatrix} Z_{mn}^{pp} & Z_{mn}^{pi} \\ Z_{mn}^{ip} & Z_{mn}^{ii} \end{bmatrix}^{-1} \begin{bmatrix} V_m^p \\ V_m^i \end{bmatrix}, \tag{1}$$
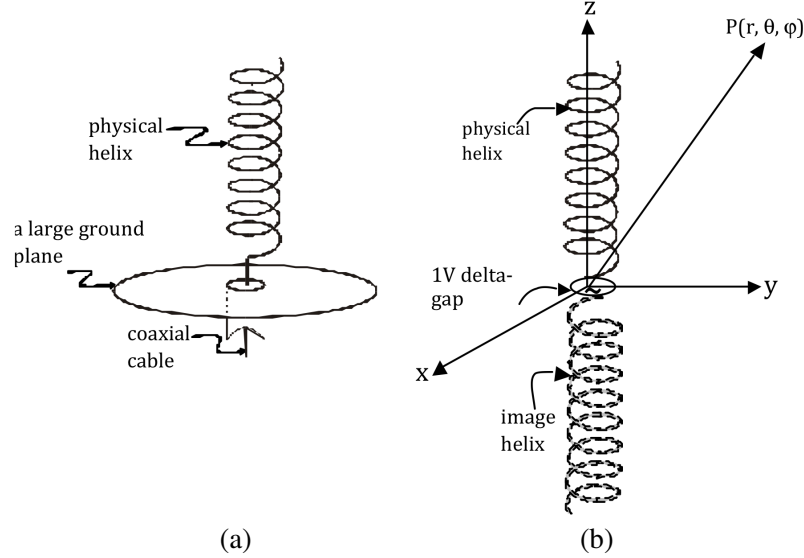
Figure 1: (a) Geometry of a monofilar helical antenna mounted on a large ground plane; (b) The image theory defined equivalent problem.

in which the subscript 'n' refers to the nth expansion; 'm' refers to the mth weighting function, and the superscripts 'p' and 'i' represent the 'physical', and 'image', respectively. Where both expansion and weighting functions are of the piece-wise linear variety given as:

$$G_n\left(\phi'\right) = \begin{cases} \frac{\phi'-\phi_{2n-1}}{\phi_{2n+1}-\phi_{2n-1}}, & \phi_{2n-1} \le \phi' \le \phi_{2n+1} \\ \frac{\phi_{2n+3}-\phi'}{\phi_{2n+3}-\phi_{2n-1}}, & \phi_{2n+1} \le \phi' \le \phi_{2n+3} \\ 0 & \text{elsewhere} \end{cases}, \tag{2}$$

for which

$$\frac{\partial G_n\left(\phi'\right)}{\partial \phi'} = \begin{cases} \frac{1}{\phi_{2n+1}-\phi_{2n-1}}, & \phi_{2n-1} \le \phi' \le \phi_{2n+1} \\ \frac{-1}{\phi_{2n+3}-\phi_{2n+1}}, & \phi_{2n+1} \le \phi' \le \phi_{2n+3} \\ 0 & \text{elsewhere} \end{cases} \tag{3}$$

It is readily established, [10], that entries into the generalized impedance matrix of (1) are given by:

$$\left[Z_{mn}^{pp}\right] = \int_0^{2\pi N}\int_0^{2\pi N} \left\{ \begin{array}{l} j\omega\mu_0 a\left(\cos\alpha\cos\left(\phi-\phi'\right)+\tan\alpha\sin\alpha\right)G_m^p\left(\phi\right)G_n^p\left(\phi'\right) \\ +\frac{1}{j\omega\varepsilon_0 a\sec\alpha}\frac{\partial G_n^p\left(\phi'\right)}{\partial\phi'}\frac{\partial G_m^p\left(\phi\right)}{\partial\phi} \end{array} \right\} \frac{e^{-jk_0 R}}{R}d\phi d\phi' \quad \text{(4a)}$$

$$\left[Z_{mn}^{pi}\right] = \int_0^{2\pi N}\int_0^{2\pi N} \left\{ \begin{array}{l} j\omega\mu_0 a\left(\cos\alpha\cos\left(\phi-\phi'\right)+\tan\alpha\sin\alpha\right)G_m^p\left(\phi\right)G_n^i\left(\phi'\right) \\ +\frac{1}{j\omega\varepsilon_0 a\sec\alpha}\frac{\partial G_n^i\left(\phi'\right)}{\partial\phi'}\frac{\partial G_m^p\left(\phi\right)}{\partial\phi} \end{array} \right\} \frac{e^{-jk_0 R}}{R}d\phi d\phi' \quad \text{(4b)}$$

$$\left[Z_{mn}^{ip}\right] = \int_0^{2\pi N}\int_0^{2\pi N} \left\{ \begin{array}{l} j\omega\mu_0 a\left(\cos\alpha\cos\left(\phi-\phi'\right)+\tan\alpha\sin\alpha\right)G_m^i\left(\phi\right)G_n^p\left(\phi'\right) \\ +\frac{1}{j\omega\varepsilon_0 a\sec\alpha}\frac{\partial T_n^i\left(\phi'\right)}{\partial\phi'}\frac{\partial G_m^i\left(\phi\right)}{\partial\phi} \end{array} \right\} \frac{e^{-jk_0 R}}{R}d\phi d\phi' \quad \text{(4c)}$$

$$\left[Z_{mn}^{ii}\right] = \int_0^{2\pi N}\int_0^{2\pi N} \left\{ \begin{array}{l} j\omega\mu_0 a\left(\cos\alpha\cos\left(\phi-\phi'\right)+\tan\alpha\sin\alpha\right)G_m^i\left(\phi\right)G_n^i\left(\phi'\right) \\ +\frac{1}{j\omega\varepsilon_0 a\sec\alpha}\frac{\partial G_n^i\left(\phi'\right)}{\partial\phi'}\frac{\partial W_m^i\left(\phi\right)}{\partial\phi} \end{array} \right\} \frac{e^{-jk_0 R}}{R}d\phi d\phi' \quad \text{(4d)}$$

In 4(a) through 4(d), the symbols 'a', 'α', and 'N' respectively stand for wire radius, helix pitch angle, and number of helix turns; and all other symbols assume their conventional meanings. And to account for the dielectric insulation, we utilize the model proposed elsewhere, [1], such that for each expansion function $G_n(\phi')$, we define a corresponding function, $G_{nd}(\phi')$ such that for a

dielectric coating thickness denoted by 'b',

$$G_{nd}(\phi') = \frac{(\varepsilon_d - \varepsilon_0)}{2\varepsilon_d} \left[\begin{array}{l} \varsigma_n \left\{ \sqrt{(b^2 + \phi_{2n+1}^2)} - \sqrt{(a^2 + \phi_{2n-1}^2)} - \sqrt{(b^2 + \phi_{2n-1}^2)} + \sqrt{(a^2 + \phi_{2n-1}^2)} \right\} \\ -\varsigma_{n+1} \left\{ \sqrt{(b^2 + \phi_{2n+3}^2)} - \sqrt{(a^2 + \phi_{2n+3}^2)} - \sqrt{(b^2 + \phi_{2n+1}^2)} + \sqrt{(a^2 + \phi_{2n-1}^2)} \right\} \end{array} \right]$$

$$\frac{\partial G_n(\phi')}{\partial \phi'} \tag{5}$$

With weighting functions defined to have the same structure, and where the Neumann functions are defined by:

$$\varsigma_n = \left\{ \begin{array}{ll} 1, & l_{2n-1} \le l' \le l_{2n+1} \\ 0, & \text{elsewhere} \end{array} \right. \tag{6}$$

$$\varsigma_{n+1} = \left\{ \begin{array}{ll} 1, & l_{2n+1} \le l' \le l_{2n+3} \\ 0, & \text{elsewhere} \end{array} \right. \tag{7}$$

Accordingly, the dielectric insulation is then accounted for by the additional generalized matrix elements characterized, for example, by:

$$[\Delta Z_{mn}^{pp}] = \int_0^{2\pi N} \int_0^{2\pi N} \left\{ j\omega\mu_0 a \left(\cos\alpha \cos(\phi - \phi') + \tan\alpha \sin\alpha \right) G_{md}^p(\phi) G_{nd}^p(\phi') \right\} \frac{e^{-jk_0 R}}{R} d\phi d\phi' \tag{8}$$

so that (1) modifies to

$$\left[\begin{array}{l} I_n^p \\ I_n^i \end{array} \right] = \left[\begin{array}{ll} \Delta Z_{mn}^{pp} + Z_{mn}^{pp} & \Delta Z_{mn}^{pi} + Z_{mn}^{pi} \\ \Delta Z_{mn}^{ip} + Z_{mn}^{ip} & \Delta Z_{mn}^{ii} + Z_{mn}^{ii} \end{array} \right]^{-1} \left[\begin{array}{l} V_m^p \\ V_m^i \end{array} \right] \tag{9}$$

to give the moment-method solution described in [1].
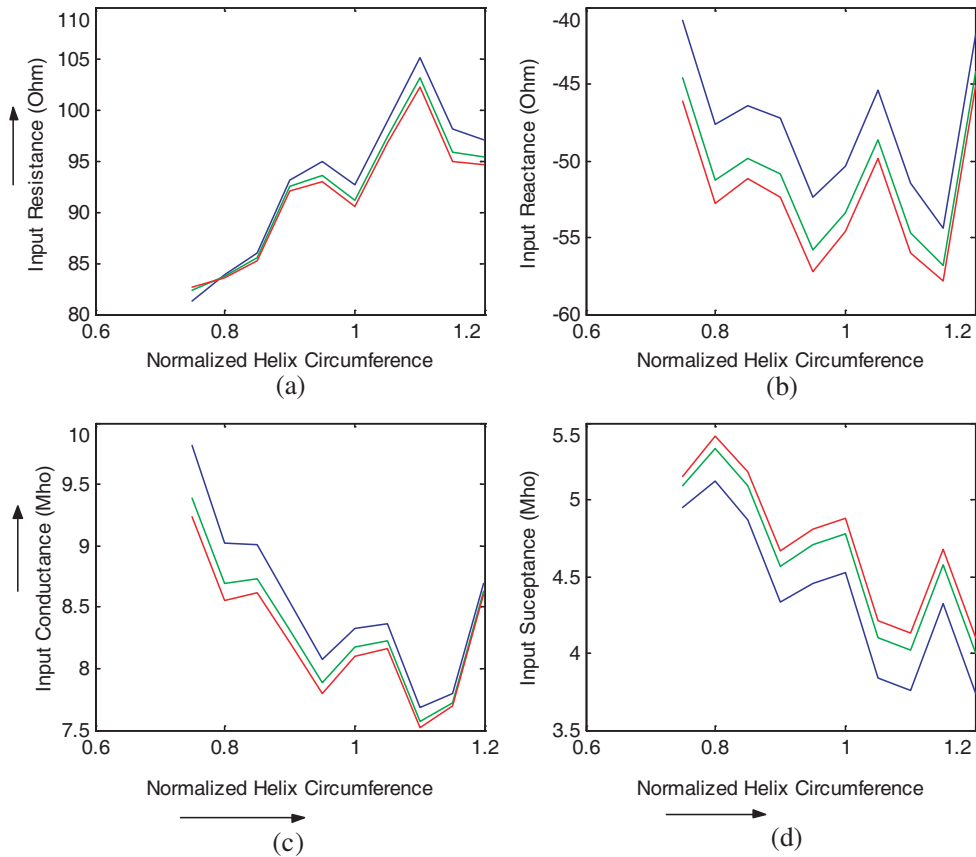
Figure 2: Variation of input impedance and admittance with normalized helix circumference for a fixed coating thickness (blue bare helix; green coated helix $\varepsilon = 2.3$; red coated helix $\varepsilon = 5.2$).
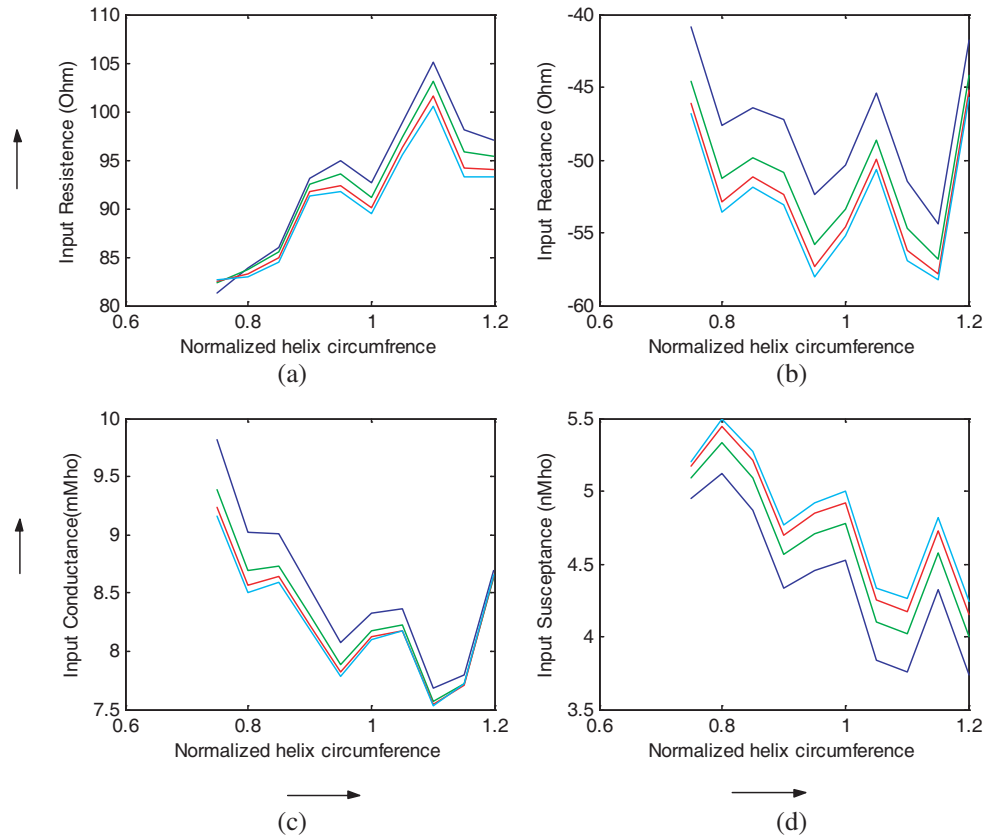
Figure 3: Variation of input impedance and admittance with normalized helix circumference for a fixed dielectric constant, (blue: bare helix; green: coated helix $b = 2a$; red coated helix $b = 3a$; and cyan coated helix $b = 4a$).

3. NUMERICAL RESULTS

Representative computational results obtained for the input impedance and admittance characteristics of the coated monofilar helical antenna backed by a large ground plane are shown in Figs. 2 and 3.

It can seen from Figs. 2(a) to 2(c), that the results suggest that for a fixed coating thickness, the effect of the dielectric insulation is to lower the values of input resistance, input reactance, and input conductance, with the decrease occurring with increase in dielectric constant. In the case of input susceptance, the reverse is the case; as susceptance increases in value with increase in dielectric constant. The input characteristics displayed in Fig. 3 also exhibit the same features as described for Fig. 2, in that we find again, that the dielectric insulation has the effect of lowering input resistance, reactance and conductance, but increasing input susceptance. In this case, the decrease occurs, for a fixed value of dielectric constant, with increase in coating thickness.

4. CONCLUSION

This paper has investigated the input characteristics of a dielectric-coated thin-wire monofilar helical antenna backed by a large ground plane. The ground plane was taken into account through the use of the image theory, and in the case of the dielectric insulation, use was made of the quasi-static formulation earlier developed by Adekola et al., [1], for a moment-method solution of the problem of coated thin-wire antennas. Numerical results obtained suggest that inclusion of the dielectric coat has the effect of lowering input resistance, reactance and conductance; with the decrease in the values of these input parameters occurring with increase in dielectric constant (for a fixed coating thickness) and with coating thickness for fixed values of dielectric constant. Since, as noted in [10], the elliptical-cylindrical helix antenna can serve as a general case for certain regular thin-wire geometries, the formulation developed in this analysis has the potential of being developed as a general case for the regular thin-wire geometries.

REFERENCES

1. Adekola, S. A., A. I. Mowete, and A. Ogunsola, "On the problem of dielectric coated wire antenna," *PIERS Proceedings*, 431–437, Moscow, Russia, Aug. 18–21, 2009.
2. Richmond, J. H. and E. H. Newman, "Dielectric coated wire antenna," *Radio Science*, Vol. 11, No. 1, 13–20, 1976.
3. Lee, J. P. Y. and K. G. Balmain, "Wire antennas coated with magnetically and electrically lossy material," *Radio Science*, Vol. 14, No. 1, 437–445, 1979.
4. Desplanches, B., A. Sharaiha, and C. Terret, "Numerical Analysis of helical antennas backed by finite ground planes," *Microwave and Optical Technology Letters*, Vol. 15, No. 6, 352–355, 1997.
5. Yamauchi, J. and H. Nakano, "Hallen-type integral equation to a system composed of wires with dielectric coating," *Electronics Letters*, Vol. 26, No. 17, 1412–1413, 1990.
6. Huddleston, P. L., L. N. Medgyesi-Mitschang, and J. M. Putnam, "Combined field integral formulation for scattering by dielecrically coated conducting bodies," *IEEE Transactions on Antennas and Propagation*, Vol. 34, No. 4, 510–520, 1986.
7. Chatterjee, A., L. Volakis, and W. J. Kent, "Scattering by a perfectly conducting and a coated thin-wire using a physical basis model," *IEEE Transactions on Antennas and Propagation*, Vol. 40, No. 7, 761–769, 1992.
8. Popovic, B. D. and A. Nesic, "Generalisation of the concept of equivalent radius of thin cylindrical antenna," *IEE Proeedings of Microwave, Optics and Antenna*, Vol. 131, No. 3, 153–158, Jun. 1984.
9. Moore, J. and M. West, "Simplified analysis of coated wire antennas and scatterers," *IEE Proceedings of Microwave, Antenna Propagation*, Vol. 142, No. 1, 14–18, Feb. 1995.
10. Adekola, S. A., A. Ike Mowete, and A. A. Ayorinde, "Compact theory of the broadband elliptical helical antenna," *European Journal of Scientific Research*, Vol. 31, No. 3, 446–490, 2009.

Antenna Design for a Portable RFID Reader

Manoel Vitório Barbin[1] and Silvio Ernesto Barbin[2]

[1]Flextronics Institute of Technology, Brazil
[2]Department of Telecommunication and Control Engineering, Polytechnic School
University of São Paulo, Brazil

Abstract— This paper presents a circular polarized antenna for a portable RFID reader operating in the 900 MHz frequency band. Size reduction is addressed as an important challenge in the antenna design since the antenna should be carried in the hand of a system operator. A high dielectric constant substrate is used for miniaturization. Further size reduction is achieved by cutting slots in the radiating patch. The feeding structure is implemented on another substrate and both circuits are stacked to constitute an electromagnetic coupled antenna. Simulation and measurement results are presented.

1. INTRODUCTION

Radio frequency identification (RFID) systems have been widely used in supply chains and logistics applications for identifying and tracking goods. In RFID systems, tags are attached to objects and readers are used for data acquisition. Data transfer between a tag and a reader is carried out through backscattering of electromagnetic waves [1]. In order to obtain an effective system, the reader must be capable to establish a reliable communication with the tags. In this way, the antenna at the reader plays an important role in the system performance. The antenna design is driven by considerations on size and weight in addition to electrical specifications like gain and return loss. Frequently, the electrical specifications are less strict for these antennas [2], being the optimization process performed in view of the whole system requirements. Following this guideline, the antenna proposed in this work was designed aiming at exhibiting small size but generating enough radiation to be used in a portable reader for identification of items stored in warehouses. The antenna is to be carried in the hand of an operator walking inside the building. Circular form was chosen for the antenna with a diameter that should not exceeding 80 mm for easy gripping with the fingers.

The present work is organized as follows. After this brief Introduction, Section 2 describes the antenna design in detail. Section 3 presents simulated and measurement results for a prototype built according to the proposed guidelines. Finally, in Section 4, conclusions are drawn.

2. ANTENNA DESIGN

In addition to the aforementioned characteristics, other important system requirements for the antenna are listed in Table 1.

Aiming at complying with the system specifications presented in Table 1, the proposed antenna was designed using a high dielectric constant substrate for size reduction but producing enough radiation to result in a reading range that covers the desired identification area. The use of a high dielectric substrate also helps in minimizing the electrical characteristics degradation of the antenna as the fields become more concentrated within the substrate. Among several substrates that could be used Arlon AD600 [3] was chosen. Some characteristics of this substrate are presented in Table 2.

Although the dielectric constant of the substrate used in the design is high enough to lead to a significant size reduction of the antenna, the obtained reduction was not sufficient for our purposes. The use of a higher dielectric constant substrate could reduce even more the size of the antenna [4].

Table 1: System characteristics.

Characteristic	Value	Note
Frequency Band	902–907.5 MHz	Licensed for RFID systems in Brazil
Reading range	1 m	Radiated power can be controlled by the reader
ID area	1 m^2	Guide for HPBW (Half Power Beam Width) specification
Polarization	Circular	Used by most RFID systems

Table 2: Specifications of the AD600 substrate.

Property	Value
Thickness	125 mils
Dielectric Constant	6.3
Dissipation Factor	0.003
Copper	1/2 oz/ft^2

However, this would also reduce the radiation intensity due to higher concentration of the fields in the dielectric. Further size reduction was achieved by cutting slots in the antenna radiation element as proposed in [5]. Two crossed slots were cut in the patch as shown in Figure 1. For slots of slight different lengths, two electromagnetic modes are excited in the structure resulting in a circular polarized wave.

Another challenge in the antenna design is the feeding method. The easiest method is to feed the antenna attaching a coaxial connector between the radiating patch and its ground plane. This method proved to be inefficient since it resulted in very poor VSWR — Voltage Standing

Figure 1: Antenna radiating patch on AD600 substrate.
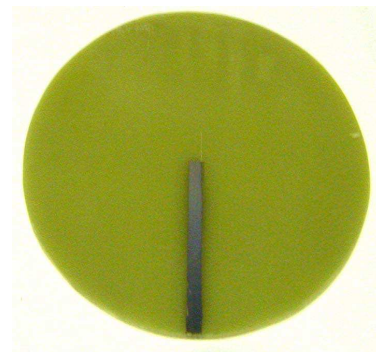
Figure 2: Feeding structure of the antenna on FR4 substrate.
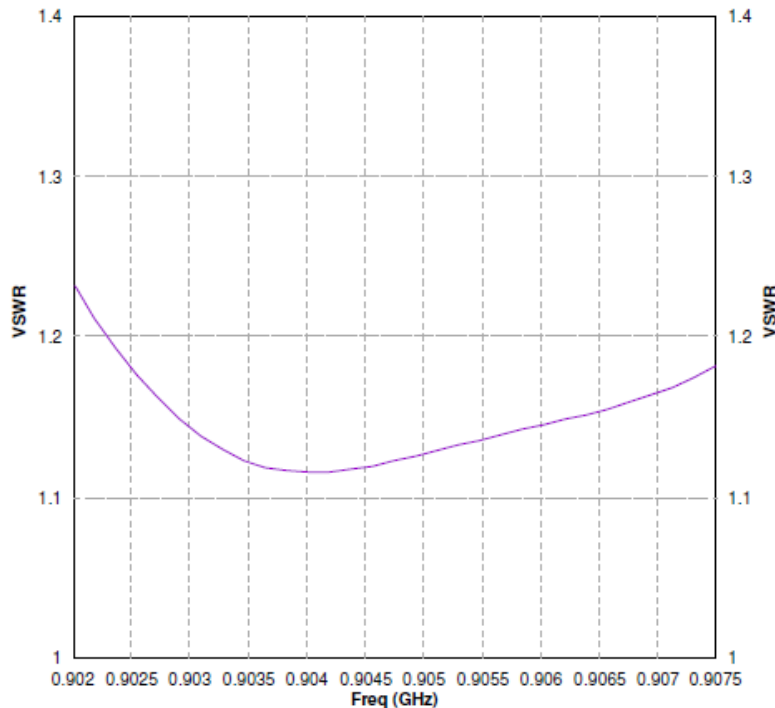
Figure 3: VSWR in the 902 MHz to 907.5 MHz frequency band.

Wave Ratio. The electromagnetic coupling feeding method described in [5] was used instead. The ground plane was removed and a 50 Ohm microstrip feeding line was implemented on a low cost FR4 substrate ($h = 1.6$ mm) which was stacked to the patch substrate. By carefully adjusting the length of the feeding line a much lower VSWR was achieved in the specified frequency band. Figure 2 shows the feeding line used in the antenna.

An SMA connector was soldered at the line input between the strip and the ground plane. Electromagnetic coupling between the line and the radiating patch is ensured through the stacking of the two substrates.

3. SIMULATION AND MEASUREMENTS RESULTS

The antenna was designed using the IE3D simulation tool by Zeland. This software is based on the Method of Moments which is known to be very efficient for the design of patch antennas. The obtained VSWR for the frequency band of interest is shown in Figure 3.

The elevation radiation pattern is presented in Figure 4. A quasi-symmetrical shape was obtained. The HPBW is approximately 110 degrees, which provides enough coverage for the RFID application discussed in Section 1.

The axial ratio for the antenna is depicted in Figure 5. A maximum value of 2.7 was obtained which is fairly acceptable for RFID systems.

A prototype of the antenna was built and measured. Slight dimensional adjustments were done afterwards for optimal performance. A commercial reader by Skytek was used in the determination
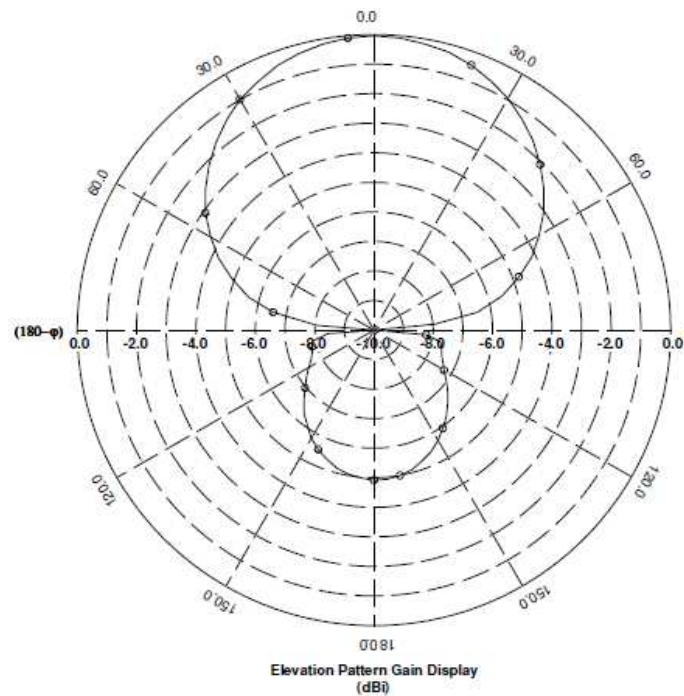
Figure 4: Radiation elevation pattern.

Table 3: Antenna and system performance in the 902 MHz to 907.5 MHz frequency band.

Parameter	Value
VSWR	< 1.3
Gain	0 dBi
Polarization	LHCP (Left Hand Circular Polarization)
Axial Ratio	< 3 dB
HPBW	$106°$
Reading range	1.2 m
ID area	$> 3\,\text{m}^2$
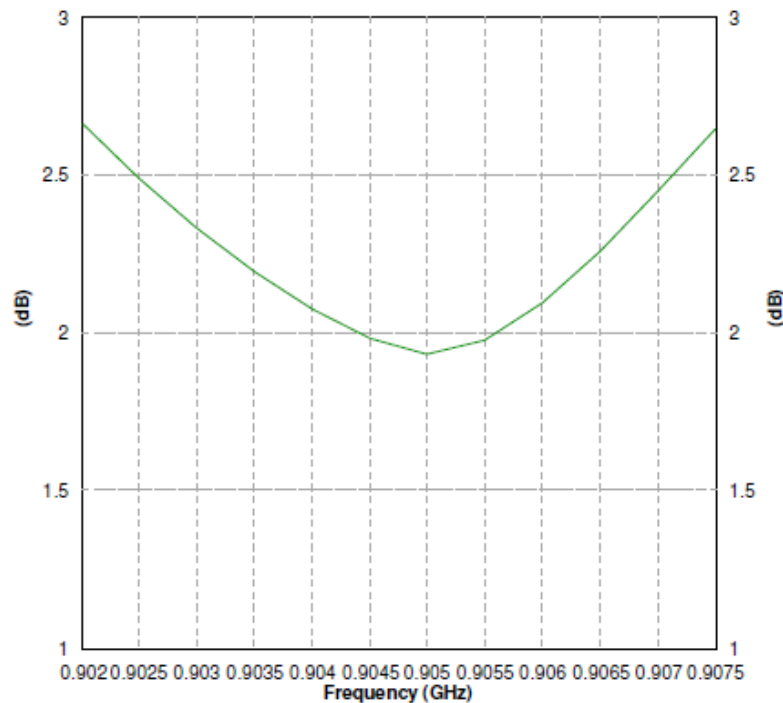
Figure 5: Axial ratio.

of the reading range. The reader uses frequency hopping in the 902 MHz to 907.5 MHz band and radiates a power of up to 30 dBm. Afterwards, the prototype was integrated to the complete system. Table 3 summarizes the obtained results.

4. CONCLUSION

An antenna for RFID readers using a stacked arrangement of two substrates was presented. One of the substrates (AD600) has a high dielectric constant to reduce the antenna size. The radiation element was designed on this substrate. Further size reduction was obtained by the introduction of slots in the radiation patch. The other substrate (FR4), used for the implementation of the feeding line, is usually found in electronic PCB designs. Electromagnetic coupling between the radiation patch and the feeding line was chosen. The obtained simulation and measurement results exhibit good agreement with the antenna specifications and comply with the system requirements.

REFERENCES

1. Finkenzeller, K., *RFID Handbook*, 2nd Edition, Wiley, England, 2004.
2. Fujimoto, K. and J. R. James, *Mobile Antenna Systems Handbook*, 2nd Edition, Artech House, Norwood, 2001.
3. AD600 — Arlon Microwave Materials, Arlon Inc., rev D, 2009, www.arlon-med.com.
4. Rao, B. R., M. A. Smolinski, C. C. Quach, and E. N. Rosario, "Triple band GPS trap loaded inverted L antenna array," *Microw. Opt. Tech. Lett.*, Vol. 38, No. 1, 35–37, Jan. 2003.
5. Iwasaki, H., "A circularly polarized small-size microstrip antenna with a cross slot," *IEEE Trans. Antennas and Propagation*, Vol. 44, 1399–1401, Oct. 1996.
6. Davidovitz, M. and Y. T. Lo, "Rigorous analysis of a circular patch antenna excited by a microstrip transmission line," *IEEE Trans. Antennas and Propagation*, Vol. 37, 949–958, Aug. 1989.

Characterization of Microwave Thin Radar Absorber Composed of Hexagonal Patch Array

L. Olivia, F. Kurniasih, and A. Munir

School of Electrical Engineering and Informatics, Institut Teknologi Bandung, Indonesia

Abstract— A feasibility to employ a doubly periodic hexagonal patch for microwave thin radar absorber is numerically investigated. The hexagonal patch that operates at the resonance frequency of resistively textured surface is incorporated with surface-mounted-resistive elements. These resistive elements are used to reduce the amount of backscatter from the surface affecting the absorption of radar absorber. By the selection of appropriate choice of the required resistive elements based on elementary circuit principles, the absorption can be optimally achieved. The construction of radar absorber is then numerically characterized under normal incident to obtain its performance. It is shown that by applying the construction elaborated in this work it has enabled a reduction in the radar absorber thickness, and that up to $-30\,\mathrm{dB}$ at resonance frequency of $3.35\,\mathrm{GHz}$ reflected wave can be obtained.

1. INTRODUCTION

Recently, patch array is becoming popular due to the planar substrates upon which the patch elements are printed. A number of applications based on patch array printed on a circuit board have been reported [1–4]. These include the use of high-impedance surface (HIS), or, artificial magnetic conductor (AMC) such as a suitably designed textured surface for antenna with reduced radar cross-section, reflected polarization with stable resonance, and microwave radar absorber [2–4]. An AMC that is usually consisted of a doubly periodic array of printed metallic patch on a grounded substrate is a physical approximation of perfect magnetic conductor (PMC) with zero degree reflection properties in only a narrow frequency band. Several forms of AMC, as well as HIS, have been investigated with or without vias-included with positive implications on manufacturing simplicity [4–7].

The advent of HIS based on a doubly periodic patch array has also opened up a new idea in the design of ultra-thin radar absorber. One of well-known approaches in the design of radar absorber material is using the Salisbury screen [8]. In this approach, the screen that is a resistive sheet is positioned on $\lambda/4$ from a conducting metal ground plane, as a result the destructive phasing that exist at the front face of the resistive sheet can cancel the reflected signal. By use of a texture surface technology comprised of HIS as a PMC, this can remove the need of HIS for a $\lambda/4$ spacing between resistive sheet and a perfectly conducting metal ground plane obtaining the reduction of absorber thickness drastically. This approach has been theoretically investigated and practically implemented with different physical structures for microwave absorber application [9, 10].

In this work, the characterization of microwave thin radar absorber is numerically investigated. The radar absorber that has thickness about $0.03\lambda_0$ is designed using textured surface technology based on the HIS principle. The construction of radar absorber employs a doubly periodic hexagonal patch to investigate feasibility usage of the different shape of patch. To reduce the amount of backscatter from the surface by controlling its surface impedance, surface-mounted-resistive elements are incorporated midway onto the array of surface. Meanwhile to investigate the characteristic of radar absorber, we numerically analyzed a unit cell comprised of a hexagonal patch that operates whereby at the resonance frequency of resistively texture surface. By using the elementary circuit principles, the appropriate value of the required resistive elements is then theoretically calculated to be used for the simulation.

2. STRUCTURE CONSTRUCTION

The structure of radar absorber used here is based on the construction in [4] but with a doubly periodic hexagonal patch placed on the different size of substrate. To conserve computational effort as illustrated in Fig. 1 a unit cell is modeled for the numerical investigation. The unit cell consists of hexagonal shape of metallic copper with the edge length of 6.58 mm and the gap between patches in y-axis direction of 2.0 mm. The patch is then placed on a single-sided thick 2.54 mm Taconic CER-10 substrate that has permittivity and $\tan\sigma$ of 10 ± 0.5 and 0.0035 respectively. The thickness of metallic copper top patch as well as the ground plane of the substrate is 0.035 mm. Here,
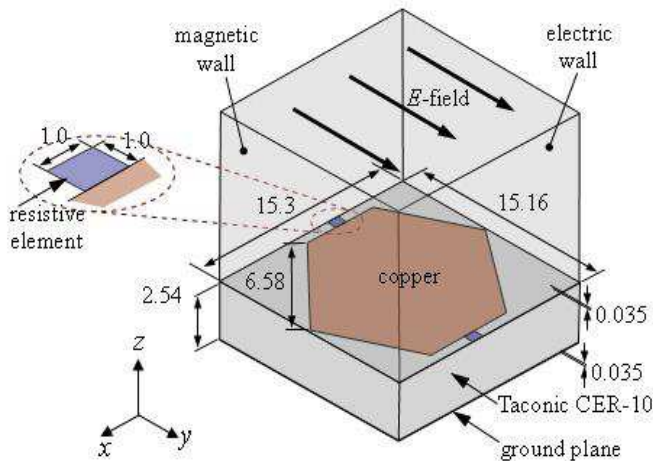
Figure 1: A doubly periodic hexagonal patch of unit cell for the investigation (unit in mm).
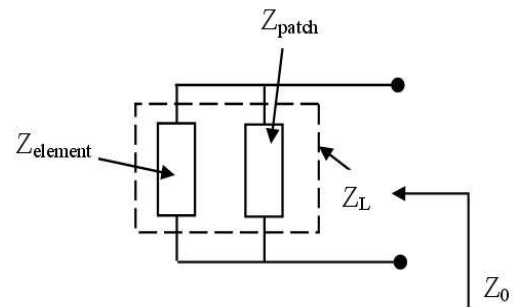
Figure 2: Transmission line model for the impedance matching analysis.

substrate and copper conductive losses are also accounted for. To reduce the amount of backscatter from the surface, surface-mounted-resistive elements are incorporated midway connecting between the adjacent patches in y-axis direction. A normal incident wave of simple TE mode in y-axis direction is applied to illuminate the patch surface and boundary conditions are applied with perfect electric conductor (PEC) or electrical walls perpendicular and perfect magnetic conductor (PMC) or magnetic walls parallel to the E-field. The selected boundary conditions are used to make the image of hexagonal patch to be a double periodic array of infinite extent.

3. IMPEDANCE MATCHING CALCULATION

As the construction operates whereby at the resonance frequency of resistively texture surface, the surface behaves like an perfect magnetic conductor, i.e., zero-phase reflection of the applied E-field at resonance frequency. The resonance frequency of such construction can be theoretically approximated by approaching the construction as a unit cell of square patch. This approach is usable to determine the values of L and C of the construction by taking into account the dimension, thickness, and permittivity of the unit cell, as a result the resonance frequency can be approximately calculated. Hence to analyze the reflection properties of the surface, a transmission line theory of lumped circuit element can be used. This approximation analysis is allowed to be applied for the construction as the size is much smaller than one wavelength. By calculating reflection coefficient (Γ) using (1), the mismatch that occurs because of the relatively large surface impedance compared with the impedance of free space can be investigated.

$$\Gamma = \frac{Z_L - Z_0}{Z_L + Z_0}, \tag{1}$$

where Z_0 is the impedance of free space ($120\pi\,\Omega$) and Z_L is the load impedance comprised of the textured surface impedance (Z_{patch}) in parallel with the impedance of resistive elements interconnecting the textured surface ($Z_{element}$) as shown in Fig. 2.

In order the mismatch to be a minimum or zero, the value of load impedance (Z_L) should be the same as the value of free space impedance (Z_0). This condition can be achieved by the selection of appropriate choice of the required $Z_{element}$ to lower the inherent of Z_{patch}. If this condition is accomplished the amount of backscatter from the surface can be suppressed maximally affecting the increase of incoming energy absorption. In connection with the free space impedance, from Fig. 2 the textured surface impedance (Z_{patch}) can be expressed as follows,

$$\frac{1}{Z_{patch}} = \frac{1}{Z_0} - \frac{1}{Z_{element}}. \tag{2}$$

From the above equation, if the value of Z_{patch} is obtained then the value of resistive elements interconnecting the textured surface ($Z_{elements}$) can be determined.
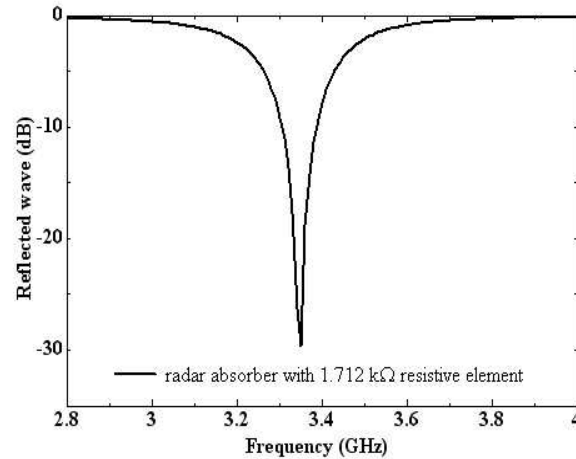
Figure 3: Simulated result of hexagonal patch incorporated with resistive element.

4. CHARACTERIZATION AND RESULT

The characterization of the radar absorber is numerically carried out under normal incident generated form a simple TE mode excitation. From the simulation result, the impedance of the textured surface (Z_{patch}) without resistive-elements, but with substrate loss, 0.0035, and copper losses, 5.8×10^7 S/m included, becomes $484\,\Omega$ at its resonant frequency of 3.35 GHz. Application of (2) yields an approximate initial value for the resistive element of $1.705\,\text{k}\Omega$ yielding a resultant parallel combination of $120\pi\,\Omega$. Then by applying (1), the reflection magnitude for each value of Z_L can be theoretically obtained. To compare the theoretical result, the hexagonal patch that operates at resonance frequency of 3.35 GHz is then incorporated with surface-mounted-resistive elements interconnecting with the adjacent patch. Since a normal incident uses a simple TE mode the variant of E-field only exists in y-axis direction, therefore the resistive-elements are necessary interconnecting only in the midway of the patch. Here, the characteristic response of unit cell with resistive-elements values swept from $1.6\,\text{k}\Omega$ to $1.8\,\text{k}\Omega$ to be around the predicted result from theoretical calculation, $1.7\,\text{k}\Omega$, is analyzed. As the prediction, the optimum result of resistive element from the simulation result is $1.712\,\text{k}\Omega$ resulting the deepest reflected wave where the textured surfaces impedance closes to the free space impedance. The result is plotted in Fig. 3 that shows up to -30 dB reflected wave can be obtained at resonance frequency with the bandwidth response is about 2.5% at 10 dB reflection loss. The narrow bandwidth response of the construction is probably caused by high Q of the used substrate.

5. CONCLUSIONS

It has been demonstrated that the HIS-based textured surface technology comprised of a doubly periodic hexagonal patch with the incorporation of surface-mounted-resistive-element upon it can be used in the construction of microwave thin radar absorber. From the characterization result, it shows that even though the bandwidth response is still narrow due to high Q of the substrate that needs to be improved, however the construction using hexagonal patch array with resistive elements of $1.712\,\text{k}\Omega$ whereupon the incident electromagnetic energy is absorbed up to 30 dB has the thickness of $0.03\lambda_0$. A simple means for the calculation of required resistive element based on elementary circuit principles has also been demonstrated to be valid. More investigation in the characterization of radar absorber is under progress where more reliable properties such as bandwidth improvement will be demonstrated later.

REFERENCES

1. Pozar, D. M. and T. A. Metzler, "Analysis of a reflectarray antenna using microstrip patches of variable size," *Electron. Lett.*, Vol. 29, 657–658, 1993.
2. Fusco, V. F. and S. W. Simms, "Textured surface slot antenna with reduced radar cross-section," *Electron. Lett.*, Vol. 43, No. 8, 438–440, 2007.
3. Simovski, C. R., P. de Maagt, and I. V. Melchakova, "High-impedance surfaces having stable resonance with respect to polarization and incidence angle," *IEEE Trans. Antennas Propagat.*, Vol. 53, No. 3, 908–914, 2005.
4. Munir, A. and V. Fusco, "Effect of surface resistor loading on high impedance surface radar absorber return loss and bandwidth," *Microwave and Optical Tech. Lett.*, Vol. 51, No. 7, 1773–1775, 2009.
5. Sievenpiper, D., L. Zhang, R. Broas, N. G. Alexopolous, and E. Yablonovitch, "High impedance electromagnetic surfaces with a forbidden frequency band," *IEEE Trans. Microwave Theory & Tech.*, Vol. 47, 2059–2074, 1999.
6. Zhang, Y., J. von Hagen, M. Younis, C. Fischer, and W. Wiesbeck, "Planar artificial magnetic conductors and patch antennas," *IEEE Trans. Antennas Propagat.*, Vol. 51, No. 10, 2704–2712, 2003.
7. Goussetis, G., A. P. Feresidis, and J. C. Vardaxoglou, "Tailoring the AMC and EBG characteristics of periodic metallic arrays printed on grounded dielectric substrate," *IEEE Trans. Antennas Propagat.*, Vol. 54, No. 1, 82–89, 2006.
8. Fante, R. L. and M. T. McCormack, "Reflection properties of the Salisbury screen," *IEEE Trans. Antennas Propagat.*, Vol. 36, 1443–1454, 1988.
9. Simms, S. and V. Fusco, "Tunable thin radar absorber using artificial magnetic ground plane with variable backplane," *Electron. Lett.*, Vol. 42, No. 21, 1197–1198, 2006.
10. Munir, A. and V. Fusco, "Characterization of microwave anisotropic thin radar absorber using artificial magnetic ground plane," *Proceeding of 2008 Asia-Pacific Microwave Conference*, 1–4, Hongkong, China, December 2008.
11. Sievenpiper, D., "High-impedance electromagnetic surfaces," Ph.D. Thesis, UCLA, 1999.

Microstrip Array Antenna with New 2D-Electromagnetic Band Gap Structure Shapes to Reduce Harmonics and Mutual Coupling

Dalia N. Elsheakh[1], **Magdy F. Iskander**[1], **Esmat A. Abdallah**[2],
Hala A. Elsadek[2], **and Hadia Elhenawy**[3]

[1]Hawaii Center for Advanced Communication, Hawaii, Honolulu, USA
[2]Electronics Research Institute, Cairo, Egypt
[3]Faculty of Engineering, Ain Shams University, Cairo, Egypt

Abstract— This paper presents microstrip array antenna integrated with novel shapes of 2D-electromagnetic band-gap structure (2D-EBG). Three different shapes of 2D-EBG are used for harmonic suppression, optimizing the current distribution on the patches and decreasing the mutual coupling between array elements. As a result the performance of the antenna array is improved. The three novel shapes of 2D-EBG presented are star, H and I shaped slots. Simulated and measured results verify the improved performance of the array antenna compared to the antenna without EBG as well as antenna array with conventional EBG shapes. The harmonic suppression and the reflection coefficients are improved by about 18 dB and the antenna size is reduced by 15% compared to the original size.

1. INTRODUCTION

Microstrip patch antennas are widely used in various applications because of low profile, low cost, light-weight and conveniently integration with RF devices. However, microstrip antennas have many disadvantages. One of these disadvantages is the excitation of surface waves that occur in the substrate layer. Surface waves are undesired because when a patch antenna radiates, a portion of total available radiated power becomes trapped along the surface of the substrate. It reduces total available power for radiation to space wave as well as there is harmonic frequency created [1]. For arrays, surface waves have a significant impact on the mutual coupling between array elements [2]. One solution to reduce surface waves is using electromagnetic band-gap (EBG) or photonic band-gap structure (PBG). Recently, there has been an increasing interest in studying the microstrip patch antenna with various periodic structures including electromagnetic band-gap (EBG) [2]. Many shapes of EBG slots have been studied for single element microstrip antenna such as circles, dumb-bells and squares. However, not many have realized in antenna arrays [3]. It has been demonstrated that the EBG structure will lead to a reduction in the side-lobe levels and improvements in the front to back ratio and overall antenna efficiency for the radiation pattern. In [4], the unique capability of the EBG structure to reduce the mutual coupling between elements of an antenna array is demonstrated. The side lobe of the antenna with one patch is caused by surface-wave diffraction at the edges of the antenna substrate, while for antenna array the side lobe is related to the pattern of the individual antenna, location of antenna in the array and the relative amplitudes of excitation [5, 6].

In this paper, microstrip patch antenna arrays with three different shapes of 2D-EBG as star shape, H shape and I shape etched on the ground plane are designed, simulated and measured. In this study, harmonic suppression and reduction of the mutual coupling effect are investigated by proposing these new shapes. The obtained results demonstrate that the 2D-EBG not only reduces the mutual coupling between the patches of antenna array, but also suppresses the second harmonic, reduces the side lobe levels and gives results better than conventional 2D-EBG shapes as circle and square. It is also shown that the novel shapes of 2D-EBG on the ground plane increases the gain of the antenna array.

2. CONFIGURATION OF 2D-EBG SHAPES

Three different shapes of 2D-EBG are presented in this paper as shown in Figure 1. The three shapes are compared with familiar conventional shapes as circular and square shapes 2D-EBG by using transmission line approach. The proposed EBG units are composed of several rectangular-shape slots (of length **L** and width **W**). This EBG cell can provide a cutoff frequency and attenuation pole. It is well known that an attenuation pole can be generated by a combination of the inductance and capacitance elements as given in [4] which presents circuit model for the cell for all 2D-EBG

structures. Here, the capacitance is provided by the transverse slot and the inductance by different shapes slots. For star shape there are four rectangular slots with $\mathbf{L} = 5$ mm, $\mathbf{W} = 1$ mm at angles $= 0°$, $45°$, $90°$ and $135°$. The second shape, which is the H shaped slot, consists of three rectangular slots with same previous dimensions. The third shape is the I shaped slot, which is obtained by rotating H shape by $90°$. The substrate with a dielectric constant of 10.2, loss tangent of 0.0019 and thickness of 2.5 mm is considered here. The microstrip feeding line on top plane has a width $\mathbf{W_f} = 2.3$ mm, corresponding to $50\,\Omega$ characteristic impedance. 2D-EBG cells are etched on the ground plane with periodicity $\mathbf{P} = 7$ mm and ratio $L/p = 0.7$ [6]. Then the reflection and transmission coefficients (S_{11} and S_{21}) are calculated using the high frequency structure simulator (HFSS).

3. ANTENNA ARRAY DESIGN

Consider an ordinary antenna array with two elements, as shown in Figure 2(a). At 5.2 GHz, the dimensions of the patches are patch width $\mathbf{W_p} = 8$ mm, patch length $\mathbf{L_p} = 7.5$ mm and microstrip feed line with length $\mathbf{L_f}$, $\mathbf{L_s} = 20$ mm, 13 mm, respectively, width $\mathbf{W_f} = 2.3$ mm and the distance between the patches is $\mathbf{d} = 19$ mm ($0.44\lambda_{5.2\,\text{GHz}}$.). It can be seen that the antenna will radiate energy at a harmonic frequency of 7.5 GHz. In order to suppress such harmonics, the band-stop characteristic of the EBG structure may be used. In this paper, the 2D-EBG shown in Figure 2(b) which is simply 2D-EBG cells are etched on the ground metal sheet.

4. RESULTS AND DISCUSSION

The first step of the design is obtaining the transmission and reflection coefficient response of the ground plane which has 2D-EBG. The response presents both conventional shape as circular and square 2D-EBG as well as the three new shapes. The second step, is applying these shapes to the ground plane of two element array antenna. The reflection coefficient of the two patches array antenna with 2D-EBG structure. The results indicate that the harmonic at 7.5 GHz is indeed suppressed as well as reducing array antenna size by about 7.5% for H-shape, 8% for star-shape and for I-shape reaches 15%. According to the characteristics of EBG, the surface wave can also be suppressed. For effective suppression of the harmonics, and for effective suppression of the surface waves, a periodic structure surrounding the patches, in addition to underneath the patches,
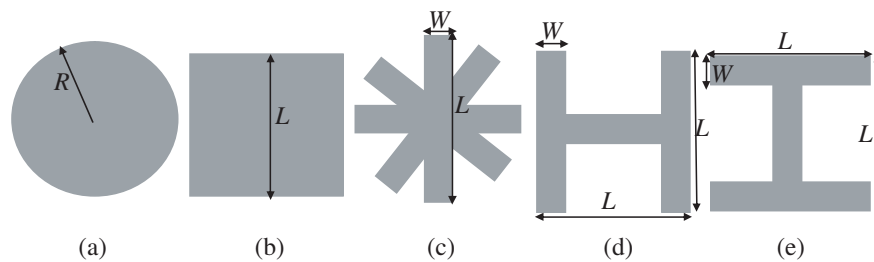
Figure 1: The different shapes of one unit cell of 2D EBG. (a) Conventional circle, (b) conventional square, (c) star, (d) H shape and (e) I-shape.
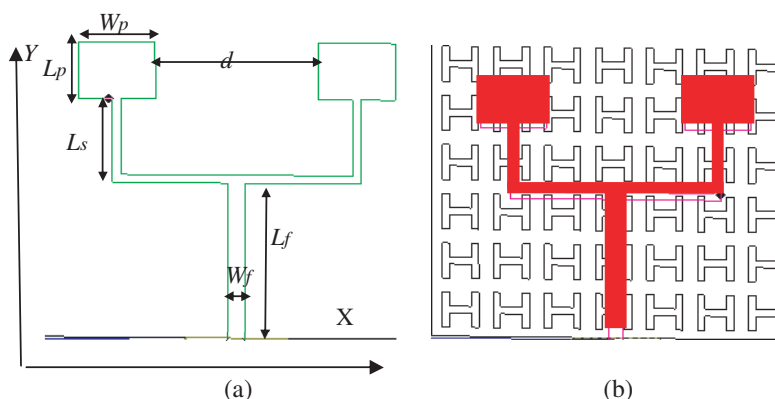
Figure 2: (a) Two-element MPAA, (b) MPAA with 2D-EBG.

are necessary. The array performance of the conventional 2D-EBG and the three new shapes of 2D-EBG are given in Table 1.

From Table 1 one can notice that; I shape gives maximum reduction in resonant array frequency than other shapes so reduce the electrical array size, star shape gives maximum average antenna gain and minimum mutual coupling while H shape gives larger antenna bandwidth than others.

The 2D-EBG structure on the ground plane changes the current distribution on the patches, and consequently the antenna gain. The surface current distributions for the various shapes. The gain of the two-element array antenna is also studied for different array antennas with and without 2D-EBG. Figure 3 shows that the antenna gain at lower frequencies for the antenna without 2D-EBG is slightly better than with EBG because it is out of band-gap. However, at higher frequencies the antenna gain with 2D-EBG is better than that without EBG by about 9 dBi maximum difference and 3 dBi in average over the entire antenna band which verifies the harmonic suppression behavior.

Finally, the two element array antennas are fabricated by using photolithographic techniques at HCAC center and measured by using E8364A vector network analyzer. The comparisons between measured and simulated reflection coefficients are shown in Figures 4 and 5 for the star and I shape, respectively. The difference between the results of simulation and measurement may be attributed to some fabrication tolerances especially in the etched slots as well as soldering discontinuities effect. The photos of the fabricated 2D-EBG antennas are shown in Figure 6. The simulated E-plane and H-plane radiation patterns for the five shapes of the 2D-EBG are shown in Figure 7.

Table 1: The effect of different 2D-EBG shapes on the antenna performance.

Shape of 2D-EBG	Antenna Gain dB @5.2 GHz	Mutual Coupling $|S_{21}|$	Harmonic level dB	Reflection Coefficient	F_o GHz	BW %	Defect Geometry, Perioficity X direction/Y direction
Without	10	-16 dB	-35	-17 dB	5.1	3	
Square	13.5	-18.5 dB	-10	-17.5 dB	5	4	Side dimension 4 mm 6 mm, 6 mm
Circular	13	-19 dB	-15	-20 dB	4.8	5	Radius 2 mm, 2 mm, 2 mm
Star	13.75	-40 dB	-9	-30 dB	4.75	5	Side length 1×4 mm^2, 6 mm, 6 mm
H	12.75	-20 dB	-10	-40 dB	5	5.1	Side length 1×5 mm^2, 6 mm, 6 mm
I	11	-30 dB	-7	-45 dB	4	5	Side length 1×5 mm^2, 6 mm, 6 mm
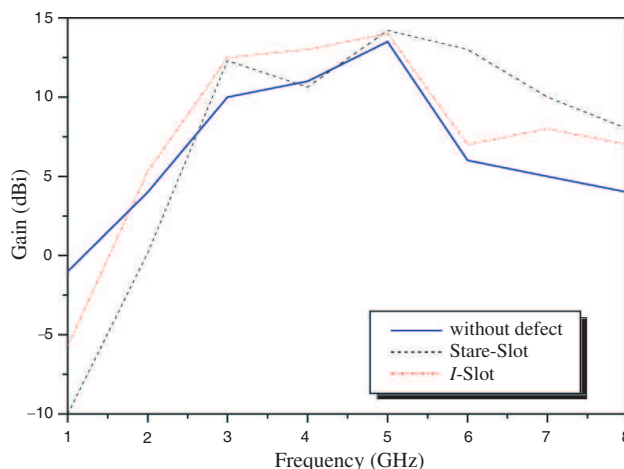
Figure 3: The Gain response for different shapes of MP array antenna without and with 2D-EBG shapes.
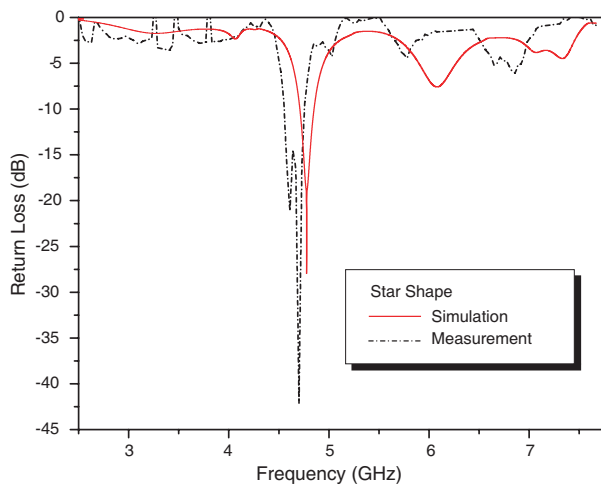
Figure 4: Comparison between measurement and simulated reflection coefficients for star shaped slot 2D-EBG.
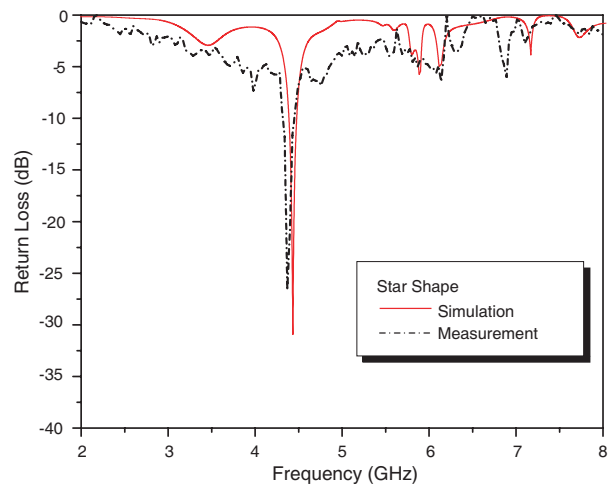
Figure 5: Comparison between measurement and simulated reflection coefficients for I shaped slot 2D-EBG.
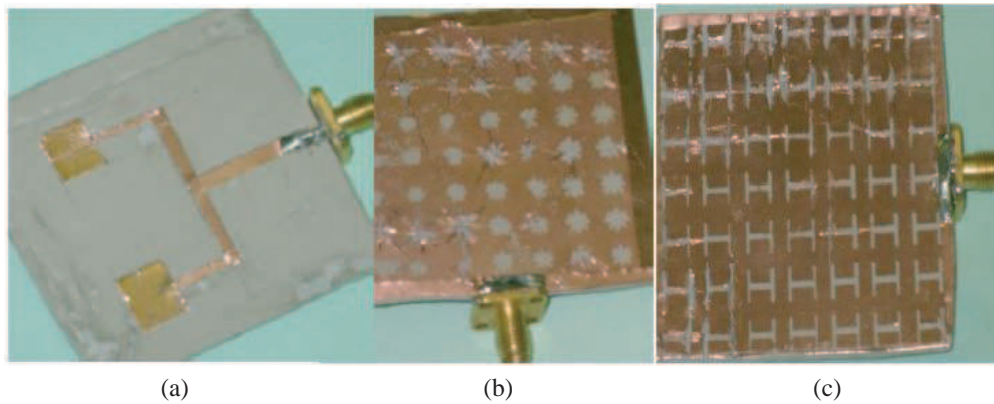
Figure 6: Photos of the fabricated antennas. (a) Radiator, (b) Star slot and (c) I slot.
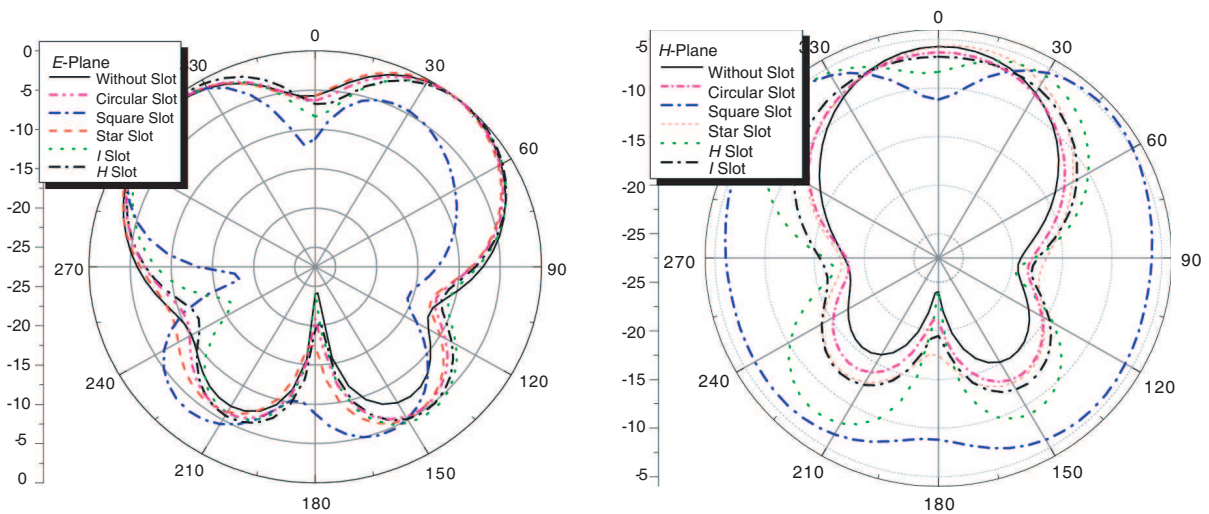
Figure 7: The simulated E-plane and H-plane radiation patterns for the five shapes of 2D-EBG.

5. CONCLUSION

In this paper, a two-element microstrip array antenna integrated with 2D-EBG on the ground plane has been investigated. Three new 2D-EBG shapes namely star-shape, Hshape and I-shape have been compared with conventional 2D-EBG shapes (square and circular). The 2D-EBG reduces the coupling between patches of the array and, hence, is useful in decreasing the maximum side-lobe level of antenna array without a change in the distance between the patches. Consequently, increase in array radiated power and gain have been achieved. The results demonstrated that the radiation properties of the antenna with 2D-EBG are improved compared to the antenna without 2D-EBG or with other conventional shapes as circular and square. The MPAA is fabricated easily and gain enhancement by 3 dBi in average is obtained. The array size is reduced by 15% than the original without 2D-EBG as well as from conventional shapes of 2D-EBG. Simulated results as well as measurements indicate that the novel design is quite effective for the harmonics suppression of microstrip patch antenna. It should be noted that the results obtained in this work can be extended to antenna array with larger number of elements.

REFERENCES

1. Gonzalo, R., P. De Maagt, and M. Sorolla, "Enhanced patch-antenna performance by suppressing surface waves using photonic-band-gap substrates," *IEEE Trans. Microwave Theory Tech.*, Vol. 47, 2131–2138, Nov. 1999.
2. Yu, A. and X. Zhang, "A novel method to improve the performance of microstrip antenna arrays using dumbbell EBG structure," *IEEE Antennas and Wireless Propagat. Lett.*, Vol. 2, 170–172, 2003.
3. Horii, Y. and M. Tsutsumi, "Harmonic control by photonic bandgap on microstrip patch antenna," *IEEE Microwave Guided Wave Lett.*, Vol. 9, 13–15, 1999.
4. Salehi, M., A. Motevasselian, A. Tavakoli, and T. Heidari, "Mutual coupling reduction of microstrip antennas using defected ground structure," *10th IEEE International Conference on Communication Systems (ICCS)*, 1–5, Oct. 2006.
5. Yang, L., Z. Feng, F. Chen, and M. Fan, "A novel compact EBG structure and its application in microstrip antenna arrays," *IEEE MTTS Digest*, 1635–1638, 2004.
6. Yang, F. and Y. Rahmate-Samii, "Applications of electromagnetic band gap (EBG) structures in microwave antenna designs," *Proc. 3rd Int. Conf. Microwave and Millimeter Wave Tech.*, 528–531, 2002.

Integrated Design of Multiple Antennas for WiFi/Bluetooth/GPS Mobile Communication

Dong Wang and Qinjiang Rao

Research in Motion Limited, Canada

Abstract— A novel dual-feed, integrated antenna for WiFi, Bluetooth and GPS applications in a portable device is described. The single antenna which has a compact size and high efficiency can be used for wireless handset applications instead of the three individual antennas in mobile handsets. The specific dual feed design allows the WiFi and Bluetooth antennas to work simultaneously. This design creates lower coupling which results in higher radiation efficiency and MIMO antenna application.

1. INTRODUCTION

The trend towards smaller mobile devices with increased functions (i.e., multipurpose handsets with multiple mobile bands including GSM, UMTS, GPS, Bluetooth and WiFi data connectivity) continuously heightens the challenges for antenna designers.

This integrated antenna design is a technique that utilizes a dual feed, single antenna to replace the three individual antennas in the mobile handset thus decreasing the occupied space. The need to reduce the coupling at the same frequency was resolved in this design.

This paper discusses compact geometry design, same frequency lower coupling performance, higher efficiency, and will also explore the GPS/WiFi/ Bluetooth applications in mobile devices.

Furthermore, there has been much interest in designing dual-feed low-coupling technique, which requires integrating three antennas into one and may also be used for MIMO antenna applications.

We focus on highly-efficient single antenna design for multiple functions in small mobile devices. We proceed in three steps, the first one being an integration of three individual antennas, then we present dual feed design to be able to run WiFi and Bluetooth simultaneously, and we resolve the coupling issue at the same frequency band.

2. ANTENNA OVERVIEW

This paper presents an antenna design for mobile phone applications such as a WiFi/Bluetooth/GPS antenna-as illustrated in Fig. 1. The antenna model consists of an IFA, a PIFA and a patch antenna elements which are dual-feed with SMA connectors. The design integrates these three elements and a dual feed to utilize single antenna instead of three individual antennas.

The dual feed structure allows WiFi and Bluetooth bands to operate simultaneously.
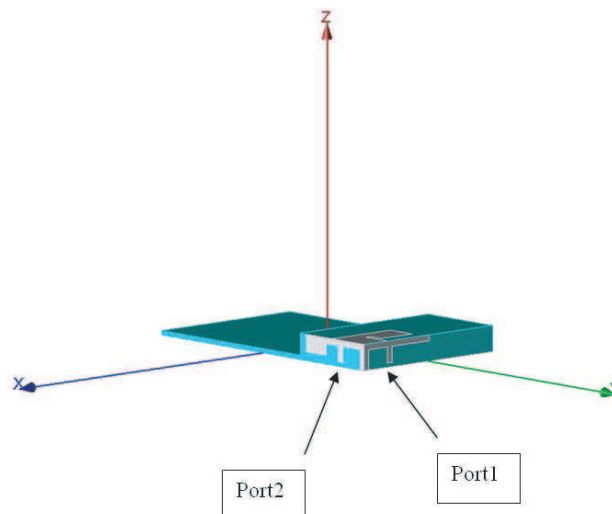
Figure 1: Proposed antenna configuration.
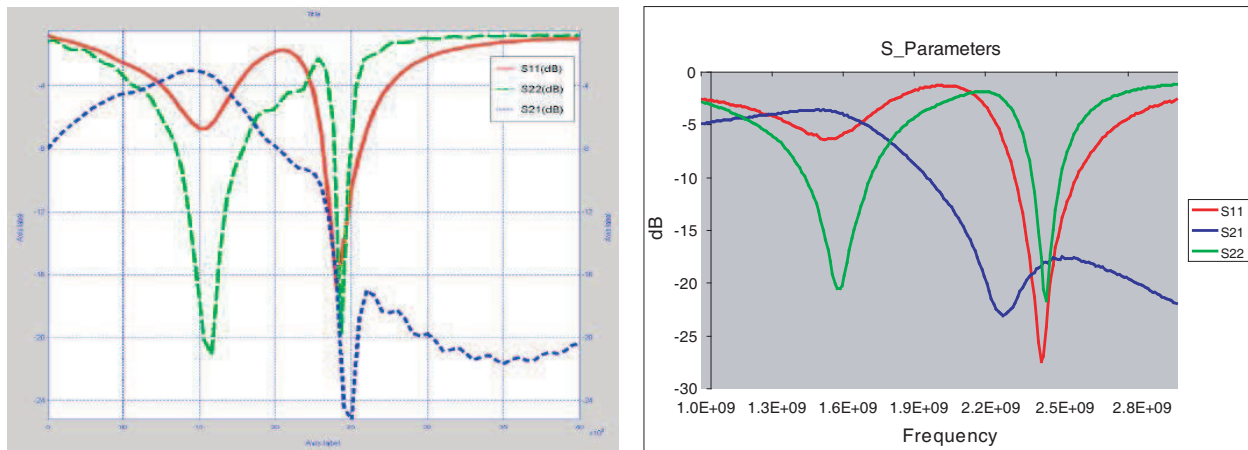
Figure 2: The calculated and measured S-parameters of the proposed antenna.
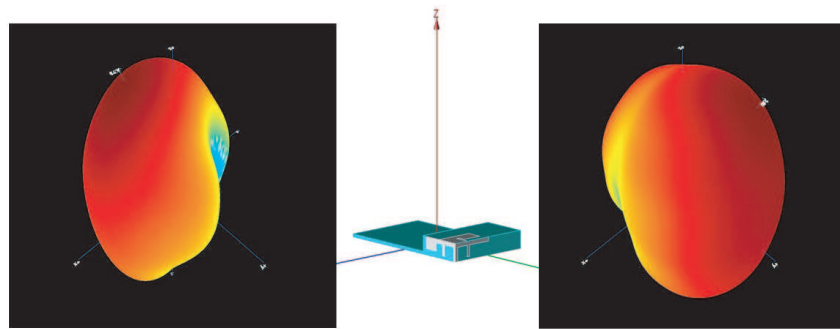
Figure 3: The measured radiation patterns of two ports at 2.45 GHz.

The design uses the GPS patch to increase the isolation. The isolation between the WiFi and Bluetooth bands can be improved by using GPS parts without any additional components.

Ideally isolation between the two feeds should be less than 15 dB, and the WiFi and Bluetooth antenna elements should have a $> 50\%$ efficiency.

3. DESIGN & SIMULATION

The model of the proposed antenna is shown in Fig. 1. The size of the proposed antenna has a small dimension of $20 \times 15 \times 8\,\text{mm}^3$ and is easy to place at the top left corner of the mobile phone.

The antenna feeds Port 1 and Port 2 are shown in Fig. 1 and are comprised of two small coaxial SMA connectors, both having an input impedance of 50 ohms.

Figure 2 shows the return loss for the design with two ports, both of which were lower than -10 dB. It is clearly observed this proposed antenna can be excited a dual-band resonant mode.

The upper GPS patch of the antenna is connected to the side of the IFAs. It is situated between the WiFi and Bluetooth antennas for increasing isolation between the WiFi and Bluetooth.

On the other hand, because the isolation between the two frequency bands is high, the WiFi and Bluetooth band characteristics are not much affected by each other. The mutual coupling between the two ports is calculated and measured at less than 15 dB at the WiFi band and Bluetooth bands.

A small area of copper was removed from the under side of the SMA connector around the feed to ensure electrical isolation.

The shorting pin of the copper strip is connected to the ground plane.

All simulations presented in this paper were calculated using the GEMS.

The proposed antenna is well resonated in the WiFi, Bluetooth and GPS bands, respectively.
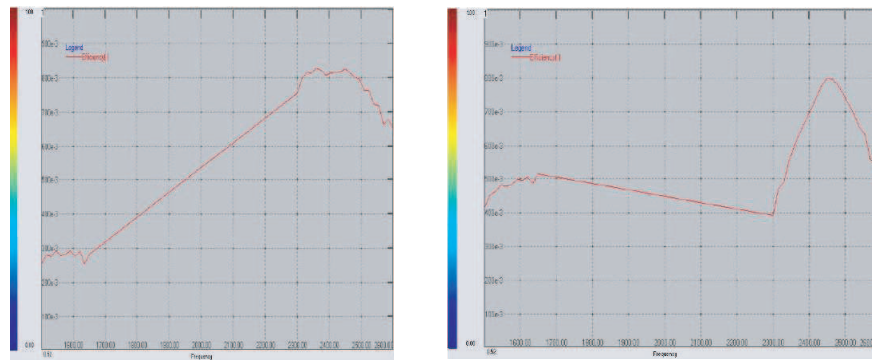
Figure 4: Measured total efficiency.

4. MEASUREMENTS & RESULTS

A prototype of the dual-feed integrated antenna was built for testing and the results compared to those predicted by simulations. S-parameters of the antenna were measured using an R&S Vector Network Analyzer.

Figure 2 shows the simulated and measured return loss for each port, whereby S_{11} is the return loss for Port 1, and S_{22} is the return loss for Port 2. The isolation between the two ports is shown as S_{21} in Fig. 2.

The bandwidth included dual-mode from 2.4 GHz to 2.5 GHz and 1.57542 GHz.

The results presented in Fig. 2 shows a close agreement between the simulated and measured S parameters.

Measured radiation patterns of Port 1 and Port 2 at 2.45 GHz are presented in Fig. 3 respectively, showing that the design produces pattern diversity.

Figure 4 gives measured total efficiencies over the WiFi, and Bluetooth bands. The total efficiency is the ratio of the power supplied to the antenna (via an RF cable) to the integrated power on a sphere surrounding it (the radiated power).

The measured efficiencies are found to be $> 70\%$ over the WiFi and Bluetooth bands, respectively. In this antenna structure, the antenna efficiency is determined by the return loss and coupling.

On the other hand, the radiation power can not go from one port to another port, which means the power loss is low thus the high efficiency design is achieved.

5. CONCLUSION

Recent research on integrated antenna for handset multiple applications is presented. The antenna design consists of a dual feed which permits the WiFi and Bluetooth to work simultaneously. The design incorporates a dual feed to utilize pattern diversity. The investigations in this paper show that realizing low coupling at the same frequency band on small terminals is relatively challenging. A low coupling technique has been demonstrated using simulation and prototype. The radiation pattern and efficiency results are shown. Future research will involve this antenna design within a handset environment and MIMO antenna applications.

ACKNOWLEDGMENT

REFERENCES

1. Geyi, W., Q. Rao, S. Ali, and D. Wang, "Handset antenna design: Practice and theory," *Progress In Electromagnetics Research*, PIER 80, 123–160, 2008.
2. Wang, D. and Q. Rao, "Patch loaded tri-monopole wideband antenna for mobile applications," *2009 IEEE International Conference on Ultra-wideband (ICUWB)*, 2009.
3. Rao, Q. and D. Wang, "Compact low coupling dual-antennas for MIMO applications in handheld devices," *2009 IEEE APS Conference*, 2009.
4. Rao, Q. and D. Wang, "Multiple input, multiple output antenna for handheld communication devices," *RIM IDF*, 34286.

5. Wang, D. and Q. Rao, "Dual-feed dual band antenna for WiFi, bluetooth and GPS applications in compact mobile device," *RIM IDF*, 36657.

6. Lindmark, B., "A dual polarized dual-band microstrip antenna for wireless communications," *IEEE Aerospace Conference Proceedings,* Vol. 3, 1998.

7. Serra, A. A., P. Nepa, G. Manara, G. Tribellini, and S. Cioci, "A wide-band dual-polarized stacked patch antenna," *IEEE Antennas and Wireless Propagation Letters*, Vol. 6, 2007.

8. Guo, Y.-X., K.-M. Luk, and K.-F. Lee, "Broadband dual polarization patch element for cellular-phone base stations," *IEEE Trans. Antennas & Propag.*, Vol. 50, No. 2, Feb. 2002.

9. GEMS Simulation Tool: www.2comu.com

Increasing Integration in Composite Patch Antenna Arrays for Dual-band and Dual-polarized Uses

Monika Hornik and Pawel Kabacik

Institute of Telecommunications, Teleinformatics and Acoustics, Wroclaw University of Technology
Wybrzeze Wyspianskiego 27, Wroclaw 50-370, Poland

Abstract— Weight significant lowering objective and dualpolarized operation, possible in more than two bands, have driven our studies on composite antennas in last three years. With ready-at-hand technology making use of several dielectric layers, we have focused research on antenna element shaping and on element dense packaging. Accomplishing high quality of polarization and enabling inter-element spacing up to a half wavelength, were other two main objectives in our studies. The results of these research are presented for antenna clusters operating with dual linear polarization at both 2.45 and 5.3 GHz.

1. INTRODUCTION

Presently advantages of operation with dual-linear polarized waveforms are becoming wider used, as availability of smaller and more productive signal processing modules widespread. Two other highly desired objectives are dualband operation and bandwidth broadening. Low weight of antennas and high scale of integration — understand in various terms — let to mention dense element clustering, arraying schemes, antenna and feed circuits packaging altogether — are among key advantages opening new areas of practical uses.

We have been carrying on studies on lightweight antenna elements for more than ten years [1–3]. With available technology making use of five layers of printed circuits and four dielectric substrate layers we could have thought on interesting element optimisations. However, to make element suitable for arraying with a spacing as short as a half wavelength in a presence of two sets of elements, we have to spent much efforts on antenna element shaping and making their dense packaging feasible. Other method for packaging together two arrays of elements is perforation of antenna elements [4]. For practical demonstration, we developed two antenna subarrays with separate array of elements for each frequency band.

Models are for operation in two bands centred at 2.45 and 5.3 GHz. Antenna structure strength, low weight, wide range of accepted environmental conditions and — last but not least good — electrical performance make this antennas suitable for much broader applications than typical wireless and mobile nodes. It must be admitted they might be too expensive for standard base station uses.

2. ANTENNA DESCRIPTION

Details of a composite panel has been developed over a two year of analysis. Presented in this paper antennas have the same layer arrangement and it is considered as optimum by the authors. To provide dual-linear operation a range of a dozen generic geometries of element were considered [5–7]. All elements in this paper utilizes circular shapes and element diameter are $\Phi_S = 51.4$ mm and $\Phi_C = 22.2$ mm, for 2.45 GHz and 5.3 GHz center frequency, respectively.

2.1. Layer Arrangement in Presented Antennas

Layer composition of the composite panel used in antenna models. Such panels make feasible lowering weight from 45 and 100 grams per $1\,\text{dcm}^2$. Desire to substantially improve optimisation of impedance element performance, calls for increase in number of layers in the composite panel. In the proposed concept, composite panels fulfil three major tasks: (i) microwave, (ii) structural and (iii) resistance to environment.

2.2. Model without C-band Element Rotation (s_c52)

Elements are fed with aperture coupled slots and make use of dual orthogonal slots to ensure high quality of polarization [8–10]. The least complicated of four antenna model discussed in this paper is shown in Figures 1 and 2.

2.3. Model with C-band Element Rotation (s_c52r)

Element rotation (Figure 3) has been applied too improve impedance and polarization performance.

Table 1: Layer structure in the presented antenna panel.

	Material	Thickness	ε_r	Function
00	copper	17.5 μm	-	markers
01	Rogers laminate	12 mil 0.305 mm	3.55	microwave substrate
02	copper	17.5 μm	-	S-band patches
03	glue	0.15 mm	2.75	bonding
04	Rohacell foam	2.6 mm	1.01	patch substrate
05	glue	0.15 mm	2.75	bonding
06	Rogers laminate	12 mil 0.305 mm	3.55	microwave substrate
07	copper	17.5 μm	-	C-band patches
08	glue	0.15 mm	2.75	bonding
09	Rohacell foam	4.4 mm	1.01	patch substrate
10	glue	0.15 mm	2.75	bonding
11	copper	17.5 μm	-	antenna ground
12	Rogers laminate	12 mil 0.305 mm	3.55	microwave substsrate
13	copper	17.5 μm	-	C-band feed lines
14	bonding film	38 μm	2.38	bonding
15	Rogers laminate	12 mil 0.305 mm	3.55	microwave substrate
16	copper	17.5 μm	-	S-band feed lines
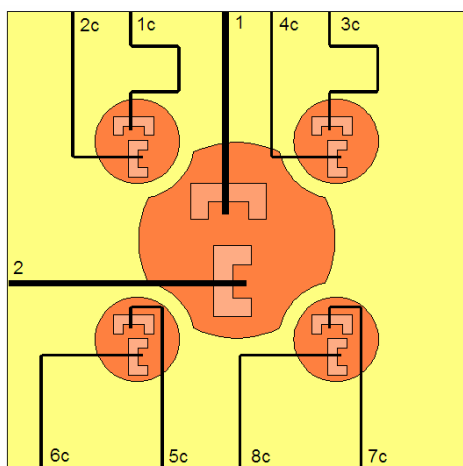
Figure 1: Geometry of patches and a feed in five element cluster s_c52.
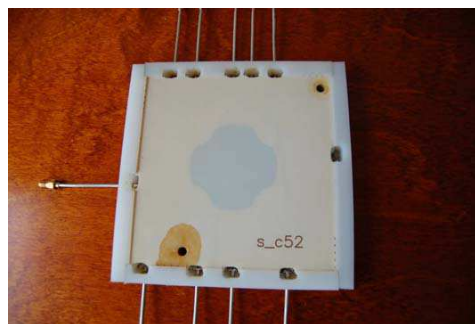
Figure 2: Top side of the s_c52 antenna model.

2.4. Model without Element Rotation (s96_c44)

The geometry is presented in Figure 4. Please note, that the same orientation of elements provide different couplings between them and it should be expected impedance and radiation properties of elements vary within the module.

2.5. Model with S- and C-band Element Rotation (s96_c44r)

Antenna subarray presented in Figures 5 and 6 make use of 0°, 90°, 180° and 270° rotation between element feed slots, to compensate some of current flows and to uniform couplings between element components.

Elements presented in Figures 1 through 7, are optimised by adopting substrate thickness different for S- and C-band patches, as well as different laminate thickness for feed lines. After analysis allowing for quasi-optimal arrangement of layers in the panel structure, two issues have attracted
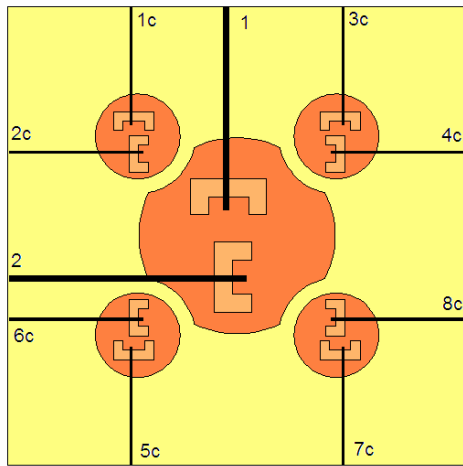
Figure 3: Geometry of five element antenna cluster with rotated orientation of aperture coupling slots between its four C-band elements.
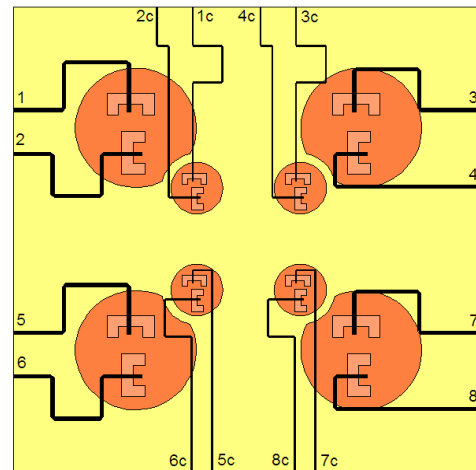
Figure 4: Geometry of eight element s96_c44 antenna module, that geometry allows for the module incorporation into antenna arrays where square grids of S- and C-band patches share one aperture.
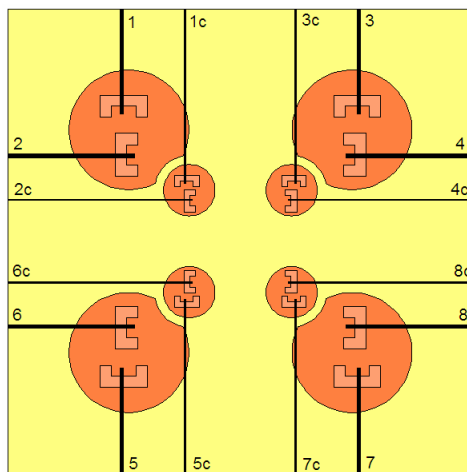
Figure 5: Geometry of eight element s96_c44r antenna module making use of 0°, 90°, 180° and 270° rotation between element feed slots.
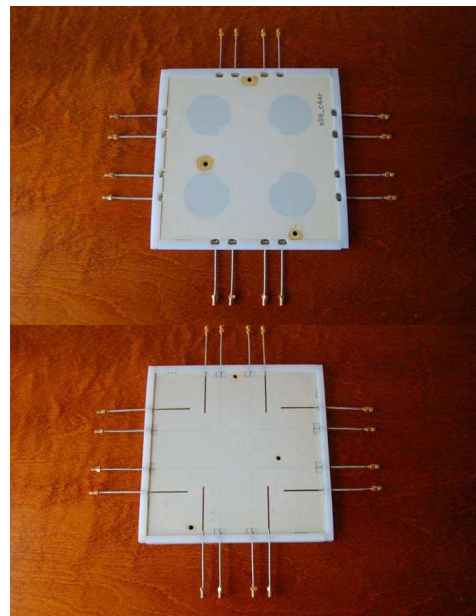
Figure 6: Patch and feed side of the s96_c44r antenna model.

major attention:

- modification of circular element area to allow for closer element spacing and at the end to open a possibility to array two arrays of patches operating at two bands,
- finding useful rotation scheme of patches to mitigate undesired effects observed with subarray scheme element making the element to be oriented all the same way.

To generate circular polarization with presented four antenna models, use of wideband directional couplers made with thin dielectrics is recommended [8, 10–12].

3. THEORETICAL AND EXPERIMENTAL RESULTS

We have used numerical simulations to design presented antenna subarrays. In a course of these studies we made use of experiences gained over several projects on various lightweight antennas,

such as [8, 9]. Measurements of antenna input impedances were carried out with ZVA50 four port and HP 8752B vector network analysers.

3.1. Numerical Simulations

Figures 7 and 8 presents examples of calculated impedance match for s96_c44r antenna. Without element rotation, these characteristics remarkable vary between ports.

3.2. Measured Return Loss Characteristics

Three manufactured antenna models were measured at their all ports and two examples of return loss plots measured at particular ports are in Figures 9 and 10. C-band patches give much more reasons to investigate some discrepancies between calculated and measured impedance character-istics. Analysing measured results — similarly as for data in plot in Figure 10 — we witness around 150 MHz downward shift in frequency characteristics. Also impedance match is worse than calculated or measured at S-band ports.

3.3. Radiation Patterns

Radiation pattern were computed with numerical methods and Suppression of cross-polar field components observed in element clusters with element rotation is illustrated in Figure 11. Mea-surements are to be completed with presently moved to an anechoic chamber our in-house developed antenna near-field measuring facility by June 2010.
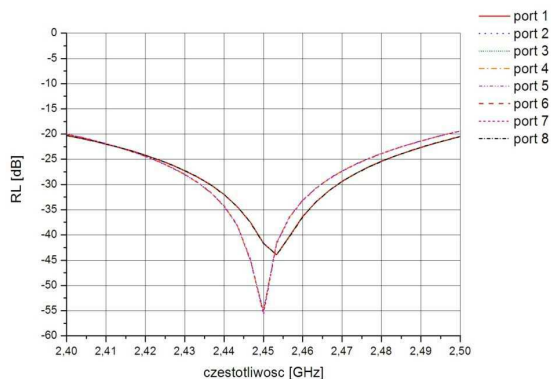
Figure 7: Calculated return loss characteristics for eight ports at four S-band elements of the s96_c44r antenna module shown in Figures 5 and 6.
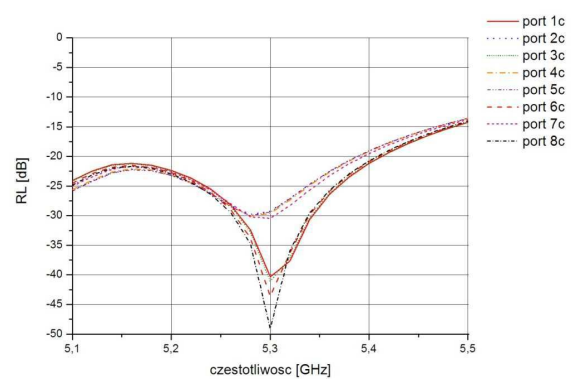
Figure 8: Calculated return loss characteristics for eight ports at four C-band elements of the s96_c44r antenna module shown in Figures 5 and 6.
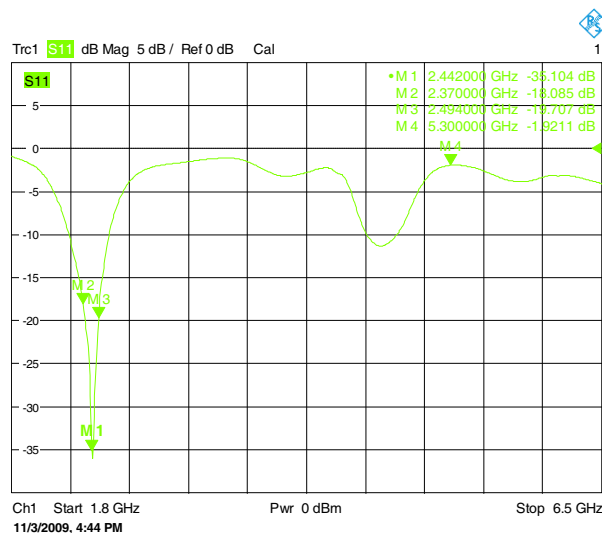
Figure 9: Measured return loss characteristic at one of S-band ports in the s96_c44r antenna module.
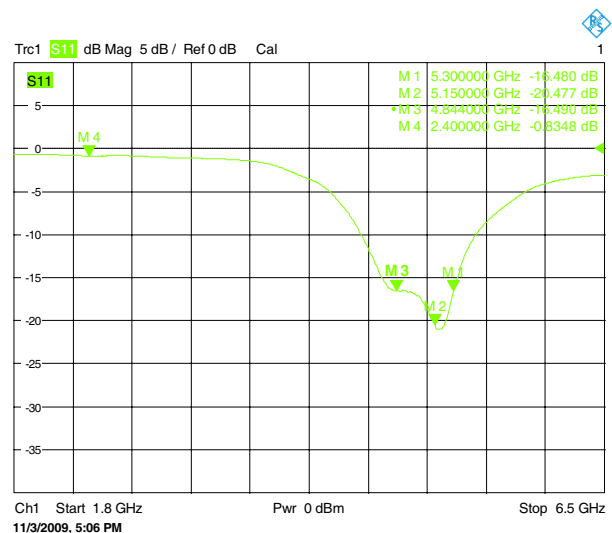
Figure 10: Measured return loss characteristic at one of C-band ports in the s96_c44r antenna module.
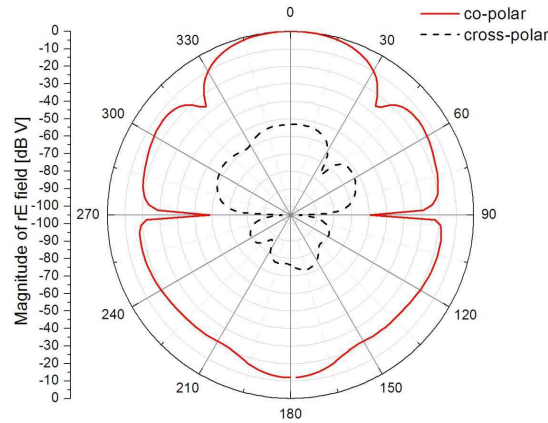
Figure 11: Calculated radiation pattern for co- and cross-polar field components, for eight element s96_c44r antenna cluster making use of rotation in S- and C-band elements.

4. CONCLUSIONS

The presented research has led us to development of antenna models operating with dual-polarization at two frequency bands. We have modified circular shape of elements to pack more densely patches sharing the same area, but operating at two bands. The concept is suited for dualband operation when there is around 1 : 2 ratio between operational frequencies. Owing to use of composite panels te antennas meet design objectives in other than electromagnetic areas: low weight, outstanding robustness to harsh mechanical and environmental conditions. The concept can be used in the whole microwave range.

It is worthwhile to say there are many emerging areas of applications where presented antenna may find applications: variety of vehicles and train platform, vessels and buoys, high engineering structures carrying wireless data nodes.

ACKNOWLEDGMENT

REFERENCES

1. Kabacik, P., G. Jaworski, M. Kamaszuk, P. Hornik, and T. Maleszka, "Lightweight conformal dual band antena for spaceborne applications," *Proc. of the European Conference on Antennas and Propagation, EuCAP 2006*, Nice, 2006.

2. Kamaszuk, M., P. Hornik, D. Guzda, and P. Kabacik, "Optimizing circular polarization within a beam of patch antenna elements," *Journal of Telecommunications and Information Technology*, No. 1, 2007.

3. Hornik, M. and P. Kabacik, "Investigations into lightweight patch element for use in dual- or multi-polarized antenna arrays," *2007 IEEE Antennas and Propagation Society International Symposium*, Honolulu, 2007.

4. Yang, X. H. and L. Shafai, "Characteristics of aperture coupled microstrip antennas with various radiating patches and coupling apertures," *IEEE Transactions on Antennas Propagation*, Vol. 43, 72–78, 1995.

5. Kabacik, P., G. Jaworski, and M. Hornik, "Small spaceborne microstrip antennas," *29th ESA Antenna Workshop on Multiple Beam and Reconfigurable Antennas, ESTEC*, 2007.

6. Kabacik, P., G. Jaworski, M. Hornik, and T. Maleszka, "Lightweight L- and S-band antenna fed by three-strip directional couplers," *2007 IEEE Antennas and Propagation Society International Symposium*, Honolulu, 2007.

7. Kamaszuk, M., P. Hornik, D. Guzda, and P. Kabacik, "Optimizing circular polarization within a beam of patch antenna elements," *Journal of Telecomms and Information Technology*, No. 1, 2007.

8. Kabacik, P., G. Jaworski, M. Hornik, T. Maleszka, P. Gorski, and D. Wydymus, "Dual-band circularly polarized spaceborne antenna made with multilayer composite lightweight panel," *Proceedings Polish Microwave Week MIKON 2008*, Wroclaw, 2008.

9. ARISS — Amateur Radio on International Space Station. Available: www.rac.ca/ariss/ and www.ariss-eu.org.

10. Kabacik, P., G. Jaworski, M. Hornik, T. Maleszka, P. Gorski, and D. Wydymus, "Columbus/ISS CP dual-band, slim antennas made with a composite multi-layer panel," *30th ESA Antenna Workshop, ESTEC*, Noordwijk, 2008.

11. Sachse, K. and A. Sawicki, "Quasi-ideal multilayer two- and three-strip directional couplers for monolithic and hybrid MIC," *IEEE Trans. on MTT*, Vol. 47, Sept. 1999.

12. Bona, M., L. Manholm, J. P. Starski, and B. Svensson, "Low-loss compact butler matrix for a microstrip antenna," *IEEE Trans. on MTT*, Vol. 50, 2069–2075, Sept. 2002.

Novel MEMS Dipole/Monopole Antenna for Wireless Systems Operating at 77 GHz

E. A. Soliman, S. Sedky, M. O. Sallam, S. Hassan, O. El Katteb,
A. K. S. Abdel Aziz, and M. Refaat

The American University in Cairo, AUC Avenue, P. O. Box 74, New Cairo 11835, Egypt

Abstract— In this paper, we present a novel MEMS antenna designed for operation at 77 GHz. The antenna consists of two right-angle metal arms which are supported by two vertical silicon walls. These walls are fabricated using bulk micromachining through Deep Reactive Ion Etching (DRIE) process. The two right-angle arms are fed via a microstrip ring coupler which has two input ports. A new process flow is introduced in this paper, which allows the realization of the proposed antenna on a single silicon wafer. The antenna is analyzed and optimized thoroughly using Ansoft/HFSS. The results show that based on the selection of port of excitation, the proposed antenna can radiate either dipole or monopole patterns. In the dipole (monopole) mode, the antenna has impedance bandwidth of 4.3% (4.2%), gain of 8.9 dBi (5.5 dBi), radiation efficiency of 94% (95%).

1. INTRODUCTION

Micromachining technology is very attractive for integrated antennas as it offers efficient packaging, high radiation efficiency, wide impedance bandwidth, and less mutual coupling between antenna elements. These advantages are more difficult to be achieved using the conventional planar technology especially at high frequencies. Research carried out on MEMS antennas can be classified into two main categories. The first category features a flat antenna, such as patch, realized on a thin membrane surrounded by air. The membrane can be fabricated via either bulk [1] or surface [2] micromachining technology. This results in reducing the effective dielectric constant of the medium around the antenna and consequently increases the bandwidth and radiation efficiency. The second category features a 3D antenna, such as horn or waveguide, realized by etching grooves in a number of silicon wafers via bulk micromachining [3]. The walls of these grooves are covered with metal. Each groove represents part of the desired 3D structure. The wafers are bonded together to form the complete 3D antenna. In this paper, a novel MEMS antenna design is presented. The proposed antenna is 3D in shape and it can be fabricated on a single silicon wafer without any need for wafer bonding or hybrid integration. The proposed antenna is capable of operating as either dipole or monopole based on the selection of the port of excitation.

2. ANTENNA STRUCTURE AND FABRICATION TECHNOLOGY

The proposed MEMS antenna is shown in Fig. 1. It has two vertical silicon walls that can be fabricated using bulk micromachining through 0.675 mm thick high resistivity silicon wafer with dielectric constant of 11.9 and conductivity of 0.05 S/m. The width, length, and depth of each wall are 70 μm, 953 μm, and 475 μm, respectively. The last two dimensions correspond to $\lambda_g/2$ and $\lambda_g/4$ at the operating frequency of 77 GHz. The thickness of the remaining silicon substrate is 200 μm. Two horizontal metal arms are covering the top surfaces of the walls. Two vertical pillars with square cross section of 55 μm × 55 μm are drilled through the entire wafer. The inner surfaces of these pillars are covered with vertical metal arms, as shown in Fig. 1. It can be seen in this figure that there are gaps between the vertical and horizontal arms. The top surface of the substrate is covered with slotted ground metal plane, through which the silicon walls are going up. This plane serves as a reflector that increases the directivity of the antenna. Moreover, it isolates between the antenna and the bulk silicon substrate, which reduces the surface wave losses and increases the radiation efficiency. All metallic parts of this structure are made of copper with thickness of 3 μm. From the bottom side of the substrate, the vertical arms are connected to the two output ports of a ring coupler made of microstrip lines. Two feeding microstrip lines are connected to the input ports of the ring coupler. The width of each line is 200 μm which corresponds to 50 Ω at 77 GHz. The ring is made of a microstrip line whose width and characteristic impedance are 88 μm and 70.7 Ω, respectively. The radius of the ring is 333 μm, and its circumference equals 2.092 mm, which corresponds to $1.5\lambda_g$ at the frequency of operation.
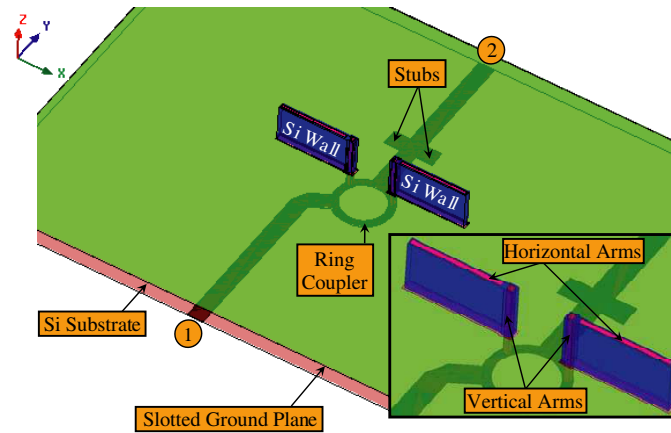
Figure 1: Structure of the new MEMS dipole/monopole antenna.

silicon (■), oxide (■), copper (■)
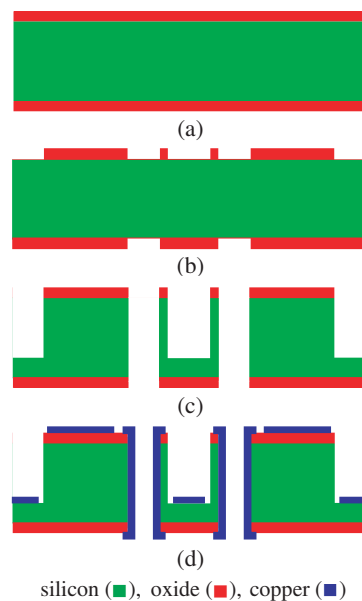
Figure 2: Proposed process flow.
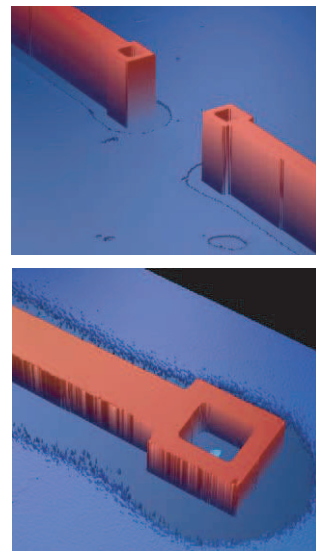
Figure 3: Photographs of the fabricated walls and pillars.

In order to fabricate the proposed structure, the process flow outlined in Fig. 2 is used. In this figure, cross-sections through the antenna arms are presented. As shown in Fig. 2(a), we start by high resistivity silicon substrate with resistivity of $2,000\,\Omega{\cdot}$cm and thickness of 0.675 mm. The substrate is coated with $4\,\mu$m SiO_2 on both sides. The first step in the process flow is to selectively etch the SiO_2 from both sides to define the openings of the pillars and from the top side to define the walls, as shown in Fig. 2(b). After this, we etch from the top side the Si volume that is not protected by SiO_2 with a depth of $475\,\mu$m. Also, the unprotected pillars' openings are etched from the bottom sides with a depth of $200\,\mu$m. The result of this step is the realization of the pillars and walls, as shown in Fig. 2(c). The last step is to cover with Cu of $3\,\mu$m thickness the following: (1) the top sides of the walls to create the horizontal arms, (2) the inner surfaces of the pillars to create the vertical arms of the antenna, (3) the top side of the substrate around the bases of the walls to create the slotted ground plane, and (4) selectively the bottom side of the substrate to create the ring coupler feeding circuit. This step is shown in Fig. 2(d). Fig. 3 shows photographs of the fabricated walls through which pillars are drilled.

3. DIPOLE MODE OF OPERATION

If the excitation signal is applied to port 1 of the ring coupler, see Fig. 1, the antenna arms will be excited with the same amount of power, but with 180° phase shift. Almost no power will be transferred to port 2. The currents on the vertical arms will be opposite to each other, while on the horizontal arms the currents will be in the same direction. Fig. 4 shows the surface current

distribution on the antenna arms due to excitation from port 1, as obtained using Ansoft/HFSS simulator at 77 GHz. In this mode of operation, the vertical currents cancel out, while the horizontal arms act as an array of two $\lambda_g/2$ dipoles. These dipoles are located a distance $\lambda_g/4$ on top of the slotted ground plane covering the top face of the silicon substrate. By applying the image method, it is possible to replace this ground plane with another two horizontal dipoles out-of-phase with the original ones and located $\lambda_g/2$ away from them. Hence, the originals dipoles and their images add to each other constructively in the broadside direction and destructively in the end-fire direction. The presence of gaps between the vertical and horizontal arms imposes current nulls around the gaps. This defines standing waves on the horizontal arms, where each wave is limited by two nulls separated by a distance of $\lambda_g/2$. The S-parameters of the proposed antenna are plotted versus frequency in Fig. 5. In this mode, the antenna is excited via port 1. The impedance bandwidth, for which $S_{11} < -10$ dB, is 4.3%. The coupling to other port, i.e., S_{21}, is less than -16 dB over the working frequency band, which indicates good isolation between the two ports. The 3D radiation pattern of this mode at the resonance frequency of 77 GHz is drawn in Fig. 6. It can be seen that the antenna is radiating mainly from the top side, while the bottom side radiation is relatively weak and results from diffraction at the truncated edges of the antenna structure. The calculated gain of the antenna is 8.9 dBi and the radiation efficiency is about 94%. Such high radiation efficiency at 77 GHz can't be achieved without the use of MEMS technology.

4. MONOPOLE MODE OF OPERATION

The excitation of this mode is via port 2. In this case, the ring coupler delivers half of the input power to each antenna side with the same phase. A negligible amount of power can couple to port 1. The surface current distribution of the monopole mode on the antenna arms at 77 GHz is plotted in Fig. 7. It can be seen that the horizontal currents are opposite to each other, which results in relatively weak radiation from them. On the other hand, the vertical currents are in the same direction. In this mode of operation, the image method should be applied twice. First, we keep the $\lambda_g/4$ parts of the vertical arms that are located on top of the ground plane, while we replace the ground with in-phase images of these parts. This results in two $\lambda_g/2$ vertical dipoles
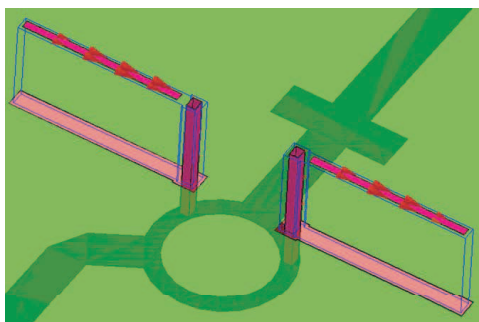
Figure 4: Surface current distribution of the dipole mode.
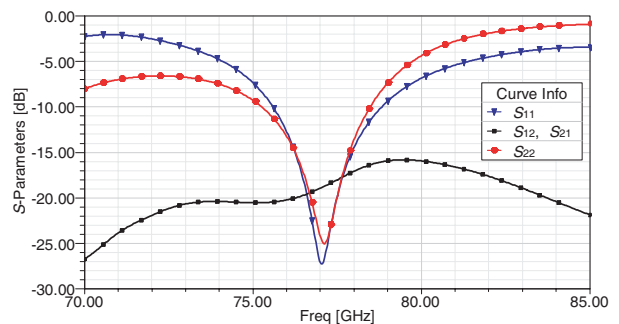
Figure 5: S-parameters of the antenna versus frequency.
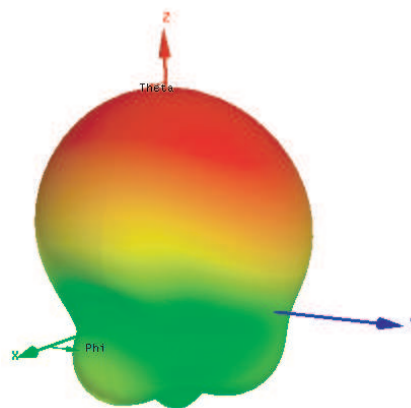
Figure 6: Radiation patterns of the dipole mode.
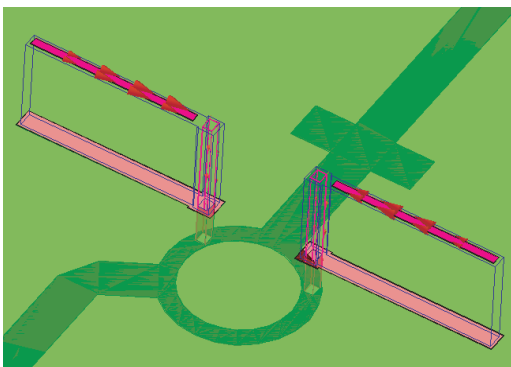
Figure 7: Surface current distribution of the monopole mode.
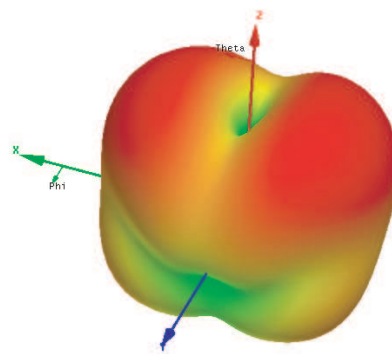
Figure 8: Radiation patterns of the monopole mode.

that radiates from the top side. Second, the $\lambda_g/8$ parts of the vertical arms that are located below the ground plane are kept, and the ground is replaced by their images. This is equivalent to two $\lambda_g/4$ vertical dipoles embedded into silicon and radiating from the bottom side. The top side radiation is more significant than that of the bottom side due to the difference in length of the radiating elements in both cases. As in the dipole mode, the disconnection of the vertical and horizontal arms imposes current nulls at the points of disconnection. This ensures standing wave patterns terminated by these currents nulls. To enhance the matching between the antenna input impedance of the monopole mode and the feeding line, two open circuit stubs are connected in parallel with the microstrip line of port 2, as shown in Fig. 1. The spacing between the inner edges of the stubs and the ring coupler is $560\,\mu$m. The free length of each stub is $200\,\mu$m. As shown in Fig. 5, the impedance bandwidth of this mode, along which S_{22} is less than $-10\,$dB, is 4.2%. Again, the coupling between the two ports is very weak as indicated by $S_{12} = S_{21} < -16\,$dB over the working bandwidth. The 3D radiation pattern at 77 GHz of the antenna in the monopole mode of operation is shown in Fig. 8. A radiation null at the broadside direction can be noticed. On the other hand, this pattern offers better coverage around the end-fire direction than that offered by the dipole mode. The gain and radiation efficiencies of the antenna in this mode are 5.5 dBi and 95%, respectively.

5. CONCLUSION

A novel MEMS antenna is introduced in this paper. It can be micromachined using a new process flow. The proposed antenna is tuned for operation at 77 GHz. It has been demonstrated that if the antenna is excited from the first port, it behaves like an array of two dipoles. The same antenna radiates like a monopole, if it is excited from the second port. The presented results show that the proposed antenna enjoys good characteristics, such as reasonable impedance bandwidth, good isolation between the feeding ports, and very high radiation efficiency for both modes of operation. In the dipole mode, the antenna is capable of transmitting/receiving waves mainly in the broadside direction, while it can't transmit/receive efficiently in the end-fire direction. In the monopole mode, the opposite is true. Consequently, the proposed antenna provides very good coverage of the entire half-space via switching between the two modes of operation.

REFERENCES

1. Ojefors, H., H. Kratz, K. Grenier, R. Plana, and A. Rydberg, "Micromachined loop antennas on low resistivity silicon substrates," *IEEE Trans. Antennas Propagat.*, Vol. 54, No. 12, 3593–3601, 2006.
2. Pan, B., et al., "Analysis and characterization of a high-performance Ka-band surface micromachined elevated patch antenna," *IEEE Antennas and Wireless Propogat. Lett.*, Vol. 5, 511–514, 2006.
3. Shenouda, B. A., L. W. Pearson, and J. E. Harris, "Etched-silicon micromachined W-band waveguides and horn antennas," *IEEE Trans. Microwave Theory Tech.*, Vol. 49, No. 4, 724–727, 2001.

Fast Electromagnetic Modeling of 3D Interconnects on Chip-package-board

Boping Wu[1], Xin Chang[1], Leung Tsang[1], and Tingting Mo[2]

[1]Department of Electrical Engineering, University of Washington in Seattle, United States
[2]School of Microelectronics, Shanghai Jiao Tong University, China

Abstract— The goal of this paper is twofold: to give a brief review of the latest research progress on electromagnetic modeling of vertical interconnects by using Foldy-Lax multiple scattering technique, to introduce a fast full-wave interconnect simulator, namely Foldy-Lax Via Tool, integrating all the extensions that recently have been made available. The kernel part of this novel approach is a mostly analytic algorithm which can significantly reduce the requirement of computational resources, making it suitable for the signal integrity analysis of a large number of vias and various via structures. We demonstrate this approach and the tool by simulating 64 vias including 18 pairs of differential-signaling vias and 18 ground vias in 8-layer board with layered and lossy dielectrics. The numerical results of signal attenuation and crosstalk are within 5% difference of accuracy up to 20 GHz compared with Ansoft HFSS. The CPU time of this tool is about three orders of magnitude faster than that of the HFSS.

1. INTRODUCTION

High speed vertical interconnects are among the key components for up-to-date 3D design and integration on chip-package-board [1]. With the ever-increasing clock rate, massively-coupled multiple vias, such as BGA, LGA, PTH, microvia and TSV, behave like efficient radiators, thereby introducing significant electromagnetic interference and signal integrity issues. The segmented via analysis with local parametric optimization is important before going into further integration. However, simple approximations, such as physical and lumped models, are inaccurate due to their incapability of including all the couplings among multiple vias. On the other hand, the network analyzer has difficulties on hardware characterization of the complete network with many ports.

Since 2001, we have used a full wave and mostly analytic method, based on the Foldy-Lax equations for multiple scattering technique, to model the randomly-positioned vias in high speed interconnect circuits [2–5]. In this paper, we give a brief description of the kernel algorithm. Then we review some important extensions. A recently developed 3D interconnect simulator is introduced and demonstrated. Comparisons are made between commercial software and hardware measurements [6].

2. FOLDY-LAX EQUATION FOR MULTIPLE SCATTERING TECHNIQUE

Via cylinders are modeled as conducting cylindrical scatterers between two parallel plates (Figure 1). In order to capture the multiple scattering among the vias (dashed arrows in Figure 1), we model the cylindrical scatterers using a cylindrical wave expansion of dyadic Green's functions G in terms of waveguide modal solutions. Based upon the magnetic Green's functions, we excite this parallel waveguide structure using a voltage source at the port, which is equivalent to a magnetic current ring source $\mathbf{M_s}$ at the antipad (solid circular arrows in Figure 1). The surface currents $\mathbf{I}$ on the cylinders (white arrows in Figure 1) are then calculated from the magnetic field $\mathbf{H}$.

$$\bar{H} = -j\omega\varepsilon \iint dx'dy' \bar{\bar{G}}(\bar{r}, \bar{r}') \cdot \bar{M}_s(\bar{r}') \tag{1}$$

The final excitation magnetic field on cylinder p is,

$$\bar{H}_{ex}^{(p)} = \sum_{m,l} w_{lm}^{TM(p)} Rg\bar{H}_m^{TM}(k_{\rho l}, k_{zl}, \bar{\rho} - \bar{\rho}_p, z \pm d/2) \tag{2}$$

where $w_{lm}^{TM(p)}$ are the exciting field coefficients to be solved by Foldy-Lax multiple scattering equations.

$$w_{ln}^{TM(q)} = a_{ln}^{TM(q)} + \sum_{\substack{p=1 \\ p \neq q}}^{N} \sum_{m=-\infty}^{\infty} H_{n-m}^{(2)}(k_{\rho l}|\bar{\rho}_p - \bar{\rho}_q|)e^{j(n-m)\phi_{\bar{\rho}_p\bar{\rho}_q}} T_m^{TM} w_{lm}^{TM(p)} \tag{3}$$

Figure 1: Multiple vias between two horizontal power/ground plates.
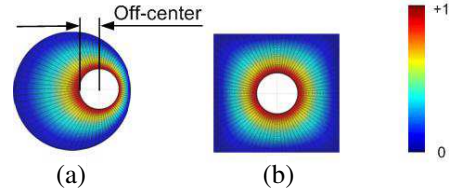
Figure 2: Potential distribution for apertures of (a) off-center via drilling in circular antipad, and (b) concentric via in squared antipad.

The Foldy-Lax multiple scattering equations state that the final exciting field of cylinder q is equal to the incident field plus the scattering fields from all other cylinders. Finally, we get the current on the pth cylinder using solved $w_{lm}^{TM(p)}$.

$$I^{(p)} = \sum_l \frac{4(-1)^l}{\eta H_0^{(2)}(k_{\rho l}a)} w_{l0}^{TM(p)} \tag{4}$$

For multilayered problems, we can get the cascaded transmission ($ABCD$) matrix by multiplying the transmission matrices of each layer [4]. This cascading method may miss some cross-layer couplings when vias are positioned closely or the antipads are shared in the middle plane. To analyze cases where there are ground vias around signal vias, the $\mathbf{Y}$ matrix corresponding to the signal vias is extracted from the entire $\mathbf{Y}$ matrix. Using this method, we do not consider any specific path for the return current. Since the ground/power plane is very large, the displacement currents between the parallel planes become dominant and are distributed all over the planes.

For vias placed closely to others, we need to include the higher-order parallel waveguide modes, $l > 0$, in order to ensure the accuracy. In general, when pitch, via center-to-center distance, is smaller than the length of via, it is advised to add the solutions of higher-order modes. The suggested value for $l_{\max}$ is given by,

$$l_{\max} = \text{round}\left[\frac{6d}{(\rho - 2a)\pi}\right] \tag{5}$$

where d is the via length and ρ is pitch. After considering the higher-order parallel waveguide modes, the crosstalk at the near end of via-pair begins to defer from the crosstalk at the far end. The near-end crosstalk is usually stronger than the far-end crosstalk. To improve the accuracy of the insertion loss, it is advised to add the self-via correction term with $L_{\max}$ for the diagonal $\mathbf{Y}$ matrix.

$$L_{\max} = \text{round}\left[\frac{6d}{a\pi}\right] \tag{6}$$

3. MODELING ARBITRARY SHAPE OF PAD AND ANTIPAD

For modeling via with arbitrary shape of pad and antipad, the finite difference method (FDM) is applied to solve the potential distribution and to numerically calculate the magnetic frill current source $\bar{M}_s$. The general expression of incident field coefficient $a_{ln}^{TM(q)}$ and the magnetic modal solutions of the parallel waveguide $\bar{m}_{-n}$ are given in paper [7]. For a typical concentric via inside the circular antipad, $\bar{M}_s$ has a closed-form expression. But for the arbitrary shape of pad and antipad, $\bar{M}_s$ can only be expressed numerically. Then $a_{ln}^{TM(q)}$ is calculated using a numerical 2D integration.

$$a_{ln}^{TM(q)} = \frac{\eta j\omega\varepsilon}{2d} \frac{(-1)^l}{k_{\rho l}^2} f_l \iint d\bar{\rho}' k_{\rho l} H_0^{(2)'}(k_{\rho l}|\bar{\rho}' - \bar{\rho}_q|)\bar{\bar{M}}_s(\bar{\rho}') \tag{7}$$

We use only 0th order cylindrical harmonic for calculating the incident field coefficient, which means $n = 0$ and $\bar{m}_{-n}$ does not have the $\hat{\rho}_{\bar{\rho}'\bar{\rho}_q}$ direction component. That is why in (7), $\bar{\bar{M}}_s(\bar{\rho}')$ has only the $\hat{\phi}_{\bar{\rho}'\bar{\rho}_q}$ direction frill component. The numerical technique of band matrix iterative method can be used in Matlab coding for efficient and accurate calculation [8]. For the incident field onto other

vias, $j \neq q$, we can numerically calculate the field coefficients as well.

$$a_{ln}^{TM(q)} = \frac{\eta j\omega\varepsilon}{2d} \frac{(-1)^{n+l}}{k_{\rho l}^2} f_l H_n^{(2)}(k_{\rho l}|\bar{\rho}_j - \bar{\rho}_q|)e^{jn\phi_{\bar{\rho}_j\bar{\rho}_q}} \iint d\bar{\rho}' k_{\rho l} J_1(k_{\rho l}|\bar{\rho}' - \bar{\rho}_j|)\bar{\bar{M}}_s(\bar{\rho}') \qquad (8)$$

This FDM based numerical technique can be adopted to treat any arbitrary shape of pad and antipad at the via-end (Figure 2).

4. MODELING DIFFERENTIAL VIA-PAIR IN SHARED ANTIPAD

For differential signaling scheme, which provides good immunity to the environment noise, via-pair is usually drilled in shared antipad [9]. We can use FDM to numerically calculate the equivalent magnetic current source by putting positive unit voltage on one pad and negative on the other (Figure 3(a)).

The accuracy and stability of the finite different solution is carefully controlled by optimizing the meshing scheme. As the shared antipad becomes large or is in irregular shape, the artificial boundaries created by the meshing scheme become impractical for describing the whole domain of the real object (Figure 3(b)). This is mainly caused by the cylindrical coordinate system formerly adopted in the Foldy-Lax scattering techniques. We have to generate more intervals on θ direction than on ρ direction, enforcing $\rho\Delta\theta$ close to $\Delta\rho$, in order to maintain a normal shape for the meshing element on every corner. Using finer meshes, by reducing the meshing size, leads to the decrease of the discretization error on the physical side. But this refinement solution may create some round-off errors in numerical calculations. We reach a point where the minimum total error occurs for a particular algorithm on a specific structure (Figure 3(c)).
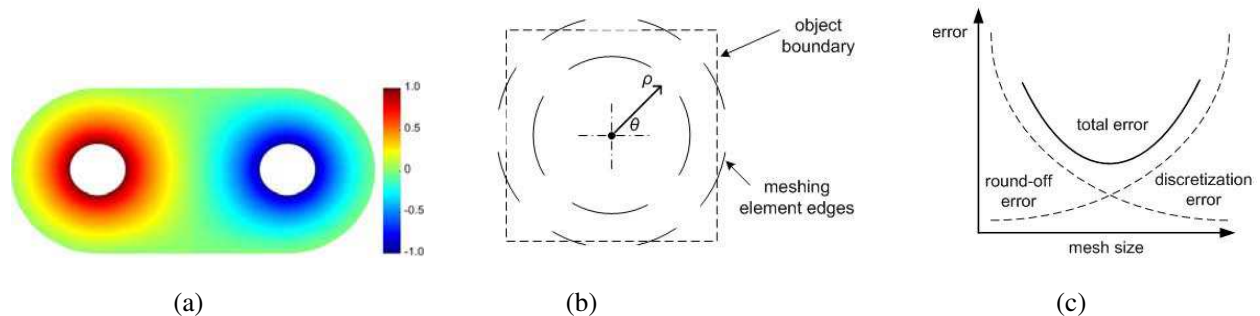
Figure 3: (a) Port potential distribution for via-pair in shared antipad, (b) solution region with lattice truncation, (c) error as a function of the mesh size.
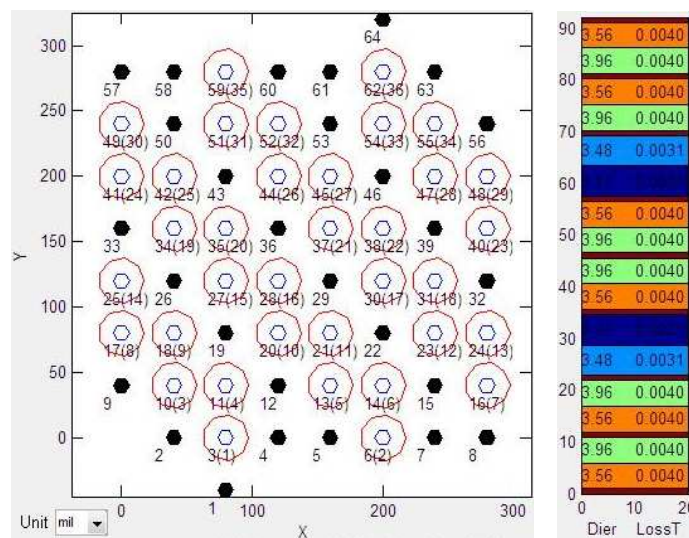
Figure 4: An example of via layout and stack information.

(a)   (b)
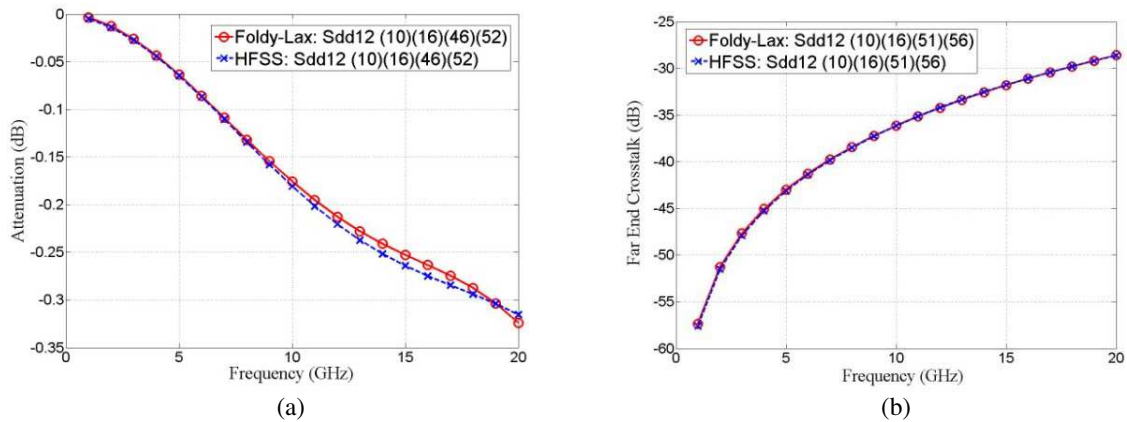
Figure 5: (a) Insertion loss of differential mode on center via pair (10)–(16), and (b) far end crosstalk of differential mode on neighboring via pairs (10)–(16) to (15)–(20).

(a)   (b)
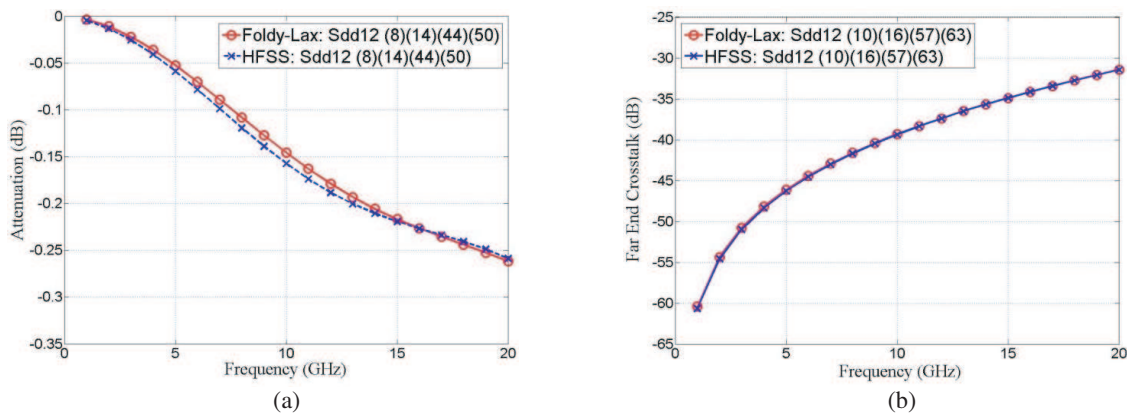
Figure 6: (a) Insertion loss of differential mode on corner via pair (8)–(14), and (b) far end crosstalk of differential mode on ex-neighboring via pairs (10)–(16) to (21)–(27).

5. FOLDY-LAX VIA TOOL AND DEMONSTRATION

Based upon the Foldy-Lax multiple scattering approach, we developed the Foldy-Lax Via Tool [11], a fast full wave 3D interconnect simulator for electromagnetic modeling massively-coupled multiple vias in multilayered and lossy electronic packaging. The current version provides a graphical user interface and several extended functions that recently have been made available. The Foldy-Lax Via Tool was tested for all the structures in the previous publications [2, 4, 7, 9, 10]. Results are within 5% difference of accuracy up to 20 GHz compared with Ansoft HFSS. The required CPU of using this tool is about three orders of magnitude faster than that of the HFSS. This tool was sent to Intel and IBM for further verification and hardware benchmarks [6].

Here we demonstrate a case of 64 vias including 18 pairs of differential-signaling vias and 18 ground vias in 8-layer board with layered and lossy dielectrics (Figure 4). The dark dots represent ground vias connecting every ground plane from top to bottom. The concentric circles represent signal via going through the antipad. Those numbers inside parentheses are noted for signal via assignment. The material properties and stack information are shown on the right side of Figure 4. To simulate this structure, Ansoft HFSS took 28 hours and 23 minutes of CPU time and 5.19 G of RAM for running 20 frequency points from 1 GHz to 20 GHz on an Intel Xeon Quad-core 3.0 G processor. The Foldy-Lax Via Tool took only 2.41 seconds of CPU time and 20M of RAM for the same structure. The insertion loss of differential mode on a center via pair is shown in Figure 5(a). Figure 5(b) illustrates the far end crosstalk (FEXT) of differential mode onto a neighboring via pair. A good agreement is achieved between Foldy-Lax Via Tool and HFSS simulations.

The insertion loss of differential mode on a corner via pair is shown in Figure 6(a). Figure 6(b) illustrates the far end crosstalk (FEXT) of differential mode onto an ex-neighboring via pair. It shows that the insertion loss of differential mode on a corner via pair (0.26 dB at 20 GHz) is smaller

than that on a center via pair (0.32 dB at 20 GHz). The FEXT is increased to around −30 dB as frequency goes 20 GHz. The FEXT of differential mode on the neighboring via pairs (−28.6 dB at 20 GHz) is stronger than that on the ex-neighboring via pairs (−31.5 dB at 20 GHz). This is mainly due to the smaller separation between the neighboring via pairs.

ACKNOWLEDGMENT

REFERENCES

1. Kam, D. G., M. B. Ritter, T. J. Beukema, J. F. Bulzacchelli, P. K. Pepeljugoski, Y. H. Kwark, L. Shan, X. Gu, C. W. Baks, R. A. John, G. Hougham, C. Schuster, R. Rimolo-Donadio, and B. Wu, "Is 25 Gb/s on-board signaling viable?" *IEEE Trans. Adv. Pkg.*, Vol. 32, No. 2, 328–344, May 2009.
2. Tsang, L., H. Chen, C.-C. Huang, and V. Jandhyala, "Modeling of multiple scattering among vias in planar waveguides using Foldy-Lax equations," *Microw. Opt. Technol. Lett.*, Vol. 31, No. 3, 201–208, Nov. 2001.
3. Tsang, L., H. Chen, C.-C. Huang, and V. Jandhyala, "Methods for modeling interactions between massively coupled multiple vias in multilayered electronic packaging structures," U.S. Patent 7 149 666, Dec. 12, 2006.
4. Ong, C.-J., D. Miller, L. Tsang, B. Wu, and C.-C. Huang, "Application of the Foldy Lax multiple scattering method to the analysis of vias in ball grid arrays and interior layers of printed circuit boards," *Microw. Opt. Technol. Lett.*, Vol. 49, No. 1, 225–231, Jan. 2007.
5. Ong, C.-J., B. Wu, L. Tsang, and X. Gu, "Full-wave solver for microstrip trace and through-hole via in layered media," *IEEE Trans. Adv. Pkg.*, Vol. 31, No. 2, 292–302, May 2008.
6. Gu, X., B. Wu, C. Baks, and L. Tsang, "Fast full wave analysis of PCB via arrays with model-to-hardware correlation," *Proc. IEEE Electrical Performance of Electronic Packaging and Systems Conf. (EPEPS'09)*, 175–178, Portland, Oregon, Oct. 19–21, 2009.
7. Wu, B. and L. Tsang, "Modeling multiple vias with arbitrary shape of antipads and pads in high speed interconnect circuits," *IEEE Microwave and Wireless Comp. Lett.*, Vol. 19, No. 1, 12–14, Jan. 2009.
8. Sadiku, M. N. O., "Finite differencing for nonrectangular systems," *Numerical Techniques in Electromagnetics with MATLAB*, 3rd Edition, CRC Press, Apr. 2009.
9. Wu, B. and L. Tsang, "Full-wave modeling of multiple vias using differential signaling and shared antipad in multilayered high speed vertical interconnects," *Progress In Electromagnetics Research*, PIER 97, 129–139, 2009.
10. Wu, B. and L. Tsang, "Signal integrity analysis of package and printed circuit board with multiple vias in substrate of layered dielectrics," *IEEE Trans. Adv. Pkg.*, in Press, 2010.
11. http://www.ee.washington.edu/research/laceo/Via_Tool/.

An $\mathcal{H}$-LU Based Direct Finite Element Solver Accelerated by Nested Dissection for Large-scale Modeling of ICs and Packages

Haixin Liu and Dan Jiao

School of Electrical and Computer Engineering, Purdue University
465 Northwestern Avenue, West Lafayette, IN 47907, USA

Abstract— In this work, we prove that for the sparse matrix resulting from a finite-element-based analysis of electrodynamic problems, its inverse has a data-sparse $\mathcal{H}$-matrix approximation with error well controlled. Based on this proof, we develop a fast direct finite element solver. In this direct solver, the $\mathcal{H}$-matrix-based LU factorization is developed, which is further accelerated by nested dissection. We show that the proposed direct solver has an $O(kN\log N)$ memory complexity and $O(k^2 N\log^2 N)$ time complexity, where k is a small number that is adaptively determined based on accuracy requirements, and N is the number of unknowns. A comparison with the state-of-the-art direct finite element solver that employs the most advanced sparse matrix solution has shown a clear advantage of the proposed solver. Applications to large-scale package modeling involving millions of unknowns have demonstrated the accuracy and almost linear complexity of the proposed direct solver. In addition, the proposed method is applicable to arbitrarily-shaped three-dimensional structures and arbitrary inhomogeneity.

1. INTRODUCTION

A finite element method (FEM) based analysis of a large-scale IC and package problem generally results in a large-scale system matrix. Although the matrix is sparse, solving it can be a computational challenge when the problem size is large. There exists a general mathematical framework called the "Hierarchical ($\mathcal{H}$) Matrix" framework [1–4], which enables a highly compact representation and efficient numerical computation of the dense matrices. It has been shown that the storage requirements and matrix-vector multiplications using $\mathcal{H}$ matrices are of complexity $O(N\log N)$, and the inverse of an $\mathcal{H}$-matrix can be obtained in $O(N\log^2 N)$ complexity. In [5, 6], we developed an $\mathcal{H}$-matrix based solver to efficiently compute and store the inverse of a finite element matrix. In this work, we develop an LU-factorization based fast finite-element solver. We then further accelerate the $\mathcal{H}$-based LU solver by Nested Dissection [7].

The main contribution of this work is four-fold. First, we theoretically prove the existence of an $\mathcal{H}$-matrix-based representation of the FEM matrix and its inverse for electrodynamic problems. The existence of an $\mathcal{H}$-matrix approximation so far was only proved for elliptic partial differential equations (PDE) [8], whereas the Maxwell's equations are hyperbolic in nature. Second, we develop an $\mathcal{H}$-matrix-based LU solver of $O(kN\log N)$ memory complexity and $O(k^2 N\log^2 N)$ time complexity for solving vector wave equations, where k is a variable that is adaptively determined based on the accuracy requirement, which is also small compared to N. The $\mathcal{H}$-based LU is further accelerated by Nested Dissection [7]. Third, we develop a theoretical analysis of the complexity and accuracy for the proposed fast direct solver. In addition, we compare the proposed direct solver with the state-of-the-art direct sparse solver such as UMFPACK 5.0 [9]. UMFPACK has incorporated almost all the advanced sparse matrix techniques such as the multifrontal method and the approximate minimum degree (AMD) ordering for solving large-scale sparse matrices. The proposed solver is shown to outperform the UMFPACK 5.0 in both matrix decomposition and matrix solution time without sacrificing accuracy.

2. ON THE EXISTENCE OF $\mathcal{H}$-MATRIX REPRESENTATION OF THE FEM MATRIX AND ITS INVERSE FOR ELECTRODYNAMIC PROBLEMS

It has been proven in the mathematical literature that the FEM matrix resulting from the analysis of elliptic partial differential equations such as a Poisson equation has an $\mathcal{H}$-matrix representation. Moreover, its inverse also allows for a date-sparse $\mathcal{H}$-matrix approximation [8]. However, the full Maxwell's equations are hyperbolic partial differential equations in nature. Therefore, the proof developed for elliptic PDE-based equations does not apply to the wave equation, which governs all the electrodynamic phenomena. The existence of an $\mathcal{H}$-matrix representation of the FEM system matrix for electrodynamic analysis is obvious based on the definition of an $\mathcal{H}$-matrix [1–4]. In the following, we rigorously prove that the *inverse* of the FEM matrix also allows for an $\mathcal{H}$-matrix representation.

Consider the electric field $\mathbf{E}$ due to an arbitrary current distribution $\mathbf{J}$ in free space. The current distribution $\mathbf{J}$ can always be decomposed into a group of electric dipoles $\tilde{I}_i l_i$, where $\tilde{I}_i$ is the current of the i-th element and l_i is the length of the i-th current element. An FEM-based solution to the second-order vector wave equation subject to boundary conditions results in a linear system of equations

$$\mathbf{Y}\{E\} = \{I\} \tag{1}$$

where the right-hand-side vector $\{I\}$ has the following entries

$$I_i = -j\omega\mu_0\tilde{I}_i l_i. \tag{2}$$

On the other hand, $\mathbf{E}$ due to any current distribution $\mathbf{J}$ can be evaluated from the following integral

$$\mathbf{E} = -j\omega\mu_0 \iiint_V \left(\mathbf{J}G_0 + \frac{1}{k_0^2}\nabla' \cdot \mathbf{J}\nabla G_0 \right) dV' \tag{3}$$

where G_0 is the free-space Green's function.

For a group of electric dipoles $\tilde{I}_i l_i$, the $\mathbf{E}$ field radiated by them at any point in the computational domain can be written as

$$\{E\} = \mathbf{Z}\{I\} \tag{4}$$

where $\{I\}$ vector is the same as that in (1), $\mathbf{Z}$ is a dense matrix having the following elements

$$\mathbf{Z}_{mn} = \frac{1}{-j\omega\mu_0} \left\{ -j\omega\mu_0\hat{t}_m(\mathbf{r}_m) \cdot \hat{l}_n(\mathbf{r}'_n)G_0(\mathbf{r}_m,\mathbf{r}'_n) - \frac{j}{\omega\varepsilon}\hat{t}_m(\mathbf{r}_m) \cdot \nabla \left[\nabla \cdot (\hat{l}_n(\mathbf{r}')G_0(\mathbf{r},\mathbf{r}')) \right] \right\} \tag{5}$$

and $\{E\}$ vector has the following entries

$$E_m = \hat{t}_m(\mathbf{r}_m) \cdot \mathbf{E}(\mathbf{r}_m) \tag{6}$$

where $\hat{t}_m$ is the unit vector tangential to the m-th edge, $\hat{l}_n$ is the unit vector tangential to the n-th current element, $\mathbf{r}_m$ denotes the center point of the m-th edge, $\mathbf{r}'_n$ denotes the point where the n-th current element is located.

Comparing (1) to (4), it is clear that the inverse of the FEM matrix $\mathbf{Y}$ is $\mathbf{Z}$. Since we have proved in [10–12] that the $\mathbf{Z}$ resulting from an integral-equation based analysis can be represented by an $\mathcal{H}$-matrix with error well controlled, we prove that $\mathbf{Y}$'s inverse has an $\mathcal{H}$-matrix representation. Following a proof similar to the above, we can show that the inverse of the FEM matrix in a non-uniform material can also be represented by an $\mathcal{H}$-matrix.

3. PROPOSED FAST DIRECT FEM SOLVER

In [5, 6], we developed an $\mathcal{H}$-inverse based fast direct FEM solver. Since what is to be solved in (1) is $\mathbf{Y}^{-1}\{I\}$ instead of $\mathbf{Y}^{-1}$, an LU-factorization-based direct solution is generally more efficient than an inverse-based direct solution. In addition, in the LU factorization, the input matrix can be overwritten by $\mathbf{L}$ and $\mathbf{U}$ factors, thus the memory usage can be saved by half.

The proposed LU-based direct solution has three components: (1) $\mathcal{H}$-based recursive LU factorization; (2) matrix solution by $\mathcal{H}$-based backward and forward substitution; and (3) acceleration by nested dissection.

3.1. Recursive LU Factorization and Matrix Solution

We use an $\mathcal{H}$-matrix block $\mathbf{Y}_{tt}$ to demonstrate the $\mathcal{H}$-LU factorization process, where t is a non-leaf cluster in the cluster tree $T_\mathcal{I}$ [5, 6]. If t is a non-leaf, block $t \times t$ is not a leaf block and hence $\mathbf{Y}_{tt}$ can be subdivided into four sub blocks:

$$\mathbf{Y}_{tt} = \begin{pmatrix} \mathbf{Y}_{t_1 t_1} & \mathbf{Y}_{t_1 t_2} \\ \mathbf{Y}_{t_2 t_1} & \mathbf{Y}_{t_2 t_2} \end{pmatrix} \tag{7}$$

where t_1 and t_2 are the children of t in the cluster tree $T_\mathcal{I}$.

Assuming $\mathbf{Y}$ can be factorized into $\mathbf{L}$ and $\mathbf{U}$ matrices, $\mathbf{Y}$ can also be written as:

$$\mathbf{Y}_{tt} = \mathbf{L}_{tt}\mathbf{U}_{tt} = \begin{pmatrix} \mathbf{L}_{t_1 t_1} & 0 \\ \mathbf{L}_{t_2 t_1} & \mathbf{L}_{t_2 t_2} \end{pmatrix} \begin{pmatrix} \mathbf{U}_{t_1 t_1} & \mathbf{U}_{t_1 t_2} \\ 0 & \mathbf{U}_{t_2 t_2} \end{pmatrix} = \begin{pmatrix} \mathbf{L}_{t_1 t_1}\mathbf{U}_{t_1 t_1} & \mathbf{L}_{t_1 t_1}\mathbf{U}_{t_1 t_2} \\ \mathbf{L}_{t_2 t_1}\mathbf{U}_{t_1 t_1} & \mathbf{L}_{t_2 t_1}\mathbf{U}_{t_1 t_2} + \mathbf{L}_{t_2 t_2}\mathbf{U}_{t_2 t_2} \end{pmatrix} \tag{8}$$

By comparing (7) and (8), the LU factorization can be computed recursively by the following four steps: 1) Compute $\mathbf{L}_{t1t1}$ and $\mathbf{U}_{t1t1}$ by $\mathcal{H}$-LU factorization $\mathbf{Y}_{t1t1}= \mathbf{L}_{t1t1}\mathbf{U}_{t1t1}$; 2) Compute $\mathbf{U}_{t1t2}$ by solving $\mathbf{L}_{t1t1}\mathbf{U}_{t1t2}= \mathbf{Y}_{t1t2}$; 3) Compute $\mathbf{L}_{t2t1}$ by solving $\mathbf{L}_{t2t1}\mathbf{U}_{t1t1}= \mathbf{Y}_{t2t1}$; and 4) Compute $\mathbf{L}_{t2t2}$ and $\mathbf{U}_{t2t2}$ by $\mathcal{H}$-LU factorization $\mathbf{L}_{t2t2}\mathbf{U}_{t2t2} = \mathbf{Y}_{t2t2} - \mathbf{L}_{t2t1}\mathbf{U}_{t1t2}$.

If $t\times t$ is a leaf block, $\mathbf{Y}_{tt}$ is not subdivided. It is stored in full matrix format, and factorized by a conventional pivoted LU factorization. Matrix solution by backward and forward substitution can be done in a similar hierarchical way.

3.2. Acceleration by Nested Dissection

It is known that the smaller the number of nonzero elements to be processed in LU factorization, the better the computational efficiency. Nested dissection [7] can be used as an ordering technique to reduce the number of non-zero blocks to be computed in the LU factorization. In addition, this scheme naturally fits the $\mathcal{H}$-based framework compared to many other ordering techniques. It serves an efficient approach to construct a block cluster tree [5].

We divide the computational domain into three parts: two domain clusters D1 and D2 which do not interact with each other and one interface cluster "I" which interacts with both domain clusters. Since the domain clusters D1 and D2 do not have interaction, their crosstalk entries in the FEM matrix $\mathbf{Y}$ are all zero. If we order the unknowns in D1 and D2 first and the unknowns in I last, the resultant matrix will have large zero blocks. These zero blocks are preserved during the LU factorization, and hence the computation cost of LU factorization is reduced.

We further partition the domain clusters D1 and D2 into three parts. This process continues until the number of unknowns in each cluster is smaller than *leafsize* ($n_{\min}$), or no interface edges can be found to divide the domain. Since the matrices in the non-zero blocks are stored and processed by $\mathcal{H}$-matrix techniques in the proposed direct solver, the computational complexity is significantly reduced compared to a conventional nested dissection based LU factorization.

4. COMPLEXITY AND ACCURACY ANALYSIS

4.1. Complexity Analysis

The storage complexity and inverse complexity of an $\mathcal{H}$-matrix are shown to be $O(kN\log N)$, and $O(kN\log^2 N)$ respectively in [6] for solving electrodynamic problems. Here, we only analyze the complexity of an $\mathcal{H}$-based LU factorization.

As can be seen from Section 3.1, the LU factorization of $\mathbf{Y}_{tt}$ is computed in four steps. In these four steps, $\mathbf{Y}_{t1t1}$, $\mathbf{Y}_{t1t2}$, and $\mathbf{Y}_{t2t1}$ are computed once, $\mathbf{Y}_{t2t2}$ is computed twice. Since in inverse, each block is computed twice, the complexity of $\mathcal{H}$-based LU factorization is bounded by the $\mathcal{H}$-based inverse, which is $O(N\log^2 N)$.

4.2. Accuracy Analysis

From the proof given in Section 2, it can be seen that the inverse of the FEM matrix $\mathbf{Y}$ has an $\mathcal{H}$-matrix-based representation. In such a representation, which block is admissible and which block is inadmissible are determined by an admissibility condition [5, 6]. Rigorously speaking, this admissibility condition should be defined based on $\mathbf{Y}^{-1}$. However, since $\mathbf{Y}^{-1}$ is unknown, we determine it based on $\mathbf{Y}$. Apparently, this will induce error. However, as analyzed in Section 2, the $\mathbf{Y}$'s inverse can be mapped to the dense matrix formed for an integral operator. For this dense matrix, the admissibility condition used to construct an $\mathcal{H}$-matrix representation has the same form as that used in the representation of the FEM matrix $\mathbf{Y}$ [10, 12]. Thus, the $\mathcal{H}$-matrix structure, i.e, which block can have a potential low-rank approximation and which block is a full matrix, is formed correctly for $\mathbf{Y}^{-1}$. In addition, the accuracy of the admissibility condition can be controlled.

In the LU factorization process, the rank of each admissible block is adaptively determined based on a required level of accuracy. If the rank is determined to be a full rank based on the adaptive scheme, then a full rank will be used. Thus, the low-rank approximation for each admissible block is also error controllable.

Based on the aforementioned two facts, the error of the proposed direct solver is controllable.

5. NUMERICAL RESULTS

A package inductor array is simulated to demonstrate the accuracy and efficiency of the proposed direct solver. The configuration of each inductor is shown in Figure 1, and a 7×7 inductor array is shown in Figure 2. In this example, $\mathcal{H}$-LU factorization with nested dissection is used to directly solve the FEM matrix. Simulation is done at $10\,\mathrm{GHz}$ for the inductor array from 2×2 to 7×7,
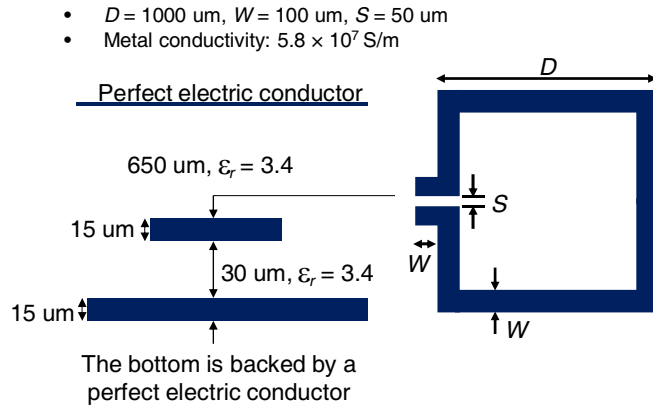
Figure 1: Geometry and material of a package inductor.
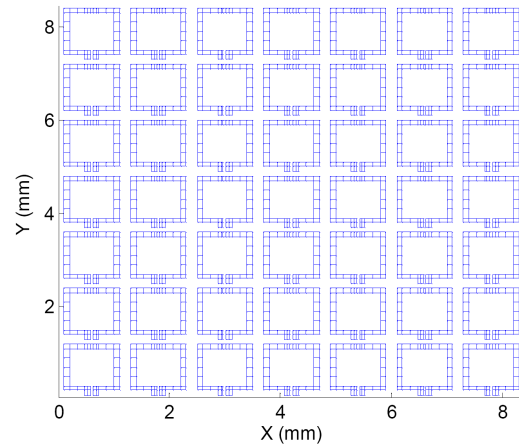
Figure 2: A 7×7 inductor array.

(a)   (b)   (c)   (d)
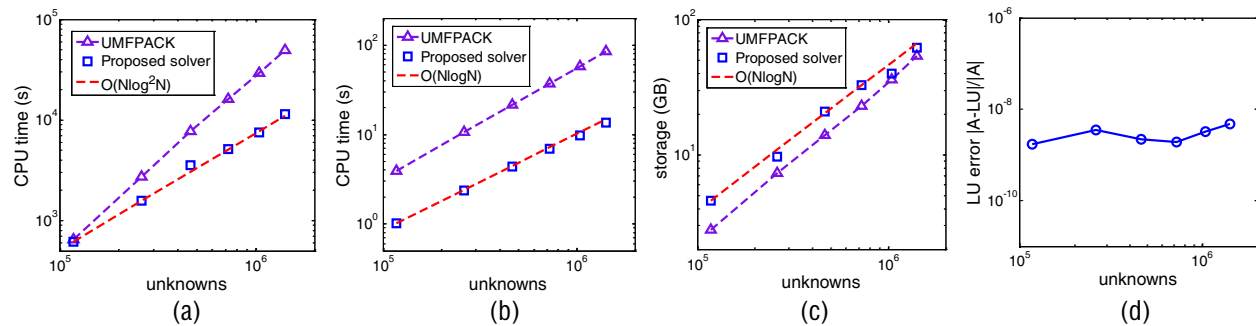
Figure 3: Performance of the proposed LU-based direct solver for simulating an inductor array from a 2×2 array to a 7×7 array. (a) CPU time for LU factorization. (b) CPU time for solving one right hand side. (c) Storage. (d) Accuracy.

the number of unknowns of which is from 117,287 to 1,415,127. The simulation parameters were chosen as: $n_{\min} = 32$ and $\eta = 1$. The rank k was adaptively decided. In Figure 3(a), we plot the LU factorization time of the proposed direct solver, and that of UMFPACK 5.0 with respect to the number of unknowns. The proposed solver demonstrates a complexity of $O(N\log^2 N)$, which agrees very well with the theoretical analysis, whereas UMFPACK has a much higher complexity. In Figure 3(b), we plot the matrix solution time of the proposed direct solver, and that of UMFPACK for one right hand side. Once again, the proposed direct solver outperforms UMFPACK. In addition, the proposed direct solver is shown to have an $O(N\log N)$ complexity in matrix solution (backward and forward substitution). In Figure 3(c), we plot the storage requirement of the proposed direct solver and that of UMFPACK in simulating this example. Even though the storage of the proposed solver is shown to be a little bit higher than that of UMFPACK, the complexity of the proposed solver is lower, and hence for larger number of unknowns, the proposed solver will outperform UMFPACK in storage. In Figure 3(d), we plot the relative error of the proposed direct FEM solver. Good accuracy is observed in the entire range. The proposed direct FEM solver has also been successfully applied to the modeling of on-chip circuits.

6. CONCLUSIONS

In this work, we proved the existence of an $\mathcal{H}$-matrix-based representation of the inverse of the FEM matrix for solving electrodynamic problems. We developed a direct LU-based FEM solver of significantly reduced complexity. The time and storage complexity were shown to be $O(N\log^2 N)$ and $O(N\log N)$ respectively. In addition, we accelerated the direct solver by nested dissection. Numerical experiments and a comparison with the state-of-the-art sparse matrix solver UMFPACK have demonstrated its superior performance in modeling large-scale circuit and package problems involving millions of unknowns.

REFERENCES

1. Hackbusch, W. and B. Khoromaskij, "A sparse matrix arithmetic based on matrices. Part I: Introduction to matrices," *Computing*, Vol. 62, 89–108, 1999.
2. Hackbusch, W. and B. N. Khoromskij, "A sparse-matrix arithmetic. Part II: Application to multi-dimensional problems," *Computing*, Vol. 64, 21–47, 2000.
3. Borm, S., L. Grasedyck, and W. Hackbusch, "Hierarchical matrices," Lecture Note 21 of the Max Planck Institute for Mathematics in the Sciences, 2003.
4. Grasedyck, L. and W. Hackbusch, "Construction and arithmetics of matrices," *Computing*, Vol. 70, No. 4, 295–344, August 2003.
5. Liu, H. and D. Jiao, "A direct finite-element-based solver of significantly reduced complexity for solving large-scale electromagnetic problems," *International Microwave Symposium (IMS)*, 4, June 2009.
6. Liu, H. and D. Jiao, "Performance analysis of the H-matrix-based fast direct solver for finite-element-based analysis of electromagnetic problems," *IEEE International Symposium on Antennas and Propagation*, 4, June 2009.
7. George, A., "Nested dissection of a regular finite element mesh," *SIAM J. on Numerical Analysis*, Vol. 10, No. 2, 345–363, April 1973.
8. Bebendorf, M. and W. Hackbusch, "Existence of $\mathcal{H}$-matrix approximants to the inverse FE-matrix of elliptic operators with L^∞-coefficients," *Numerische Mathematik*, Vol. 95, 1–28, 2003.
9. UMFPACK5.0, http://www.cise.ufl.edu/research/sparse/umfpack/.
10. Chai, W. and D. Jiao, "$\mathcal{H}$- and $\mathcal{H}^2$-matrix-based fast integral-equation solvers for large-scale electromagnetic analysis," *IET Microwaves, Antennas & Propagation*, accepted for publication, 2009.
11. Chai, W. and D. Jiao, "An $\mathcal{H}^2$-matrix-based integral-equation solver of reduced complexity and controlled accuracy for solving electrodynamic problems," *IEEE Trans. Antennas Propagat.*, Vol. 57, No. 10, 3147–3159, October 2009.
12. Chai, W. and D. Jiao, "An $\mathcal{H}^2$-matrix-based integral-equation solver of linear-complexity for large-scale full-wave modeling of 3D circuits," *IEEE 17th Conference on Electrical Performance of Electronic Packaging (EPEP)*, 283–286, October 2008.

Application of Two Mixed Potential Integral Equations to Electromagnetic-circuit Simulation of Three-dimensional Interconnects in Layered Media

N. Kurt-Karsilayan[1] and K. A. Michalski[2]

[1]Texas A&M University and Mentor Graphics Corporation, USA
[2]Texas A&M University, USA

Abstract— Electromagnetic-circuit simulation of three-dimensional (3-D) arbitrary-shaped conducting objects over conducting substrate layers is addressed. The electromagnetic-circuit surface integral equations are presented for two mixed potential integral equation (MPIE) forms of electric field integral equation (EFIE) based on the Michalski-Mosig formulation where different sets of layered kernels are involved. Various new ways of applying external voltage and current sources are discussed in detail. Numerical results are presented for validation of the proposed methods.

1. INTRODUCTION

Electromagnetic-circuit simulation of 3-D interconnects and the substrate in integrated circuits (IC), printed circuit boards or packages continues to be an important research topic as the switching frequency, density and complexity of processes and designs continue to increase [1].

Electromagnetic-circuit integral equation (IE) solvers can be grouped based on volume integral equation (VIE) and surface integral equation (SIE), where volumes and surfaces of the conductors are discretized, respectively. The majority of the existing full-wave IE approaches treat planar layered media similar to the conducting objects, by discretizing the dielectric interfaces and the substrate, and using full-wave free-space Green functions [2–5]. Since modern IC processes include tens of dielectric layers, discretizing each dielectric interface and the substrate region causes significant increase in the number of unknowns. Several full-wave SIE methods published in recent years treat conductors as 2-D surfaces with impedance boundary conditions and use layered, instead of free-space kernels [6, 7]. However, these methods are based on the assumption of 2.5-D simulation of regular rectangular objects where only the upper and lower surfaces of the conductors are modeled. A recent full-wave VIE method [8] uses layered medium kernels limited to only two half spaces where the kernels are approximated with discrete complex image method. The disadvantage of the VIE approach is that finer discretization of the conductor cross-sections is needed for higher frequencies which increases the number of unknowns.

In this paper, a new full-wave, surface impedance equation method for electromagnetic-circuit simulation of 3-D arbitrary-shaped conducting objects in layered media is proposed. Two MPIE forms are used for the parasitic extraction problem where different sets of layered medium kernels are involved. Unlike most of the existing approaches, no assumptions are made for the layered media Green functions since the Sommerfeld integrals are computed directly for controllable accuracy. Since the layer information is independent of the interconnect geometries, the Sommerfeld integrals can be computed one time and used later during the geometry processing. Another contribution of this paper is that several ways of applying external voltage and current sources are discussed in detail. In Sections 2 and 3, the electromagnetic-circuit formulation and discretization are summarized, respectively. Section 4 contains numerical results for validating the proposed methods. Section 5 contains concluding remarks.

2. ELECTROMAGNETIC-CIRCUIT INTEGRAL FORMULATION

According to the equivalence principle [9], the original problem in Fig. 1(a) can be separated into interior and exterior equivalent problems where the Green functions for the interior and the exterior regions can be used, respectively. Since interconnects have finite high conductivity, they can be considered as lossy objects with surface impedance boundary condition [6, 7, 10, 11]. This eliminates the need of interior equations and magnetic surface current in Fig. 1(b), therefore the number of unknowns is reduced significantly. The layered Green functions [12–15] are used in the exterior equivalent problem in Fig. 1(c). Contacts or terminals represent the interface between

(a) Original problem   (b) Interior equivalence   (c) Exterior equivalence
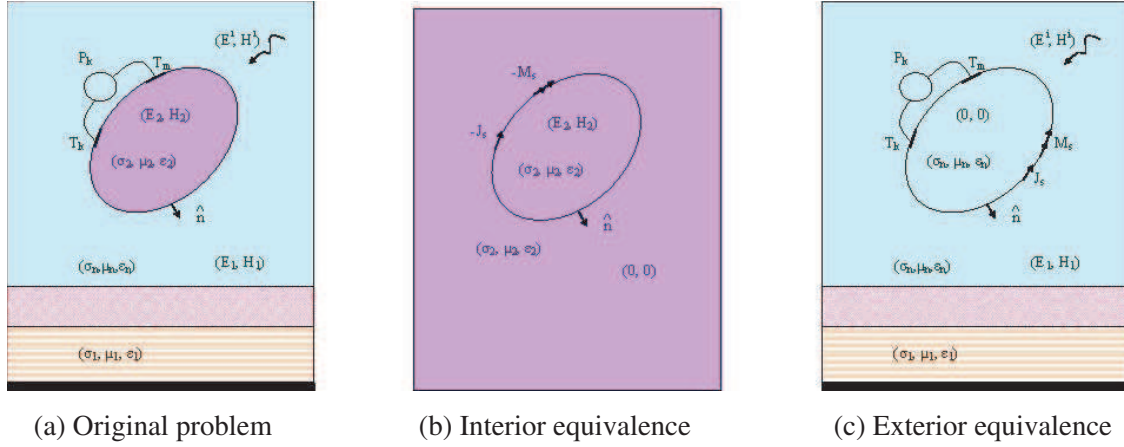
Figure 1: Equivalence principle.

electromagnetic and circuit domains which are denoted as $T_{k,m}$ in Figs. 1(a) and 1(c). A port denoted as P_k in Fig. 1(a) is associated with two terminals.

The tangential electric field on the surface satisfy the following condition,

$$\left(\mathbf{E}^i + \mathbf{E}^s\right)_{\text{tan}} = Z_s\mathbf{J}_s, \quad Z_s = \frac{1+j}{\sigma\delta}, \quad \delta = \frac{1}{\sqrt{\pi f \mu \sigma}}, \tag{1}$$

where J_s, Z_s, $\mathbf{E}^i$, $\mathbf{E}^s$, σ and δ represent the surface current density, surface impedance, possible incident electric field, the scattered electric field, the conductivity and the skin depth, respectively.

The continuity equations at non-contact and contact surfaces are stated as follows,

$$- j\omega\rho_e = \left\{ \begin{array}{ll} \boldsymbol{\nabla}'_s \cdot \mathbf{J}_s, & \mathbf{r}' \in S_{nc}, \\ \boldsymbol{\nabla}'_s \cdot \mathbf{J}_s - K_c, & \mathbf{r}' \in S_c, \end{array} \right. \tag{2}$$

where ρ_e, K_c, S_c and S_{nc} represent the charge density, the current density injected through the contact, the contact and the non-contact surfaces, respectively.

The set of electromagnetic-circuit equations for MPIE form I is as follows,

$$Z_s\mathbf{J}_s + \oint \left[j\omega\mu_0\mathbf{G}^A \cdot \mathbf{J}_s - \frac{1}{j\omega\epsilon_0}\boldsymbol{\nabla}\left(G^\phi\boldsymbol{\nabla}'_s \cdot \mathbf{J}_s\right) \right] dS' = \mathbf{E}^i_{\text{tan}}, \quad \mathbf{r}' \in S_{nc}, \tag{3}$$

$$Z_s\mathbf{J}_s + \oint \left[j\omega\mu_0\mathbf{G}^A \cdot \mathbf{J}_s - \frac{1}{j\omega\epsilon_0}\boldsymbol{\nabla}\left(G^\phi\left(\boldsymbol{\nabla}'_s \cdot \mathbf{J}_s - K_c\right)\right) \right] dS' = \mathbf{E}^i_{\text{tan}}, \quad \mathbf{r}' \in S_c, \tag{4}$$

$$V_c = -\frac{1}{j\omega\epsilon_0} \oint \left[G^\phi\left(\boldsymbol{\nabla}'_s \cdot \mathbf{J}_s - K_c\right) \right] dS', \quad \mathbf{r}' \in S_c, \tag{5}$$

where V_c, $\mathbf{G}^A$ and G^ϕ represent the contact potential, the dyadic vector and scalar potential kernels, respectively.

The set of electromagnetic-circuit equations for MPIE form II is as follows,

$$Z_s\mathbf{J}_s + \oint \left[j\omega\mu_0\mathbf{G}^A \cdot \mathbf{J}_s - \frac{1}{j\omega\epsilon_0}\boldsymbol{\nabla}\left(G^\phi\boldsymbol{\nabla}'_s \cdot \mathbf{J}_s + \hat{z}C^\phi \cdot \mathbf{J}_s\right) \right] dS' = \mathbf{E}^i_{\text{tan}}, \quad \mathbf{r}' \in S_{nc}, \tag{6}$$

$$Z_s\mathbf{J}_s + \oint \left[j\omega\mu_0\mathbf{G}^A \cdot \mathbf{J}_s - \frac{1}{j\omega\epsilon_0}\boldsymbol{\nabla}\left(G^\phi\left(\boldsymbol{\nabla}'_s \cdot \mathbf{J}_s - K_c\right) + \hat{z}C^\phi \cdot \mathbf{J}_s\right) \right] dS' = \mathbf{E}^i_{\text{tan}}, \quad \mathbf{r}' \in S_c, \tag{7}$$

$$V_c = -\frac{1}{j\omega\epsilon_0} \oint \left[G^\phi\left(\boldsymbol{\nabla}'_s \cdot \mathbf{J}_s - K_c\right) + \hat{z}C^\phi \cdot \mathbf{J}_s \right] dS', \quad \mathbf{r}' \in S_c, \tag{8}$$

where C^ϕ is the correction kernel for the scalar potential [14].

The kernels for two MPIE forms are summarized in Table 1 where ρ, ϕ and S_n represent the horizontal distance between the source and the observation points, the angle between x-coordinate and ρ, and the Sommerfeld-type integrals with Bessel functions of order n, respectively. V_s^m, I_s^m

Table 1: Summary of kernel properties.

MPIE form(s)	Kernel	Expression
I, II	$G^A_{xx}(\rho, z\vert z')$	$\dfrac{1}{j\omega\mu_0}S_0\{V^h_i\}$
I	$G^A_{zz}(\rho; z\vert z')$	$-j\omega\mu_0 S_0\left\{\left(\dfrac{\mu_t}{\epsilon'_z} + \dfrac{\mu'_t}{\epsilon_z}\right)\dfrac{I^e_v}{k^2_0} + \mu_t\mu'_t\dfrac{I^h_v - I^e_v}{k^2_\rho}\right\}$
I	$G^A_{xz}(\rho; z\vert z')$	$-\cos\phi S_1\left\{\mu'_t\dfrac{(V^h_v - V^e_v)}{k_\rho}\right\}$
I	$G^A_{yz}(\rho; z\vert z')$	$-\sin\phi S_1\left\{\mu'_t\dfrac{(V^h_v - V^e_v)}{k_\rho}\right\}$
I, II	$G^\phi(\rho, z\vert z')$	$-j\omega\epsilon_0 S_0\left\{\dfrac{V^h_i - V^e_i}{k^2_\rho}\right\}$
I, II	$G^A_{zx}(\rho, z\vert z')$	$-\cos\phi S_1\left\{\mu_t\dfrac{(I^h_i - I^e_i)}{k_\rho}\right\}$
I, II	$G^A_{zy}(\rho, z\vert z')$	$-\sin\phi S_1\left\{\mu_t\dfrac{(I^h_i - I^e_i)}{k_\rho}\right\}$
II	$G^A_{zz}(\rho, z\vert z')$	$\dfrac{1}{j\omega\epsilon_0}S_0\left\{\dfrac{\mu_t}{\epsilon'_z}I^e_v\right\}$
II	$C^\phi(\rho, z\vert z')$	$k^2_0 S_0\left\{\dfrac{\mu'_t}{k^2_\rho}(V^h_v - V^e_v)\right\}$

Figure 2: Current definition.

represent the transmission line Green functions (TLGF), where $s = v$ or $s = i$, and $m = e$ (TM) or $m = h$ (TE) [14, 15]. Note that primed coordinates or parameters correspond to the source point or the corresponding layer, whereas unprimed coordinates or parameters correspond to the observation point or the corresponding layer.

The rest of the equations are as follows,

$$I_c = \sum_{n=1}^{N_c} K^n_c, \quad [I_c] = [Q]^T[I_p], \quad [V_p] = [Q][V_c], \quad [R][I_p] + [P][V_p] = [U], \tag{9}$$

where K^n_c, I_c, V_c, I_p, V_p and U represent the normal current at contact element n, contact currents, contact voltages, port currents, port voltages and current or voltage sources, respectively. Reference current directions are illustrated in Fig. 2.

3. DISCRETIZATION

Method of moments is used to transform the continuous surface integrals to a linear matrix system [16]. Each conductor surface is discretized with triangles and well-known Rao-Wilton-Glisson (RWG) functions are used for basis and testing functions over triangles. An RWG function is

defined over pairs of triangle surfaces as follows [17],

$$\mathbf{\Lambda}_i(\mathbf{r}) = \begin{cases} l_i \frac{\boldsymbol{\rho}_i^+}{2S^+}, & \mathbf{r} \in S^+ \\ l_i \frac{\boldsymbol{\rho}_i^-}{2S^-}, & \mathbf{r} \in S^- \end{cases} , \quad \nabla \cdot \mathbf{\Lambda}_i(\mathbf{r}) = \begin{cases} \frac{l_i}{S^+}, & \mathbf{r} \in S^+ \\ -\frac{l_i}{S^-}, & \mathbf{r} \in S^- \end{cases} \tag{10}$$

Two more basis functions are used in addition to RWG functions for expanding the voltages and the currents over each contact surface.

$$\upsilon_n = \begin{cases} 1, & \mathbf{r}' \in S_n \\ 0, & \mathbf{r}' \notin S_n \end{cases} , \quad \varphi_n = \begin{cases} \frac{1}{S_n}, & \mathbf{r}' \in S_n \\ 0, & \mathbf{r}' \notin S_n \end{cases} \tag{11}$$

Surface current density, contact voltage, and contact current density are expanded as follows,

$$\mathbf{J} = \sum_{i=1}^{N_e} \mathbf{\Lambda}_i J_i, \quad V_c = \sum_{n=1}^{N_c} \upsilon_n V_c^n, \quad K_c = \sum_{n=1}^{N_c} \varphi_n K_c^n \tag{12}$$

where N_e, $\mathbf{\Lambda}_i$ and J_i represent the number of independent edges, the RWG function and the normal current at edge i, respectively. N_c, K_c^n and V_c^n are the number of contact elements associated with contact c, the injected normal current and the potential at contact element n, respectively. Each contact surface is equipotential.

Testing and expanding the integral equations in (3)–(8) with the corresponding functions provides the following matrix system,

$$\begin{bmatrix} A & C & 0 & 0 & 0 & 0 \\ E & F & 0 & G & 0 & 0 \\ 0 & L & I & 0 & 0 & 0 \\ 0 & 0 & 0 & -Q & 0 & I \\ 0 & 0 & I & 0 & -Q^T & 0 \\ 0 & 0 & 0 & 0 & R & P \end{bmatrix} \begin{bmatrix} J \\ K \\ I_c \\ V_c \\ I_p \\ V_p \end{bmatrix} = \begin{bmatrix} E^g \\ 0 \\ 0 \\ 0 \\ 0 \\ U \end{bmatrix} \tag{13}$$

where U is either a voltage or a current source, and J, K, I_c, V_c, I_p, V_p are the unknown vectors for the surface currents, the normal currents, the terminal currents, the terminal voltages, the port currents and the port voltages of size N_e, N_c, N_t, N_t, N_p, and N_p, respectively. Note that, N_e, N_c, N_t and N_p are non-boundary edge, contact element, terminal and port counts, respectively. Sub-matrix expressions for each MPIE form are summarized in Table 2 where $\langle \mathbf{f}, \mathbf{g} \rangle = \oint \mathbf{f} \cdot \mathbf{g} dS'$.

Note that, the sub-matrix A corresponds to the electromagnetic part of the system, C, E, F, G, L represent the sub-matrices for electromagnetic and circuit interactions. The rest of the sub-matrices correspond to the Kirchoff current and voltage laws in the circuit domain.

The term for dyadic vector potential kernel $\mathbf{G}^A$ for MPIE I is expanded as follows,

$$\langle \mathbf{\Lambda}_i, \mathbf{G}^A, \mathbf{\Lambda}_j \rangle = \langle \mathbf{\Lambda}_i, (\mathbf{xx} + \mathbf{yy}) G_{xx}^A + \mathbf{zz} G_{zz}^A + \mathbf{zx} G_{zx}^A + \mathbf{zy} G_{zy}^A + \mathbf{xz} G_{xz}^A + \mathbf{yz} G_{yz}^A, \mathbf{\Lambda}_j \rangle \tag{14}$$

Table 2: Summary of sub-matrix expressions.

Matrix	MPIE	Expression
A	I	$j\omega\mu_0 \langle \mathbf{\Lambda}_i, \mathbf{G}^A, \mathbf{\Lambda}_j \rangle + \frac{1}{j\omega\epsilon_0} \langle \nabla \cdot \mathbf{\Lambda}_i, G^\phi, \nabla \cdot \mathbf{\Lambda}_j \rangle + Z_s \langle \mathbf{\Lambda}_i, \mathbf{\Lambda}_j \rangle$
A	II	$j\omega\mu_0 \langle \mathbf{\Lambda}_i, \mathbf{G}^A, \mathbf{\Lambda}_j \rangle + \frac{1}{j\omega\epsilon_0} \left(\langle \nabla \cdot \mathbf{\Lambda}_i, G^\phi, \nabla \cdot \mathbf{\Lambda}_j \rangle + \langle \nabla \cdot \mathbf{\Lambda}_i, C^\phi \hat{\mathbf{z}}, \mathbf{\Lambda}_j \rangle \right) + Z_s \langle \mathbf{\Lambda}_i, \mathbf{\Lambda}_j \rangle$
E	I	$\frac{1}{j\omega\epsilon_0} \langle \varphi_m, G^\phi, \nabla \cdot \mathbf{\Lambda}_j \rangle$
E	II	$\frac{1}{j\omega\epsilon_0} \left(\langle \varphi_m, G^\phi, \nabla \cdot \mathbf{\Lambda}_j \rangle + \langle \varphi_m, \hat{\mathbf{z}} C^\phi, \mathbf{\Lambda}_j \rangle \right)$
C	I, II	$-\frac{1}{j\omega\epsilon_0} \langle \nabla \cdot \mathbf{\Lambda}_i, G^\phi, \varphi_n \rangle$
F	I, II	$-\frac{1}{j\omega\epsilon_0} \langle \varphi_m, G^\phi, \varphi_n \rangle$
G	I, II	$\langle \varphi_m, \upsilon_n \rangle$
E^g	I, II	$\langle \mathbf{\Lambda}_i, \mathbf{E}^i \rangle$

Table 3: Comparison of wire impedance for MPIE form I and II using RWG method.

GHz	Form I (Ω)	Form II (Ω)	$\frac{|FormII|-|FormI|}{|FormI|}$ (%)
0.01	$0.0152 + 0.1587i$	$0.0161 + 0.1594i$	0.5
0.1	$0.2501 + 1.2924i$	$0.2523 + 1.2942i$	0.2
1	$9.9282 + 12.7142i$	$9.9165 + 12.7159i$	-0.04
10	$6.5038 + 0.4896i$	$6.4322 + 0.404i$	-1.2

Table 4: Analysis of different excitations.

Excitation Type	Output	Value
Unit voltage at the port	Admittance	$1.2736E-003 - 6.0208E-002i$
Unit current at the port	Impedance	$0.3512 + 16.6017i$
Unit voltage at terminal 1	Terminal currents	$\mp 1.2699E-003 \pm 6.0033E-002$
Unit current at terminal 1	Voltage at terminal 1	$-29.8780 - 1427.6176$
Unit current at terminal 1	Voltage at terminal 2	$-30.0536 - 1435.9187$

The term for dyadic vector potential kernel $\mathbf{G}^A$ for MPIE II is stated as follows,

$$\langle \mathbf{\Lambda}_i, \mathbf{G}^A, \mathbf{\Lambda}_j \rangle = \langle \mathbf{\Lambda}_i, (\mathbf{xx} + \mathbf{yy})G_{xx}^A + \mathbf{zz}G_{zz}^A + \mathbf{xz}G_{xz}^A + \mathbf{yz}G_{yz}^A, \mathbf{\Lambda}_j \rangle \tag{15}$$

When the excitation is through a voltage source at a port, the solution for the unknown vector, I_p, directly provides port admittance values. Similarly, when the excitation is through a current source at a port, the solution for the unknown vector, V_p provides the port impedance values. Another excitation method can be through the terminals where the other node of the supply is grounded. In this case, port current and voltage equations are not used in (13).

4. NUMERICAL RESULTS

Impedance value of a single wire of size $0.5 \times 0.5 \times 5\,\text{mm}$ over a single substrate is compared in Table 3 for two forms of MPIE. Note that, the same mesh is used for both cases. The substrate has conductivity of $1000\,\text{S/m}$ and permittivity and permeability constants of 12 and 1, respectively.

Four different excitations are applied to the single wire at $1\,\text{GHz}$ in free-space and reported in Table 4. The wire is discretized such that the total and contact element counts are 116 and 12, respectively. The edge, terminal and port counts are 174, 2, and 1, respectively. It is shown that with different port excitations, the port impedances or admittances can be directly obtained. The impedance value obtained by port current excitation is in fact equal to the inverse of the admittance value obtained by port voltage excitation. It is also observed that the terminal currents for terminal voltage excitation are consistent with the admittance value obtained by port voltage excitation.

5. CONCLUSION

Two MPIE forms of EFIE based on the Michalski-Mosig formulations are presented for electromagnetic-circuit interactions of 3-D interconnects in layered media over conducting substrate layers. It is shown that the two MPIE forms provide consistent results. MPIE II can be used instead of MPIE I when majority of the interconnects have significant side surfaces, since one less kernel is computed due to vertical currents. Port and terminal excitations are elaborated in detail for electromagnetic-circuit simulation.

REFERENCES

1. Ruehli, A. E. and A. C. Cangellaris, "Progress in the methodologies for the electrical modeling of interconnects and electronic packages," *Proc. IEEE*, Vol. 89, No. 5, 740–771, May 2001.
2. Ponnapalli, S., A. Deutsch, and R. Bertin, "A package analysis tool based on a method of moments surface formulation," *IEEE Trans. Compon., Hybrids, Manuf. Technol.*, Vol. 16, No. 8, 884–892, Dec. 1993.
3. Chew, W. C., J. Jin, E. Michielssen, and J. Song, *Fast and Efficient Algorithms in Computational Electromagnetics*, Artech House, Norwood, MA, 2001.

4. Zhu, Z., B. Song, and J. White, "Algorithms in FastImp: A fast and wideband impedance extraction program for complicated 3-D geometries," *Proc. Design Automa. Conf.*, 712–717, Anaheim, CA, Jun. 2003.

5. Chakraborty, S. and V. Jandhyala, "Surface-based broadband electromagnetic-circuit simulation of lossy conductors," *IEE Proc. — Microw., Antennas Propag.*, Vol. 153, No. 2, 191–198, Apr. 2006.

6. Kapur, S. and D. E. Long, "Large-scale full-wave simulation," *Proc. Design Automa. Conf.*, 806–809, San Diego, CA, Jun. 2004.

7. Ling, F., V. I. Okhmatovski, W. Harris, S. McCracken, and A. Dengi, "Large-scale broad-band parasitic extraction for fast layout verification of 3-D RF and mixed-signal on-chip structures," *IEEE Trans. Microw. Theory Tech.*, Vol. 53, No. 1, 264–273, Jan. 2005.

8. Hu, X., J. White, J. H. Lee, and L. Daniel, "Analysis of full-wave conductor system impedance over substrate using novel integration techniques," *Proc. Design Automa. Conf.*, 147–152, San Diego, CA, Jun. 2005.

9. Harrington, R., *Time-harmonic Electromagnetic Fields*, IEEE Press, Wiley Interscience,, Piscataway, NJ, 2001.

10. Theron, I. P. and J. H. Cloete, "On the surface impedance used to model the conductor losses of microstrip structures," *IEE Proc. — Microw., Antennas Propag.*, Vol. 142, No. 1, 35–40, 1995.

11. Wang, Y., D. Gope, V. Jandhyala, and C. J. R. Shi, "Generalized Kirchoff's current and voltage law formulation for coupled circuit-electromagnetic simulation with surface integral equations," *IEEE Trans. Microw. Theory Tech.*, Vol. 52, No. 7, 1673–1682, Jul. 2004.

12. Michalski, K. A. and D. Zheng, "Electromagnetic scattering and radiation by surfaces of arbitrary shape in layered media, Part I: Theory," *IEEE Trans. Antennas Propag.*, Vol. 38, No. 3, 335–344, Mar. 1990.

13. Michalski, K. A. and D. Zheng, "Electromagnetic scattering and radiation by surfaces of arbitrary shape in layered media, Part II: Implementation and results for contiguous half-spaces," *IEEE Trans. Antennas Propag.*, Vol. 38, No. 3, 345–352, Mar. 1990.

14. Michalski, K. A. and J. R. Mosig, "Multilayered media Green's functions in integral equation formulations," *IEEE Trans. Antennas Propag.*, Vol. 45, No. 3, 508–519, Mar. 1997.

15. Michalski, K. A., "Electromagnetic field computation in planar multilayers," *Encyclopedia of RF and Microwave Engineering*, K. Chang, Ed., Vol. 2, 1163–1190, John Wiley, 2005.

16. Harrington, R., *Field Computation by Moment Methods*, IEEE Press, Piscataway, NJ, 1993.

17. Rao, S., D. Wilton, and A. Glisson, "Electromagnetic scattering by surfaces of arbitrary shape," *IEEE Trans. Antennas Propag.*, Vol. 30, No. 3, 409–418, May 1982.

Spectral Shift of an Electromagnetic Gaussian Schell-model Beam

Shijun Zhu and Yangjian Cai

School of Physical Science and Technology, Soochow University, Suzhou 215006, China

Abstract— By using a tensor method, spectral changes of a focused electromagnetic Gaussian Schell-model (EGSM) beam with twist phase. Our results show that the spectral shift of twisted EGSM beam is closely related to the degree of polarization, twist phase and correlation coefficients of the initial beam.

1. INTRODUCTION

Gaussian Schell-model (GSM) beam is a typical scalar partially coherent beam whose spectral degree of coherence and the intensity distribution are Gaussian functions [1–3]. A more general partially coherent beam can possess a twist phase. Twisted GSM beam was introduced by Simon and Mukunda [4]. In the past several years, Electromagnetic Gaussin Schell-model (EGSM) beam (i.e., vectorial GSM beam) has attracted more and more attention owing to its importance in theories of coherence and polarization of light and in some applications, e.g., free-space optical communications [5–8]. More recently, Cai and Korotkova introduced twisted EGSM beam, and studied its propagation in free space [9] and its radiation force on a Rayleigh dielectric particle [10].

The spectral changes of scalar GSM and twisted GSM beams focused by a thin lens were studied in [11, 12]. To our knowledge no results have been reported up until now on spectral changes of an electromagnetic GSM beam with or without twist phase focused by a thin lens. This paper is aimed to investigate spectral shift of a focused twisted EGSM beam.

2. THEORY

The second-order statistical properties of a twisted EGSM beam can be characterized by the 2×2 cross-spectral density matrix $\overleftrightarrow{W}(\mathbf{r}_1, \mathbf{r}_2; 0)$ specified at any two points with position vectors $\mathbf{r}_1$ and $\mathbf{r}_2$ in the source plane with elements [9]

$$W_{\alpha\beta}(\tilde{\mathbf{r}}, \omega, 0) = \frac{A_\alpha A_\beta B_{\alpha\beta} \Gamma_0^2}{(\omega - \omega_0)^2 + \Gamma_0^2} \exp\left[-\frac{i\omega}{2c}\tilde{\mathbf{r}}^T \mathbf{M}_{0\alpha\beta}^{-1}\tilde{\mathbf{r}}\right], \quad (\alpha = x, y; \ \beta = x, y), \tag{1}$$

where A_α is the square root of the spectral density of electric field component E_α, $B_{\alpha\beta} = |B_{\alpha\beta}| \exp(i\phi)$ is the correlation coefficient between the E_x and E_y field components, satisfying the relation $B_{\alpha\beta} = B_{\beta\alpha}^*$, $\mathbf{M}_{0\alpha\beta}^{-1}$ is a 4×4 matrix of the form [9]

$$\mathbf{M}_{0\alpha\beta}^{-1} = \begin{pmatrix} \frac{1}{ik}\left(\frac{1}{2\sigma_{\alpha\beta}^2} + \frac{1}{\delta_{\alpha\beta}^2}\right)\mathbf{I} & \frac{i}{k\delta_{\alpha\beta}^2}\mathbf{I} + \mu_{\alpha\beta}\mathbf{J} \\ \frac{i}{k\delta_{\alpha\beta}^2}\mathbf{I} + \mu_{\alpha\beta}\mathbf{J}^T & \frac{1}{ik}\left(\frac{1}{2\sigma_{\alpha\beta}^2} + \frac{1}{\delta_{\alpha\beta}^2}\right)\mathbf{I} \end{pmatrix}, \tag{2}$$

where $\sigma_{\alpha\beta}$ and $\delta_{\alpha\beta}$ denote the widths of the spectral density and correlation coefficient, respectively. $\mu_{\alpha\beta}$ represents the twist factor and is limited by $\mu_{\alpha\beta}^2 \leq 1/(k^2\delta_{\alpha\beta}^4)$ if $\alpha = \beta$ due to the non-negativity requirement of the cross-spectral density (Eq. (1)) [9]. A_α, $B_{\alpha\beta}$, $\sigma_{\alpha\beta}$, $\delta_{\alpha\beta}$ and $\mu_{\alpha\beta}$ are independent of position but, in general, depend on the frequency. Here we have assumed that the initial spectrum is of the Lorentz type with ω_0 being the central frequency and Γ_0 being the half-width at half-maximum, ω is the angular frequency. $k = \omega/c$ is the wave number with c being the velocity of light in vacuum.

After propagating through an axially nonsymmetric $ABCD$ optical system, the elements of the cross-spectral density matrix can be expressed in the following tensor form [9, 13]

$$W_{\alpha\beta}(\tilde{\rho}, \omega, z) = \frac{A_\alpha A_\beta B_{\alpha\beta} \Gamma_0^2}{(\omega - \omega_0)^2 + \Gamma_0^2}\left[\det\left(\bar{\mathbf{A}} + \bar{\mathbf{B}}\mathbf{M}_{0\alpha\beta}^{-1}\right)\right]^{-1/2} \exp\left[-\frac{i\omega}{2c}\tilde{\rho}^T \mathbf{M}_{1\alpha\beta}^{-1}\tilde{\rho}\right], \quad (\alpha = x, y; \ \beta = x, y) \tag{3}$$

where det stands for the determinant of a matrix, $\tilde{\rho} \equiv (\rho_1 \ \rho_2)$ with ρ_1 and ρ_2 being the transverse position vectors in the output plane, while $\mathbf{M}_{1\alpha\beta}^{-1}$ and $\mathbf{M}_{0\alpha\beta}^{-1}$ are related by the following known

tensor $ABCD$ law [13]

$$\mathbf{M}_{1\alpha\beta}^{-1} = \left(\bar{\mathbf{C}} + \bar{\mathbf{D}}\mathbf{M}_{0\alpha\beta}^{-1}\right)\left(\bar{\mathbf{A}} + \bar{\mathbf{B}}\mathbf{M}_{0\alpha\beta}^{-1}\right)^{-1}. \tag{4}$$

Here $\bar{\mathbf{A}}$, $\bar{\mathbf{B}}$, $\bar{\mathbf{C}}$ and $\bar{\mathbf{D}}$ are 4×4 matrices of the form:

$$\bar{\mathbf{A}} = \begin{pmatrix} \mathbf{A} & 0\mathbf{I} \\ 0\mathbf{I} & \mathbf{A}^* \end{pmatrix}, \quad \bar{\mathbf{B}} = \begin{pmatrix} \mathbf{B} & 0\mathbf{I} \\ 0\mathbf{I} & -\mathbf{B}^* \end{pmatrix}, \quad \bar{\mathbf{C}} = \begin{pmatrix} \mathbf{C} & 0\mathbf{I} \\ 0\mathbf{I} & -\mathbf{C}^* \end{pmatrix}, \quad \bar{\mathbf{D}} = \begin{pmatrix} \mathbf{D} & 0\mathbf{I} \\ 0\mathbf{I} & \mathbf{D}^* \end{pmatrix}. \tag{5}$$

where $\mathbf{A}$, $\mathbf{B}, \mathbf{C}$ and $\mathbf{D}$ are the 2×2 sub-matrices of the $ABCD$ optical system, and "*" in Eq. (9) is required for an general optical system with loss or gain.

3. NUMERICAL RESULTS

The focusing geometry is shown in Fig. 1, where the thin lens with focal length f is located at $z = z_1$ and the exit plane is located at z. Here the transformation matrix of the total optical system between the source plane and the exit plane has the form

$$\begin{pmatrix} \mathbf{A} & \mathbf{B} \\ \mathbf{C} & \mathbf{D} \end{pmatrix} = \begin{pmatrix} \mathbf{I} & (z - z_1)\mathbf{I} \\ 0 & \mathbf{I} \end{pmatrix}\begin{pmatrix} \mathbf{I} & 0\mathbf{I} \\ -(1/f)\mathbf{I} & \mathbf{I} \end{pmatrix}\begin{pmatrix} \mathbf{I} & z_1\mathbf{I} \\ 0\mathbf{I} & \mathbf{I} \end{pmatrix} = \begin{pmatrix} (1-Z)\mathbf{I} & (z - z_1 Z)\mathbf{I} \\ -(1/f)\mathbf{I} & (1 - z_1/f)\mathbf{I} \end{pmatrix}. \tag{6}$$

with $Z = (z - z_1)/f$. The spectral density at point ρ is then given by the formula

$$S(\rho, z, \omega) \equiv \mathrm{Tr}\overleftrightarrow{\mathbf{W}}(\rho, \rho, z, \omega) = W_{xx}(\rho, \rho, z, \omega) + W_{yy}(\rho, \rho, z, \omega). \tag{7}$$

We can calculate the spectral shift of the focused twisted EGSM beam focused by a thin lens by using Eqs. (3)–(7).

In this paper, we only consider the twisted EGSM beam that is generated by a stochastic electromagnetic source whose cross-spectral density matrix is diagonal, i.e., of the form

$$\overleftrightarrow{\mathbf{W}}(\mathbf{r}_1, \mathbf{r}_2, 0, \omega) = \begin{pmatrix} W_{xx}(\mathbf{r}_1, \mathbf{r}_2, 0, \omega) & 0 \\ 0 & W_{yy}(\mathbf{r}_1, \mathbf{r}_2, 0, \omega) \end{pmatrix}. \tag{8}$$

The degree of polarization of the initial source beam at point $\mathbf{r}$ can be expressed as follows [5]

$$P_0(\mathbf{r}, 0, \omega) = \sqrt{1 - \frac{4\det\overleftrightarrow{\mathbf{W}}(\mathbf{r}, \mathbf{r}, 0, \omega)}{[\mathrm{Tr}\overleftrightarrow{\mathbf{W}}(\mathbf{r}, \mathbf{r}, 0, \omega)]^2}}. \tag{9}$$

Under the condition of $W_{xx}(\mathbf{r}_1, \mathbf{r}_2, 0, \omega) = 0$ or $W_{yy}(\mathbf{r}_1, \mathbf{r}_2, 0, \omega) = 0$, the twisted electromagnetic GSM beam reduces to a scalar twisted GSM beam with $P_0(r, 0, \omega) = 1$. In the following numerical examples, we set $\sigma_x = \sigma_y = 3\,\mathrm{mm}$, $A_x = 1$, $B_{xx} = B_{yy} = 1$, $f = 100\,\mathrm{mm}$ and $z_1 = 200\,\mathrm{mm}$. In this case, the polarization properties are uniform across the source plane with $P_0(r, 0, \omega) = |\frac{A_x^2 - A_y^2}{A_x^2 + A_y^2}|$, and the degree of polarization at source plane varies as the value of A_y varies. The parameters used in all numerical calculations are set to $\omega_0 = 3.2 \times 10^{15}\,\mathrm{rad/s}$ and $\Gamma_0 = 0.6 \times 10^{15}\,\mathrm{rad/s}$.
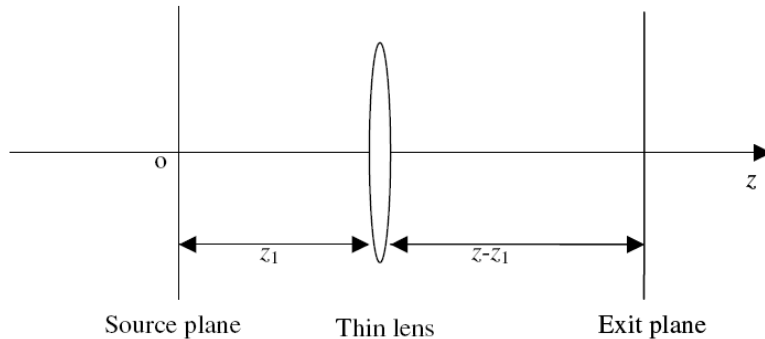

Figure 1: Focusing geometry.

Figure 2: On-axis normalized spectrum $S(0, z, \omega)/S(0, z, \omega)_{\max}$ of a focused electromagnetic GSM beam without twist phase ($\gamma_{xx} = \gamma_{yy} = 0$) at several propagation distances.
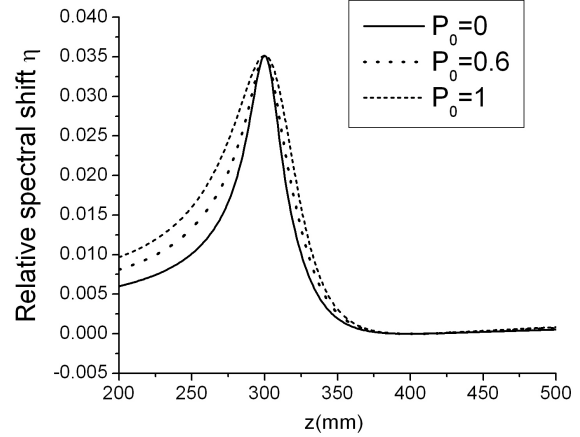
Figure 3: On-axis relative spectral shift η of a focused electromagnetic GSM beam without twist phase ($\gamma_{xx} = \gamma_{yy} = 0$) versus propagation distance for different values of the degree of polarization of the initial beam with $\delta_{xx} = 0.01\,\text{mm}$ and $\delta_{yy} = 0.02\,\text{mm}$.
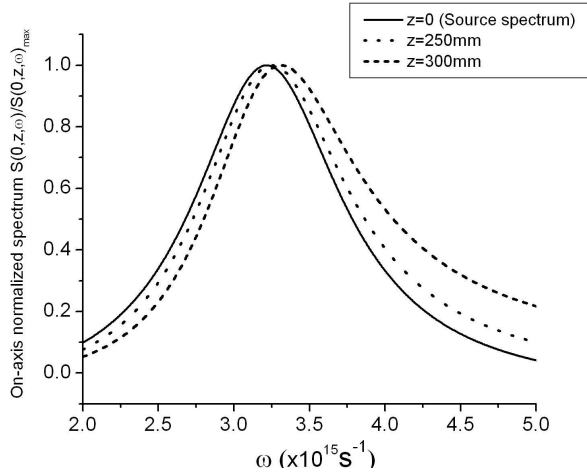
We calculate in Fig. 2 the on-axis normalized spectrum $S(0, z, \omega)/S(0, z, \omega)_{\max}$ of a focused electromagnetic GSM beam without twist phase ($\gamma_{xx} = \gamma_{yy} = 0$) at several propagation distances with $P_0 = 0.6$, $\delta_{xx} = 0.01\,\text{mm}$, $\delta_{yy} = 0.02\,\text{mm}$. For the convenience of comparison, the source spectrum is also calculated (see solid line of Fig. 2). One finds from Fig. 2 that spectrum profile of the on-axis normalized spectrum the focused electromagnetic GSM beam behind the thin lens is similar to the source spectrum, but its peak position is blue-shifted. This phenomenon also occurs for a focused scalar GSM beam as shown in [11, 12].

Now we discuss the dependence of the relative spectral shift of a focused electromagnetic GSM beam on its initial degree of coherence and other beam parameters. The spectral shift $\Delta\omega$ is the difference between the peak frequency ω_m of the spectrum of the field after propagation and the peak frequency ω_0 of the source spectrum. A positive value of $\Delta\omega$ denotes a blue shift, while a negative value represents a red shift. We will study the variation of the relative spectral shift, which is defined as

$$\eta = (\omega_m - \omega_0)/\omega_0. \tag{10}$$

Figure 3 shows the on-axis relative spectral shift η of a focused electromagnetic GSM beam without twist phase ($\gamma_{xx} = \gamma_{yy} = 0$) versus propagation distance for different values of the degree of polarization of the initial beam with $\delta_{xx} = 0.01\,\text{mm}$ and $\delta_{yy} = 0.02\,\text{mm}$. One finds from Fig. 3 that the maximum relative spectral shift of a focused electromagnetic GSM beam occurs at the back focal plane, while the minimum relative spectral shift (i.e., no spectral shift) occurs at the image plane ($z = 400\,\text{mm}$). The results are in agreement with the results derived for the case of scalar GSM beam [11, 12]. It is also evident that the degree of polarization of the initial beam affects the relative spectral shift strongly. The relative spectral shift increases as the degree of polarization increases, while we should note that the position of the maximum relative spectral shift and the position of the zero spectral shift are independent of the degree of polarization.

Figure 4 shows the on-axis relative spectral shift η of a focused twisted electromagnetic GSM beam versus propagation distance for different values of the twist factors γ_{xx} and γ_{yy} with $P_0 = 0.6$, $\delta_{xx} = 0.01\,\text{mm}$ and $\delta_{yy} = 0.02\,\text{mm}$. From Fig. 4, we find that the twist phase has significant influence on the relative spectral shift on propagation. The relative spectral shift on propagation and the maximum relative spectral shift at the back focal plane increase as the absolute values of the twist factors decrease, while zero spectral shift still occurs at the image plane.

All above discussions are confined to the on-axis spectrum and relative spectral shift. In Fig. 5, we calculate the relative spectral shift of a focused twisted electromagnetic GSM beam versus the transverse coordinate x for different values of the degree of polarization of the initial beam at $z = 350\,\text{mm}$ with $\gamma_{xx} = 0.003\,(\text{mm})^{-1}$, $\gamma_{yy} = 0.0002\,(\text{mm})^{-1}$, $\delta_{xx} = 0.01\,\text{mm}$ and $\delta_{yy} = 0.02\,\text{mm}$.
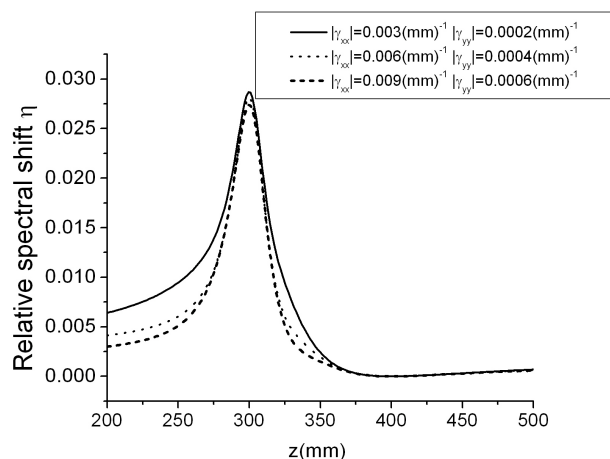
Figure 4: On-axis relative spectral shift η of a focused twisted electromagnetic GSM beam versus propagation distance for different values of the twist factors γ_{xx} and γ_{yy} with $P_0 = 0.6$, $\delta_{xx} = 0.01\,\mathrm{mm}$ and $\delta_{yy} = 0.02\,\mathrm{mm}$.
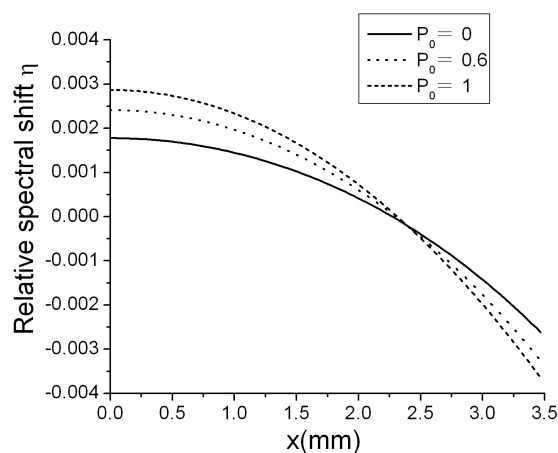
Figure 5: Relative spectral shift of a focused twisted electromagnetic GSM beam versus the transverse coordinate x for different values of the degree of polarization of the initial beam at $z = 350\,\mathrm{mm}$ with $\gamma_{xx} = 0.003\,(\mathrm{mm})^{-1}$, $\gamma_{yy} = 0.0002\,(\mathrm{mm})^{-1}$, $\delta_{xx} = 0.01\,\mathrm{mm}$ and $\delta_{yy} = 0.02\,\mathrm{mm}$.

One finds from Fig. 5 that the relative spectral shift gradually decreases as the transverse coordinate x increases, red shift can be observed when x is enough large. For certain value of transverse coordinate x, no spectral shift occurs. Furthermore, the absolute value of the relative spectral shift increases as the initial degree of polarization increases. Numerical results (not present here to save space) also show that the absolute value of the relative spectral shift decreases as the absolute values of initial twist factors (γ_{xx} and γ_{yy}) increases.

4. CONCLUSION

The spectral shift of a focused twisted EGSM beam focused has been studied in detail. Dependence of the spectral shifts on the degree of polarization, twist phase and correlation coefficients of the initial beam is explored numerically. It is shown that the relative spectral shift of focused twisted EGSM beam is related to the initial beam's parameters, the blue shift occurs at on-axis points, while the red shift can occur at off-axis points.

REFERENCES

1. Mandel, L. and E. Wolf, *Optical Coherence and Quantum Optics*, Cambridge U. Press, 1995.
2. Wolf, E. and E. Collett, "Partially coherent sources which produce same far-field intensity distribution as a laser," *Opt. Commun.*, Vol. 25, 293–296, 1978.
3. Wang, F. and Y. Cai, "Experimental observation of fractional Fourier transform for a partially coherent optical beam with Gaussian statistics," *J. Opt. Soc. Am. A*, Vol. 24, 1937–1944, 2007.
4. Simon, R. and N. Mukunda, "Twist phase in Gaussian-beam optics," *J. Opt. Soc. Am. A*, Vol. 15, 2373–2382, 1998.
5. Wolf, E., "Unified theory of coherence and polarization of random electromagnetic beams," *Phys. Lett. A*, Vol. 312, 263–267, 2003.
6. Gori, F., M. Santarsiero, G. Piquero, R. Borghi, A. Mondello, and R. Simon, "Partially polarized Gaussian Schell-model beams," *J. Opt. A: Pure Appl. Opt.*, Vol. 3, 1–9, 2001.
7. Cai, Y., O. Korotkova, H. T. Eyyuboğlu, and Y. Baykal, "Active laser radar systems with stochastic electromagnetic beams in turbulent atmosphere," *Opt. Express*, Vol. 16, 15835–15846, 2008.

8. Yao, M., Y. Cai, H. T. Eyyuboğlu, Y. Baykal, and O. Korotkova, "The evolution of the degree of polarization of an electromagnetic Gaussian Schell-model beam in a Gaussian cavity," *Opt. Lett.*, Vol. 33, 2266–2268, 2008.

9. Cai, Y. and O. Korotkova, "Twist phase-induced polarization changes in electromagnetic Gaussian Schell-model beams," *Appl. Phys. B*, Vol. 96, 499–507, 2009.

10. Zhao, C., Y. Cai, and O. Korotkova, "Radiation force of scalar and electromagnetic twisted Gaussian Schell-model beams," *Opt. Express*, Vol. 17, 21472–21487, 2009.

11. Palma, C., G. Cincotti, and G. Guattari, "Spectral shift of a Gaussian Schell-model beam beyond a thin lens," *IEEE. J. Quantum Electron.*, Vol. 34, 378–83, 1998.

12. Cai, Y., Y. Huang, and Q. Lin, "Spectral shift of partially coherent twisted anisotropic Gaussian-Schell-model beams focused by a thin lens," *J. Opt. A: Pure App. Opt.*, Vol. 5, 397–401, 2003.

13. Lin, Q. and Y. Cai, "Tensor ABCD law for partially coherent twisted anisotropic Gaussian-Schell model beams," *Opt. Lett.*, Vol. 27, 216–218, 2002.

A Fiber Optic Evanescent Wave Sensor for Measuring Refractive Index Change of Liquids

Chenghua Sui, **Pinghui Wu**, and **Gaoyao Wei**
Institute of Laser and Optoelectronic Technology
Zhejiang University of Technology, Hangzhou 310023, China

Abstract— We demonstrate a novel sensor capable of detecting small refractive index change of liquids using single microfiber. The sensor is based on the principle of optical heterodyne frequency modulation technique and is used to measure the variation of refractive index with concentration of glucose in distilled water. Our experimental results show that the device exhibits the capability of measuring an index variation of $\sim 10^{-5}$. The stability of the sensor, high sensitivity and the simplicity of the design, low cost of fabrication, compact size, and easy integration with optoelectronic devices, make it suitable for chemical, biomedical, pharmaceutical and process control applications.

1. INTRODUCTION

In the past few years, evanescent-field-based optical sensors have been under intensive investigation for deployment as biological and/or chemical sensors. For these applications, small size, high sensitivity, high selectivity, and low detection limits are the dominant requirements. Optical microfiber sensors meet all these criteria due to they have excellent properties such as low cost, low loss, and very large evanescent fields [1–3]. Among the various sensing schemes, refractive index sensing is widely employed since many biological or chemical specimens can be identified by measuring their refractive indices. However, in free space the fabrication of these microfibers with high reliability is challenging due to problems of stability, degradation, coupling, and cleanness. In this paper we demonstrate a robust evanescent wave sensor capable of detecting small refractive index change of liquids using single microfiber. Compared with the multiple-microfiber scheme that relies on the average response of many microfibers, single microfiber detection presents special advantages of high sensitivity and fast response.

2. EXPERIMENTAL

For chemical and biological sensing, compared with the multiple-microfiber scheme that relies on the average response of many microfibers, single microfiber detection presents special advantages of high sensitivity and fast response. In this work, we used a single microfiber as sensing element for detecting specimens in aqueous solutions. As shown in Fig. 1, a certain length of a microfiber is immersed in the solution to be detected, and the microfiber guides light as a single-mode waveguide. An extreme small refractive index change around the microfiber will lead to a change of the propagation constant of the propagating mode, thereby shifting the optical phase of the guided light ($\Delta\Phi$) [4]. For the purpose of detecting slight changes with high sensitivity, we use optical heterodyne frequency modulation technique to measure the phase shift of the probing light.

To study the performance of the sensor, we use the sensor to detect the variation of the refractive indices of glucose solutions with different concentrations, which allow arbitrarily small change of refractive index. The schematic diagram of the sensor is shown in Fig. 2. It consists of light source, oscillator, frequency mixer, photoelectric transducer, oscilloscope, flow cell, microfiber, and lead fiber. Light from a He-Ne laser (with a central wavelength of 632.8 nm) is modulated by O_1 which is used as local oscillator, and has frequency at 100 MHz. The laser is focused on the left end of fiber, and it propagates along the fiber and is coupled into the microfiber. After traveling through the microfiber, the light from the other end of the fiber is translated to electric signal by photoelectric transducer, and then is mixed with another electric signal from O_2 which has frequency at 99.545 MHz by M_2. The mixed frequency is used as measured heterodyne frequency signal y_2. At the same time another electric signal from the M_1 which is mixed by the frequency from O_1 and O_2, is used as reference heterodyne frequency signal y_1. In this case, the optical phase shift (i.e., $\Delta\Phi = |y_1 - y_2|$) will be monitored by a two channel digital oscilloscope, and the information of specimens can be retrieved.

In our experiment, in order to perform the low-loss input and output connections, the microfiber (approximately 1.2 µm in diameter and 5 mm of effective interaction length), which was fabricated
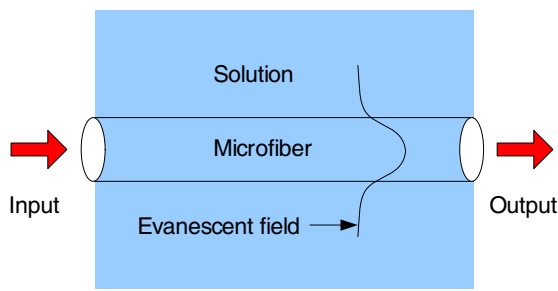
Figure 1: A microfiber sensing element in solution.
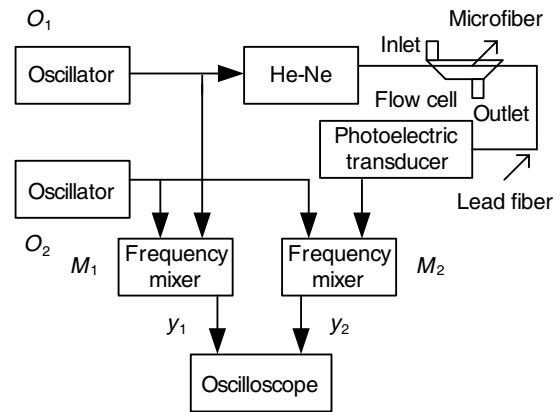
Figure 2: Schematic of the sensor with optical heterodyne frequency modulation technique.
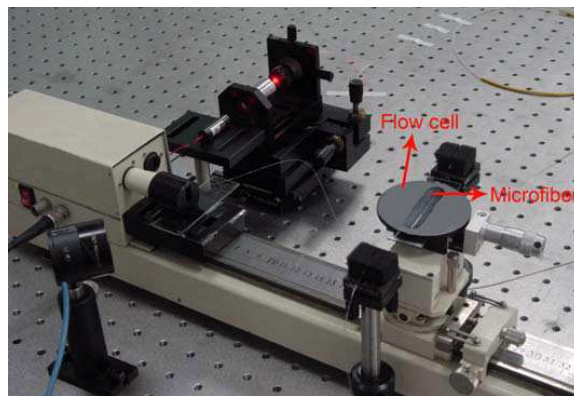
Figure 3: Photograph of the experimental set-up used to test the sensor.

by flamed-heated taper-drawing of a sing-mode fiber (Corning SMF 28) [1], was connected to optical fiber at both extremities by conical transition regions. Several solutions were prepared with different glucose concentrations in distilled water, with the refractive indices varying from 1.3322 to 1.3340 in step of 0.0003, as determined by an Abbe refractometer operating at room temperature. A flow cell was made of Aluminum with an inlet and an outlet to allow the solutions flow in and out. We first immersed the microfiber in distilled water (refractive index is 1.3322), and then modify the refractive index by delivering glucose solutions into the sensitive area using a microlitre syringe. In Fig. 3 we show the photograph of the experimental set-up that was used to test the sensor.

3. RESULTS AND DISCUSSION

Figure 4 shows the response of the sensor in different refractive indices. As expected, the reference heterodyne frequency signal is fixed, and the measured heterodyne frequency signal shifts towards the left as the refractive index increases. The experimental data were obtained with the sensor and calculated is plotted in Fig. 5. For comparison, using the parameters described above, phase shifts can be obtained by numerically solving Maxwell's equations [4]. Thus in Fig. 5 we also plot the theoretical prediction of the phase shifts as a function of the refractive index variation. It is clear that the experimental values are in close agreement with the theoretical values. Moreover, the curve shows excellent linear dependence of the phase shift on the increasing refractive index. The sensitivity of the sensor, defined as the slope of the line, was evaluated to be about 3655 rad. This number is much higher than conventional optic fiber sensors. In addition, the sensitivity can be enhanced with the decreasing of the microfiber diameter. For example, when the fiber diameter is 800 nm, the sensitivity can up to ~ 9910 rad. We believe that higher sensitivity can be achieved by improving the manufacturing technology.

Beside the sensitivity, the detection limit is a very important parameter to evaluate the sensing capability of a device. In practice, the detection limit of the sensor is limited by the performance
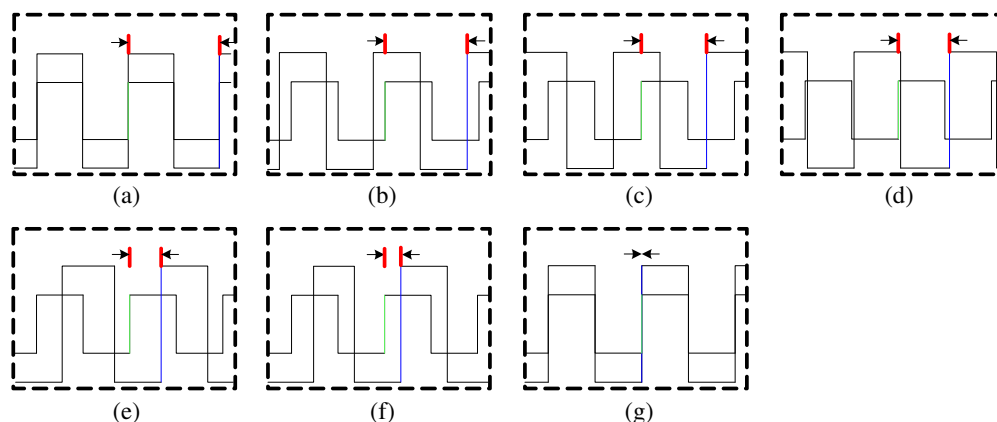
Figure 4: Response of the sensor in different refractive indices: (a) 1.3322, (b) 1.3325, (c) 1.3328, (d) 1.3331, (e) 1.3334, (f) 1.3337, (g) 1.3340. (Green line is reference signal, blue line is measured signal).
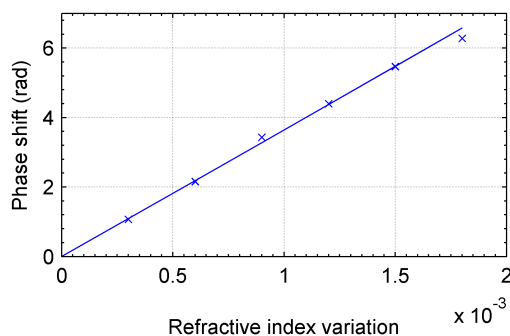
Figure 5: Comparison of experimental ($\times$) and theoretical (solid line) phase shifts as a function of the refractive index variation.

of the whole measuring system. In our experiment, the bandwidth of the oscilloscope is 40 MHz, which indicates the sensor has the potential to detect an index variation of $\sim 10^{-5}$.

4. CONCLUSION

In summary, a simple sensor has been designed and developed for sensing the variation of refractive index with concentration of glucose in distilled water. The sensing principle is based on the heterodyne frequency modulation technique. In the sensor, phase shifting is caused by the refractive index changes in the environment of the microfiber. The fabrication process and the testing of the prototype sensing devices have been described, showing the potential measurement accuracy to be the order of $\sim 10^{-5}$. Advantages of the sensor reported here include high sensitivity, easy fabrication, compact size, and easy integration with optoelectronic devices. Therefore, the sensor can be applied to many fields, including bio/chemical analyses, environmental monitoring, and pharmaceutical and process control.

ACKNOWLEDGMENT

REFERENCES

1. Tong, L. M., R. R. Gattass, J. B. Ashcom, S. L. He, J. Y. Lou, M. Y. Shen, I. Maxwell, and E. Mazur, "Subwavelength-diameter silica wires for low-loss optical wave guiding," *Nature*, Vol. 426, No. 6968, 816–819, 2003.

2. Brambilla, G., V. Finazzi, and D. J. Richardson, "Ultra-low-loss optical fiber nanotapers," *Opt. Express*, Vol. 12, No. 10, 2258–2263, 2004.

3. Leon-Saval, S. G., T. A. Birks, W. J. Wadsworth, P. S. J. Russell, and M. W. Mason, "Supercontinuum generation in submicron fibre waveguides," *Opt. Express*, Vol. 12, No. 13, 2864–2869, 2004.

4. Lou, J. Y., L. M. Tong, and Z. Z. Ye, "Modeling of silica nanowires for optical sensing," *Opt. Express*, Vol. 13, No. 6, 2135–2140, 2005.

Ultrasonic Wave Detection in Atmospheric Pressure Plasma Using Fraunhofer Diffraction Effect

Toshiyuki Nakamiya[1], **Fumiaki Mitsugi**[2], **Shota Suyama**[2], **Tomoaki Ikegami**[2],
Yoshito Sonoda[1], **Yoichiro Iwasaki**[1], **and Ryoichi Tsuda**[1]

[1]Graduate School of Industrial Engineering, Tokai University
Toroku 9-1-1, Kumamoto 862-8652, Japan
[2]Graduate School of Science and Technology, Kumamoto University
Kurokami 2-39-1, Kumamoto 860-0082, Japan

Abstract— We present a new diagnostic system to measure audible sound or ultrasonic wave emitted from electric discharge using Fraunhofer diffraction effect of visible laser beam by compression wave of atmosphere. This new system is called the optical wave microphone by us and is very useful for the detection of sound wave without disturbing the sound field. Moreover, this system is available for the use in the strong electric field. In this work, we applied the optical wave microphone to observe the emission of the ultrasonic wave from a Coplanar DBD (Dielectric Barrier Discharge) in air. Time-resolved waveform of the applied voltage, the current and the ultrasonic wave were measured simultaneously and examined the fundamental relationship between the micro discharge and the acoustic properties. The Fast Fourier Transform (FFT) is applied to discriminate the acoustic sound of the Coplanar DBD discharge and the dominant frequency components. We expect that the understanding of acoustic and ultrasonic properties gives more details of electric discharges and also develops new applications in the field of medical diagnostics, environment system and so on.

1. INTRODUCTION

The dielectric barrier discharge (DBD) has attracted much interest due to the promising applications such as pollutant gas removal and ozonizer. In addition, recently, coplanar type surface discharge, which is one of the DBDs, has been researched as a plasma actuator which applies the ionic wind originated from the discharge [1]. Most of electric discharges emit acoustic ($20 \sim 20,000\,\mathrm{Hz}$) and ultrasonic (over $20\,\mathrm{kHz}$) waves [2–4]. Continuous and pulsed voltages initiate the electric breakdown which generates pressure deviation from equilibrium pressure. The sound waves are generated by the pressure change causing local compression and rarefaction. We focus on the sound and ultrasonic waves which are emitted from the discharge because the sound signal includes the information about the discharge and the atmospheric condition around the discharge. We have previously used a conventional condenser microphone to detect the discharge sound [2–4]. However, the frequency range can not cover over $100\,\mathrm{kHz}$ which may be generated by the pulsed discharge. Moreover, it is not suitable to place the condenser microphone between or near the electrodes of the discharge device because it affects the electric field between the electrodes.

Therefore, we applied a new diagnostic method of an optical wave microphone to detect the sound and ultrasonic waves [5, 6]. The optical wave microphone is based on Fraunhofer diffraction between the sound wave and the laser beam. Then, it is composed of a laser, a lens and a detector. This method is very useful to detect not only audible sound but also ultrasonic wave without disturbing the sound field and the electric field in case of the discharge. This method also has potential to diagnose plasma of the discharge during the operation.

In this paper, we measured the ultrasonic wave emitted from the coplanar DBD using the optical wave microphone. The condenser microphone was also used for comparison. The time-resolved waveforms of the applied voltage, the current and the ultrasonic wave were measured simultaneously and the relationships were analyzed. The FFT (Fast Fourier Transform) analysis was also performed to identify the frequency components.

2. EXPERIMENTAL PROCEDURE

2.1. Principal of Optical Wave Microphone

The most fundamental construction of the optical wave microphone consists of a laser, a lens and a photo detector. The sound wave should exist between the laser and the lens. When the incident laser beam crosses a sound wave, diffracted waves are generated and propagate with the penetrating
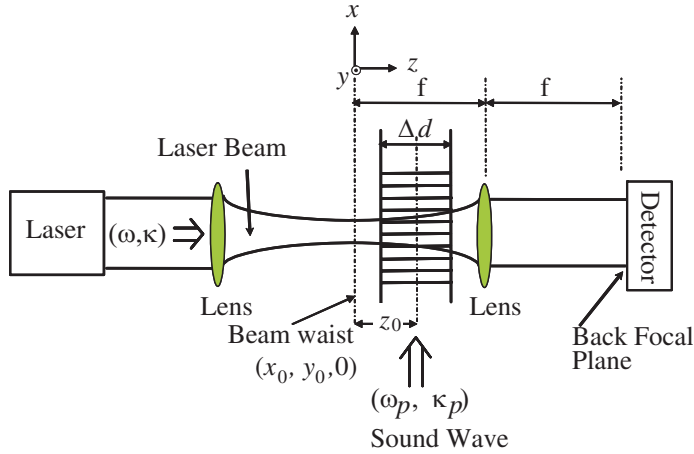
Figure 1: Schematic representation of optical wave microphone.
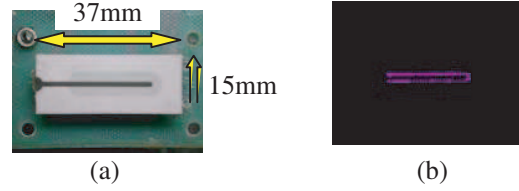
Figure 2: Photographs of (a) coplanar DBD device and (b) light emission from the discharge.

beam through the Fourier optical lens and reach the observing plane, which is set at the Fraunhofer diffraction region or in the back focal plane of the lens. The diffracted optical waves are homodyne-detected by using the penetrating optical wave as a local oscillating power. The spatial intensity of diffracted waves of higher orders is much smaller than that of the first order wave and can be neglected. The spatial intensity of the first vibration elements (I_{ac}) of the resultant optical field at the back focal plane is given by the following equation [7–10].

$$I_{ac} = I_0 \Delta\phi_0 \left[\exp\left\{ -\left(u^2 + (u-\theta)^2 \right) \right\} - \exp\left\{ -(u^2 + (u+\theta)^2) \right\} \right] \sin \omega_p t \tag{1}$$

where $I_0 = (2P_0/\pi w_f^2) \exp[-2(y_f/w_f)^2]$, (x_f, y_f): x_f and y_f denote the location coordinate on a detection face, and the y direction in the direction parallel to the forward direction of the sound wave, $u = x_f/W_f$: The normalized x-coordinate in the back focal plane, $\theta = k_p W_0/2$: The normalized wave number, ω_P: The angular frequency of sound field, W_f: The beam size in the focal plane, $k_p(= 2\pi/\lambda_p)$: The wave number of sound wave, W_0: The spot size, P_0: The total incident power, $k_i(= 2\pi/\lambda_i)$: The wave number of incident beam, λ_i: The wave length of probing beam, $\phi_0 = \kappa_i(\mu_0 - 1)\Delta d$: The time-constant of component of phase modulation, $\Delta\phi_0 = \kappa_i \Delta\mu_0 \Delta d = \kappa_i(\mu_0 - 1)\Delta d \Delta p/\gamma p$: The time-dependent component of phase modulation, μ_0: The reflective index of air, γ: The specific heat ratio, Δd: The width of sound wave, p: The air pressure, Δp: The intensity of sound wave, $\rho = z_0/Z_R$: The spatial position parameter of sound wave normalized by the Rayleigh zone, z_0: The distance from the beam waist to the wave position, and $Z_R = \kappa_i W_0^2/2$: The Rayleigh zone.

2.2. Experimental Setup

Figure 2(a) is a photo of the coplanar DBD device ($37\,\text{mm} \times 15\,\text{mm}$). There are a line type top electrode and a plane type back electrode which is buried inside the ceramics. This type of discharge has generally been used as an ozonizer but has recently attracted much attention because of its potential as a plasma actuator. The coplanar DBD was generated in the air by applying the high voltage (approximately $6\,\text{kVpp}$, sine wave, $28.6\,\text{kHz}$) between the electrodes of the device. The light emission mainly emitted from N_2 second positive band is observed as can be seen in Fig. 2(b).

The discharge also emits the audible sound wave and the ultrasonic wave. We measured the time-resolved waveforms of the applied voltage, the current and the sound using the measurement system shown in Fig. 3. The applied voltage and the current were measured by a high voltage probe and a current transformer (frequency range $= 1\,\text{kHz}–1\,\text{MHz}$), respectively. The discharge sound was detected by the optical wave microphone and a condenser microphone (Rion, UC-29, $20\,\text{Hz}–100\,\text{kHz}$) for comparison. The condenser microphone was fixed at $2\,\text{cm}$ above the device. The discharge sound crosses the laser beam at the region between the laser and the Lens1. The probing diode laser beam ($685\,\text{nm}$, $28\,\text{mW}$, $\phi 2\,\text{mm}$) runs $1\,\text{cm}$ above the discharge device and the diffracted laser beam is performed the optical Fourier transform by the Lens1 and detected by a photodiode detector. In this experiment, the diameter of the laser beam which arrives at the
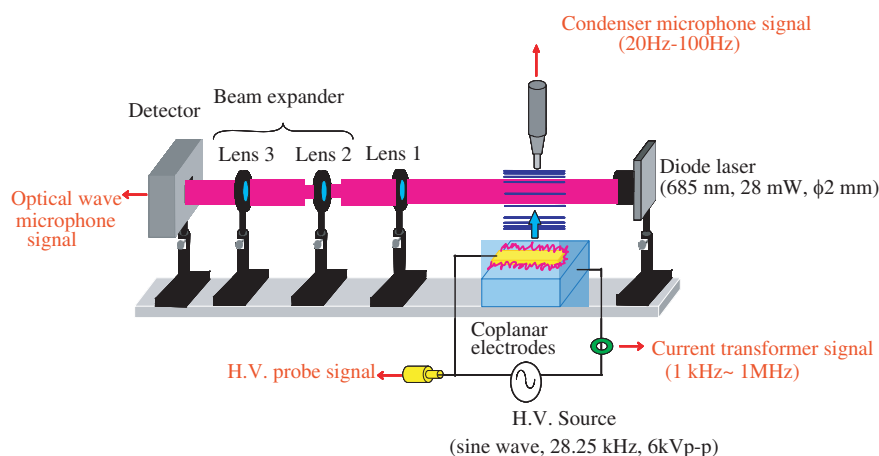
Figure 3: Experimental setup to detect the discharge sound using optical wave microphone.
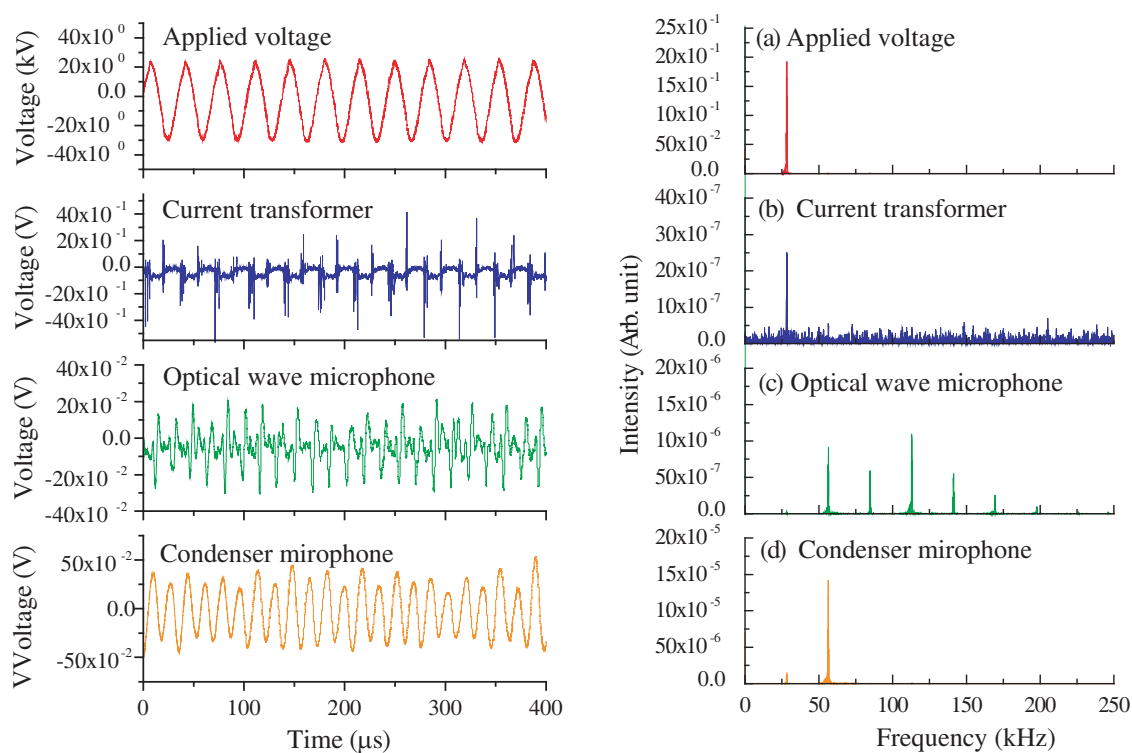
Figure 4: Typical voltage waveforms and FFT spectra obtained from (a) High voltage probe. (b) Current transformer. (c) Optical wave microphone and (d) Condenser microphone.

detector is adjusted by a beam expander (Lens2 and Lens3) with taking into account that of the detector. The time-resolved waveforms from the applied voltage probe, the current transformer, the condenser microphone and the optical wave microphone were stored simultaneously in the digital oscilloscope (Tektronix TDS3034) and the FFT analysis was performed.

3. RESULTS AND DISCUSSION

Figure 4 shows the typical voltage waveforms obtained from (a) high voltage probe, (b) current transformer, (c) condenser microphone and (d) the optical wave microphone in air. The measurement time is 400 μs. When the high voltage is applied to the electrodes, the discharge current appears and the discharge sound has been generated. The discharge sound is detected by the optical wave microphone and the condenser microphone. These generation time of the discharge current and the sound signal are fairly in good agreements.

The results of FFT analysis are shown in the range of 0 to 250 kHz. The coplanar DBD occurs

two times in a cycle of applied voltage. The FFT result for the current transformers presents in Fig. 4(b) and the large peak appears at 28.3 kHz which almost corresponds to the frequency of the applied voltage due to the relatively large displacement current. The FFT result for the optical wave microphone is shown in Fig. 4(c). It contains many frequency components such as 56.5, 84.6, 113.0, 141.3, 169.4 and 197.8 kHz. These values are almost same with 2nd, 3rd, 4th, 5th, 6th, and 7th harmonics frequency of applied voltage. Fig. 4(c) may be shown that the electric wind, which is due to the migration of ions inside plasma, is produced or/and the discharge device is vibrated by the applied voltage. The FFT result of the condenser microphone (Fig. 4(d)) shows that the main frequency components are 28.2 and 56.4 kHz. The condenser microphone is difficulte to detect the high frequency components that the optical wave microphone have detected, because the optical wave microphone is more sensitive compared with the condenser microphone at the high frequency region.

4. CONCLUSION

The sound signal generated by the coplanar DBD was detected by the optical wave microphone and the condenser microphone, and the discharge sound was analyzed by FFT. The optical wave microphone is very convenient to detect the ultrasonic wave generated by coplanar DBD over 100kHz which condenser microphone can not detect.

ACKNOWLEDGMENT

REFERENCES

1. Laurentie, J. C., J. Jolibois, and E. Moreau, "Surface dielectric barrier discharge: Effect of encapsulation of the grounded electrode on the electromechanical characteristics of the plasma actuator," *Journal of Electrostatics*, Vol. 67, 93–98, 2009.
2. Nakamiya, T., K. Ebihara, T. Ikegami, Y. Sonoda, and R. Tsuda, "Acoustic spectra characteristics of creeping discharge," *The 5th Asia-Pacific International Symposium on the Basic and Application of Plasma Technology*, Vol. 5, 82–85, 2007.
3. Nakamiya, T., K. Ebihara, T. Ikegami, Y. Sonoda, and R. Tsuda, "Acoustic signal analysis in the creeping discharge," *Journal of Physics: Conf.*, Vol. 100, 062016, 2008.
4. Nakamiya, T., T. Tanaka, K. Ebihara, T. Ikegami, and R. Tsuda, "Acoustic signal analysis in the partial discharge by short time fourier transformation," *The Papers of Technical Meeting on Plasma Science and Technology, IEE Japan*, Vol. PST-04-80, 45–49, 2004.
5. Nakamiya, T., Y. Sonoda, T. Ikegami, F. Mitsugi, K. Ebihara, and R. Tsuda, "Measurement of electric discharge sound by Fraunhofer diffraction and analysis," *Przegląd Elektrotechniczny (Electrical Review)*, Vol. 2009, No. 5, 143–146, 2009.
6. Nakamiya, T., F. Mitsugi, S. Suyama, T. Ikegami, Y. Sonoda, Y. Iwasaki, and R. Tsuda, "Investigation of electric discharge sound in atmospheric pressure plasma," *Journal of AOT's*, Vol. 13, 43–49, 2010.
7. Evans, D. E., M. von Hellermann, and E. Holzhauer, *Plasma Phys. Control. Fusion*, Vol. 24, 819, 1982.
8. Sonoda, Y., Y. Suetsugu, K. Muraoka, and M. Akazaki, *Plasma Phys. Control. Fusion*, Vol. 25, 1113, 1983.
9. Sonoda, Y. and M. Akazaki, "Measurement of low-frequency ultrsonic waves by fraunhofer diffraction," *Jpn. J. Appl. Phys.*, Vol. 33, 3110–3114, 1994.
10. Evans, D. E., E. J. Doyle, D. Frigione, M. von Hellermann, and A. Murdoch, *Plasma Phys.*, Vol. 25, 617, 1983.

Dielectric-dielectric Composite Photonic Crystals for Negative Refraction of Unpolarized Electromagnetic Waves

N. Yogesh and V. Subramanian

Microwave Laboratory, Department of Physics
Indian Institute of Technology Madras, Chennai-600 036, India

Abstract— The investigations on negative refraction of unpolarized microwaves in dielectric-dielectric composite photonic crystals are presented. Similar to metal-dielectric composite photonic crystals, common negative refraction regime for both polarization modes (transverse electric and transverse magnetic) are also found in these dielectric composites. This paper further investigates the beam steering ability of an unpolarized microwave in these composites by analyzing the angular dispersion characteristics of both polarization modes. One can utilize this beam steering ability in the fields of far-field imaging and microwave devices.

1. INTRODUCTION

The theoretical framework given by Veselago [1] on the properties of linear, isotropic and homogenous medium which possessing simultaneous negative values of permittivity (ε_r) and permeability (μ_r) revealed the phenomena of left-handed electromagnetism such as negative refraction, reversal of Doppler shift and Cherenkov radiation. Among these, the negative refraction is given prominent attention since it leads to the sub-wavelength imaging as suggested by Veselago and later by Pendry [2]. Apart from natural materials, the experimental evidence of negative refraction was found in an artificial composite medium called as metamaterials consisting of periodic arrangement of metallic wires (responsible for negative permittivity) and split-ring resonators (responsible for negative permeability) in the plasmonic resonance regime [3].

Notably, the subject of negative refraction not only confined with search of simultaneous negative values of ε_r and μ_r in composite medium but also extended into class of periodic arrangement of dielectric/magnetic constituents in air/dielectrics called photonic crystals (PC). The unusual refraction is also found in these PCs [4], which are categorized as 1) AANR — all angle negative refraction [5], in which the periodic medium possess neither negative permittivity nor negative permeability and 2) left-handed behavior [6], in which the group and phase velocity vectors are anti parallel with each other inside the PC.

Based on these behaviors, PCs are also identified as potential candidate for sub-wavelength imaging systems [7] and also revealed other promising applications including super-prism effect [8] and wave confinement [9]. However, these applications are for either transverse electric (TE) or transverse magnetic (TM) modes. Other than one-dimensional periodic systems (Only for the case of normal incidence), in higher dimensional systems, the degeneracy of polarization modes splits up into either TE or TM. In the broader sense, other than lasers, specific polarization of electro magnetic (e-m) waves cannot be expected. This defines the problem of finding the common anomalous dispersion characteristics for both polarization modes in PCs and it was first addressed by X. Zhang [10] in a metal-dielectric composite PC. Though common negative refraction regime for both the polarization modes are found in these composites, the use of metal leads to undesired losses. Another possible drawback is the truncation and termination effect. In fact, any real time applications of PC are possible only through proper truncation at both the input and output interfaces. In such a case, one cannot maintain the common negative refraction regime as far as the phase is concerned, even though the frequencies are matched.

Among these issues, it is natural to ask, is it possible to have common negative refractive regime for both polarization modes with pure, real, positive dielectric constituents? This paper addresses this issue with the analysis of dielectric-dielectric composite PC and presents the numerical demonstration of negative refractive behavior and super-lens effect for both the polarization modes. Owing to the applications in radiating systems in microwave length-scales, the beam steering aspect in these PC is also addressed.

2. BAND STRUCTURE ANALYSIS

It is a well known fact that the unusual refraction in PCs can either be based on partial band gap effects [11] or be based on negative slope of higher bands [12]. In the latter case, the PCs

are characterized with the negative phase index. To find the common negative refraction for both polarization modes, one should have common band gaps with common band edge frequencies (almost not possible alone with dielectric constituents) or should utilize the common negative slope from band profiles of both the modes. As far as the band gap effect is concerned, the dielectric rods in air medium highly favors to TM mode (electric field parallel to the axis of the dielectric cylinders) and the air holes in dielectric substrate favors to TE mode (magnetic field parallel to the axis of the dielectric cylinders). If one merges these structures with dielectric components, the resulting PC configuration would be dielectric constituents in dielectric background (referred as dielectric-dielectric composite PC). By varying the index contrast between the background and core, one can have various polarization devices such as beam splitter and even a device with common dispersion characteristics for both the polarization modes.

The composite PC studied in this work consists of dielectric square rods with the relative permittivity (ε_r) of 3.6 (for example ebonite rods) arranged in dielectric background with the relative permittivity (ε_r) of 5.5 (ordinary glass medium) in a square lattice basis. The normalized size of the square rod would be $0.3a$. To account for the truncation effect, the square shape is considered among the circular, triangular and hexagon shapes. Band structure calculations are carried out using MPB [13], which treats the Maxwell's wave equation as the Hermitian eigenvalue problem with the plane wave basis and are plotted in Figs. 1(a) and 1(b), which specify the two modes of operations with respect to specific symmetry points M and Γ respectively. It should be noted that such low filling fraction of ebonite (around 9%) in the glass medium (91%) doesn't leads to the formation of band gap for either TE or TM. As from Figs. 1(a) and 1(b), one can utilize the negative slope of the bands for unusual refraction behavior. The choice of utilization of band profiles in the specific symmetry directions of ΓM and ΓX is best revealed through the plot of Equifrequency contours (EFC) for selected frequencies and it is given in Fig. 2.

It is clear from Fig. 2(a) that the frequencies ranging form 0.216 to 0.245 ($2\pi c/a$) are all concave with respect to M point and cannot be used for negative refraction behavior, even though they show common dispersion for both TE and TM modes. Since the negative refraction behavior with respect to M point requires all convex contours so that e-m wave incident towards the ΓM direction bends towards the same side of the normal according to the boundary condition. Higher frequencies such as 0.273 ($2\pi c/a$) can be looked for negative refraction due to their flatness but it is not common for both TE and TM modes. On the other hand, Fig. 2(b) shows the EFC for the second band for TE and TM modes, in which the contours are convex with respect to Γ symmetry point. Hence an e-m wave incident towards ΓX direction for the range of frequencies 0.3 to 0.32 ($2\pi c/a$) (choice is also based on Fig. 1(b)) shows the unusual refraction behavior and super-lens effect for both TE and TM modes. It is also to be noted that the uniqueness of dispersion trend departs as frequency increases further from (0.32 ($2\pi c/a$) onwards), though shape remains same for both TE and TM modes.

Before proceeding with field pattern analysis, one can look for the considerable population of Bloch's modes for TE and TM in the target range of 0.3 to 0.32 ($2\pi c/a$) by plotting the density of

(a)   (b)
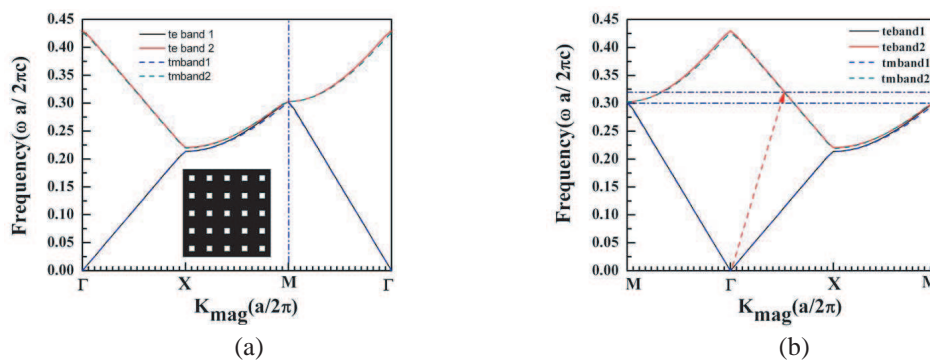
Figure 1: (a) Shows the band profile of the composite PC studied in this work. The inset shows the geometry of the composite PC. The dash-dotted line represents the mode of operation towards the M symmetry point. Γ, X and M are the highest symmetry points of the irreducible Brillouine zone of the square lattice. (b) The band profile specifies the mode of operation in Γ point. The dotted line shows incident radiation direction. The dash-dotted lines specifies the frequency of interest in the range of 0.3 to 0.32 ($2\pi c/a$). 'a' is the lattice constant.

states for both the polarizations and it is given in Fig. 3(a). This assures the further refinement of frequency range for common dispersion, in which the range of frequencies 0.319 to 0.3198 $(2\pi c/a)$, the states are equally populated for both TE and TM (indicated in Fig. 3(a) with dash-dotted lines).

For the normalized frequency (ω) of 0.319 $(2\pi c/a)$, EFCs in PC (for both TE and TM) and in air medium are plotted in Fig. 3(b). Rightness of the system (positive or negative) is decided by the band slope (Fig. 1(b)), EFC curvature (Fig. 2(b)) and construction line (parallel component of the incident wave vector (Fig. 3(b)) for a given frequency. It is evident from Figs. 2(b) and 3(b) that as frequency increases, the radius of curvature of EFC contours is shrinking towards the Γ symmetry point. Moreover the band slope is negative for this frequency regime. This implies the left-handed behavior, in which the group and phase velocity vectors are anti-parallel with each other. By considering these things in to the boundary condition (referring with construction line), an incident ray with an inclined angle toward the ΓX symmetry direction shows positive refraction of the beam accompanied by the negative refraction of the phases. It is to be noted that whether the refraction behavior of the PC for second band frequencies is positive or negative and even multi-refringence, the phase velocity is always negative inside the PC. Interestingly, the convex curvature of the EFC with respect to Γ symmetry point and negative refraction of the phase component are fair enough to focus the e-m wave radiation along with sub-wavelength feature in the form of point source placed near the PC slab.
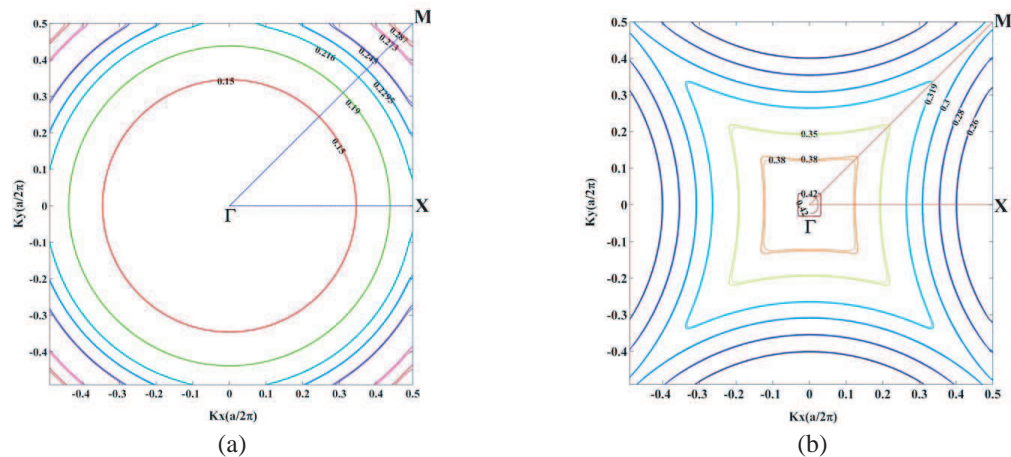
Figure 2: (a) Shows EFC plot corresponding to the band 1 frequencies for both the polarization modes. (b) Shows the EFC plot for the band 2 frequencies. TE and TM modes are differentiated by solid and dotted lines respectively.
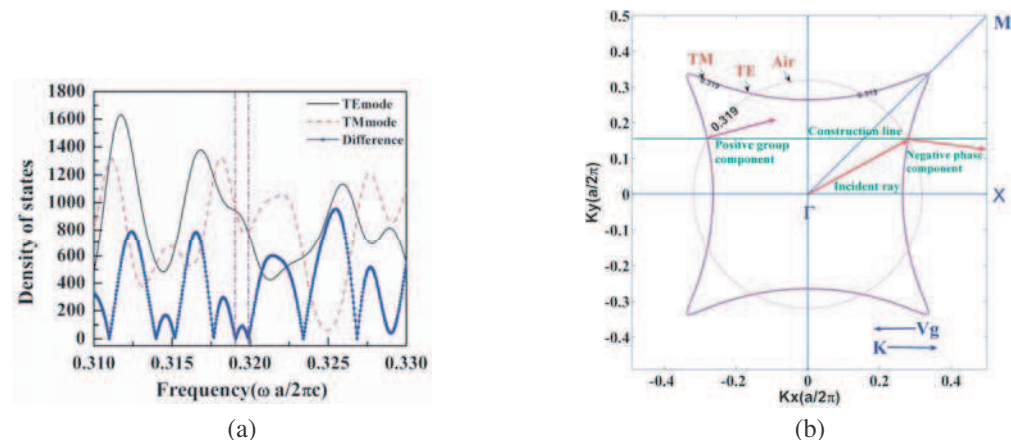
Figure 3: (a) The plot of density of states in the range of frequencies 0.31 to 0.33 $(2\pi c/a)$. Equally populated states are indicated with dash-dotted lines. (b) Shows the ray picture corresponding to the frequency of 0.319 $(2\pi c/a)$ for both TE and TM modes.

3. ANOMALOUS REFRACTION AND SUPER-LENS EFFECT

The analysis of fields in the composite PC for both TE and TM modes are carried out in finite-element methodology based electromagnetic solver FEMLAB [14]. The PC slab of 23 layers in lengthwise and 7 layers in breadth wise is taken in a computational domain, around which low reflecting boundary conditions are employed to minimize the reflections. To study the anomalous dispersion in composite PC, the computational domain is discretized with extra fine meshes along with refinement (in order to avoid the numerical dispersion at higher frequencies) A plane wave source of size 5 cm is taken and the wave is launched at an incident angle of $15°$. For a specific microwave length-scale (a) of 1.2 cm, the normalized frequency (ω) 0.319 $(2\pi c/a)$ corresponds to the operating frequency of 7.975 GHz. The field patterns of Ez (TM) and Hz (TE) corresponding to this frequency shows unusual refractive behavior for both the polarization modes as per the ray picture given in Fig. 3(b). It should be noted from Fig. 4(b) that change of termination scheme $(0.2a)$ employed at the input/output interface of the composite PC strongly influences the refractive behavior of both TE and TM modes, in which common unusual refraction regime delimited by the phase components (Here the phase delay (TE) and phase advance (TM) are referred with respect to the initial phases of the time averaged field components of both TE and TM modes given in Fig. 4(a)).

Beside the termination effect, the common objective is to show the imaging behavior of the proposed composite PC for both TE and TM modes. Hence further computations are carried out for point source object placed near the PC slab. The field patterns given in Fig. 5 clearly demonstrate the super-lens effect for both the polarization modes, for a point source object placed at $0.18a$ $(a$ — fundamental length-scale) from left side of the composite PC slab. The slab width is taken to be $6.3a$ and the operating wavelength chosen for imaging behavior is 3.7654 cm (7.96735 GHz). In a normalized scale this frequency corresponds to 0.3187 $(2\pi c/a)$, which shows the common dispersion behavior for both TE and TM modes. The computed spot sizes (full width at half maximum) from the normalized intensity distribution of both the modes given in Fig. 5(b) are 0.345λ for TE and
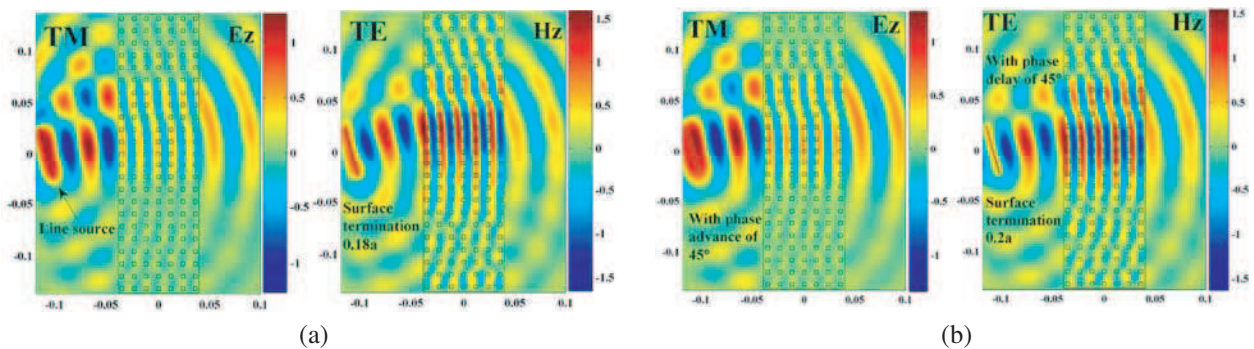
Figure 4: Shows the time averaged field patterns corresponding to both the polarization modes at 7.975 GHz. Plane wave source is inclined at angle of $(\theta_{incident})$ $15°$. The domain is taken in SI units (meter). (b) Shows the effect of termination when it is changed from $0.18a$ to $0.2a$ and other parameters are remaining same.
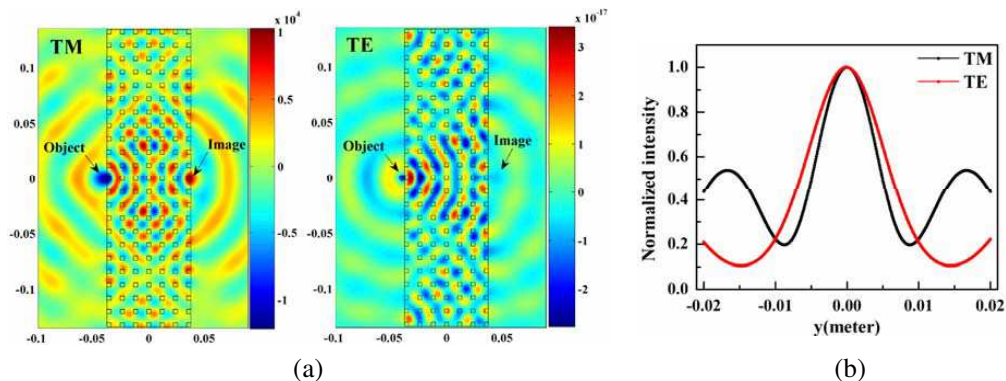
Figure 5: Shows the imaging behavior of composite PC for both TM and TE modes for point source object placed at $0.18a$ from left side of the PC slab. The operating wavelength is 3.7654 cm (7.96735 GHz). The color bar indicates the electric (TM) and magnetic (TE) field strengths respectively. (b) Shows the intensity plot of images for both TE and TM modes. X axis represents the scanning length in y direction.

0.264λ for TM. This demonstrates the super-lens effect of the proposed composite PC irrespective of the polarization state of the e-m wave.

Since the proposed PC mostly resembles the uniform glass medium (91%), the results have to be compared and verified with respect to propagation of wave in a uniform glass medium for the same parameters and it is given in Fig. 6. By comparing the Figs. 5 and 6, one can realize the importance of modulation effect of the dielectric constituents (the need of PC) against the ordinary glass medium, in which a uniform glass does not show the imaging effect for both TE and TM modes. This preserves the necessity of dielectric-dielectric composite PC for common dispersion characteristics so that one can have near field lens even for an unpolarized e-m wave.

4. BEAM STEERING ASPECT

It is advantageous to have common dispersion regime, which is favorable for beam steering ability to both TE and TM modes. As one step further, the beam steering aspect is addressed in dielectric-dielectric composite PC. In this work triangular lattice is considered instead of square lattice and other parameters of the composite PC are remaining unchanged. The wave-vector diagram given in Fig. 7 reveals the common beam steering aspect to both TE and TM modes for composite PC with triangular basis.

An e-m wave with an angular frequency of $0.2705\,(2\pi c/a)$ incident on composite PC towards ΓK symmetry direction with various incident angles ranging from $12°$ to $36°$ shows two interesting features common to both TE and TM modes. The first one involves the beam steering ability: For an incident angle ranging from $12°$ to $34°$, the beam steering is almost unique inside the PC, where the computed steering angle from the ray picture is around $50°$. But when an incident angle slightly changed from $34°$ to $35°$, the propagation is entirely different (one can refer Fig. 7.), in which beam steering angle reduced to $15°$ due to the anomalous behavior of PC (one can see the change of curvature of the EFC in Fig. 7). For this case, the composite PC acts as demagnifier with demagnification of the order of 35 for both the polarization modes.

The second feature corresponds to the frequency dispersive steering: As per the ray picture, at an incident angle of $35°$, the angular frequencies of $0.295\,(2\pi c/a)$ and $0.2705\,(2\pi c/a)$ are steered with beam steering angle of $40°$ and $15°$ respectively. In this case, the composite PC supports the distinct, duplex transmission of frequency components regardless of their polarization states and it is the desired aspect for far-field radiometers, in which the composite PC may be looked as a filter/demultiplexing channel for radiant energy in the narrow band of frequencies.

Pertaining to these applications, the future scope of the present work is to optimizing the common dispersion characteristics with respect to truncation/termination at the input/output interfaces of the composite PC.
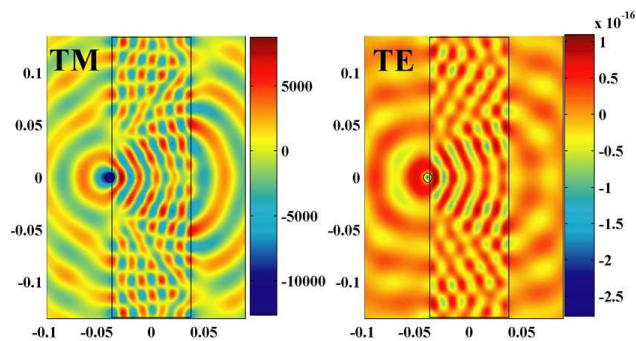
Figure 6: Wave propagation in a uniform glass medium for both the TE and TM modes. The point source is operated at the same wavelength of $3.7654\,\mathrm{cm}$.
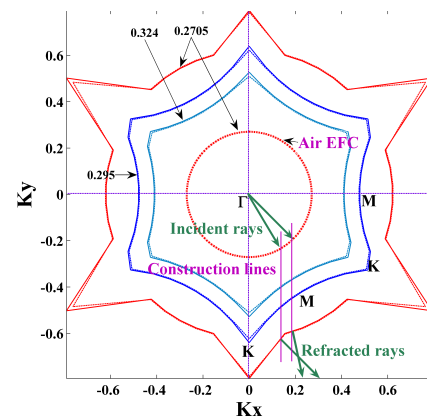
Figure 7: EFC contours of both TE (solid line) and TM (dotted line) modes for selected frequencies in second band of triangular lattice composite PC. The geometrical ray picture corresponds to angular frequency (ω) of $0.2705\,(2\pi c/a)$ reveals the beam steering ability of the proposed composite PC. Γ, M and K are the highest symmetry points of the irreducible Brillouine zone of the triangular lattice.

5. CONCLUSIONS

The aim of utilizing the composite PC made of real, positive dielectric constituents for common dispersion characteristics of TE and TM modes is addressed in this work. Based on the negative refraction of the phases, super-lens effect for the both the polarization modes are demonstrated numerically. Unlike in pure left-handed medium, there is no internal focusing found in these dielectric composite PC. Since the composite PC shows imaging effect for both the polarization modes, one can look into the possibility of removing the restriction on specific polarization state of the e-m wave source. The investigations on composite PC in triangular lattice basis reveal the common beam steering aspect for both TE and TM modes. By optimizing the common dispersion behavior against truncation/termination effect of the PC, the beam steering aspect can be employed in far-field radiometers and microwave devices.

REFERENCES

1. Veselago, V. G., "The electrodynamics of substances with simultaneous negative values of ε and μ," *Sov. Phys. Uspekhi*, Vol. 10, No. 4, 509–514, 1968.
2. Pendry, J. B., "Negative refraction makes a perfect lens," *Phys. Rev. Lett.*, Vol. 85, No. 18, 3966–3969, 2000.
3. Shelby, R. A., D. R. Smith, and S. Schultz, "Experimental verification of a negative index of a refraction," *Science*, Vol. 292, 77–79, 2001.
4. Notomi, M., "Theory of light propagation in strongly modulated photonic crystals: Refraction like behavior in the vicinity of the photonic band gap," *Phys. Rev. B*, Vol. 62, 10696–10705, 2000.
5. Luo, C., S. G. Johnson, J. D. Joannopoulos, and J. B. Pendry, "All-angle negative refraction without negative effective index," *Phys. Rev. B.*, Vol. 65, 201104(R), 2002.
6. Parimi, P. V., W. T. Lu, P. Vodo, J. Sokoloff, J. S. Derov, and S. Sridhar, "Negative refraction and left-handed behavior in two-dimensional photonic crystals," *Phys. Rev. Lett.*, Vol. 92, 127401, 2004.
7. Luo, C., S. G. Johnson, and J. D. Joannopoulos, "Sub-wavelength imaging in photonic crystals," *Phys. Rev. B.*, Vol. 68, 045115, 2003.
8. Kosaka. H, T. Kawashima, A. Tomita, M. Notomi, T. Tamamura, T. Sato, and S. Kawakami, "Superprism phenomena in photonic crystals," *Phys. Rev. B.*, Vol. 58, R10096–R10099, 1998.
9. Ramakrishna, S. A., S. Guenneau, S. Enoch, G. Tayeb, and B. Gralak, "Confining light with negative refraction in checkerboard metamaterials and photonic crystals," *Phys. Rev. A.*, Vol. 75, 063830, 2007.
10. Zhang, X., "Absolute negative refraction and imaging of unpolarized electromagnetic waves by two-dimensional photonic crystals," *Phys. Rev. B.*, Vol. 70, 205102, 2004.
11. Kuo, C.-H. and Z. Ye, "Negative-refraction-like behavior revealed by arrays of dielectric cylinders," *Phys. Rev. E.*, Vol. 70, 026608, 2004.
12. Qiu, M., L. Thylén, M. Swillo, and B. Jaskorzynska, "Wave propagation through a photonic crystal in a negative phase refractive-index region," *IEEE J. Quantum. Electron.*, Vol. 9, No. 1, 106–110, 2003.
13. Johnson, S. G. and J. D. Joannopoulos, "Block-iterative frequency-domain methods for Maxwell's equations in a plane wave basis," *Opt. Express.*, Vol. 8, No. 3, 173–190, 2001, http://ab-initio.mit.edu/mpb.
14. Whiteman, J. R., *The Mathematics of Finite Elements and Applications*, John Wiley and Sons, Chichester, 1998, EM solver is at http://www.comsol.com.

Light Scattering from 3-D Nanoscale Disordered Media

G. Berginc[1] and C. Bourrely[2]

[1]THALES, 2 Avenue Gay Lussac, 78995 Elancourt Cedex, France
[2]Center for Theoretical Physics, CNRS-Luminy Case 90, 13288 Marseille Cedex 9, France

Abstract— Random volume and surface scattering is a topic, which has been studied in many domains such as optical wave propagation in turbulent media, plasmonics and surface optics. Useful phenomena in the optical range can be produced by random media with randomly rough surfaces. Designing these disordered slabs with rough surfaces can produce new optical components, which can transmit or scatter optical field with specified angular, spatial or spectral properties. Understanding how light interacts with disordered matter is a fundamental issue in optoelectronics and photonics and has huge consequences in communications, imaging and sensing. In this paper, we consider a three-dimensional disordered medium with randomly rough interfaces. This structure describes a device based on metallic nanoparticles embedded in insulators or dielectric media. We present a theory of transport based on the Bethe-Salpeter equation. The calculation of the intensities scattered by the considered structure for the ladder and most-crossed contributions is given by a Green tensor, which satisfies a Bethe-Salpeter equation.

1. INTRODUCTION

Random media have attracted much attention, not only in electromagnetic wave propagation, but also in solid-state physics. The governing equation can be written in the form of a Bethe-Salpeter equation. The problem is then reduced to find a good approximation to the solution of this equation. For a three-dimensional system composed of a random medium bounded by two randomly rough surfaces, the Bethe-Salpeter is constructed in order that the medium and the boundaries are treated on the same footing. This unified Bethe-Salpeter equation enables us to obtain a general expression, whatever the choice of the scattering operators used at the boundaries. The Quasi-Crystalline Coherent Potential Approximation (QC-CPA) is taken into account for the contribution of the random medium, which is made of spherical particles of given permittivity in a homogeneous background medium. The boundaries are described by random functions. In [1–4], we developed a general formalism based on Green functions to calculate the diffuse intensity. With these Green functions, we can separate the contributions of the surfaces and the volume. The procedure is to write the Maxwell equations as an integral form with the help of the Green functions and to apply the Wigner transform to the derived equation. Starting from the wave equation, we are able to take into account new contributions to the scattered intensity such as enhanced backscattering and the correlations between the scatterers which can not be introduced by the phenomenological radiometric approach. We use an unified approach to describe how the waves interact with the randomly rough boundaries. The main advantage of this approach is that the equations we obtained are very similar to the equations used to describe the electromagnetic waves scattered by an infinite random medium.

2. INCOHERENT SPECIFIC INTENSITY AND CROSS-SECTION

We consider harmonic waves with $e^{-i\omega t}$ dependence. We are going to study a three-dimensional slab (see Fig. 1), which is composed of an incident medium of permittivity ϵ_0, a first randomly rough boundary, a random medium defined by a permittivity ϵ_1 which contains scatterers, a second randomly rough boundary at the distance $z = -H$ and a semi-infinite homogeneous medium with a permittivity ϵ_2. In this approach, the main quantity we used to describe the scattering process is the specific intensity, which can be defined as a Stokes vector or a tensor if the polarization of the electromagnetic wave is taken into account. For a random layer with rough interfaces, the incoherent specific intensity can be decomposed into four parts.

$$\overline{\overline{\mathcal{I}}}^{incoh} = \overline{\overline{\mathcal{I}}}^{incoh}_{L=0} + \overline{\overline{\mathcal{I}}}^{incoh}_{L=1} + \overline{\overline{\mathcal{I}}}^{incoh}_{Ladder} + \overline{\overline{\mathcal{I}}}^{incoh}_{Crossed}, \tag{1}$$

where the contributions are given by:

$$\boldsymbol{\mathcal{I}}_{L=0}^{incoh}(\boldsymbol{R},\boldsymbol{k}) = e_0 \int_{V_0} \mathrm{d}^3\boldsymbol{r}\exp^{-i\boldsymbol{k}\cdot\boldsymbol{r}}\left[<\boldsymbol{E}_S^{0\,s}\!\left(\boldsymbol{R}\!+\!\frac{\boldsymbol{r}}{2}\right)\!\otimes\boldsymbol{E}_S^{0s*}\!\left(\boldsymbol{R}\!-\!\frac{\boldsymbol{r}}{2}\right)>_S - <\boldsymbol{E}_S^{0\,s}\!\left(\boldsymbol{R}\!+\!\frac{\boldsymbol{r}}{2}\right)>\otimes<\boldsymbol{E}_S^{0s*}\!\left(\boldsymbol{R}\!-\!\frac{\boldsymbol{r}}{2}\right)>_S\right],\ (2)$$

$$\boldsymbol{\mathcal{I}}_{L=1}^{incoh}(\boldsymbol{R},\boldsymbol{k}) = e_0 \int_{V_0} \mathrm{d}^3\boldsymbol{r}\,\exp^{-i\boldsymbol{k}\cdot\boldsymbol{r}}\,\overline{\boldsymbol{\mathcal{G}}}_{<S>}^{01} : \overline{\boldsymbol{\mathcal{P}}}^{11} :< \boldsymbol{E}^{1t}\otimes\boldsymbol{E}^{1t}>_S \left(\boldsymbol{R}+\frac{\boldsymbol{r}}{2},\boldsymbol{R}-\frac{\boldsymbol{r}}{2}\right), \tag{3}$$

$$\boldsymbol{\mathcal{I}}_{Ladder}^{incoh}(\boldsymbol{R},\boldsymbol{k}) = e_0 \int_{V_0} \mathrm{d}^3\boldsymbol{r}\exp^{-i\boldsymbol{k}\cdot\boldsymbol{r}}\,\overline{\boldsymbol{\mathcal{G}}}_{<S>}^{01} : \overline{\boldsymbol{\mathcal{P}}}^{11} : \overline{\boldsymbol{\mathcal{G}}}_{\ll SV\gg}^{11} : \overline{\boldsymbol{\mathcal{P}}}^{11} :< \boldsymbol{E}^{1t}\otimes\boldsymbol{E}^{1t}>_S\!\left(\boldsymbol{R}+\frac{\boldsymbol{r}}{2},\boldsymbol{R}-\frac{\boldsymbol{r}}{2}\right), \tag{4}$$

$$\boldsymbol{\mathcal{I}}_{Crossed}^{incoh}(\boldsymbol{R},\boldsymbol{k}) = e_0 \int_{V_0} \mathrm{d}^3\boldsymbol{r}\exp^{-i\boldsymbol{k}\cdot\boldsymbol{r}}\left[\overline{\boldsymbol{\mathcal{G}}}_{<S>}^{01} : \overline{\boldsymbol{\mathcal{P}}}^{11} : \overline{\boldsymbol{\mathcal{G}}}_{\ll SV\gg}^{11} : \overline{\boldsymbol{\mathcal{P}}}^{11} :< \boldsymbol{E}^{1t}\otimes\boldsymbol{E}^{1t}>_S\right]^{T_R}\!\left(\boldsymbol{R}+\frac{\boldsymbol{r}}{2},\boldsymbol{R}-\frac{\boldsymbol{r}}{2}\right), \tag{5}$$

with $e_0 = \epsilon_{vac}\,c_{vac}\,n_0/2$. ϵ_{vac} and c_{vac} are respectively the permittivity and the speed of light in vacuum. n_0 is the optical index of the medium 0. T_R defines the right transpose of a tensor. The superscripts of the operators and the Green functions correspond respectively to the receiver location and the source location (0 for the medium 0, 1 for the medium 1, 2 for the medium 2). The first term $\overline{\boldsymbol{\mathcal{I}}}_{L=0}^{incoh}$ gives the scattering by the slab with rough boundaries and defined by an effective permittivity given by the QC-CP approximation [1]. The second term $\overline{\boldsymbol{\mathcal{I}}}_{L=1}^{incoh}$ is related to the first approximation where only one process of scattering by a particle is taken into account. The two last terms $\overline{\boldsymbol{\mathcal{I}}}_{Ladder}^{incoh}$ and $\overline{\boldsymbol{\mathcal{I}}}_{Crossed}^{incoh}$ correspond respectively to the ladder approximation and the most-crossed approximation. The tensor $\overline{\boldsymbol{\mathcal{P}}}^{11}$ describes the intensity scattered by the first particle the wave encounters. The expression of this tensor is given by the the Quasi-Crystalline Coherent Potential Approximation (QC-CPA). This intensity operator is determined by using the energy conservation principle and takes into account the correlations with the other particles. Under the QC-CPA, the effective permittivity satisfies a non-linear system of equations. Introducing these equation in a Ward identity, we obtain an expression, called the modified ladder approximation for the intensity operator $\overline{\boldsymbol{\mathcal{P}}}^{11}$ which satisfies the energy conservation. The operator $\overline{\boldsymbol{\mathcal{G}}}_{\ll SV\gg}^{11}$ is the Green tensor which contains the interaction between the scatterers and the surfaces. We will study its expression in the following section. The lower index $\ll SV \gg$ represents the average over the randomly rough surfaces and the disordered medium. The fields $\boldsymbol{E}_S^{0s}(\boldsymbol{r})$, $\boldsymbol{E}_S^{1t}(\boldsymbol{r})$ represent respectively the field scattered by the interfaces without any interaction with the scatterers and the field transmitted in the layer before an interaction with the scatterers. Their expressions are given by:

$$\boldsymbol{E}_S^{0s}(\boldsymbol{r}) = \int \frac{\mathrm{d}^2\boldsymbol{p}}{(2\pi)^2}\, e^{i\,\boldsymbol{p}\cdot\boldsymbol{x}+i\,\alpha_0(\boldsymbol{p})\,z}\,\overline{\boldsymbol{S}}^{0+,0-}(\boldsymbol{p}|\boldsymbol{p}_0)\cdot\boldsymbol{E}^{0\,i}(\boldsymbol{p}_0), \tag{6}$$
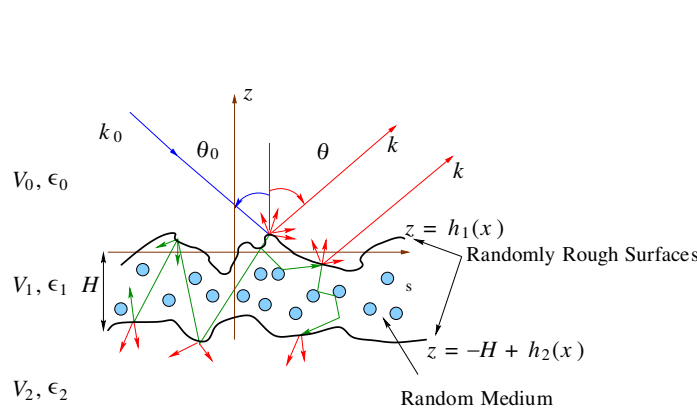

Figure 1: Random volume with rough boundaries.
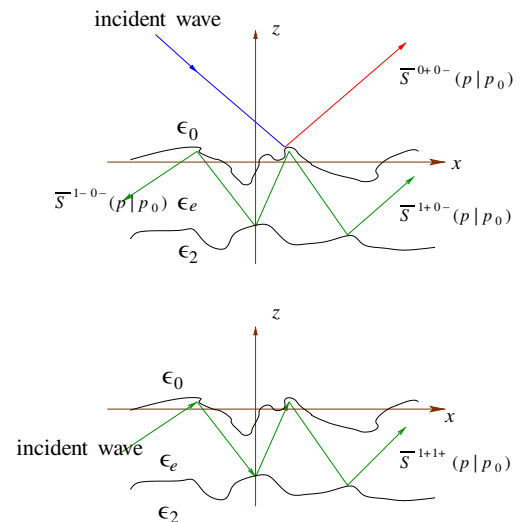
Figure 2: Definition of the scattering operators.

$$\boldsymbol{E}_S^{1\,t}(\boldsymbol{x},z) = \int \frac{\mathrm{d}^2\boldsymbol{p}}{(2\pi)^2} e^{\mathrm{i}\,\boldsymbol{p}\cdot\boldsymbol{x}} \left[e^{\mathrm{i}\,\alpha_1(\boldsymbol{p})\,z}\overline{\boldsymbol{S}}^{1+,0-}(\boldsymbol{p}|\boldsymbol{p}_0) + e^{-\mathrm{i}\,\alpha_1(\boldsymbol{p})\,z}\overline{\boldsymbol{S}}^{1-,0-}(\boldsymbol{p}|\boldsymbol{p}_0) \right] \cdot \boldsymbol{E}^{0\,i}(\boldsymbol{p}_0). \qquad (7)$$

With the definitions of the wave vectors $\boldsymbol{k}_{\boldsymbol{p}}^{0\pm}$ and $\boldsymbol{k}_{\boldsymbol{p}}^{1\pm}$ by:

$$\boldsymbol{k}_{\boldsymbol{p}}^{0\pm} \equiv \boldsymbol{p} \pm \alpha_0(\boldsymbol{p})\hat{\boldsymbol{e}}_z, \qquad (8)$$

$$\boldsymbol{k}_{\boldsymbol{p}}^{1\pm} \equiv \boldsymbol{p} \pm \alpha_1(\boldsymbol{p})\hat{\boldsymbol{e}}_z. \qquad (9)$$

we have,

$$\alpha_0(\boldsymbol{p}) = \sqrt{K_0^2 - \boldsymbol{p}^2}, \quad \alpha_1(\boldsymbol{p}) = \sqrt{K_1^2 - \boldsymbol{p}^2}. \qquad (10)$$

with:

$$K_0^2 = \epsilon_0 \left(\frac{\omega}{c_{vac}} \right)^2, \quad K_1^2 = \epsilon_1 \left(\frac{\omega}{c_{vac}} \right)^2. \qquad (11)$$

We define an upgoing wave if the wave vector is directed along $z > 0$ ($a = +$), and a downgoing wave if the wave vector is directed along $z < 0$ ($a = -$). For example, $\overline{\boldsymbol{S}}^{1+,0-}(\boldsymbol{p}|\boldsymbol{p}_0)$ describes the scattering operator of an incident downgoing wave from medium 0 which is scattered into an upgoing wave in medium 1, that is to say, the source in the medium 0 generates in the medium 1 a transmitted downgoing wave, which after a reflection on the second rough surface generates an upgoing wave. In Fig. 2, we define the representations of different scattering operators. The relation between the specific intensity and the cross-section is given by a product of two tensors:

$$4\pi \cos\theta\, \boldsymbol{\mathcal{I}}^{incoh}(\boldsymbol{R},\hat{\boldsymbol{k}}) = \overline{\sigma}^{incoh}(\hat{\boldsymbol{k}}|\hat{\boldsymbol{k}}_0) : \boldsymbol{\mathcal{J}}^{0i}(\hat{\boldsymbol{k}}_0), \qquad (12)$$

where

$$\boldsymbol{\mathcal{J}}^{0i}(\hat{\boldsymbol{k}}_0) = e_0\, \boldsymbol{E}^i(\hat{\boldsymbol{k}}_0) \otimes \boldsymbol{E}^{0i\,*}(\hat{\boldsymbol{k}}_0). \qquad (13)$$

In (13), we have a tensorial product of two vectors.

3. GREEN TENSOR $\overline{\boldsymbol{\mathcal{G}}}_{\ll SV \gg}^{11}$

As seen in the previous chapter, the contributions for the most-crossed and the ladder diagrams are determined by the Green tensor $\overline{\boldsymbol{\mathcal{G}}}_{\ll SV \gg}^{11}$, which satisfies a Bethe-Salpeter equation. It contains the second order and the higher orders describing the scattering by particles. The Fig. 3 gives a representation of the scattering process for the ladder approximation. To calculate the previous expressions, we need to estimate the tensor $\overline{\boldsymbol{\mathcal{G}}}_{\ll SV \gg}^{11}$, as no exact solution exists for the expression of the Green tensor, we rely on a perturbative method. In [3, 4], we calculated this tensor for the first-order approximation. In this paper, we take into account the second-order approximation. The very first results for this second-order approximation was given in [5, 6]. The Green tensor $\overline{\boldsymbol{\mathcal{G}}}_{\ll SV \gg}^{11}$ is given by the Bethe-Salpeter equation as follows:

$$\overline{\boldsymbol{\mathcal{G}}}_{\ll SV \gg}^{11} = \overline{\boldsymbol{\mathcal{G}}}_{\infty <S>}^{11} + \overline{\boldsymbol{\mathcal{G}}}_{\infty <S>}^{11} : \overline{\boldsymbol{\mathcal{P}}}^{11} : \overline{\boldsymbol{\mathcal{G}}}_{\ll SV \gg}^{11}, \qquad (14)$$

where the previous tensors are defined by the following tensorial products of the Green functions:

$$\overline{\boldsymbol{\mathcal{G}}}_{\ll SV \gg}^{11} = \ll \overline{\boldsymbol{G}}_{SV}^{11} \otimes \overline{\boldsymbol{G}}_{SV}^{11\,*} \gg_{SV}, \qquad (15)$$

$$\overline{\boldsymbol{\mathcal{G}}}_{\infty <S>}^{11} = < \overline{\boldsymbol{G}}_{S}^{11} \otimes \overline{\boldsymbol{G}}_{S}^{11\,*} >_{S}, \qquad (16)$$

By iterating the Bethe-Salpeter Eq. (??) we obtain the following perturbative development:

$$\overline{\boldsymbol{\mathcal{G}}}_{\ll SV \gg}^{11} = \overline{\boldsymbol{\mathcal{G}}}_{\infty <S>}^{11} + \overline{\boldsymbol{\mathcal{G}}}_{\infty <S>}^{11} : \overline{\boldsymbol{\mathcal{P}}}^{11} : \overline{\boldsymbol{\mathcal{G}}}_{\infty <S>}^{11} + \overline{\boldsymbol{\mathcal{G}}}_{\infty <S>}^{11} : \overline{\boldsymbol{\mathcal{P}}}^{11} : \overline{\boldsymbol{\mathcal{G}}}_{\infty <S>}^{11} : \overline{\boldsymbol{\mathcal{P}}}^{11} : \overline{\boldsymbol{\mathcal{G}}}_{\infty <S>}^{11} + \dots \qquad (17)$$

It can be noticed that the first-order Green tensor expansion represents an approximation of a double-scattering theory for the cross-section while the second-order corresponds to an approximation of a third-order scattering for the cross-section. This second-order expansion is taken into account in the simulation we present in the next section.
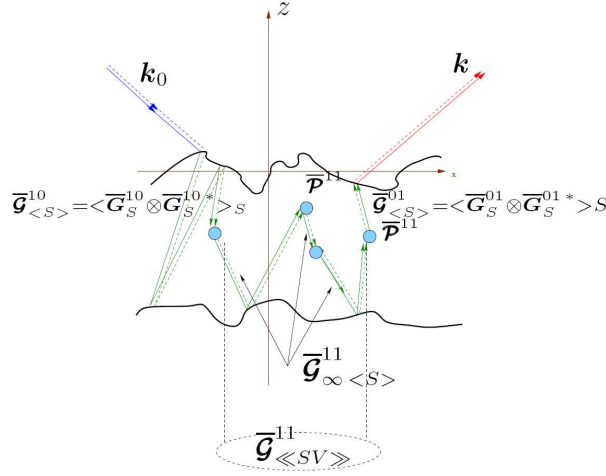
Figure 3: k Scattering processes for the ladder approximation. The solid and dashed lines represent respectively the propagating wave on the right and left sides of the tensorial products $\overline{\boldsymbol{\mathcal{G}}}^{11}_{\ll SV \gg} = \ll \overline{\boldsymbol{G}}^{11}_{SV} \otimes \overline{\boldsymbol{G}}^{11\,*}_{SV} \gg_{SV}$. The Green functions $\overline{\boldsymbol{G}}^{1a1a_0}_S$ are calculated with the scattering operators $\overline{\boldsymbol{S}}^{1a1a_0}$ defined previously.
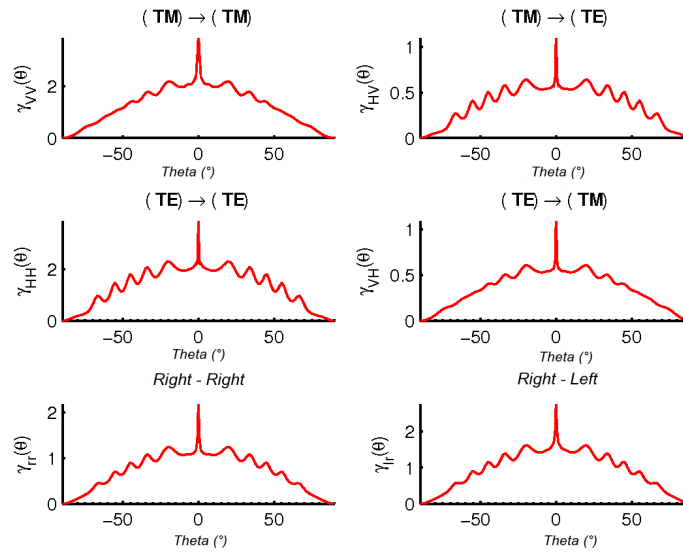
Figure 4: Cross-section of a slab with an effective permittivity $\epsilon_e = 2.37 + \mathrm{i}\,1.747 10^{-2}$. The disordered medium contains nanoscale metallic particles, the upper surface of the slab is a randomly rough surface, the angle of incidence is $\theta_0 = 0°$, the incident wavelength $\lambda = 1.5\,\mu m$.

4. CROSS-SECTION CALCULATION

Calculations of the intensity cross-sections require multi-dimensional integrations on two-dimensional wave vectors. We use an integration method of Gauss-Legendre with N points. We have to cope with oscillating expressions. To increase the precision of integration, we develop an integration method taking into account suitable domains of integration.

We compute the incoherent cross-section in the plane of incidence for a slab, which is defined as follows. The incident medium is vacuum ($\epsilon_0 = 1$). The layer depth is $H = 5\lambda$, its permittivity is $\epsilon_1 = 2$. The upper layer boundary is defined as a slightly randomly rough surface defined by the RMS height of the surface $\sigma/\lambda = 0.01$ and the correlation length is given by $l/\lambda = 0.3$. The lower boundary is a flat surface, which separates the layer from a semi-infinite medium of permittivity $\epsilon_2 = 16$. The wavelength is given by: $\lambda = 1.5\,\mu m$. The medium contains two types of spherical metallic particles defined as Rayleigh spherical scatterers. The radius of the first type of particles is $r_1 = \lambda/20$. The volume fraction of these particles is $f_{vol1} = 0.0125$. For the second type of particles,

the radius is $r_2 = \lambda/200$, the volume fraction is $f_{vol2} = 0.0375$. The global volume fraction is 5%. We obtain (Fig. 4) the total incoherent cross-section for an incident angle $\theta = 0°$, for the co- and cross-polarization components and the circular polarization components (right to right and right to left). The backscattering enhancement is due to the most-crossed diagram contributions, we can notice that the second order of the Green tensor expansion is about 5% of the first order. We have highlighted the backscattering enhancement peak due to the scattering by nanoscale particles in the disordered slab, which is a new result for the 3D configuration considered in this paper.

5. CONCLUSION

This paper was devoted to a theory of transport based on a Bethe-Salpeter equation. We presented a multiple scattering theory (up to third-order) for a random slab with discrete nanoscale scatterers and bounded with randomly rough surfaces. A new expansion of the Green tensor up to second order was developed, and calculations of the incoherent cross-sections were performed taking into account polarization components with the Mueller matrix. We observed the backscattering enhancement peaks for the most-crossed contribution and for all polarization components.

REFERENCES
 1. Soubret, A. and G. Berginc, arXiv:physics/0312117, 2003.
 2. Soubret, A. and G. Berginc, arXiv:physics/0312133, 2003.
 3. Soubret, A. and G. Berginc, arXiv:physics/0312136, 2003.
 4. Berginc, G. and C. Bourrely, "Electromagnetic wave scattering from a random layer with randomly rough interfaces," *Progress In Electromagnetics Research Symposium Abstracts*, 88, Prague, Czech Repulic, August 27–30, 2007.
 5. Berginc, G. and C. Bourrely, "Electromagnetic wave scattering from a random layer with rough interfaces I: Multiple scattering theory," *Progress In Electromagnetics Research Symposium Abstracts*, 205, Cambridge, USA, July 2–6, 2008.
 6. Berginc, G. and C. Bourrely, "Electromagnetic wave scattering from a random layer with rough interfaces II: Numerical experiments," *Progress In Electromagnetics Research Symposium Abstracts*, 206, Cambridge, USA, July 2–6, 2008.

Analysis of Dispersion Properties of Waveguide Based on Metamaterials

S. Bouali and T. Aguili

Syscom, National Engineering School of Tunis, Tunisia

Abstract— This paper presents an analysis of dispersion properties of rectangular waveguide filled with dielectric, and periodically loaded with obstacles (irises), using the transmission line theory of metamaterials. The rectangular waveguide discussed in this paper is periodically loaded with obstacles. By defining the matrix chain of the strucure and using Floquet's theorem we obtain the equation of dispersion of the structure. This structure produce a set of allowed and forbidden frequency bands which is plotted and discussed, the results of this analysis are presented.

1. INTRODUCTION

Electromagnetic metamaterials are broadly defined as artificial effectively homogeneous electromagnetic structures with unusual properties not readily available in nature. An effectively homogeneous structure is a structure whose structural average cell size L is much smaller than the guided wavelength ($L < \lambda g/4$) [1]. Metamaterials have attracted much attention from the optical/electromagnetic community; they can be essentially modeled by one-dimensional (1D) transmission lines (TLs), whose propagation direction represents any direction in the material [1]. Many important property of metamaterials have attracted significant research interest like the miniaturization of antennas and other microwave circuit components, like waveguide and filters. In the present paper, we focus our analysis on the electromagnetic dispersion in rectangular waveguide filled with dielectric and periodically loaded with obstacles (irises), this electromagnetic dispersion is examined between 1 GHz and 300 GHz, a numerically analysis is given.

2. TRANSMISSION LINE ANALYSIS

We consider a rectangular waveguide filled with dielectric and periodically loaded with obstacles (irises) (Figure 1) The rectangular waveguide is considered as an infinite repetition of unit cell which is represented in Figure 2.

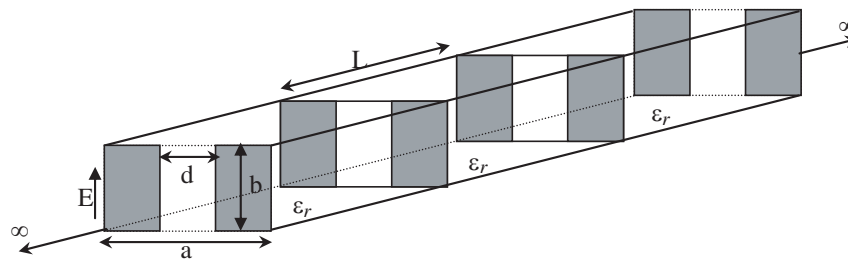Figure 1: Schema of a rectangular waveguide periodically loaded with obstacles (irises).
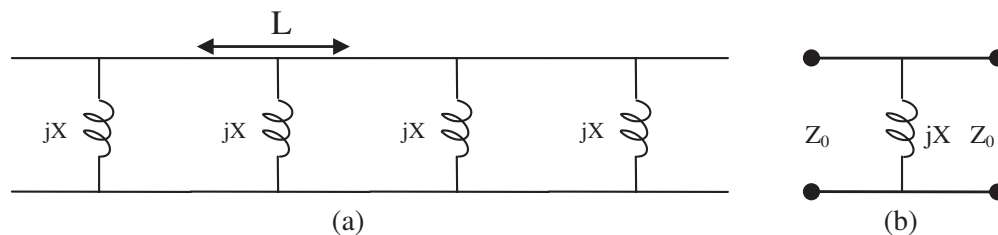

Figure 2: (a): Scheme the equivalent circuit of the wave guide. (b) Schema of the unit cell (one irise).

This unit cell consists of a transmission line, the line's length is L, we place at the center of this line a lumped inductive obstacles jX (witch X is symmetrical window formed by zero thickness
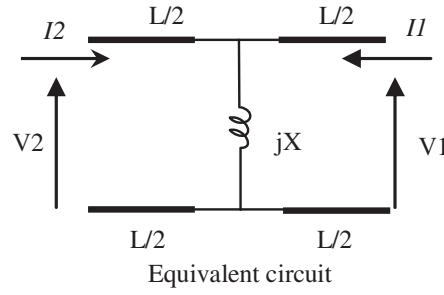
Figure 3: Schema of the unit cell.

obstacles with edges parallel to the electric field (H10-mode in rectangular guide), X depend on the frequency [2].

We consider a unit cell as a three part network: one half $(L/2)$ of the transmission line, the loading element JX, and another half $(L/2)$ of the transmission line Figure 3.

And X is given by:

$$X = \frac{Z_0 a}{\lambda_g} \tan^2 \frac{\pi d}{2a} \left\{ 1 + \frac{3}{4} \left[\frac{1}{\sqrt{1 - \left(\frac{2a}{3\lambda}\right)^2}} - 1 \right] \sin^2 \frac{\pi d}{a} + 2 \left(\frac{a}{\lambda}\right)^2 \left[\frac{1 - \frac{4}{\pi} \frac{E(\alpha) - \beta^2 F(\alpha)}{\alpha^2} *}{\frac{E(\beta) - \alpha^2 F(\beta)}{\beta^2} - \frac{1}{12} \sin^2 \frac{\pi d}{a}} \right] \right\} \quad (1)$$

where $\alpha = \sin \frac{\pi d}{2a}$, $\beta = \cos \frac{\pi d}{2a}$ and $F(\alpha)$, $E(\alpha)$ are respectively complete elliptic integral of the first and second kinds.

The network of the TL of Figure 2(a) constitueted by the repetition of the unit cell of Figure 3 where the matrix chain is obtained by cascading three matrixes: the matrix chain of the half $L/2$ $(C_{L/2})$ of the transmission line, the matrix chain of the obstacle $jX(C_e)$ and the matrix chain of the half $L/2$ $(C_{L/2})$ of the transmission line wich are given by:

$$C_{L/2} = \begin{pmatrix} \cosh\left(\gamma \frac{L}{2}\right) & Z_C \sinh\left(\gamma \frac{L}{2}\right) \\ Y_C \sinh\left(\gamma \frac{L}{2}\right) & \cosh\left(\gamma \frac{L}{2}\right) \end{pmatrix} \text{ and } C_e = \begin{pmatrix} 1 & 0 \\ JX & 1 \end{pmatrix} \quad (2)$$

where γ the transmission line propagation constant, L is the length of the transmission line and Z_C is a characteristic impedance of a waveguide defined by the transmission line $L/2$ $(Z_C = Z_0)$. The matrix of the unit cell is given by:

$$C_T = C_{L/2} \cdot C_e \cdot C_{L/2} = \begin{pmatrix} Ch(\gamma L) + \frac{JX}{2Y_c} sh(\gamma L) & Z_c Sh(\gamma L) + \frac{JX}{Y_c^2} Sh^2(\gamma L) \\ Y_c Sh(\gamma L) + JX Ch^2(\gamma L) & Ch(\gamma l) + \frac{JX}{2Y_c} Sh(\gamma L) \end{pmatrix} \quad (3)$$

By using the model of transmission line presented at Figure 2 Floquet's theorem for periodic structure we obtain two equations of dispersion: Equation (4) gives the dispersion diagram with attenuation and Equation (5) gives the dispersion diagram without attenuation:

$$G(f) = ch\left(\alpha_P \frac{L}{2}\right) = \frac{\cos(\beta L)}{\cos(\beta_P \frac{L}{2})} - \frac{X Z_C}{2} \sin(\beta L) \text{ with } \beta_P \frac{L}{2} = n\pi \quad (4)$$

$$H(f) = \cos\left(\beta_P \frac{L}{2}\right) = \cos(\beta L) - \frac{X Z_C}{2} \sin(\beta L) \text{ with } \alpha_P = 0 \quad (5)$$

We consider the function

$$G(f) = \cos(\beta L) - \frac{X Z_C}{2} \sin(\beta L) \quad (6)$$

with X is given by (2) and Z_C is equal to Z_0 and

$$Z_C = Z_0 = Z_{TE(10)} = \frac{C \mu_0}{\sqrt{\varepsilon_r - \left(\frac{C}{2bf}\right)^2}} \quad (7)$$

The attenuation constant and the phase constant are given by:

$$\alpha_P = \frac{2}{L} ach \left(\frac{\cos(\beta L)}{\cos(\beta_P \frac{L}{2})} - \frac{XZ_C}{2} \sin(\beta L) \right) \text{ with } \beta_P \frac{L}{2} = n\pi \tag{8}$$

$$\beta_P = \frac{2}{L} ar\cos \left(\cos(\beta L) - \frac{XZ_C}{2} \sin(\beta L) \right) \text{ with } \alpha_P = 0 \tag{9}$$

There are two equations of dispersion (4) and (5) witch are plotted, for Equation (4), if $ch(\alpha pL/2) > 1$, the periodic structure supports a propagation waves, else $(ch(\alpha pL/2) < 1)$ no wave can propagate along the structure. In Equation (5), if $\cos(\beta pL/2)$ is varying between -1 and $+1$ the structure supports a propagation waves, else no wave can propagate along the structure.

3. SIMULATION AND RESULTS

To simulate the structure we can vary two parameters the permittivity (ε_r) or the width of the opening of the iris (d). For this work we propose that the length of the unit cell L is fixed, and we present the results for several cases by varying (ε_r) and d. The dispersion curve with attenuation is obtained by plotting $G(f)$, the frequency ranges corresponding to $G(f)$ larger than 1 indicate the pass band while the frequency regions with $G(f) < 1$ correspond to the stop band. For the dispersion curve without attenuation to have propagation $G(f)$ should be between -1 and $+1$. The attenuation constant and phase constant were calculated and plotted.
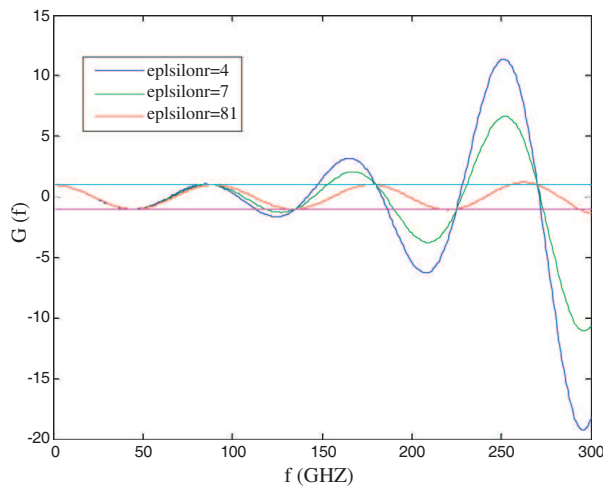
Figure 4: Diagram dispersion for three values of ε_r.
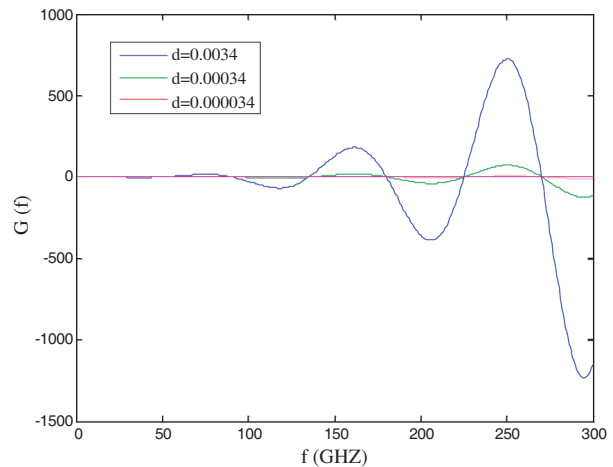
Figure 5: Diagram dispersion for three values of d.
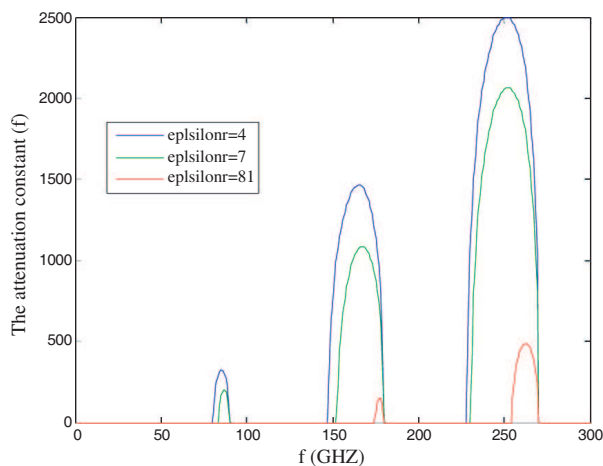
Figure 6: The attenuation constant for three values of ε_r.
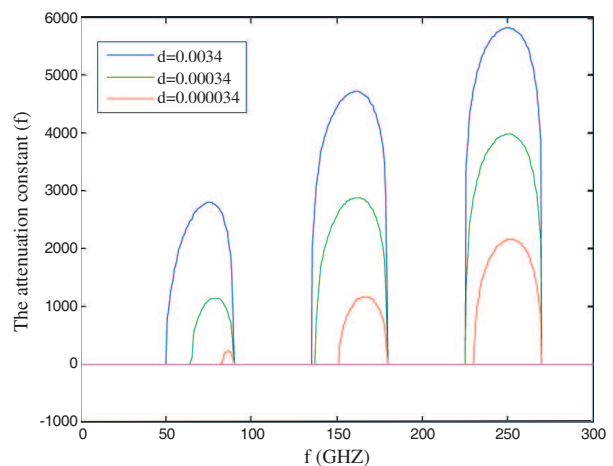
Figure 7: The attenuation constant for three values of d.

The frequency ranges corresponding to $G(f)$ larger than 1 in Figure 5 (respectively Figure 6) indicate the pass band propagation with attenuation ($\alpha p \neq 0$ (Figure 6 (respectively Figure 7)) and $\beta p \neq$ (Figure 8 (respectively Figure 9)), the frequency ranges corresponding to $-1 < G(f) < 1$ indicate the pass band (propagation without attenuation ($\alpha p = 0$ (Figure 6 (respectively Figure 7) and $\beta p \neq$ (Figure 8 (respectively Figure 9)), the frequency ranges corresponding to $G(f) < -1$ correspond to the stop band.
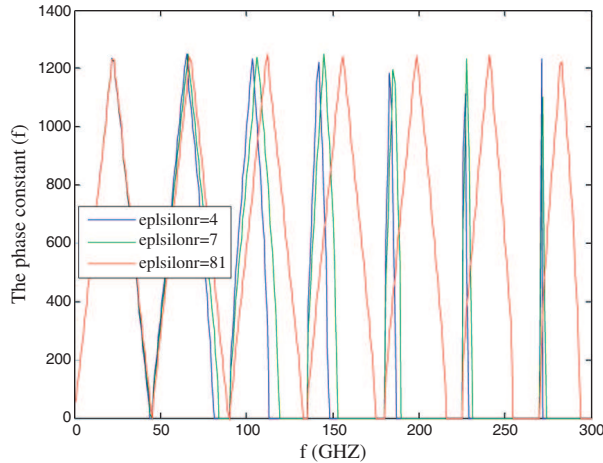
Figure 8: The phase constant for three values of ε_r.
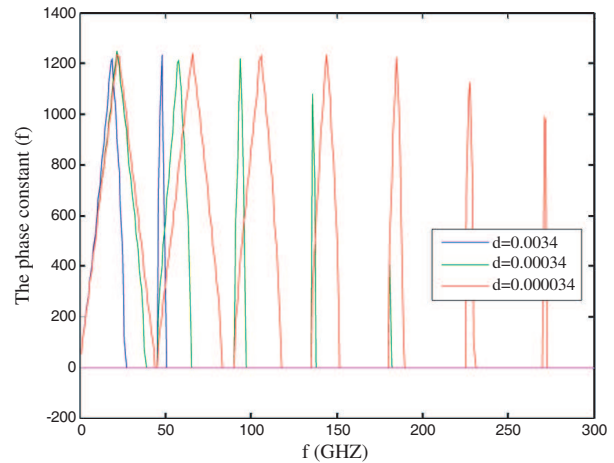
Figure 9: The phase constant for three values of d.

4. CONCLUSION

We have analyzed the dispersion properties of rectangular waveguide filled with dielectric, and periodically loaded with obstacles (irises). The general dispersion relation of our structure has been formulated using the TL approach and solved using Floquet theory; we obtained tow equation which depends of the attenuation and phase constant. We simulated these equations using MATLAB. The results revel the presence of stop and pass band. The frequency ranges corresponding to the stop and pass band depend on the physical configuration of the periodic structure like the permittivity relative (ε_r) of the wave guide and the width of the opening of the iris (d), the bandwith and the frequency range of stop and pass band Can be controlled by modifying the permittivity of the waveguide either by optimizing the dimensions of the iris.

REFERENCES

1. Caloz, C. and T. Itoh, *Electromagnetic Metamaterials: Transmission Line Theory and Microwave Applications*, John Wiley & Sons, Inc., 2006.
2. Marcuvitz, N., *Waveguide Handbook*, Peter Peregrinus Ltd on behalf of the Institution of Electrical Engineers, 1986.
3. Yablonovitch, E., "Photonic band-gap structures," *J. Opt. Soc. Amer. B*, Vol. 10, No. 2, 283–294, Feb. 1993.
4. Bouali, S. and T. Aguili, "The study of electromagnetic dispersion in the periodic structures," *MMS*, 2008.

Stability of Bragg Grating Solitons in a Cubic-quintic Nonlinear Medium with Dispersive Reflectivity

Sahan Dasanayaka and Javid Atai

School of Electrical and Information Engineering, The University of Sydney, NSW, 2006, Australia

Abstract— Quiescent solitons in a Bragg grating in a cubic-quintic medium with dispersive reflectivity are investigated. Two disjoint families of solitons exist, as in the cubic-quintic model, but with expanded regions of stability due to the dispersive reflectivity.

1. INTRODUCTION

Periodic variation of the refractive index along an optical fiber produces a fiber Bragg grating (FBG). The cross-coupling between counter-propagating waves in an FBG results in a strong effective dispersion that is approximately 6 orders of magnitude greater than the underlying chromatic dispersion of the fiber [1, 2]. At sufficiently high intensities the FBG-induced dispersion may be counterbalanced by nonlinearity resulting in the formation of a Bragg grating soliton.

Bragg grating solitons have been the subject of intense theoretical and experimental research over the past two decades (see for example Refs. [2–5]). In a uniform Bragg grating, the governing equations for nonlinear pulse propagation have been derived using coupled mode theory (CMT) [2]. In this case, BG solitons form a two-parameter family of solutions. One of these parameters is related to soliton's velocity, which can range between zero and the speed of light in the medium, and the other is dependent on the detuning frequency, peak power and soliton width. Due to their potential application in optical buffers and storage devices, significant efforts have been directed toward the generation of zero-velocity (quiescent) solitons.

The existence and stability of solitons have also been investigated in more sophisticated systems. For example, in Ref. [6], it was reported that in a medium with a cubic-quintic nonlinearity two disjoint families of BG solitons exist. In Refs. [7, 8], the existence and stability of solitons in a *nonuniform* Bragg grating was considered. A key result in these works is that reflectivity dispersion leads to the expansion of the stability region of the standard model.

In this paper, we investigate the effect of reflectivity dispersion on the existence and stability of quiescent solitons in a cubic-quintic medium. The model is as follows:

$$
\begin{aligned}
iu_t + iu_x + \left[\frac{1}{2}|u|^2 + |v|^2\right] u - \nu \left[\frac{1}{4}|u|^4 + \frac{3}{2}|u|^2|v|^2 + \frac{3}{4}|v|^4\right] u + v + mv_{xx} = 0 \\
iv_t - iv_x + \left[\frac{1}{2}|v|^2 + |u|^2\right] u - \nu \left[\frac{1}{4}|v|^4 + \frac{3}{2}|v|^2|u|^2 + \frac{3}{4}|u|^4\right] v + u + mu_{xx} = 0
\end{aligned}
\tag{1}
$$

where u and v are the forward and backward propagating components, m accounts for the strength of the dispersive reflectivity and $\nu > 0$ is a parameter to control the strength of quintic nonlinearity.

2. SOLITON SOLUTIONS

To obtain soliton solutions, the ansatz $u(x,t) = U(x)e^{-i\omega t}$ and $v(x,t) = V(x)e^{-i\omega t}$ are substituted into (1) resulting in the following system of coupled equations:

$$
\begin{aligned}
-mV_{xx} = \omega + iU_x + \left[\frac{1}{2}|U|^2 + |V|^2\right] U - \nu \left[\frac{1}{4}|U|^4 + \frac{3}{2}|U|^2|V|^2 + \frac{3}{4}|V|^4\right] U + V, \\
-mU_{xx} = \omega - iV_x + \left[\frac{1}{2}|V|^2 + |U|^2\right] V - \nu \left[\frac{1}{4}|V|^4 + \frac{3}{2}|V|^2|U|^2 + \frac{3}{4}|U|^4\right] V + U.
\end{aligned}
\tag{2}
$$

These equations are then solved solved by means of a relaxation algorithm. It is found that, similar to the cubic-quintic model without dispersive reflectivity [6], there are two disjoint families of solitons in this model. The soliton families are separated by the border $1 - \omega = \frac{27}{160\nu}$. An important difference between between the soliton families is in their phase structures and parities. In one of the families the Re $\Re(u(x))$ and $\Re(v(x))$ are even, and $\Im(u(x))$ and $\Im(v(x))$ are odd functions of x. In the other family, the parities of the real and imaginary parts of the solutions are opposite. It is also found that, for moderate values of dispersive reflectivity parameter, sidelobes appear in the solitons' profile.

3. STABILITY ANALYSIS

We have investigated the stability of both families of solitons by numerically solving Eq. (1). Figure 1 shows the stability regions for BG solitons in a cubic-quintic nonlinear medium for $m = 0.1$. The two families of solitons are separated by the same analytical curve as in the model with no dispersive reflectivity.

Comparing Figure 1 with the stability diagram in Ref. [6], it is readily seen that the stable regions for both families of solitons have been expanded as a result of dispersive reflectivity. This is consistent with the findings of Ref. [7] where it was shown that the presence of dispersive reflectivity leads to the expansion of the stability region in the cubic model. The stabilization effect due to dispersive reflectivity may be explained qualitatively as follows: in the proximity of soliton's center, which has largest negative curvature, the effective reflectivity is reduced due to the presence of terms proportional to m. This amounts to the creation of a defect which has the property of attracting gap solitons and stabilizing them [7].

Examples of stable and unstable propagation for both types of solitons are given in Figures 2 and 3. For both families of solitons, the degree of instability generally increases as the distance from the stability border increases. For example, since the soliton in Figure 2(b) is near a stability boundary, it radiates a small amount of energy and evolves to a stable pulse. This indicates that the stable solitons are robust objects. However, slightly further away from that boundary, the soliton rapidly decays into radiation as shown in Figure 3(b).
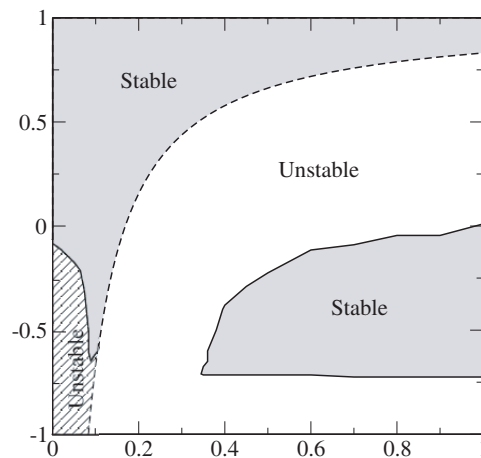
Figure 1: Stability diagram for $m = 0.1$. The dashed curve separates the two families of solitons and is defined by $1 - \omega = 27/(160\nu)$.
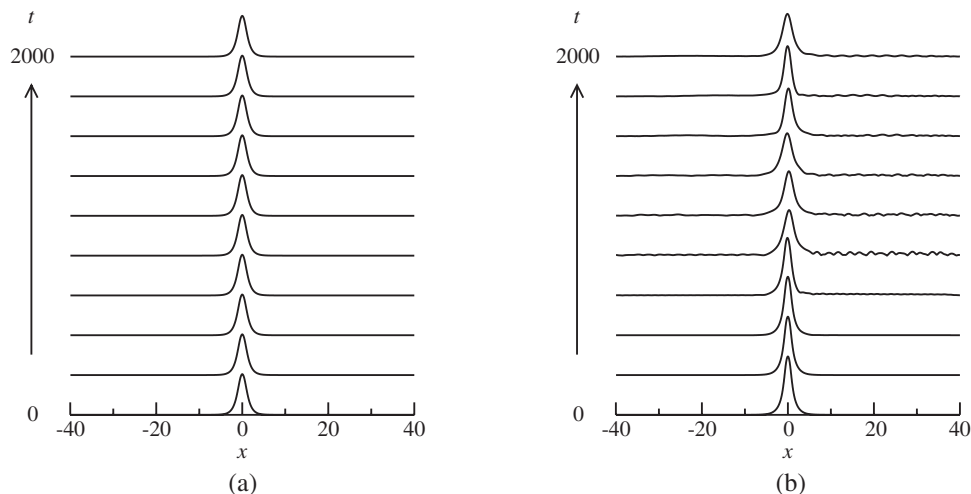
Figure 2: Examples of soliton evolution. (a) A stable soliton with $\omega = 0.20$, $\nu = 0.05$ and (b) an unstable soliton with $\omega = -0.60$, $\nu = 0.05$.
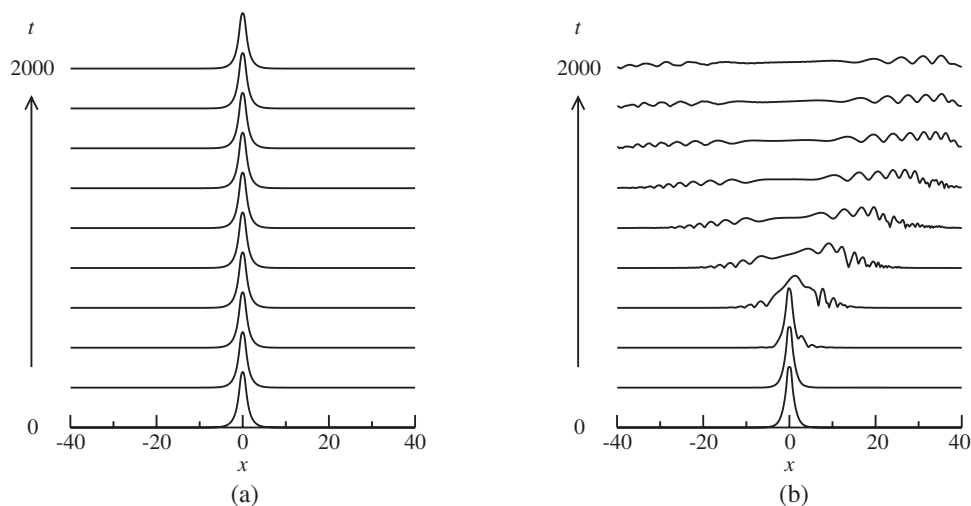
Figure 3: Examples of soliton evolution. (a) A stable soliton with $\omega = -0.60$, $\nu = 0.50$ and (b) an unstable soliton with $\omega = 0.20$, $\nu = 0.50$.

4. CONCLUSION

The existence and stability of quiescent Bragg grating solitons in a cubic-quintic non-linear medium with dispersive reflectivity have been investigated numerically. It is found that the model supports two disjoint families of solitons. The presence of dispersive reflectivity expands the stability region for both families.

REFERENCES

1. Russell, P. St. J., *J. Mod. Opt.*, Vol. 38, 1599, 1991.
2. De Sterke, C. M. and J. E. Sipe, *Prog. Opt.*, Vol. 33, 203, 1994.
3. Aceves, A. B. and S. Wabnitz, *Phys. Lett. A*, Vol. 141, 37, 1989.
4. Eggleton, B. J., C. M. De Sterke, and R. E. Slusher, *J. Opt. Soc. Am. B*, Vol. 14, 2980, 1997.
5. Taverner, D., N. G. R. Broderick, D. T. Richardson, R. I. Laming, and M. Ibsen, *Opt. Lett.*, Vol. 23, 328, 1998.
6. Atai, J. and B. A. Malomed, *Phys. Lett. A*, Vol. 284, 247, 2001.
7. Atai, J. and B. A. Malomed, *Phys. Lett. A*, Vol. 342, 404, 2005.
8. Neill, D. R., J. Atai, and B. A. Malomed, *J. Opt. A: Pure Appl. Opt.*, Vol. 10, 085105, 2008.

The "Missing Mass" in the Universe May Be Represented by the Dynamic-mass of the Photons

Antonio Puccini

Department of Neurophysiology of Order of Malta, Naples, Italy

Abstract— As we know the *missing mass* in the universe represents more than 90% of the universe mass. The hadronic matter, in fact, corresponds only to a very small part of the total (about 4%). It is not known what the *missing mass* is represented of. It is thought that it is made of weakly interactive massive particles (WIMPS). Massive particles (100 times heavier than a proton) which interact very little with the matter, even less than neutrinos. It may also be a super symmetric particle, or something else.

We calculated that the momentum of a photon of the optic band, with a normal wavelength, along with the formula $p = h/\lambda$, will be $6.625 \cdot 10^{-27}$ [erg $\cdot$ s]$/5.7 \cdot 10^{-5}$ [cm], which corresponds to $1.1623 \cdot 10^{-22}$ [g $\cdot$ cm/s]. Thus we have that the photon has really a significant *dynamic mass*, about 100 times bigger than the mass of the proton. It is curious to notice that it corresponds just to the hypothetic mass given to the WIMPs.

Moreover, if we consider, along with what Weinberg tells us in "The First Three Minutes", that for each nuclear particle (proton or neutron) there is a billion of photons, we may think that the photons can contribute to fill the vacuum of the missing mass in the universe.

1. INTRODUCTION

At the beginning of the 30's Fritz Zwicky noticed that peripheral stars rotating around the centre of a galaxy have such a speed that the gravity force should not be able to keep them in orbit. Zwicky assumed the existence of an invisible mass on which the gravity force acted. He hypothesized the existence of a *missing mass* (MM). An invisible mass whose gravitational effect adds to the visible matter's. In this way account balanced.

We learn from R. Giacconi and W. Tucker "such differences between the observed mass and the gravitational mass were already noticed by Jan Oort Leida University, in 1941 and M. Schwarzchild from Princeton in 1954. However, most astronomers ignored the problem until late 70's. Things changed radically when new optical instruments were developed as well as more powerful X and radio telescopes. New instruments allowed Vera Rubin and her stuff at the Carnegie Institute to measure orbital speeds far away from the centre of a galaxy. They obtained accurate evaluations of mass galaxies. They learned that the mass calculated from orbital speeds is much bigger than the mass inferred from the optical image of the galaxy. Apparently galaxies are immersed in a halo of invisible matter. These results were confirmed by radio observations, showing that galaxy invisible halos must contain about ten times more mass than what can be seen in the visible and radio waves. Apparently the mass is hidden in a kind of shape which so far we have not been able to observe" [1].

Also recent observations have showed that the motion of both the galaxy and the stars in the galaxies, is to be imputed to a quantity of mass significantly bigger than what can be detected with the optical band or other electromagnetic radiations. X and radio frequency surveys confirm the results: non observable mass is at least 90% bigger than the total mass of the universe.

2. DISCUSSION

What is the invisible mass of the universe (MM) made of? The hadronic matter is only about 4% of the total mass. "Cosmological considerations seem to exclude that the MM is under the shape of a normal baryonic matter" [1]. Most scientists agree that it is made of WIMPs (Weakly Interactive Mass Particles), that is very massive super symmetric particles (100 times heavier than a proton). They interact very little with the matter, even less than neutrinos.

WIMPs are being searched at the Gran Sasso and in particle accelerators, however, no definite result has been obtained so far. Though neutrinos seem to have a little mass it is still not enough to consider that they may represent the MM. As Giacconi and Tucker remind us it would require that "the fraction of invisible mass around the galaxies was much less than the one in the clusters, but observations do not agree with such predictions" [1]. Some other authors maintain that the MM is represented by an antimatter particle, a hypothetical "symmetric partner" of the neutrino,

the one to be searched in the big particle accelerators. It has also been thought that the MM is made of exotic particles such as axions. It is likely that these particle formed at the beginning of the universe, about one million second after the Big Bang, however they have never been observed.

If we look around we simply notice that the universe is full of light, full of electromagnetic radiation (EMR) with different frequencies. Besides, as we learn from Margherita Hack "the density of radiant energy (photons) in the universe is about one thousand millions bigger than the density of the matter. This shows the big quantity of energy generated by the destruction of couple of particles and antiparticles. We owe our existence to the little difference between the number of particles and antiparticles. Otherwise, we would have a universe without matter, with only radiation" [2].

Steven Weinberg in *The First Three Minutes* wrote: "going back to the early universe there has always been a number of photons for proton or neutron between 100 millions and 20 thousand millions. In order to simply things I will round it off and consider that in the universe there is, and there has always been, *only* one thousand millions of photons for each nuclear particle" [3].

In short the ratio between baryonic particles and radiant particles, or photons (Ps), tends to correspond to one to one thousand millions! Yes, Ps are not ethereal radiation but particles. Richard Feynman taught Cal Tech students "I want to emphasize that light comes in this form — particles. It is very important to know that light behaves like particles, especially for those of you who have gone to school, where you were probably told something about light behaving like waves. I'm telling you the way it DOES behave — like particles. Light is made of particle" [4]. In the same way Weinberg said: "we have to renounce to the classical idea of radiation in terms of EMWs, we have used so far, and use the more modern *quantum* vision, according to which the radiation is made of particles known as *photons*. A normal luminous wave has a high number of photons which travel together. Each of them carry a very well defined energy and a momentum" [3].

We see than, as all elementary particle, also the P has a its own *momentum* (p) represented in the formula

$$p = h/\lambda \tag{1}$$

where h is Planck's constant, corresponding to $6.625 \cdot 10^{-27}$ [erg·s], and λ represents the wave length of the considered radiant particle. The mean wave length of a P in the optical band corresponds to 570 nanometres. A nanometre corresponds to 10^{-9} [mt], which in the *cgs* metric system corresponds to 10^{-7} [cm]. Hence 570 nanometres correspond to $5.7 \cdot 10^{-5}$ [cm].

Let's consider the *momentum* of a P in the optical band, with a mean wave length:

$$p = \frac{6.625 \cdot 10^{-27} \, [\text{erg} \cdot \text{s}]}{5.7 \cdot 10^{-5} \, [\text{cm}]} \tag{2}$$

Since $1\text{erg} = \frac{\text{g·cm}}{\text{s}^2} \cdot \text{cm}$, that is $1\text{erg} = \frac{\text{g·cm}^2}{\text{s}^2}$, we can write (2) in another way:

$$p = \frac{6.625 \cdot 10^{-27} \left[\frac{\text{g·cm}^2}{\text{s}}\right]}{5.7 \cdot 10^{-5} \, [\text{cm}]} \tag{3}$$

We can develop the (3):

$$p = 1.1623 \cdot 10^{-22} \left[\frac{\text{g} \cdot \text{cm}}{\text{s}}\right] \tag{4}$$

This is the value of the *momentum* of a P in the optical band. It shows that a common EMR particle is not so ethereal [5, 6].

If we consider that a common baryonic particle, that is the proton, weighs $1.6726 \cdot 10^{-24}$ [g], we have that a common visible P carries a *dynamic mass* equal to the mass of 100 protons (curiously it corresponds just to the mass given to the hypothetic WIMPs). This is particularly significant if we consider that for each proton in the universe there are about one thousand millions Ps. The universe is full of Ps.

3. CONCLUSION

To better under stand what MM is made of, we should point our attention on invisible matter halos in which galaxies are immersed and surrounded.

One of the most spectacular examples of invisible halos was showed around the big elliptic galaxy M87 by Fabricant and Gorenstein, and by Forman and Jones (at Harvard-Smithsonian Centre for Astrophysics). The data were collected with the X ray counter from *Einstein* [1]. We learn from Giacconi and Tucker "every time there is a central galaxy in a cluster of galaxies we find that it is surrounded by a wide X ray crown and, implicitly, by a big halo of invisible mass" [1]. Why can't we think these halos are made mainly of EMR belonging to non visible bands? In this case, the value of the P *momentum*, coming from our calculations, may contribute to represent the invisible mass, the MM, which adds a gravitational mass about 10 times bigger than the mass observed in stars and in galaxy gasses.

If we consider a P of the most energetic radio band, let's say with a wave length about 10^{-3} [cm], we have that its *momentum* corresponds about 10^{-24} [g·cm/s], which is superimposable to the mass of a proton. On its turn a XP, with a wave length 10^{-8} [cm], will carry a *momentum*, that is a dynamic mass, about 10^{-19} [g·cm/s], that is 10^5 times bigger than the mass of the proton.

In short, if invisible halos surrounding the galaxies were made mainly of EMR, we could explain the gravitational effect 10 times bigger than the visible mass and better understand the mystery of the MM. Thus, according to Zwicky the invisible mass (MM) represents the mass on which the gravity force (GF) acts. However, if we consider the MM as made of radiant energy, that is Ps, how can the GF, coming from the big masses at the centre of the galaxy, act at the periphery on particles considered mass less?

However this is not surprising. It is known that the EMR, the Ps, *feel* the GF. "Einstein's prediction based on his General Theory of Relativity says that the light feels the GF. Thus, during a sun eclipse it has been possible to observe that the light of far away stars, going pass the sun, rather than spread in a straight line, made a curved path towards the sun itself" [7]. Not only does the light, EMR, *feel* the GF, Ps can also make a gravitational effect. At this proposal we learn from Weinberg: "At the beginning of the history of universe, it was the total density of energy, of the various Ps, electrons, positrons, etc. to provide the source of the universe gravitational fields. Not only are gravitational fields generated by the mass of the particles but by any form of energy too. The Earth is orbiting around the Sun with a speed slightly higher than the one it would have if the sun wasn't hot, because the energy in the heat of the Sun contributes (though slightly) to its gravitational force" [3]. Besides: "Any particle having energy (mass) creates a gravitational field. According to Einstein, in its gravitation theory (General Relativity) mass and energy are related, so any object having energy attracts gravitationally other object" [7].

It is normal to wonder: how can a mass less particle such as the P to *feel* the GF, or even exert a gravitational effect? But it is just so! An explanation may come from the *momentum* of the P. We have seen how calculations show that the *momentum* of the P carries a dynamic mass completely superimposable to the hadronic mass. That is why the P can behave in the same way as a baryon, that is as a massive particle, probably giving the real consistency to the invisible mass, the MM, necessary to make the account balance in the motion of galaxies and cluster of galaxies.

REFERENCES

1. Giacconi, R. and W. H. Tucker, *The X-Ray Universe. The Quest for Cosmic Fire from Black Holes to Intergalactic Space*, Mondadori Ed., 170–179, Milano, 2003.
2. Hack, M., *Dove Nascono le Stelle*, Sperling & Kupfer Ed., 177, Milano, 2004.
3. Weinberg, S., *The First Three Minutes. A Modern View of the Origin of the Universe*, Mondadori Ed., 65–66, 87, 100, 161, Milano, 1977.
4. Feynman, R. P., *QED. The Strange Theory of Light and Matter*, Adelphi Ed., 30–31, Milano, 1989.
5. Puccini, A., "About the zero mass of photon," *Progress In Electromagnetics Research*, PIER 55, 117–146, 2005.
6. Puccini, A., "Light weighs," *Progress In Electromagnetics Research B*, Vol. 8, 161–177, 2008.
7. Kane, G., *The Particle Garden*, TEA Ed., 172, 215, 182, Milano, 2002.

The Inflationist Expansion of the Universe Was Conducted by Very High Energy Photons

Antonio Puccini

Department of Neurophysiology, Order of Malta, Naples, Italy

Abstract— The inflationist expansion of the universe was probably conducted by very energetic photons (Ps) since the Big Bang represents a source of very high electromagnetic emission. We think that the Ps emitted had an energy bigger than gamma Ps (10^{27} Hz). The fact that these Ps induced the inflationist event coincides with the extremely homogeneous and isotropic presence of the bottom cosmic radiation, which is just the phantom of the electromagnetic radiation initially emitted with the Big Bang.

There is no satisfactory physical explanation to justify expansion speed of the inflationist phase, much bigger than the speed of light. However, if we consider that the inflation was basically conducted by these extremely energetic Ps, we may be able to explain the high speed expansion. It may be explained with the Quantum Mechanics, through the Uncertainty Principle: $\Delta_E \cdot \Delta_T \geq h/2\pi$.

Indeed, if we apply this principle to the electromagnetic radiation, we have that the bigger the Energy of the P, the bigger its speed.

1. INTRODUCTION

The most accepted theory on the origins of the universe (U), known as *the standard model*, says that the universe started with a big explosion. Two important points support the theory: 1) the galaxies recession; 2) the feeble bottom fossil radiation, or *cosmic microwave radiation* (CMR) — foreseen by Gamov [1] and detected by Penzias and Wilson [2] — which comes from every direction in the U and which is verifiable everywhere. "The reasons to believe in an explosive origin of the universe come from a theory study of Einstein *field equation* in a cosmologic context, carried out by Friedmann 1922. Later, in 1929, Hubble discovered that far galaxies are actually departing from us, implying that the matter of the U is the result of a huge explosion, known as Big Bang (BB). Cosmological models of the class studied by Friedmann are called *Friedmann-Lemaitre-Robertson Walker models* — (FLRW). A FLRW model is characterized by the fact that it is completely *spatially homogeneous and isotropic*. This shortly means that the U appears similar in all directions, thus it has a O(3) rotational symmetry group. *Spatially homogeneous* means that the U, at any changing, appears equal in every point of the space too. These two hypothesis represent a good agreement with observations of the matter distribution on a very big scale and with the nature of the black-body radiation. It really seems that *homogeneous and isotropic* cosmologies are excellent approximations of the structure of the real U" [3].

2. DISCUSSION

First we should state that "Alan Guth, trying to find a model of the U in which many initial different configurations could have evolved in something similar to the present U, suggested that the primitive U may have gone through a very rapid expansion period. According to Guth, in an extremely small fraction of second the ray of the U grew 10^{30} times. Any irregularity in the U was *levelled* by the expansion, as the creases of a balloon as we inflate it. In this way the *Inflationary Theory* (IT) explains how the present regular and uniform state of the U could have emerged also from many different and non uniform initial states" [4]. With the IT [5, 6] Guth manages to solve two big problems of cosmology, unsolved by the FLRW models: the horizon and flatness problems. 1) The *flatness problem* comes out when we use a *flat* geometry for the U. According to a number of estimations the present density of the U is completely superimposable to the one just a second later the BB, concluding that the cosmos is incredibly *flat* [7]. 2) The *horizon problem* was born from the study of the CMR: how can this radiation be so homogeneous in all possible spatial directions? The homogeneity cannot come from an exchange of information between them since, in all directions, the points with a distance bigger than their reciprocal cosmic horizon cannot see each other [7]. As described by Guth and Pi "the inflationary-U scenario was proposed as a possible solution to the horizon flatness, and monopole problems. In this scenario the U supercools by many orders of magnitude below the critical temperature of a grand unified theory (GUT) phase transition, and in

the process it exponentially expands by an enormous factor. In this 'new inflationary U', the entire observed U emerges from a single bubble or fluctuation. The U expands exponentially as the Higgs field φ slowly 'rolls' down the potential, and the energy is then rapidly themalized when φ begins to oscillate about its minimum. We will examine the consequences of the quantum fluctuations of the scalar field φ which occur during the era of exponential expansion. We find that the new inflationary U leads to $\delta\rho/\rho$ which is roughly independent of scale, but with a magnitudo of $\approx$ 50" [6]. The IT postulates that our U is part of a bigger super-U which and was born, respecting the concepts of the Quantum Mechanics, after a *vacuum fluctuation* which occurred in the super-U. Einstein cosmological constant can be considered the mathematical representation of the *vacuum energy* and, inserting it in its *field equation*, makes the IT more congruous:

$$R_{\mu\nu} - 1/2g_{\mu\nu}R - \lambda g_{\mu\nu} = -8\pi G T_{\mu\nu} \tag{1}$$

where $R_{\mu\nu}$ is Ricci bending tensor Ricci, R its *trace*, λ the cosmological constant, $g_{\mu\nu}$ is Riemann metric tensor (it measures the distance in a bent space), G Newton gravitational constant ($6,6742 \cdot 10^{-11}$ [m^{3}kg^{-1}s^{-2}]) and $T_{\mu\nu}$ represents Einstein tensor Energy-Impulse.

Hawking pointed some problems among them the fact that in the primordial U, very hot, "there was not enough time so that the heat could pass from a region to the other" [4]. Strictly connected there is the surprising homogeneous and isotropic distribution of CMR and thus the *flatness problem*. An explanation may come from the isotropic diffusion (set up with the BB, and sped up by the *inflationary phase*) of highly energetic γ Ps, carrying the heat wherever they go (that is in every corner of the primordial U). The result is a "uniform distribution of the energy" [4]. In this way we can explain the present h*omogeneity* and *isotropism* of the CMR. As Hawking says: "the temperature is just a measure of the mean energy (or speed) of the particles" [4]. Thus, 'temperature, energy and/or mean velocity' are pretty correlated.

We learn from Weinberg "the density of energy (that is energy per litre) of the EMR expresses the number of Ps (per litre) multiplied the mean kinetic energy (MKE). The MKE is just proportional to the temperature. On its turn the density of energy is proportional to the fourth power of the temperature (T): with $T = 1°$K the energy density of the black-body radiation is $4,72$ eV per litre. With $T = 10°$K will be $4,72 \cdot 10$ per litre; Thus with a temperature of $10^{11}°$K, according to Stefan-Boltzmann Law, will be $4,72 \cdot 10^{44}$ eV per litre" [8].

Kirkoff (1860) studying the radiation coming from the sun, understood that the ratio between the energy emitted by a heated body (black-body radiation) as electromagnetic radiation (EMR) and the absorbed energy, was a *function (P)*, as indicated by (2):

$$P(\lambda, T) \tag{2}$$

where λ is the wave length and T the absolute temperature.

It was already clear the inversely proportional relation between the λ of a EMR and T. As a consequence the directly proportional relation between the frequency (f) of a EMR and T [9]. In short, as T increases, f increases too, and with it the energy of the EMR we are examining. In fact, Feynman says: "the MKE is thus some *function of the temperature*. The best way to do it would be *to call the MKE itself the temperature*" [10]. We also know that " the emission of a black-body, according to the wave length (λ) depends only by the temperature of the body, and not by the matter it is made of. This emission is represented by a bell curve (Planck curve) which has a maximum intensity (B_λ) of the emitted radiation with a wave length as shorter as bigger the temperature: B_λ is a *function* of λ. The emission of the primordial U, a plasma, was the one of a black-body with very high temperature" [11].

We learn again from Weinberg that " the primordial U was full of light. Light must not be considered as something different from the particle: the Quantum Theory tells us that the light is made of particle known as Ps. Each P carries a well defined quantity of energy and motion (*momentum*) depending on the wave length of the light" [8]. Indeed "the CMR is made of those Ps which filled the U just after the BB, which ever since have just gone around the world, losing energy" [12]. The CMR in 13,7 thousand millions years has lost a lot of energy, both as heat — in fact its temperature is just 3°K above absolute zero — and as energy of motion, or rather *momentum (p)*, and frequency (f), which in every electromagnetic wave are inversely proportional to the wave length (λ). In fact $p = h/\lambda$ (h is Planck constant), and $f = c/\lambda$ (c is the light speed in vacuum).

The λ of the CMR detected by Penzias and Wilson is 7,35 cm [2, 8]. Thus we can calculated the frequency (f) of the CMR:

$$f = c/\lambda = 2,9979 \cdot 10^{10}\,[\text{cm/s}]/7,35\,[\text{cm}] = 0,40787 \cdot 10^{10}\,[\text{cm/s}] \cdot [1/\text{cm}] = 4,0787 \cdot 10^{9}\,[1/\text{s}] \quad (3)$$

This is the frequency of the CMR, related to $\lambda = 7,35\,[\text{cm}]$. If λ was close to 3 cm, as may come from more detections, then the f of the CMR would correspond to $10^{10}\,[1/\text{s}]$. As we know also λ, with time, has become longer and longer, we may presume it was very short when it was emitted. It is useful to keep in mind that "the typical wave length (λ), around which most of the black-body radiation is concentrated corresponds to $\lambda = 0,29\,[\text{cm}]$ with a temperature (T) of 1°K" [8]. Let's examine a P of the *U-inflationary*, with T around $3 \cdot 10^{10}$°K. In order to get its λ, we need to divide 0,29 for T, that is:

$$\lambda = 0,29/3 \cdot 10^{10} = 9,666 \cdot 10^{-12}\,[\text{cm}] \quad (4)$$

It is seven poker shorter than the λ of the visible light. Of course if the T of the *inflationary phase* had been about $3 \cdot 10^{11}$°K, we would have had: $\lambda = 9,666 \cdot 10^{-13}\,[\text{cm}]$. Let's analyse the corresponding energy (E) and the corresponding frequency (f):

$$f = c/\lambda = 2,9979 \cdot 10^{10}\,[\text{cm/s}]/9,666 \cdot 10^{-12}\,[\text{cm}] = 0,31015 \cdot 10^{22}\,[\text{cm/s}][1/\text{cm}] = 3,1015 \cdot 10^{21}\,[1/\text{s}] \quad (5)$$

A T of one power bigger would increase the frequency of the P of the *inflationary phase*. In this phase Ps had to have probably a f at least 10 millions times bigger than a common visible light. Finally let's analyze the energy (E) of the primordial Ps. As Planck pointed out, the Energy of the P is given by the formula:

$$E = h \cdot f = 6,625 \cdot 10^{-27}\,[\text{erg} \cdot \text{s}] \cdot 3,1015 \cdot 10^{21}\,[1/\text{s}] = 20,54744 \cdot 10^{-6}\,[\text{erg}] = 2,054744 \cdot 10^{-5}\,[\text{erg}] \quad (6)$$

Since $1\,\text{eV} = 1,602 \cdot 10^{-12}\,[\text{erg}]$, we can measure the energy of the primordial P in eV:

$$E = 2,054744/1,602 \cdot 10^{-5}/10^{-12} = 1,282 \cdot 10^{7}\,\text{eV} \quad (7)$$

We notice that, as the f, also the E of the primordial P is ten million times bigger than the energy of the solar light (2,48 eV). We can get to the same value from a different path. We know that the P with $\lambda = 1\,\text{cm}$ has an Energy of (E) = 0,000124 eV [8]. Thus we divide this value for λ of the primordial P:

$$E = 0,000124\,[\text{eV}]/9,666 \cdot 10^{-12}\,[\text{cm}] = 0,00001282 \cdot 10^{12} = 1,282 \cdot 10^{7}\,\text{eV} \quad (8)$$

If at that time the temperature had been of a power bigger, the energy of the P would have been around 10^{8} eV. Hawking says: "the temperature is just a measure of the mean energy (or speed) of a particle" [4]. What were the particles in the primordial U? Weinberg tells us: "at the origins of the U the light was the main ingredient of the U. There were basically Ps, as well as neutrinos and electrons, with their respective anti-particle. The common matter was just a negligible contamination: there has been a number of Ps for proton or neutron between 100 millions and 20 thousand millions" [8].

3. CONCLUSIONS

In short, light dominate the U. What kind of light was it? It was highly energetic EMR, mostly (or totally) invisible, since it was basically made of high energy Ps, mainly γ Ps.

Thus, if the particles of the primordial U were mainly Ps, then the Ps underwent the influence of the very high temperature, which increased considerably "their mean energy and speed", along with Hawking. Those primordial Ps must have been extremely hot and fast. Their motion energy was provided by the big initial push and the high heat and, as Weinberg underlines, "by the continuous annihilation electron-positron which has given the Ps a temperature (and thus a motion energy) 35% higher than neutrino's" [8]. Such continuous annihilation, as we learn from Quantum Mechanics, are produced by quantum fluctuations generated by the *vacuum energy*, that is the same energy which set up the *inflationary phase*.

The IT postulates that the U in its first fraction of second expanded very quickly, with an exponential speed, thanks to an unusual form of energy (the *vacuum energy*). The latter created a gravitational repulsion able to provide the motive-power for the cosmic expansion. It pushed

the U towards a critic density, explaining at the same time the *homogeneity of the space*. It also gives a solution to the *horizon problem*. Why can't we think that primordial Ps underwent, at high temperature, an acceleration that today we cannot think of? That is, those Ps, γ prevalently, having an energy of at least 10^7 eV and a frequency bigger than 10^{21} Hz, with extremely high temperature underwent an as much high acceleration, faster than the visible light, with an exponential increase of their energy and frequency, even bigger than the powerful γ Ps we know. Besides, highly energetic γ Ps may provide an explanation to the "extremely quick expansion" [4] set up by the *inflationary phase*. They may also provide a physical substrate to the extremely quick expansion (much quicker than the light), and a solution to the *horizon problem*.

In this way we have a physical substrate to explain how the *inflationary expansion* propagated: it was carried by high energetic and very fast Ps. Probably this explanation may appear in conflict with common physical ideas, however we have to consider that "the inflation occurred at a speed much bigger than the speed of light, it occurred when the U was empty. The insuperable limit of the speed of light is applied to the matter, but the matter did not exist yet, or rather there were quantum fluctuations of the vacuum" [11].

Eventually in order to try to accept the idea that in a past there may have been, though for a very short moment, such a violent and quick expansion of the U to be able to exceed the speed of light itself, we can take in consideration Heisenberg's Uncertainty Principle:

$$\Delta_E \cdot \Delta_T \geq h/2\pi \tag{9}$$

If we apply Heisenberg's Uncertainty Principle to EMR, we have that the higher the energy an electromagnetic wave carries, the shorter its time of travelling and hence the higher the speed of the wave" [13]. It was the multitude of primordial highly energetic Ps, γ Ps with very high frequency, to represent the physical support to justify the velocity of the *inflationary expansion*, much bigger than the speed of light. Besides as Feynman says: "no one has ever found (or even thought of) a way around the uncertainty principle. So we must assume that it describes a basic characteristic of nature" [10].

REFERENCES

1. Alpher, R., H. Bethe, and G. Gamov, *Physical Review*, Vol. 73, 803, 1948.
2. Penzias, A. A. and R. W. Wilson, *Astrophysics Journal*, Vol. 142, 419, 1965.
3. Penrose, R., *The Road to Reality*, Vol. 704, 717–718, RCS, Milano, 2005.
4. Hawking, S., *A Briefer History of Time*, Vol. 84, 89–90, Rizzoli, Milano, 2005.
5. Guth, A., *Physical Review D*, Vol. 23, No. 2, 347–356, 1981.
6. Guth, A. and S.-Y. Pi, *Physical Review Letters*, Vol. 49, No. 15, 1110–1113, 1982.
7. Aczel, A. D., *God's Equation*, 155–156, Il Saggiatore, Milano, 2004.
8. Weinberg, S., *The First Three Minutes: A Modern View of the Origin of the Universe*, Mondadori, Milano, 2001.
9. Puccini, A., "Light weighs," *Progress In Electromagnetics Research B*, Vol. 8, 161–177, 2008.
10. Feynman, R. P., *Feynman's Lectures on Physics*, Zanichelli, Bologna, 2004.
11. Hack, M., *Dove Nascono Le Stelle*, 189–190, Sperling & Kupfer, Milano, 2005.
12. Gratton, L., *Relatività, Cosmologia, Astrofisica*, Vol. 202, Torino, Boringhieri, 1976.
13. Puccini, A., "Uncertainty principle and electromagnetic waves," *Journal of Electromagnetic Waves and Applications*, Vol. 19, No. 7, 885–890, 2005.

Self-field Theory — A Possible Gravitational Structure for Galaxies

A. H. J. Fleming

Biophotonics Research Institute, Melbourne, Australia

Abstract— This report brings two seemingly unrelated phenomena together: the EPR paradox, a thought exercise Einstein used to infer quantum mechanics was incomplete, and the orbital rotation of solar systems in galaxies, mainly invariant with radial distance from the galactic centre that has been hypothetically explained via dark matter, a halo of matter invisible to Earth thought to surround galaxies. Self-Field Theory (SFT) is a new bispinorial description of electromagnetic (EM) interactions applying across physics. SFT utilizes exact closed-form solutions of the Maxwell-Lorentz (ML) equations containing two curl and two divergence equations. The eigenvalue equations indicate a photonic level physics sitting underneath the atomic level physics via two new quantum numbers relating to the phase length of photons and the discretization of the motions of atomic particles. Hence electrons and protons are in dynamic balance via photons acting as binding energy within atoms at the EM level while photons and other bosons again act as binding energy at the gravitational level between planets and suns. Strong nuclear (SN) regions of atoms can be described via trispinorial forms involving a modified system of ML equations incorporating three curl and three divergence equations instead of the two curl and two divergence equations of EM interactions. There is correspondence between the internal boson structure and the form of the gravitational structure: the photon corresponds to bi-rotational motion while the gluon corresponds to tri-rotational motion. There is an acoustic (A-) field in addition to the electrical and magnetic fields that binds the galactic constituents together within a 3-D system of forces that stiffens the galaxy into one viscous mass. The dynamics of solar systems orbiting within galaxies can be described using such trispinorial motions.

1. INTRODUCTION

Historically a widespread and considered opinion existed from 1687 till the 1930s that gravitation throughout all levels of interaction within the Universe was similar to that in the Solar System as proposed mathematically by Newton. Lagrange in the late 1700's followed the mechanical and astronomical paths in Newton's footsteps confirming and extending the application of Newton's gravitational laws to the full extent of the then known Universe. This was a time pre-quantum physics and pre-relativity during the 18th century when the Universe was thought of as a nebula, the term 'galaxy' did not appear in any index, and 'cosmogony' was used in discussing how the Solar System formed out of the Universe. In 1915, Einstein extended Newton's inverse square law to a system of geodesic equations that took into account the speed of light treated as an observable constant; this in effect was an extension to a second degree of freedom within gravitation at the level of the Solar System. In the 1920's Hubble used the 100 inch telescope at Mount Wilson to discover that the local 'star groups' were in fact other galaxies. He subsequently discovered cosmological redshift, a discovery that lead eventually to the theory of the Big Bang. In 1931, Oort observed the red-shift of stars near the Galactic Plane (GP). He found that the variation of orbital speeds with radial distance away from the Galactic Centre (GC) were fairly invariant unlike the Solar System where orbital speeds diminish. Zwicky in 1932 extended this finding by studying galaxies within the Coma Cluster measuring similar results. If gravitation were Newtonian, the stars should fly apart; the Milky Way Galaxy and its myriad counterparts within the Universe were thus now problematic in terms of their gravitational structure. Over the intervening years to the present one hypothesis is that dark matter including Massively Compact Halo Objects, and Weakly Interacting Massive Particles supplies the missing matter. Another hypothesis is MOdified Newtonian Dynamics that heuristically changes Newton's constant of gravitation to match the observed rotational speeds.

A recent separate line of inquiry was opened up when cycles of biodiversity were found to exist within the fossil record. Rohde and Muller found cycles at 62 Myrs. Medvedev and Melott confirmed the cycles and discussed them in terms of the Solar System's oscillatory motions orthogonal to the Galactic Plane (GP). Fleming in a parallel talk in this same PIERS session also found further reasons linked to the extinction of large structured mammals to support the finding of cycles of biodiversity within a tri-rotational system of dynamics. Galactic resonances of the A- and EM energy match the evidence of cycles within the fossil record. The orbital speeds of galaxies also match the presence of the acoustic field than Hans Jenny demonstrated was linked to the formation

of solid structures. (A planet acts approximately as a solid; magnetic moments cause plate slippage or earthquake within planets where moments vary with material and depth). This tri-rotational dynamics can be linked to SFT via a modified system of ML equations to describe regions where the SN interactions occur. The normal ML equations become modified where Maxwell's equations usually consist of two curl and two divergence equation, four in total, become six by adding an extra curl and an extra divergence equation. These six equations support a system of quarks and gluons within the nucleus that have a three-way interaction between triplets of particles and rotate in three orthogonal directions, this tri-rotational motion linking to the recent analysis of the galactic tide by Klacka.

2. EPR AND BOSON STREAMS

The well-known EPR paradox lies at the heart of the way SFT sees gravitational physics at the Solar System level which can be described as a dipolar interaction between atoms either within their near- or far-field zones of interaction where far-field can include AU distances. Einstein challenged quantum theory that he saw as incomplete in a paper that contained the paradox. As a consequence of this historical debate quantum entanglement is now understood as a way in which parts of a QM system are connected. The quantum states of the constituent parts are linked together so that one part cannot be properly described without mention of all other parts within the system. Einstein referred to this as 'spooky action at a distance'. SFT too sees quantum theory as incomplete. SFT suggests a missing coordinate within the photon that is the underlying reason for Heisenberg's Uncertainty Principle and its incomplete knowledge at the photonic level. Within atomic and molecular physics according to SFT photons link many atoms together. This is the underlying photon level of interaction applying to matter within the Universe. SFT sees two extra quantum numbers that are linked to the discretization of the paths of the bi-rotations of the electron and proton within the atom which are created by the photon in its role as binding energy. This applies to crystals where atoms rotate in synchronized fashion and to biological systems where biophotons emitted from DNA acting as a hydrated liquid crystal at metaphase link to other objects in the view of the biological system. This usually implies the biological capacity for optical sight but can encompass other forms of biophotonic emission and detection. This includes the complete body-fields of biological systems in general but is found in specialized physiological tissues such as the elasmobranch fish that use pores, the ampullae of Lorenzini, on the periphery of their dorsal fins for predation.

The physics of this photon level interaction can be a resonance phenomenon as is the case inside atoms, molecules, or crystals where it acts as a binding energy and its phase length can range over multiples of $\pi/2$. The interaction can also be a long-range dipole-dipole effect, or gravitation whereby the molecules in a massive conglomerate are linked to other nearby or remotely located massive conglomerates. The phase lengths involved are now averaged across a range of different wavelengths where the individual and ensemble masses may not be in dynamic equilibrium depending on the dynamic state of the gravitational system involved. Again photons or the various derivatives of their flux densities, including the radial derivatives act as a binding energy between masses. At the atomic level there are very few streams of photons, the streams act only between couples of atoms and the photons move in double rotations as per the general solution of partial differential equations. At the level of the Solar System the streams couple all conglomerates via an interconnected array of forces. The photons emitted and absorbed by the atoms within the conglomerates still stream only between atoms taken two at a time. Photons as distinct from gluonic bosons for example cannot physically form streams between more than two atoms at any one time. Gluonic structures on the other hand can form streams between triplets of quarks depending on the energy density available inside nuclei. Gluons can also form long-range or gravitational forces between remotely located quarks residing in different massive conglomerates. The individual quarks interact only in triplets; however conglomerates at the macroscopic level interact with all other conglomerates.

It is noted that like photons within the Solar System, if the strong force gluons exist outside the nuclei they will lose and then regain some of their energy during transit through deep space converting into lower energy fields that are carried as a binding energy within the Galaxy. When they reach their destination the energy rises until they reach the particular nucleus they connect to when they again have sufficient energy to interact via elastic collision as is the case with photons acting as binding energy. It appears from SFT that some bosonic collisions are involved in this gravitational role. This role of bosons as binding energy between more massive particles is the

underlying driver for the existence of streams of field particles noted to exist at the Solar System level and used by NASA. Physically what may be found is that these streams exist in deep space waiting to be discovered as regions of relatively higher energy when compared with normal deep space. If a probe should enter one of these streams it may find the energy density rises beyond that of ordinary space where no such streams exist. In fact such a system of streams has been used by Lo working at the Jet Propulsion Laboratory at California Institute of Technology and the National Aeronautics and Space Administration to design a low-energy transit for the Genesis mission flight path. The streams have been described as "*a 'freeway' through the solar system resembling a vast array of virtual winding tunnels and conduits around the Sun and planets ... can slash the amount of fuel needed for future space missions.*" At present such streams are applied as staging points for interplanetary travel. Similar streams composed of various bosons may exist at all levels of gravitational structure.

3. BOSONS AND GRAVITATIONAL STRUCTURE

Binney and Tremaine in 1987 approximated the galactic tide within the GP as a function of x and y with no gravitational effect due to the z direction using a Cartesian system at the Galactic Centre. Klacka in 2009 derived an equation of motion for the galactic tide that included the z-component. Thus there are three components of galactic gravitation distinct from the two components of gravitation of the Solar System. These three components of gravitation link directly to SFT where the SN forces involve three degrees of freedom. Fleming has recently discussed the relationship between gravitation and the differential forms of ML equations. While the photon has an internal structure consisting of two internal particles having equal mass the gluon can by analogy be described as a three-particle internal structure each of equal mass. As discussed below the ML equations in the SN region controlling the motions of quarks may be differentiated to form a tri-rotational gravitational system.

At the EM level the ML equations are written in matrix form where each particle has two spinor motions σ_i^{EM} and a current κ_j^{EM}.

$$M_{ij}^{\mathrm{EM}} \sigma_i^{\mathrm{EM}} = \kappa_j^{\mathrm{EM}} \tag{1}$$

The motion of the electron is an exact EM self-field solution, its position at any time is the sum of two spinors forming a bispinorial motion $\sigma_o^{\mathrm{EM}}(r_o, \omega_o)$ and $\sigma_c^{\mathrm{EM}}(r_c, \omega_c)$ where the distance of the electron is written as a sum of the spinors not a Pythagorean root mean square but a function of orthogonal orbital and cyclotron spinors:

$$r^{\mathrm{EM}}\left(r_o^{\mathrm{EM}}, \omega_o^{\mathrm{EM}}, r_c^{\mathrm{EM}}, \omega_c^{\mathrm{EM}}\right) = r_o^{\mathrm{EM}} e^{j\omega_o t} + r_c^{\mathrm{EM}} e^{j\omega_c t} \tag{2}$$

Direct substitution of such bispinors into the eigensystem of ML equations provides a closed-form system of atomic solutions. At the EM level the motion of the electron has four unknowns as visualized in Fig. 1.

Figure 1: Plot of bispinorial solution for electron motion in $r_o - \phi_o$ and $r_c - \theta_c$ planes where $r_o = 4r_c$ and $\omega_c = 16\omega_o$.
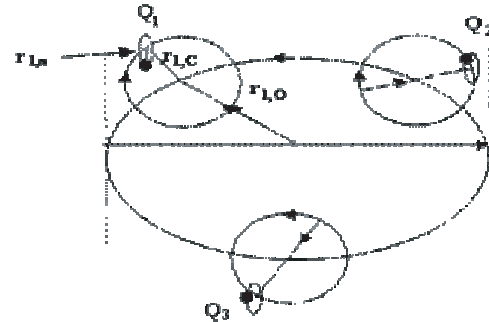

Figure 2: Model of proton consisting of three quarks each having three degrees of rotational freedom.

A parallel formulation exists at the SN level where each quark is proposed to have three spinor motions σ_i^{SN} and a SN current κ_j^{SN}.

$$M_{ij}^{\mathrm{SN}} \sigma_i^{\mathrm{SN}} = \kappa_j^{\mathrm{SN}} \tag{3}$$
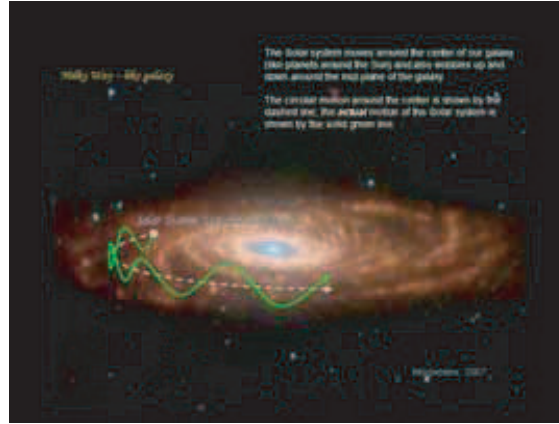
Figure 3: Galactic dynamics: typical sun orbiting around the centre of a galaxy (Credit: Medvedev and Melott).

The motion of the quarks may be an exact SN self-field solution, its position the sum of three spinors forming a tri-spinorial motion $\sigma_o^{\text{SN}}(r_o, \omega_o)$, $\sigma_c^{\text{SN}}(r_c, \omega_c)$, and $\sigma_t^{\text{SN}}(r_t, \omega_t)$; the total distance of the quark can be written as a sum of three spinors again, not a Pythagorean root mean square, but a function of orthogonal spinors, one orbital, one cyclotron, the third designated tangential:

$$r^{\text{SN}}\left(r_o^{\text{SN}}, \omega_o^{\text{SN}}, r_c^{\text{SN}}, \omega_c^{\text{SN}}, r_t^{\text{SN}}, \omega_t^{\text{SN}}\right) = r_o^{\text{SN}}e^{j\omega_o^{\text{SN}}t} + r_c^{\text{SN}}e^{j\omega_c^{\text{SN}}t} + r_t^{\text{SN}}e^{j\omega_t^{\text{SN}}t} \tag{4}$$

Direct substitution of these trispinors into the SN eigensystem of ML equations provides a closed-form system of nuclear solutions. At the SN level SFT has six unknowns per particle.

Differential forms of the EM (DEM) and SN (DSN) ML matrices exist where the rotations can take place in orthogonal planes to their undifferentiated SFT forms; these planes now include the axial spins of a planet or solar system as distinct from the cyclotron motions of an electron or quark:

$$M_{ij}^{\text{DEM}}\sigma_i^{\text{DEM}} = \kappa_j^{\text{DEM}} \tag{5}$$

$$M_{ij}^{\text{DSN}}\sigma_i^{\text{DSN}} = \kappa_j^{\text{DSN}} \tag{6}$$

4. CONCLUSION

According to SFT galactic gravitation may be related to a differential form of the SN ML equations: The internal three-particle structure of the gluon, and the tri-rotational dynamics of quarks within atomic nucleus, corresponds to the tri-rotational gravitational dynamics (Fig. 3). Looking at the general picture that emerges from SFT, in terms of the bosonic structures involved, and observing the evidence from cosmology, it seems the Universe is segmented into layers of structure that depend on the spatial variation of energy density to form Solar Systems, Galaxies, Super Clusters, and perhaps the Universe itself. According to SFT each layer has its own gravitational structure depending on the energy density and the bosons available as a function of space-time.

REFERENCES

1. Williams, H. S., *The Story of Nineteenth Century Science*, Harper and Brothers, 1900.
2. Rohde, R. A. and R. A. Muller, "Cycles in fossil diversity," *Nature*, Vol. 434, 208–210, 2004.
3. Medvedev, M. V. and A. L. Melott, "Do extragalactic cosmic rays induce cycles in fossil diversity?" *Astrophys. J.*, Vol. 664, 879–889, 2007.
4. Jenny, H., *Cymatics: A Study of Wave Phenomena and Vibration*, 3rd Edition, Macromedia Press, July 2001.
5. Lo, M. W. and M. J. Chung, "Lunar sample return via the interplanetary superhighway," *JPL, TRS*, 1992.
6. Binney, J. and S. Tremaine, *Galactic Dynamics*, Princeton University Press, 1987.
7. Klacka, J., *Galactic Tide*, arXiv-0912.3112v1 [astro-ph.GA], December 16, 2009.
8. Fleming, A. H. J., "Electromagnetic self-field theory and its application to the hydrogen atom," *Physics Essays*, Vol. 18, No. 3, 265–285, 2005.

9. Fleming, A. H. J., "Self-field theory, analytic spectroscopy of the ordinary photon," *Proc. 2nd Electromagnetics Health and Environment Intl. Conf.*, 18–23, Wroclaw, Poland, 2007.
10. Fleming, A. H. J., *Self-Field Theory — A New Mathematical Description of Physics*, Pan Stanford Publishing, to be published, 2010.

Self-field Theory-biodiversity May Be a Resonance Process

A. H. J. Fleming

Biophotonics Research Institute, Melbourne, Australia

Abstract— Self-Field Theory (SFT) is a new description of electromagnetic (EM) interactions that utilizes closed-form solutions of the Maxwell-Lorentz (ML) equations. Bispinorial motions apply to the motions of EM field-particles and interacting particles including electrons and protons. The strong nuclear region of atoms may be similarly described via trispinors involving modified ML equations incorporating three curl and three divergence equations that include electric, magnetic, and acoustic fields. The complicated dynamics of suns can be described via a system of galactic gravitational fields. The bispinorial motions of EM interactions are extended to trispinorial motions corresponding to the tri-rotational galactic dynamics. Thus SFT can be applied to the dynamics of suns and their planets. Corresponding to the last 500 Myr history of Earth's fossil diversity a strong Fourier component at around 62 Myr was found. This cycle corresponds to the motion of the Solar System as it bobs up and down around the Galactic Centre. It has been suggested that at points of maximum amplitude in its orbit the Earth is relatively unprotected from nearby gamma-ray bursts. Other possibilities are proposed including the hypothesis that the bulk modulus of biological tissues may drop with the density of galactic matter as the Earth moves to the upper and lower edge of the Galaxy near its maximum amplitude in the plane orthogonal to the Galactic Plane. The effects to the fields on Earth depend on the mutual system of the Galaxy and may be deleterious to the integrity of biological tissue similar to the observation that prolonged stays in free space affect bone, muscle, perfusion and blood pressure. Further it is known that DNA is sensitive to certain EM frequencies which correspond to stages of the cell-cycle. This paper examines these galactic, gravitational, and biological interactions and suggests that biodiversity on Earth may be a resonance process corresponding to the energy density and spectral fingerprint within our Milky Way Galaxy.

1. INTRODUCTION

The general meaning of biodiversity is the variation of life across all level of organization. Recently there have been some interesting findings of cycles within domains of biodiversity. In 2005 Rohde and Muller performed a statistical analysis of Sepkoski's compendium on the stratigraphic appearance of 36.380 marine species sorting the genera into the 295 time periods used by Sepkoski. They produced a plot of diversity against time and found a strong Fourier component at 62 Myr. They suggested 7 possible reasons for the cycles but were themselves unconvinced by any of these hypotheses only suggesting that such strong statistical evidence should be explicable. In 2007 Medvedev and Melott re-examined the initial data and confirmed the findings of a biodiversity cycle of 62 Myr suggesting that cosmic ray extinction events may be responsible as the Solar System bobs up and down. At its maxima the Earth is less protected from nearby cosmic ray events. While cosmic ray events may be more prevalent at the maximum amplitudes of Earth's galactic motion, there are other possible factors of biodiversity.

If the energy density at the Earth's surface were constant, this would imply an infinite and possibly homogeneous region surrounding the Solar System and the Earth. In fact the Galaxy is observed to resemble something between an ellipsoid and a flat disk. Unlike the Solar System there is depth and structure orthogonal to the GP and also the Galaxy has a reasonably constant orbital speed unlike the orbital speed relationship found within the Solar System. The Galaxy therefore rotates approximately like a solid. Acoustic fields are known to be involved in structural integrity. Hans Jenny (1904–1972) studied the interaction of acoustics on the formation of structure within particulate substances such as sand, liquid, and iron filings examining the resonant acoustic modes on a sheet of metal. As the Earth and Solar System move up and down orthogonal to the Galactic Plane, the electric (E-), magnetic (H-), and acoustic (A-) fields on the Earth's surface vary. The Galaxy may be considered to be represented by particles, the Solar System and the Black Hole at the Galactic Centre (GC) moving within an ellipsoidal galactic structure. It can be seen that the E-, H-, and A-fields on the Earth's surface will vary with distance above and below the Galactic Plane (GP). This cyclic variation is partly due to the falling-off in energy density near the upper and lower edges of the Galaxy as the mass density changes abruptly to that of intergalactic space. The associated variation in the fields may be involved in the observed cycles of biodiversity.

2. GALACTIC DYNAMICS

Historically there has been a widespread and implicit assumption that gravitation throughout all levels within the Universe is similar to that in the Solar System as proposed mathematically by Newton in 1687 and Einstein in 1915. Using a Cartesian system centred at the GC Binney and Tremaine in 1987 approximated the galactic tide within the GP as a function of x and y with no gravitational effect due to the z direction. Klacka however in 2009 derived an equation of motion for the galactic tide that included the z-component. Thus there are now accepted to be three components of galactic gravitation as distinct from the two components of gravitation at the level of the Solar System. These three components of gravitation suggest a link to SFT where the strong nuclear forces involve three degrees of freedom. SFT suggests that the strong nuclear fields controlling the motions of charged particles in atoms satisfy the following adaptation of the Maxwell-Lorentz equations. In general, the region is assumed isotropic and homogeneous and ε_n, μ_n and ν_n are invariant scalars. Where nuclear sub-particles, quarks, carrying units of elementary charge q_q are studied, the modified Maxwell-Lorentz equations can be written

$$\nabla \cdot \vec{E} = \frac{q_q}{v_q} \tag{1a}$$

$$\nabla \cdot \vec{H} = 0 \tag{1b}$$

$$\nabla \cdot \vec{N} = 0 \tag{1c}$$

$$\nabla \times \vec{E} + \mu_n \frac{\partial \vec{H}}{dt} = 0 \tag{1d}$$

$$\nabla \times \vec{H} - \varepsilon_n \frac{\partial \vec{E}}{dt} = \frac{\pi}{s_q} q_q \vec{v} \tag{1e}$$

$$\nabla \times \vec{N} + \nu_n \frac{\partial \vec{E}}{dt} = 0 \tag{1f}$$

where the modified Lorentz equation for the forces acting on the quarks is

$$\vec{F} = q_q \vec{E} + q_q \vec{v} \times \vec{B} + q_q \vec{v} \times \vec{M} \tag{1g}$$

and constitutive equations $\vec{B} = \mu_n \vec{H}$, $\vec{D} = \varepsilon_n \vec{E}$ and $\vec{M} = \nu_n \vec{N}$ where ε_n, μ_n and ν_n are invariant scalars, the nuclear constitutive parameters similar to those of free space, ε_0 and μ_0, except the energy density within the nucleus now depends upon the three gluon fields $dU_N = \rho_N dV = \frac{1}{2}(\varepsilon_0 \tilde{E} \cdot \tilde{E} + \mu_0 \tilde{H} \cdot \tilde{H} + \nu_0 \tilde{N} \cdot \tilde{N})dV$ where $\tilde{N}$ is termed the nuclear field and $\tilde{M}$ is the nuclear flux density. As with $c = (\varepsilon_0 \mu_0)^{-1/2}$ there are corresponding relationships between the gluon speed and the ratios of the three fields. These modified equations provide three orthogonal rotations per quark. Where the photon and the phonon are seen to be composite in structure it emerges that the nuclear field is in fact an acoustic field.

In terms of gravitation the above system may be differentiated thus converting into a tripolar form to become a long-range strong nuclear tripole-tripole system of forces between nuclei. Thus there is a long range three-way interaction between strong nuclear masses taken as triplets. This gravitational structure is an extension to that proposed for gravitation at the Solar System level where EM dipole-dipole forces are involved and bispinors apply between pairs of masses as in Newton's and Einstein's gravitational models. In the case of the Galaxy it is the addition of the longitudinal or acoustic field to the EM forces that adds the solidity to the Galactic structure that is observed via the particularly high orbital speeds observed within galaxies. This form of gravitational structure is discussed in a parallel session at this same PIERS conference. The main features in terms of biodiversity cycles are a rotation in the (R, z) plane where $R = \sqrt{x^2 + y^2}$ and the presence of a photon-phonon gluonic field involving E-, H- and A-fields. Like the streams of photons the binding energy within atoms, there will be streams of gluonic bosons acting as the binding energy within the Galaxy. The density of these streams and the energy within the Galaxy itself will fall off near the upper and lower edges of the Galaxy. If the Solar System's motion orthogonal to the GP approaches these upper and lower edges then the fields will vary at these points in its motion.

3. THE ROLE OF ACOUSTIC AND ELECTROMAGNETIC RESONANCE IN BIODIVERSITY

As the Earth bobs up and down to its maxima in its motion within the Solar System around the Galactic Centre, it moves to regions where the acoustic fields are diminished and the structural integrity of matter on Earth is reduced limiting the ability of species to maintain their physiological integrity. Physiological integrity refers in part to the mechanisms a body uses to reach a state of constancy, homeostasis, and adaptation, and includes perfusion, nutrition and oxygenation. Tissues that were solid at or near the GP will be more viscous or more solidified, and may not have the required structural integrity for life to be as viable at the maxima points in the galactic motion. There is a link between fluid dynamics and acoustics that is pertinent to the current discussion. As is known the speed of sound is given by $c_s = \sqrt{k/\rho_0}$ where ρ_0 is the mean density and κ is the bulk modulus measuring a substance's resistance to compression. Similar equations hold for gases, liquids, and solids as well as biological tissues. If the bulk modulus of tissues falls below a certain threshold the tissue will lose its structural integrity. This is similar to the observation of space sickness that astronauts enduring prolonged stays in free space can suffer deleterious effects to bone, muscle, perfusion and blood pressure. This might also be the case for large structures such as the dinosaurs that roamed the Earth some 60 Myr ago a time of near maximum excursion form the GP.

Similar to the variation in acoustic fields near the upper and lower edges of the Galaxy, a similar effect happens with the E- and H-fields that are also involved in the galactic gravitational structure. Again the energy density of matter falls off near these edges. In this case, the Galaxy's Black Hole near the centre of the Galaxy is a negative source of energy unlike the Sun near the centre of the Solar System which is a positive source of energy. SFT indicates a fractal view of the Universe and its gravitational structures. This includes an oscillating series of gravitational forces that goes beyond the galactic level; energy density in the bulk medium within the Universe is observably convergent rather than divergent. Hence as the Solar System bobs up and down, the relative energy due to the Galaxy is reduced and the Solar System may get slightly warmer than while moving near the GP. Reproductive processes including mitosis within species may become marginally less viable as the frequencies of the energy required during the cell cycle are modified away from their values within a more 'habitable zone'. 'Goldilocks Zones' are thought necessary to sustain life both at the Solar System and the Galactic levels. Popp has investigated the spectral emissions from the DNA of numerous life forms finding wavelengths from 200–800 nm. Longer wavelengths, and larger species, might be associated with galactic dynamics closer to the GP as the ambient temperature deep inside the Galaxy would be expected to be relatively cooler.

4. CONCLUSION

It is possible that the cause of the cycles in the observed record of biodiversity relates to two distinct effects: (1) There may be a reduced viability of biological tissue to withstand the drop-off in compressibility at the maximum excursions from the GP leaving the tissues of some species less resistant to the forces wanting to implode their structure, especially larger structured species. The loss of bulk modulus would appear to have left some species unable to function at a primary level. (2) It appears that biodiversity may also be related to the energy density within the Galaxy. Cells, tissues, and organs may have evolved to be more viable near the GP so as to resonate with the available energy density at those points within its dynamic motion. The biophoton may not only be involved within the body but within dynamics of the Galaxy giving a spectroscopic test for extraterrestrial life.

REFERENCES

1. Rohde, R. A. and R. A. Muller, "Cycles in fossil diversity," *Nature*, Vol. 434, 208–210, 2004.
2. Medvedev, M. V. and A. L. Melott, "Do extragalactic cosmic rays induce cycles in fossil diversity?" *Astrophys. J.*, Vol. 664, 879–889, 2007.
3. Fleming, A. H. J., "Electromagnetic self-field theory and its application to the hydrogen atom," *Physics Essays*, Vol. 18, No. 3, 265–285, 2005.
4. Fleming, A. H. J., "Self-field theory, analytic spectroscopy of the ordinary photon," *Proc. 2nd Electromagnetics Health and Environment Intl Conf.*, 18–23, Wroclaw, Poland, 2007.
5. Fleming, A. H. J., *Self-field Theory — A New Mathematical Description of Physics*, Pan Stanford Publishing, 2010.

6. Jenny, H., *Cymatics: A Study of Wave Phenomena and Vibration*, 3rd Edition, Macromedia Press, Jul. 2001.

7. Binney, J. and S. Tremaine, *Galactic Dynamics*, Princeton University Press, 1987.

8. Klacka, J., Galactic Tide, arXiv-0912.3112v1 [astro-ph.GA], Dec. 16, 2009.

9. Popp, F. A., Q. Gu, and K. H. Li, "Biophoton emission: Experimental background and theoretical approaches," *Modern Physics Letters B*, Vol. 8, 1269–1296, 1994.

Self-field Theory-biophotons and EPR

A. H. J. Fleming

Biophotonics Research Institute, Melbourne, Australia

Abstract— The EPR paradox lies at the heart of the way Self-Field Theory (SFT) sees physics and biophysics. Einstein coauthored a paper on the paradox that challenged quantum theory he saw as incomplete. Quantum entanglement is now understood as the way in which parts of a quantum mechanical system are connected. The quantum states of the constituent parts are linked; one part cannot be properly described without mention of all other parts within the system. Einstein referred to this as 'spooky action at a distance'. SFT too sees quantum theory as incomplete. SFT suggests a missing coordinate within the photon that is the underlying reason for Heisenberg's uncertainty principle and its lack of knowledge concerning photons. Like entanglement SFT suggests that photons link all atoms together as in a crystal lattice. In solid crystals according to SFT the atoms rotate in synchronized fashion. Photon interactions apply between many if not all atoms within the Universe in which dipole-dipole electromagnetic (EM) inter atomic forces exist as streams of photons between masses. DNA is an example of a liquid crystal capable of 'stiffening' as the biophotonic states change within the cell cycle. Biophotons link to objects around a biological system. This includes the biological ability of optical sight but can include other biophotons within the complete body-field. Biophotons are found in specialized physiological tissues including elasmobranch fish that use jelly-filled canals called the ampullae of Lorenzini on the lower peripheries of their fins for predation. As well as being absorbed, biophotons are emitted by biological systems.

1. INTRODUCTION

The EPR paradox refers to a paper in which Einstein challenged quantum theory that he saw as incomplete. As a consequence of this historical debate quantum entanglement is now understood as a way in which parts of a QM system connect. The constituent states are linked together so that one part cannot be properly described without mention of other parts within the system. Einstein referred to this as 'spooky action at a distance'. SFT too sees quantum theory as incomplete. SFT suggests a missing coordinate within the photon that is the underlying reason for Heisenberg's Uncertainty Principle (HUP) and its incomplete knowledge at the photonic level. Within atomic and molecular physics according to SFT photons link many atoms together. This is the underlying photon level of interaction applying to matter within the Universe. SFT sees two extra quantum numbers that are linked to the discretization of the paths of the double rotations of the electron and proton within the atom which are related to the photon in its role as binding energy. This applies to crystals where atoms rotate in synchronized fashion and to biological systems where biophotons emitted from DNA acting as a hydrated liquid crystal at metaphase can link to other objects in the view of the biological system. This usually implies the biological capacity for optical sight but can encompass other forms of biophotonic emission and detection. This includes the complete body-fields of biological systems in general but is found in specialized physiological tissues such as the elasmobranch fish that use pores, the ampullae of Lorenzini, on the periphery of their dorsal fins for predation. As discussed in the following Einstein was right; it is now realised that an interconnection existing between living and non-living systems has been overlooked while quantum theory failed to see the photonic and biophotonic level interaction.

2. HEISENBERG UNCERTAINTY PRINCIPLE — THE INCOMPLETE PHOTON

The uncertainty principle was first proposed by Heisenberg in 1927. HUP is now presented in the original form given by Heisenberg. Assume the wave packet illustrated by Fig. 1 consists of sinusoidal plane waves of wavelengths close to λ_0. There are approximately $n = \Delta x/\lambda_0$ wavelengths within the packet. Outside the limits of the wave packet the waves must cancel each other by interference. This only occurs if at least $n + 1$ waves fall inside the limits of the wave. Thus we may write

$$\frac{\Delta x}{\lambda - \Delta \lambda} \geq n + 1 \tag{1}$$

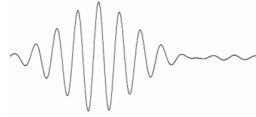In (1), $\Delta \lambda$ is the approximate range of wavelengths. Thus

Figure 1: Wave packet with uncertainty Δx in position and Δp in momentum.

$$\frac{\Delta x \Delta \lambda}{\lambda_0^2} \geq 1 \tag{2}$$

The group velocity of the wave can be written

$$v_g = \frac{h}{m_p \lambda_0} \tag{3}$$

The spreading of the wave is thus characterized by a range of velocities

$$\Delta v_g = \frac{\hbar}{m_p \lambda_0^2} \Delta \lambda_0 \tag{4}$$

By definition $\Delta p = m_p \Delta v_{gx}$ hence

$$\Delta p_x \Delta x \geq \hbar \tag{5}$$

HUP may also be written in the corresponding form

$$\Delta t \Delta E \geq \hbar \tag{6}$$

The inequality relationship (6) applies to photons, electrons, and in fact any quantum system The equation for the orbital motion of the electron lies at the heart of SFT and is given in (7) for comparison. Apart from the approximation of energy and time in the uncertainty relationship and the replacement of the 'greater than' relationship by an exact relationship the two equations are strikingly alike. Quantum theory is thus seen as an incomplete formulation as Einstein had long suspected. SFT provides a completion of the Bohr model that did not include any magnetic effect on the electron.

$$m_e v_o^2 = 2\hbar\omega \tag{7}$$

According to SFT the photon can be modeled as two point masses of opposite charge, similar to the hydrogen atom, but of equal mass. Due to the mass equality the eigenstructure is continuous in this case since a resonance condition holds at every energy state in agreement with Einstein's theory of the photoelectric effect proposed in 1905 and the equation relating photon energy to its frequency $E = h\nu$. If such a photon moves past an observation point, the resulting effect is approximately as shown in Fig. 1. The wave packet conceptualized around the time of the discovery of quantum theory is thus seen to be an approximation to the physics. The SFT domain of the photon ω_γ is seen to be below $\omega_\gamma \leq \frac{m_\gamma c^2}{2\hbar}$ or $\alpha/8 \approx 0.912 \times 10^{-3}\,\mathrm{rad\ sec^{-1}}$ where the inverse fine structure constant $\alpha = \frac{v_e}{c} = \frac{4 m_\gamma c^2}{\hbar \omega_\gamma}$ and where the mass of the photon has been estimated[1] $m_\gamma = 0.387 \times 10^{-55}\,\mathrm{kg}$. Below this level, possibly in deep-space at the edge of the Universe, the photon's self-energy is significant and it basically 'freezes' and can remain in an isolated state where it performs bispinorial rotations about a point in space. Above this energy level the photon's self-energy becomes insignificant and it obeys outside influences to its motion moving at the speed of light. In this mode the photon acts as a binding energy between inanimate particles and in a more specialized role within biological systems.

---

[1]In SFT each photon is assumed to transit between electron and proton in atoms via a series of resonant elastic collisions. The phase length during transit, $\pi/2$ maintains the periodicity of the atom providing a method for analytically comparing the energy of the photon with that of the electron $m_\gamma c2 = \frac{\hbar \omega_\gamma v_e}{4c} = \frac{q^2 \omega_\gamma}{16\pi\varepsilon_0 c}$, where ω_γ is the integer transit frequency of the photon within each cycle of the electron. In order for the atom to maintain its periodicity N_γ the number of complete transits per atomic cycle must be an integer. Ignoring any non-linearities, the electron's motion can be modeled as piece-wise linear. This collision-based form of periodic motion by the electron illustrates the non-classical, quantum nature of SFT. Assuming a polygonal motion circumscribes a circle representing the Bohr mageton, the photon collision frequency is estimated as 53 to several places of significance from the known value of the Landég-factor assumed precisely known from both measurement and quantum electrodynamics theory. In earlier reports of the mass of the photon this collision frequency integer was reported as 54, however reexamination reveals the best fit to six significant figures is a polygon of 53 sides. In an attempt to best model the collision process a form of finite difference model was used in these tests by adding half the difference between the inscribed and circumscribed areas of n-sided polygons ranging from $n = 50, \ldots, 60$.
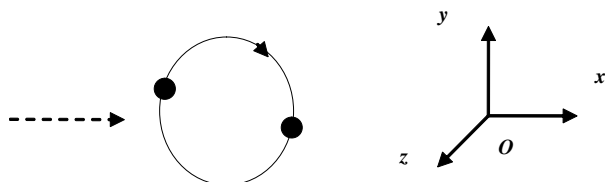
Figure 2: Composite photon moving past point O along x axis rotating in x-y plane.
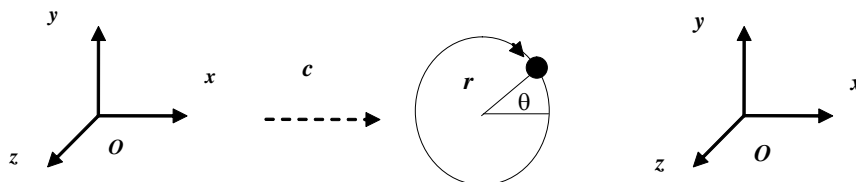

Figure 3: Single particle photon moves past point O along x axis rotating in x-y plane.

From Fig. 3, we might model the wave packet in a somewhat unphysical fashion, as a single particle rotating around a centre of motion while translating along the x axis. In this case uncertainty Δx in the x direction involves a trigonometric function in θ and the scalar radius r of the photon's internal motion. Δx is seen to range from positive to negative in keeping with the wave motion. Similarly the uncertainty in momentum Δp is also a function of θ and r as well as the particle's mass and also ranges from negative to positive. Attempting to investigate uncertainty in this case leads to an unphysical result. It is only when the photon is modeled by two particles as in Fig. 2 the uncertainty function becomes balanced by the symmetry of the sub-photonic particles and uncertainty is obviated. HUP can be considered a theoretical error leading to numerical inaccuracy. SFT is a mutual effect between two particles that obviates uncertainty, rendering the motion of the photon deterministic.

The equations of HUP can be seen to be closely related to the central equations of SFT where the motion of the electron is analyzed. These equations are exact whereas in HUP they are inequalities. In this case the motion of the electron is modeled via an infinite mass proton, similar to the one-particle photon model of Fig. 3. In this case, the model is not unphysical in the sense that this is a reasonable approximation to the physics using a simplifying assumption. Note that Heisenberg assumes neither the group mass is a variable depending on relativistic speed nor is it zero. Heisenberg prefaced the derivation of his principle of uncertainty:

'The uncertainty relation specifies the limits within which the particle picture can be applied. Any use of the words "position" and "velocity" with an accuracy exceeding that given by Equations (5), (6) is just as meaningless as the use of words whose sense is not defined' .... 'In this connection one should particularly remember that the human language permits the construction of sentences which do not involve any consequences and which therefore have no content at all-in spite of the fact that these sentences produce some kind of picture in our imagination; e.g., the statement that besides our world there exists another world with which any connection is impossible in principle, does not lead to any experimental consequence, but does produce some kind of picture in the mind. Obviously such a statement can neither be proved nor disproved. One should be especially careful using the words "reality", "actually" etc., since these words very often lead to statements of the type just mentioned.'

It is noted that while uncertainty for any model can be zero this only tells us something about the model's theoretical basis; it tells us little about how the model stands up to experiment. It is this observation that leads us to conclude that uncertainty is a form of theoretical inaccuracy as distinct to a numerical inaccuracy. It was Heisenberg's opinion that the photon could not be understood in a deterministic fashion. While he was correct that any attempt to use photons to examine a photon would disturb the experiment, this does not prevent us from examining the insides of the photon mathematically. Experimentally we may simply use numbers of photons to test individual photons. When we see blue light in the day sky we are not perturbing all photons with blue wavelengths but only those photons that reach our eyes. Hence we might assume the vast majority of the photons in this part of the sky will have an associated blue energy.

SFT yields exact equations rather than the inequality Equations (5), (6). Heisenberg's statements seem more about an afterlife rather than scientific comments about uncertainty being a fabric of reality which was their context. If one were able to ask their great-great-grandmother whether she believed in the reality of television her answer would depend on whether she had ever lived in the age of television. Otherwise she would have denied such a preposterous suggestion, and her view would have been supported by thousands of years of human experience. Similarly, quantum mathematicians might deny the existence of deterministic equations of motion for the electron in the atom. Depending on whether they knew of the modern variant of SFT, they might think physics was a fixed and constant commodity, as immutable as life on Earth, or perhaps more

pertinent Planck's 'constant'. Now we can perceive a complete world of theory inside the photon that promises to yield new physical understandings. Perhaps this HUP episode of science in the early and late 20th century gives us a more complete understanding of the differences between modeling and reality. We accept the assumptions of a scientific model on faith in order to find a way forwards via theory to an understanding of reality. The more two-way reflections there are between physics and any theory the more refined becomes our perception. Ironically we must keep our cerebral antennae open to outside broadcast without closing off reception as was the case at the 5th Solvay Conference in 1927 when Heisenberg and Bohr suggested *"We regard quantum mechanics as a complete theory for which the fundamental physical and mathematical hypotheses are no longer susceptible of modification."*

One last comment can be made about the mathematics of uncertainty and the equations of SFT. As has been demonstrated both are remarkably similar and it remains a historical quirk of fate that SFT did not emerge before WWII. It may be that the scientific world does not move with any haste. That may be been both a good and a bad thing — good in that no presumptuous errors are made but bad in that the world has to wait eighty odd years to finally begin to peer inside the photon with all the physical and biophysical structure that this knowledge contains.

3. CONNECTIVITY AND BIOPHOTONS

In their normal role biophotons convey energy and information to parts of a biological system in addition to their role as a binding energy at the EM level. One form of photonic information is phase length whereby biological systems can infer positions and lengths of their surroundings for various purposes including sight, touch, smell, motion, location and predation. A body's fields connect it with its environment. These whole-body fields or biophotons are no different to ordinary connective photons except that they perform this informative role. Within the body biophotons can perform this informative role and in addition provide the distribution of energy to its cells, organs, and tissues. The DNA is central to this role of supplying energy during the cell-cycle. SFT suggests that self-organization within the cell occurs because of the reducing level of energy as the cycle proceeds. Biophotons provide both the information and the energy when a group of cells decides to replicate their own species.

4. CONCLUSIONS

In the light of SFT, uncertainty is seen as an approximation to the physics of the photon, the electron, the nucleus, and any system, including life-forms studied using the quantum formulation of the 20th century. The model of the photon as a wave-packet is the reason for its numerical basis. As Einstein long suspected and attempted to demonstrate via EPR quantum theory is incomplete. It is the exact solutions to the Maxwell-Lorentz equations and the photonic and biophotonic level revealed by SFT that yields quantitative knowledge of a biological system.

REFERENCES

1. Nakamura, J. and M. Hiramatsu, "Ultra-weak photon emission from human hand: Influence of temperature and oxygen concentration on emission," *Journal of Photochemistry and Photobiology B: Biology*, Vol. 80, 156–160, 2005.
2. Heisenberg, W., C. Eckart, and F. C. Hoyt, *The Physical Principles of the Quantum Theory*, Dover, 1930.
3. Fleming, A. H. J., "Electromagnetic self-field theory and its application to the hydrogen atom," *Physics Essays*, Vol. 18, No. 3, 265–285, 2005.
4. Fleming, A. H. J., "Self-field theory, analytic spectroscopy of the ordinary photon," *Proc. 2nd Electromagnetics Health and Environment Intl Conf.*, Wroclaw, Poland, 18–23, 2007.
5. Fleming, A. H. J., *Self-field Theory — A New Mathematical Description of Physics*, Pan Stanford Publishing, 2010 (to be published).

Subsurface Sub-terahertz and Terahertz Tomography

A. A. Vertiy, H. Cetinkaya, and M. Tekbas

International Laboratory for High Technology, Material Institute, TUBITAK-MRC
Gebze/Kocaeli, Turkey

Abstract— Development of millimeter and sub-millimeter wavelengths technologies is one of the most promising research areas, especially for applications in so called terahertz imaging. In the paper we consider a tomography approach for obtaining 3-D imaging in frequency range from 100 GHz up to 325 GHz. We apply the modernized image reconstruction method, based on developed earlier, for low frequency, surface imaging procedure [1]. We managed to significantly improve the image resolution by newly designed probes for millimeter and sub-millimeter wave range measurements. The images obtained demonstrate that the built measurement system and the image reconstruction method can be used for non-destructive testing applications such as the imaging of manufacturing defect on wafer.

1. INTRODUCTION

In a view of growing importance of surface and subsurface imaging, for example, in medical and non-destructive testing, the tomography technologies have been receiving a proper attention [1, 2]. For higher resolution imaging, the changeover to high frequencies is required. Our paper is devoted to development of the sub-terahertz and terahertz tomography that allows us to get quite clear imagine.

TUBITAK — International Laboratory for High Technologies (ILHT) has already realized tomography applications [3–5]. In this study, the tomography method that we employ, based on evaluating of the distribution of equivalent currents induced on the target, was originally proposed and verified at frequency 3 GHz in the work [1]. We built the microwave measurement setup and successfully used the method in 10 GHz and 40 GHz rangers for surface and subsurface tomography imaging in non-destructive testing and biological applications. Herein it is shown that similar method can give good results also at sub-terahertz (100 GHz) and terahertz (325 GHz) frequencies for surface and subsurface applications. The essential resolution improvement in W band was achieved with using newly designed dielectric probes. The experimental results obtained at the sub-millimeter wave band demonstrate the wide practical application of the method and the proposed measurement setup.

2. PROBLEM FORMULATION

Let us consider a three-dimensional object of volume V that is illuminated by a plane linearly polarized wave of E-polarization $(E_\parallel)$; the wave incident angle is θ^i. The surrounding isotropic medium is supposed uniform and defined by its permittivity ε and conductivity σ. The media permeability is $\mu = 1$.

Let $\vec{E}$ represent the total electric field, $\vec{E}^i$ is an incident field and $\vec{E}^s$ is a scattered field which is excited by the equivalent electric currents (polarization currents), so $\vec{E} = \vec{E}^i + \vec{E}^s$. The equivalent electric currents are defined as

$$\vec{J}_{ob}(x, y, z) = \left(k_{ob}^2(x, y, z) - k^2\right)\vec{E}(x, y, z), \tag{1}$$

where k_{ob} and k are the wave numbers for the object medium and vacuum correspondently, the time dependence is chosen in the form $e^{-i\omega t}$.

The scattered field $\vec{E}_\parallel^s$, that is parallel to z, inside and outside the object can be calculated by using its integral representation. If one assumes that the depolarization is negligible, and polarization current is normalized by incident field $E_z^i(\theta^i, x, y)$, the scattered field $\psi(\theta^i, x, y, z)$ can be presented in the form

$$\psi(\theta^i, x, y, z) = k^2 \iiint\limits_V E_z^i\left(\theta^i, x', y'\right) K\left(\theta^i, x', y', z'\right) G\left(x, y, z; x', y', z'\right) dx'dy'dz', \tag{2}$$

where $G(x, y, z; x', y', z')$ is free space Green function, $K(\theta^i, x', y', z')$ is a normalized polarization current and $E_z^i(\theta^i, x, y) = e^{ik(x\sin\theta^i + y\cos\theta^i)}$ is an incident plane wave.

Let us define the two-dimensional Fourier transform $\hat{\psi}(\theta^i, v_1, y, v_3)$ of the scattered field $\psi(\theta^i, x, y, z)$ on a scanning plane at $y=constant$ and also the three-dimensional Fourier transform $\hat{K}(\theta^i, \alpha, \beta, \chi)$ of $K(\theta^i, x, y, z)$

$$\hat{\psi}\left(\theta^i, v_1, y, v_3\right) = \int\limits_{-\infty}^{\infty} \int\limits_{-\infty}^{\infty} \psi(\theta^i, x, y, z)e^{-2\pi i(v_1 x + v_3 z)}dxdz, \tag{3}$$

$$\hat{K}(\theta^i, \alpha, \beta, \chi) = \int\limits_{-\infty}^{\infty} \int\limits_{-\infty}^{\infty} \int\limits_{-\infty}^{\infty} K(\theta^i, x, y, z)e^{-2\pi i(\alpha x + \beta y + \chi z)}dxdydz. \tag{4}$$

Applying the two-dimensional Fourier transform for (2) along x and z directions, one can obtain the following equation:

$$\hat{\psi}(\theta^i, v_1, y, v_3) = k^2 \int\limits_{-\infty}^{\infty} \int\limits_{-\infty}^{\infty} \int\limits_{-\infty}^{\infty} e^{ik(x'\sin\theta^i + y'\cos\theta^i)} K(\theta^i, x', y', z') \underbrace{\frac{i}{2} \frac{e^{-2\pi i v_1 x'} e^{i\gamma(y'-y)} e^{-2\pi i v_3 z'}}{\gamma}}_{g(v_1, y, v_3; x', y', z')} dx'dy'dz', \tag{5}$$

where $g(v_1, y, v_3; x', y', z')$ is the two-dimensional Fourier transform of Green function, and $\gamma = 2\pi v_2 = \sqrt{k^2 - 4\pi^2(v_1^2 + v_3^2)}$ is the wave number.

After some manipulations, the Equation (5) becomes

$$\hat{K}(\theta^i, \alpha, \beta, \chi) = \hat{\psi}\left(\theta^i, v_1, y, v_3\right) \frac{2\gamma}{k^2 i e^{-i\gamma y}}, \tag{6}$$

where α, β, and χ have the following presentations

$$\alpha = v_1 - \frac{k}{2\pi}\sin\theta^i, \quad \beta = -\frac{1}{2\pi}\left(\gamma + k\cos\theta^i\right), \quad \chi = v_3 \tag{7}$$

3. EXPERIMENTAL SETUP AND APPLICATIONS

Our measurement system includes the specially designed PNA Control Software, installed in control computer for scanner system data acquisition, to be able to control all measurement setup, network analyzer (Agilent PNA N5260A), Probe Station (Cascade Probstation, summit 12000 B-S), and Scanner-Positioner Control Computer (see Figure 1). Thus, control computer for scanner system data acquisition performs a role of master computer. In our design the Scanner-Positioner Control Computer only controls the Scanner-Positioner System. Also, data acquisition over x-y scan area on the object is performed by PNA Control Software. The Probe Station Positioner goes to the coordinate point, assigned by PNA Control Software, to make a measurement. In a such way the measured data is collected. Moreover, the measurement is processed by using the network analyzer (Agilent PNA N5260A) for different frequencies. During these experiments, all of measurements are made at 32 different frequencies with a constant frequency step. We use the frequency range [98 GHz, 102 GHz] for millimeter wave measurements. Sub-millimeter wave measurements are conducted in the interval from 300 GHz to 320 GHz.

The crucial component of our experimental setup is dielectric probes. Figure 1(b) shows the W-band dielectric probe, made from Teflon. We used it for millimeter wave measurements. In Figure 1(c) a dielectric probe, made from Duroid and inserted into the horn antenna, was used at sub-millimeter wave measurements. For subsurface measurements at millimeter wave range the two different types of undersurface objects were used. One of them was cardboard capital letter C shown in Figures 2(a) and (b), the height, width and thickness of which were 40 mm, 40 mm, and 0.8 mm, respectively. Another object was metal capital letter A shown in Figures 2(c) and (d). Its height, width and thickness were 40 mm, 40 mm, and 0.2 mm, respectively.

Also the surface and subsurface tomography measurements were made at sub-millimeter wave measurements for similar object that was copper capital letter A placed on FR4 PCB (see Figure 3). Its dimensions are height 5.78 mm, width 3.81 mm, and the thickness 1 mm.

It should be indicated that thicknesses of Teflon, used as layers for millimeter and sub-millimeter wave measurements, were 5 mm and 3 mm, respectively.
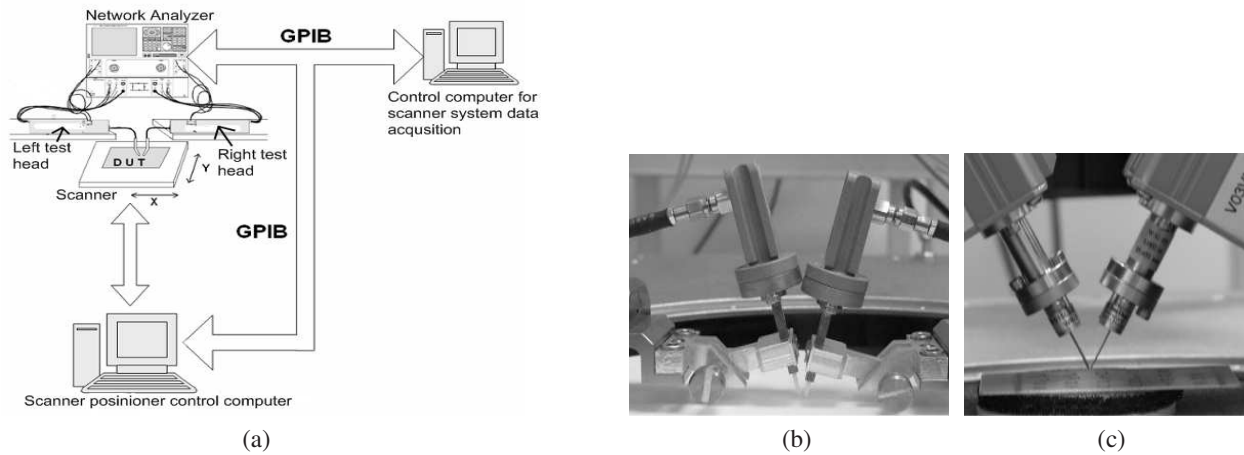
(a)   (b)   (c)

Figure 1: (a) The measurement system and designed probes for measurements at (b) 100 GHz and at (c) 300 GHz.

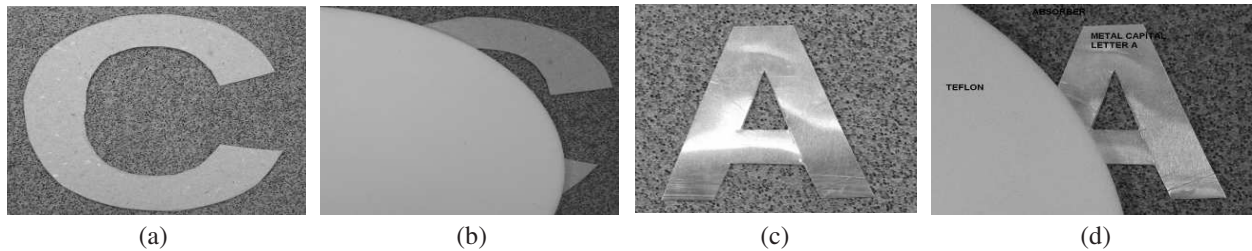(a)   (b)   (c)   (d)

Figure 2: (a) Cardboard capital letter C and (b) cardboard capital letter C under Teflon, (c) metal capital letter A and (d) metal capital letter A under Teflon.
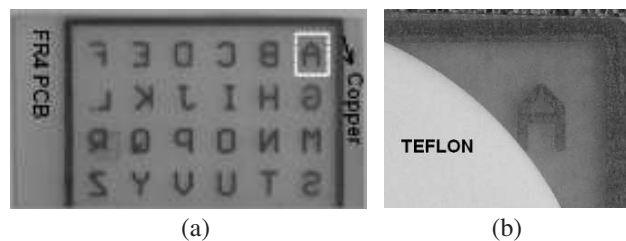

(a)   (b)

Figure 3: (a) Copper capital letter A, placed on FR4 PCB and (b) copper capital letter A, placed on FR4 PCB, under Teflon.

4. EXPERIMENTAL RESULTS

Firstly, note that measurement plane consisted of 100×100 grids in all measurements. One grid size was 0.5×0.5 mm^2 in millimeter wave measurements and in sub-millimeter wave measurements one grid sizes was 0.25×0.25 mm^2. The image visualization was done by using IRIS Explorer™ software [6].

The dielectric objects are more difficult for measurement because of the scattered field produced by a dielectric object is much weaker than that by metallic object. We present the image reconstruction of a dielectric object, cardboard capital letter C (see Figure 4). It demonstrates that accurate scattering data is able to be collected from dielectric target and high quality images can be generated. The target geometry under Teflon layer is shown in Figures 2(a) and (b). Measured data and subsurface tomography reconstruction for cardboard letter C are shown in Figure 4.

The shape of metal capital letter A under Teflon layer is shown in Figures 2(c) and (d). The measured data and tomography reconstruction of the metal letter A located under Teflon are shown in Figure 5.

Copper capital letter A on FR4 PCB, used for surface and subsurface imaging at 300 GHz, is shown in Figure 3. The measured data and tomography reconstructions for surface and subsurface imagine of copper capital letter A on FR4 PCB are shown in Figures 6 and 7, respectively.

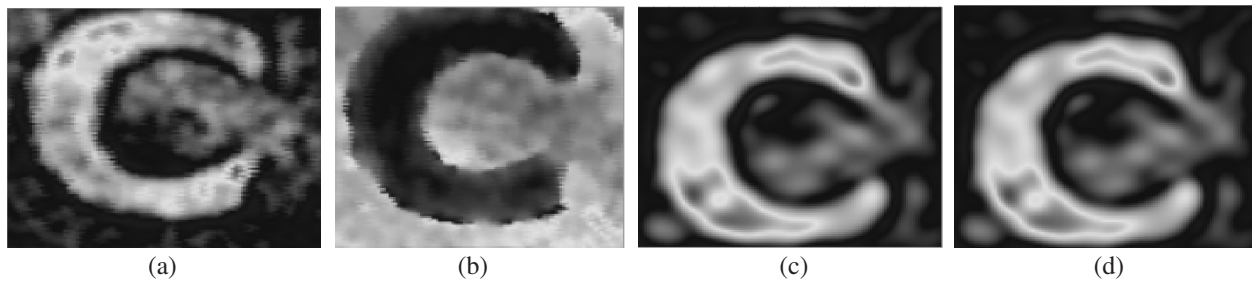(a)   (b)   (c)   (d)

Figure 4: (a) Amplitude and (b) phase distributions and the tomography reconstruction for depths of (c) 0.001 m and (d) 0.002 m, for cardboard object at 98 GHz–102 GHz.

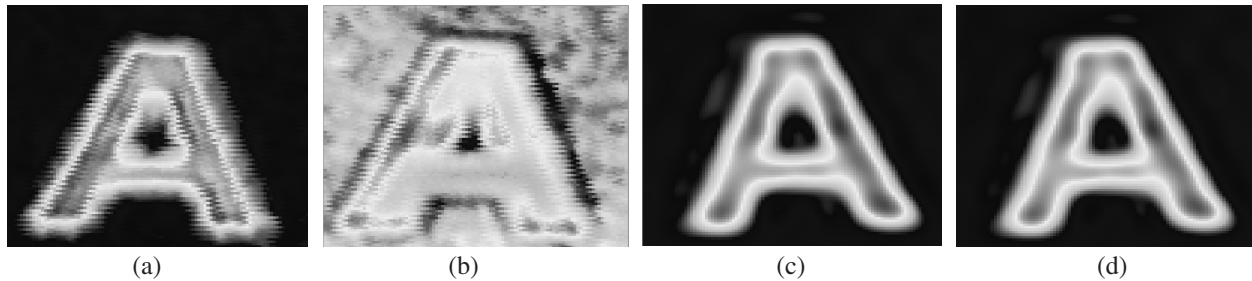(a)   (b)   (c)   (d)

Figure 5: (a) Amplitude, (b) phase distributions and the tomography reconstruction for depths of (c) 0.005 m and (d) 0.006 m For subsurface located metal letter A at 98 GHz–102 GHz.
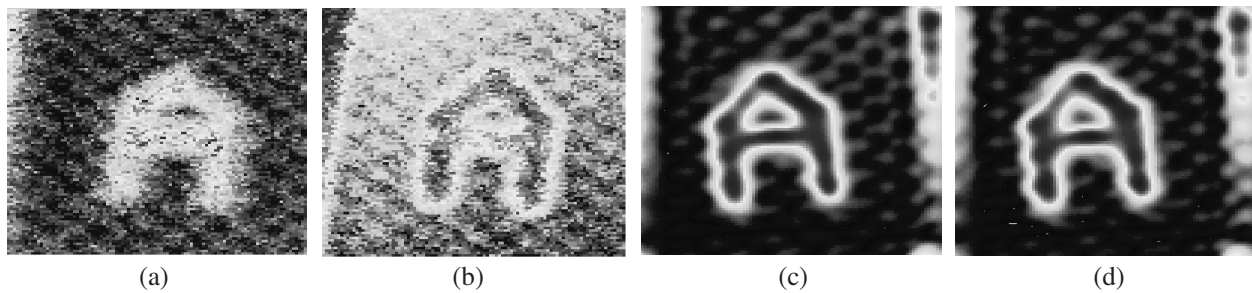

(a)   (b)   (c)   (d)

Figure 6: (a) Amplitude, (b) phase distributions and the tomography reconstruction for depths of (c) 0.0015 m and (d) 0.0020 m for copper capital letter A placed on FR4 PCB at 300 GHz–320 GHz.

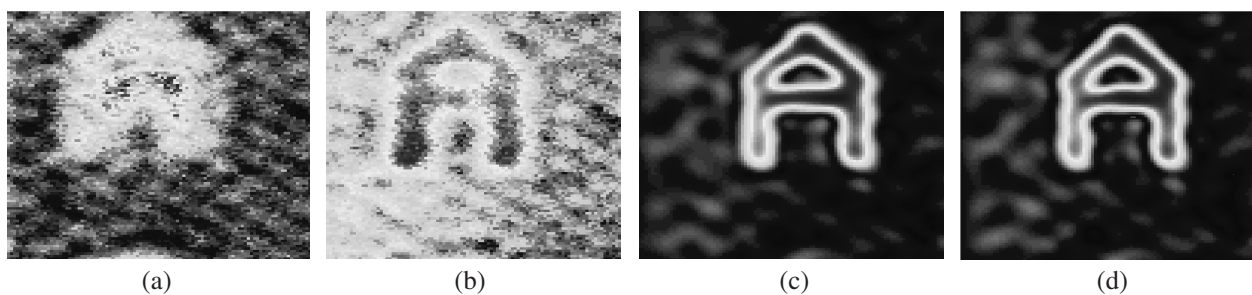(a)   (b)   (c)   (d)

Figure 7: (a) Amplitude, (b) phase distributions and the tomography reconstruction for depths of (c) 0.003 m and (d) 0.004 m for copper capital letter A placed on FR4 PCB at 300 GHz–320 GHz.

5. CONCLUSION

The experimental setup was designed and built for sub-terahertz and terahertz frequencies measurements. This imaging system and reconstruction algorithm have demonstrated good results to be used for different types of technological and scientific applications. Thus, our further studies will be focused on non-destructive imaging and wafer imaging which is important for non-destructive control system to detect manufacturing defect on wafer. Also the algorithm used in our system can be extended for medical imaging.

REFERENCES

1. Pichot C., L. Jofre, G. Perronnet, and J. C. Bolomey, "Active microwave imaging of inhomogeneous bodies," *IEEE Transaction on Antenna and Propagation*, Vol. 33, No. 4, 416–423, April 1985.

2. Candy, J. V. and C. Pichot, "Active microwave imaging: A model-based approach," *IEEE Transaction on Antenna and Propagation*, Vol. 39, No. 3, 285–290, March 1991.

3. Vertiy, A. A., S. P. Gavrilov, S. Aksoy, I. V. Voynovskyy, A. M. Kudelya, and V. N. Stepanyuk, "Reconstruction of microwave images of the subsurface objects by diffraction tomography and stepped-frequency radar methods," *Zarubejnaya Radioelektronika, Uspehi Sovremennoy Radioelektroniki*, Vol. 7, 17–52, 2001.

4. Vertiy, A. A., S. P. Gavrilov, I. V. Voynovskyy, V. N. Stepanyuk, and S. Ozbek, "The millimeter wave tomography application for the subsurface imaging," *International Journal of Infrared and Millimeter Waves*, Vol. 23, No. 10, 1413–1444, 2002.

5. Vertiy, A. A. and S. P. Gavrilov, "Application of tomography method in millimeter wavelengths band II. Experimental," *International Journal of Infrared and Millimeter Waves*, Vol. 18, No. 9, 1761–1781, 1997.

6. http://www.nag.co.uk/Welcome_IEC.asp.

Advanced Studies of the Differential Phase Shift in the Azimuthally Magnetized Circular Ferrite Waveguide

Mariana Nikolova Georgieva-Grosse[1] and Georgi Nikolov Georgiev[2]

[1]Meterstrasse 4, D-70839 Gerlingen, Germany
[2]Faculty of Mathematics and Informatics, University of Veliko Tirnovo "St. St. Cyril and Methodius"
BG-5000 Veliko Tirnovo, Bulgaria

Abstract— Two iterative methods are elaborated to determine the boundaries of the domain in that the circular waveguide, uniformly filled with azimuthally magnetized ferrite, provides differential phase shift for the normal TE_{01} mode. The peculiarities of the cut-off state of configuration and of its limiting one at higher frequencies in which the transmission for negative magnetization ceases, are the physical grounds for their formulation. The conception of first (second) approach is to compute the value of normalized in a suitable manner critical guide radius (radius, corresponding to a point of a specific envelope line in the phase portrait, depicting the limiting state) for a fixed numerical equivalent of the off-diagonal ferrite permeability tensor element in two ways: by a definite formula and by the root of structure's characteristic equation, derived through a certain complex Kummer function. The root is counted over and over again for a changing negative (positive) imaginary part of the first complex parameter of the latter, until the results for the radius coincide with a prescribed accuracy. The value of the imaginary part at that this happens is employed to reckon the phase constant of propagating mode, relevant to the state considered. The differential phase shift equals this constant in the first case, whereas in the second one, it is found from it by simple algebra. Varying the off-diagonal element, the borders of the domain in question are traced. The outcomes are presented graphically. The maximum value differential phase shift might attain at all is also calculated.

1. INTRODUCTION

The availability of phase shifting properties is the basic feature of the circular waveguide with azimuthally magnetized ferrite, operating in the normal TE_{01} mode [1, 2]. Due to the complexity of the problem for their investigation [2], still they are not completely known.

Making a step forward, here, two iterative procedures are developed to outline the limits of the region in which the properties mentioned are exhibited. The study is based on special working regimes of geometry and the main point in it is the repeated numerical solution of its characteristic equation [1, 2], altering the imaginary part of the first complex parameter of wave function.

2. METHOD FOR COMPUTATION OF THE DIFFERENTIAL PHASE SHIFT AT CUT-OFF

2.1. Physical Background

The propagation of normal TE_{0n} modes in the circular waveguide, entirely filled with ferrite, magnetized azimuthally by an infinitely thin central wire, is governed by the equation [1, 2]:

$$\Phi\left(a, c; x_0\right) = 0, \tag{1}$$

written through the complex Kummer confluent hypergeometric function [3] in that $a = c/2 - jk$ — complex, $c = 3$, $x_0 = jz_0$, $k = \alpha\bar{\beta}/(2\bar{\beta}_2)$, $z_0 = 2\bar{\beta}_2\bar{r}_0$; k, z_0 — real, $-\infty < k < +\infty$, $z_0 > 0$, $\mathrm{sgn}k = \mathrm{sgn}\alpha$ ($\alpha = \gamma M_r/\omega$ — off-diagonal ferrite permeability tensor element, $-1 < \alpha < 1$, γ — gyromagnetic ratio, M_r — ferrite remanent magnetization, ω — angular frequency of the wave, $\bar{\beta} = \beta/(\beta_0\sqrt{\varepsilon_r})$, $\bar{\beta}_2 = \beta_2/(\beta_0\sqrt{\varepsilon_r})$, $\bar{r}_0 = \beta_0 r_0\sqrt{\varepsilon_r}$, β — phase constant, $\beta_2 = [\omega^2\varepsilon_0\mu_0\varepsilon_r(1-\alpha^2) - \beta^2]^{1/2}$ — radial wavenumber, r_0 — guide radius, $\beta_0 = \omega\sqrt{\varepsilon_0\mu_0}$ — free space phase constant, ε_r — ferrite relative permittivity), (see, inset Fig. 1(b); (r, ϑ, z) — a cylindrical co-ordinate system). The eigenvalue spectrum of the fields examined is determined by the relation $\bar{\beta}_2 = \zeta_{k,n}^{(c)}/(2\bar{r}_0)$, ($\zeta_{k,n}^{(c)}$ — nth positive purely imaginary root of Eq. (1), $n = 1, 2, 3, \ldots$) [1, 2]. Under certain conditions waves with different phase constants $\bar{\beta}_+$ and $\bar{\beta}_-$ may be sustained for $\alpha_+ > 0$ and $\alpha_- < 0$, resp. and the structure may afford differential phase shift $\Delta\bar{\beta} = \bar{\beta}_- - \bar{\beta}_+$ [1, 2]. At cut-off no transmission is possible when $\alpha_+ > 0$ and hence $\bar{\beta}_{cr+} = 0$ (the relevant number $k_{cr+} = 0$). If $\alpha_- < 0$, however, two modes are observed here. The first of them is in cut-off regime and for it $\bar{\beta}_{cr-} = 0$ (the pertinent to it $k_{cr-} = 0$). The second is propagating with constant $\bar{\beta}_{c-} \neq 0$ (the answering to it $k_{c-} \neq 0$,

$k_{c-} < k_{cr-}$) and for it phase shift $\Delta\bar{\beta}_{cr} = \bar{\beta}_{c-}$ may be obtained. The abscissa of the cut-off point (the normalized critical guide radius, corresponding to the cut-off frequency) [1]

$$\bar{r}_{0cr} = \zeta_{0,n}^{(c)} / \left[2(1 - \alpha_{cr}^2)^{1/2} \right] \tag{2}$$

in which $\zeta_{0,n}^{(c)} = \mathbf{7.66341\ 19404\ 1502}5$ provided $c = 3$ and $n = 1$ specifies the lower limit of the domain in which $\Delta\bar{\beta}$ is available for a given $|\alpha| \equiv |\alpha_{cr}|$ [1]. The subscripts "+" ("−") distinguish the quantities, relating to the positive (negative) magnetization; and the ones "cr" ("$c-$") those, corresponding to cut-off (to transmission state for $\alpha_- < 0$, linked with the cut-off.) In what follows normal TE_{01} mode ($n = 1$) is treated only.

2.2. Description of the Method

A value of the off-diagonal tensor element α_-^{ch} is chosen and the one of critical radius $\bar{r}_{0cr}^{comp}$ is figured for it from formula (2). Two arbitrary negative values $k_{-,1}^{ch}$ and $k_{-,2}^{ch}$ ($k_{-,1}^{ch} < k_{-,2}^{ch} < 0$) of the imaginary part k of the complex first parameter of Kummer function are selected. Then, the pertinent to them roots $\zeta_{k_{-,1}^{ch},n}^{(c)}$ and $\zeta_{k_{-,2}^{ch},n}^{(c)}$ ($\zeta_{k_{-,1}^{ch},n}^{(c)} < \zeta_{k_{-,2}^{ch},n}^{(c)}$) of Eq. (1) are counted up. Afterwards the numbers, corresponding to α_-^{ch}, $k_{-,1}^{ch}$, $\zeta_{k_{-,1}^{ch},n}^{(c)}$, resp. to α_-^{ch}, $k_{-,2}^{ch}$, $\zeta_{k_{-,2}^{ch},n}^{(c)}$, are substituted in [1,2]:

$$\bar{r}_0 = \left(k\zeta_{k,n}^{(c)}/\alpha \right) \left\{ \left[1 + (\alpha/(2k))^2 \right] / \left(1 - \alpha^2 \right) \right\}^{1/2}. \tag{3}$$

The relevant numerical equivalents $\bar{r}_{0-,1}^{comp}$ and $\bar{r}_{0-,2}^{comp}$ ($\bar{r}_{0-,1}^{comp} > \bar{r}_{0-,2}^{comp}$, $\bar{r}_{0-,1}^{comp} = \bar{r}_{0-,2}^{comp}$, or $\bar{r}_{0-,2}^{-comp} > \bar{r}_{0-,1}^{-comp}$) are compared with $\bar{r}_{0cr}^{comp}$. If $\bar{r}_{0cr}^{comp} > \bar{r}_{0-,1}^{comp} > \bar{r}_{0-,2}^{comp}$, $\bar{r}_{0cr}^{comp} > \bar{r}_{0-,1}^{comp} = \bar{r}_{0-,2}^{comp}$, $\bar{r}_{0cr}^{comp} > \bar{r}_{0-,2}^{comp} > \bar{r}_{0-,1}^{comp}$ or $\bar{r}_{0-,1}^{comp} > \bar{r}_{0-,2}^{comp} > \bar{r}_{0cr}^{comp}$, a new couple $k_{-,1}^{ch}$ and $k_{-,2}^{ch}$ is picked out and the computations are repeated. In case $\bar{r}_{0-,1}^{comp} > \bar{r}_{0cr}^{comp} > \bar{r}_{0-,2}^{comp}$, obviously an interval is found, containing $\bar{r}_{0cr}^{comp}$. Its left and right-hand sides and the ones of the relevant interval for k are assumed as zeroth approximations to $\bar{r}_{0c-}$ and to k_{c-} sought. Accordingly, it is postulated: $k_{c-,left}^{(0)ch} \equiv k_{-,1}^{ch}$ and $k_{c-,right}^{(0)ch} \equiv k_{-,2}^{ch}$, and $\bar{r}_{0c-,right}^{(0)comp} \equiv \bar{r}_{0-,1}^{comp}$ and $\bar{r}_{0c-,left}^{(0)comp} \equiv \bar{r}_{0-,2}^{comp}$. [Note that $\bar{r}_{0c-,right}^{(0)comp}$ ($\bar{r}_{0c-,left}^{(0)comp}$) corresponds to $k_{-,left}^{(0)ch}$ ($k_{-,right}^{(0)ch}$).] For the intervals mentioned it holds: $\Delta\bar{r}_{0c-}^{(0)comp} = [\bar{r}_{0c-,left}^{(0)comp}, \bar{r}_{0c-,right}^{(0)comp}]$ and $\Delta k_{c-}^{(0)ch} = [k_{c-,left}^{(0)ch}, k_{c-,right}^{(0)ch}]$. A positive integer m^{ch}, larger than 1 is taken and $\Delta k_{c-}^{(0)ch}$ is divided in m^{ch} parts (e.g., $m^{ch} = 10$) by the points $k_{c-,left}^{(0)ch} + q\Delta k_{c-}^{(0)ch}/m^{ch}$, $q = 1, 2, \ldots, (m^{ch} - 1)$. The relevant values of critical radius are calculated at each of them, using formula (3), as described above and are confronted with $\bar{r}_{0cr}^{comp}$. The closest lying ones of them are accepted as first approximations to $\bar{r}_{0c-}$, resp. the ends of the interval for k, pertinent to them are considered as first approximations to k_{c-}. Let $\Delta k_{c-}^{(1)ch} = [k_{c-,left}^{(1)ch}, k_{c-,right}^{(1)ch}]$, $\Delta k_{c-}^{(1)ch} = \Delta k_{c-}^{(0)ch}/m^{ch}$, $k_{c-,left}^{(1)ch} = k_{c-,left}^{(0)ch} + p\Delta k_{c-}^{(0)ch}/m^{ch}$ and $k_{c-,right}^{(1)ch} = k_{c-,left}^{(0)ch} + (p+1)\Delta k_{c-}^{(0)ch}/m^{ch}$, $p = 0, 1, 2, \ldots, (m^{ch} - 1)$. Subsequently, it is proceeded in a similar manner. A period is put to the procedure when for the sth approximation it is

Table 1: Numerical values of the quantities $\bar{r}_{0cr}^{comp}$, k_{c-}^{comp}, $\zeta_{k_{c-}^{comp},n}^{(c)comp}$, $\bar{\beta}_{c-}^{comp}$ for normal TE_{01} mode ($n = 1$, $c = 3$) in case $|\alpha_-^{ch}| = 0\,(0.05)\,0.95$.

$|\alpha_-^{ch}|$	$\bar{r}_{0cr}^{comp}$	k_{c-}^{comp}	$\zeta_{k_{c-}^{comp},n}^{(c)comp}$	$\bar{\beta}_{c-}^{comp}$	$|\alpha_-^{ch}|$	$\bar{r}_{0cr}^{comp}$	k_{c-}^{comp}	$\zeta_{k_{c-}^{comp},n}^{(c)comp}$	$\bar{\beta}_{c-}^{comp}$
0.00	3.8317059702	0	7.6634119404	0	0.50	4.4244729467	−0.0699479911	7.3799884609	0.2333454734
0.05	3.8365046020	−0.0006703491	7.6606584723	0.0267708018	0.55	4.5879647204	−0.0854474814	7.3182761633	0.2478136937
0.10	3.8510093970	−0.0026847101	7.6523887042	0.0533482080	0.60	4.7896324628	−0.1027792656	7.2497506373	0.2592836548
0.15	3.8755540011	−0.0060530880	7.6385744186	0.0795360920	0.65	5.0421548754	−0.1220620712	7.1741176590	0.2671896876
0.20	3.9107185297	−0.0107923718	7.6191681596	0.1051327202	0.70	5.3654615579	−0.1434365616	7.0910375386	0.2708098913
0.25	3.9573689094	−0.0169266648	7.5941025807	0.1299275671	0.75	5.7929949110	−0.1670698767	7.0011180926	0.2691777189
0.30	4.0167192673	−0.0244877655	7.5632895029	0.1536976220	0.80	6.3861766170	−0.1931615125	6.9009059204	0.2609130441
0.35	4.0904266862	−0.0335158201	7.5266186553	0.1762029217	0.85	7.2737887180	−0.2219510189	6.7928754908	0.2438547332
0.40	4.1807339641	−0.0440601738	7.4839560565	0.1971809302	0.90	8.7905363713	−0.2537282117	6.6754153573	0.2140864435
0.45	4.2906869538	−0.0561804620	7.4351419842	0.2163392050	0.95	12.2712800587	−0.2888469234	6.5478105544	0.1622371762

Table 2: Numerical values of the quantities $\bar{r}_{0cr}^{comp}$, k_{c-}^{comp}, $\zeta_{k_{c-}^{comp},n}^{(c)comp}$, $\bar{\beta}_{c-}^{comp}$ for normal TE_{01} mode ($n = 1$, $c = 3$) as a function of $|\alpha_{-}^{ch}|$ and the number of iteration N.

N	$\|\alpha_{-}^{ch}\|$	$\bar{r}_{0cr}^{comp}$	k_{c-}^{comp}	$\zeta_{k_{c-}^{comp},n}^{(c)comp}$	$\bar{\beta}_{c-}^{comp}$
1	0.71	**5.44**120 54140 95902	**– 0.14**797 66433 55093	**7.07**349 43608 16384	**0.27094** 03659 94200
	0.72	**5.52**139 65117 19297	**– 0.15**260 84546 93197	**7.05**563 43925 85650	**0.27085** 27380 82768
2	0.711	**5.44**901 80876 07954	**– 0.14843** 56717 89717	**7.07**172 26767 30265	**0.27094 15763** 57058
	0.712	**5.45**687 55786 04664	**– 0.14889** 56189 84702	**7.06**994 78213 55382	**0.27094** 05966 42416
3	0.7110	**5.44**901 80876 07954	**– 0.14843** 56717 89717	**7.07172** 26767 30265	**0.27094 15763** 57058
	0.7111	**5.44**980 18135 56626	**– 0.14848** 16251 40066	**7.07154** 53339 58063	**0.27094 15770** 98444
4	0.71105	**5.44940** 98945 36816	**– 0.14845** 86473 16348	**7.07163** 40093 08488	**0.27094 15794** 65945
	0.71106	**5.44948** 82693 71959	**– 0.14846** 32426 97318	**7.07161** 62748 72712	**0.27094 15794** 30593
5	0.711051	**5.44941** 77318 18561	**– 0.14845** 91068 50310	**7.07163** 22358 79183	**0.27094 15794** 72267
	0.711052	**5.44942** 55691 45142	**– 0.14845** 95663 85191	**7.07163** 04624 46706	**0.27094 15794** 76399
	0.711053	**5.44943 34065** 16560	**– 0.14846 00259** 20991	**7.07162 86890** 11056	**0.27094 15794 78**340
	0.711054	**5.44944** 12439 32815	**– 0.14846 04854** 57710	**7.07162** 69155 72236	**0.27094 15794 78**092
	0.711055	**5.44944** 90813 93909	**– 0.14846 09449** 95348	**7.07162** 51421 30241	**0.27094 15794** 75652
	0.711056	**5.44945** 69188 99841	**– 0.14846 14045** 33904	**7.07162** 33686 85080	**0.27094 15794** 71021

fulfilled: $\bar{r}_{0c-,right}^{(s)comp} - \bar{r}_{0cr}^{comp} < \varepsilon^{ch}$, $\bar{r}_{0cr}^{comp} - \bar{r}_{0c-,left}^{(s)comp} < \varepsilon^{ch}$ or $\bar{r}_{0c-,right}^{(s)comp} - \bar{r}_{0c-,left}^{(s)comp} < \varepsilon^{ch}$ where $\bar{r}_{0c-,left}^{(s)comp} < \bar{r}_0^{comp} < \bar{r}_{0c-,right}^{(s)comp}$ (ε^{ch} — positive real number, less than unity, specifying the prescribed accuracy) or eventually if $\bar{r}_{0c-,right}^{(s)comp} \equiv \bar{r}_{0cr}^{comp}$ or $\bar{r}_{0c-,left}^{(s)comp} \equiv \bar{r}_{0cr}^{comp}$ (possibly provided $\bar{r}_{0-,1}^{comp} \equiv \bar{r}_{0cr}^{comp}$ or $\bar{r}_{0-,2}^{comp} \equiv \bar{r}_{0cr}^{comp}$). The value of $\bar{r}_{0c-,right}^{(s)comp}$ ($\bar{r}_{0c-,right}^{(s)comp}$ or $\bar{r}_{0-,1}^{comp}$) or $\bar{r}_{0c-,left}^{(s)comp}$ ($\bar{r}_{0c-,left}^{(s)comp}$ or $\bar{r}_{0-,2}^{comp}$), situated closer to (coinciding with) $\bar{r}_{0cr}^{comp}$ is accepted as such of $\bar{r}_{0c-}$. The corresponding numerical equivalent of k ($k_{c-,left}^{(s)ch}$ or eventually $k_{-,1}^{ch}$, or $k_{c-,right}^{(s)ch}$ or possibly $k_{-,2}^{ch}$) is taken as one of k_{c-}. Putting α_{-}^{ch} and k_{c-} in [1, 2]:

$$\bar{\beta} = \left\{ \left(1 - \alpha^2\right) / \left[1 + \left(\alpha / (2k)\right)^2\right] \right\}^{1/2} \tag{4}$$

yields $\bar{\beta}_{c-}$. Then α_{-}^{ch} is changed and everything begins over again. (The superscript "ch" ("comp") is attached to the symbols, typifying the parameters chosen (the quantities computed).)

2.3. Numerical Results

Table 1 lists the findings of numerical investigation for $|\alpha_{-}^{ch}| = 0\,(0.05)\,0.95$. It is seen that $\Delta\bar{\beta}_{cr}$ has a maximum in the interval $|\alpha_{-}^{ch}| = \langle 0.65 \div 0.75 \rangle$, at $|\alpha_{-}^{ch}| \approx 0.7$. To fix its exact value and location, an iterative scheme is worked out. The idea is to shrink gradually the interval pointed out until a satisfactory accuracy is achieved. The outcomes of subsequent steps are presented in Table 2,

Table 3: Numerical values of the quantities $\bar{\beta}_{en-}^{comp}$, $\bar{r}_{0en-}^{comp}$, k_{e+}^{comp}, $\zeta_{k_{e+}^{comp},n}^{(c)comp}$, $\bar{\beta}_{e+}^{comp}$, $\Delta\bar{\beta}_{en-}^{comp}$ for normal TE_{01} mode ($n = 1$, $c = 3$) in case $|\alpha_{en-}^{ch}| = 0.1\,(0.1)\,0.9$.

| $\|\alpha_{en-}^{ch}\|$	$\bar{\beta}_{en-}^{comp}$	$\bar{r}_{0en-}^{comp}$	k_{e+}^{comp}	$\zeta_{k_{e+}^{comp},n}^{(c)comp}$	$\bar{\beta}_{e+}^{comp}$	$\Delta\bar{\beta}_{en-}^{comp}$
0.1	0.99498 74371	66.26871 71806	0.62727 20906	10.47839 74657	0.99184 14847	0.00314 59524
0.2	0.97979 58971	33.64810 02126	0.62261 45744	10.45625 73535	0.96739 75917	0.01239 83054
0.3	0.95393 92014	23.04009 20625	0.61480 52939	10.41916 06870	0.92675 48542	0.02718 43472
0.4	0.91651 51390	17.98566 61016	0.60377 21866	10.36680 59161	0.87002 46408	0.04649 04982
0.5	0.86602 54038	15.22739 18940	0.58941 03296	10.29875 67018	0.79727 29178	0.06875 24860
0.6	0.8	13.73677 93891	0.57157 74770	10.21442 64949	0.70835 81917	0.09164 18083
0.7	0.71414 28429	13.18994 64667	0.55008 76358	10.11305 67386	0.60252 24792	0.11162 03637
0.8	0.6	13.73677 93891	0.52470 20192	9.99368 68569	0.47715 94859	0.12284 05141
0.9	0.43588 98944	16.80764 43978	0.49511 63490	9.85511 32849	0.32256 66973	0.11332 31970
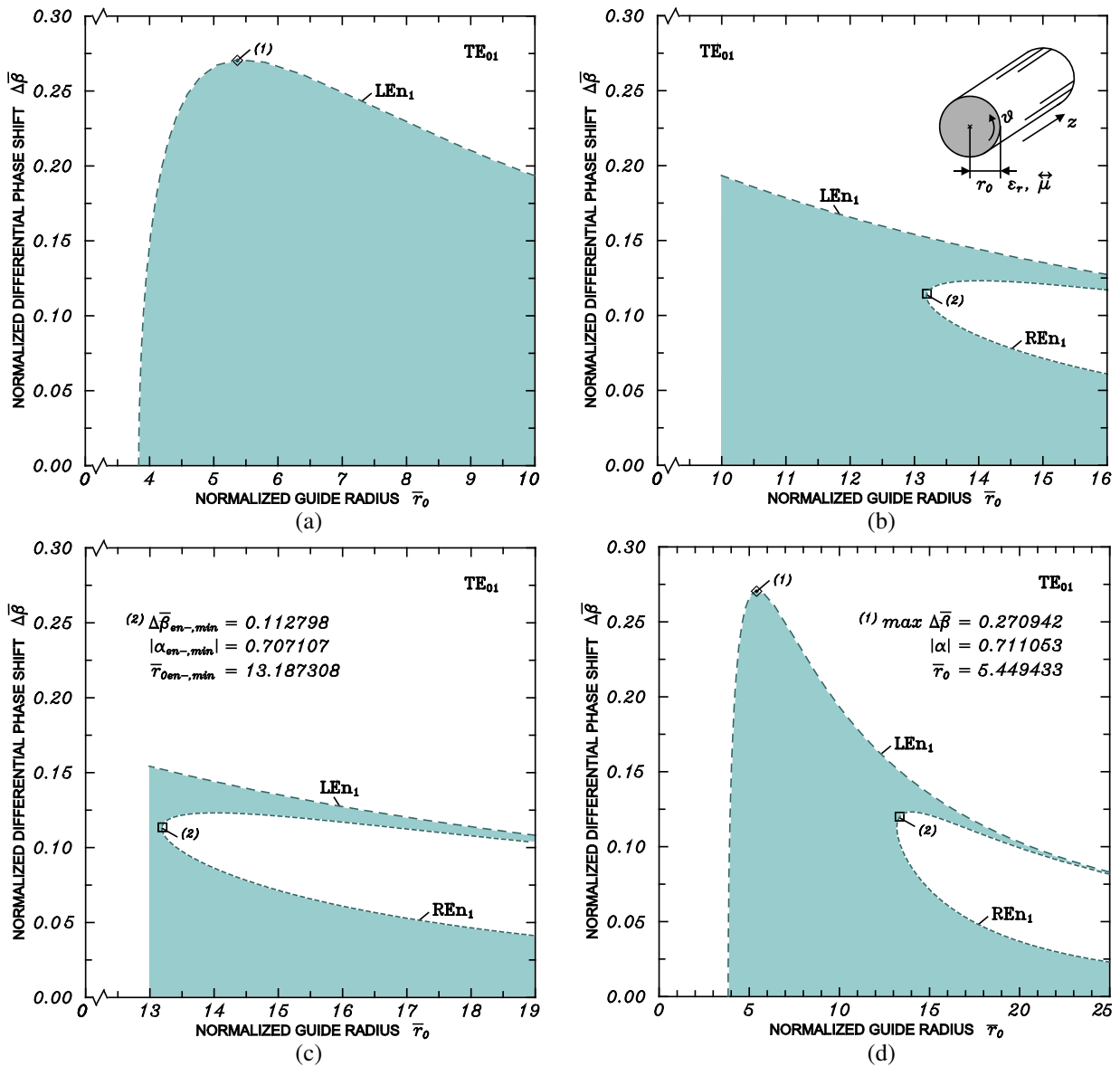
Figure 1: Domain of existence of the differential phase shift of the azimuthally magnetized circular ferrite waveguide in case of normal TE_{01} mode for $\bar{r}_0$ in the intervals: (a) $\langle 3.5 \div 10 \rangle$; (b) $\langle 10 \div 16 \rangle$; (c) $\langle 13 \div 19 \rangle$ and (d) $\langle 0 \div 25 \rangle$.

showing that the maximum value the differential phase shift might attain at all, is $\max \Delta \bar{\beta}_{cr} =$ **0.27094 15794 78**340, obtained at $|\alpha^{ch}_-| =$ **0.711053** and $\bar{r}^{comp}_{0cr} =$ **5.44943 34065** 16560. (The digits in a given result, being identical with these in the final one, are distinguished by bold face type.)

3. METHOD FOR COMPUTATION OF THE DIFFERENTIAL PHASE SHIFT AT THE ENVELOPE OF PHASE CHARACTERISTICS FOR NEGATIVE MAGNETIZATION

3.1. Physical Background

In case of negative magnetization an envelope line of equation $\bar{\beta}_{en-} = \bar{\beta}_{en-}(\bar{r}_{0en-})$ where [1]:

$$\bar{r}_{0en-} = L(c,n) / \left[|\alpha_{en-}| \left(1 - \alpha^2_{en-} \right)^{1/2} \right], \tag{5}$$

$$\bar{\beta}_{en-} = \left(1 - \alpha^2_{en-} \right)^{1/2}, \tag{6}$$

(α_{en-} is a parameter) restricts the propagation of normal TE_{0n} modes in the waveguide examined from the side of higher frequencies. For $\alpha_+ > 0$ there is no such boundary. The symbol $L(c,n)$ in Eq. (5) stands for a certain positive real number, defined through the relation: $\lim\limits_{k_- \to -\infty} |k_-| \zeta^{(c)}_{k_-,n} =$

$\lim_{k_- \to -\infty} |a_-|\zeta_{k_-,n}^{(c)} = L(c,n)$ [1]. In particular, if $c = 3$, $n = 1$ (corresponding to TE_{01} mode), it is valid: $L(c,n) = 6.59365\,41068$. Obviously, the quantities $\bar{r}_{0en-}$ are co-ordinates of both the curve mentioned and of the upper limit of the domain in which phase shift is produced. Its value here is given by the formula $\Delta\bar{\beta}_{en-} = \bar{\beta}_{en-} - \bar{\beta}_{e+}$. (The subscript "en−" ("e+") marks the quantities, characterizing the envelope (the point from the $\bar{\beta}_+(\bar{r}_0)$ — curve for certain $|\alpha|$ of abscissa equal to that of the end point of the $\bar{\beta}_-(\bar{r}_0)$ — one for the same $|\alpha|$ at the envelope).

3.2. Description of the Method

As before, a numerical equivalent of the element $|\alpha^{ch}|$ is selected. Next, the relevant ones of the guide radius $\bar{r}_{0en-}^{comp}$ and the phase constant $\bar{\beta}_{en-}^{comp}$ are reckoned from Eqs. (5) and (6). Then, the iterative scheme, described in Section 2.2, is effectuated for positive values of parameter k_+^{ch} to get k_{e+}^{comp} and $\zeta_{k_{e+}^{comp},n}^{(c)}$, resp. $\bar{r}_{0e+}^{comp}$ and $\bar{\beta}_{e+}^{comp}$ looked for. The computations go on until the inequality $|\bar{r}_{0en-}^{comp} - \bar{r}_{0e+}^{comp}| < \varepsilon^{ch}$ becomes true. $\Delta\bar{\beta}_{en-}$ is determined as a difference between $\bar{\beta}_{en-}^{comp}$ and $\bar{\beta}_{e+}^{comp}$.

3.3. Numerical Results

Table 3 yields the upshots of computations for $|\alpha_{en-}^{ch}| = 0.1\,(0.1)\,0.9$. As seen, the function $\bar{r}_{0en-} = \bar{r}_{0en-}(|\alpha_{en-}^{ch}|)$ possesses a minimum. It follows from expression (5) that $\bar{r}_{0en-,\min} = 2L(c,n) = 13.187308$ is obtained at $|\alpha_{en-,\min}^{ch}| = 1/\sqrt{2} = 0.707107$. For it $\Delta\bar{\beta}_{en-,\min} = 0.112798$.

4. DOMAIN OF EXISTENCE OF THE DIFFERENTIAL PHASE SHIFT

The LEn_1 — dashed and the REn_1 — dotted lines in Figs. 1(a)–(d) depict the limits of the domain in which $\Delta\bar{\beta}$ is afforded (represented by blue colour), linked with the cut-off frequencies and with the envelope of the $\bar{\beta}_-(\bar{r}_0)$ — characteristics [1], resp. It is seen that for specific $\bar{r}_0 \in [\zeta_{0,n}^{(c)}/2, 2L(c,n)]$, $\Delta\bar{\beta}$ is produced for all $|\alpha| \in [0, |\alpha_{cr}|]$, $|\alpha_{cr}| = \sqrt{1 - (\zeta_{0,n}^{(c)}/(2\bar{r}_0))^2}$ and its value changes from the $\bar{r}_0$ — axis to the LEn_1 — line. The maximum of the latter (the maximum value of $\Delta\bar{\beta}$ which the relevant geometry might yield at all) is marked in Figs. 1(a), (d) by the points (1). Provided $\bar{r}_0 \in [2L(c,n), +\infty]$, there are two zones below and above the REn_1 — curve in which $\Delta\bar{\beta}$ is available, separated by one where it is not observed. In the lower (upper) zone phase shift is obtained for $|\alpha| \in [0, |\alpha_2|]$ ($|\alpha| \in [|\alpha_1|, |\alpha_{cr}|]$), $|\alpha_{1,2}| = 0.5\sqrt{1 \pm (1 - 4(L(c,n)/\bar{r}_0))^2}$. There is no $\Delta\bar{\beta}$, if $|\alpha| \in [|\alpha_2|, |\alpha_1|]$. The abscissa $\bar{r}_{0en-,\min} = 2L(c,n)$ of point (2) delimits both intervals for $\bar{r}_0$.

5. CONCLUSION

Two approaches for tracing the borderlines of the area in which the circular ferrite waveguide with azimuthal magnetization, brings forth differential phase shift in case of normal TE_{01} mode, are presented. The idea is to use the special features of the phase characteristics of geometry for negative magnetization established earlier: double-valuedness at cut-off and existence of a particular envelope curve in the phase chart, restricting them from the side of higher frequencies. The method of successive approximations is employed whose main point is the repeated numerical solution of the structure's characteristic equation, written by a definite complex Kummer function. The results are displayed graphically in normalized form and are analyzed.

REFERENCES

1. Georgiev, G. N. and M. N. Georgieva-Grosse, "A new property of the complex Kummer function and its application to waveguide propagation," *IEEE Antennas Wireless Propagat. Lett.*, Vol. 2, 306–309, December 2003.
2. Georgiev, G. N. and M. N. Georgieva-Grosse, "Iterative method for differential phase shift computation in the azimuthally magnetized circular ferrite waveguide," *PIERS Online*, Vol. 6, No. 4, 365–369, 2010.
3. Tricomi, F. G., *Funzioni Ipergeometriche Confluenti*, Edizioni Cremonese, Rome, Italy, 1954.

Research of a Solid Object Impacting on the Water Surface

Ching-Jer Huang and Tsung-Mo Tien

National Cheng-Kung University, Taiwan

Abstract— The high-speed camera and an underwater hydrophone were applied to measure the trajectory and the underwater sounds of a solid object impacting on the water surface. The analysis methods include Fast Fourier Transform and Gabor Transform, not only reveal sounds in frequency domain but also in time-frequency domain. It is found that the frequency spectrum for the solid object impacting the water surface less than 10 kHz. Through this analysis, a better understanding of the mechanism of a solid object impacting on the water surface will be helpful to ocean remote sensing.

1. INTRODUCTION

Sounds in the ocean are mainly caused by marine lives, waves, currents and navigating ships. Different sound sources have its specific frequency characteristics, and also result in analytical complexities. The phenomena of a solid object impacting on water surface is quite complicated, which involves many fluid mechanical effects, such as splash inception, cavity formation, surface seal and bubble pinch off so on and so forth.

Worthington (1908) was the first one who showed that different roughness of the object will lead to different splashes. Richardson (1948) tried to describe mechanism of the cavity formation when the sphere impacts at the water surface in terms of potential flow and drag force. Albert (1951) used high-speed camera to investigate the effects of cavity that result from different sizes of sphere entering the water. It is noticeable that when the object impacting water surface, air volume will be entrained and induce bubble plume and sounds start to radiate during the process. When the frequency of the underwater sounds is revealed, the bubble size, R_0, can be easily determined from Minnaert's equation (1933)

$$\omega_0 = \frac{1}{R_0}\sqrt{\frac{3\gamma p_0}{\rho}}$$

where, ω_0 is the resonant frequency of the bubble; p_0, the ambient pressure of the bubble; ρ, the density of the surrounding fluid; and γ, the ratio of the specific heat ($\gamma = 1.4$ for air). Duclaux et al. (2007) made a laboratory experiments to take pictures on the cavity generated by solid impacting
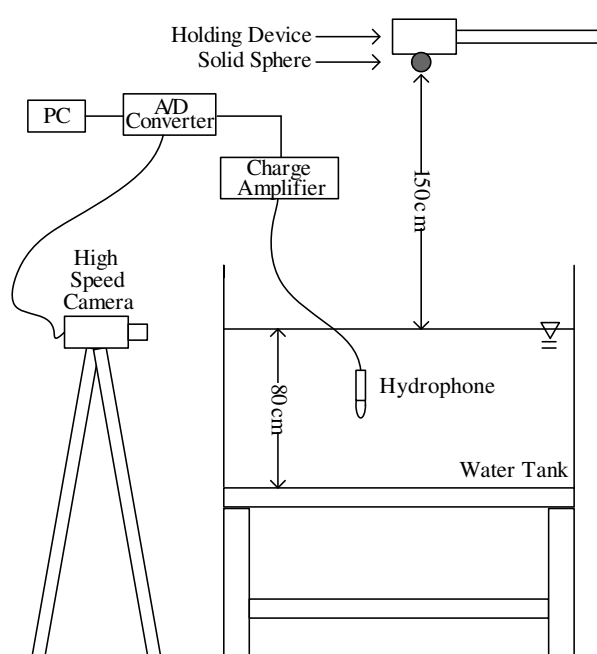

Figure 1: Schematic diagram of the experimental setup.

on water surface at high Weber number and Reynolds number. Minh and Gustav (2009) used numerical method to simulate the process of splash phenomenon and flow field. The purpose of this article is trying to find out the frequency characteristics when a solid object impacting on the water surface.

2. EXPERIMENTAL SET-UP

Experiments were carried out in a glass-walled water tank at Fiber Optic Sensing and Acoustics Laboratory at the Department of Hydraulic and Ocean Engineering, National Cheng Kung University, Taiwan. The tank has a dimension of 150 cm long, 90 cm wide and 100 cm high, and which is applied to measure underwater sounds when solid object impact on the water surface. The steel sphere (diameter = 3 inches; weight = 1, 800 g) was set up at 150 cm by an electromagnet above the water surface. The high-speed camera and underwater hydrophone were applied to measure the trajectory of a solid object impact on the water surface and the underwater sounds simultaneously. Figure 1 shows the schematic diagram of the experimental setup. The sampling frequency of the hydrophone is 100 kHz and the recording time is 2 seconds, signals are received by a hydrophone (Brüel and Kjær, type 8014) and amplified by a conditioning charge amplifier. Signals will be sent to the data acquisition system for further analysis.

Figure 2 shows the time series result of the underwater sound signals while the steel ball (diameter = 3 inches) hits the water surface. By considering the water depth and the efficient field of view (FOV) that high speed camera can capture, the analysis record in this study is 0.172 second. Figure 3 represents the range of image when the steel ball (diameter = 3 inches) hits the water surface. After the steel ball leaves the FOV that can be captured, it is difficult to
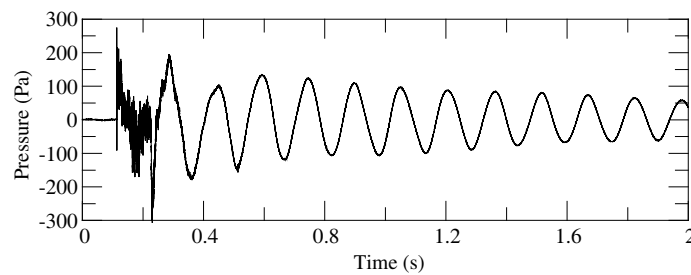

Figure 2: The underwater signals produced by steel ball ($d = 3$ inches).

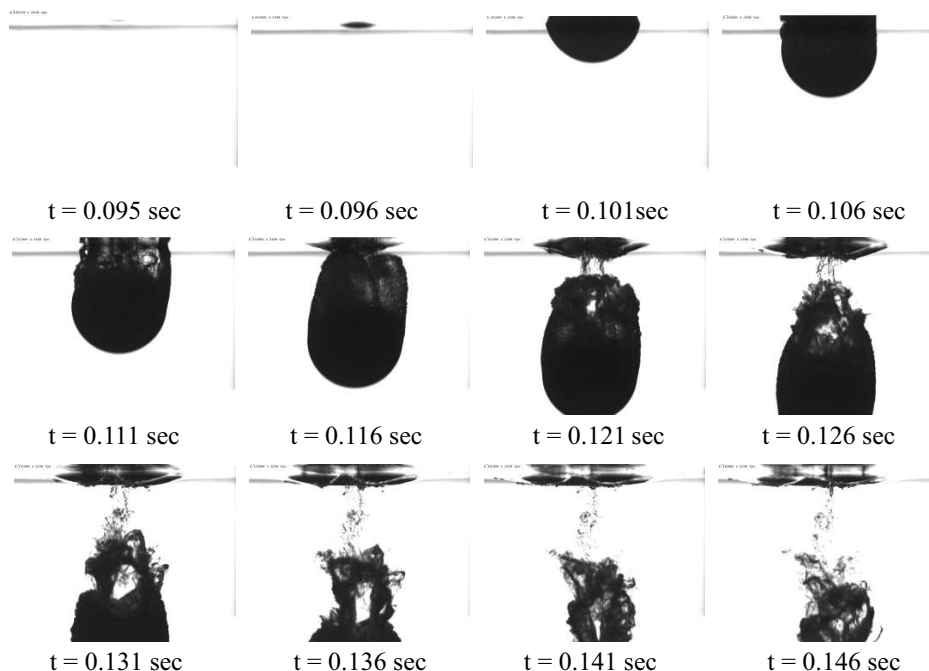| t = 0.095 sec | t = 0.096 sec | t = 0.101sec | t = 0.106 sec |
| t = 0.111 sec | t = 0.116 sec | t = 0.121 sec | t = 0.126 sec |
| t = 0.131 sec | t = 0.136 sec | t = 0.141 sec | t = 0.146 sec |

Figure 3: The steel ball impacts on water surface with the release height at 150 cm ($\Delta t = 5$ ms).

distinguish the physical phenomenon from the original signals. Figure 4(b) is the FFT result of the original signals, it is obvious that the energy of the impacting has a tendency to lower frequency. Figure 4(c) presents the FFT result within 500 Hz. Figure 4(d) presents the time series data in time-frequency domain obtained by use of Gabor transform.
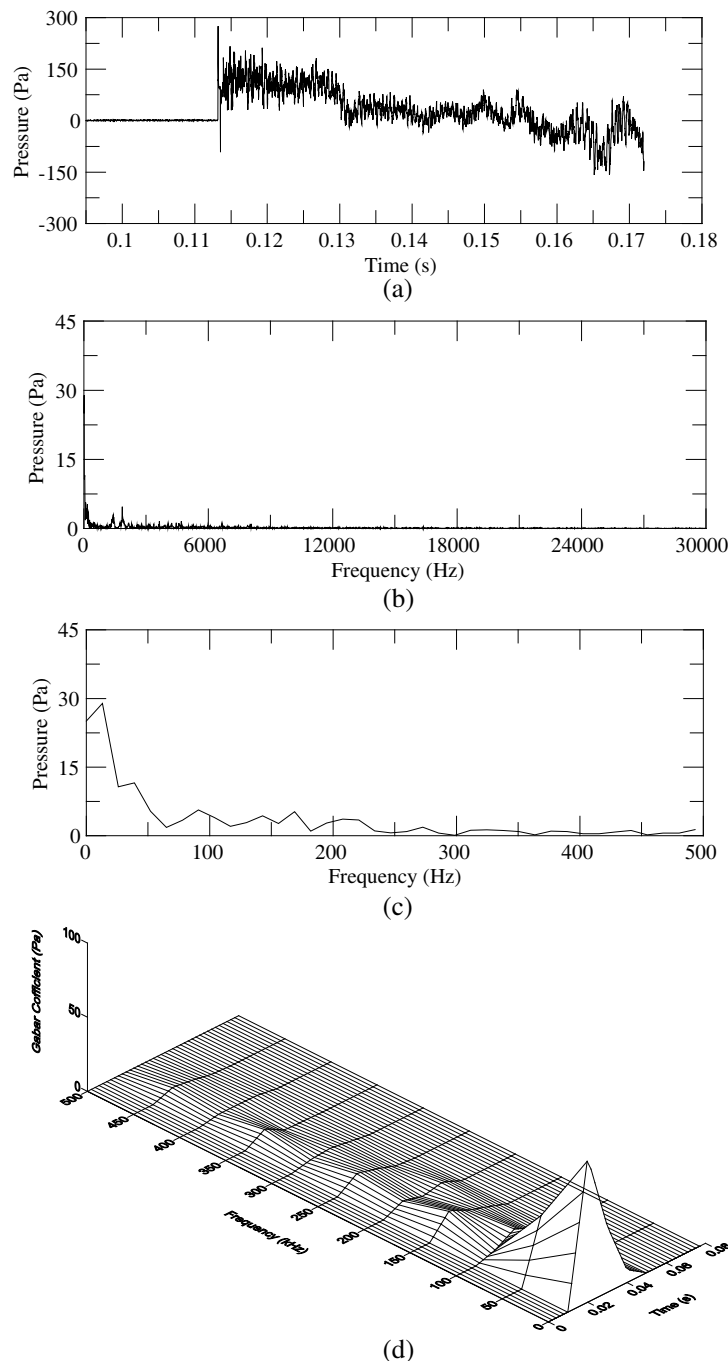

Figure 4: The underwater signals produced by steel ball ($d = 3$ inches), (a) Original time series data, (b)(c) FFT results over the entire frequency domain. (d) Gabor representation of the time domain signal.

3. CONCLUSION

In this study, the underwater signals are analyzed by using Fast Fourier Transform (FFT) and Gabor Transform to explore the characteristic of signals in the time and frequency domains. From the results showed in the figures, the frequency spectrum that induced by steel ball impacting on water surface is distributed within 10 kHz, and more precisely that energy focus at the frequency lower than 100 Hz.

REFERENCES

1. Albert, M., "Effect of surface condition of a sphere on its water-entry cavity," *J. Appl. Phys.*, Vol. 22, 1219–1222, 1951.

2. Duclaux, V., F. Caillé, C. Duez, L. Bocquet, C. Clanet, and C. Ybert, "Dynamics of transient cavities," *J. Fluid Mech.*, Vol. 591, 1–19, 2007.

3. Minnaert, M., "On musical air bubbles and the sounds of running water," *Phil. Mag.*, Vol. 16, 235–248, 1933.

4. Minh, D. Q. and A. Gustav, "The splash of a solid sphere impacting on a liquid surface: Numerical simulation of the influence of wetting," *Phys. Fluids*, Vol. 21, 0221021–02210212, 2009.

5. Richardson, E. G., "The impact of a solid on a liquid surface," *Proc. Phys. Soc.*, Vol. 61, 352–267, 1948.

6. Worthington, A. M., *A Study of Splashes*, Macmillan, New York, reprinted 1963, 1908.

A Rectangular Patch Antenna Technique for the Determination of Moisture Content in Soil

K. Y. You[1], J. Salleh[1], Z. Abbas[2], and L. L. You[3]

[1]Radio Communication Engineering Department, University Teknologi Malaysia
UTM Skudai 81310, Malaysia
[2]Department of Physics, University Putra Malaysia, UPM Serdang 43400, Malaysia
[3]Department of Human Biology, School of Medicine and Health Sciences
International Medical University, Kuala Lumpur 57000, Malaysia

Abstract— This paper presents a compact and low cost rectangular patch antenna that was used as a sensor for real time agriculture measurements. There were two types of rectangular patch sensor have been fabricated using FR4 printed circuit board and tested on soil (peat and loam). Both sensors were designed based on resonant and reflection principle which were operated at frequency range from 1.5 GHz to 3 GHz. The peat and loam soil were measured in a range of moisture content, $m.c$ from 0% to 30% and the fraction bond water in these soil samples were also analyzed.

1. INTRODUCTION

Sensors system is an important tool aimed at improving soil performance and soil quality. Generally, the sensors used in monitoring the soil quality are based on the physical and chemical properties of the soil. The physical properties include colour, texture, structure and moisture content in the soil [1]. In this paper, only moisture properties of the soil were studied.

Moisture content, $m.c$ in soil is essential characteristic in agriculture, civil engineering and hydrology, since the consistency and workability of a clayey soil strongly depend on its moisture content, $m.c$. Due to this reason, many of microwave sensors have been designed to give a real-time, simple, sensitive, small size and low cost for soil moisture measurement. In this study, these mentioned features of the sensors are considered although the focus of this study only on rectangular patch sensors.

Here, there were two rectangular patch sensors have been fabricated using microstrip feeding method and both patches were printed on low cost FR4 board, respectively. The first patch sensor was designed to give a single-resonant frequency and the second modified patch sensor is designed to provide dual-resonant frequencies at the range frequency between 1.5 GHz to 3 GHz. Finally, the sensors were used to estimate the moisture content in soil.

2. PRINCIPLE OF MOIS SOIL MEASUREMENT USING MICROWAVE PATCH SENSOR

In practical, the microstrip patch sensors use capacitance principle to measure the complex reflection coefficient, Γ of the soil samples [3]. The microstrip patch is filled with a soil sample, when the amount of ingredients or moisture changes in the soil samples, the patch sensor measures a change in capacitance, then produces a resonance frequency shift and a broadening of the resonance curve compared to free space. The volume of water in the total volume of dry soil most heavily influences the dielectric permittivity of the soil sample because the dielectric of water (80 at DC frequencies) is much greater than the other constituents of the materials in soil sample, For instance, the approximated relative permittivity value of mineral in soil is 4, the approximated value of organic matter is 4 and air is equal to 1 [4].

In generally, the water contained in the soil can be in bound water and free water conditions. The bound water fraction is not same for different kind of soil depend on it texture. Loam is the soil has a high water holding capacity as compared to other soil due to the loam soil contain a lot of organic matter. The organic matter in loam soil can hold more water than mineral substances. Thus, the water holding capacity or maximum fraction of bound water can be improved by adding organic matter [1, 2]. Since the changes of reflection coefficient, Γ are depended on the amount of organic matter and moisture content, $m.c$ in soil, thus the measurements can be directly correlated with a change in moisture content, $m.c$ and organic matter of the soil samples.

Normally, the moisture content, $m.c$ in soil are measured at microwave frequency range between 0.4 GHz to 2.45 GHz, due to the polarization of molecule water is sensitive at the frequency range.

At very low frequency ($< 0.4\,\mathrm{GHz}$), the reflection coefficient, Γ is not so sensitive to soil moisture variations. While, at high frequency ($> 3\,\mathrm{GHz}$), the measurements are strongly affect by the surface roughness of soil samples [2] and it will decrease the precision and repeatability of measurements.

3. METHODOLOGY

The rectangular patch sensors were designed using Microwave Office software (AWR) in order to obtain the sensitive operation frequency range between $1.5\,\mathrm{GHz}$ and $3\,\mathrm{GHz}$. Both rectangular patch sensors were constructed using low cost FR4 printer circuit board (PCB) with thickness substrate, $h = 1.6\,\mathrm{mm}$, relative permittivity substrate, $\varepsilon_r = 4.2$ and loss tangent substrate, $\tan \delta = 0.035$. All dimension of rectangular were sketched by using AutoCAD software and printed on an act paper, then attached on PCB using ironing technique. Finally, the PCB was etched and fabricated with acrylic sample holder as shown in Figures 1(a), (b) and (c).

For the preparation of soil samples, all soil samples were first dried at $100 \pm 0.5°\mathrm{C}$ in an oven for 24 hours. After drying, a certain weight of water was mixed with $100\,\mathrm{g}$ of dry soil in a small beaker. The mixed soil sample was subsequently filled into the sample holder up to a height of $65\,\mathrm{mm}$ of a sensor. The reflection coefficient, Γ of the mixed soil samples were measured by E5071C Network Analyzer at frequency range between $1.5\,\mathrm{GHz}$ to $3\,\mathrm{GHz}$. The relative moisture content, $m.c$ in soil samples, in percentage (dry basis), was calculated from:

$$m.c = \frac{m_{\mathrm{water}}}{m_{\mathrm{water}} + m_{\mathrm{dry\ soil}}} \times 100\% \tag{1}$$

where m_{water} and $m_{\mathrm{dry\ soil}}$ are the weight of water and weight of dry soil sample, respectively.

The dimensions of the both sensor are shown in Figures 2(a) and (b). Prior to the measurement, an one-port calibration was required to implement at the BB' plane using a $3.5\,\mathrm{mm}$ calibration kit (open, short and load) as shown Figures 2(c). Under the assumption of quasi-TEM mode, the measured reflection coefficient, $\Gamma_{BB'}$ of the sample at the plane BB' can be de-embedded to the junction between the coaxial line and the microstrip line, which coincide with the calibration plane AA' to give a reflection coefficient, $\Gamma_{AA'}$ by

$$\Gamma_{AA'} = \Gamma_{BB'} \exp\left(2jk_c z\right) \tag{2}$$

where k_c and z are the propagation constant and the length in meter (including fringing effect length) for coaxial line.

4. RESULTS AND DISCUSSION

In this study, a minimum sample thickness required to assume an infinite medium was investigated based on measurement and simulation results. The significant sample thickness was estimated based on distance at which the measured reflection coefficient, $|\Gamma|$ become constant when the plate was moved certain far from the patch sensor. Figure 3 shows the simulations results and measured
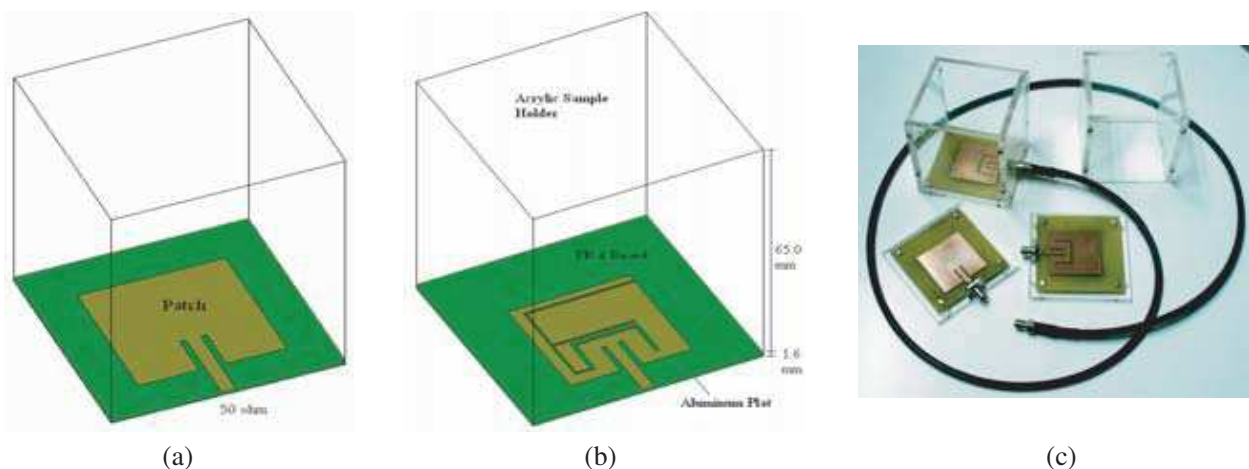

| (a) | (b) | (c) |

Figure 1: (a) Conversional rectangular patch sensor. (b) Modified rectangular patch sensor. (c) Actual configuration sensors.

(a)   (b)
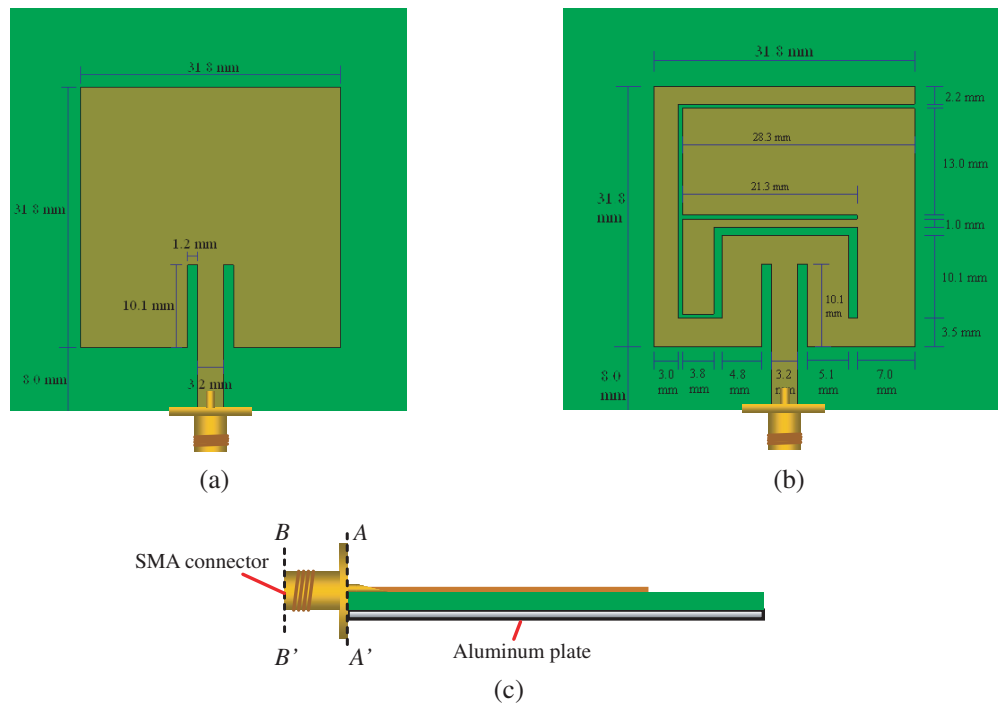

(c)

Figure 2: (a) Dimension for conventional patch sensor. (b) Dimension for modified patch sensor. (c) Side view for both patch sensors.

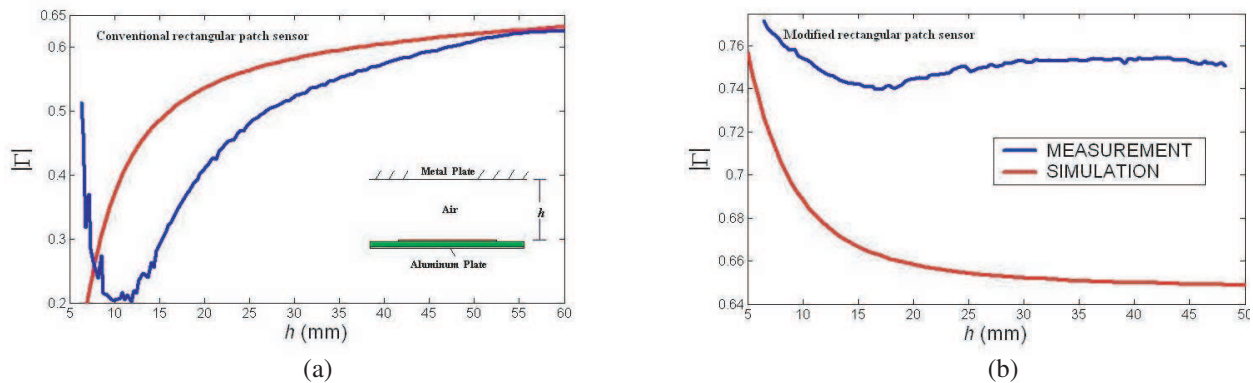(a)   (b)

Figure 3: Variation in magnitude of reflection coefficient, $|\Gamma|$ with air thickness, h at 2.4 GHz for (a) conventional rectangular patch sensor and (b) modified rectangular patch sensor.

reflection coefficient, $|\Gamma|$ results versus distance, h between patch sensor and metal plate. Results obtained shows that when the air layer thickness, h exceeded 60 mm, the measured magnitude reflection coefficient $|\Gamma|$ at 2.4 GHz remains unchanged for conversional rectangular patch sensor, as well as for modified rectangular patch sensor, the $|\Gamma|$ became constant when h only exceeded 30 mm. It can be concluded that the sensing area for conversional rectangular patch was two times larger than modified rectangular patch, since the radiation field for conversional rectangular patch was in omnidirectional shape.

Figures 4(a), (b), (c) and (d) show the comparison results of the measured and simulation reflection coefficient, Γ for both rectangular patch sensors. There are slightly deviation between simulation and measurement for conventional patch compared to modified patch. The small coupled gap line on the modified patch is the main factor to cause the high error in fabrication. In addition, the iron etching method is implemented to give a significantly low cost fabrication processes, nevertheless this technique will make the overall microstrip line enlarge up to 0.5 mm than actual design size. This tolerance is due to thermal expansion during the ironing process. Besides that, the errors may cause by the uncertainty of permittivity, ε_r and loss tangent, $\tan\delta$ for low

cost FR4 substrate. In our design, we assumed that the permittivity of FR4 substrate is a constant value, $\varepsilon_r = 4.2$. However, in real case, there are slightly change of permittivity, ε_r for the FR4 with operated frequency. The part of soldering and the quality of SMA connectors are also the important factor to affect the deviation between simulation and measurement results. In addition, cable movement and cable connection mismatch are normally constributed to the measurement error. Equation (2) is important for phase matching at the junction between coaxial line and microstrip line by referring to the simulation phase results. In this study, the z was given 0.019 m when the measured phase was shifted to match the simulation results as shown in Figures 4(a) and (b).

Figure 5 illustrates the reflection coefficient, Γ varied with percentage moisture content, $m.c$ for peat and loam soil at 2.05 GHz, which the frequency is within the sensitive region (resonant region) for both sensors. From Figure 5, we found that the maximum percentage bound water for loam soil is approximate 18% $m.c$, while the peat soil can only achieve 12% $m.c$. The main elements in loam soil are sand, silt and clay, thus it can retain water easier than peat soil [1, 2]. The measured phase shift, Ø vary slightly curve with the amount of moisture content, $m.c$ in the loam and peat soil. Obviously, the magnitude of reflection coefficient, $|\Gamma|$ are less sensitive and less precise to moisture content, $m.c$ in soil sample. From the fitting curve line in Figure 5, it is obvious that the measured phase shift, Ø using modified patch sensor was more sensitive to the soil moisture content, $m.c$ than conventional patch sensor. The coupled gap line on the rectangular patch can improve the sensitivity sensor to the sample under test, since the extra coupled gap line will increase the capacitive properties of the patch. Based on the measurement, we found that the phase of reflection coefficient, Ø is most flexible parameter to relate the moisture content, $m.c$ in soil samples. From roughly view, both soil samples were fully saturated by water above 30% moisture content, $m.c$. In future, the further investigation in bound water, geometrical particle effects and water-phase configuration for soil sample are required in order to obtain a detail physical background and trend of measured reflection coefficient respect to soil moisture content, $m.c$.
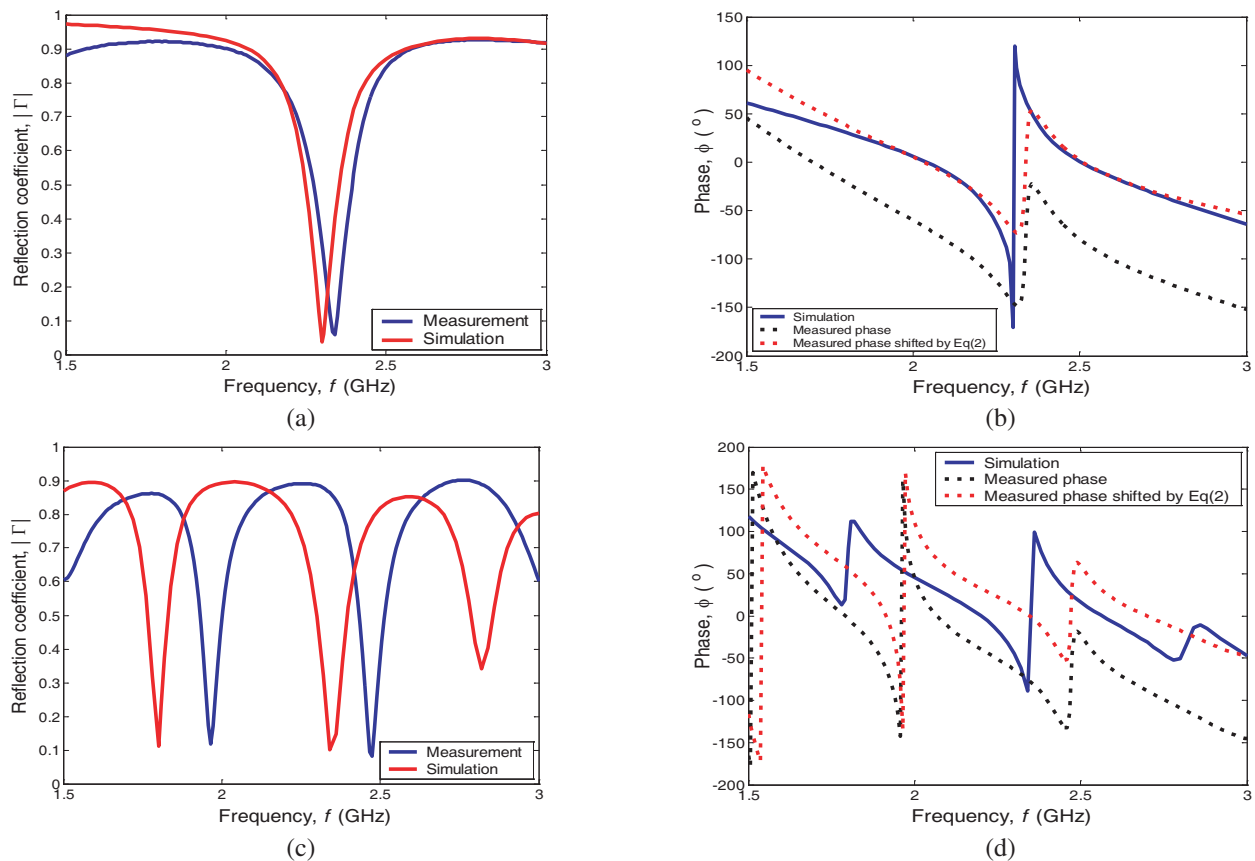

Figure 4: Variation in reflection coefficient, Γ (magnitude and phase) with frequency for (a) (b) conventional rectangular patch sensor and (c) (d) modified rectangular patch sensor.
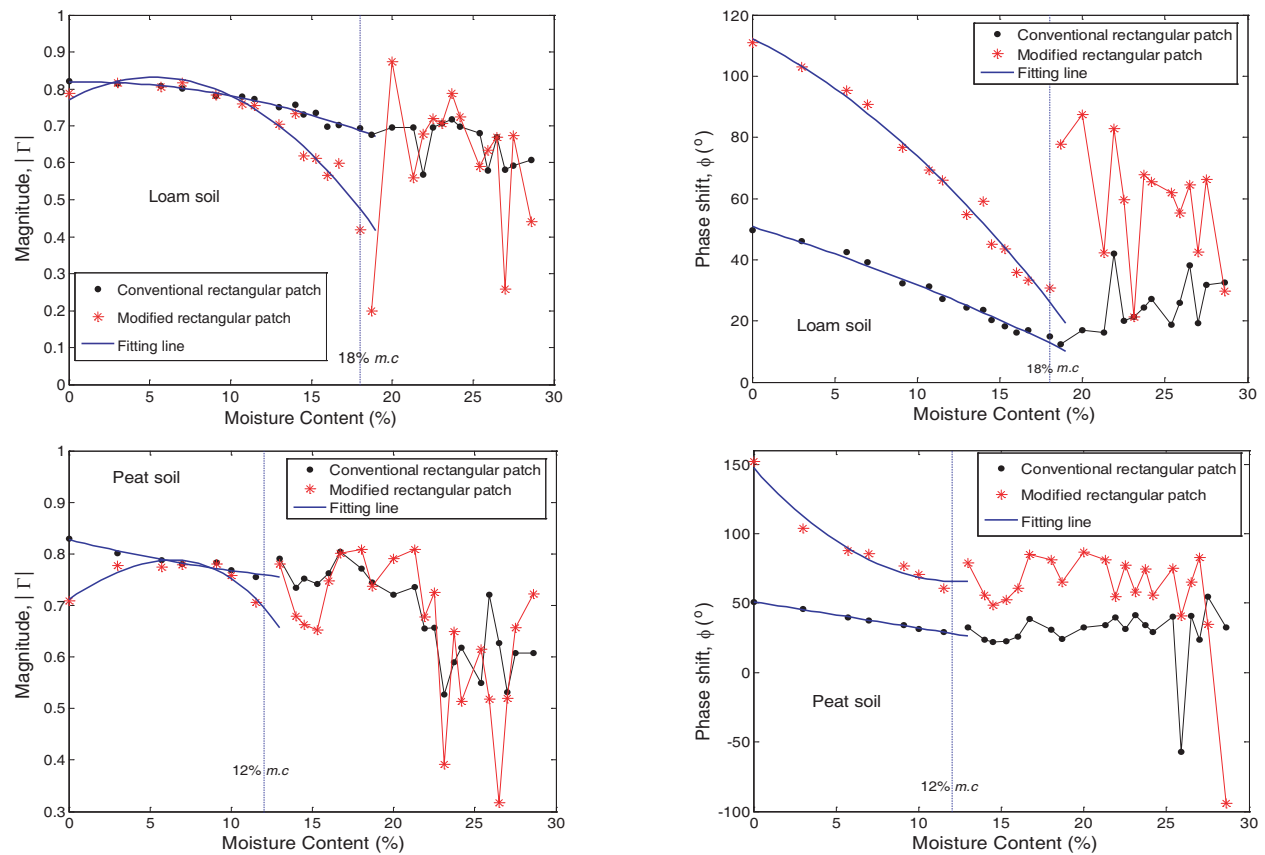
Figure 5: Variation in reflection coefficient, Γ with percentage moisture content, $m.c$ in peat and loam soil at 2.05 GHz at room temperature 25°C.

5. CONCLUSION

In this study, the single and dual resonant rectangular patch sensors have been developed for moisture soil measurement. This work provides a simple and sensitive of microwave sensors for testing and monitoring soil and pests in order to minimize the chemical fertilizer and nutrients put into the soil at certain time and location.

ACKNOWLEDGMENT

REFERENCES

1. Mirsal, I. A., *Soil Pollution: Origin, Monitoring & Remediation*, 2nd Edition, Springer, New York, 2008.
2. Behari, J., *Microwave Dielectric Behavior of Wet Soils*, Springer, New York, 2005.
3. Nyfors, N. and P. Vainikainen, *Industrial Microwave Sensors*, Artech House, Norwood, MA, 1989.
4. Kaatze, U., *Electromagnetic Aquametry*, K. Kupfer, Ed., Springer, New York, 2005.
5. David, A. S.-H., *Multiband Integrated Antennas for 4G Terminals*, Artech House, Norwood, MA, 2008.
6. Cataldo, A., G. Monti, E. De Benedetto, G. Cannazza, and L. Tarricone, "A noninvasive resonance-based method for moisture content evaluation through microstrip antennas," *IEEE Transaction on Instrumentation and Measurement*, Vol. 58, No. 5, 1420–1426, 2009.
7. You, K. Y., Z. Abbas, and K. Khalid, "Application of microwave moisture sensor for determination of oil palm fruits ripeness," *Measurement Science Review*, Vol. 10, No. 1, 7–14, 2010.

Monitored Solar Cycle in Relation to an Approximated Model

Shigehisa Nakamura

Kyoto University, Kyoto, Japan

Abstract— This is a note concerning a significant trend of the 11 year cycle in the solar activity. The monitored solar cycle for about 100 years has been studied by the scientists in order to develop a numerical model for the solar cycle in a scope of dynamical electromagnetism. This solar cycle model could be a key to an answer at considering any one of the geophysical processes on the planet earth.

1. INTRODUCTION

This is a note to help a significant trend of the 11 year cycle in the solar activity. The monitored solar cycle for about 100 years is studied by an approximated model in order to understand a specific property of solar activity in a scope of dynamical electromagnetism. Chapman [l, 2] and Stix [3], for example, noted the early state of the researches related to the solar cycle and solar activity specified by the sun spots number index in an annual time unit. This solar cycle model could be a key to an answer at considering any one of the geophysical processes on the earth as a planet in the solar system.

2. MAXWELL EQUATIONS

In order to start for studying solar cycle, Maxwell equations are introduced first for the magnetic field B, the electric field E, and the electric current density j, i.e.,

$$\text{div} \quad B = 0, \tag{1}$$
$$\text{curl} \quad B = \mu j, \tag{2}$$
$$\text{curl} \quad E = -(\partial/\partial t)B, \tag{3}$$

where, the mark μ is the magnetic permeability (for free space, in this case). In equation of (2), an approximation is assumed for non-relativistic, or slow phenomena (neglected the displacement current).

When the field is in a material with electric conductivity σ, the current is σ times the electric field (known as Ohm's law). When the material is in motion, it is taken into account of that the law valid in the co-moving frame of reference (i.e., $j = \sigma E$). In a case of motion (say, v for $v \ll c$), transformation to the frame at rest is as $j = j$ and $E = E + v \times B$. Then, $J = \sigma(E + v \times B)$. Eliminating E and j in the above equations, the induction equation is written as

$$(\partial/\partial t)B = \text{curl}(v \times B) - \text{curl}(\eta \, \text{curl} \, B), \tag{4}$$

where, magnetic diffusivity is $\eta = 1/(\mu\sigma)$.

3. MEAN-FIELD ELECTRODYNAMICS

The solar cycle could be solved referring essentially to the Maxwell equations for the magnetic field B, the electric field E, and the electric current density j [1]. Then, an induction equation is reduced. Electric conductivity of the sun could be determined as that of the ionized gas (or plasma) following to Spitzer (1962). For the case of the dynamo problem in terms of a mean magnetic field, $B = [B] + b$, where $[B]$ may be understood as an average over longitude or, more generally, as an ensemble average. Then, $[b] = 0$. In a same way, $v = [v] + u$. Substituting these two into the induction equation, fluctuating part is obtained after separating the mean part.

Following Moffatt (1978) with some assumptions, the mean part $[B]$ and the fluctuating part b can be separately described, i.e.,

$$(\partial/\partial t)\,[B] = \text{curl}\,([v] \times [B] + \varepsilon - \eta \, \text{curl}\,[B]), \tag{5}$$
$$(\partial/\partial t)\,b = \text{curl}\,([v] \times b + u \times [B]) + G - \eta \, \text{curl}\, b), \tag{6}$$

where, $\varepsilon = [u \times b]$, and $G = u \times B - [u \times b]$.

Under some specific condition, the value of ε is shown as following, i.e.,

$$\varepsilon = \alpha[B] \cdot \beta \operatorname{curl}[B] + \ldots, \tag{7}$$

where,

$$\alpha = -(1/3) \int_0^\infty \left[u(t) \operatorname{curl} u\left(t - t'\right) \right] dt', \quad \text{and} \quad \beta = (1/3) \int_0^\infty \left[u(t) u\left(t - t'\right) \right] dt', \tag{8}$$

One of the way to describe feature of the mean-field induction equation is the term involving a (that is called as the α effect).

Following to Knause (1967), $\alpha \simeq +1\,\Omega$ (or $-1\,\Omega$) is the mean angular velocity of the Sun. The sign of α depends on helicity of the flow in the solar convection.

Stix (1976) has shown the meridional cross sections for contours of constant toroidal field strength and poloidal lines of force (cf. Figure 1). The arrows are indicating strength and sign of polar field. An illustration is given in an adjusted time scale for 11 years for each half-cycle.

Theoretical butterfly diagram (contours of constant toroidal field) in an oscillatory kinematic $\alpha\,\Omega$ dynamo is shown by Steenbeck and Krause in 1969 (cf. Figure 2).
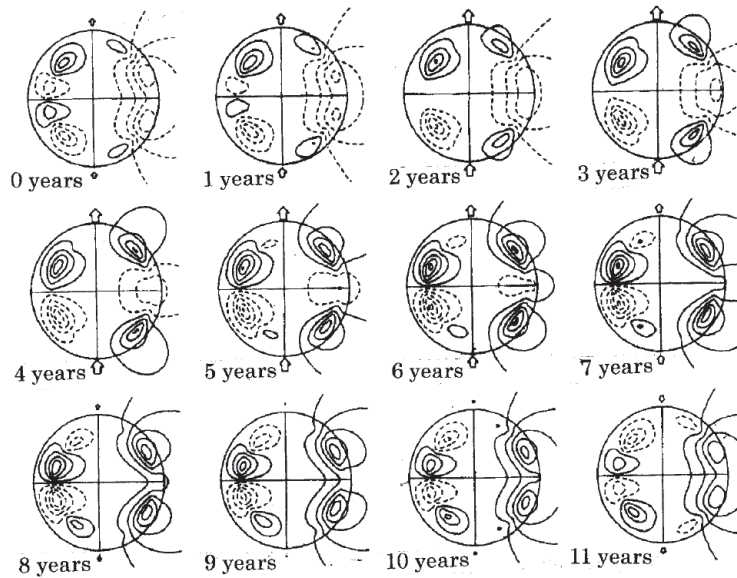
Figure 1: Oscillatory kinematic $\alpha\,\Omega$ dynamo model. In each illustration in every year, the meridional cross section is shown as (1), (1) on the right-contours of constant toroidal field strength, (2) on the left-contours of constant poloidal lines of force, (3) arrows indicate strength and sign of the polar field, (4) time scale is adjusted to 11 years for each half-cycle, (5) refer to Stix (1976).
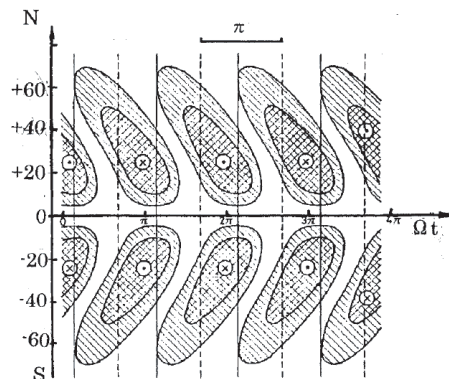

Figure 2: Theoretical butterfly diagram (contours of constant toroidal field) in an oscillatory kinematic $\alpha\,\Omega$ dynamo model (cf. Steenbeck and Krause, 1969).

The numerical results noted above is obtained under several assumption with some conditions, so that specific patterns could be demonstrated on the bases of the dynamical theory in an approximated forms as introduced by Stix [1].

The author here has to notice that the scientists should have their understanding of the specific pattern in the solar activity at considering the geophysical processes on the planet earth.

4. CHAOTIC DYNAMO

As a dynamic system, the magnetohydrodynamic dynamo is capable of chaotic behaviour. Such can be seen from the numerical integrations mentioned, for example, by Stix [1]. A simplified expression of the model can be written as follow, i.e.,

$$(\partial/\partial t)A = 2DB - A, \tag{9}$$
$$(\partial/\partial t)B = iA - (1/2)i\Omega A' - B, \tag{10}$$
$$(\partial/\partial t)\Omega = -iAB - v\Omega. \tag{11}$$

where, A' is complex conjugate of A.

System (9) to (11) is a complex generalization of a system first studied by Lorenz in 1963 as a model of turbulent convection. The system in this work likes to the Lornz system. It has chaotic solutions but also has solutions which are periodic in time.

5. DISCUSSION AND CONCLUSIONS

A theoretical background is introduced in a form of shortened expression. This might be helpful for realizing the monitored solar activity or the 11 year cycle of the sun spots number index. This work might be well related to the various geophysical processes found on the planet earth. Nevertheless, it is yet necessary to consider how complicated processes appear in the earth as well as in the sun.

It should be aware of an advanced research to be promoted even at present for our dynamical understanding of the sun as well as the planet earth where we are living.

REFERENCES

1. Chapman, S. and J. Bartels, *Geomagnetism*, 1049, Oxford University Press, London, 1940.
2. Chapman, S., *Solar Plasma, Geomagnetism, and Aurora*, 141, Gordon and Breach, New-York, 1964.
3. Stix, M., *The Sun — An Introduction, Astronomy and Astrophysics Library*, 390, Springer-Verlag, 1989.

Satellite Monitoring of Lunar Shadow on the Earth at Solar Eclipse

S. Nakamura

Kyoto University, Japan

Abstract— This an introduction to a satellite monitoring of the lunar shadow tracking on the earth surface at the predicted solar eclipse. One of the specific events is the one on 22 July 2009 in the low latitude zone of the western Pacific. A brief notice is given in relation of the solar eclipse on the planet earth in a scope of geophysical science.

1. INTRODUCTION

This is an introduction to a satellite monitoring of the lunar shadow tracking on the earth surface at the predicted solar eclipse. This is a part of the extensive research work at the Shirahama Oceanographic Observatory, Kyoto University. The project was started in 1960. For this project an offshore fixed tower was settled in the northwestern Pacific after one of the project leaders, Professor Shoitiro Hayami of Geophysics, in Kyoto University. Professor Hayami had ever been a member of the observation group for a solar eclipse on an island, Losop Island, in the north western Pacific in an early year around 1930.

In advance of the 50years Anniversary of "the Shirahama Oceanographic Tower", we had a chance for the satellite monitoring of the solar eclipse. This is the first time of the satellite monitoring of the predicted solar eclipse on the earth surface.

On 22 July 2009, the solar eclipse track passed just neighbor of the Japanese Islands. This solar eclipse might be a tiny impact to "the geophysical processes on the earth" now.

After reviewing the history of human activity on the earth, we can aware that the processes on the planet earth have been governed in the solar system.

Essentially, research on the "Solar Eclipse" has been promoted in the fields related to the section of "Astronomy". Hence, it should be raised as an interdisciplinary research on the solar activity in relation to the global processes on the earth.

The author here introduces a notice to the solar eclipse observed on the earth after his idea for a satellite monitoring of a solar eclipse in a scope of his interests.

2. SATELLITE MONITORING

In this work, the author introduces first some note to the lunar shadow on the earth surface at the solar eclipse. As a special reference, the event of the solar eclipse on the date of 22 July 2009 is taken for his convenience. The reference data was obtained by the satellite GMS-2 which has been operated on a synchronized orbital motion with the earth at the height of 800 km just above the earth's surface on the equator.

The satellite GMS-2 is operated for the purpose of monitoring the various geophysical processes on the earth. A sensor mounted on the satellite has a function to send us about the information of the various geophysical processes including the radiations out of the earth radiation. The author concentrated his interest in this work to the data of the earth surface pattern monitored as a passive signal in the visible band of the solar radiation reflected on the earth surface and of the earth radiation out of the earth surface.

As for the temperature, it is described in an accuracy of 0.5 degree C. The author has a wish to have the interested date in a form of an accuracy of 0.1 degree C In order to have a more detailed pattern as a reduced result from the satellite monitoring data.

By this time, the author has worked to see what satellite thermal pattern on the ocean surface or the land surface could be obtained in the infrared band of the radiation out of the ocean surface or the land surface.

The data of the satellite GMS-2 is successively processed and distributed through the Web-site by the Japanese Meteorological Agency as the service for public and citizen uses.

The resolution of a pixel size in an imagery of the earth surface pattern is about 4 km square. Nevertheless, we have to be aware of some restriction at utilizing the data obtained by the satellite GMS-2. Some part of the data should be strictly processed after the exactly assured reference of the data.
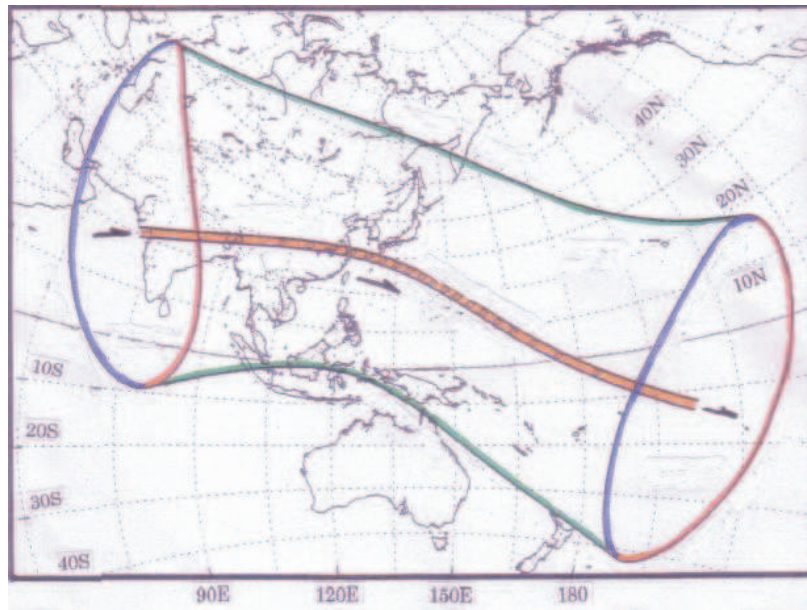
Figure 1: Solar eclipse shadow belt on the earth surface on 2009 July 22 (Refer to the National Astronomical Observatory). 1. Orange color line for the main shadow belt zone. 2. Red color line at each case of the west and ease parts for the start of the solar eclipse at sun rise and at sun set. 3. Blue color line at each case of the west and ease parts. for the end of the solar eclipse at sun rise and at sun set. 4. Green color lines for the northern and southern limits of the sub-shadow belt centering the main shadow zone. 5. Arrows (in Black color mark) shows the shadow movement with the time elapse.

3. PREDEICTED SOLAR ECLIPSE

Each one of the solar eclipses is predicted properly by the National Astronimical Observatory, Tokyo to issue every year in the series of the annual publication as the "Chronological Scientific Tables", which is available for the public and citizen use as well as the scientists in the related fields to the astronomy and geophysics. The edition No. 82 of this Table is for 2009.

In Figure 1, an illustration of the lunar shadow zone on the earth surface at the event on 22 July 2009 is introduced in a modified form of the original 2009 issue of the National Astronomical Observatory.

Main shadow zone is shown along an expected line track. Shadow zones at the start and at the end of the solar eclipse are also shown by the distorted circle as a projection of the main and sub shadow zones covering the interested zones.

As for the main solar eclipse shadow, the astronomical prediction about the solar eclipse on 22 July 2009 could be specified by the factors related to the main shadow, that is to say, to indicate the location and time of the solar eclipse shadow. After the evaluation by the National Astronomical Observatory, the specifying data set is given as follow;

	Time (JST)	Location
Start of partial ecliptic shadow	2009 July 22/ 08 h 58.3 m	84 43'E/ 19 03'N
Start of main ecliptic shadow	2009 July 22/ 09 h 52.8 m	70 31'E/ 20 21'N
Meridional Center (Concentric)	2009 July 22/ 11 h 33.0 m	143 22'E/ 24 37'N
End of main eclipse shadow	2009 July 22/ 13 h 17.8 m	157 41'W/ 12 55'S
End of partial ecliptic shadow	2009 July 22/ 14 h 12.4 m	171 51'W/ 14 14'S

At the time of the meridional center, a bright ring of the solar beam is formed by the fringe (4%) of the sun.

4. TRACKING OF SOLAR ECLIPTIC SHADOW

A data set for the solar eclipse shadow on the earth surface was issued as a special data set through the Web-site by the Japanese Meteorolgical Agency.

The data set consist the northern hemisphere as a synthesized foot print of the monitoring sensor of the satellite GMS-2 to demonstrate the movement of the solar ecliptic shadow pattern in a step of 15 min from the time of 0900-JST to 1400-JST. The data is simply distributed the solar ecliptic shadow pattern reduced after processing the signal radiation for the visible band which was monitored by the sensor mounted on the satellite GMS-2.

The solar ecliptic shadow pattern could be seen along a path projected on the earth following the factors shown above to specify the solar eclipse event. Nevertheless, the cloud distribution was the contaminating factor at seeing the solar ecliptic shadow.

With the author's experience of the daily pattern of the earth surface, especially, of the ocean surface, the author found that the shadow pattern reduced after processing the earth radiation of the visual band is coarsely consistent to the astronomical prediction.

It was unfortunate this time that no data was supplied for the reduced pattern in the infrared band. So that, it is expected what thermal pattern was obtained in the shadow zone at the interested solar eclipse event to the details in the successive work.

5. CONCLUSIONS

A satellite monitored solar eclipse shadow on the earth was introduced. This time, the available data was the radiation in the infrared band reflected on the earth surface and radiated out of the earth surface. The data was obtained by the satellite GMS-2.

The astronomical prediction of the solar eclipse on 22 July 2009 was consistent to the reduced result after processing the data of the satellite monitoring of the radiation in the visible band.

It should be encouraged to promote a research on the thermal pattern a t an event of the predicted solar eclipse by a satellite monitoring of the solar eclipse.

Referring to the data obtained and monitored by the satellite, the special and timely pattern of an interested solar eclipse shadow can be seen to help for realizing a more detailed knowledge of an environmental and the other geophysical processes instead of the limited numbers of the discrete local observations obtained on the earth surface in the past.

Monitored Solar Cycle in Relation to Sea Surface Temperature at Azores in the Northeast Atlantic Ocean

S. Nakamura

Kyoto University, Japan

Abstract— This is a brief note to the monitored solar cycle in relation to the sea surface temperature at a station in the ocean. First of all, a short note on the monitored solar cycle as a part of "Astronomy". One of the most classic interests for the scientists is "global magnetism" of the sun just like the main magnetic field of the earth. A note is given to a part of the observed result of sea surface temperature trend fit well to sun spot number index trend introduced in 2009 by the Azores Science group.

1. INTRODUCTION

This is a brief note to the monitored solar cycle in relation to the sea surface temperature at a station in the ocean. First of all, the author introduces a short note on the monitored solar cycle as a part of astronomy. It must be familiar to the scientists what the author notes as a briefing of the astronomical knowledge especially for realizing what should be considered about the relation between the sea surface temperature variations at Azores in the Atlantic Ocean and the sun spot number index variations during the time period of 1960 to 2007. A notice is given whether the fitting trends of the two factors could be possible to extend for the following several ten years.

2. SOLAR CYCLE

A convenient index of the solar cycle is the sun spot relative number, for example, Chapman ever written in his publication in 1964 [1]. As for the two types of "sun spot models", the first one is an empirical one. The second one is the magnetohydrostatic model. These models has been developed, for example, by Stix, 1989 [2].

A part of solar cycle variation of sun spots is introduced in a diagram, for example, as found in Figure 1. So-called solar cycle has been well known by the geophysical scientists though its dynamical mechanism has been extensively studied in the fields related to astronomy.

This 11 year cycle was found first by Schwabe in 1844. Hale had the first scientist of the magnetic field in sun spots in 1908. Hale had observed them by 1923 and formulated his polarity rules on his bases of three consecutive cycles. That is to say, Hale's rules are so as that:

(1) the magnetic orientation of leader and follower spots in bipolar groups remains the same in each hemisphere over each 11-year cycle,

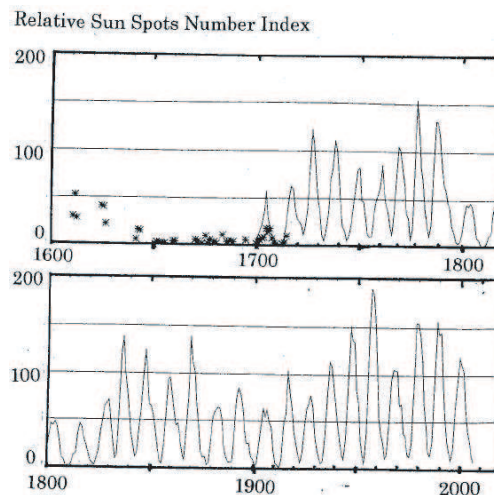(2) the bipolar groups in the two hemispheres have opposite magnetic orientation,

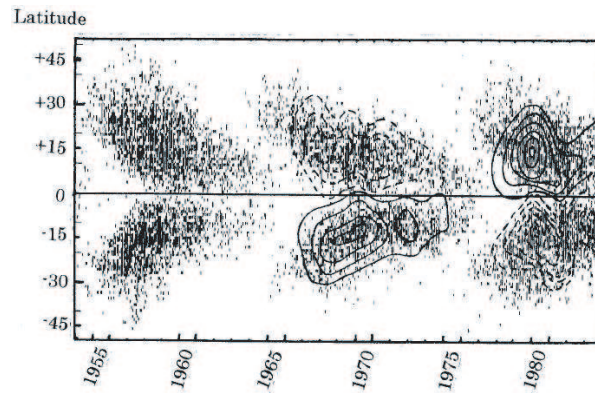Figure 1: Solar cycle variation of sun spots.

Figure 2: Butterfly diagram from Mt. Wilson Observatory (courtesy R. Howard, National Solar Observatory). Note: (1) Contours of radial mean field (from Mt. Wilson and Stanford magnetograms), (2) each vertical bar marks a sun spot, (3) the contours are (a) for solid positive $27\,\mu\mathrm{T}$, $54\,\mu\mathrm{T}$,..., (b) for dashed negative $-27\,\mu\mathrm{T}$, $-54\,\mu\mathrm{T}$,....

(3) the magnetic orientation of bipolar groups reverses from one cycle to the next.

Chapman [1] and Stix [2] had noted in his publication to a more detailed terms. For example, trends of the solar cycle variation of sun spots, prominences, and faculae. The numbers of northern and southern polar faculae are drawn with a sign in order to indicate the alternating magnetic polarity (which was published by Sheeley in 1964). Stix [1] had given the signs of plus or mipus mark magnetic reversals at the poles in 1974.

3. BUTTERFLY DIAGRAM

Another important result is known as butterfly diagram introduced by Maunder in 1922. The systematic behaviour of bipolar sun spot groups is readily understood in terms of a subsurface mean toroidal magnetic field, which is a field where lines of force are circles around the solar axis [1, 2].

In addition to the mean toroidal field there is a mean poloidal magnetic field. Cowling (1934) stated first the line-of-sight component of the magnetic vector field **B**. The mean field electrodynamics has been developed since 1955 by Parker and his followers.

4. SEA SURFACE TEMPERATURE

In 2007, the Azores Scientific Group showed that the observed sea surface temperature during the time period of 1960 to 2007 has shown a significant trend to fit the solar cycle variation of sun spots for four consecutive solar cycles. Nevertheless, it is hard to accept what has introduced by the Azores Group for helping to understand any global trend of the sea surface temperature on the planet earth. The scientists for dynamics of the ocean and atmosphere have found already any dynamical processes of the geophysical fluid motions are not so simple to see on a basis of a Limited data observed on the earth surface. The Azores Group had a lucky position of their station for obtaining their interesting finding.

5. DISCUSSIONS AND CONCLUSIONS

The author here has to note whether the Azores Scientific Group could show a same trend for their extensive observation of the sea surface temperature in relation to solar spots for about several ten years trends of the two physical factors.

The ocean scientists have learned that the sea surface thermal pattern on the earth is not so simple that it is hard to take it easy to relate the sea surface temperature variations at Azores in the Atlantic Ocean to the sun spots number variations as an index of the solar activity.

The ocean water has a complicated system of the ocean water motion between the earth crust surface and the atmospheric layer under an affect of the solar radiation.

So that, a global understanding of the ocean thermal transferring system should be taken into consideration at discussing on the sea surface temperature variations for obtaining a more reasonable understanding in a physical scope.

Finally, it is expected that a more advanced research should be promoted for a dynamical understanding of the various processes appear on the earth under the effect of the solar radiation.

REFERENCES

1. Chapman, S., *Solar Plasma, Geomagnetism, and Aurora*, 141, Gordon and Breach, New-York, 1964.
2. Stix, M., *The Sun: An Introduction*, 390, Springer-Verlag, 1989.

A Pattern Synthesis Technique for Multiplicative Arrays

Herbert M. Aumann

MIT Lincoln Laboratory, Lexington, Massachusetts, USA

Abstract— A technique is presented for synthesizing the antenna pattern of a multiplicative array. It is shown that the antenna pattern of two multiplicatively combined orthogonal linear subarrays of $(2N - 1)$ and $(2M - 1)$ elements can be made to match the antenna pattern of an $N \times M$ element planar array. Any planar array excitation function can be implemented provided that the planar array excitation function is separable. The excitation functions of the subarrays are shown to be the auto-convolution of the corresponding principal axis excitation functions of the planar array. The technique is illustrated by synthesizing a multiplicative array pattern with a two-dimensional 30-dB Chebyshev taper.

1. INTRODUCTION

Multiplicative arrays have been widely used in radio astronomy because of their excellent angular resolution and low cost. A well known example is the Mills Cross array [1, 2]. It consists of two conventionally summed linear subarrays that are oriented orthogonal to each other. The outputs of the subarrays are cross-correlated to form an antenna pattern. Although multiplicative arrays provide a greatly reduced element count when compared with conventional planar arrays, they have not found much acceptance in radar applications because of their reputed high sidelobes, degraded signal-to-noise ratio, and poor multiple target discrimination [3–5].

In this paper, we present a technique for improving the sidelobe performance of a multiplicative array. MacPhie [6] matched the power pattern of a Mills Cross array to that of a planar array with uniform illumination. We generalize this concept to show that, with proper choice of excitation, we can match the antenna pattern of a planar array with an arbitrary excitation.

In Section 2, we show that the antenna pattern of a planar array can be expressed as a product of two subarray patterns. In Section 3, we will derive the excitation functions of the multiplicative subarrays. An example of the technique is given in Section 4.

2. PLANAR ARRAY PATTERN

Most array pattern synthesis techniques are carried out in the voltage domain, even though the end product, the directional response of the array, is always presented as a power pattern in decibel. Since the directional response of a multiplicative array has already the units of power, we will determine an excitation function that best matches its pattern to the power pattern of a planar array.

Consider the power pattern of a conventional array consisting of $N \times M$ isotropic elements on a rectangular grid having uniform $\lambda/2$ element spacing, as illustrated in Fig. 1. It is well known that the array factor $\mathbf{D}$ in (u, v)-space is given by

$$\mathbf{D}(u, v) = \mathcal{F}^{-1}(\mathbf{A}), \tag{1}$$

where $\mathcal{F}^{-1}$ denotes a two-dimensional inverse Fourier transform and $\mathbf{A}$ is the planar array excitation function. Excitation functions are usually chosen to be separable along the x- and y-axis. In fact, the synthesis technique described in Section 3 requires $\mathbf{A}$ to be separable, that is

$$\mathbf{A} = \mathbf{e}_x^t \cdot \mathbf{e}_y, \tag{2}$$

where t denotes a transposition, and $\mathbf{e}_x(n)$, $n = 1, \ldots, N$ and $\mathbf{e}_y(m)$, $m = 1, \ldots, M$ can be any conventional array taper and may include a beam steering phase shift. When Eq. (2) is substituted into Eq. (1), the Fourier transform separability property [6] can be applied

$$\mathbf{D} = \mathcal{F}^{-1}\left(\mathbf{e}_x^t \cdot \mathbf{e}_y\right) = \mathcal{F}^{-1}\left(\mathbf{e}_x^t\right) \cdot \mathcal{F}^{-1}\left(\mathbf{e}_y\right), \tag{3}$$

where $\cdot$ indicates a vector multiplication. The power pattern $\mathbf{P}$ of a planar array is then given by

$$\mathbf{P} = \mathbf{D} \times \mathbf{D}^* = \left\{\mathcal{F}^{-1}\left(\mathbf{e}_x^t\right) \cdot \mathcal{F}^{-1}\left(\mathbf{e}_y\right)\right\} \times \left\{\mathcal{F}^{-1}\left(\mathbf{e}_x^t\right) \cdot \mathcal{F}^{-1}\left(\mathbf{e}_y\right)\right\}^*, \tag{4}$$

where $*$ denotes the complex conjugate and $\times$ is an element-by-element, or Hadamard [7], multiplication. By applying the distributive property of a Hadamard product, Eq. (4) can be rewritten as

$$\mathbf{P} = \left\{ \mathcal{F}^{-1}\left(\mathbf{e}_x^t\right) \times \left[\mathcal{F}^{-1}\left(\mathbf{e}_x^t\right)\right]^* \right\} \cdot \left\{ \mathcal{F}^{-1}\left(\mathbf{e}_y\right) \times \left[\mathcal{F}^{-1}\left(\mathbf{e}_y\right)\right]^* \right\}. \tag{5}$$

The above equation suggests that the antenna pattern of a planar array with separable excitation can be expressed in the form of two multiplied antenna patterns.

3. MULTIPLICATIVE ARRAY EXCITATION

Consider the pattern of a multiplicative array consisting of two separate, orthogonal, linear subarrays as shown in Fig. 2. The multiplicative array pattern $\mathbf{P}_m$ is defined by

$$\mathbf{P}_m = \mathbf{D}_1^t \cdot \mathbf{D}_2, \tag{6}$$

where $\mathbf{D}_1$ and $\mathbf{D}_2$ are the subarray patterns with excitations $\mathbf{e}_1(l)$, $l = 1, \ldots, L$ and $\mathbf{e}_2(k)$, $k = 1, \ldots, K$. The excitation functions are chosen to be auto-convolutions of $\mathbf{e}_x$ and $\mathbf{e}_y$, such that

$$\begin{aligned}
\mathbf{e}_1(l) &= \mathbf{e}_x \otimes \mathbf{e}_x, \quad l = 1, \ldots, (2N-1) \\
\mathbf{e}_2(k) &= \mathbf{e}_y \otimes \mathbf{e}_y, \quad k = 1, \ldots, (2M-1)'
\end{aligned} \tag{7}$$

where $\otimes$ denotes convolution. This choice will allow us to match Eq. (5) and Eq. (6). Substituting Eq. (7) into Eq. (1) and Eq. (6) and applying the Fourier convolution theorem [6] yields

$$\mathbf{P}_m = \mathcal{F}^{-1}\left(\mathbf{e}_1^t\right) \cdot \mathcal{F}^{-1}(\mathbf{e}_1) = \left\{ \mathcal{F}^{-1}\left(\mathbf{e}_x^t\right) \times \mathcal{F}^{-1}\left(\mathbf{e}_x^t\right) \right\} \cdot \left\{ \mathcal{F}^{-1}\left(\mathbf{e}_y\right) \times \mathcal{F}^{-1}\left(\mathbf{e}_y\right) \right\}. \tag{8}$$

For Eq. (5) and Eq. (8) to be identical, the excitation functions $\mathbf{e}_x$ and $\mathbf{e}_y$ must meet the following conjugate symmetry condition

$$\mathbf{e}_x^* = \mathbf{e}_x \cdot \mathbf{J} \quad \text{and} \quad \mathbf{e}_y^* = \mathbf{e}_y \cdot \mathbf{J}, \tag{9}$$

where $\mathbf{J}$ is a per-symmetric identity matrix [8]. All conventional array taper and beam steering excitation functions satisfy this condition.
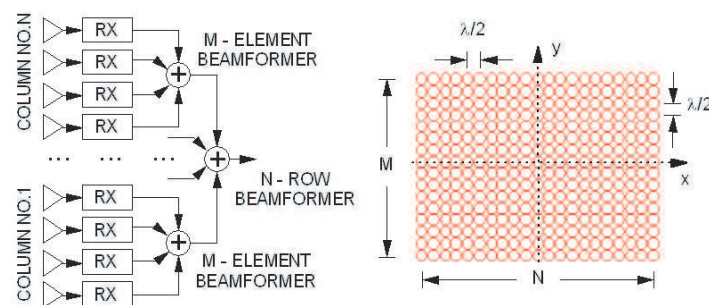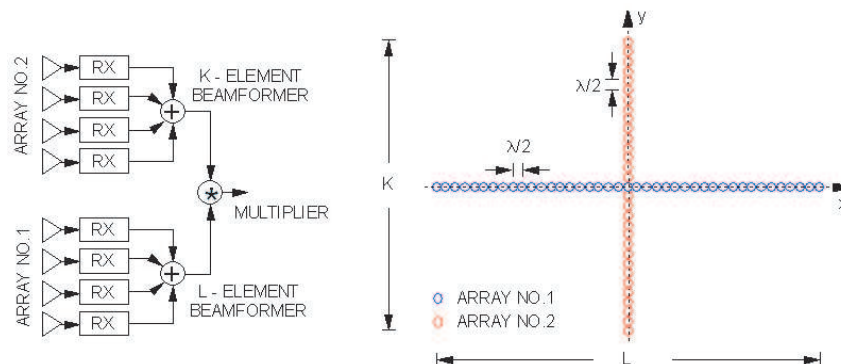

Figure 1: Conventional planar array.

Figure 2: Equivalent multiplicative array.

It can be shown that if $\mathbf{e}_x$ and $\mathbf{e}_y$ exhibit conjugate symmetry, then $\mathbf{e}_1$ and $\mathbf{e}_2$ in Eq. (7) will also be conjugate symmetric. Furthermore, the subarrays do not have to have colocated phase centers as shown in Fig. 2. The magnitude of the multiplicative pattern in Eq. (6) will not change when the phase centers of $\mathbf{D}_1$ and $\mathbf{D}_2$ are displaced, provided that $\mathbf{D}_1$ and $\mathbf{D}_2$ remain orthogonal.

4. EXAMPLE

The synthesis technique is illustrated by a numerical example of an $N = M = 21$ element array of isotropic elements on a grid with $\lambda/2$ spacing. A 30-dB Chebyshev taper is applied in the x-
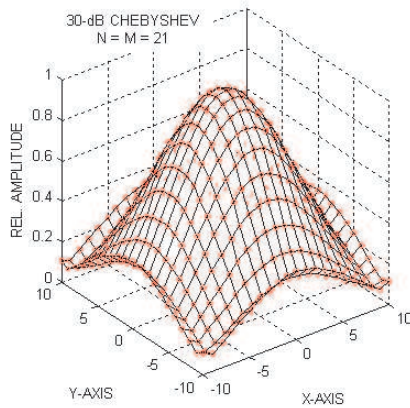
Figure 3: Planar array excitation.
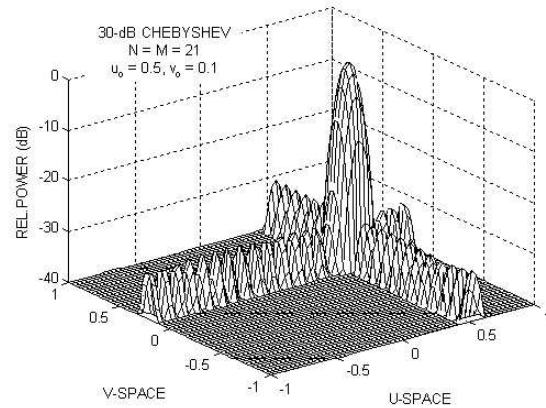
Figure 4: Planar array pattern.
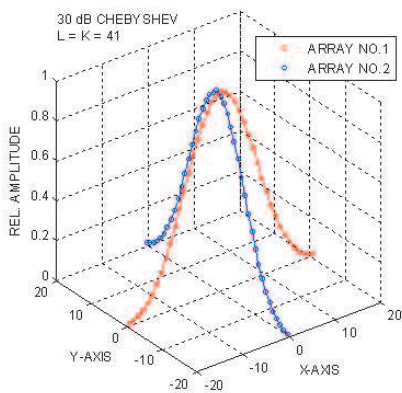
Figure 5: Multiplicative array excitation.
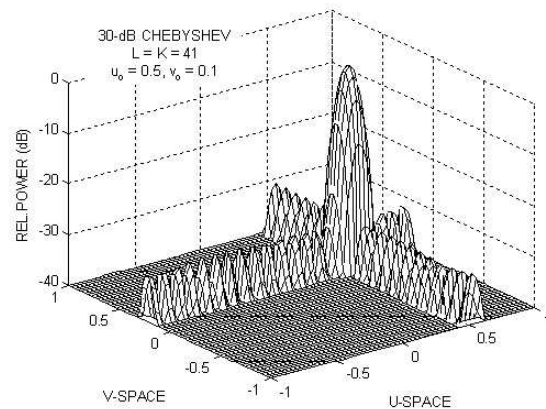
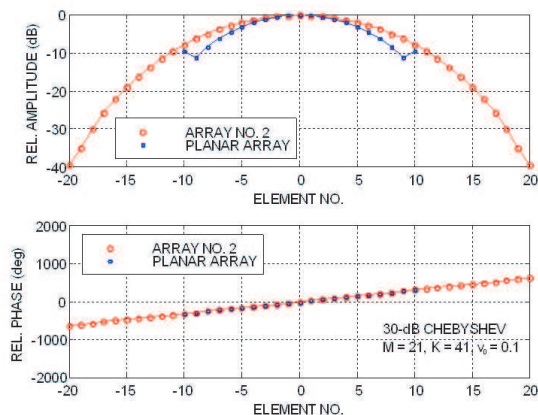Figure 6: Multiplicative array patten.
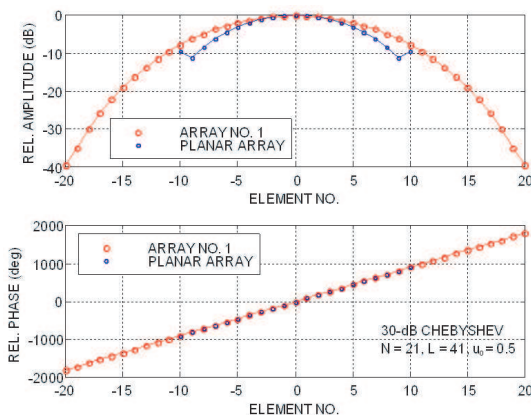
Figure 7: x-axis excitation.

Figure 8: y-axis excitation.

direction and y-direction and the array is steered to $u_o = 0.5$ and $v_o = 0.1$. The planar array excitation $\mathbf{A}$ and the corresponding antenna pattern $\mathbf{P}$ are shown in Fig. 3 and Fig. 4.

The excitations $\mathbf{e}_1$ and $\mathbf{e}_2$ were calculated from Eq. (7) and are shown in Fig. 5. Note that the multiplicative array contains less than one-fifth the elements of the equivalent planar array. Yet the multiplicative array pattern $\mathbf{P}_m$, in Fig. 6, is identical to the planar array pattern $\mathbf{P}$, in Fig. 4.

The conjugate symmetry condition in Eq. (9) is verified by comparison, in Fig. 7 and Fig. 8, of the amplitude and phase of the multiplicative array excitations with those of the planar array excitations along the x- and y-axis.

5. CONCLUSION

In this paper, we have demonstrated that the antenna power pattern of a multiplicative array consisting of a $(2N - 1)$ element linear array and an orthogonal $(2M - 1)$ element linear array can be made identical to the power pattern of a $N \times M$ element planar array if the excitations of the linear arrays are chosen to be the auto-convolution of the planar array excitations along the major axes. Conventional pattern synthesis techniques can be applied to determine the excitation of the planar array. The technique is not affected by subarray phase center displacement, nor does it interfere with array beam steering.

ACKNOWLEDGMENT

REFERENCES

1. Mills, B. Y. and A. G. Little, "A high resolution aerial system of a new type," *Australian J. Phys.*, Vol. 6., 272–278, 1953.
2. Grill, M., F. Honary, E. Nielsen, T. Hagfors, G. Dekoulis, P. Chapman, and H. Yamagishi, "A new imaging riometer based on mills cross technique," *7th International Symposium on Communication Theory and Applications*, 2003.
3. Davies, D. E. N and C. R. Ward, "Low sidelobe patterns from thinned arrays using multiplicative processing," *Proc. IEE*, Vol. 237, Pt. F, 9–15, 1980.
4. Nielsen, E., F. Honary, and M. Grill, "Time resolution of cosmic noise observations with a correlation experiment," *Annales Geophysicae*, Vol. 22, 1687–1689, 2004.
5. Pedinoff, M. E. and A. A. Ksienski, "Multiple target response of data processing antennas," *IEEE Trans. on Antennas and Propagation*, Vol. 10, 112–126, 1962.
6. MacPhie, R. H., "A mills cross multiplicative array with the power pattern of a conventional planar array," *2007 IEEE Antennas and Propagation International Symposium*, 5961–5964, Charleston, North Carolina, USA, July 2007.
7. Mitra, S. K., *Digital Signal Processing*, 3rd Edition, McGraw-Hill, Boston, MA, 2005.
8. Golub, G. H. and C. F. Van Loan, *Matrix Computations*, 3rd Edition, John Hopkins University Press, Baltimore, MD, 1996.

Interleaved Array Antennas Design — (Almost) Deterministic Strategies

Massimiliano Simeoni[1], Ioan E. Lager[1], Cristian I. Coman[2], and Christian Trampuz[1]

[1]International Research Centre for Telecommunications and Radar (IRCTR)
Faculty of Electrical Engineering, Mathematics and Computer Science
Delft University of Technology, CD Delft, The Netherlands
[2]NATO Consultation, Command and Control Agency (NC3A), 2597 AK the Hague, The Netherlands

Abstract— The synthesis strategies to be used for designing array antennas implementing the *shared-aperture* concept are described and discussed. The presented techniques range from fully deterministic approaches to semi-deterministic ones up to purely statistical design strategies. The pros and cons of each technique are ascertained.

1. INTRODUCTION

The quest for increasingly performing antenna front-ends has been stimulated in the last years by the necessity of implementing complex functions in radars and communication systems. In particular, modern sensing systems require the (array) antennas to be able to perform a number of *concurrent* tasks, such as, for instance, operating at different frequency bands, different polarizations, different scanning directions, etc. The coexistence of several array antennas performing concomitantly the different tasks often results in bulky antenna systems that are difficult to deploy on moving platforms such as ships, airplanes or satellites.

A convenient way to address this problem is to *co-locate* the array antennas responsible for the different services (functionalities) to be concurrently provided. The so-called *shared-aperture* concept [1, 2] can then be adopted to realize multi-functional array antennas. The different functionalities are ascribed to sub-arrays of elementary radiators, the sub-arrays sharing a common physical area that constitute the complete antenna aperture.

An early implementation of this concept is reported in [3] where the elementary antennas composing the sub-arrays are deployed on interleaved, uniform grids. A later contribution [4] proposed a complementary partition of a linear array in two sub-arrays exhibiting narrow radiation beams and grating lobes free operation. The shared-aperture concept was successively exploited to achieve multi-frequency operation [2] and polarization-agility capability [5]. Moreover the possibility to integrate the transmitter and the receiver antennas of a frequency modulated, continuous wave (FMCW) radar by making use of the shared-aperture concept was demonstrated in [6].

In this paper, some techniques that can be used to design interleaved array antennas implementing the shared-aperture concept are described. The reader is conducted through a path that, starts from strictly deterministic methods, passes through an intermediate step, and leads to fully stochastic approaches. The advantages and drawbacks introduced by the different techniques are analyzed in detail. It is worth noting that none of the techniques described in this work invokes any kind of iterative optimization procedure, this enabling a time effective design strategy for any of the presented methods.

2. COMPLEMENTARY APERTURE DIVISION AND SUB-ARRAY INTERLEAVING

The shared-aperture concept can be implemented in two different ways: the available antenna system aperture is subdivided in separate areas over which the different sub-arrays are deployed; the antenna aperture is shared between the different sub-arrays in an interleaved manner. The former approach keeps the different sub-arrays separated that, in turn, has a twofold advantageous effect: it conveniently minimizes the interference between the different functionalities and allows for using classic (uniform) array antenna design strategies. However, the fact that the different sub-arrays are confined to limited areas on the antenna aperture entails significant difficulties in achieving highly directive radiation patterns. Conversely, the latter solution, schematically represented in Fig. 1, benefits from exploiting the entire extent of the antenna aperture for each of the sub-arrays, at the expense of an increased cross-talk between the individual sub-arrays and a more complex design. Furthermore, this approach offers the additional advantage of implementing different sub-arrays having their phase centers virtually co-located, this feature being particularly useful in some applications (e.g., radar systems).

For the reasons above enumerated, the interleaved, shared-aperture strategy has been consistently adopted at the International Research Centre for Telecommunications and Radar (IRCTR), Delft University of Technology, for the design of multi-functional array antennas.

3. RIGOROUS TOOLS FOR COMPLEMENTARY APERTURE DIVISION

The design of a shared-aperture antenna consisting of two sub-arrays (i.e., implementing two concurrent services) can be achieved by partitioning an existing set of radiators (for instance deployed on a uniform rectangular grid) in two sub-sets. A convenient manner to achieve this is by calling upon rigorous, deterministic methods that exploit the properties of some binary numeric sequences.

In particular, the so-called Cyclic Difference Sets (CDS), sets of numbers, commonly used in the field of cryptography and communication technology [7], can be made use of to this end. The seminal work [8] describes in details the procedure to generate a thinned array by removing elements from a uniform array deployed on a regular grid. The remarkable auto-correlation properties of the CDS guarantee that, by deploying elements at all positions vacated by the thinning algorithm, a second (sub-)array can be obtained that has very similar radiation properties in terms of beamwidths and average side lobe levels (SLL). This observation amounts to the CDS placement strategy offering the handle to achieve a *complementary division* of the initial fully populated aperture [9]. A shared-aperture antenna architecture obtained in this way is shown in Fig. 2(a), where the dark gray squares represent the elements belonging to the first sub-array while the white ones correspond to the second sub-array. A generalization of this technique was proposed in [10] where, by concatenating several CDS and by adopting an appropriate partitioning scheme, a shared-aperture consisting of up to eight sub-arrays was designed. The eight sub-arrays showed very similar radiation patterns even in conjunction with beam scanning.

An alternative for obtaining shared-aperture antennas consisting of two interleaved sub-arrays is to provided by the Hadamard non-cyclic Difference Sets (HDS), as shown in [11]. An example of such array architectures is depicted in Fig. 2(b). This approach enables the synthesis of square arrays with almost 50% partitioning of the elements between the two sub-arrays. The degree of similarity between the radiation characteristics of the two sub-arrays is slightly lower than in the case of adopting the CDS.

Unfortunately, only a limited variety of Difference Sets, cyclic or not, exists, this inducing significant limitations in the range of array antennas to be designed in this manner. One manner to alleviate this drawback is by resorting to the wider class of Almost Difference Sets (ADS) [12]. In [13] the ADS were employed for designing linear thinned arrays with well controlled and predictable SLL. Again, the empty spaces left by the thinning of an initially fully populated array can be exploited for deploying a complementary (sub-)array, thus adding an additional, concurrent function to the overall array architecture. It must, however, be stated that this class of sets, although larger than that of (non-)cyclic Difference Sets, is still finite, this resulting, again, in array design limitations.
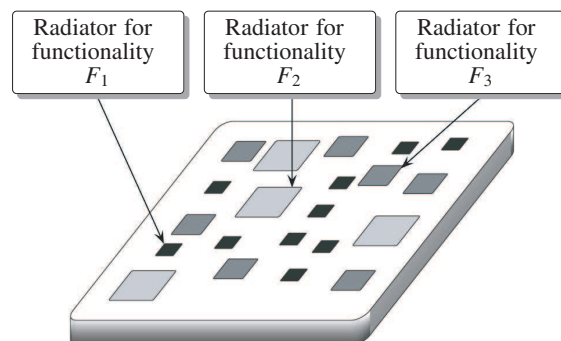

Figure 1: Illustrative for the shared-aperture antenna concept: different sets of radiators (sub-arrays) implement different functionalities.

4. DEVIATING FROM RIGOR

The previous section singled out the complementary division of a fully populated array by means of a CDS placement strategy as a convenient modality to implement two concurrent functions, with the high degree of similarity between the generated beams being cited as one of the most attractive features of the resulting design. While instrumental in some applications, such as the one described
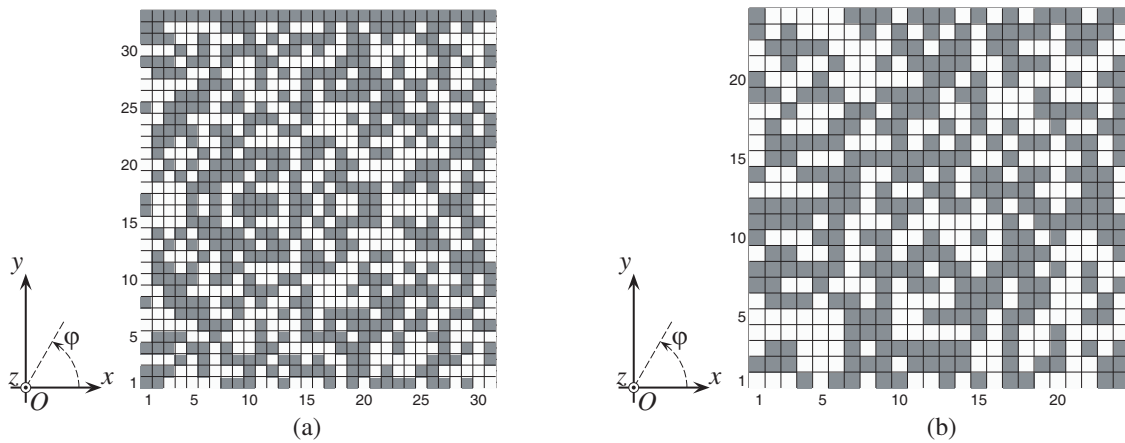
Figure 2: Shared-aperture antenna architectures obtained by using difference sets. (a) CDS, (b) HDS.

in [5], this similarity may result in some cases in sub-optimal operation. For example, [9] discussed the case of an interleaved, transmit-receive antenna for FMCW radars. The antenna aperture in [9] is partitioned in transmit (Tx) and receive (Rx) sub-arrays. In this case, the rigorous application of the CDS placement results in peak SLL in the two-way radiation pattern in the range of −26 dB. However, by resorting to an effective additional trimming artifice, this peak SLL could be reduced by 4 and 6.2 dB in the two main radiation planes, respectively, the relevant array architecture being shown in Fig. 3. It is important to note that the design procedure discussed in [9] relies on a full grid search over a feasible space that was cleverly reduced by making use of the properties of the CDS.

5. ONCE PANDORA'S BOX WAS OPEN

One of the important observation of [9] was that deviating from the rigorous CDS placement strategy does not result in substantial deterioration of the overall radiation properties of the obtained array. In particular, similarly to the case of antennas designed with the rigorous application of the method advocated in [8], there were no high lobes in the far sidelobes region. While the additional trimming in [9] was quite reduced, it was intriguing to investigate whether this preservation of adequate radiation properties remains valid in the case of drastic thinnings. This idea was the more so interesting since it opened the path towards generating interleaved arrays that are completely devoid of the intrinsic limitations of the CDS blueprints.

The validity of this design strategy was demonstrated in [14] where the sub-array interleaving was combined with thinning strategies aimed at obtaining very low SLL. The design procedures presented in [14] were entirely based on stochastic methods. More specifically, shared-aperture array antennas were obtained in successive steps. In the first place, the total array aperture consisting of elementary radiators deployed over a regular rectangular lattice were randomly subdivided in two sub-arrays. Note that this approach can be straightforwardly extended to a higher number of sub-arrays. The resulting arrangement of the sub-array radiators across the aperture was homogeneous, such that to preserve as much as possible the beamwidth set by the initial dimensions of the complete antenna aperture, but irregular, in order to prevent large periodicity sidelobes. By observing that the prescribed low SLL in array antennas can be achieved by varying the current distribution over the aperture, a *density tapering* strategy, mimicking the customary amplitude tapering techniques,
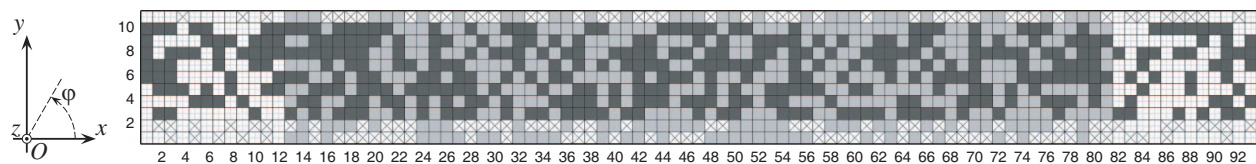

Figure 3: Antenna aperture's architecture obtained by trimming a CDS-generated shared-aperture array. The dark squares correspond to the Tx sub-array and the light ones to the Rx sub-array. The crosses indicate the trimmed elements in the Tx sub-array and the pluses the trimmed elements in the Rx one.

was then applied. The antenna aperture was subdivided in areas over which a certain illumination function is prescribed by the design algorithm (e.g., the Taylor algorithm [16]). Over each area a thinning procedure, again performed randomly over the elements of the relevant sub-arrays, enabled replicating the prescribed illumination function, higher thinning rate corresponding to lower values of the illumination function. The density tapering was shown to be an effective strategy, provided that the number of elements is sufficiently large for statistically mimicking the required current density distribution on the aperture. An example of such an array is depicted in Fig. 4, again the case of a transmit-receive antenna for the FMCW radar applications being considered. In Fig. 4(a) the subdivision of the array aperture in several areas is clearly visible, each area is associated with a given thinning rate that translates into a given value of the illumination function. The actual array configuration is shown in Fig. 4(b) where the decreasing density of antenna elements towards the edges of the aperture is easily recognizable.

This discussion is concluded by briefly touching upon a completely different (almost) deterministic vehicle for designing non-periodic array antennas that was discussed in details in [15]. It also relies on reproducing a prescribed aperture current distribution in combination with a placement along a spiral that ensures an almost full randomization of the inter-element spacing. While the applicability of this approach to the design of interleaved arrays remains to be demonstrated, the algorithm further evidences the versatility and effectiveness of resorting to readily available mathematical instruments for addressing highly demanding radiation requirements.
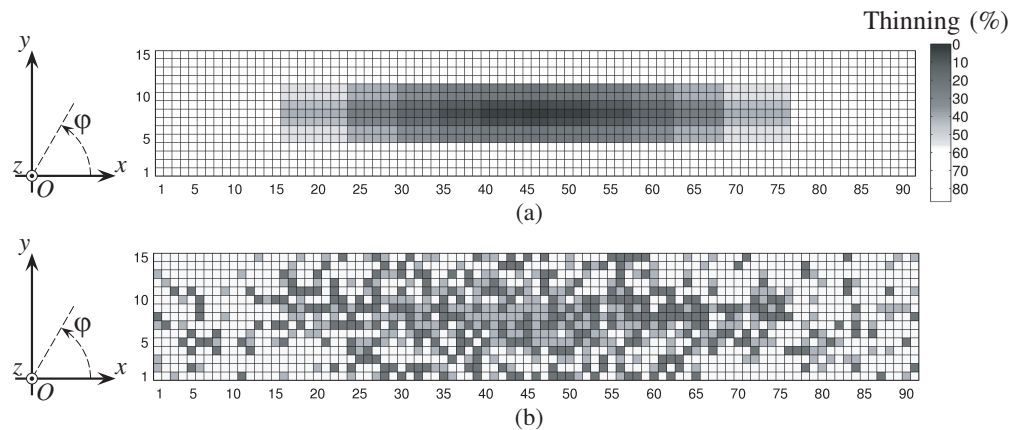

Figure 4: Thinned, interleaved array architecture replicating a Taylor amplitude taper. (a) The thinning rate, in percents, in the various regions of the aperture, (b) the resulting array architecture: the dark gray squares correspond to the transmit sub-array, the light gray ones to the receive sub-array and the white ones to the eliminated elements (58%).

6. CONCLUSION

An illustrative selections of antenna array synthesis methods employed for implementing the shared-aperture concept was discussed. The presented architectures concurrently support two functionalities, this resulting in a substantial enhancement of the array antenna performance. The employed design methods make use of deterministic mathematical instruments or invoke effective (random) optimization approaches for tailoring the radiation properties. Due to their efficiency, the discussed strategies are suitable for tackling the design of (very) large array antennas.

ACKNOWLEDGMENT

REFERENCES

1. Coman, C. I., I. E. Lager, and L. P. Ligthart, "Multifunction antennas — The interleaved sparse sub-arrays approach," *Proc. 36th European Microwave Conference — EuMC*, 1794–1797, Manchester, UK, Sep. 2006,

2. Coman, C. I., "Shared aperture array antennas composed of differently sized elements arranged in sparse sub-arrays," Ph.D. Dissertation, Delft University of Technology, Jan. 2006.

3. Pozar, D. M and S. D. Targonski, "A Shared-aperture dual-band dual-polarized microstrip array," *IEEE Trans. Antennas and Propagat.*, Vol. 49, No. 2, 150–157, Feb. 2001.

4. Haupt, R. L., "Interleaved thinned linear arrays," *IEEE Trans. Antennas and Propagat.*, Vol. 53, No. 9, 2858–2864, Sep. 2005.

5. Simeoni, M., I. E. Lager, C. I. Coman, and A. G. Roederer, "Implementation of polarization agility in planar phased-array antennas by means of interleaved subarrays," *Radio Science*, Vol. 44, RS5013, Oct. 2009.

6. Trampuz, C., M. Simeoni, I. E. Lager, and L. P. Ligthart, "Complementarity based design of antenna systems for FMCW radar," *Proc. 5th European Radar Conference — EuRAD*, 216–219, Amsterdam, The Netherlands, Oct. 2008.

7. Golomb, S. W. and G. Gong, *Signal Design for Good Correlation: For Wireless Communication, Cryptography, and Radar*, Cambridge University Press, Cambridge, 2005.

8. Leeper, D. G., "Isophoric arrays — Massively thinned phased arrays with well-controlled sidelobes," *IEEE Trans. Antennas and Propagat.*, Vol. 47, No. 12, 1825–1835, Dec. 1999.

9. Lager, I. E., C. Trampuz, M. Simeoni, and L. P. Ligthart, "Interleaved array antennas for FMCW radar applications," *IEEE Trans. Antennas and Propagat.*, Vol. 57, No. 8, 2486–2490, Aug. 2009.

10. Coman, C. I., I. E. Lager, and L. P. Ligthart, "A deterministic solution to the problem of interleaving multiple sparse array antennas," *Proc. 2nd European Radar Conference — EuRAD*, 243–246, Paris, France, Oct. 2005.

11. Kopilovich, L. E., "Square array antennas based on hadamard difference sets," *IEEE Trans. Antennas and Propagat.*, Vol. 56, No. 1, 263–266, Jan. 2008.

12. Arasu, K. T., C. Ding, T. Helleseth, P. V. Kumar, and H. M. Martinsen, "Almost difference sets and their sequences with optimal autocorrelation," *IEEE Trans. Inf. Theory*, Vol. 47, No. 7, 2934–2943, Nov. 2001.

13. Oliveri, G., M. Donelli, and A. Massa, "Linear array thinning exploiting almost difference sets," *IEEE Trans. Antennas and Propagat.*, Vol. 57, No. 12, 3800–3812, Dec. 2009.

14. Trampuz, C., M. Simeoni, I. E. Lager, and L. P. Ligthart, "Low sidelobe interleaved transmit-receive antennas for FMCW radar applications," *IEEE Antennas Propagat. Symp. Dig.*, Charleston, USA, Jun. 2009.

15. Viganó, M. C., G. Toso, G. Caille, C. Mangenot, and I. E. Lager, "Sunflower array antenna with adjustable density taper," *Int. Journal of Antennas and Propagation, Hindawi Publ. Corp.*, Vol. 2009, Article ID 624035, 2009.

16. Taylor, T. T., "Design of line-source antennas for narrow beam-width and low sidelobes," *IRE Trans. on Antennas and Propagation*, Vol. 3, 16–28, Jan. 1955.

A Complete MIMO System Built on a Single RF Communication Ends

Vlasis Barousis, Athanasios G. Kanatas, and George Efthymoglou

University of Piraeus, Greece

Abstract— It is well known that Multiple Input-Multiple Output systems enhance significantly the spectral efficiency of wireless communication systems. However, their remarkable hardware and computational burden hinders the wide deployment of such architectures in modern systems. In this paper, we present an alternative MIMO architecture built on parasitic antenna structures with small inter-element distance. We show that exploiting appropriately the beamforming capabilities of such antennas, a cost efficient MIMO transceiver architecture emerges, with low implementation complexity. Our proposal is evaluated against the corresponding conventional MIMO systems in terms of bit error rate and capacity, and the results show a satisfactory performance.

1. INTRODUCTION

It is well known that Multiple Input-Multiple Output (MIMO) architectures improve significantly the performance of wireless communication systems. Depending on the system design, the effect of multiple antennas might be twofold; In spatial multiplexing mode, the objective is the data rate maximization, by exploiting appropriately the structure of the channel matrix to obtain independent signaling paths that can be used to support independent data streams. Alternatively, in diversity mode the multiple antennas are jointly used in order to effectively mitigate the negative effects of fading, thus improving the overall system reliability. However, the benefits of such systems are obtained at the cost of remarkable implementation complexity. Indeed, in conventional MIMO systems with Uniform Linear Arrays (ULAs) at both ends, the number of required Radio-Frequency (RF) chains equal to the number of antenna elements. Thus, increasing the number of elements the hardware complexity also increases. Obviously, the power consumption is increased accordingly. Although the deployment of such systems is quite realistic at base stations, such complex architectures are prohibitive in battery powered Mobile Terminals (MTs) due to additional implementation issues such as size and energy restrictions. Thus, although the promising performance of MIMO systems necessitates their implementation to modern wireless communications, the corresponding hardware complexity hinders the wide application of such systems.

Recently, remarkable research work is drawn in order to investigate alternative MIMO architectures with reduced hardware complexity, while maintaining the total performance close to the levels of conventional MIMO approach. Indeed, antenna selection [1, 2], and antenna subarray formation [3, 4] constitute different approaches towards this aim. Such architectures, are signal processing techniques applied at the spatial domain of a typical antenna array with fixed geometry and intend to reduce the required RF chains for a given number of antenna elements. Recently, another approach with completely different treatment has appeared, labeled as beamspace MIMO [5–7]. In this case, instead of considering antenna arrays with multiple RF chains parasitic antenna structures with a single active port are considered. Such antennas are known as Electronically Steerable Parasitic Antenna Radiators (ESPAR) and are low power consumption antenna structures [8], with fast beamforming capabilities [9]. In particular, such antennas consist of a single active element which is surrounded by several parasitic (or passive) elements in linear or planar arrangement. Beamforming abilities are achieved by tuning the varactors loaded directly to the parasitic elements. Since a single active element is present, a single driving port is required, thus reducing dramatically the implementation cost and power consumption. However, the concept of spatial sampling (as in case of ULAs) cannot be considered, implying that known MIMO signal processing techniques cannot be used directly. Instead, the beamforming capabilities of such antennas allow the angular sampling of the incident field from a single physical location. Thus, the Beamspace MIMO functionality is studied at the angular or beamspace domain. In contrast to the preceeding work on this topic, we study the Beamspace approach at both communication ends. In particular, in Section 2 the beamspace system architecture is analytically presented followed by extensive performance comparisons in terms of bit error rate (BER) and ergodic capacity, in Section 3. The paper ends with the results summarized in Section 4.

2. BEAMSPACE MIMO ARCHITECTURE

In this paper, we propose the implementation of a MIMO transceiver based on a single RF front end, by mapping symbols in the beamspace domain using orthogonal radiation patterns, instead of the traditional approach of sending different symbol streams in different antenna elements. The requirement for orthogonal basis patterns is justified in Section 3.

First, let us consider a typical single user MIMO link. Following a geometrical modeling of the scattering environment, the channel matrix is given by:

$$\mathbf{H} = \sum_{i=1}^{L} b_i \mathbf{a}_R(\theta_{R,i}) \mathbf{a}_T^H(\theta_{T,i}) = \mathbf{A}_R(\hat{\theta}_R) \mathbf{H}_b \mathbf{A}_T^H(\hat{\theta}_T) \tag{1}$$

where L is the number of paths between the beamspace transmitter and receiver, $\mathbf{a}_T$, $\mathbf{a}_R$ are the transmit and receive steering vectors and $\hat{\theta}_T$, $\hat{\theta}_R$ are the direction vectors of the angles of departure (AoDs) and angles of arrival (AoAs) of all paths respectively. Moreover, $\mathbf{H}_b$ is an $(L \times L)$ diagonal matrix which contains the complex path gains denoted as b_i, $i = 1 \dots L$, while $\mathbf{A}_T(\hat{\theta}_T)$, $\mathbf{A}_R(\hat{\theta}_R)$ are the transmit and receive steering matrices respectively.

The authors in [5], show that in case of using a Beamspace transmitter and a ULA-receiver, the channel matrix becomes $\mathbf{H}' = \mathbf{A}_R(\hat{\theta}_R)\mathbf{H}_b\mathbf{B}_T$, where $\mathbf{B}_T$ is a $(M_T \times L)$ matrix each row of which contains L samples of an orthogonal pattern. Based on the analysis therein, the extension to the full Beamspace MIMO system is straightforward, and the channel matrix in this case is expressed as:

$$\mathbf{H}_{bs} = \mathbf{B}_R^H \mathbf{H}_b \mathbf{B}_T \tag{2}$$

where matrix $\mathbf{B}_R$ is defined accordingly. Thus, the beamspace input-output relationship is:

$$\mathbf{y} = \mathbf{H}_{bs}\mathbf{x} + \mathbf{n} \Leftrightarrow \mathbf{y} = \mathbf{B}_R^H \mathbf{H}_b \mathbf{B}_T \mathbf{x} + \mathbf{n} \Leftrightarrow \mathbf{y} = \mathbf{B}_R^H \mathbf{H}_b P_T^{(\mathbf{x})}\left(\hat{\theta}_T\right) + \mathbf{n} \tag{3}$$

where $P_T^{(\mathbf{x})}(\hat{\theta}_T) = \mathbf{B}_T\mathbf{x}$ defines a $(L \times 1)$ vector containing angular samples of the actual transmit radiation pattern at each time slot. Note that the samples of the transmit pattern emerge as a linear combination of the sampled basis patterns and the transmit symbol vector:

$$P_T^{(\mathbf{x})}\left(\hat{\theta}_T\right) = \left[\begin{array}{ccc} B_{T,1}\left(\hat{\theta}_T\right) & \dots & B_{T,M_T}\left(\hat{\theta}_T\right) \end{array} \right] \left[\begin{array}{c} x_1 \\ \vdots \\ x_{M_T} \end{array} \right] \tag{4}$$

Therefore, at each time slot, the beamspace transmitter constructs a radiation pattern given by $P_T^{(\mathbf{x})}(\hat{\theta}_T) = \sum_{k=1}^{M_T} x_k B_{T,k}(\theta)$, where $B_{T,k}(\theta)$, $k = 1, \dots M_T$ are the orthogonal basis patterns used at the transmitter, and $\mathbf{x} = [\begin{array}{ccc} x_1 & \dots & x_M \end{array}]^T$ is the symbol vector emerged, e.g., directly from a PSK constellation.

Regarding the receiving mode, since just a single active port is present, instead of sampling the incident waves in the spatial domain (i.e., antenna domain) as in the typical case, samples are obtained at the beamspace from the same physical location. This is achieved by altering the receive radiation pattern during a time slot among all othogonal basis patterns. A similar approach also has been suggested in [10], where a parasitic antenna operates in the receiving mode as a switch antenna with rotating radiation pattern. However, in our case instead of considering the rotated versions of the same narrow beam, the sampling of incident wave field is achieved by using the orthogonal basis patterns sequentially during each symbol period. Therefore, this operation can be viewed as oversampling the incident wave field at the receiver [10].

In order to evaluate the performance of the proposed scheme, a 3 element ESPAR antenna with inter-element distance $d = \lambda/16$ is considered. The radiation pattern of a such antenna is given by:

$$\begin{aligned} G(\theta) &= \mathbf{i}^T \mathbf{s}(\theta) = i_0 + i_1 e^{ja\cos(\theta)} + i_1 e^{-ja\cos(\theta)} \\ &= i_0 + (i_1 + i_2)\cos(a\cos(\theta)) + j(i_1 - i_2)\sin(a\cos(\theta)) \end{aligned} \tag{5}$$

where $\mathbf{i} = [\begin{array}{ccc} i_0 & i_1 & i_2 \end{array}]^T$ and $\mathbf{s}(\theta) = [\begin{array}{ccc} 1 & e^{ja\cos(\theta)} & e^{-ja\cos(\theta)} \end{array}]^T$, are the current vector and the steering vector of the ESPAR respectively, while $a = 2\pi d/\lambda$ represents the normalized distance
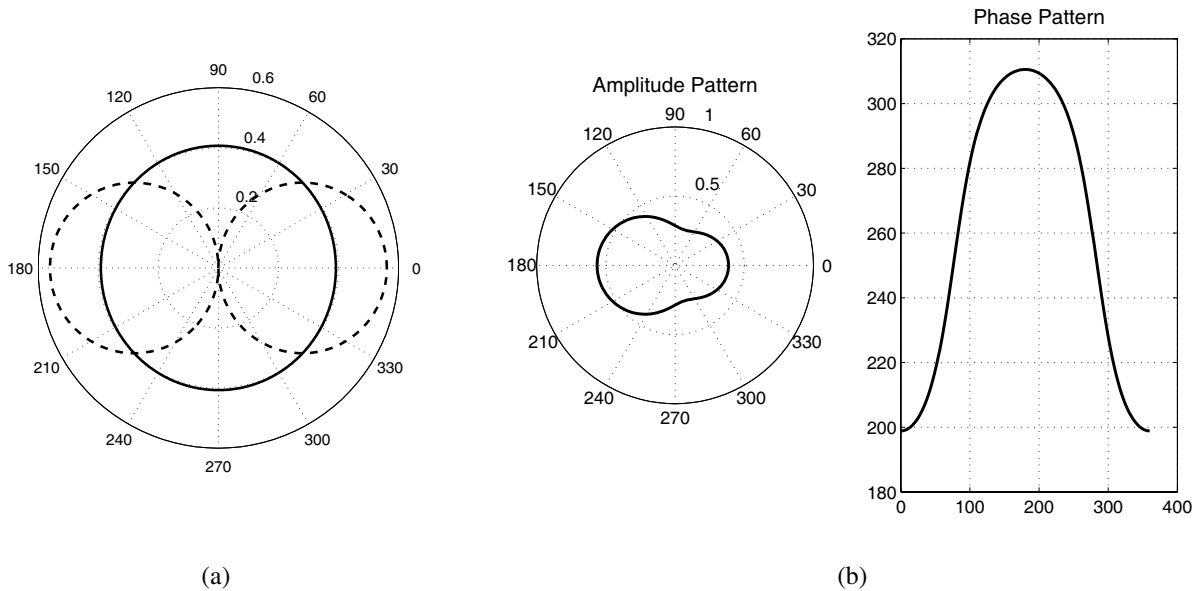
Figure 1: (a) Orthogonal basis patterns of (6), (b) example of actual pattern, for a specific symbol vector.

between elements. Thus, when both the transmitter and the receiver are equipped with a 3 element ESPAR, there are two orthogonal basis patterns:

$$B_{T,k}(\theta) = B_{R,k}(\theta) = \begin{cases} i_0 + (i_1 + i_2)\cos(a\cos(\theta)) & k = 1 \\ (i_1 - i_2)\sin(a\cos(\theta)) & k = 2 \end{cases} \tag{6}$$

where, i_0 is the current running on the active element and i_1, i_2 are the induced currents at the parasitic elements. Thus, different currents on the ESPAR elements produce different radiation patterns. Fig. 1(a) shows the two basis patterns normalized to unity power, while Fig. 1(b) shows an example radiation pattern $P_T^{(\mathbf{x})}(\widehat{\theta}_T)$ corresponding to an arbitrary chosen symbol vector $\mathbf{x} = [\ e^{j7\pi/8} \quad e^{-j\pi/2}\ ]$. It is noted that ESPAR antennas with different characteristics (i.e., number of elements, distance between elements and geometry) may produce larger number of basis patterns, thus leading to higher order beamspace MIMO systems while preserving low hardware complexity.

3. PERFORMANCE EVALUATION

In this Section, we evaluate the performance of beamspace MIMO systems against the corresponding conventional approach. In terms of bit error rate (BER), Fig. 2 shows that our approach performs equivalently to the typical MIMO architecture. We note that the curves in Fig. 2 correspond to a 16-PSK modulation scheme. However, although the beamspace approach leads to obvious advantages regarding complexity, the radiation pattern switching at the receiver within a symbol period has a negative impact. In particular, as mentioned in Section 2, the operation of using at the receiver different patterns sequentially can be viewed as oversampling the incident wave field. In this case, the SNR as seen at the receiver (henceforth called effective SNR) is decreased by the oversampling factor [10], which is equal to the number of pattern changes within a symbol period. Thus, when the received SNR in case of a conventional MIMO is $\gamma_{conv} = E/N_0$, in beamspace MIMO will be $\gamma_{bs} = E/(M_R N_0)$. Therefore, the SNR loss due to oversampling is given as:

$$\gamma_{loss}^{(\mathrm{dB})} = \gamma_{conv}^{(\mathrm{dB})} - \gamma_{bs}^{(\mathrm{dB})} = 10\log_{10}(M_R) \tag{7}$$

Thus, since in our case $M_R = 2$, beamspace MIMO receiver experience $3\,\mathrm{dB}$ SNR loss against the typical MIMO receiver.

The effect of SNR loss is clearly viewed in Fig. 3, where an indicative comparison in terms of capacity Cumulative Distribution Functions (CDFs), for two different values of γ_{conv} is shown. Moreover, it is known that transmit or receive signal correlation may affect significantly the spectral efficiency of conventional MIMO systems [11, 12]. For a given scattering environment increasing the
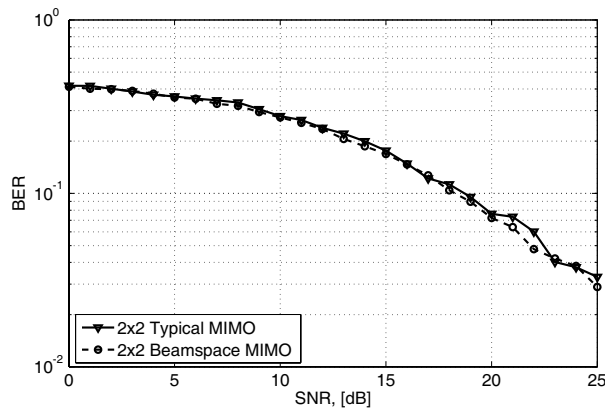
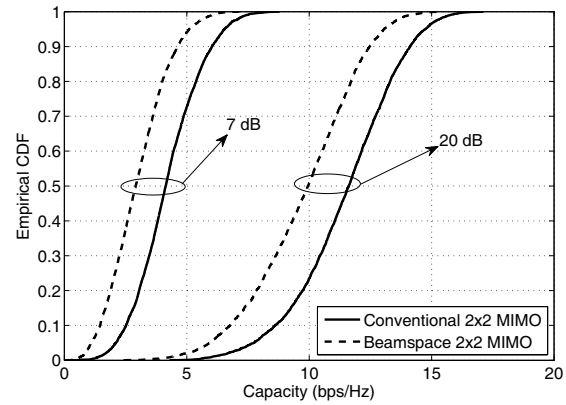Figure 2: Bit error rate comparison for 16-PSK modulation.

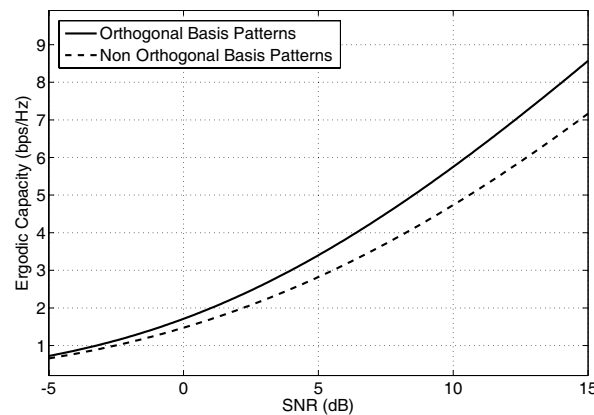Figure 3: Capacity CDF comparisons.

Figure 4: Effect of basis pattern selection on Ergodic capacity.

distance between the antenna elements at both ends the signals are decorrelated, thus the open loop capacity performance is maximized. Accordingly, in beamspace MIMO approach spectral efficiency maximization requires orthogonal basis radiation patterns. This is observed in Fig. 4, where ergodic capacity is plotted in two cases, one using the basis patterns in (6), and one using one pattern of (6), and the cardioid pattern $B(\theta) = 1 + \cos(\theta)$. Fig. 4 clearly depicts the performance degradation in the latter case. Note that the selection of the cardioid pattern as an example is reasonable, since it has been already considered in beamspace MIMO [5–7]. Also, in case of clustered channels the scattering distribution (as seen by the transmitter and the receiver) is not uniform any more. This fact affects the orthogonality of the basis patterns in (6), implying possible performance degradation in terms of spectral efficiency.

4. CONCLUSION

In this paper, an alternative MIMO transceiver architecture is proposed with simplified hardware complexity compared to the equivalent conventional MIMO systems. The performance results confirm that it is possible to exploit parasitic antenna structures to the design of efficient MIMO transceivers with a single RF chain at both communication ends. Although the proposed architecture induces an SNR loss compared to the conventional MIMO systems, this drawback is acceptable thinking the significant hardware savings.

REFERENCES

1. Molisch, A. F., M. Z. Win, Y. S. Choi, and J. H. Winters, "Capacity of MIMO systems with antenna selection," *IEEE Transactions on Wireless Communications*, Vol. 4, No. 4, 1759–1772, 2005.
2. Karamalis, P., N. Skentos, and A. Kanatas, "Selecting array configurations for MIMO systems: An evolutionary computation approach," *IEEE Transactions on Wireless Communications*, Vol. 3, No. 6, 1994–1998, 2004.

3. Theofilakos, P. and A. G. Kanatas, "Capacity performance of adaptive receive antenna sub-array formation for MIMO systems," *EURASIP Journal on Wireless Communications and Networking*, Vol. 2007, 2007.

4. Kanatas, A. G., "A receive antenna subarray formation algorithm for MIMO systems," *IEEE Communications Letters*, Vol. 11, No. 5, 396–398, 2007.

5. Kalis, A., A. G. Kanatas, and C. Papadias, "A novel approach to MIMO transmission using a single RF front end," *IEEE Journal on Selected Areas in Communications*, Vol. 26, No. 6, 972–980, 2008.

6. Kalis, A., A. G. Kanatas, and C. Papadias, "An ESPAR antenna for beamspace-MIMO systems using PSK modulation schemes," *Proceedings of IEEE International Conference on Communications*, Glasgow, UK, June 2007.

7. Barousis, V., A. G. Kanatas, A. Kalis, and C. B. Papadias, "Closed-loop beamspace MIMO systems with low hardware complexity," *Proceedings of IEEE VTC*, Barcelona, Spain, April 2009.

8. Ohira, T. and K. Gyoda, "Electronically steerable passive array radiator antennas for low-cost analog adaptive beamforming," *Proceedings of Phased Array Systems and Technology*, Dana Point, CA, USA, May 2000

9. Sun, C., A. Hirata, T. Ohira, and N. C. Karmakar, "Fast beamforming of electronically steerable parasitic array radiator antennas: Theory and experiment," *IEEE Transactions on Antennas and Propagation*, Vol. 52, No. 6, 1819–1832, 2004.

10. Bains, R. and R. R. Muller, "Using parasitic elements for implementing the rotating antenna for MIMO receivers," *IEEE Transactions on Wireless Communications*, Vol. 7, No. 11, 4522–4533, 2008.

11. Foschini, G. J. and M. J. Gans, "On limits of wireless communication in a fading environment when using multiple antennas," *Wireless Personal Communications*, Vol. 6, 311–335, 1998.

12. Telatar, I. E., "Capacity of multi-antenna Gaussian channels," *European Transactions on Telecommunications*, Vol. 10, No. 6, 585–595, 1999.

Artificial Magneto-superstrates for Gain and Efficiency Improvement of Microstrip Antenna Arrays

H. Attia, O. Siddiqui, and O. M. Ramahi

University of Waterloo, Canada

Abstract— This paper presents an engineered magneto-dielectric superstrates designed to enhance the gain and efficiency of a microstrip antenna array without any substantial increase in the antenna profile. The broadside coupled split ring resonator (SRR) inclusions are used in the design of the superstrate. Numerical full-wave simulations of a 4×1 linear microstrip antenna array working at the resonance frequency of 2.18 GHz and covered by the superstrate show a gain enhancement of about 3.5 dB and an efficiency improvement of 10%. The total height of the proposed structure, is $\lambda_0/7$ where λ_0 is the free-space operating wavelength.

1. INTRODUCTION

The magnetic metamaterials demonstrate larger than unity permeability (μ) values due to the fact that they are magnetically polarized under the influence of electromagnetic (EM) field. However, such materials do not occur naturally in the microwave regime because the inertia of their atomic system is not able to track the high frequency EM field. Another related metamaterial is the magneto-dielectric which can be polarized both electrically and magnetically when exposed to an applied EM field, so that it has both relative permeability (μ) and permittivity (ε) greater than one [1, 2]. There are many potential applications of magneto-dielectrics particularly where miniaturization of microwave components is desired. For example, magneto-dielectric materials have been utilized recently as substrates for miniaturization of microstrip antenna [3, 4], and as superstrates for gain enhancement of planar antenna [5]. In [6], High-permittivity materials have been used as superstrates for gain enhancements where a half wave-length thickness of the superstrates was required to achieve the gain-enhancement, resulting in high profile antenna systems. On the other hand, the antenna profile can be substantially reduced by using magneto-dielectric superstrates because of the simultaneously large permittivity and permeability.

In this work, a magneto-dielectric superstrate using modified split ring resonators (SRR) is designed for gain and efficiency enhancement of microstrip antenna arrays. The designed SRR-based material has effective positive values for the effective permeability and permittivity at the resonance frequency of the antenna array. The antenna system is simulated using Microwave CST Studio and the effect of superstrate on the far-field antenna parameters is investigated. In particular, a significant enhancement in gain and efficiency of the antenna is demonstrated. The proposed method is anticipated to combat some of the downsides of the microstrip array antennas such as feed network losses and gain reduction due to surface wave radiations. Other contemporary trends of gain enhancement include the use of non-magnetic dielectric [6] or electromagnetic bandgap structures (EBG) [7, 8] as superstrates. However, they all require fairly thick superstrates layers, leading to a significant increase of antenna profile. In [5], the use of magneto-dielectric materials as a gain enhancing superstrate is investigated without practical design considerations.

2. THE PROPOSED ARTIFICIAL MAGNETIC SUPERSTRATE

The SRR unit cell of the proposed artificial magneto-dielectric is shown in Fig. 1(a). The SRR inclusion consists of two parallel broken square loops printed on both sides of the host dielectric Rogers RO4350 substrate that has a thickness of 0.762 mm, a relative permittivity (ε_r) of 3.48, and a loss tangent ($\tan \delta$) of 0.004.

The SRR unit cell is analytically modeled by obtaining its effective relative permeability as [1, 2]

$$\mu_{r_{eff}} = 1 - \frac{j\omega L_{eff} S}{\Delta x \Delta z \left(R_{eff} - \frac{j}{\omega C_{eff}} + j\omega L_{eff} \right)} \tag{1}$$

where S is the surface area of the inclusion $(l_x \times l_y)$ Δx and Δz are the unit cell sizes in x and z directions as shown in Fig. 1(a). The dimensions of the designed SRR unit cell are $\Delta x = \Delta y = 8.5$ mm, $\Delta z = 2.762$ mm, $l_x = l_y = 6.5$ mm, $w = 0.3$ mm. The width of metallic strips (s) is equal
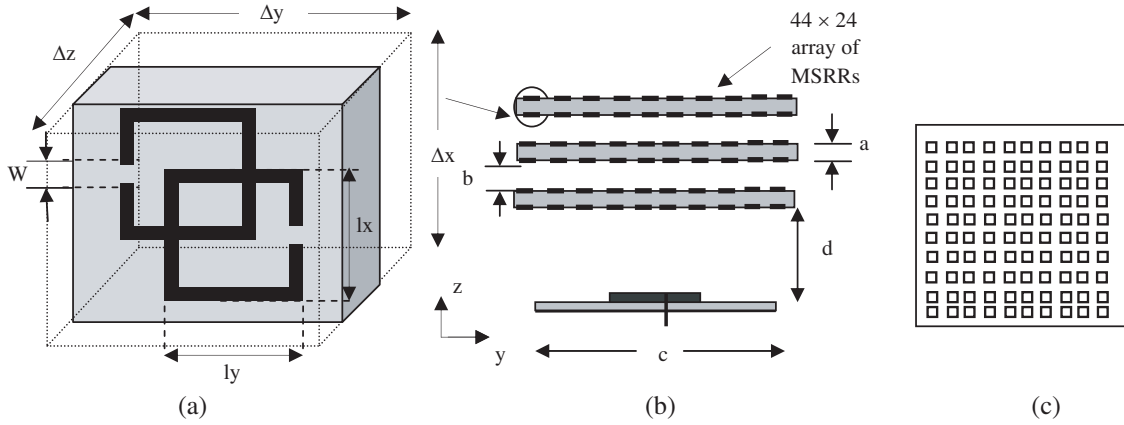
Figure 1: Geometry of a 4×1 microstrip antenna array covered by an engineered magnetic superstrate. (a) SRR unit cell. (b) Side view. (c) Top view. ($a = 0.762\,\text{mm}$, $b = 2\,\text{mm}$, $c = 210\,\text{mm}$ and $d = 12\,\text{mm}$).
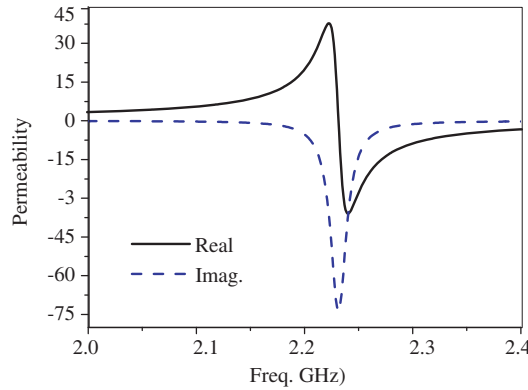

Figure 2: Analytically calculated relative permeability of the SRRs.

to $0.3\,\text{mm}$, and the metallic strips are assumed to be made of copper. Formulas for R_{eff}, C_{eff} and L_{eff} can be found in [1]. The effective relative permeability calculated from (1) is depicted in Fig. 2.

As shown in Fig. 1(c), one layer of the superstrate is constructed by arranging an 44×24 array of SRRs. The superstrates consists of three layers of the SRR arrays, aligned in the XY plane and separated from each other by $2\,\text{mm}$ air layers, as depicted in Fig. 1(b). It may be noted that only z-directed magnetic fields are coupled to the superstrates layers. Any incident magnetic field in the x or y direction will not couple to the SRR inclusion resulting in a permeability equal to that of free-space in those directions. Hence, the anisotropic permeability tensor is given by

$$\bar{\bar{\mu}} = \mu_o \begin{bmatrix} 1 & 0 & 0 \\ 0 & 1 & 0 \\ 0 & 0 & \mu_{r\_eff} \end{bmatrix} \tag{2}$$

The effective permittivity of the artificial materials arises from the capacitive gap regions of width 'w' between the SRR inclusions and also from the gap regions between the vertically stacked metallic inclusions (unit cells). The unit cell thus reacts to the incident x-and y-directed electric field to produce the capacitive effect.

The resulting x- and y-directed effective permittivity is given by [3]

$$\varepsilon_{r_{eff}} = \varepsilon_{r_{diel}} \left[1 + \frac{\Delta z l_x}{\Delta x \Delta y} \frac{K(\sqrt{1 - g^2})}{K(g)} \right], \quad g = \frac{\frac{S}{2}}{\frac{S}{2} + w}, \quad K(g) = \int_0^{\frac{\pi}{2}} \frac{d\theta}{\sqrt{1 - g^2 \sin^2 \theta}} \tag{3}$$

However, in case of z-directed electric field, the metamaterials superstrate will experience an effective permittivity equal to that of its host dielectric as the electric field would be perpendicular to

the plane of the unit cell. Thus, the permittivity matrix of the magneto-dielectric is given by

$$\bar{\bar{\varepsilon}} = \varepsilon_o \begin{bmatrix} \varepsilon_{r\_eff} & 0 & 0 \\ 0 & \varepsilon_{r\_eff} & 0 \\ 0 & 0 & \varepsilon_{r\_diel} \end{bmatrix} \tag{4}$$

3. THE ANTENNA SYSTEM SIMULATIONS

The 4×1 antenna array used to demonstrate the gain and efficiency enhancement is shown in Fig. 3(a). The antenna elements are printed on the substrate that is identical to the one mentioned in the previous section. The separation between adjacent antenna elements is optimized for obtaining the highest gain. Each antenna is designed to operate at a center frequency of 2.18 GHz which lies in the UMTS band. The feeding network provides a zero progressive phase to the antenna elements to obtain broadside radiation. At the operating frequency, the ε_{r_eff} and μ_{r_eff} are given respectively by 5.62 and 15. All simulations are performed using the full-wave electromagnetic simulation tool CST taking into account the actual structure of the SRR based superstrate.

First, in order to show the coupling between the magnetic field and the SRR unit cell, the distribution of the magnetic field due to the antenna array system when the superstrate is removed is plotted in Fig. 3(b). As shown in the figure, the dominant component of the magnetic field vector lies in the z direction. This confirms that the superstrate with permeability tensor given in (2) is indeed suitable for the microwave antenna array considered in this example.

Using the CST simulation package, the optimized distance between the patch antenna and superstrate is determined by parametric analysis to be 12 mm. When the gain is optimized, the resulting overall antenna profile is only $\lambda_o/7$ (where λ_o is the free-space wavelength at the resonance frequency). As shown in the gain plot given in Fig. 3(c), the gain in the broadside direction is improved by about 3.5 dB at the antenna resonance. The return loss plot, also depicted in Fig. 3(c), shows that the antenna array is matched, before and after the application of the superstrates.

A slight change in the resonant frequency and the antenna bandwidth is observed because of the change in the near field properties of the antenna when the superstrates is added. To further illustrate the effect of superstrate on the antenna gain, a comparison of the far-field radiation patterns is provided in Fig. 4(a). The overall pattern shape before and after the addition of superstrates are identical showing that the principle E-plane of the antenna array is not disturbed. Finally, Fig. 4(b) provides the efficiency of the antenna before and after the addition of the superstrates.
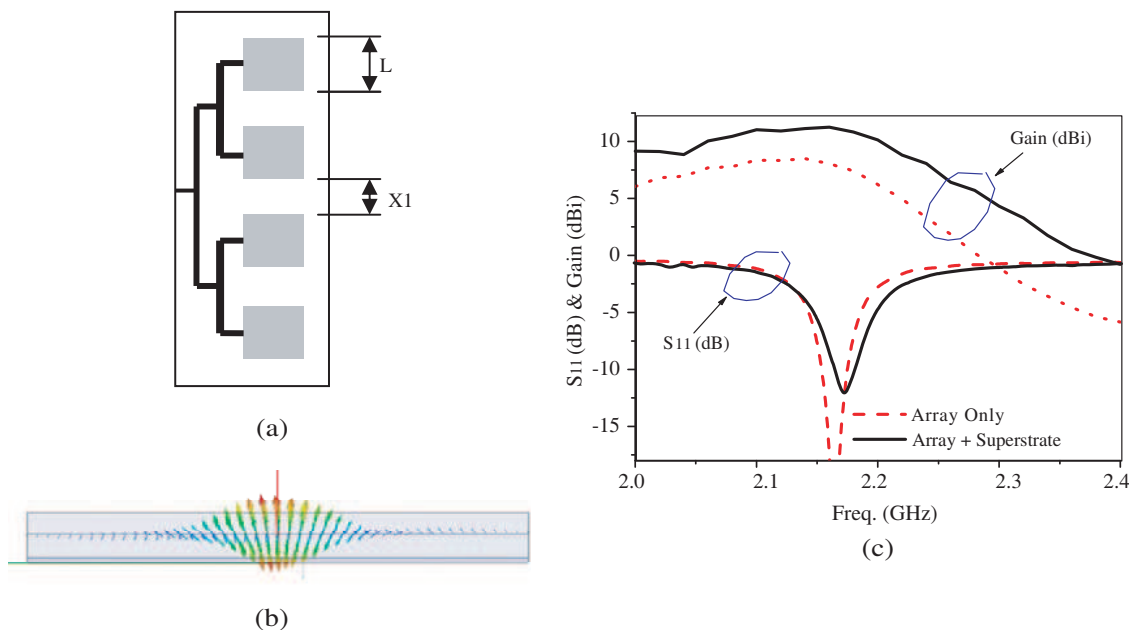

Figure 3: (a) Top view of a conventional 4×1 microstrip antenna array with $L = 36$ mm, and $X_1 = 24.5$ mm. (b) A snapshot of the magnetic field vectors plotted on a surface at the superstrate location when the superstrate is removed. (c) The return loss and gain of the microstrip antenna array before and after using the artificial magnetic superstrate.
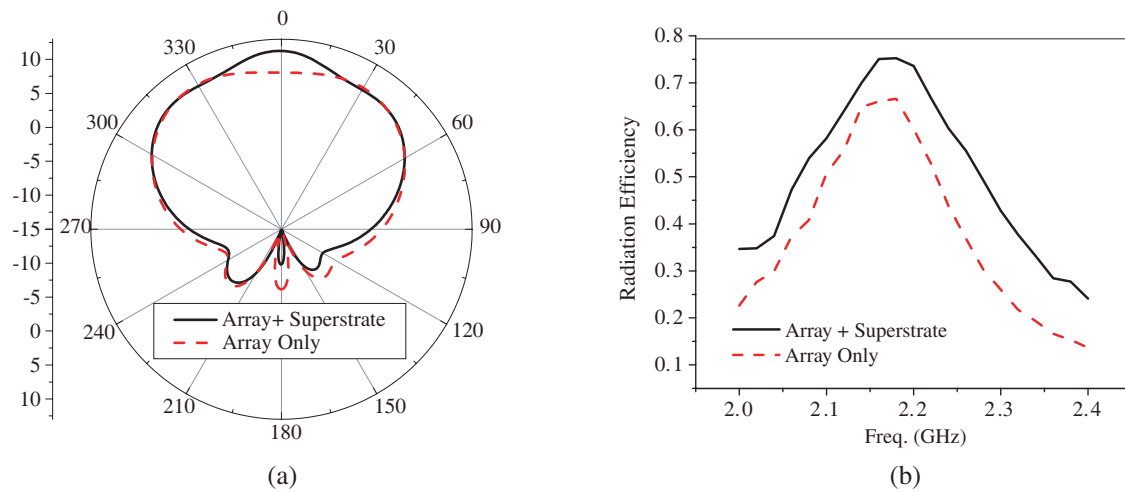
(a)   (b)

Figure 4: (a) The E-plane radiation pattern of the microstrip antenna array before and after using the superstrate. (b) The radiation efficiency before and after using the artificial magnetic superstrate.

A 10% increase in efficiency shows that the losses due to surface waves are somehow reduced. This can be understood by considering the inherent anisotropy of the band gap structure.

4. CONCLUSION

A magneto-dielectric superstrate constructed by split-ring-resonators is used with a 4×1 linear microstrip array to enhance its far-field properties. The distance between the patches and the superstrates is optimized to achieve a gain enhancement of about 3.5 dB. The antenna properties such as radiation patterns and the return loss characteristics are not significantly affected by the superstrates. However, there is an improvement in efficiency of about 10%. An overall profile of $\lambda_o/7$ resulted when the superstrates is added, which is appreciably better than the other techniques of gain enhancements such as EBG based superstrates.

REFERENCES

1. Maslovski, S. I., P. M. T. Ikonen, I. Kolmakov, S. A. Tretyakov, and M. Kaunisto, "Artificial magnetic materials based on the new magnetic particle: Metasolenoid," *Progress In Electromagnetics Research*, PIER 54, 61–81, 2005.

2. Yousefi, L. and O. M. Ramhi, "New artificial magnetic materials based on fractal hilbert curves," *2007 IEEE International Workshop on Antenna Technology: Small and Smart Antennas and Novel Metamaterials*, Cambridge, UK, Mar. 2007.

3. Buell, K., H. Mosallaei, and K. Sarabandi, "A substrate for small patch antennas providing tunable miniaturization factors," *IEEE Trans. Microwave Theory Tech.*, Vol. 54, No. 1, 135–146, Jan. 2006.

4. Mookiah, P. and K. R. Dandekar, "Metamaterial-substrate antenna array for MIMO communication system," *IEEE Trans. Antennas Propagation*, Vol. 57, No. 10, 3283–3292, Oct. 2009.

5. Foroozesh, A. and L. Shafai, "Size reduction of a microstrip antenna with dielectric superstrate using meta-materials: Artificial magnetic conductors versus magneto-dielectrics," *Proceeding of IEEE Antennas and Propagation Society International Symposium*, 11–14, Jul. 2006.

6. Jackson, D. R. and N. G. Alexopoulos, "Gain enhancement methods for printed circuit antennas," *IEEE Trans. Antennas Propagation*, Vol. 33, No. 9, 976–987, Sep. 1985.

7. Attia, H. and O. M. Ramahi, "EBG superstrate for gain and bandwidth enhancement of microstrip array antennas," *Proceeding of IEEE Antennas and Propag. Society International Symposium*, 1–4, Jul. 2008.

8. Lee, Y. J., J. Yeo, R. Mittra, and W. S. Park, "Application of electromagnetic bandgap (EBG) superstrates with controllable defects for a class of patch antennas as spatial angular filters," *IEEE Trans. Antennas Propagation*, Vol. 53, No. 1, 224–235, Jan. 2005.

Rectangular Ring Antenna for On-body Communication System

N. Zainudin and M. R. Kamarudin

Wireless Communication Centre (WCC), Faculty of Electrical Engineering
Universiti Teknologi Malaysia, Skudai Johor, Malaysia

Abstract— The demand of smaller and compact antennas in modern mobile and wireless communication system has been increasing. Because of low cost and process simplicity, printed monopole antennas are popular candidates for these applications and applicable in body centric communications. A simple and compact microstrip-fed printed monopole antenna is proposed in this design. The antenna is composed of a rectangular ring for operating frequency at 2.45 GHz. The configuration has rectangular base with rectangular slot cut inside the patch resulting the rectangular ring. The dimension of the patch is 12 mm × 26 mm with ring width size of 1 mm along the patch. The size of partial ground plane is 20 mm × 9 mm while the dimension of substrate used is 20 mm × 40 mm. The antenna are fabricated of FR4 substrate with thickness of 1.6 mm, dielectric permittivity, is 4.7 and tangent loss is 0.019. The designed antenna had bees successfully simulated using CST Microwave Studio. It was found that the antenna operates well at 2.45 GHz. Return Loss measurement had been done using network analyzer and both simulated and measured results are in good agreement. The antenna covers bandwidth from 2.35 GHz to 2.8 GHz which is 17.54%.

1. INTRODUCTION

Modern wireless systems are placing greater demands on antenna designs. Due to its increasing applications in the personal communications systems, body-centric wireless communication has become major field of interest for researchers [1]. The antennas of such systems are also required for compact and small size [2–4]. In various research, printed monopole antenna have been received much attention due to their wideband matching characteristic, omnidirectional radiation patterns, high radiation efficiency and compact size [5–7].

The ever increasing use of wireless devices in on-body communications drives research to establish more reliable and efficient link between the devices mounted on the body. Thus, wearable devices should be designed in term of functionality and the human comfort [8].

In this paper, a rectangular ring antenna fed by 50 ohm microstrip feed line was proposed for on-body communications. This antenna has many advantages, such as small size, low-profile, simple structure and easy to fabricate. The design of the antenna was performed using the CST Studio software. The following sections describe the configuration, design and performance of the proposed antenna.
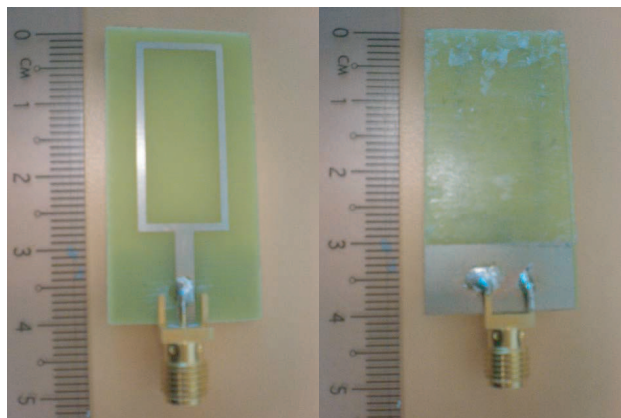

Figure 1: Antenna prototype front view and back view.

2. ANTENNA DESIGN AND GEOMETRY

Figure 2 illustrates the geometry of the proposed printed antenna with a rectangular radiator and a finite-size system ground plane. The overall size of the antenna is 20 mm × 40 mm. The radiator and

ground plane are etched on the opposite sides of a FR4 board ($\varepsilon_r = 4.7$ and 1.6 mm in thickness). The antenna consists of rectangular radiator (12 mm × 26 mm) and a rectangular notch cut from the radiator. The radiator is fed by a microstrip line of 2.4 mm width and 12 mm length located at the center with a 3 mm feed gap. The ground plane has a vertical length of 9 mm.

3. RESULTS AND DISCUSSION

The simulated antenna performance is analyze using CST Microwave Studio Suite and measured using spectrum analyzer. To increase the impedance matching bandwidth, an overall adjustment of the geometrical parameters is performed for the 2.45 GHz band respectively. Both the feed gap and the position of feed point can be used to adjust the impedance matching. The length of the ground plane was optimized to achieve a miniaturized design with good impedance matching. In order to further reduce the overall size of the printed antenna, a rectangular slot is notched onto the radiator. All the measured results show satisfactory performance and good agreement with the simulated results. From the simulations and measurements, the optimized dimensions are: $L_{sub} = 20$ mm, $W_{sub} = 40$ mm, $L = 12$ mm, $W = 26$ mm, $L_g = 9$ mm, $L_{feed} = 12$ mm, $g = 3$ mm and $d = 2.4$ mm, $h = 1.6$ mm.

Figure 3 shows the simulated and measured frequency response of return loss at 2.45 GHz for the proposed antenna. As can be seen from the measured result, the antenna is excited at 2.45 GHz with a -10 dB impedance bandwidth of 450 MHz (2.35–2.8 GHz). This indicates that the proposed
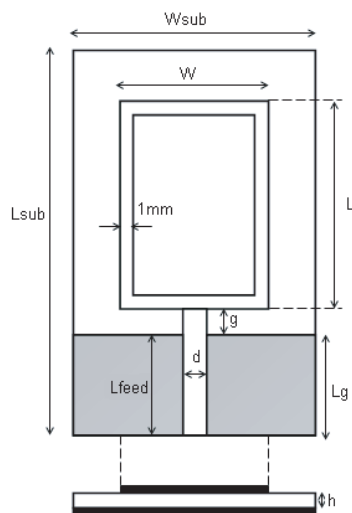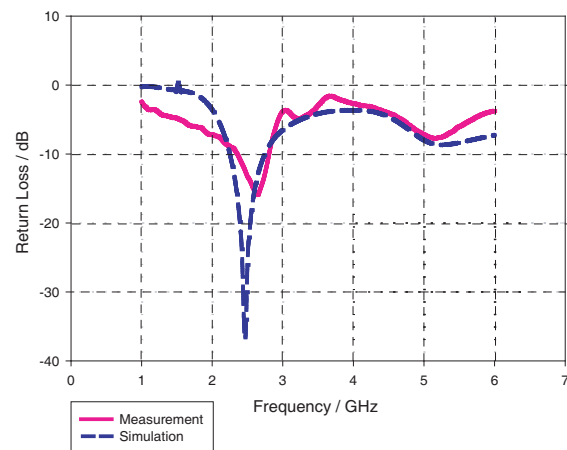

Figure 2: Antenna configuration.

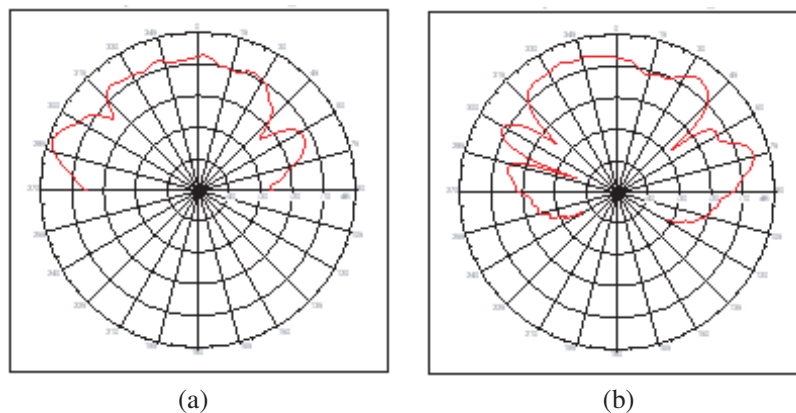Figure 3: Simulated and measured return loss for rectangular ring antenna.

(a)   (b)

Figure 4: Measured radiation pattern for rectangular ring antenna. (a) H-plane at 2.45 GHz, (b) E-plane at 2.45 GHz.

antenna can operate at 2.45 GHz unlicensed ISM band and applicable for wireless communication and on-body communication bands. Figure 4 shows the measuerd far-field radiation patterns for E-plane and H-plane of the proposed antenna at the operation band. The simulated results show that the radiation patterns of the antenna are bidirectional in the E-plane and omni directional in the H-plane.

4. CONCLUSION

A rectangular monopole antenna fed by 50 ohm microstrip line is presented in this paper. With an overall adjustment of the geometrical parameters, the proposed antenna was successfully designed to operate at 2.45 GHz frequency band for on-body communications and have a corresponding bandwidth of 17.54% respectively. The final measured result shows satisfactory performance and good agreement with the simulated result. The antenna has small physical size and can be easily integrated in wearable devices.

REFERENCES

1. Hall, P. S. and Y. Hao, *Antennas and Propogation for Body Centric Wireless Communications*, Artech House, Boston, London, 2006.
2. Gemperle, F., C. Kasabach, J. Stivoric, M. Bauer, and R. Martin, "Design for wearability," *Proceedings of the 2nd IEEE International Symposium on Wearable Computers*, 116–122, Oct. 19–20, 1998.
3. Hall, P. S., M. Ricci, and T. M. Hee, "Characterization of on-body communication channels," *Proceedings of 3rd International Conference on Microwave and Millimeter Wave Technology*, 770–772, Aug. 17–19, 2002.
4. Kamarudin, M. R., Y. I. Nechayev, and P. S. Hall, "Antennas for on-body communication systems," *IEEE International Workshop on Antenna Technology: Small Antennas and Novel Metamaterials*, 17–20, March 7–9, 2005.
5. Pan, C.-Y., T.-S. Horng, W.-S. Chen, and C.-H. Huang, "Dual wideband printed monopole antenna for WLAN/Wimax applications," *IEEE Antennas and Wireless Propagation Letters*, Vol. 6, 149–151, 2007.
6. Kim, T. H. and D. C. Park, "CPW-fed compact monopole antenna for dual-band WLAN applications," *Electron. Lett.,* Vol. 41, No. 6, 292–293, Mar. 2005.
7. Kuo, Y. L. and K. L. Wong, "Printed double-T monopole antenna for 2.4/5.2 GHz dual band WLAN operations," *IEEE Trans. Antennas Propag.*, Vol. 51, No. 9, 2187–2192, Sep. 2003.
8. Bodine, K. and F. Gemperle, "Effects of functionality on perceived comfort of wearables," *Proceedings of the 7th IEEE International Symposium on Wearable Computers*, 57–60, Oct. 21–23, 2003.

A New Fractal Antenna for Super Wideband Applications

Abolfazl Azari

Young Researchers Club, Isalmic Azad University, Gonabad Branch, Iran

Abstract— Modern communication systems require small size and wideband antennas. Fractal geometries have been used to fabricate multi-band and broad-band antennas. In addition, fractal geometries can be miniaturized the size of antennas.

In this work, I have investigated a new fractal antenna with multi-band and broad-band properties. The proposed design is a loaded the 2nd iteration of a new fractal geometry to a square loop antenna. The simulation is performed via SuperNEC electromagnetic simulator software. The simulation results show that the proposed antenna is applicable in 1–30 GHz frequency range. Radiation patterns are also studied.

1. INTRODUCTION

Antenna plays such an important role in communication systems and one of the main components of ultra wideband (UWB) communication systems is an UWB antenna. UWB communication systems require smaller antennas with more bandwidth, thus the design, simulation and fabrication of these antennas are very important. This is the cause of widespread research on UWB antennas in recent years. One of the good solution is using fractal geometry to design of UWB antennas. Applying fractals to the antenna elements allows for smaller size, multi-band and broad-band properties [1–4].

Fractals have self-similar shapes and can be subdivided in parts such that each part is a reduced size copy of the whole. Self-similarity of fractals causes multi-band and broad-band properties and their complicated shapes provide design of antennas with smaller size. Fractals have convoluted and jagged shapes with many corners that these discontinuities increase bandwidth and the effective radiation of antennas. Fractals can be placed long electrical length in to a small area using their ability of space-filling [5–9].

Fractals describe by one algorithm or repetitive function, iterating several times that integral dimension does not define for them.

Several wire antenna configurations based on fractal geometries have been investigated including Koch, Minkowski, Hilbert, and fractal tree antennas in recent years. These antennas have been simulated using the moment method, as well as fabricated and measured.

In this paper, a new fractal geometry is presented. By applying this fractal generator to square loop antenna elements, I have achieved a super wideband antenna.

The moment method based electromagnetic simulator SuperNEC has been used for the design and simulation of the proposed antenna. According to the results this new fractal antenna is applicable in 1 GHz–30 GHz. Also, the radiation patterns are studied in multi frequencies.

2. ANTENNA SPECIFICATIONS

The geometric construction of this new fractal curve starts with a straight line, called the initiator, which is shown in Figure 1 ($n = 0$). This is partitioned in to four equal parts, and the two centric segments are replaced with three others of the same length which are formed like a trapezoid with the indentation angle $\theta = 60°$. This is the first iterated version of the new fractal geometry and is called the generator, which is shown in Figure 1 ($n = 1$). The process is repeated in the generation of the 2nd iteration, which is shown in Figure 1 ($n = 2$).

Each segment in the first iteration (generator) is 1/4 the length of the initiator. There are five such segments. Thus for the nth iteration, the length of the curve is $(5/4)^n$.

An iterative function system (IFS) can be used to define the generator. The transformations to obtain the segments of the generator are:

$$W_1 = \begin{bmatrix} \frac{1}{4} & 0 & 0 \\ 0 & \frac{1}{4} & 0 \\ 0 & 0 & 1 \end{bmatrix} \quad W_2 = \begin{bmatrix} \frac{1}{4}\cos 60° & -\frac{1}{4}\sin 60° & \frac{1}{4} \\ \frac{1}{4}\sin 60° & \frac{1}{4}\cos 60° & 0 \\ 0 & 0 & 1 \end{bmatrix} \quad W_3 = \begin{bmatrix} \frac{1}{4} & 0 & \frac{3}{8} \\ 0 & \frac{1}{4} & \frac{1}{4}\sin 60° \\ 0 & 0 & 1 \end{bmatrix}$$

$$W_4 = \begin{bmatrix} \frac{1}{4}\cos 60° & \frac{1}{4}\sin 60° & \frac{5}{8} \\ -\frac{1}{4}\sin 60° & \frac{1}{4}\cos 60° & \frac{1}{4}\sin 60° \\ 0 & 0 & 1 \end{bmatrix} \quad W_5 = \begin{bmatrix} \frac{1}{4} & 0 & \frac{3}{4} \\ 0 & \frac{1}{4} & 0 \\ 0 & 0 & 1 \end{bmatrix} \tag{1}$$

The generator is then obtained as:

$$W(A) = W_1(A) \cup W_2(A) \cup W_3(A) \cup W_4(A) \cup W_5(A) \tag{2}$$

This process can be repeated for higher iterations of this fractal geometry. Also, the similarity dimension of the geometry can be calculated as:

$$D = \frac{\log 5}{\log 4} = 1.16096 \tag{3}$$

The proposed design is based on a loaded the 2nd iteration of the new generator to a square loop antenna. If the length of each side at square is assumed to be "X", with applying the 2nd iteration of this generator, the length will be $X \times (5/4)^2$.

In this paper, I have supposed the length of each side at square loop is 8 cm and 2 mm in diameter. The feed location is placed at the corner.

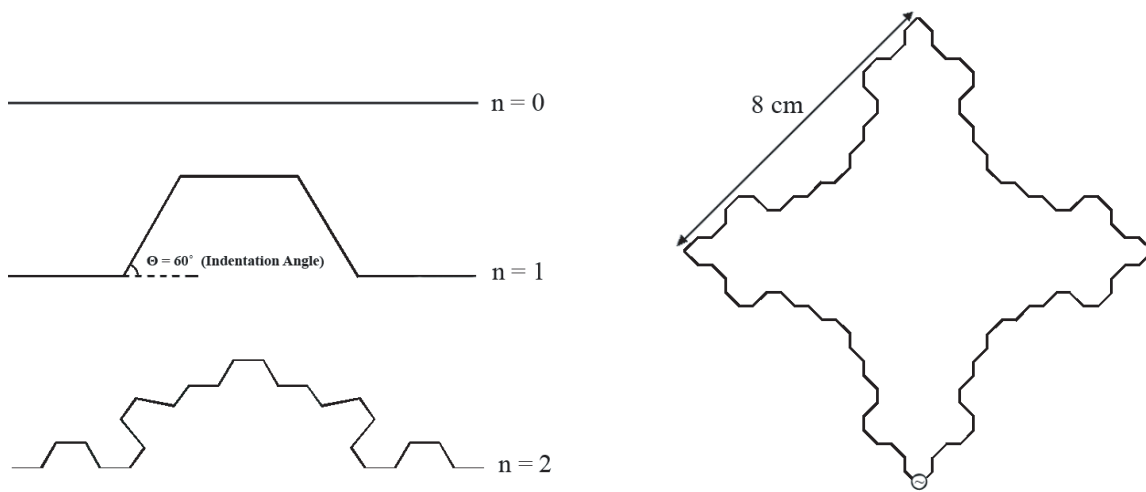The structure of this fractal antenna is shown in Figure 2.

Figure 1: Iterations of the proposed fractal geometry.

Figure 2: Antenna structure.

Simulation Results: The MOM (method of moments) is a very powerful technique which can be applied to the analysis of three dimensional structures. MOM is used for simulation of this antenna based on the SuperNEC electromagnetic simulator software. One starts with defining the antenna structure for software. The wire conductivity of all conductors is assumed to be 5.7E7. The voltage source is 1 volt and the frequency range is from 1 GHz–35 GHz.

Figure 3 shows the simulated VSWR (voltage standing wave ratio) in entire bandwidth.

According to the simulated VSWR, this super wideband antenna is applied between frequencies 1 GHz–30 GHz and approximately can be matched with a 50 Ω coaxial cable.

Also, Figures 4 and 5 present real and imaginary parts of the input impedance.
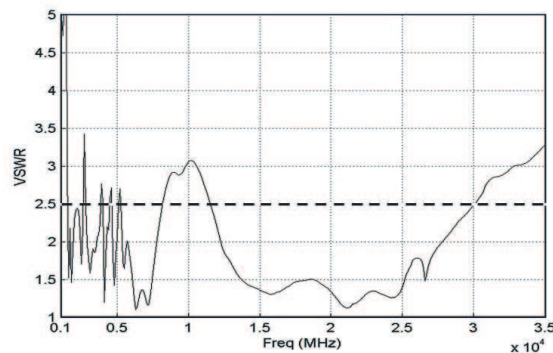

Figure 3: VSWR for the proposed fractal antenna.

To study the radiation pattern, Figure 6 shows radiation patterns for five frequencies including 1 GHz, 10 GHz, 20 GHz, 30 GHz, and 35 GHz for the xy, xz, and yz planes.
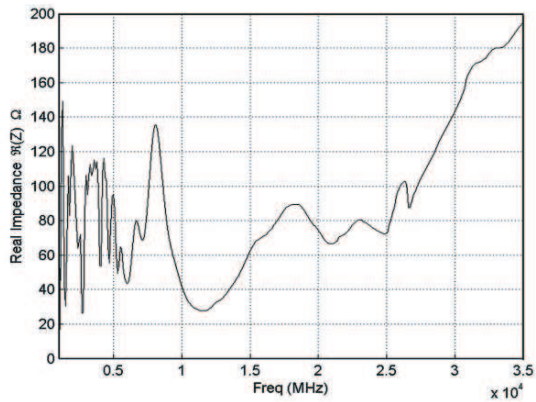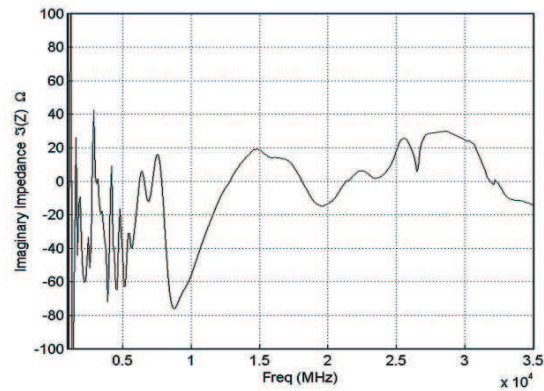

Figure 4: Real part of the input impedance.

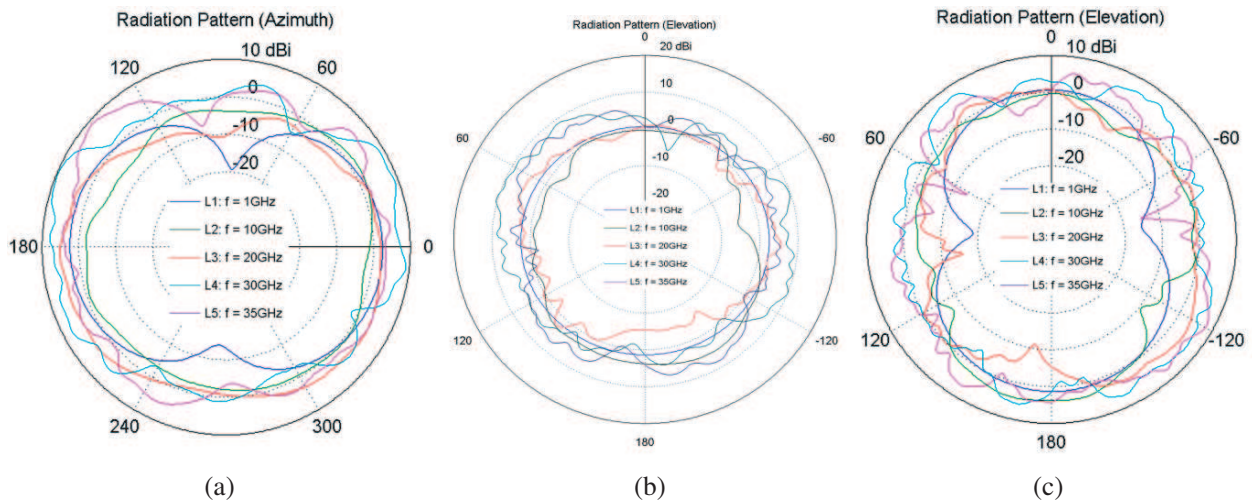Figure 5: Imaginary part of the input impedance.

(a)   (b)   (c)

Figure 6: (a) Radiation pattern (xy plane). (b) Radiation pattern (xz plane). (c) Radiation pattern (yz plane).

3. CONCLUSION

The concepts of fractals can be applied to the design of ultra wideband antennas. Applying fractals to antennas allows for miniaturization of antennas with multi-band and broad-band properties.

The proposed design is a loaded 2nd iteration of a new fractal geometry to a square loop antenna. The proposed structure has a dimensions of $8 \times 8\,\text{cm}^2$.

The simulated results conducted by the SuperNEC electromagnetic simulator. Due to the simulation results, the proposed design is a super wideband antenna which is applicable for frequencies between 1 GHz–30 GHz.

This super wideband antenna is simple to design and easy to fabricate.

REFERENCES

1. Gianvittorio, J. P., "Fractals, MEMS, and FSS electromagnetic devices miniaturization and multiple resonances," Dissertation, University of California, Los Angeles, 2003.
2. Werner, D. H. and S. Ganguly, "An overview of fractal antenna engineering research," *IEEE Antennas and Propagation Magazine*, Vol. 45, 38–57, Feb. 2003.
3. Vinoy, K. J., "Fractal shaped antenna elements for wide- and multi-band wireless applications," Thesis, Pennsylvania, Aug. 2002.

4. Gianvittorio, J. P. and Y. R. Samii, "Fractal antennas: A novel antenna miniaturization technique and applications," *IEEE Antennas and Propagation Magazine*, Vol. 44, No. 1, Feb. 2002.

5. Werner, D. H. and R. Mittra, *Frontiers in Electromagnetics*, IEEE Press, New York, 2000.

6. Puente, C., J. Romeu, R. Pous, J. Ramis, and A. Hijazo, "Small but long koch fractal monopole," *Electronics Letters*, 1998.

7. Cohen, N., " Fractal antenna application in wireless telecommunications," *Proceedings of Electronics Industries Forum of New England*, 43–49, 1997.

8. Gouyet, J., *Physics and Fractal Structures*, Springer, New York, 1996.

9. Falconer, K. J., *Fractal Geometry: Mathematical Foundations and Applications*, John Wiley & Sons, New York, 1990.

10. Azari, A. and J. Rowhani, "Ultra wideband fractal microstrip antenna design," *Progress In Electromagnetics Research C*, Vol. 2, 7–12, 2008.

11. Azari, A., "Super wideband fractal antenna design," *IEEE MAPE*, Beijing, China, 2009.

12. Azari, A., "A new fractal monopole antenna for super wideband applications," *IEEE MICC*, Kuala lumpur, Malaysia, 2009.

13. Azari, A. and J. Rowhani, "Ultra wideband fractal antenna design," *IASTED ARP*, Maryland, USA, 2008.

Koch Fractal Antenna for UWB Applications

Javad Rohani[1] and Abolfazl Azari[2]

[1]Islamic Azad University, Gonabad Branch, Iran
[2]Young Researchers Club, Islamic Azad University, Gonabad Branch, Iran

Abstract— Fractals have very unique properties, Therefore in recent years, antenna designers use fractal geometry in ultra wideband antennas designing.

In this paper, we have achieved an ultra wideband antenna by applying a Koch fractal geometry to a wire square loop antenna. Modelling and simulation is performed via SuperNEC electromagnetic simulator. Also, optimization is performed via GAO (genetic algorithm optimiser). This antenna is easy to be fabricated and has successfully demonstrated multi-band and broad-band characteristics. Results of simulations show that the proposed antenna has very good performance in bandwidth and Radiation pattern.

1. INTRODUCTION

Communication systems require antennas with more bandwidth and smaller dimensions compared to conventional antennas. Fractal geometry is a very good solution to fabricate these antennas. This causes widespread researches about fractal antennas recently [1].

Fractals create from self-similar elements, which are iterated in different directions and their general shape does not change by increasing iterations. Self similarity of fractals causes wideband and multi-band properties [2, 3].

fractals are highly complicated shapes and having many corners, that these discontinuities increase bandwidth and effective radiation of antennas. In design of fractal antennas, using their ability of space filling can be placed long electrical lengths in to small areas [4, 5].

The Koch fractal curve is one of the most well-known fractal shapes. The Koch curve is generated by replacing the middle third of each segment with two sides of an equilateral triangle. The resulting curve is comprised of four segments of equal length.

In this paper, an UWB antenna is proposed based on a loaded 2nd iteration Koch fractal geometry. In addition, genetic algorithm is implemented to optimize the length of antenna for maximum bandwidth.
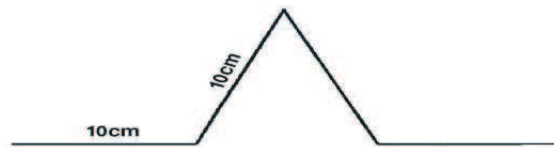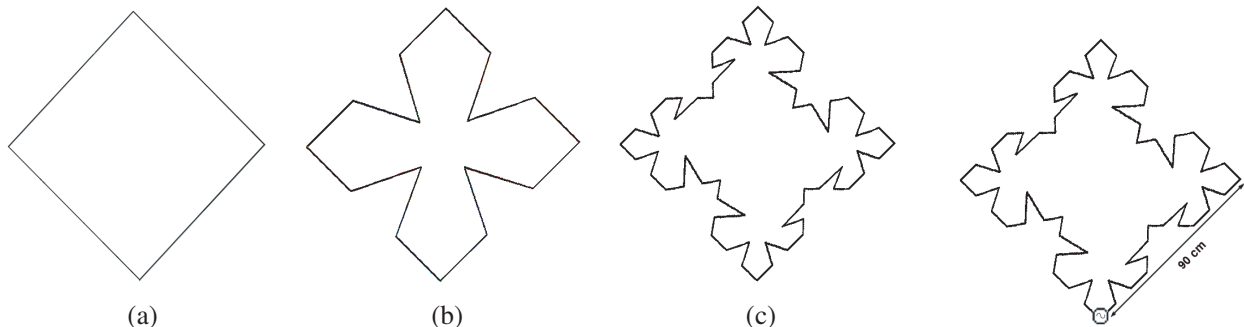

Figure 1: Fractal generator.

(a)   (b)   (c)

Figure 2: (a) Iteration 0. (b) Iteration 1. (c) Iteration 2.

Figure 3: Antenna structure.

2. ANTENNA DESIGN

This fractal antenna is an iterative model to a normal square loop with a generator of the shape shown in Fig. 1.

Figure 2(a) shows a normal wire square loop that the length of each side is 90 cm and a wire diameter of 2 mm. By replacing each straight wire with the proposed generator shape, we get a new shape as shown in Fig. 2(b), the second iteration is shown in Fig. 2(c).

Results show, increasing iterations do not have more effects on antenna parameters, thus we have supposed second iteration. The feeding position is placed according to Fig. 3.

Simulation Results: The MOM (method of moment) is used for simulation this antenna with SuperNec electromagnetic simulator software. First we define the fractal geometry for software, then we specify the location of feeding. A voltage source is 1 volt and a frequency rang is 10 MHz to 10 GHz.

In addition, GAO (genetic algorithm optimiser) is applied to optimize the length of antenna for maximum bandwidth.

Figures 4 and 5 show S_{11} (return loss) and VSWR (voltage standing wave ratio).

According to Figs. 4 and 5, we conclude that it is an ultra wideband antenna and it is operational in frequencies between 100 MHz to 10 GHz because in these frequencies approximately $S_{11} < -10$ dB or VSWR < 2.

Figure 6 shows the maximum gain versus frequency.

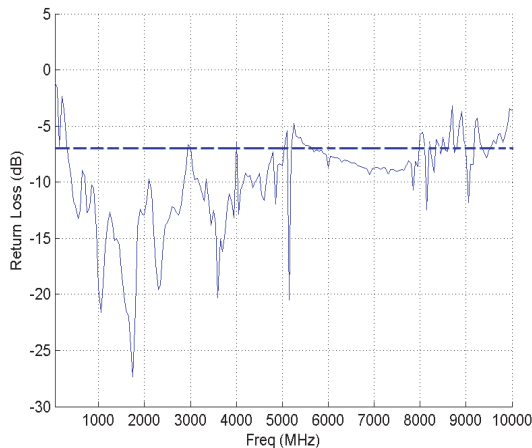To study radiation pattern, Fig. 7 depicts the radiation pattern in 1 GHz, 6 GHz and 10 GHz frequencies.

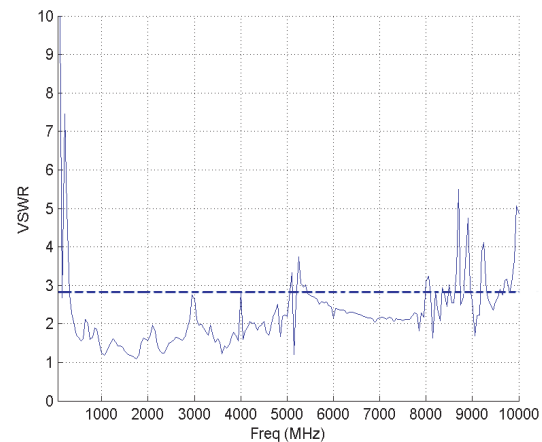
Figure 4: S_{11} (return loss).
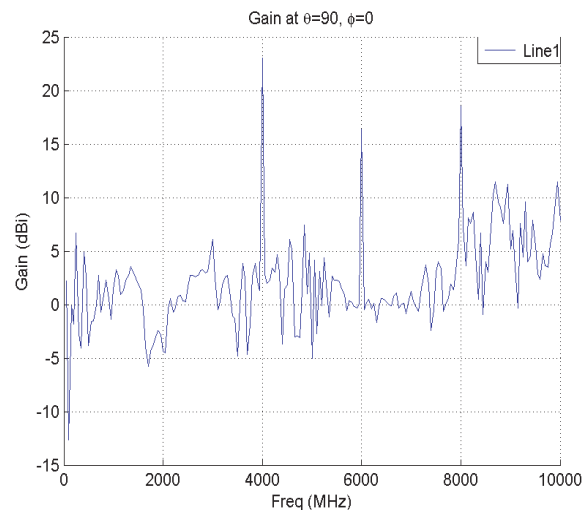

Figure 5: VSWR (voltage standing wave ratio).

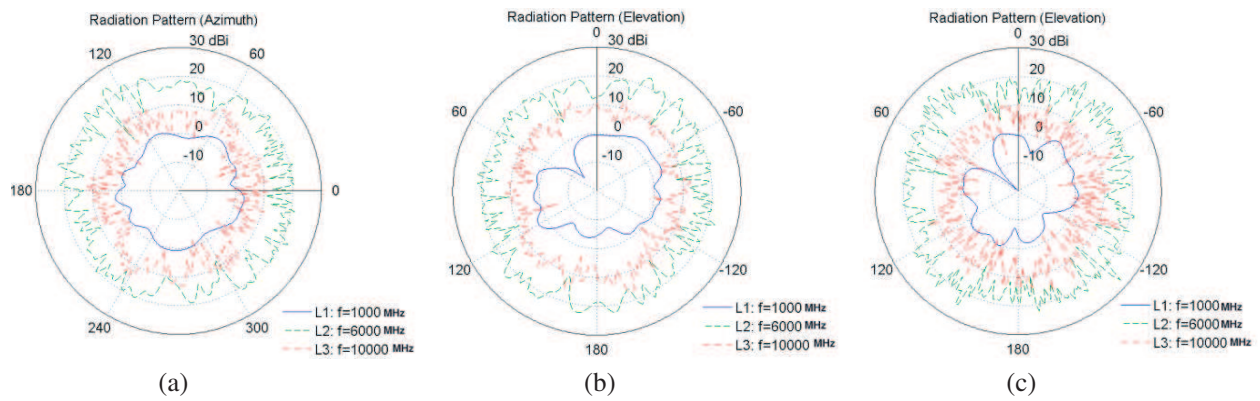Figure 6: Maximum gain versus frequency.

Figure 7: (a) Radiation pattern (xy plane). (b) Radiation pattern (xz plane). (c) Radiation pattern (yz plane).

3. CONCLUSION

Using fractal geometry can result in achieving an ultra wideband antenna. The proposed design is a loaded 2nd iteration of Koch fractal antenna and optimize it's length to achieve maximum bandwidth with GAO. Wideband and multi-band characteristics of the proposed antenna and significant gain are also observed.

REFERENCES

1. Azari, A. and J. Rowhani, "Ultra wideband fractal microstrip antenna design," *Progress In Electromagnetics Research C*, Vol. 2, 7–12, 2008.
2. Cohen, N., "Fractal antenna options for wideband and beyond wireless," Calgary, 2003.
3. Cohen, N., "Fractal antenna application in wireless telecommunications," 1997.
4. Werner, D. H. and R. Mittra, *Frontiers in Electromagnetics*, IEEE Press, 2000.
5. Gouyet, J., *Physics and Fractal Structures*, Springer, New York, 1996.
6. Makarov, S. N., *Antenna and EM Modelling with Matlab*, John Wiley and Sons, Inc., New York, 2002.
7. Mandelbrot, B. B., *The Fractal Geometry of Nature*, Freeman, San Francisco, CA, 1983.
8. Azari, A. and J. Rowhani, "Ultra wideband fractal antenna design," *IASTED ARP*, Maryland, USA, 2008.
9. Azari, A., "Super wideband fractal antenna design," *IEEE MAPE*, Beijing, China, 2009.
10. Azari, A., "A new fractal monopole antenna for super wideband applications," *IEEE MICC*, Kuala Lumpur, Malaysia, 2009.
11. Gianvittorio, J. P., "Fractals, MEMS, and FSS electromagnetic devices: Miniaturization and multiple resonances," Dissertation, University of California, Los Angeles, 2003.

Miniaturized RF MEMS Switch Matrices

K. Y. Chan[1], R. R. Mansour[2], and R. Ramer[1]

[1]School of Electrical Engineering and Telecommunications
University of New South Wales, Australia
[2]Centre for Integrated RF Engineering (CIRFE), University of Waterloo, Canada

Abstract— This paper proposes novel implementations of wideband large switch matrices. The solution is based on constructing switch matrices using unit cells. It gives an account of the design and characteristics of two unique novel cell units, a switch cell and a semi-T switch cell. The simulations of these cells demonstrated excellent RF performance. Three distinct switch matrix topologies using these cells are introduced and compared. They are the crossbar, staircase and L-matrix topology.

1. INTRODUCTION

Microwave switches are the key building blocks in modern communications systems. Mechanical and semiconductor switches are the dominating technologies for RF switches. Coaxial switches are the most frequently found mechanical switches, while PIN diode and FET transistor switches are the most recognized semiconductor types. Mechanical switches have the advantage of providing excellent RF performance, but are bulky and expensive. Semiconductors on the other hand are very small in size but with poor RF performance. These highlight the need of new technology for switch and more importantly, switch matrix. Microwave switch matrices are used for signal routing and system redundancy purposes. Switch matrix provides freedom for interconnections between different ports. More importantly, they enable the ability to optimize the bandwidth usage based on beam linking systems [1].

Micro-Electro-Mechanical Systems (MEMS) have been widely investigated. MEMS are widely used in many areas including sensors and actuators. They are being extensively studied for RF/Microwave applications in recent decades. The most developed MEMS in the RF/Microwave field are RF MEMS switches including both contact type and capacitive type configurations. RF MEMS switches are emerging as one of the most promising candidates of replacing the existing technologies including mechanical switches and semiconductor switches. RF MEMS switches have the advantages of both. Not only they are small in size but also demonstrate good RF performance with low inter-modulation distortion [2].

It is apparent that, although RF MEMS switches have been widely investigated, only limited research has concentrated on switch matrices. A monolithic switch matrix topology was reported in [3]. It has several drawbacks: The design is limited in matrix size due to the fact that single-pole N-throw (SPNT) switches are required. Such a requirement creates complications in large structures and therefore the topology cannot be easily expanded to larger switch matrices. Furthermore the design makes use of capacitive coupled transitions from one side of the substrate to the other side. This results in the limitation of the operation bandwidth as well as the introduction of backside patterning which inherently leads to manufacturing and fabrication difficulties.

To overcome such problems this paper proposes the use of cell units to construct switch matrices. Two novel miniaturized cell units are designed, they are a switch cell and a semi-T switch cell. With these cell units, three distinct novel switch matrix topologies are introduced. They are the crossbar, the staircase and the L-matrix topologies as shown in Figure 1. All topologies provide flexibility matrix and each of them has unique advantages which will be discussed in later section.

2. SWITCH CELL UNITS

In this paper, two miniaturized switch cell units are presented. They are the switch cell (Figure 2(a)) and the semi-T switch cell (Figure 2(b)). As major building blocks of switch matrix, they enable flexible switch matrix order and topology. In both designs, a CPW dimensions of $15\,\mu m/20\,\mu m/15\,\mu m$ (G/S/G) has been selected to achieve miniaturization. Symbols and circuit models of the proposed cell units are shown in Figures 2(a) and (b).

Both switches either operates in state 1, thru state or in state 2, turn state. As the name suggested state 1, thru state, makes connections between opposite ports, i.e., 1 and 2 and ports 3 and 4 while state 2, turn state, connects adjacent ports. One could noticed that the major different

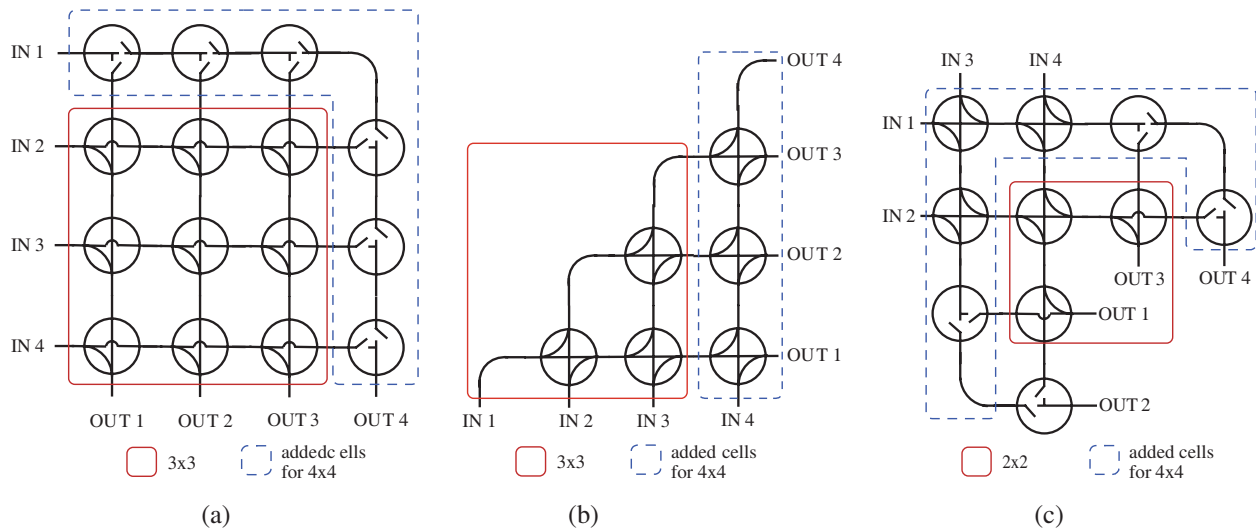(a)   (b)   (c)

Figure 1: (a) Crossbar, (b) staircase and (c) L-matrix topology.
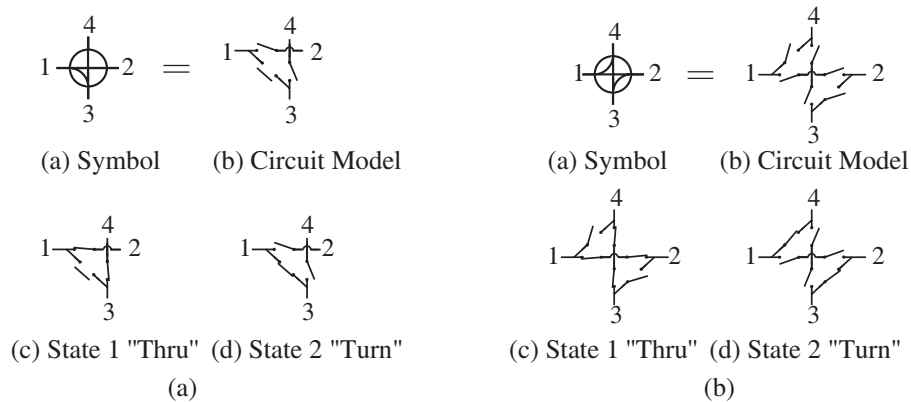

Figure 2: Symbol and circuit model of the proposed (a) switch cell and (b) semi-T switch cell.

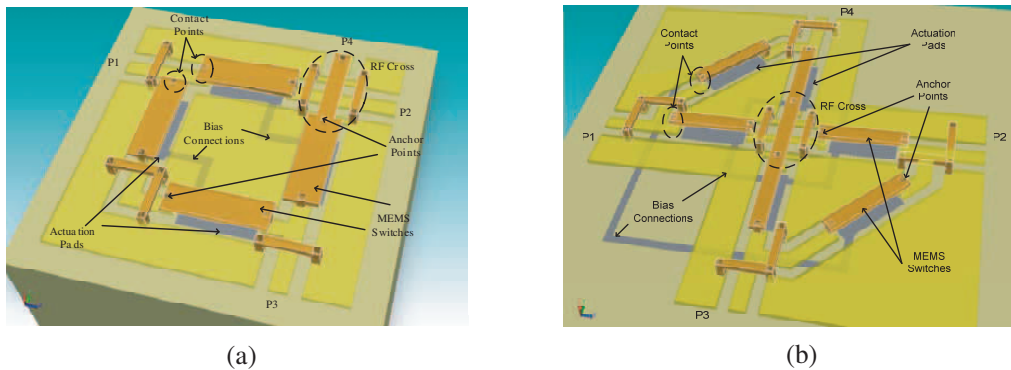(a)   (b)

Figure 3: 3D model of the proposed (a) switch cell and (b) semi-T switch cell.

between the switch cell and semi-T switch is in the turn state. For the switch cell, the turn state connects ports 1 and 3 while for the semi-T switch cell, it connects both ports 1 and 4 and ports 2 and 3. Notice that although number of MEMS switches are used in the cells, all the MEMS switches works in groups according to the states. Therefore both cells only require 2 control signals. 3D models of the proposed cells are shown in Figure 3. Notice that the switch cell uses two MEMS switches on the turn path while the semi-T switch only uses one. This is to reduce the overall MEMS switch number in the semi-T switch design. With the purpose of overall size reduction, the upper signal path of the RF cross shares the anchors of the two adjacent MEMS on both cells. The overall size of the designs are $250\,\mu m \times 250\,\mu m$ for the switch cell and $350\,\mu m \times 350\,\mu m$ for the semi-T switch.
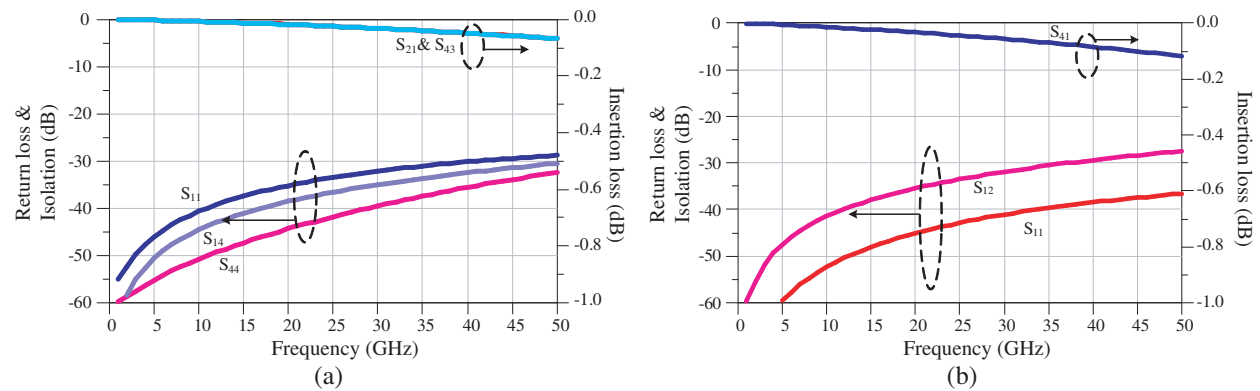
Figure 4: The RF performance of the switch cell at (a) thru state and (b) turn state.
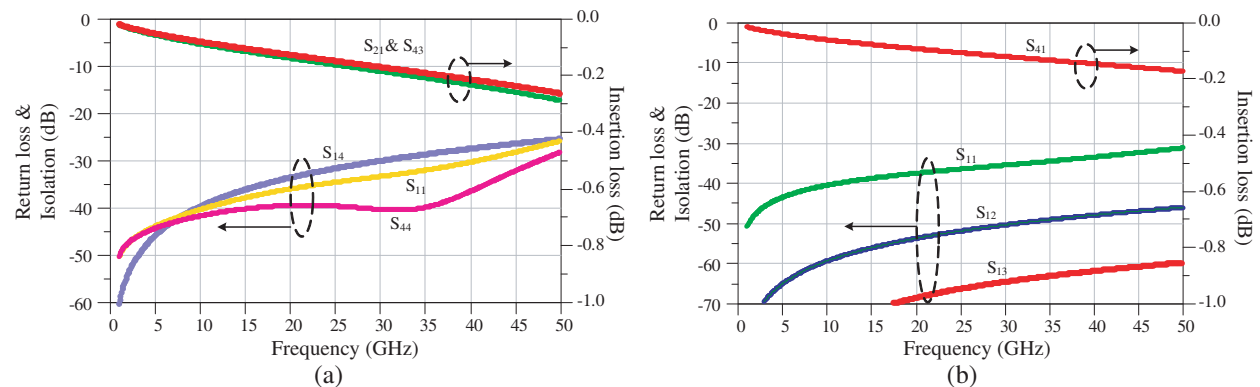

Figure 5: The RF performance of the switch cell at (a) thru state and (b) turn state.

Figure 4 shows the simulated RF performance of the switch cell at both the thru and turn states. The simulation shows that the cell demonstrated return loss (S_{11} and S_{44}) better than 30 dB while maintaining isolation (S_{41}) better than 30 dB at state 1 across DC to 50 GHz. It also shows that while at state 2, the cell achieves better than 30 dB return loss (S_{11}) and 25 dB isolation (S_{12}) across the same range.

Figure 5 demonstrated the semi-T switch cell simulated RF performance at both the thru and turn states. The simulation shows return loss (S_{11} and S_{44}) better than 25 dB while maintaining isolation (S_{41}) better than 25 dB at state 1 across DC to 50 GHz. At state 2, the cell achieves better than 30 dB return loss (S_{11}) and 40 dB isolation (S_{12}) across the same range.

Notices that in all the simulation results, contact resistance from closed MEMS switches are not included. It is not included due to the difficulties in estimating the value as it is fabrication dependent and it is not easy to include in the simulations. Therefore, all the insertion loss values presented in the figures are not compared. However, it can be noticed that the semi-T switches have a considerable highly insertion loss when compare to the switch cell.

3. SWITCH MATRIX TOPOLOGY

In Figure 1, three different switch matrix topologies are introduced. They are the crossbar, the staircase and the L-matrix topologies. Noticed that the introduced topologies offer switch matrix order flexibility. Meaning that switch matrix could be designed with infinite orders theoretically. As shown in the figure, all three topologies allow easy expansion of matrix order. Figure 1(a) shows that by cascading addition row and column, a 4×4 switch matrix crossbar switch matrix could be constructed from a 3×3 one. A 4×4 staircase matrix could also be constructed from a 3×3 one by adding a column to the output ports as shown in Figure 1(b). Similarly, for the L-matrix topology, a 4×4 switch matrix is acquired by adding cells around a 2×2 one. One should notice that because of the inherent property of the L-matrix topology, only even order switch matrix could be designed.

Microwave crossbar switch matrix offers the simplest and direct approach to a microwave switch matrix design. It provides wide band frequency of operation with the simplest design as it only utilizes the proposed switch cell units. However, due to quadratic increase in unit cells as matrix
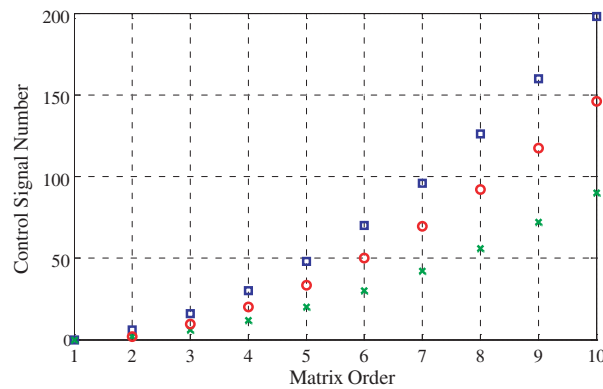
Figure 6: A control signal number comparison between the three proposed switch matrix topologies.

order increases, many control signals are required. For the case of our proposed switch cell, each unit cell requires least two control signals. The overall number control signal for an $N \times N$ switch matrix would be $2(N^2 - 1)$ which becomes impractical. To overcome such a problem, staircase matrix topology as shown is proposed. It can achieve any connections between inputs and outputs while maintaining the expandable characteristic of a crossbar matrix. Although the increase in cell number is still a quadratic function, the rate is much slower. The number of cell requires is only $N(N-1)/2$ which gives $N(N-1)$ control signal number.

Although the proposed crossbar and staircase switch matrix topologies offer efficient RF performance and design flexibility, there is a large insertion loss and phase difference between the longest and shortest paths. For several applications such as beam-forming networks large insertion loss and phase variations across different paths would cause problems and add to the complexity of the entire system. To solve such problems L-matrix topology is proposed. This topology has been proven to provide a more uniform path length distribution across all possible paths in the matrix even with the growth of the matrix order [4]. It is a unique feature that outmatches both the crossbar and staircase topologies. However, although it is superior in the path length variation, it still requires a larger number of cell units compare to the staircase topology. The number of cell required is $3/4N^2 - 2$ which requires $3/2N^2 - 4$ control signals. Figure 6 shows a comparison of control signal number between the three topologies as the matrix order increases. It can be noticed from the figure that staircase give the smallest control signal number as it requires the smallest number of cell unit.

4. CONCLUSION

A new concept producing large scalable $N \times N$ switch matrices has been proposed in this paper. This concept is based on switch cell development. The paper includes the design and characteristics of the switch cell and the semi-T switch which are the basic building blocks of switch matrices. Three distinct switch matrix topologies using these cell units are proposed with their advantages and disadvantages detailed.

REFERENCES

1. Assal, F., R. Gupta, K. Betaharon, A. Zaghloul, and J. Apple, "A wide band satellite microwave switch matrix for SS/TDMA communications," *IEEE Journal on Selected Areas in Communications*, Vol. 1, 223–231, 1983.
2. Rebeiz, G. M., *RF MEMS Theory, Design, and Technology*, John Wiley & Sons, 2003.
3. Daneshmand, M., R. R. Mansour, P. Mousavi, C. Savio, B. Yassini, A. Zybura, and Y. Ming, "Integrated interconnect networks for RF switch matrix applications," *IEEE Transactions on Microwave Theory and Techniques*, Vol. 53, 12–21, 2005.
4. Chan, K. Y., M. Daneshmand, R. R. Mansour, and R. Ramer, "Scalable RF MEMS switch matrices: Methodology and design," *IEEE Transactions on Microwave Theory and Techniques*, Vol. 57, No. 6, 1612–1621, June 2009.

Spectrally Coded Multiplexing Based on FBG Pairs

Binbin Yan[1, 2]**, Paul A. Childs**[2, 3]**, Chongxiu Yu**[1]**, Xinzhu Sang**[1]**,**
Daxiong Xu[1]**, and Gang-Ding Peng**[2]

[1]Key Laboratory of Information Photonics and Optical Communications of Ministry of Education
Beijing University of Posts and Telecommunications, Beijing 100876, China
[2]School of Electrical Engineering and Telecommunications
University of New South Wales, Sydney 2052, Australia
[3]Department of Electronic Engineering, Tsinghua University, Beijing 100084, China

Abstract— We propose a spectrally coded multiplexing (SCM) technique based on FBG pair sensors formed by two identical sub-gratings and an interval. Each FBG pair in multiplexing network has the same Bragg wavelength but a unique interval that determines them to have different wavelength-frequencies and allows them to be multiplexed by use of SCM. The multiplexed signals are demodulated by using fast Fourier transform (FFT) and identifying amplitudes in Fourier spectra of FBG pairs. Combining SCM with WDM, the number of multiplexed FBG pairs can be greatly improved. The performance of proposed SCM has been demonstrated through differential strain sensing measurements. Experimental results showed that the measurement error of the multiplexed system is within $8\mu\varepsilon$ and the crosstalk $< 40\mu\varepsilon$ for differential strain applied up to $378\mu\varepsilon$.

1. INTRODUCTION

Fiber-optic sensors, especially fiber Bragg grating (FBG) sensors, have been widely used in measurements of strain, temperature, pressure, dynamic magnetic field, etc. FBG sensors have many attractive attributes, such as high sensitivity, safety, immunity to electric interference, small size, capability of measuring different kinds of physical parameters, easy to be multiplexed and so on [1]. For structural health monitoring (SHM) of large scale structures, the number of multiplexed sensors needs to be enhanced. It is also necessary to eliminate the influence of temperature on strain measurement. The conventional multiplexing techniques for FBG-based sensors are wavelength division multiplexing (WDM) and time division multiplexing (TDM). However, the maximum number of sensor that can be multiplexed is limited by the ratio of the spectral width of light source divided by the width of the spectral slot allocated to individual sensor in WDM; TDM requires the use of long delay lines which would reduce the structural integrity of host material if embedded.

Recently, several more advanced multiplexing techniques have been reported in the literature. For example, Paul A. Childs [2] has proposed a multiplexing scheme for expanding the channel count of a FBG strain sensor system. The scheme uses carrier modulated FBG and the sensing signal is demodulated by extracting the phase in Fourier spectra of reflected signal from each FBG sensor. Allan C. L. Wong [3] et al., have reported a multiplexing technique by using amplitude-modulated chirped fiber Bragg gratings (CFBG). The discrete wavelet transform is employed in order to demodulate the multiplexed signal and a wavelet denoising technique is used to reduce the noise. Y. J. Rao [4] et al., have proposed fiber-optic Fabry-Perot sensors formed by CFBG pairs for a large number of multiplexing. They use fast Fourier transform (FFT) to demodulate the multiplexed signal. In these multiplexing techniques, the grating sensors are able to spectrally overlap each other, having same central wavelength, bandwidth and reflectivity, but different reflective spectral forms. These multiplexing schemes provide a new multiplexing dimension of freedom and allow the spectra of gratings overlapping. They can be classified as spectrally coded multiplexing (SCM).

In this paper, we propose a spectrally coded multiplexing based on FBG pair sensors that allow each FBG pair to be spectrally overlapped. The sensing signal is demodulated by extracting the amplitude in Fourier spectra of reflected spectra of FBG pairs. The differential strain measurements are performed to demonstrate the performance of proposed SCM.

2. MULTIPLEXING PRINCIPLE AND DEMODULATION

To realize spectrally overlapped multiplexing, we take into account FBG pair sensors as shown in Figure 1. The FBG pair is formed by two sub-gratings and an interval. L_1 and L_2 are the sub-grating length; d is the length of interval between two sub-gratings. For a symmetrical FBG
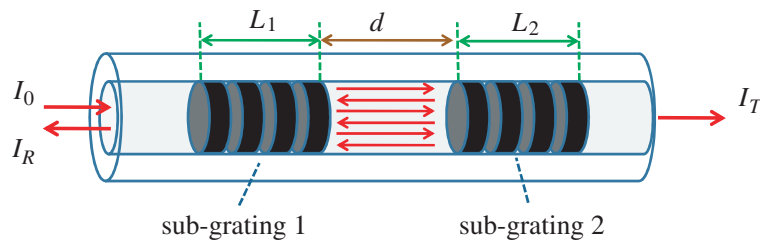
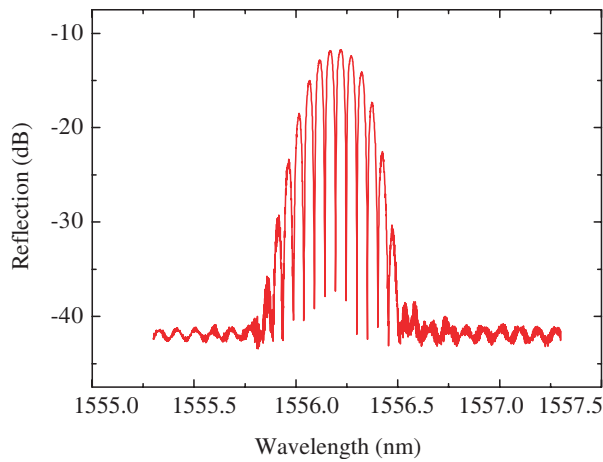Figure 1: The structure of FBG pair sensor.

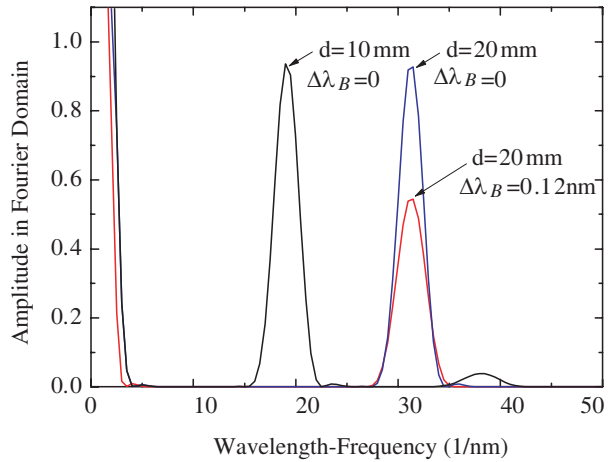Figure 2: A typical reflected spectrum of FBG pair.

Figure 3: The Fourier spectra of FBG pairs.

pair, i.e., identical sub-gratings, the reflection coefficient of FBG pair can be approximated by the expression:

$$r = r_g[1 + \exp(-i\varphi_p)] \tag{1}$$

here, r_g is the reflection coefficient of sub-grating, $\varphi_p = 4\pi n L_p/\lambda$ is the phase in FBG pair, $L_p = L + d$ ($L = L_1 = L_2$) is the length of the resonant cavity formed by two sub-gratings which determines the resonant frequency of reflected spectrum of FBG pair. It can be seen from Eq. (1) that the reflection of FBG pair is cosine function of wavelength within its reflected bandwidth. The resonant frequency, namely wavelength-frequency, depends on the length of interval between two sub-gratings for the same length of sub-gratings. Hence, the FBG pairs, having same Bragg wavelength, bandwidth and reflectivity, are still uniquely distinguishable from one another in Fourier domain by taking FFT as long as they have different length of interval. In other words, FBG pair is capable of realizing spectral encoding because the variable length of interval can induce different spectral form.

A typical reflected spectrum for a free FBG pair with an interval of 10 mm long is shown in Figure 2. For the FBG pair which can be treated as a FBG-FP structure, the mismatched Bragg wavelengths of two sub-gratings will degrade the resonance in the cavity. The resonance intensity decreases as the increase of mismatched quantity in Bragg wavelengths. Such a capability can be used for monitoring differential strain in a structure. To demodulate the differential strain induced change in resonant spectra, we take FFT which is a good algorithm for harmonic analysis. Figure 3 illustrates the Fourier spectra for FBG pairs of $d = 10$ mm and $d = 20$ mm. With increasing the differential strain loaded on the FBG pair, the peak-amplitude of Fourier spectra decreases monotonically and the peaks in Fourier domain are separated for different d value. Hence, the sensing signal can be demodulated by extracting the peak-amplitude in Fourier domain. The FBG pairs can be multiplexed in Fourier domain because FBG pair with a particular interval only occupies identical wavelength-frequency band even their reflective spectra are overlapped over one another. Also, two sub-gratings can effectively counteract the effect of environmental temperature during measuring strain.
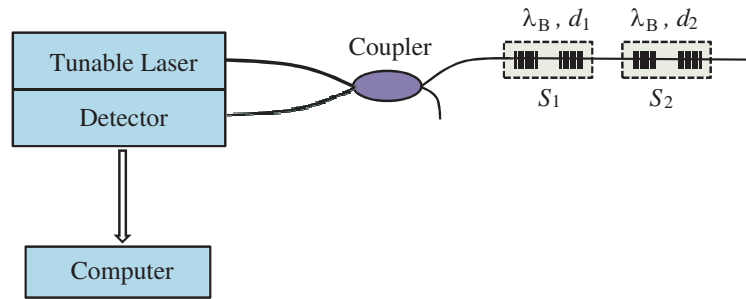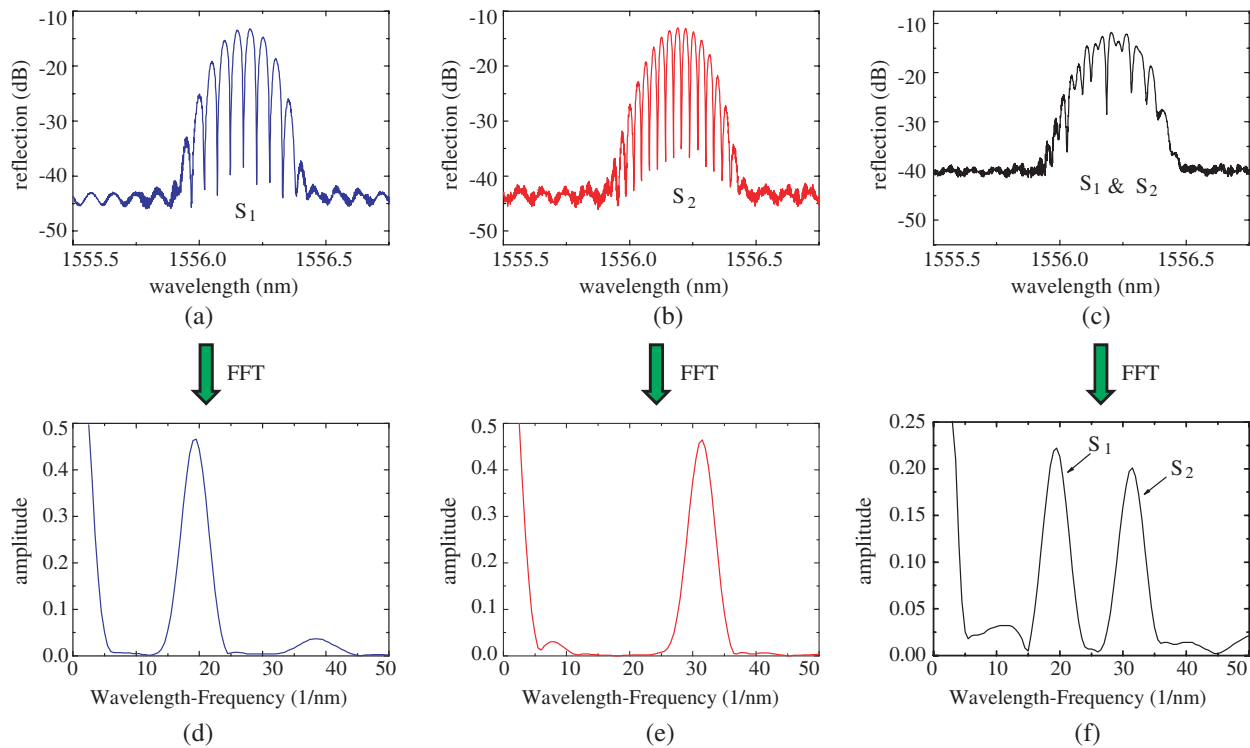
Figure 4: The experiment setup.

Figure 5: The reflected spectra and Fourier spectra of FBG pairs.

3. EXPERIMENTS AND DISCUSSIONS

We demonstrate the feasibility of the FBG pair based differential strain sensors under SCM. The experimental setup is shown in Figure 4. A laser light from tunable laser module (Agilent, 81640A) was launched to two multiplexed FBG pairs, S_1 and S_2, via a 3-dB coupler. The FBG pairs were fabricated at the UNSW grating writing facility with same Bragg wavelength of 1556.2 nm by using uniform phase mask. The length of all sub-gratings is 6 mm. The apodization with flatted cosine profile for each sub-grating was achieved by dithering the phase mask as the UV beam scanned across it. Whereas S_1 and S_2 was written with intervals of 10 mm and 20 mm, respectively, in order to separate them in Fourier domain. The reflected spectra and Fourier spectra of S_1 and S_2 are shown in Figures 5(a), (b), (d) and (e). The multiplexed signal was reflected back to the power sensor module (Agilent, 81635A) and then was sent to a computer to be processed digitally. The wavelength resolution of tunable laser module was set as 1 pm which can ensure the required high accuracy of differential strain measurement. The measured multiplexed signal is shown in Figure 5(c) for free S_1 and S_2. By taking FFT, we can obtain the Fourier spectrum of multiplexed signal as shown in Figure 5(f). The measurand (differential micro strain) can be extracted by monitoring the amplitudes of peaks in Fourier domain.

In experiments, two FBG pairs were spliced together as shown in Figure 4 and were suspended vertically. FBG pair S_1 was loaded using a plastic tray with washers hung between two sub-gratings
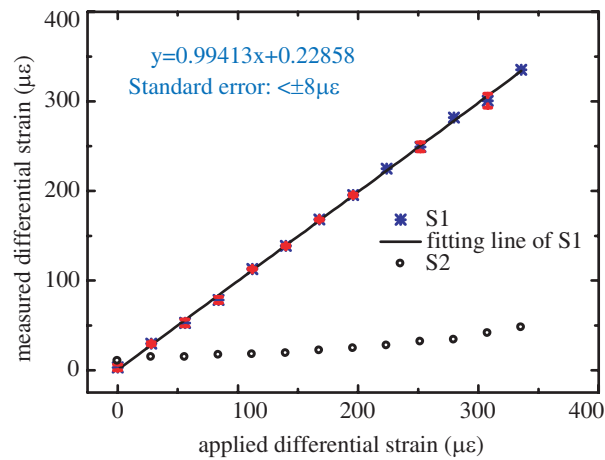
Figure 6: The experiment results.

that mean a differential strain applied to S_1. FBG pair S_2 kept free from any strain and was used to measure crosstalk. Each washer weights 0.49 g, and total of 60 washers were used which plus plastic tray corresponds to $378\mu\varepsilon$. Figure 6 shows the measured differential strain responses of S_1 and S_2 with the applied differential strain. The solid line is fitting line for S_1. It can be seen that the differential strain measured by S_1 has very high accuracy of lower than $\pm8\mu\varepsilon$. However, there was a little bit high crosstalk ($< 40\mu\varepsilon$). This problem can be reduced by taking a logarithm linearization of reflected spectrum.

4. CONCLUSION

We have demonstrated SCM technique based on FBG pair sensors by performing temperature-insensitive differential strain measurement. An amplitude demodulation technique based on FFT has been used to identify the measurand-induced change in spectra of the FBG pair sensors. The demodulation does not need complicated demodulating electronic equipments because it is carried out digitally by computer processing. Combining WDM and SCM, the number of multiplexed FBG pair based sensors could be greatly improved. Experimental results showed that the measurement error of the multiplexed system is within $\pm8\mu\varepsilon$ and the crosstalk is less than $40\mu\varepsilon$ for differential strain applied up to $378\mu\varepsilon$. The proposed sensors are able to monitor the cracking of large scale structures.

ACKNOWLEDGMENT

REFERENCES

1. Kersey, A. D., M. A. Davis, H. J. Patrick, M. LeBlanc, K. P. Koo, C. G. Askins, M. A. Putnam, and E. J. Friebele, "Fiber grating sensors," *Journal of Lightwave Technology*, Vol. 15, No. 8, 1442–1463, 1997.
2. Childs, P., "An FBG sensing system utilizing both WDM and a novel harmonic division scheme," *Journal of Lightwave Technology*, Vol. 23, No. 1, 348–354, 2005.
3. Wong, A. C. L., P. A. Childs, and G.-D. Peng, "Multiplexing technique using amplitude-modulated chirped fiber Bragg gratings," *Optics Letters*, Vol. 32, No. 13, 1887–1889, 2007.
4. Rao, Y. J., Z. L. Ran, and C. X. Zhou, "Fiber-optic Fabry-Perot sensors based on a combination of spatial-frequency division multiplexing and wavelength division multiplexing formed by chirped fiber Bragg grating pairs," *Applied Optics*, Vol. 45, No. 23, 5815–5818, 2006.

Bioelectrical Impedance Analysis by Multiple Frequencies for Health Care Refrigerator

Bo-Rim Ryu[1], Haeseong Jeong[2], and Heung-Gyoon Ryu[2]

[1]Seoul National University, Korea
[2]Chungbuk National University, Korea

Abstract— In this paper, we like to study the bioelectrical impedance analysis and propose a smart refrigerator for ubiquitous health care. A smart refrigerator has an additional function enabling users to keep in track of their health by the newly equipped installation. Also, it is equipped with a body fat analyzer that is used in gym and hospitals in order to receive health care in a ubiquitous environment. This proposed method is measured for body impedance and recognized for body composition by using bioelectrical impedance analysis (BIA). Also, we expect that medical center manages user's condition such as amount of body fat, muscle, body water and etc. through internet in a ubiquitous environment. This proposed method has two merits. It can be used to measure more often and much cheaper than body fat analyzer in gym and hospitals.

1. INTRODUCTION

As the telecommunication has gradually developed to become ubiquitous, health care also reflected the influence of mobile telecommunication progressing from hospitals, telemedicine, e-Health and u-Health respectively. Health care patients will receive, in such ubiquitous environments, treatment in physical environments without being exposed regardless of the time or space. A smart refrigerator has an additional function enabling users to keep in track of their health by the newly equipped installation.

This paper's purpose are to measure body composition such as body fat, basal metabolism, muscle mass, etc. by using 'Bioelectrical Impedance Analysis (BIA)', and do health care. The idea of the smart refrigerator was brought up by the fact that it is a home appliance that operates 24 hours which encourages users to check and treat their health condition frequently. The body fat analyzer is incongruent in the gym and hospital in order to measure on occasion. Therefore, the smart refrigerator is proposed for measuring body condition in a breeze at the house. Also, it is proposed for cheaper health care. In this paper, we explain the principle of bioelectrical impedance analysis (BIA) for health care through smart refrigerator in ubiquitous environment. Afterwards, we will explain the composition method of smart refrigerator. Also, we recognize that the supposed technique is adaptive through the measurement and evaluation.

2. BIOELECTRICAL IMPEDANCE ANALYSIS (BIA)

The bioelectrical impedance analysis (BIA) is to predict body composition by using difference of electrical conductivity for biological character of body tissue [1, 2]. The body tissue is divided both fat and free-fat. Also, the electrical conductivity is relative to amounts of water and electrolyte, and decreases when the shape of a cell is similar to a circle. Since the fat tissue is made by the cell of a circle, and has a little water, it has an insulator character. On the other hand, the muscle and the water have a conductor character. Whenever a small amount of AC current passes through the body, the current is flowed along the water of high conductivity. According to conductivity of each body such as total body water, fat mass, muscle mass and etc., the impedance occurs differently, and then we measure and analyze body tissue by using BIA. We suppose that the body, which is determined through height and weight, is made by one cylinder or 5 cylinders and measure through the amount of total body water and body fat mass. The body impedance is measured by a method which separately measures the trunk of body, arm and leg impedance.

The resistance of a length of homogeneous conductive material of uniform cross-sectional area is proportional to its length and inversely proportional to its cross sectional area. Hence, resistance can be expressed as

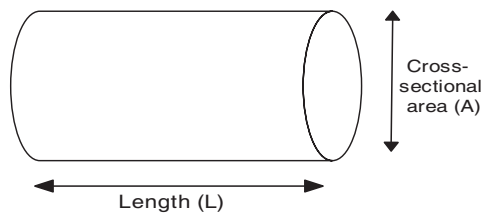$$R = \rho \frac{L}{A} = \rho \frac{L^2}{V} \tag{1}$$

Figure 1: Principles of BIA model.
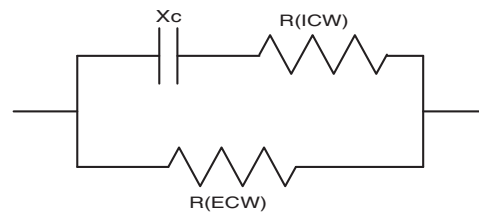
Figure 2: Electrical model of the human body.
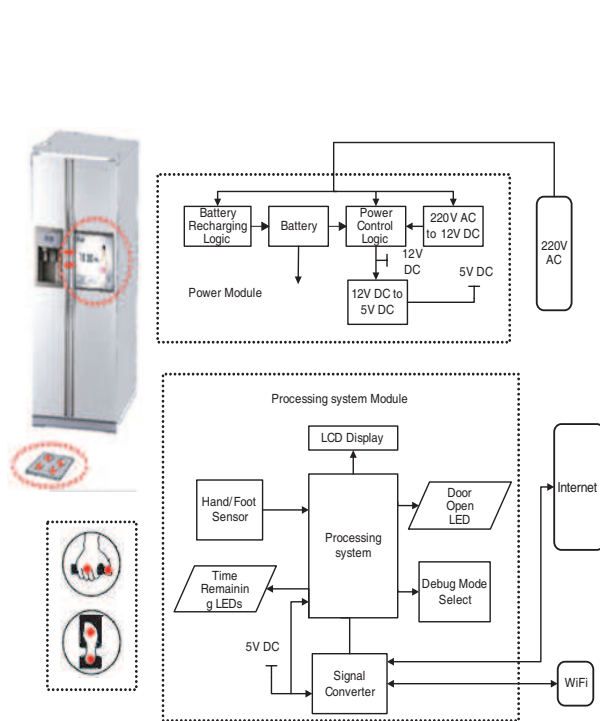
Figure 3: Block diagram of overall system.
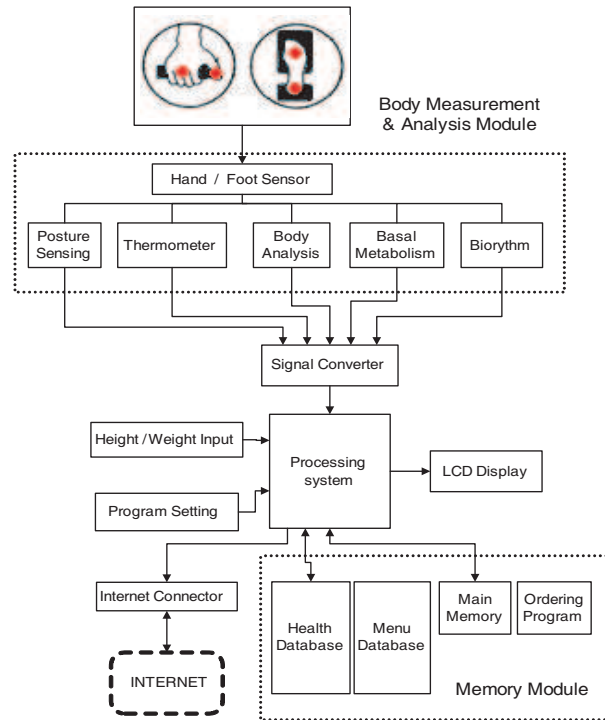
Figure 4: Body measurement and analysis module.

Figure 5: Composition of handle sensor and foot sensor.

where ρ is the resistivity of the conducting material and $V = AL$. Also, the equation of volume can be expressed as

$$V = \rho \frac{\text{height}^2}{R} \tag{2}$$

where $\frac{\text{height}^2}{R}$ is impedance index, and it is calculated to volume.

The original problem of BIA method is very different to segmental resister. Therefore, we suppose that the body is made by 5 cylinders [3].

When we inquire of body character by using BIA, we suppose that the human body consists of resistance and capacitance connected in parallel or in series. The resister (R) arises from extracellular fluid and intracellular fluid, and the capacitance (C) from cell membranes. In this parallel model, two or more resistors and capacitors are connected in parallel, with the current passing at high frequencies through the intracellular space and at low frequencies passing through the extracellular space.

There are two methods for measuring BIA which is the bi-polar method and the Tetra-polar method. The two methods are used to contact electrodes. The contact resisters occur when body connect to electrode. The Bi-polar method is simple because it consists of current electrode and

voltage electrode at unity. But it has low accuracy because of high contact resister. On the other hand, the Tetra-polar method is complex because current electrode and voltage electrode is used separately. However, it has high accuracy because of low contact resister. Also, it is very accurate because of same part from the wrist and the ankle. In addition to that, we separately measure to the resister of arm, leg and trunk. In this paper, we use multi-frequency analysis by using $1\,\text{kHz} \sim 1000\,\text{kHz}$ frequency band. Below $100\,\text{kHz}$, the current does not penetrate the cell membrane and therefore the current passes through the extracellular fluid. Therefore, below $100\,\text{kHz}$ is used to measure the extracellular water (ECW). At above $100\,\text{kHz}$, the current penetrates the cell membrane. Therefore, above $100\,\text{kHz}$ can be used to measure the total body water (TBW). In multi-frequency, we exactly measure intracellular water and extracellular water. The correlation of total body water (TBW), intracellular water (ICW) and extracellular water can be expressed as,

$$\text{TBW} = \text{ICW} + \text{ECW} \tag{3}$$

We measure intracellular water, extracellular and total body water by using this correlation. It can help measure body water balance, treat several diseases and protect various diseases.

3. DESIGN OF HEALTH CARE REFRIGERATOR

We will apply principal of BIA to smart refrigerator. Figure 3 is a block diagram of an overall system. It consists of power module and processing system module. The power module part is converted to $12\,\text{V}$ DC voltage by using $220\,\text{V}$ AC voltage. And the power control logic converts to $5\,\text{V}$ DC voltage. Also, the smart refrigerator consists of battery recharging logic and battery part. Figure 4 on the other hand is a block diagram of body measurement and analysis module. It consists of body measurement and analysis module part, memory module part and processing module part. And we will explain Input part, Sensor part, Processor part, Operation part and Output part. Enter height, age and sex in order to correctly measure since the body is non-uniform.

Handle sensor and foot sensor are made by contact electrode in Figure 5 [3]. The contact electrode is red point in Figure 5. The composition of sensor part in smart refrigerator is equipped to the handle sensor in knob of Refrigerator, and the foot sensor is equipped under the Refrigerator. We use Tetra-polar 8-Point Tactile Electrode System in order to correctly measure. Therefore, the handle sensor is made to connect to thumb and palm, and the foot sensor is made to connect to front sole and rear sole.
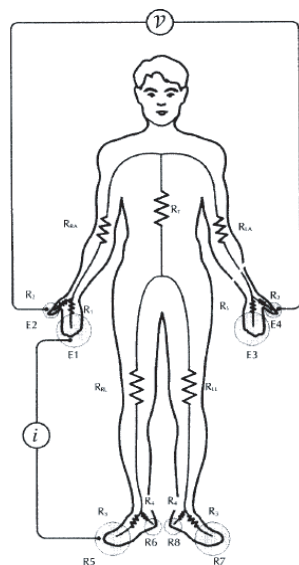

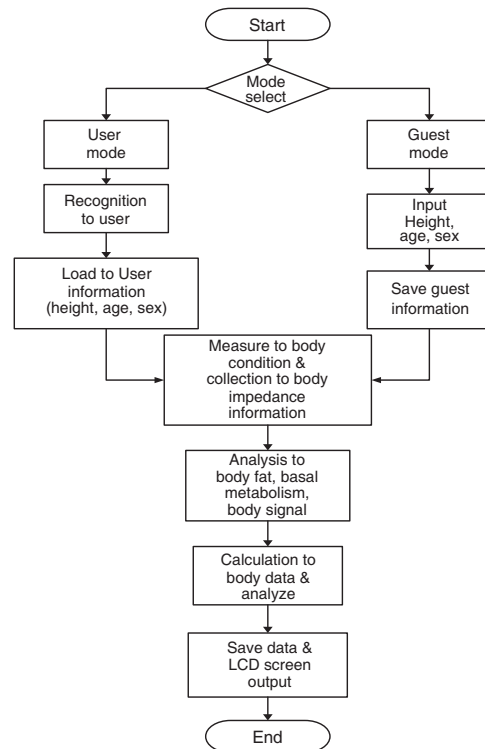Figure 6: Segmental impedance measurement.

Figure 7: Main control algorithm.

The impedance is measured by using Handle sensor and Foot sensor in Sensor part and we suppose that the body consists of five cylindrical conductors. And we measure segmental impedance by using multi-frequency.

Suppose that we measure the impedance of right arm (R_{RA}). In order to measure to R_{RA}, current terminals are connected to right palm electrode (E_1) and right front sole (E_5), and voltage pick-up terminals are connected to right thumb electrode (E_2) and left thumb electrode (E_4). The current is flowed through right palm (R_1), right arm (R_{RA}), trunk (R_T) and right leg (R_{RL}). And the voltage is measured through right thumb (R_1), right arm (R_{RA}), left arm (R_{LA}), left thumb (R_2). The current path and measured voltage loop become reiteration and then we measure the resistance of right arm (R_{RA}).

The other impedance is similar to the method of the right arm. The current source put on the same method when we measured the right arm impedance, and the voltage is measured to the left thumb electrode (E_4) and left rear sole electrode (E_8) in order to measure impedance of trunk. Also, the voltage is measured to right rear sole electrode (E_6) and left rear sole electrode (E_8) in order to measure impedance of leg. In order to measure left segmental impedance, the current source is connected to left palm electrode (E_3) and left front sole electrode (E_7), and the voltage measurement method is same as the right side method in order to measure left arm and leg impedance. The equation for calculation to FFMI (Fat Free-Mass Index), FMI (Fat Mass Index) and BMI (Body Mass Index) is as follows. In the processor part that calculates body fat, muscle mass and total body water, etc. by using the algorithms, take advantage of Equations (1)–(3).

$$
\begin{aligned}
\text{FFMI} &= \frac{\text{fat} - \text{free mass}}{\text{height}^2} \left(\frac{\text{kg}}{\text{m}^2}\right) \\
\text{FMI} &= \frac{\text{fat} - \text{mass}}{\text{height}^2} \left(\frac{\text{kg}}{\text{m}^2}\right) \\
\text{BMI} &= \text{FFMI} + \text{FMI}
\end{aligned}
\tag{4}
$$

The data is managed by using Equations (1)–(4) and suitable algorithms. The data is known for body condition, encouragement exercise and encouragement menu in the operation part.

4. MEASUREMENT AND EVALUATION

The Table 1 is Measurement specifications about smart refrigerator. 1) Segmental impedance measurement in Multi-frequency. 2) Body component analysis. 3) BMI, Percent body fat and Waist-Hip ratio measurement, etc.

The Table 2 is Segmental impedance measurement in Multi-frequency. The segmental impedance of RA (Right Arm), LA (Left Arm), TR (Trunk, Body), RL (Right Leg), and LL (Left Leg) is measured. And we use multi-frequency to measure the impedance. In multi-frequency, electrical current is passed through the body and we measure the body impedance. It is calculated to total body water, muscle mass, fat free mass and fat mass by using BIA through right arm, right leg, left arm and left leg. In the frequency band of 1, 5, 50, 250, 500 and 1000 kHz, 30 kinds of impedance are measured in right arm, right leg, left arm and left leg and 15 kinds of reactance are measured in each right arm, right leg, trunk, left arm and left leg.

Table 3 is body component analysis. We analyze weight, total body water, muscle mass, fat free mass and fat mass by using handle sensor, foot sensor and weight sensor.

$$
\text{Total body water (L)} = \text{ICW} + \text{ECW} \tag{5}
$$
$$
\text{Soft lean mass (kg)} = \text{TBW} + \text{Protein mass} \tag{6}
$$
$$
\text{FFM (kg)} = \text{SLM} + \text{Mineral mass} \tag{7}
$$
$$
\text{Weight (kg)} = \text{FFM} + \text{Fat mass} \tag{8}
$$

Table 4 indicates BMI (kg/m^2), percent body fat and waist-hip ratio. BMI is calculated for Equation (4) and percent body fat is calculated in the following equation.

$$
\text{Percent Body Fat (\%)} = \frac{\text{Amount of body fat}}{\text{weight}} \times 10 \tag{9}
$$

For males below thirty, percent body fat is normal from 14% to 20%, a little bit overweight from 21% to 25 %, and obese over 26%. Otherwise, it is normal from 17 % to 23%, a little bit overweight

from 24% to 28%, obese over 29%. On the other hand, for females under thirty, percent body fat is normal from 17 % to 24%, a little bit overweight from 25% to 29% and obese over 30%. Otherwise, percent body fat is normal from 20 % to 27%, a little bit overweight from 28% to 32%, obese over 33%.

Also, the distribution of body fat is relatively low to muscle mass in case of the female during pregnancy and function of hormone, and the activity of lipolysis in hip and the femoral region is very low, therefore, the body fat is crowded in the lower part of the body. The activity of lipolysis in the upper part of body is relatively low. Therefore, the body fat is crowded in the upper part of the body in case of male.

In the paper, the impedance is measured by using BIA method, and the minuteness current is flowed through arm and leg in order to measure impedance. In multi-frequency, 30 kinds of impedance are measured, and 15 kinds of reactance are measured.

Table 1: Measurement specifications.

Electrode Method	Tetra-polar 8-Point Tactile Electrode System
Frequency	1 kHz, 5 kHz, 50 kHz, 250 kHz, 500 kHz, 1000 kHz (1 MHz)
Measurement Items	Resistance (R), Reactance (X_c), Phase Angle (φ)
Measurement Sites	Right Arm, Left Arm, Trunk, Right Leg, Left Leg
Outputs	Intracellular Water (ICW) Extracellular Water (ECW) Total Body Water (TBW) Skeletal Muscle Mass (SMM) Body Fat Mass (FAT) Edema Visceral Fat Area (VFA) Lean Balance
Applied Rating Current	100μA (1 kHz), 500μA (others)
Power Consumption	60 VA
Power Source	100–240 V∼, 50/60
Display Type	640 × 480 Color TFT LCD
External Interface	RS-232C 3EA, USB (Ver. 1.1) 2EA, Ethernet (10/100 Base-T) 1EA
Printer Interface	IEEE1284 (25 pin parallel)
Dimensions	520 (W) × 870 (L) × 1200 (H): mm
Machine Weight	45 kg
Measurement Duration	Less than 2 minutes
Operation Environment	10 ∼ 40°C (50 ∼ 104°F), 30 ∼ 80% RH
Storage Environment	0 ∼ 40°C (32 ∼ 104°F), 30 ∼ 80% RH
Optimum Pressure	500 ∼ 1060 hPa
Weight Range	10 ∼ 250 kg (22 ∼ 551 lbs)
Age Range	6 ∼ 99 years
Height Range	110 ∼ 220 cm (43.3 ∼ 86.6 in)

Table 2: Segmental impedance measurement.

	RA	LA	TR	RL	LL
frequency	**Object No. 1**				
1 kHz	368.4	348.1	32.0	272.8	272.1
5 kHz	360.7	340.7	30.9	266.8	266.4
50 kHz	321.9	299.7	26.1	233.3	231.5
250 kHz	286.0	268.2	21.8	208.8	206.8
500 kHz	274.3	258.6	20.4	202.7	201.4
1000 kHz	265.4	251.0	18.7	200.6	199.4
frequency	**Object No. 2**				
1 kHz	395.0	399.8	29.4	299.2	296.2
5 kHz	380.6	387.7	27.7	291.2	287.7
50 kHz	327.8	337.3	22.9	247.7	244.8
250 kHz	290.5	301.0	19.6	221.3	218.9
500 kHz	277.1	287.6	18.3	215.3	213.5
1000 kHz	267.5	277.2	16.9	212.9	211.1
frequency	**Object No. 3**				
1 kHz	352.5	368.2	30.4	281.2	281.3
5 kHz	343.9	360.6	28.8	274.0	274.5
50 kHz	302.8	318.7	24.0	233.8	234.7
250 kHz	270.7	286.4	20.0	208.2	208.1
500 kHz	260.5	275.6	18.6	202.3	202.3
1000 kHz	252.6	265.9	17.4	199.5	199.7
frequency	**Object No. 4**				
1 kHz	377.4	375.1	28.9	279.4	270.0
5 kHz	367.9	367.8	27.8	272.1	263.1
50 kHz	320.1	324.7	22.9	231.3	223.9
250 kHz	287.8	294.1	19.2	204.9	199.2
500 kHz	278.0	284.7	18.1	199.1	194.1
1000 kHz	269.0	276.1	17.1	197.2	192.9
frequency	**Object No. 5**				
1 kHz	362.3	370.8	30.7	245.8	246.3
5 kHz	355.0	363.0	29.5	239.7	240.5
50 kHz	318.1	325.8	25.2	207.9	210.3
250 kHz	290.5	299.0	21.2	187.0	190.0
500 kHz	280.6	290.0	19.9	182.3	185.4
1000 kHz	272.6	281.5	18.7	181.5	184.3

Table 3: Body component analysis.

	age	height	weight	Total body water	Muscle mass	Fat free mass	Fat mass
1	25	170	59.2	36.7	46.6	50.0	9.2
2	27	183	82.0	47.2	59.7	63.9	18.1
3	22	174	62.2	39.2	49.7	53.3	8.9
4	24	173	68.4	39.8	50.5	54.2	14.2
5	24	171	67.3	37.2	47.0	50.5	16.8

Table 4: BMI, body fat rate and abdominal fat measurement.

	BMI	Body fat (%)	Waist–Hip ratio
1	20.5	15.6	0.79
2	24.5	22.0	0.86
3	20.5	14.3	0.78
4	22.9	20.8	0.83
5	23.0	25.0	0.83

5. CONCLUSION

In this paper, we propose a smart refrigerator in order to measure body condition in ubiquitous environment. This proposed method is measured for body impedance and calculated composition using bioelectrical impedance analysis. The purpose of this paper is to exchange data among houses, health care centers and hospitals through optical fiber on occasion. Also, the purpose of this paper is to exactly check body condition by using BIA on occasion in ubiquitous environment. Therefore, if we use smart refrigerator, we can manage health condition on occasion among health care center, hospital and refrigerator by checking the condition of somebody's health. We are expecting to reduce fee for medical treatment.

REFERENCES

1. Kyle, U. G., et al., "Bioelectrical impedance analysis — part I: Review of principles and methods," *Elservior*, 1226–1243, June 4, 2004.
2. Kyle, U. G., et al., "Bioelectrical impedance analysis — part II: Utilization in clinical practice," *Elservior*, 1430–1453, September 7, 2004.
3. Cha, K. C., et al., "Segmental bioelectrical impedance analysis (SBIA) for determining body composition," *Korean J. Community Nutrition*, Vol. 2, No. 2, 179–186, 1997.
4. Kim, M.-G., et al., "Assessment of fat-free mass using segmental bioelectrical impedance analysis," *The Korean Journal of Physical Education*, Vol. 39, No. 3, 391–400, 2000.
5. Ryu, B.-R., H.-G. Ryu, and T. S. Lee, "Design of smart refrigerator for ubiquitous healthcare," *Proceeding of the IET Conference on Assisted Living*, The IET, Savoy Place, London, UK, March 24–25, 2009.

Simulations of Multi-Photon Absorption Spectra for Fullerene Derivatives $C_{60} > C_2H_4NH_3(Polyaniline)_n$ Based on First-principle Calculations

W.-D. Cheng and J.-Y. Wang

State Key Laboratory of Structural Chemistry
Fujian Institute of Research on the Structure of Matter, Chinese Academy of Sciences
Fuzhou, Fujian 350002, China

Abstract— The sum over states formula following after the calculations of time-dependent density functional theory has been employed to model 2-photon and 3-photon absorption spectra of fullerene derivatives $C_{60} > C_2H_4NH_3(\text{polyaniline})_n$. The calculated results show that the multi-photon absorption cross sections are increasing in the order of n values of $1 < 2 < 3$ for $C_{60} > C_2H_4NH_3(\text{polyaniline})_n$. The electronic origin of multi-photon absorption has been identified with respect to the molecular orbitals involved in charge transfer process. It shows that the increases of donor polyaniline extent result in a large multi–photon absorption cross section in $C_{60} > C_2H_4NH_3(\text{polyaniline})_n$.

1. INTRODUCTION

Multi-photon absorption has become a focused topic in photo-physics since the late 1980s [1, 2]. This is due to its demand in applications of many fields, such as three-dimensional (3D) optical data storage and microfabrication, photodynamic therapy and bioimaging, and optical power limiting, etc [3–5]. In order to meet the requirements of actual applications, scientists have made great efforts to develop new materials with large two-photon absorption (2PA) and three-photon absorption (3PA) cross section. The previous studies revealed that the charge transfers effectively enhance the two-photon absorptivity [6]. Generally, the covalently linked compounds showing favorable intramolecular charge transfers will improve multi-photon absorption property. An aniline or polyaniline as a donor linking to the C_{60} as an acceptor via a pyrrolidine spacer, the formed compound may exists with large multi-photon absorption cross sections. The nonlinear optical (NLO) properties of polyaniline and the size effect of the oligomer on the photophysical properties of the dyads or triads have been investigated intensively [7, 8]. It is crucial for the understanding the relationships between the NLO response (multi-photon absorption) and molecular structure in a rational design of new multi-photon absorption materials. However, there is little information available about the dependence of the multi-photon absorption properties of fullerene derivatives on the size of the linked oligomer. In this work, we will model the 2PA and 3PA absorption spectra and understand the origination of multi-photon absorption for fullerene derivatives $C_{60} > C_2H_4NH_3(\text{polyaniline})_n$ ($n = 1$–3).

2. MODLING PROCESS AND METHOD

The molecular 2PA cross section $\delta(\omega)$ can be characterized by the imaginary part of the molecular third-order nonlinear polarizability, $\delta(\omega) = 32\pi^4\hbar/(n\lambda)^2 F^4 \text{Im}\gamma(-\omega; \omega, \omega, -\omega)$ and an average 2PA cross section of $\langle\delta(\omega)\rangle = 32\pi^4\hbar/(n\lambda)^2 F^4 \langle\text{Im}\gamma(-\omega; \omega, \omega, -\omega)\rangle$, in which the third-order polizability γ at degenerate four-wave mixing process can be calculated by sum over states (SOS) method [9]. The 3PA cross section σ can be derived from the imaginary part of the fifth-order polarizability $\varepsilon(-\omega; \omega, -\omega, \omega, -\omega, \omega)$. However, the numerical calculation of this polarizability through the full SOS approach is a formidable task. Under resonant conditions, the 3PA cross section can be expressed as [10]

$$\sigma(\omega) = 4\pi^2(\hbar\omega)^3 L^6 / \left(\hbar^3 c^5 n^3\right) \Sigma_f \left|T_{g\to f}^{ijk}\right|^2 \left\{\Gamma / \left(E_{gf} - 3\hbar\omega\right)^2 + \Gamma^2\right\},$$

where c is the speed of light in vacuum, L denotes a local field correction (equal to 1 for vacuum), $\hbar\omega$ is the photon energy of the incident light, and Γ is a Lorentzian broadening factor (set to 0.1 eV in the calculations). $T_{g\to f}$ corresponds to the three photon transition amplitude from the ground state to a final three-photon state f, with tensor ijk elements given by

$$T_{g\to f}^{ijk} = P_{ijk}\Sigma_{m,n} \langle g|\mu_i|m\rangle \langle m|\mu_j|n\rangle\langle n|\mu_k|f\rangle/(E_{gm} - \hbar\omega - i\Gamma)(E_{gn} - 2\hbar\omega - i\Gamma)$$

the third-order transition moment has to be orientationally averaged as devised by McClain [11]. For linearly and circular polarized lights the three-photon probabilities are separately given by

$$\delta_L^{3PA} = 1/35(3\Sigma_{ijk}T_{ijk}T_{ijk} + 2\Sigma_{ijk}T_{iij}T_{kkj}) \quad \text{and}$$
$$\delta_C^{3PA} = 1/35(5\Sigma_{ijk}T_{ijk}T_{ijk} - 2\Sigma_{ijk}T_{iij}T_{kkj})$$

Before doing the 2PA and 3PA cross section calculations, the equilibrium geometrical structures of $C_{60} > C_2H_4NH_3(\text{polyaniline})_n$ ($n = 1$–3) are separately optimized by B3LYP method at 6-31G* level, and their state-state transition energies and moments that are taken as inputs of SOS and transition probability $|T_{g \to f}^{ijk}|^2$ is computed by the calculated results using TDDFT at TDB3LYP/3-21G* level coded in GAUSSIAN03.

3. RESULTS AND DISCUSSIONS

3.1. Two-photon Absorption Spectra

Figure 1 shows the plots of average frequency-dependent 2PA cross sections $\langle\delta(\omega)\rangle$ of title compounds for $n = 1$–3. The maximum $\langle\delta(\omega)\rangle$ are 1361, 3559 and 4424 GM, and corresponding to wavelengths of 679, 1012 and 1263 nm for $n = 1, 2, 3$, individually. The 2PA cross sections increase and the corresponding wavelengths are red-shifts as the condensed aniline extents are from 1 to 3. The origination of 2PA enhancement is understood from state-dependent second hyperpolarizability contributing to the $\langle\delta(\omega)\rangle$ at a given wavelength. As mentioned above, the $\delta(\omega)$ value only depends on the imaginary part of the second hyperpolarizability, $\text{Im}\gamma(-\omega; \omega, \omega, -\omega)$, while the input frequency is given at the vacuum medium. Accordingly, the two-photon states contributing to $\text{Im}\gamma(-\omega; \omega, \omega, -\omega)$ also contribute to $\delta(\omega)$ value. From the simulation of average $\text{Im}\gamma(-\omega; \omega, \omega, -\omega)$ value vs two-photon state at the characteristic wavelength, as shown in Figure 2, we can find that states S_2 and S_{22} for $n = 1$, states S_{14}, S_{15} and S_{19} for $n = 2$, and states S_2 and S_5 for $n = 3$ make the most contributions to $\text{Im}\gamma(-\omega; \omega, \omega, -\omega)$, i.e., to the $\langle\delta(\omega)\rangle$ values at a given wavelength for the title compounds, respectively. An analysis in term of calculated results by the configuration interactions, we find some occupied and empty molecular orbitals involving charge transfer processes. For example, state S_2 of the title compound for $n = 1$ is mostly constructed by the configuration state interaction function $0.7068(MO_{220} \to MO_{222})$, and state S_5 of the title compound for $n = 3$ is mostly constructed by the configuration state interaction function $0.7055(MO_{267} \to MO_{270})$. Figure 3 gives a representation and only shows the orbitals mostly contributing to S_5 of the title compounds for $n = 3$. Accordingly, we can conclude that the charge transfers from the polyaniline to the C_{60} make great contribution to $\langle\delta(\omega)\rangle$ at the resonant wavelength of 679, 1012 and 1263 nm for the title compounds for $n = 1$ to 3, respectively.
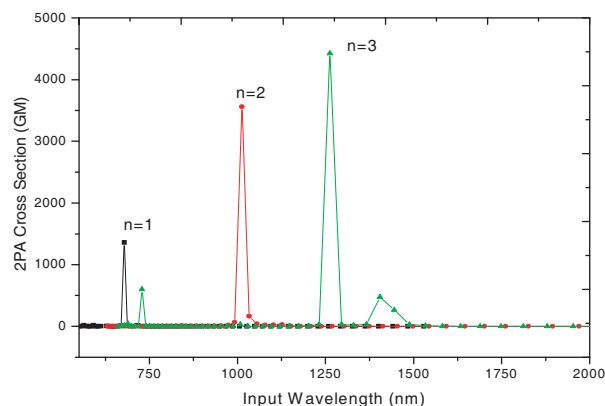

Figure 1: Wavelength-dependent 2PA cross sections.

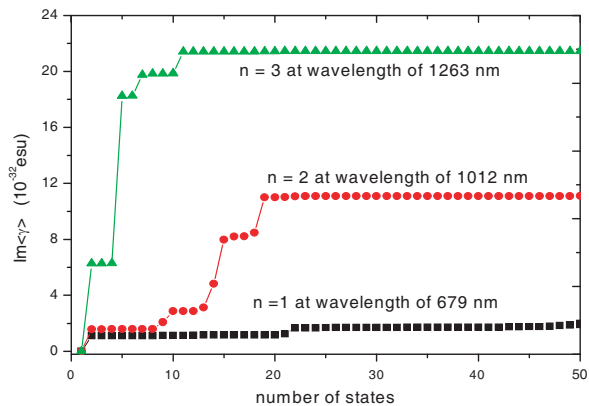Figure 2: State-dependent imaginary part of third-order polarizabilities at given wavelength.

3.2. Three-photon Absorption Spectra

3PA is cubic-dependent on incident-light intensity and it may be superior to 2PA in the penetration depth of the excitation volume. 3PA affords the possibility of using a much longer excitation wavelength. Figure 4 shows the plots of wavelength-dependent 3PA cross sections at average linear

light-polarization for the title compounds ($n = 1$–3), respectively. The peak value of 3PA cross section σ from the circular light polarization is larger than that from linear light polarization. Hereafter, we only consider the 3PA properties of the average linear light-polarization. It is found that the largest 3PA cross section $\langle\sigma\rangle$ values are 58, 1059 and 2701 GM' ($1\text{GM}' = 10^{-80}\ \text{cm}^6\text{s}^2$) at wavelengths of 1294, 1051 and 1381 nm for the title compounds ($n = 1$–3), respectively. These findings tell us the 3PA cross sections are also increasing as the polyaniline condensation is enhancement. The phenomenon can be understood from the state-dependent 3PA cross section at the characteristic wavelength corresponding to the largest 3PA cross section. Figure 5 gives the plots of 3PA cross section $\langle\sigma(\omega)\rangle$ vs state numbers at the given wavelengths of 1294, 1051 and 1381 nm for the title compounds ($n = 1$–3), respectively. It shows that S_{21} and S_{22} for $n = 1$, S_{48} for $n = 2$, and S_{26} for $n = 3$ make the most contributions to $\langle\sigma(\omega)\rangle$ values of the title compounds, respectively. States S_{21} and S_{22} are mainly constructed by the configurations of $0.7006(\text{MO}_{220} \rightarrow \text{MO}_{224})$ and $0.6977(\text{MO}_{220} \rightarrow \text{MO}_{225})$, respectively. The occupied molecular orbital of MO_{220} consists of contributions from the $[\text{C}_{60} > \text{C}_2\text{H}_4\text{NH}_3]$ cage and polyaniline fragment by about 11% and 89%, while the unoccupied molecular orbitals of MO_{224} and MO_{225} both contain contributions from the $[\text{C}_{60} > \text{C}_2\text{H}_4\text{NH}_3]$ by about 100%, respectively. For $n = 2$, state S_{48} is mostly constructed by the configuration of $0.3954(\text{MO}_{241} \rightarrow \text{MO}_{248})$–$0.3256(\text{MO}_{243} \rightarrow \text{MO}_{248})$, in which the occupied molecular orbitals of both MO_{241} and MO_{243} contain contributions from the (polyaniline)$_2$ fragment by about 35% and 57%, respectively, while the unoccupied molecular orbital of MO_{248} contains contribution from the $[\text{C}_{60} > \text{C}_2\text{H}_4\text{NH}_3]$ by about 100%. For $n = 3$, state S_{26} is mostly constructed by the configurations of $0.6718(\text{MO}_{261} \rightarrow \text{MO}_{269})$, and the occupied MO_{261} contains contribution from the $[\text{C}_{60} > \text{C}_2\text{H}_4\text{NH}_3]$ by about 18%, while the unoccupied MO_{269} contains contribution from the $[\text{C}_{60} > \text{C}_2\text{H}_4\text{NH}_3]$ by about 92%. Therefore it can be found that the charge transfers from the fragment (polyaniline)$_n$ to cage $[\text{C}_{60} > \text{C}_2\text{H}_4\text{NH}_3]$ make a great contribution to $\langle\sigma(\omega)\rangle$ at the peak position for the title compounds.

for n = 3, MO$_{267}$ (HOMO − 1)   MO$_{270}$ (LUMO + 1)
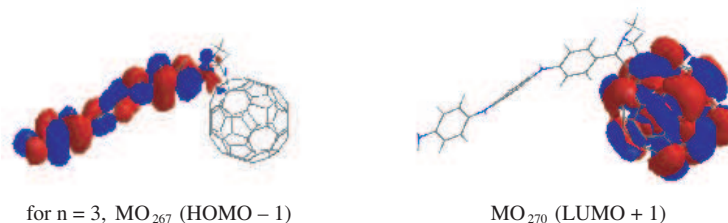
Figure 3: For fullerene derivatives $\text{C}_{60} > \text{C}_2\text{H}_4\text{NH}_3(\text{polyaniline})_n$ ($n = 3$), molecular orbitals involving charge transfer processes.
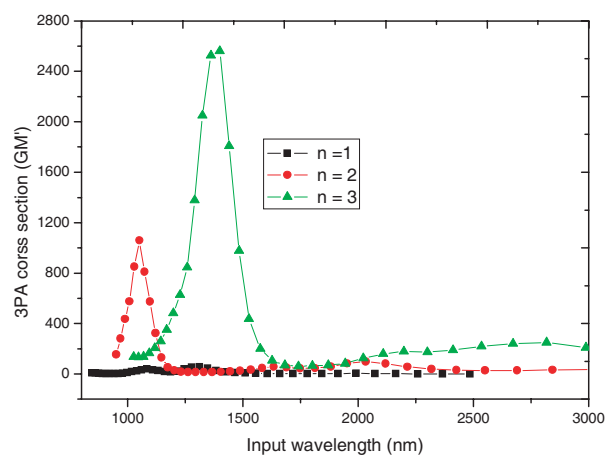

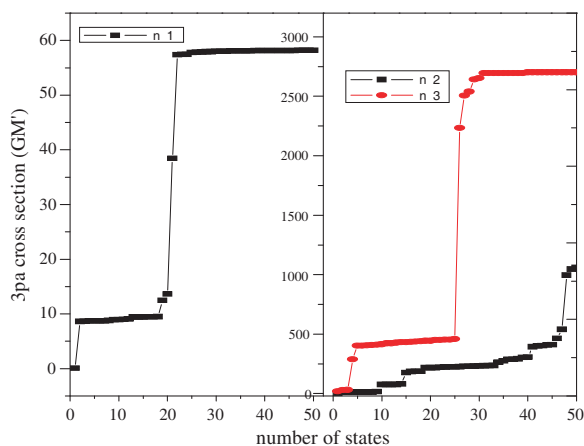Figure 4: Wavelength-dependent 3pa cross sections.

Figure 5: State-dependent 3pa cross sections.

4. CONCLUSION

In summary, TDDFT combined with SOS formula has been employed to model the 2PA and 3PA spectra of $C_{60} > C_2H_4NH_3$(polyaniline)$_n$. The 2PA and 3PA cross sections are increasing as the condensed aniline extents are from 1 to 3 in $C_{60} > C_2H_4NH_3$(polyaniline)$_n$. The electronic origin of 2PA and 3PA has been identified in view of the state-dependent multi-photon absorption cross sections and the molecular orbitals involved in the charge transfer processes. The charge transfers from the polyaniline to the C_{60} derivatives make great contributions to multi-photon absorption spectra for $C_{60} > C_2H_4NH_3$(polyaniline)$_n$ compounds.

REFERENCES

1. Kim, H. M., Y. O. Lee, C. S. Lim, J. S. Kim, and B. R. Cho, "Two-photon absorption properties of alkynyl-conjugated pyrene derivatives," *J. Org. Chem.*, Vol. 73, 5127–5130, 2008.
2. Fu, J., L. A. Padilha, D. J. Hagan, E. W. Van Stryland, O. V. Przhonska, M. V. Bondar, Y. L. Slominsky, and A. D. Kachkovski, "Molecular structure — Two-photon absorption property relations in polymethine dyes," *J. Opt. Soc. Am. B*, Vol. 24, 56–66, 2007.
3. Walker, E., A. Dvornikov, K. Coblentz, S. Esener, and P. Rentzepis, "Toward terabyte two-photon 3D disk," *Optics Express*, Vol. 15, 12264–12275, 2007.
4. Kawata, S. and Y. Kawata, "Three-dimensional optical data storage using photochromic materials," *Chem. Rev.*, Vol. 100, 1777–1788, 2000.
5. Sehoon, K., H. Heng, E. P. Haridas, C. Yiping, and N. P. Paras, "Intraparticle energy transfer and fluorescence photoconversion in nanoparticles: An optical highlighter nanoprobe for two-photon bioimaging," *Chem. Mater.*, Vol. 19, 5650–5656, 2007.
6. Shen, J., W.-D. Cheng, D.-S. Wu, Y.-Z. Lan, F.-F. Li, S.-P. Huang, H. Zhang, and Y.-J. Gong, "Theoretical study of two-photon absorption in donor-acceptor chromophores tetraalkylammonium halide/carbon tetrabromide," *J. Phys. Chem. A*, Vol. 110, 10330–10335, 2006.
7. Kanato, H., K. Takimiya, T. Otsubo, Y. Aso, T. Nakamura, Y. Araki, and O. Ito, "Synthesis and photophysical properties of ferrocene-oligothiophene-fullerene triads," *J. Org. Chem.*, Vol. 69, 7183–7189, 2004.
8. Obara, Y., K. Takimiya, Y. Aso, and T. Otsubo, "Synthesis and photophysical properties of [60]fullerene-oligo(thienylene-ethynylene) dyads," *Tetrahedron Letters*, Vol. 42, 6877–6881, 2001.
9. Cheng, W.-D., D.-S. Wu, X.-D. Li, Y.-Z. Lan, H. Zhang, D.-G. Chen, Y.-J. Gong, Y.-C. Zhang, F.-F. Li, J. Shen, and Z.-G. Kan, "Design of single-walled carbon nanotubes with a large two-photon absorption cross section," *Phys. Rev. B*, Vol. 70, 155401-6, 2004.
10. Lin, N., X. Zhao, J. X. Yang, M. H. Jiang, J. C. Liu, C. K. Wang, W. Shi, J. Meng, and J. Weng, "Theoretical study of one-, two-, and three-photon absorption properties for a series of Y-shaped molecules," *J. Chem. Phys.*, Vol. 124, 024704-9, 2006.
11. McClain, W. M., "Excited state symmetry assignment through polarized 2-photon absorption studies of fluids," *J. Chem. Phys.*, Vol. 55, 2789-8, 1971.

Computational Modeling of Electromagnetically Induced Heating of Magnetic Nanoparticle Materials for Hyperthermic Cancer Treatment

L. Rast and J. G. Harrison

Department of Physics, University of Alabama at Birmingham, Birmingham, Alabama 35294, USA

Abstract— We present work on the computational modeling of electromagnetically induced heating in the hyperthermic treatment of cancer using fluid-dispersed magnetic nanoparticles. Magnetic nanoparticle hyperthermia can be used as a complement to chemotherapy or for direct targeting and destruction of tumors through heat treatment. The ability of nanoscale materials to provide an extremely localized therapeutic effect is a major advantage over traditional methods of treatment. When an AC magnetic field is applied to a ferrofluid, Brownian rotation and Néel relaxation of induced magnetic moments result in power dissipation. In order to achieve appreciable volumetric heating, while maintaining safe values of frequency and magnetic field strength, and to reduce the risk of spot heating of healthy tissue, it is necessary to determine an ideal range of input parameters for the driving magnetic field as well as the complex susceptibility of the ferrofluid. We do this by the coupling of the solution of Maxwell's equations in a model of the tumor and surrounding tissue as input to the solution to the Pennes' Bioheat Equation (PBE). In this study, we solve both sets of equations via the Finite Difference Time Domain (FDTD) method as implemented in the program SEMCAD X (by SPEAG, Schmid & Partner Engineering). We use a multilayer model of the human head made up of perfused dermal and skeletal layers and a grey-matter region surrounding a composite region of tumor tissue and the magnetic nanoparticle fluid. The tumor/ferrofluid composite material properties are represented as mean values of the material properties of both constituents, assuming homogeneity of the region. The AC magnetic excitation of the system (within $100\,\text{kHz}$–$2\,\text{MHz}$ frequency range) is provided by square Helmholtz coils, which provide a uniform magnetic field in the region of interest. The power density derived from the electromagnetic field calculation serves as an input term to the bioheat equation and therefore determines the heating due to the ferrofluid. Results for several variations of input parameters will be presented.

1. INTRODUCTION

The raising of an organism's body temperature to about 5 or more degrees Celsius above its normal value is referred to as hyperthermia. Artificially induced hyperthermia may be used for therapeutic treatments and is especially effective for cancer treatment [1]. A sustained temperature above $42°\text{C}$ can cause cell apoptosis, and a sustained temperature above $45°\text{C}$ causes cell necrosis, resulting in irreversible damage to cell function, or heat-induced sensitization of cells to radiation and some cytotoxic drugs [2, 3].

Hyperthermia has fewer side effects than traditional chemotherapy or radiotherapy. The body naturally uses one type of hyperthermia, a fever, to fight many types of diseases (such as viruses and bacteria) by slowing their proliferation. Magnetic materials under the influence of an AC magnetic field are particularly convenient for hyperthermic applications. Since 1957, when investigations of the applications of magnetic materials for hyperthermia began, a wide variety of magnetic materials, field strengths, and frequencies have been used in these experiments. Human clinical trials have recently begun as a result of the increased safety and efficacy of magnetic nanomaterials for hyperthermia [4].

The subject of this research is the computational modeling of electromagnetic and thermal effects during the hyperthermic treatment of cancer using magnetic nanoparticles. These magnetic nanoparticle systems can be utilized both as drug delivery agents for chemotherapy and for direct targeting and destruction of tumors through heat treatment. This method of treatment would be much less invasive than many current treatment options. Additionally, since these are nanoscale devices, the energy deposition in the cancer cells would be extremely localized. This should cause very minimal damage to surrounding tissue, making these systems superior to traditional hyperthermic treatment. The clinical use of magnetic nanoparticles requires that enough volumetric heating power to destroy tumor cells must be produced, while maintaining safe magnetic field strengths and frequencies. The safe and useful range of magnetic field strengths and frequencies for these applications are considered to be $0 < H < 15\,\text{kA/m}$ and $0.05 < f < 1.2\,\text{MHz}$. Higher

field strengths can lead to various problems such as aggregation of magnetic materials, leading to embolisms. Lower frequencies can cause stimulation of the skeletal or peripheral muscles, or even stimulation of the cardiac muscles and arrhythmias. It has also been established that exposure to fields where the product of $H_0 f$ (where H_0 is the magnitude of the applied magnetic field) is less than $4.85 \times 10^8 \, \mathrm{Am^{-1}s^{-1}}$ is safe for use in humans. This restriction limits tissue heating power and may be relaxed depending on the diameter of the region being treated and the severity of the illness [5].

In addition to the restrictions on these input parameters mentioned in previous sections, one must also consider the delivery of the magnetic nanoparticles to the tumor region. This is of particular concern for the treatment of deep-seated brain tumors, where direct injection of the magnetic material to the tumor site is impractical. In order to cross the blood-brain barrier or blood-brain-tumor barrier, particles must be quite small ($\sim 12\,\mathrm{nm}$ magnetic core size to cross the blood-brain-tumor barrier) [6].

It is therefore necessary to determine a set of ideal input parameters, including χ'', and the effect of brain tumor perfusion rates on heating of the tumor region and possible spot heating in order to aid in design of clinical trails for magnetic nanoparticle hyperthermia in the brain. The effect of various brain tumor perfusion rates will be the focus of this study.

2. THEORY: HEATING MECHANISMS OF MAGNETIC NANOPARTICLE FLUIDS

An electrically conductive body subject to an AC magnetic field will have induced electrical currents that give rise to heating due to the resistance of the material. Smythe found an analytical expression for the time averaged power dissipation of an inductively heated sphere [7]. If it is assumed that the particles are smaller than the domain size, and $\mu = \mu_0$ (we use SI units throughout), the Smythe formula simplifies, so that the series expansion (after multiplication by the number of spheres in a sample, $n = 3\pi/4\phi R^3$, where ϕ is the volume fraction of nanoparticles in the fluid) yields the time-averaged power dissipation per unit volume:

$$P = \frac{\phi\sigma(\pi R B f)^2}{5} \tag{1}$$

(1) Applies for small particles where $f \ll fc$, where

$$f_c = (\pi R^2 \mu_0 \sigma)^{-1} \tag{2}$$

$\sigma \equiv$ electrical conductivity $= 200\,\Omega^{-1}\mathrm{cm}^{-1}$ for magnetite, so $f_c = 5 \times 10^{17}\,\mathrm{Hz}$ for $R = 5\,\mathrm{nm}$, then if $B = 0.06\,\mathrm{T}$ and $\phi \equiv$ volume fraction of magnetic nanoparticles in the fluid $= 0.071$ (representative typical values for clinical hyperthermia with a ferrofluid), $P = 2.5 \times 10^{-10}\,\mathrm{Wcm^{-3}}$. If instead, $\sigma = 9.3 \times 10^4\,\Omega^{-1}\mathrm{cm}^{-1}$ (for iron), $P = 1.2 \times 10^{-7}\,\mathrm{Wcm^{-3}}$. Since appreciable heating occurs due to magnetic nanoparticle fluid hyperthermia, there must be some heating mechanism other than induction for these materials [4].

The heating processes for a magnetic nanoparticle fluid was detailed by Rosensweig based on the Debye model for dielectric dispersion in polar fluids [8]. When an alternating magnetic field is applied to a ferrofluid, the magnetic moments of the magnetic nanoparticles rotate to align with the changing field. As the magnetic field decreases, the magnetic moments rotate back to their equilibrium positions. Rotation of the particles in the viscous medium (called Brownian rotation) and rotation of the magnetic moments (Néel relaxation) both result in power dissipation due to friction. A phase lagging between the applied magnetic field and rotation of the magnetic moments due to friction results in heating. High heating rates are achieved in the regime of particle size where the Néel mechanism does not dominate the relaxation processes. The volumetric heating power (P) of a ferrofluid is given by [8]:

$$P = f\Delta U = \mu_0 \pi \chi'' f H_0^2 \tag{3}$$

where $\chi'' \equiv$ the imaginary component of the magnetic susceptibility function, $f \equiv$ the frequency of the AC magnetic field, and $H_0 \equiv$ the magnitude of the applied magnetic field. Since the change in direction of magnetization lags the magnetic field, (i.e., χ'' is nonzero) work is converted into thermal energy [6]. Heat generation of magnetic nanoparticle fluids has a square dependence on H, leading to greater heating than ferromagnetic or paramagnetic materials at the same magnetic field

strength. Heat generation for magnetic fluids is often expressed in terms of the specific absorption rate (SAR), where

$$\text{SAR} \times \text{particle density} = P \tag{4}$$

At $f = 300\,\text{kHz}$, $H = 14\,\text{kAm}^{-1}$, SAR $= 209\,\text{Wg}^{-1}$ for superparamagnetic ferrofluids. At $f = 300\,\text{kHz}$, $H = 14\,\text{kAm}^{-1}$, SAR $= 75\,\text{Wg}^{-1}$ for ferromagnetic magnetite [4].

The heat flow equation for tissue, including the effects of perfusion of blood and metabolic heating is given by the PBE [4, 8]:

$$\rho c \partial T / \partial t = \nabla \cdot (k \nabla T) + \rho_b c_b w (T - T_b) + Q_m + Q_s \tag{5}$$

where ρ is the tissue density, c is the specific heat for the tissue, k is the thermal conductivity of the tissue, ρ_b is the blood density, c_b is the specific heat for blood, w is the blood perfusion rate, $T_b = $ blood temperature, $Q_m = $ metabolic heating, $Q_s = $ heat added to the system from a source, such as heating due to the ferrofluid in an AC field [8, 9]. In the case of magnetic fluid hyperthermia, the Q_s term is the energy deposition due to heating of the magnetic fluid in an AC magnetic field. This heating power is given by Equation (3).

3. MODEL

In this research, the program Semcad X [10] will be used to solve the Pennes bioheat Equation (5) for a tissue volume, such as the human head with a cancerous region with imbedded magnetic nanoparticles using the Finite Difference Time Domain (FDTD) method. Semcad uses the FDTD solver with volume mesh techniques applied to a 3D model in order to solve Maxwell's equations in PDE form in the region of interest. The electromagnetic results are then used in the thermal simulation to solve the PBE and determine the heating. In order to perform the calculation, the user must provide dielectric, magnetic and thermal properties of all materials, the excitation for the coils (for example, the current or voltage), the AC frequency, and specify a solver (such as the FDTD solver).

The current version of the model uses square Helmholtz coils to provide the AC magnetic field. Square Helmholtz coils are capable of producing a magnetic field more uniform than the more commonly seen circular Helmholtz coils [11].
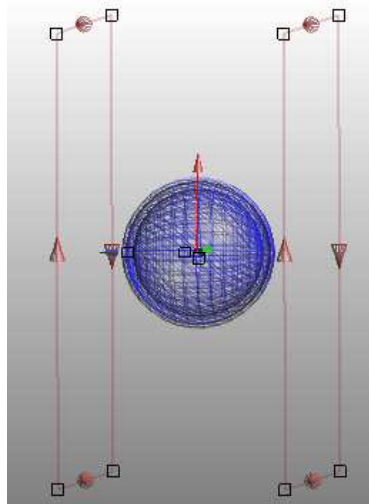

Figure 1: Square Helmholtz coils and multi-tissue layer model of the human head, including a central composite region of tumor tissue and the magnetic nanoparticle fluid. In both examples, the tumor/ferrofluid composite material properties were mean values of both material properties, assuming homogeneity of the region.

4. BENCHMARKING: FIELD UNIFORMITY

5. RESULTS

Results for $f = 1\,\text{MHz}$ are plotted in Figure 3 for temperature vs. time inside the composite tumor region. Material properties and perfusion rates of the tissue were those detailed by Duck [12] and

are similar to those found in the current literature [13]. Conductivities and permittivities for the tissues at the various frequencies were obtained using the publicly available program atsf.exe [14].
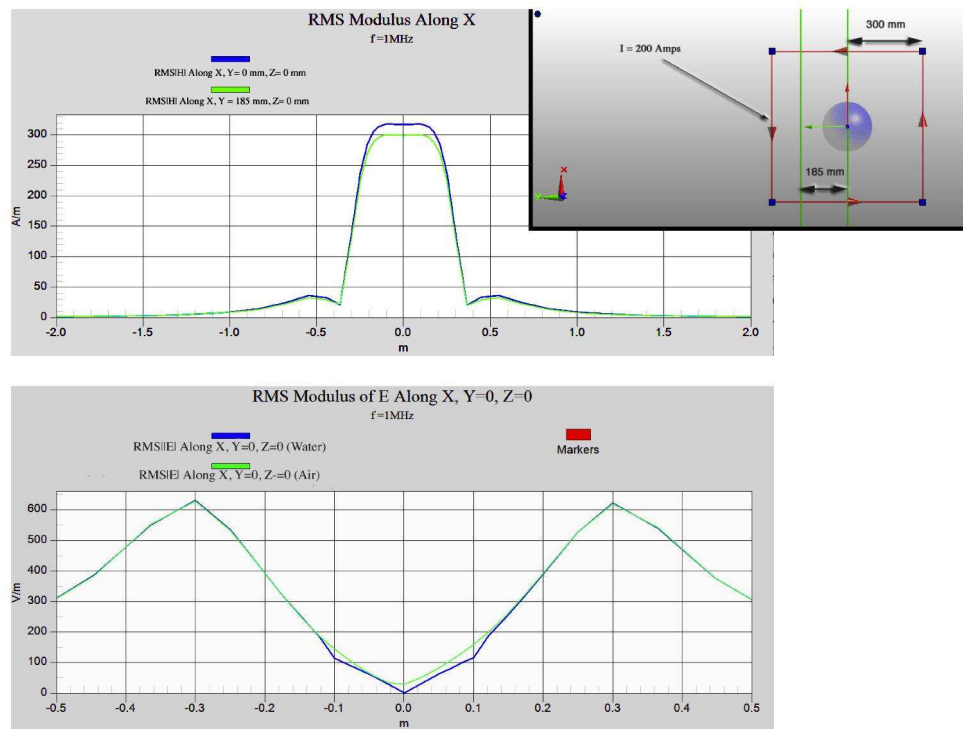

Figure 2: Calculations were first performed in order to verify uniformity of the magnetic and electric field due to the square Helmholtz coils. Above is shown RMS$|H|$ along the x axis (see inset model diagram for coordinate system) at $y = 0$, $z = 0$ (blue line) and $y = 185$ mm, $z = 0$ (green line). It can be seen that RMS$|H|$ is uniform within 6% at 185 mm from the origin along the y axis. Below is shown RMS$|E|$ for the square Helmholtz coils with and without loading of a dielectric sphere (the dielectric is water in this case). A slight decrease in RMS$|E|$ field amplitude is seen in the region of interest. RMS$|E|$ remains uniform in the region of interest. Similar results were obtained for frequencies between 30 kHz and 3 MHz.
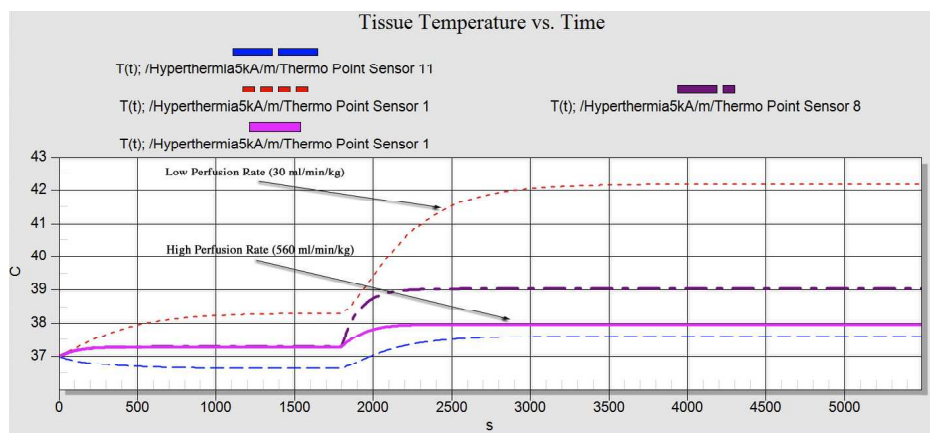
Figure 3: Temperature vs. time for heating at $f = 1$ MHz. The applied field, $H_0 = 5$ kA/m. The imaginary susceptibility of the ferrofluid is set to $\chi'' = 5$, an experimentally realistic value at 1 MHz [15]. Thermal sensors were placed on the boundary, labeled "Sensor 11" (skin layer), inside the healthy grey matter at 4 cm, labeled "Sensor 8", and inside the composite tumor region (at the center in this case), labeled "Sensor 1". In the calculations, the low perfusion rate for the tumor region was 30 ml/min/kg, while the high value was 560 ml/min/kg, the same value as the surrounding grey matter.

An increase in temperature in the composite tumor region for a low perfusion rate (30 ml/min/kg), due to the thermal deposition from the electromagnetic field, is suppressed when the perfusion rate of the tumor region is increased to match that of the surrounding healthy brain tissue.

6. CONCLUSIONS

It was shown (Figure 3) that there exists a marked increase in tissue temperature near the center of the tumor region for a low rate of tumor blood perfusion. For normal perfusion rates within the tumor region, the temperature of the composite tumor/ferrofluid remains nearly that of the skin boundary layer through out the simulation. It is necessary to further investigate this effect for various parameter input values, in order to determine how perfusion rates, i.e., the metabolic response of a patient, influence the thermal damage done to both tumor and healthy tissue in magnetic nanoparticle hyperthermia.

ACKNOWLEDGMENT

REFERENCES

1. Bagaria, H. G., J. L. Phillips, D. E. Nikles, and D. T. Johnson, "Self-regulated magnetic fluid hyperthermia," *AIChE Annual Meeting Conference Proceedings*, 14336–14340, Cincinnati, OH, USA, Oct. 30, 2005.
2. Lv, Y.-G., Z.-S. Deng, and J. Liu, "3-D numerical study on the induced heating effects of embedded micro/nanoparticles on human body subject to external medical electromagnetic field," *IEEE Transactions on Nanobioscience*, Vol. 4, No. 4, 284–292, 2005.
3. Lim, C.-U., Y. Zhang, and M. H. Fox, "Cell cycle dependent apoptosis and cell cycle blocks induced by hyperthermia in HL-60 cells," *Int. J. Hyperther.*, Vol. 22, No. 1, 77–91, 2006.
4. Pankhurst, Q. A., J. Connolly, S. K. Jones, and J. Dobson, "Applications of magnetic nanoparticles in biomedicine," *J. Phys. D.: Appl. Phys.*, Vol. 36, R167–R181, 2003.
5. Atkinson, W. J., I. A. Brezovich, et al., "Usable frequencies in hyperthermia with thermal seeds," *IEEE Transactions on Biomedical Engineering*, Vol. 31, No. 1, 70–75, 1984.
6. Sarin, H., A. S Kanevsky, H. Wu, et al., "Effective transvascular delivery of nanoparticles across the blood-brain tumor barrier into malignant glioma cells," *Journal of Translational Medicine*, Vol. 6, No. 80, 2008.
7. Smythe, W., *Static and Dynamic Electricity*, 375–378, McGraw-Hill, New York, 1968.
8. Rosensweig, R. E., "Heating magnetic fluid with alternating magnetic field," *Journal of Magnetism and Magnetic Materials*, Vol. 252, 370–374, 2002.
9. Pennes, H., "Analysis of tissue and arterial blood temperatures in the resting human forearm," *Journal of Applied Physiology*, Vol. 1, No. 2, 1948.
10. Semcad, X., "Semcad X reference manual," SPEAG — Schmid & Partner Engineering AG, http://www.semcad.com.
11. Kirschvink, J. L., "Uniform magnetic fields and double-wrapped coil systems: Improved techniques for the design of bioelectromagnetic experiments," *Bioelectromagnetics*, Vol. 13, 401–411,1992.
12. Duck, F., *Physical Properties of Tissue: A Comprehensive Reference Book*, 13–29, 329, Academic, San Diego, 1990.
13. Van De Kamer, J. B., et al., "The significance of accurate dielectric tissue data for hyperthermia treatment planning," *Int. J. Hyperther.*, Vol. 17, No. 2, 123–142, 2001.
14. Andreuccetti, D., R. Fossi, and C. Petrucci, *FAC-CNR*, Florence, Italy, 1997–2007.
15. Hergt, R., et al., "Magnetic particle hyperthermia: Nanoparticle magnetism and materials development for cancer therapy," *J. Phys.: Condens. Matter*, Vol. 18, S2919–S2934, 2006.

The Effects of Breast Tissue Heterogeneity on Data-adaptive Beamforming

D. Byrne, M. O'Halloran, E. Jones, and M. Glavin

Bioelectronic Cluster, National Centre for Biomedical Engineering and Science (NCBES)
College of Engineering and Informatics, National University of Ireland Galway
University Road, Galway, Ireland

Abstract— Ultrawideband (UWB) Microwave Imaging is an emerging technology for breast cancer detection which is based on the dielectric contrast between normal and cancerous tissues at microwave frequencies. The breast is illuminated by a UWB pulse and reflected signals are used to determine the presence and location of significant dielectric scatterers, which may be representative of cancerous tissue within the breast. Beamformers are used to spatially focus the reflected signals and to compensate for path dependent attenuation and phase effects. These beamformers can be divided into two distinct categories: Data-Independent and Data-Adaptive beamformers. Data-Independent beamformers typically use an assumed channel model to compensate for path-dependent propagation effects. Conversely, Data-Adaptive beamformers attempt to directly estimate the actual channel based on signals reflected from the breast. Recent studies by Lazebnik et al. indicate that the range of dielectric properties of normal breast tissue is much greater than reported previously. This presents a much more difficult imaging problem due to dielectric heterogeneity. Difficulties encountered by data-independent beamformers in locating tumors within dielectrically heterogeneous breasts have been documented previously. In this paper, the effects of heterogeneity on data-adaptive beamformers is investigated. 2D MRI-derived breast models with varying levels of dielectric heterogeneity are used to evaluate the data-adaptive beamformers.

1. INTRODUCTION

In 2009, there were 1,479,350 new cases of breast cancer documented in the US alone [1], while the estimated mortality rate in Europe was over 1.7 million [2]. Ultrawideband (UWB) radar imaging is a promising emerging imaging modality which illuminates the breast with a sub-nanosecond microwave pulse with a large bandwidth. The dielectric contrast between tissue types, notably malignant and normal tissues, causes scattering reflections within the breast. The corresponding backscatter signals are recorded and time-domain image formation techniques are implemented in order to determine the spatial location of a tumor.

Data-Adaptive (DA) Beamforming [3] describes how signals recorded by an antenna array are manipulated in order to achieve unit gain from a desired direction while suppressing signals of the same frequency from unwanted directions. The signal originating from the desired direction is estimated by varying the weights (or steering vector) applied to the antenna array. Prior to the introduction of the Robust Capon Beamformer (RCB) [4], the performance of the DA beamformer was significantly degraded by errors in the steering vector [5]. The RCB approach was first implemented by Guo et al. [5] for microwave breast imaging. Xie et al. [6] extended the approach for a Multistatic Adaptive Microwave Imaging (MAMI) radar aperture by implementing the RCB algorithm in two stages (referred to as MAMI 1 herein). The MAMI 1 method was extended to incorporate an alternative data-slicing technique (MAMI 2) [7] and both methods were combined under the moniker MAMI C. This paper attempts to examine the methodology of a number of DA algorithms, including RCB, MAMI 1, MAMI 2 and MAMI C. These methods are compared against a Data-Independent (DI) Delay And Sum (DAS) beamformer on two FDTD breast models with varying levels of dielectric heterogeneity. The first model is a dielectric homogeneous breast while the second represents a dielectrically heterogenous phantom, containing both adipose and fibroglandular tissue. Section two details the DA image formation systems, while the numerical breast model model is documented in section three and DA beamforming results are illustrated and discussed in the final section.

2. DATA-ADAPTIVE METHODS

2.1. Robust Capon Beamforming

The DA RCB [8] for the early detection of breast cancer was implemented by Guo et al. [5]. Before the application of the RCB, the signals are appropriately time aligned and compensated (if required)

as in a weighted DAS system [9]. In a system with M antenna array elements and N time samples, the pre-processed input signal is described by:

$$y_i(t) = \hat{\mathbf{a}}(t)s_i(t) + \mathbf{e}_i(t) \qquad 0 \le t \le (N-1) \tag{1}$$

where the scalar $s_i(t)$ denotes the backscattered signal at the ith antenna, $\hat{\mathbf{a}}$ refers to the array steering vector and $\mathbf{e}_i$ is a vector containing unwanted noise and interference. The RCB can be described as:

$$\min_w \mathbf{w}^T \hat{\mathbf{R}} \mathbf{w} \quad \text{subject to} \quad \mathbf{w}^T \hat{\mathbf{a}} = 1 \tag{2}$$

with a solution of

$$\hat{\mathbf{w}}_{\text{RCB}} = \frac{\hat{\mathbf{R}}^{-1} \hat{\mathbf{a}}}{\hat{\mathbf{a}}^T \hat{\mathbf{R}}^{-1} \hat{\mathbf{a}}} \tag{3}$$

With $\hat{\mathbf{w}}_{\text{RCB}}$ containing the beamformer coefficients and the sample covariance matrix $\hat{\mathbf{R}}$ equated as:

$$\hat{\mathbf{R}} = \frac{1}{N} \sum_{t=0}^{N-1} \mathbf{y}(t)\mathbf{y}^T(t) \tag{4}$$

where $\mathbf{y}(t) = [y_1(t), y_2(t), \ldots, y_M]^T$. SCB assumes the steering vector is known a priori however this hypothesis is prone to errors, due to variance in the channel [4, 5]. The RCB operates on the assumption that the true steering vector $\hat{\mathbf{a}}$ is constrained by $||\hat{\mathbf{a}} - \bar{\mathbf{a}}|| \le \epsilon$, where $\bar{\mathbf{a}} = (\mathbf{1}_{M \times 1})$ represents an assumed steering vector and ϵ is a user defined variable describing the error in $\hat{\mathbf{a}}$. The derivation of $\hat{\mathbf{a}}$ is documented in [4].

The energy at a specific voxel ($\mathbf{r} = [x, y, z]$) can then be calculated as:

$$I(\mathbf{r}) = \sum_{t=0}^{N-1} \hat{s}_{\text{RCB}}^2(t) \tag{5}$$

where $\hat{s}_{\text{RCB}}(t) = \mathbf{w}_{\text{RCB}}^T \cdot \mathbf{y}(t)$.

2.2. Multistatic Adaptive Microwave Imaging

The MAMI method by Xie et al. [6] involves a two stage computation of the RCB algorithm. The output of the first stage provides M waveform estimates which correspond to M transmitted signals, and a second stage is required to calculate a scalar waveform output for the complete system. The pre-processed input vector for transmitter i at sample t is described by:

$$\mathbf{y}_i(t) = [y_{i,1}(t), y_{i,2}(t), \ldots, y_{i,M}(t)]^T, \qquad \mathbf{y}_i(t) \in \mathbf{R}^{M \times 1} \tag{6}$$

and the sample covariance matrix $\hat{\mathbf{R}}_Y(t)$ is calculated as:

$$\hat{\mathbf{R}}_Y(t) = \frac{1}{M} \mathbf{Y}(t)\mathbf{Y}^T(t) \tag{7}$$

where

$$\mathbf{Y}(t) = [\mathbf{y}_1(t), \mathbf{y}_2(t), \ldots, \mathbf{y}_M(t)] \qquad \mathbf{Y}(t) \in \mathbf{R}^{M \times M} \tag{8}$$

The modified MAMI weight vector is given by:

$$\hat{\mathbf{w}}_{S1}(t) = \frac{||\hat{\mathbf{a}}(t)||}{\sqrt{M}} \frac{\left(\left[\left(\frac{1}{\lambda} \right) \mathbf{I} + \hat{\mathbf{R}}_Y(t) \right]^{-1} \bar{\mathbf{a}} \right)}{\bar{\mathbf{a}}^T \left[\left(\frac{1}{\lambda} \right) \mathbf{I} + \hat{\mathbf{R}}_Y(t) \right]^{-1} \hat{\mathbf{R}}_Y(t) \left[\left(\frac{1}{\lambda} \right) \mathbf{I} + \hat{\mathbf{R}}_Y(t) \right]^{-1} \bar{\mathbf{a}}} \tag{9}$$

with subscript $S1$ implying Stage I, $\hat{\mathbf{a}}$ and λ are obtained as in [4].

The Stage I waveform estimate is written as: $\hat{\mathbf{s}}(t) = [\hat{\mathbf{w}}_{S1}^T(t)\mathbf{Y}(t)]^T$, a snapshot from an M element waveform estimation vector from which a scalar estimate must be recovered ($\hat{s}(t)$). The

Stage I output ($\hat{s}(t)$) is used as the input argument to the RCB method in Stage II, where the sample covariance matrix is now determined by:

$$\hat{\mathbf{R}}_S = \frac{1}{N} \sum_{t=0}^{N-1} \hat{\mathbf{s}}(t)\hat{\mathbf{s}}^T(t) \tag{10}$$

All other steps are calculated for a single RCB iteration, as in Stage I, resulting in a weighted output: $\hat{s}(t) = \hat{\mathbf{w}}_{S2}(t)\hat{\mathbf{s}}(t)$. The energy at a specific voxel can be calculated using Eq. (5).

The MAMI formulation was extended by Xie et al. [7], sampling the pre-processed input signal as described by Eq. (6) and alternatively by antenna transmitter index, shown below for the ith transmitter:

$$\mathbf{y}_i = [y_i(0), y_i(1), \ldots, y_i(N-1)], \qquad \mathbf{y}_i(t) \in \mathbf{R}^{M \times N} \tag{11}$$

This data slicing method is referred to as MAMI 2, which outperforms the original MAMI method for high Signal to Clutter (S/C) scenarios but is inferior when there is low S/C. The second stage RCB application is identical to MAMI 1. The combined MAMI (MAMI C) et al. [7] approach implements the first stages of MAMI 1 and MAMI 2, concatenating both outputs as the waveform estimates input to the final stage.

3. BREAST MODEL

All backscatter data is obtained using a 2D Finite-Difference Time-Domain (FDTD) model of the breast [10]. The model is that of a naturally flattened breast from a patient lying in the supine position. The adipose/fibroglandular tissue distribution is derived from an anatomically correct breast phantom, similar to the 2D model developed by Li et al. [9]. Figure 1 describes a heterogenous breast where a conformal array consisting of 14 antenna elements, modeled as electric current sources, is located on the surface of the naturally flattened breast (represented by 14 blue dots). Fibroglandular regions appear as white and the adipose tissue as black. A homogenous

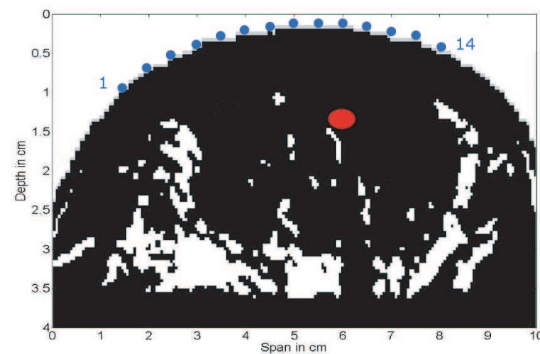| Tissue	ϵ_r	χ_1	σ	t_0
Skin	15.63	8.2	0.82	12.6
Tumor	7	47	0.15	7
Adipose (Low)	3.10	1.70	0.036	14
Fibroglandular (Low)	11	38	0.738	12
Adipose (Medium)	3.20	1.65	0.035	16
Fibroglandular (Medium)	11.2	38	0.738	12
Adipose (High)	4.75	2.95	0.083	15.5
Fibroglandular (High)	15.2	39	0.738	12.75

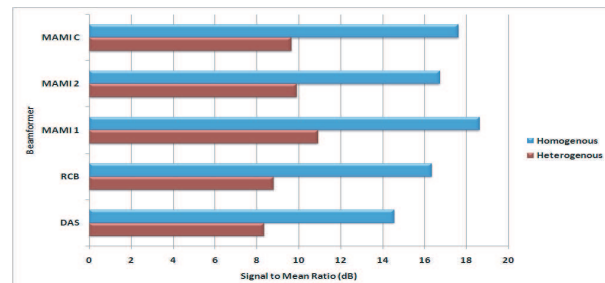Table 1: Debye parameters for the FDTD model.

Figure 1: Antenna configuration of breast model with a tumor located at (1.5 cm, 6 cm).
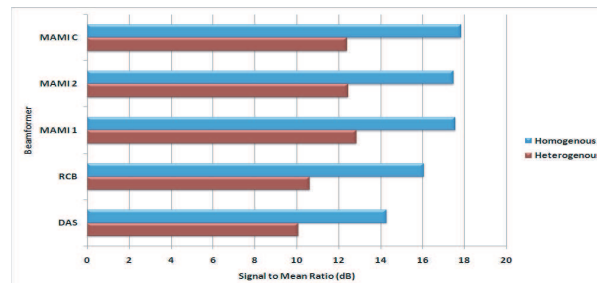
(a)   (b)

Figure 2: Signal to Mean (S/Mn) ratio results for each beamformer. (a) Tumor at (1.5 cm, 3.0 cm). (b) Tumor at (2 cm, 3.0 cm).

dielectric profile is obtained by setting all regions within the breast to a variation of adipose tissue. The model includes a 2 mm layer of skin. A specific location within the FDTD model is defined as follows (*depth*, *span*). For test purposes, a malignant tumor of 10 mm in diameter is located at (1.5 cm, 3 cm) for one test scenario and at (2 cm, 3 cm) in an alternate test scenario. The dispersive properties of breast tissue are incorporated into the FDTD model using a single-pole Debye model [11]. The dielectric properties of adipose and fibroglandular tissue used in the FDTD model are based on a recent study from Lazebnik et al. [12, 13]. The Debye parameters for skin obtained from published data by Gabriel et al. [14], while the Debye parameters for malignant tissue are those used by Bond [15]. The Debye parameters for each type of tissue are shown in Table 1.

The grid resolution, dx, is 0.5 mm and the time step dt is defined as 0.833 ps ($dt = \frac{dx}{2c}$). Each data-adaptive imaging technique is applied to an identical breast imaging scenario and artifact removal system. As a preprocessing step, an ideal artifact removal algorithm, described previously by Bond et al. [15] was used to remove the early stage artifact and reflections from the air skin interface. Before further processing, the signals are downsampled from 1200 GHz (the time step in the FDTD simulation) to 50 GHz. The input signal is a 150-ps differentiated Gaussian pulse, with a center frequency of 7.5 GHz and a -3 dB bandwidth of 9 GHz.
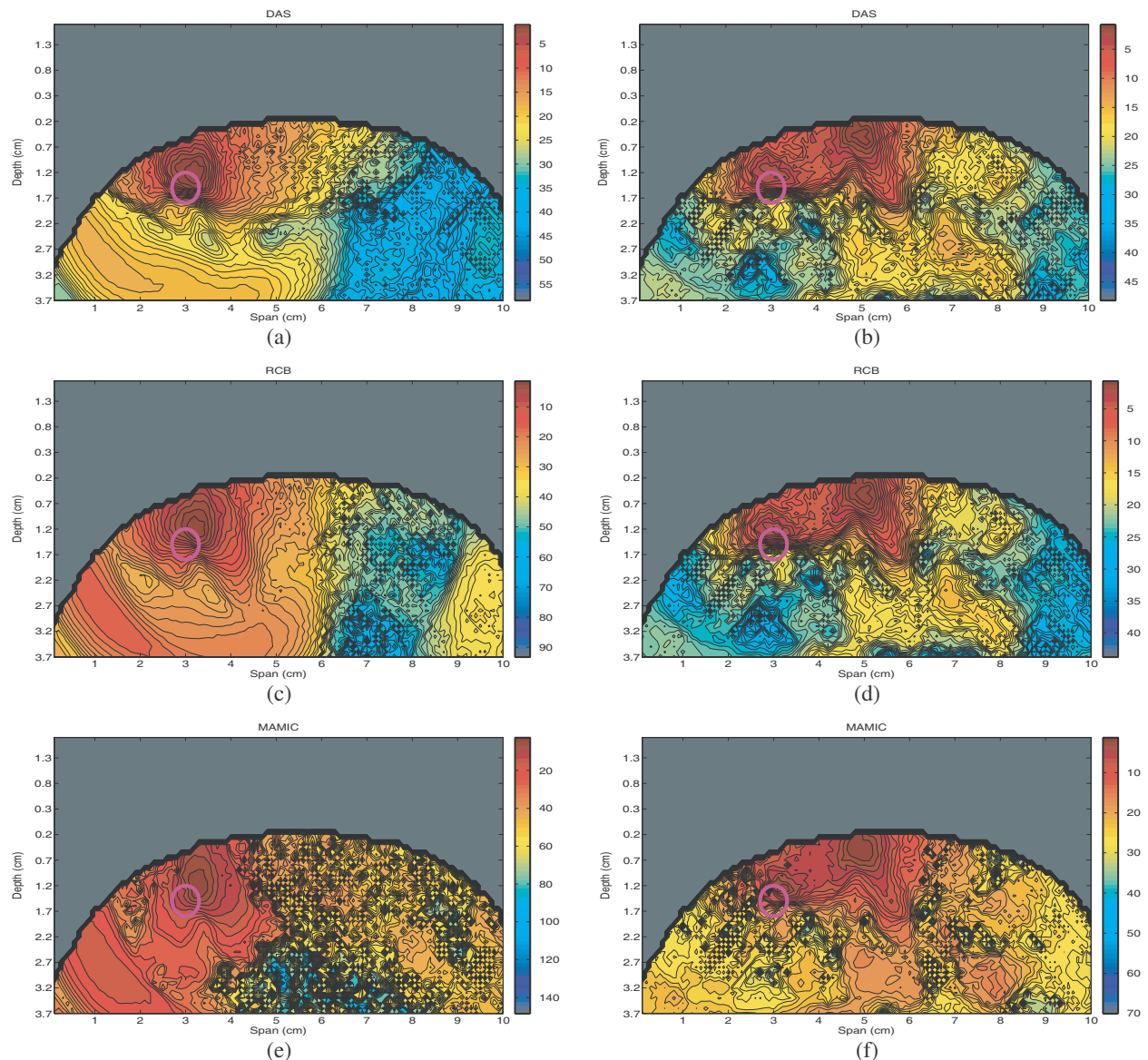

Figure 3: Beamformed Images with a malignant tumor a depth of 1.5 cm and span of 3 cm. (a) Homogenous DAS. (b) Heterogenous DAS. (c) Homogenous RCB. (d) Heterogenous RCB. (e) Homogenous MAMI C. (f) Heterogenous MAMI C.

Table 2: Signal to mean (S/Mn) ratio results.

Beamformer	(Depth, Span) (cm)	S/Mn (dB) Homogenous	S/Mn (dB) Heterogenous
DAS	(1.5, 3.0)	14.2745	10.0562
DAS	(2.0, 3.0)	14.5424	8.3229
RCB	(1.5, 3.0)	16.0488	10.5968
RCB	(2.0, 3.0)	16.3335	8.7940
MAMI 1	(1.5, 3.0)	17.5469	12.8182
MAMI 1	(2.0, 3.0)	18.5988	10.8877
MAMI 2	(1.5, 3.0)	17.4582	12.4146
MAMI 2	(2.0, 3.0)	16.7077	9.8914
MAMI C	(1.5, 3.0)	17.8104	12.3705
MAMI C	(2.0, 3.0)	17.6071	9.6422

4. CONCLUSION

A malignant tumor with $10\,\text{mm}$ diameter is modeled at $(1.5\,\text{cm}, 3\,\text{cm})$ in Figure 3, indicated by a pink ellipse. Resultant tumor scatterers are located 1 to $3\,\text{mm}$ shallower than the modeled location, as its response is assumed as a point scatterer. System performance is evaluated in terms of the Signal to Mean ratio (S/Mn), defined as the ratio of maximum energy at the tumor location to the mean energy of the imaged breast.

S/Mn results are documented in Table 2 for the inclusion of a single tumor located at $(2\,\text{cm}, 3\,\text{cm})$ and at $(1.5\,\text{cm}, 3\,\text{cm})$. A second significant scatterer occurs at $(0.6\,\text{cm}, 5\,\text{cm})$ in the heterogenous breast, due to the presence of dense fibroglandular tissue. In all cases of dielectric heterogeneity, DA methods offer a significant improvement in S/Mn results, as described in Figures 2(a) and 2(b). MAMI 1, MAMI 2 and MAMI C (Figures 3(e) & 3(f)) outperform DAS (Figures 3(a) & 3(b)) in both dielectric profiles. RCB (Figures 3(c) & 3(d)) performs poorly in a heterogeneous breast, highlighting the necessity for a second stage RCB application, but still performs well in a homogenous environment when compared to the other methods.

In this paper, a representative selection of existing DA UWB breast imaging algorithms have been described. Results indicate that the documented DA breast imaging methods outperform DAS for the relatively simple testing scenario examined here. MAMI 1 and MAMI C are the most effective adaptive algorithms for both a homogenous and heterogenous breast phantom. Although previously assumed to offer improved performance in a heterogenous imaging scenario [7], MAMI 2 gives similar results to MAMI 1 in this case. Future work will involve testing the algorithms in an even more difficult imaging scenario, modeling multiple tumors and extending the beamformers to a 3D environment.

ACKNOWLEDGMENT

REFERENCES

1. American Cancer Society, "Cancer facts and figures," Technical Report, Atlanta, 2009.
2. Ferlay, J., P. Autier, M. Boniol, M. Heanue, M. Colombet, and P. Boyle, "Estimates of the cancer incidence and mortality in europe in 2006," *Annals of Oncology*, Vol. 18, 581–592, 2007.
3. Capon, J., "High-resolution frequency-wavenumber spectrum analysis," *Proceedings of the IEEE*, Vol. 57, 1408–1417, 1969.
4. Li, J., P. Stoica, and Z. Wang, "On robust capon beamforming and diagonal loading," *IEEE Transactions on Signal Processing*, Vol. 51, No. 7, 1702–1715, July 2003.
5. Guo, B., Y. Wang, J. Li, P. Stoica, and R. Wu, "Microwave imaging via adaptive beamforming methods for breast cancer detection," *Journal of Electromagnetic Waves and Applications*, Vol. 20, No. 1, 53–63, 2006.
6. Xie, Y., B. Guo, L. Xu, J. Li, and P. Stoica, "Multi-static adaptive microwave imaging for early breast cancer detection," *IEEE Transactions on Biomedical Engineering*, Vol. 53, 1647–1657, 2006.

7. Xie, Y., B. Guo, J. Li, and P. Stoica, "Novel multistatic adaptive microwave imaging methods for early breast cancer detection," *EURASIP Journal on Applied Signal Processing*, Vol. 2006, 1–13, 2006.

8. Li, J. and P. Stoica, *Robust Adaptive Beamforming*, John Wiley & Sons, Hoboken, NJ, 2006.

9. Li, X. and S. C. Hagness, "A confocal microwave imaging algorithm for breast cancer detection," *IEEE Microwave and Wireless Communications Letters*, Vol. 11, 130–132, 2001.

10. Taflove, A. and S. C. Hagness, *Computational Electrodynamics: The Finite-difference Time-domain Method*, Artech House Publishers, June 30, 2005.

11. Kunz, F., K. Leubbers, and R. Hunsberger, "Finite difference time domain recursive convolution for secondorder dispersive materials," *Antennas and Propagation Society International Symposium*, 1992.

12. Lazebnik, M., L. McCartney, D. Popovic, C. B. Watkins, M. J. Lindstrom, J. Harter, S. Sewall, A. Magliocco, J. H. Booske, M. Okoniewski, and S. C. Hagness, "A large-scale study of the ultrawideband microwave dielectric properties of normal breast tissue obtained from reduction surgeries," *Physics in Medicine and Biology*, Vol. 52, 2637–2656, 2007.

13. Lazebnik, M., D. Popovic, L. McCartney, C. B. Watkins, M. J. Lindstrom, J. Harter, S. Sewall, T. Ogilvie, A. Magliocco, T. M. Breslin, W. Temple, D. Mew, J. H. Booske, M. Okoniewski, and S. C. Hagness, "A large-scale study of the ultrawideband microwave dielectric properties of normal, benign and malignant breast tissues obtained from cancer surgeries," *Physics in Medicine and Biology*, Vol. 52, 6093–6115, 2007.

14. Gabriel, S., R. W. Lau, and C. Gabriel, "The dielectric properties of biological tissues: II. Measurements in the frequency range 10 Hz to 20 GHz," *Physics in Medicine and Biology*, Vol. 41, No. 11, 2251–2269, November 1996.

15. Bond, E. J., X. Li, S. C. Hagness, and B. D. Van Veen, "Microwave imaging via space-time beamforming for early detection of breast cancer," *IEEE Transactions on Antennas and Propagation*, 1690–1705, 2003.

Numerical Simulation of Inductive Phase Shift Due a Brain Hematoma

R. Rojas and A. O. Rodriguez

Centro de Investigacion en Imagenologia Medica, Universidad Autonoma Metropolitana Iztapalapa
Av. San Rafael Atlixco 186, Mexico DF 09340, Mexico

Abstract— We show a theoretically electromagnetic induction method to detect the changes of fluid volume into an organic tissue. This method is technique to detect a phase shift through measurements of induced electrical currents due a RF signal. This method was designed for volumetric brain edema monitoring. Circular and planar magnetron coils were evaluated and compared for their ability to detect edema in the brain through volumetric inductive phase shift spectroscopy. The circular coil was considered as a single turn wire and the magnetron surface coil configuration was based on the principle of the cavity magnetron with successive slots. The brain cavity was modeled as an idealized sphere transversely centered with respect to the coils. The volumetric sensitivity to changes in the brain was examined by inserting in the brain cavity a spherical edema/haematoma. Spectra of inductive phase shift induced in a second circular or magnetron receiver coils were estimated between frequencies from 100 kHz to 50 MHz. Phase shift shows sensitivity to the presence of the edema/haematoma increased with frequency. The use of a planar magnetron as the receiver coil produced a substantial increase in sensitivity, in particular at higher frequency of 50 MHz.

1. INTRODUCTION

Trauma to the head may results in the accumulation of liquids or blood in certain region of the brain. Edema is a medical condition in which the relative amount of liquid in tissue or organs increases. Haematoma is a pathological condition in which accumulation of blood occurs in a specific region. The characteristic of brain edema/haematoma is that it develops in a delayed and gradually progressive fashion after a head trauma or event has occurred, over a period of hours or days, and is a cause of substantial mortality [1]. Detection of edema/haematoma in the brain is essential for assessment of the medical condition and treatment. Because the complex electrical properties of edema/haematoma are substantially different from a hose of normal tissue, various measurements of electrical properties of the brain where proposed to non-invasive detect the changes in there [2–6].

In order to optimize the detection technology we have explored, in a recent study, the possible use of a magnetron coil [7] on the inductive volumetric phase shift of the brain in the presence of a edema/haematoma. We have compared the sensitivity of a magnetron coil with that of a circular coil. The results have shown that the magnetron coil has a somewhat greater sensitivity to the detection of a edema/haematoma than the circular coil. This study reveals that the location of the edema/haematoma has a substantial effect on the sensitivity of the magnetron and circular coils. Furthermore, we find that at certain different frequencies the various locations of the edema/haematoma produce no volumetric phase shift.

2. METHOD

2.1. Time-harmonic, Quasi-static Magnetic and Electric Field

In the time-harmonic case, we omit the displacement currents in Ampere's equation [8]:

$$\nabla \times \vec{H} - \frac{\partial \vec{D}}{\partial t} = \vec{J} \quad \text{(Maxwell-Ampere's law)} \tag{1}$$

where $\vec{H}$ is the magnetic field intensity (A/m), $\vec{D}$ is the electric displacement (C/m^2), $\vec{J}$ is the electric current density (A/m^2) and t is the time. Using the current density in a conductive medium through the Lorentz force in Eq. (1), we obtain:

$$\nabla \times \vec{H} - \frac{\partial \vec{D}}{\partial t} = \sigma(\vec{E} + \vec{v} \times \vec{B}) + \vec{J}^e \tag{2}$$

where σ is the medium conductivity (S/m), $\vec{E}$ is the electric field intensity (V/m), $\vec{v}$ is the relative velocity, $\vec{B}$ is the magnetic field density (T), and $\vec{J}^e$ is a current density generated externally. Expressing the magnetic and electric fields in terms of the magnetic vector potential ($\vec{A}$) and the electric scalar potential (V):

$$\vec{B} = \nabla \times \vec{A} \tag{3}$$

$$\vec{E} = -\nabla V - \frac{\partial \vec{A}}{\partial t} \tag{4}$$

The complete constitutive equation used for the magnetic and electric fields are:

$$\vec{B} = \mu \left(\vec{H} + \vec{M} \right) \tag{5}$$

$$\vec{D} = \varepsilon \vec{E} + \vec{P} \tag{6}$$

where $\vec{M}$ is the magnetization vector (A/m), $\vec{P}$ is the electric vector polarization (C/m^2), μ is the medium permeability (H/m) and ε is the medium permittivity (F/m). Using the Eqs. (5) and (6) in Eq. (2) we obtain:

$$\nabla \times \left(\mu^{-1} \vec{B} - \vec{M} \right) - \frac{\partial \left(\varepsilon \vec{E} + \vec{P} \right)}{\partial t} = \sigma \left(\vec{E} + \vec{v} \times \vec{B} \right) + \vec{J}^e \tag{7}$$

Using Eqs. (3) and (4) in Eq. (7):

$$\nabla \times \left(\mu^{-1} \nabla \times \vec{A} - \vec{M} \right) - \frac{\partial \left(\varepsilon \left(-\nabla V - \frac{\partial \vec{A}}{\partial t} \right) + \vec{P} \right)}{\partial t} = \sigma \left(-\nabla V - \frac{\partial \vec{A}}{\partial t} + \vec{v} \times \nabla \times \vec{A} \right) + \vec{J}^e \tag{8}$$

In Eq. (8), we have considered a non-moving geometry ($\vec{v} = 0$) and no external electric potential gradient ($\nabla V = 0$) on the border of the brain sphere, to simplify initial conditions in symmetry boundaries. In addition, we have assumed that the border of the sphere surrounding the system is grounded, then:

$$\sigma \frac{\partial \vec{A}}{\partial t} + \varepsilon \frac{\partial^2 \vec{A}}{\partial t^2} + \nabla \times \left(\mu^{-1} \nabla \times \vec{A} \right) = \vec{J}^e \tag{9}$$

A time-harmonic function using Euler's formulation can be written as:

$$\vec{A}(\vec{r}, t) = \mathrm{Re} \left[\vec{A}(\vec{r}) e^{j(\omega t + \phi)} \right] = \mathrm{Re} \left[\vec{A}(\vec{r}) e^{j\phi} e^{j\omega t} \right] \tag{10}$$

where ω is the angular frequency, ϕ is the phase angle, and $\vec{A}(\vec{r}) e^{j\phi}$ is the phasor. Using this function in Eq. (9) we obtain:

$$\left(j\omega\sigma - \omega^2 \varepsilon \right) \vec{A} + \nabla \times \left(\mu^{-1} \nabla \times \vec{A} \right) = \vec{J}^e \tag{11}$$

2.2. Inductive Phase Shift Estimation

Following the proposed spherical model and coil configurations (Fig. 1), consider an alternating current $I e^{j\omega t}$ flowing trough the inductor coil, according to Hugo and Burk [9], the presence of a spherical conductive sample (the brain cavity) produces changes in the receiver coil impedance as a function of the electrical properties of the sample (σ, ε). In this work an arbitrary edema/haematoma represents volumetric changes in those properties.

The impedance of the receiver coil could be characterized by complex voltage $V(\omega)$ and current $I(\omega)$ defined as:

$$Z(\omega) = R(\omega) + jX(\omega) = \frac{V(\omega)}{I(\omega)} \tag{12}$$

where $R(\omega)$ and $X(\omega)$ are the coil resistance and reactance respectively. Thus, the induced receiver coil current could be separated in their complex coefficients [10] given by:

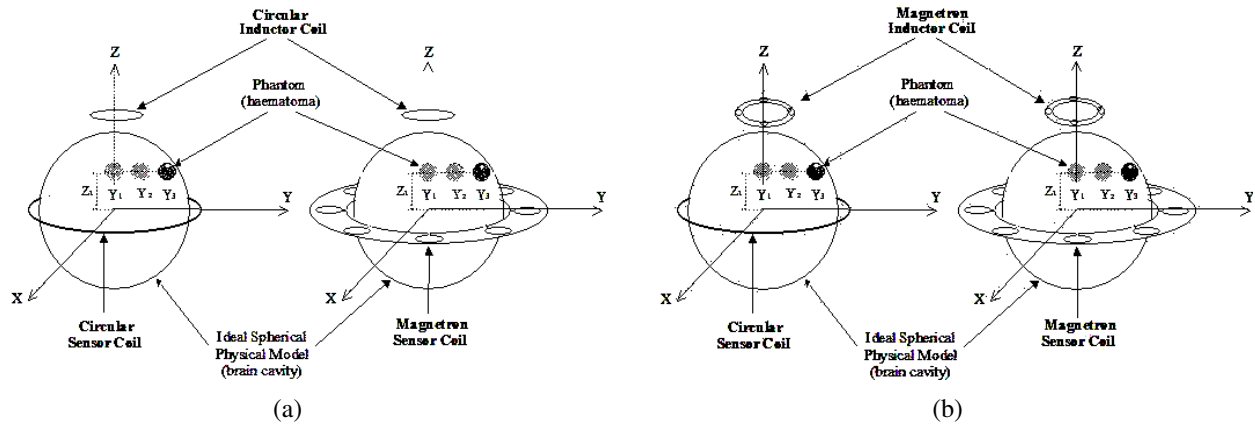$$I(t) = I(\cos(\omega t + \phi) + j \sin(\omega t + \phi)) \tag{13}$$

Figure 1: (a) Models with single circular inductor coil. (b) Models with magnetron inductor coil.

where its argument could be obtained by:

$$\omega t + \phi = \tan^{-1}\frac{\mathrm{Im}I(t)}{\mathrm{Re}I(t)} = \tan^{-1}\frac{\sin(\omega t + \phi)}{\cos(\omega t + \phi)} \tag{14}$$

We define a basal induced current argument in the receiver coil as $(\omega t + \phi)$ and the argument influenced by the edema/haematoma presence as $(\omega t + \phi_1)$. To estimate the inductive phase shift $(\Delta\phi)$ we can use the argument differences at specific frequency and time according to the following expression:

$$\Delta\phi = (\omega t + \phi_1) - (\omega t + \phi) = \phi_1 - \phi \tag{15}$$

3. SIMULATION METHOD

We use a commercial software (COMSOL MULTIPHYSICS) [11], which uses the Finite Element Method to solve Eq. (11) for the magnetic vector potential. We simulate the $\vec{B}$ for every circular/magnetron coil configuration by alternating currents in the inductor coils at the frequencies 0.1, 1, 10 and 50 MHz.

The simulation follows the next geometrical and electrical considerations: the brain cavity model is a sphere of radius 13 cm, the haematoma is a sphere of radius 2.6 cm in arbitrary position inside the brain cavity. The electrical conductivity and permitivity values for brain and blood were considered isotropic and were taken from Gabriel et al. [12]. The circular and magnetron coils were designed by copper electrical properties, thickness 0.4 cm and radii as follows: circular-inductor; inner and external radii of 14 and 14.5 cm respectively, magnetron-inductor; inner and external radii of 14 and 18.6 cm respectively with eight successive slots with radii 1.86 cm, circular-receiver; inner and external radii of 1.4 and 1.45 cm respectively, magnetron-receiver; inner and external radii of 1.9 and 2.5 cm respectively with eight successive slots with radii 0.3 cm.

4. RESULTS AND DISCUSSION

Figure 2 shows the $\vec{B}$ lines simulated at 1 MHz for the proposed circular/magnetron coil configurations. Spatial distribution differences as a function of the inductor/sensor elements are evident. Circular-receivers (Figs. 2(a) and (b)) shows $\vec{B}$ irregularly distributed. Magnetron receivers (Figs. 2(c) and (d)) shows high $\vec{B}$ uniformly distributed. Fig. 3 shows spectra of inductive phase shift in the bandwidth of 100 kHz to 50 MHz. Data are homogenized respect to basal values. The sensitivity increases as a function of frequency and is significantly higher for the magnetron-receiver configurations.

Magnetron coils as elements with high efficient factor produced high magnetic flux densities uniformly distributed in the spherical sample [10], however; spatial distribution differences observed in Fig. 2 correspond to the coil configurations evaluated. Those differences suggest specific mutual inductances associated to the inductor and receiver geometrical properties, is expected that the high magnetic flux density observed for the magnetron-receiver configurations reflect its high inductive phase shift values estimated in Fig. 3. The sensitivity increase as a function of frequency is explained by the effect of water content at high frequencies [13]; where the increase in the conductivity arises from the rotational relaxation of the water dipoles.
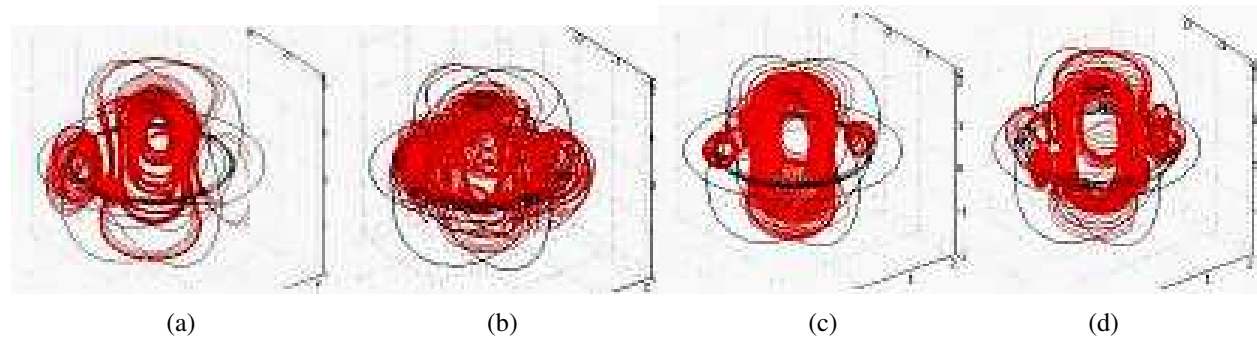
(a)   (b)   (c)   (d)

Figure 2: Spatial distribution of magnetic densities simulated at 1 MHz. Four circular/magnetron coil configurations as inductor/sensor elements are shown: (a) circular-inductor/circular-receiver, (b) magnetron-inductor/circular-receiver, (c) circular-inductor/magnetron-receiver and (d) magnetron-inductor/magnetron receiver.
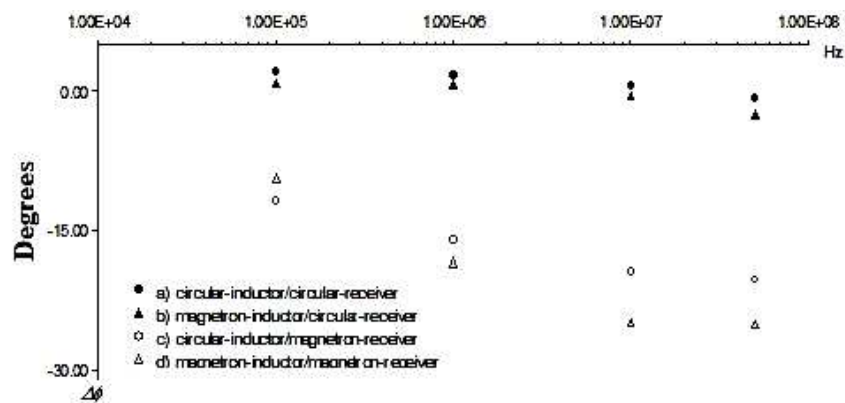

Figure 3: Spectra of inductive phase shift at the frequencies 0.1, 1, 10 and 50 MHz.

5. CONCLUSIONS

The computational simulation shows that measuring the relative spectroscopic distribution of induction phase shift has the potential for being a simple method to produce a robust means for non-contact detection of occurrence of edema/haematoma in the bulk of brain. The circular/magnetron coils evaluated in this study suggest that a system with a magnetron receiver is a feasible configuration for an easy and practical application.

REFERENCES

1. Ayata, C. and A. H. Ropper, "Ischaemic brain oedema," *Journal of Clinical Neuroscience*, Vol. 9, No. 2, 113–124, 2002.
2. Kyle, A. H., C. T. Chan, and A. I. Minchinton, "Characterization of three-dimensional tissue cultures using electrical impedance spectroscopy," *Biophys. J.*, Vol. 76, 2640–2648, 1999.
3. Zeiback, A. and N. H. Saunders, "A feasibility study of in vivo electromagnetic imaging," *Phys. Med. Biol.*, Vol. 38, 151–160, 1993.
4. Korzhenevsky, A. V. and V. A. Cherepenin, "Magnetic induction tomography," *Comm. J. Technol. Electron.*, Vol. 42, No. 4, 469–474, 1997.
5. Korzhenevsky, A. V. and V. A. Cherepenin, "Progress in realization of magnetic induction tomography," *Ann. NY. Acad. Sci.*, Vol. 873, 346–352, 1999.
6. Griffiths, H., "Magnetic induction tomography," *Meas. Sci. Technol.*, Vol. 12, 1126–1131, 2001.
7. González, C. A., "Magnetron surface coil for brain MR Imaging," *Arch. of Med. Res.*, Vol. 37, 804–807, 2006.
8. Purcell, E. M., *Electricity and Magnetism*, Berkeley Physics Course, California, 1984.
9. Hugo, G. R. and S. K. Burke, "Impedance changes in a coil due to a nearby small conducting sphere," *J. Phys. D: Appl. Phys.*, Vol. 21, 33–38, 1988.

10. Taghjian, A. D. and S. R. Best, "Impedance bandwidth, and Q of antennas," *IEEE Trans. on Anten. and Prop.*, Vol. 53, No. 4, 1298–1325, 2005.

11. COMSOL, *Electromagnetic Module User's Guide*, COMSOL, Inc., 2005.

12. Gabriel, S., R. W. Lau, and C. Gabriel, "The dielectric properties of biological tissues: III parametric models for the dielectric spectrum of tissues," *Phys. Med. Biol.*, Vol. 41, 2271–2293, 1996.

13. Schepps, J. L. and K. R. Foster, "The UHF and microwave dielectric properties of normal and tumor tissues: Variations in dielectric properties with tissue water content," *Phys. Med. Biol.*, Vol. 25, No. 6, 1149–1159, 1980.